Iowa Research Online
The University of Iowa's Institutional Repository

University of Iowa
Iowa Research Online

Theses and Dissertations

Spring 2010

A LES study on gravity currents propagating over roughness elements

Talia Ekin Tokyay
University of Iowa

Follow this and additional works at: https://ir.uiowa.edu/etd

Part of the Civil and Environmental Engineering Commons

Copyright © 2010 Talia Ekin Tokyay

This dissertation is available at Iowa Research Online: https://ir.uiowa.edu/etd/610

Recommended Citation

Tokyay, Talia Ekin. "A LES study on gravity currents propagating over roughness elements." PhD (Doctor of Philosophy) thesis, University of Iowa, 2010.
https://doi.org/10.17077/etd.4d5mck91

Follow this and additional works at: https://ir.uiowa.edu/etd

Part of the Civil and Environmental Engineering Commons

A LES STUDY ON GRAVITY CURRENTS PROPAGATING OVER ROUGHNESS ELEMENTS

by

Talia Ekin Tokyay

An Abstract

Of a thesis submitted in partial fulfillment
of the requirements for the Doctor of
Philosophy degree in Civil and Environmental Engineering
in the Graduate College of
The University of Iowa

May 2010

Thesis Supervisor: Associate Professor George S. Constantinescu

ABSTRACT

Predicting the evolution of turbulent gravity currents is of great interest in many areas of geophysics and engineering, in particular due to their impact on the environment. In most practical applications in river, coastal and ocean engineering, gravity currents propagate over loose surfaces containing large scale bedforms (e.g., dunes). In others, arrays of obstacles (e.g., ribs) are often used as protective measures on hilly terrains to stop or slow down gravity currents in the form of powder-snow avalanches. To predict the capacity of a turbulent gravity current propagating over a loose bed to entrain, carry, and deposit sediment requires a detailed understanding of its structure and the role played by the large-scale instabilities present in the flow.

The present study uses high-resolution Large Eddy Simulation to study the physics of high Reynolds number compositional Boussinesq gravity currents with large and small volume of release in lock-exchange configurations and their dynamic effects on various obstacles (e.g., bedforms, flow retarding obstacles, submerged dams that are used to control sediment deposition in reservoirs). The study shows that gravity currents propagating over large-scale roughness elements reach a turbulent drag-dominated regime in which the front velocity decays proportional to $t^{-1/2}$, similar to the case of gravity currents propagating within a porous medium. Though the establishment of a regime in which the flow evolution is mainly determined by the balance between the turbulent drag and the buoyancy force driving the flow was expected, the fact that the law of decay of the front velocity with time is identical for gravity currents propagating over roughness elements and in a porous medium of uniform porosity is not obvious.

The simulations provide detailed information on the temporal evolutions of the front velocity, energy balance, sediment entrainment capacity and the flow instabilities, and of the distributions of the density, velocity, local dissipation rate and bed shear stresses at different stages of the propagation of the gravity current. The study investigates of the effect of the shape and relative size of the obstacles, with respect to the current height, on the structure of the current and on the differences with the simpler, but much more widely studied case of a gravity current propagating over a flat smooth surface. For example, the simulation results are used to explain why gravity currents propagating over dunes have a much larger capacity to entrain sediment than gravity currents propagating over ribs of the same height and with similar spacing.

Accurate estimation of the effects of the impact of a gravity current on structures (e.g., submerged dams in reservoirs, snow retarding devices) situated along its path is very important from an engineering point of view. The simulations of gravity currents propagating past arrays of ribs or isolated dams are used to estimate the characteristic times and magnitudes of the hydrodynamic impact forces on these obstacles. This information is crucial for the proper design of these structures. The study shows the critical role played by flow disturbances (e.g., backward propagating hydraulic jumps) that form as a result of the interaction between the current and the large-scale obstacles. Finally, the study investigates scale effects between the Reynolds numbers at which most experimental investigations of gravity currents are conducted and Reynolds numbers at field scale.

Abstract Approved: ________________________________
Thesis Supervisor

____
Title and Department

____
Date

A LES STUDY ON GRAVITY CURRENTS PROPAGATING OVER ROUGHNESS ELEMENTS

by

Talia Ekin Tokyay

A thesis submitted in partial fulfillment
of the requirements for the Doctor of
Philosophy degree in Civil and Environmental Engineering
in the Graduate College of
The University of Iowa

May 2010

Thesis Supervisor: Associate Professor George S. Constantinescu

Graduate College
The University of Iowa
Iowa City, Iowa

CERTIFICATE OF APPROVAL

PH.D. THESIS

This is to certify that the Ph.D. thesis of

Talia Ekin Tokyay

has been approved by the Examining Committee
for the thesis requirement for the Doctor of Philosophy
degree in Civil and Environmental Engineering at the May 2010 graduation.

Thesis Committee: ______________________________
George S. Constantinescu, Thesis Supervisor

____
Jacob Odgaard

____
Marian Muste

____
Albert Ratner

____
James Buchholz

To My Mom, My Dad and Sumit

ACKNOWLEDGMENTS

I would like to thank my adviser for all his help and effort in putting together this dissertation. He also helped me gain insight on so many different applications of CFD by providing the opportunity to work on several projects with him for seven years. I am also thankful to my committee members for giving me their precious time and their significant feedback which improved my dissertation and my presentation skills.

Above all I would like to thank my family in Turkey and in India for being there for me in tough times, my mom, my biggest support and mentor, who always had time for me and answered all of my questions on hydraulics and everything else, my father who always gives wonderful feedback and cheers me up, and who taught me to love my job, and to my dearest husband, who has the resilience to listen to me on the phone for several hours when I need someone to hear me, and to all of my friends in Iowa City who were great supports in every sense.

ABSTRACT

Predicting the evolution of turbulent gravity currents is of great interest in many areas of geophysics and engineering, in particular due to their impact on the environment. In most practical applications in river, coastal and ocean engineering, gravity currents propagate over loose surfaces containing large scale bedforms (e.g., dunes). In others, arrays of obstacles (e.g., ribs) are often used as protective measures on hilly terrains to stop or slow down gravity currents in the form of powder-snow avalanches. To predict the capacity of a turbulent gravity current propagating over a loose bed to entrain, carry, and deposit sediment requires a detailed understanding of its structure and the role played by the large-scale instabilities present in the flow.

The present study uses high-resolution Large Eddy Simulation to study the physics of high Reynolds number compositional Boussinesq gravity currents with large and small volume of release in lock-exchange configurations and their dynamic effects on various obstacles (e.g., bedforms, flow retarding obstacles, submerged dams that are used to control sediment deposition in reservoirs). The study shows that gravity currents propagating over large-scale roughness elements reach a turbulent drag-dominated regime in which the front velocity decays proportional to $t^{-1/2}$, similar to the case of gravity currents propagating within a porous medium. Though the establishment of a regime in which the flow evolution is mainly determined by the balance between the turbulent drag and the buoyancy force driving the flow was expected, the fact that the law of decay of the front velocity with time is identical for gravity currents propagating over roughness elements and in a porous medium of uniform porosity is not obvious.

The simulations provide detailed information on the temporal evolutions of the front velocity, energy balance, sediment entrainment capacity and the flow instabilities, and of the distributions of the density, velocity, local dissipation rate and bed

shear stresses at different stages of the propagation of the gravity current. The study investigates of the effect of the shape and relative size of the obstacles, with respect to the current height, on the structure of the current and on the differences with the simpler, but much more widely studied case of a gravity current propagating over a flat smooth surface. For example, the simulation results are used to explain why gravity currents propagating over dunes have a much larger capacity to entrain sediment than gravity currents propagating over ribs of the same height and with similar spacing.

Accurate estimation of the effects of the impact of a gravity current on structures (e.g., submerged dams in reservoirs, snow retarding devices) situated along its path is very important from an engineering point of view. The simulations of gravity currents propagating past arrays of ribs or isolated dams are used to estimate the characteristic times and magnitudes of the hydrodynamic impact forces on these obstacles. This information is crucial for the proper design of these structures. The study shows the critical role played by flow disturbances (e.g., backward propagating hydraulic jumps) that form as a result of the interaction between the current and the large-scale obstacles. Finally, the study investigates scale effects between the Reynolds numbers at which most experimental investigations of gravity currents are conducted and Reynolds numbers at field scale.

TABLE OF CONTENTS

LIST OF TABLES viii

LIST OF FIGURES x

CHAPTER 1 INTRODUCTION 1
  1.1 Background 1
  1.2 The Role of High-Resolution Eddy-Resolving Numerical Simulations 5
  1.3 Description of Problems 8
    1.3.1 Gravity currents with a large volume of release propagating over an array of obstacles 10
    1.3.2 Gravity currents with a small volume of release propagating over an array of obstacles 13
    1.3.3 Gravity currents propagating over an isolated obstacle (submerged dam) 14
  1.3 Research Objectives 18

CHAPTER 2 LITERATURE REVIEW 25
  2.1 Theoretical and Experimental Studies 25
    2.1.1 Gravity currents propagating over a flat surface 25
    2.1.2 Interaction of gravity currents with obstacles 29
    2.1.3 Gravity currents propagating over rough surfaces 33
  2.2 Numerical Studies 36
    2.2.1 Integral and RANS Models 36
    2.2.2 DNS and LES studies of gravity currents propagating over flat smooth surfaces 37
    2.2.3 Studies of interaction of gravity currents with obstacles or deformed bottom topography 42

CHAPTER 3 NUMERICAL METHOD 54
  3.1 Description of Governing Equations, Subgrid-Scale Model and Numerical Algorithms 54
  3.2 Previous Validation Studies 57
  3.3 Grid Dependency and Schmidt Number Sensitivity Study 58

CHAPTER 4 GRAVITY CURRENTS WITH A LARGE VOLUME OF RELEASE (R<<1) PROPAGATING OVER AN ARRAY OF 2-D OBSTACLES 63
  4.1 Description of Test Cases 63
  4.2 Structure of the gravity current in the head and dissipative wake regions 66
  4.3 Front velocity 71
  4.4 Structure of the tail of the gravity current 75
  4.5 Analysis of the time variation of the mass fluxes and mass balance for the heavier lock fluid 78
  4.6 Mean flow and turbulence structure in between two successive obstacles situated at a large distance behind the front 81
    4.6.1. Analysis of the 2-D flow and turbulence structure 82
    4.6.2. Analysis of the 1-D flow and turbulence structure 89
  4.7 Drag force on the ribs 99

4.8 Energy budget and dissipation rate 110
4.9. Total dissipation rate 115
4.10 Near-wall flow structure.. 121
4.11 Bed friction velocity 125
4.12 Sediment entrainment capacity... 132
4.13 The case of a gravity current propagating over an array of closely-spaced 2D ribs 140
4.14 Summary and Conclusions 148

CHAPTER 5 GRAVITY CURRENTS WITH VOLUME OF RELEASE (R=O(1)) PROPAGATING OVER AN ARRAY OF 2-D OBSTACLES................. 218
5.1 Description of Test Cases.. 218
5.2 Structure of the gravity current with a small volume of release 222
5.3 Interaction of the head region with the bottom-mounted obstacles....... 236
5.4 Front velocity... 242
5.5 Dynamics of flow disturbances propagating within the gravity current 247
5.6 Analysis of the time variation of the mass fluxes and mass balance for the heavier lock fluid 252
5.7 Drag force on the ribs 258
5.8 Energy budget and dissipation rate 263
5.9 Bed friction velocity 269
5.10 Sediment entrainment capacity... 282
5.11 Summary and Conclusions 288

CHAPTER 6 GRAVITY CURRENT-SUBMERGED DAM INTERACTION 370
6.1 Introduction 370
6.2 Description of Test Cases... 375
6.3 Flow regimes 380
6.4 Comparison of the main flow parameters describing the flow past the obstacle among the test cases 383
6.5 Validation and comparison with predictions given by theoretical models 391
6.6 Analysis of the temporal changes in the structure of the gravity current as a result of its interaction with the obstacle................................ 400
6.7 Drag force on the obstacle.. 412
6.8 Mean flow and turbulence statistics around the obstacle during the quasi-steady state regimes... 422
6.9 Sediment entrainment capacity.. 429
6.10 Summary and Conclusions 433

CHAPTER 7 CONCLUSIONS AND FUTURE WORK 476
7.1 Conclusion... 476
7.2 Future Work 484

REFERENCES 487

LIST OF TABLES

Table. 4.1. Main parameters of the simulations and computational domain for the full depth gravity current simulations with a large volume of release. 156

Table 5.1 Main parameters of the simulations and computational domain for the simulations of gravity currents with a small volume of release. 294

Table 5.2 Comparison of the non-dimensional times and front positions corresponding to the end of the slumping phase, the start of the buoyancy-inertia phase and the start of the drag-dominated phase in the simulations of gravity currents with a small volume of release. 295

Table 5.3 Summary of non-dimensional times and front velocities when the front is situated at $x_f/(H/2)=17$ in the low and high Reynolds number simulations of gravity currents with a small volume of release. 296

Table 6.1 Main geometrical parameters of the simulations with a lock-exchange gravity current and with a constant-flux gravity current. 437

Table 6.2 Comparison of the front velocities of the gravity current before and after it passed the obstacle and of the velocities of the first two waves of the undular bore. (u_{b1}/u_b)“ denotes the non-dimensional bore velocity assuming a sharp bore is present and applying the continuity equation across the moving front. This is a standard assumption made in all the theoretical models used to predict the interaction of a gravity current with an obstacle. 438

Table 6.3 Comparison of the main flow parameters during the first type of quasi-steady regime, SS1. 439

Table 6.4 Comparison of the main flow parameters during the second type of quasi-steady regime, SS2. 440

Table 6.5 Comparison of the LES and theoretical model predictions of the main parameters describing the evolution of the flow before and after the gravity current passes the obstacle (during the first type of quasi-steady regime). 441

Table 6.6 Comparison of the predictions of the models of Lane–Serff et al. (1995) and Oehy and Schleiss (2007) with those given by LES for the proportion of the incoming flux that continues over the obstacle during the first type of quasi-steady regime. 442

Table 6.7 Comparison of the predictions of the models of Lane–Serff et al. (1995) and Oehy and Schleiss (2007) with those given by LES for the ratio between the depth of the lower layer behind the bore and the depth of the undisturbed lower layer upstream of the bore during the first type of quasi-steady regime. 443

Table 6.8 Main flow parameters predicted by LES and theoretical models that are used to estimate the pressure forces on the upstream and downstream faces of the obstacle during the two quasi steady regimes. 444

Table 6.9 Comparison between the predictions of LES obtained by integrating the pressure over the two faces of the obstacle and those obtained using the flow parameters predicted by the theoretical models and applying the momentum equation (subscript "T") of the mean pressure on the upstream face of the obstacle, $\mathrm{P}^{+}/\rho u_b^2$, mean pressure on the downstream face of the obstacle, $\mathrm{P}^{-}/\rho u_b^2$, and mean pressure difference between the upstream and downstream faces of the obstacle, $\Delta\mathrm{P}/\rho u_b^2$ during the two quasi steady regimes. Also shown are the predictions of these three quantities obtained using the momentum equation and the flow parameters predicted by LES (subscript "LES"). 445

LIST OF FIGURES

Figure 1.1. Picture of a gravity current showing the head, dissipative wake and tail regions from the experimental study of Sequeiros et al. (2009) on self-accelerating gravity currents in slightly tilted channels. 20

Figure 1.2. Visualization of gravity currents in the environment. a) salinity current (Simpson, 1987); b) morning glory phenomenon, an example of a temperature driven gravity current, c) snow-powder avalanche, an example of particle-laden gravity current. 20

Figure 1.3. Visualization of the interface of a bottom propagating gravity current from the 3-D LES simulation (Re~47,750) of Ooi et al. (2009) using a concentration isosurface. The red arrows point toward the lobes and clefts at the front of the current and the interfacial Kelvin-Helmholtz billows forming behind the head. 21

Figure 1.4. Sketch of the flow during the slumping phase for the case of a full depth release lock-exchange flow. The gate is positioned far from the extremities of the channel ($x_0/H>>1$). The evolution of the forward and backward propagating Boussinesq gravity currents is anti-symmetric. 22

Figure 1.5. Sketch showing relative dimensions of the 2-D ribs and dunes used in the simulations. 22

Figure 1.6. Sketch of the computational domain and flow for the partial-depth lock-release cases. a) slumping phase before the backward propagating current starts interacting with the rear wall; b) slumping phase after bore formation; c) buoyancy-turbulent drag or buoyancy-inertia self-similar phase. The buoyancy-turbulent drag regime can be present only if the bottom boundary is rough. 23

Figure 1.7. Sketch of the computational domain for the case of a lock-release gravity current interacting with a bottom obstacle corresponding to a submerged dam. 24

Figure 2.1. The shadowgraph of a gravity current head from the study of Simpson and Britter (1979). 47

Figure 2.2. A typical image of the flow from the study of Lane-Serff et al. (1995) showing the reflected jump and the flow continuing over the triangular obstacle. 47

Figure 2.3. Comparison of the interface profile, η(x,t), from the study of Tanino et al. (2005). a) slumping phase for gravity currents propagating over smooth surfaces; b) buoyancy-turbulent drag regime for gravity currents propagating over a porous medium (array of vertical emerged cylinders). ... 48

Figure 2.4. Evolution of a lock-exchange gravity current at Re~1,000 during the slumping phase from the 3-D DNS simulation performed by Härtel et al. (2000a) 49

Figure 2.5. Visualization of interface of an axisymmetric gravity current in one quadrant of the computational domain in the 3-D DNS simulation (Re~3,000) of Cantero et al. (2007) using a concentration isosurface. 50

Figure 2.6. Visualization of the flow structure in the near wall region at t/t_0=5 from a 3-D LES simulation with R=1.0 and Re=47,750 performed by Ooi et al. (2009). a) vertical vorticity contours on the bottom wall; b) streamwise velocity contours showing the high and low streaks of streamwise velocity in a plane located at about 11 wall units from the bottom wall; c) spanwise-averaged concentration contours. The light and dark vorticity contours in frame a correspond to $\omega_y = 2u_b / h$ and $\omega_y = -2u_b / h$, respectively. The solid and dashed lines in frame c correspond to the C=0.9 and C=0.1 concentration levels, respectively. 51

Figure 2.7. Evolution of the concentration, 2-D streamline patterns and vorticity fields during the impact stage for a gravity current propagating over a square cylinder mounted on the bottom wall of a channel. The simulation was conducted for a full depth release case by Gonzalez-Juez et al., (2009b). 52

Figure 2.8 Temporal evolutions of drag (a) and lift (b) predicted by the 3-D simulation (dashed line) and 2-D simulation (dash-dotted line) of the flow past a bottom-mounted rectangular cylinder performed by Gonzalez-Juez et al. (2009b) are compared to the experiments of Ermanyuk and Gavrilov (2005b) (solid lines)... 53

Figure 2.9 Effect of the Reynolds number on the drag (a) and lift (b) fluctuations from simulations (Gonzalez-Juez et al., 2009b) conducted with partial depth gravity currents (H/h=5): Re = 2,000 (thick solid line), Re = 4,000 (dashed line), Re = 10,000 (thin solid line)... 53

Figure 3.1. Concentration contours in a two dimensional (streamwise-vertical) plane during the later stages of the slumping phase for a lock exchange current with a high volume of release (R<<1). a) Sc=1; b) Sc=600. 61

Figure 3.2. Visualization of the structure of the lock-exchange bottom propagating current and bed friction velocity at t = $10t_o$. a) Concentration distribution in a streamwise-vertical section; b) bed friction velocity distribution. The top frame shows the finer mesh results (nz=72). The bottom frame shows the coarser mesh results (nz=48). 61

Figure 3.3 Comparison of the spanwise-averaged bed friction velocity distribution at t=$14t_0$.. 62

Figure 4.1 Sketch of the flow during the slumping phase for the case of a full depth release lock-exchange flow. The gate is positioned far from the extremities of the channel (x_0/H>>1). The top and bottom no-slip walls are horizontal... 156

Figure 4.2 Structure of the gravity current at a time when the front is situated close to x/H=19 in the low Reynolds number simulations with flat bed and with obstacles of height D=0.15H. a) concentration, C; b) velocity magnitude, u_{mag}/u_b; c) pressure, $p / \rho u_b^2$. The aspect ratio is 1:2 in the x-y contour plots. 157

Figure 4.3 Visualization of the changes in the structure of the gravity as the current overtakes the fourth dune in the LR-D15 simulation. The concentration field is shown. 158

Figure 4.4 Visualization of the interface between the gravity current and the lighter ambient current using a 3-D concentration iso-surface (C=0.1) in the LR-D30 simulation. a) t=36t_0; b) t=40t_0; c) t=42t_0; d) t=48_0; e) t=36t_0, view from above; d) t=48_0, view from above. 159

Figure 4.5 Visualization of the changes in the structure of the gravity as the current propagates between the third and the fourth rib in the LR-R15 simulation. The concentration field is shown. 160

Figure 4.6 Visualization of the interface between the gravity current and the lighter ambient current using a 3-D concentration iso-surface (C=0.1) in the LR-R15 simulation. a) t=20t_0; b) t=22t_0; c) t=24_0; d) t=26_0; e) t=20t_0, view from above; d) t=26_0, view from above. 161

Figure 4.7 Visualization of the changes in the structure of the gravity as the current overtakes the second rib in the LR-D30 simulation (a-d). Also shown in frame e) is the structure of the current in the LR-R30 simulation when the front is situated at the same position as in frame d). The concentration field is shown. 162

Figure 4.8 Time variation of the non-dimensional position of the front, x_f/H, function of the non-dimensional time, t/t_0 in the low and high Reynolds number simulations with flat bed and with obstacles of height D=0.15H. 163

Figure 4.9 Time variation of the non-dimensional position of the front, x_f/H, function of the non-dimensional time, t/t_0 in the low Reynolds number simulations with flat bed and with obstacles of height D=0.15H and D=0.3H. 163

Figure 4.10 Visualization of the structure of the tail in the low Reynolds number simulations with a flat bed and with obstacles of height D=0.15H at times when the front is situated close to x/H=18.5. a) concentration, C; b) out-of-plane vorticity, $\omega_z H / u_b$; c) streamwise velocity, u/u_b; d) velocity magnitude, u_{mag}/u_b. 164

Figure 4.11 Visualization of the structure of the tail in the low Reynolds number simulations with obstacles of height D=0.3H at times when the front is situated close to x/H=18.5. a) concentration, C; b) out-of-plane vorticity, $\omega_z H / u_b$; c) velocity magnitude, u_{mag}/u_b. 165

Figure 4.12 Distribution of the Froude number along the gravity current in the LR-D30 simulation at the time instant when x_f/H=18.5. Also shown is the iso-concentration contour C=0.5 in a vertical plane at the same time instant. 165

Figure 4.13 Concentration distribution in a cross-flow (y-z) section (x/H=10.5) cutting through the tail of the current in the LR-D15 simulation................ 166

Figure 4.14 Time variation of the total volumetric flux of heavier fluid $Q_i = (1/u_b H^2)\int CudA$ and of the volumetric flux of heavier fluid moving upstream $Q\text{-}_i = (1/u_b H^2)\int Cu\_dA$ a) Q_i, LR-D15; b) $Q\text{-}_i$, LR-D15; c) Q_i, LR-R15; d) $Q\text{-}_i$, LR-R15. The flux Q_i in frames a) and c) is plotted at x/H=0 and at the sections cutting through the crests of Dune 1 to Dune 5 or the downstream faces of Rib 1 to Rib 5. The flux $Q\text{-}_i$ in frames b) and c) is plotted for Dune 1 and Dune 2 and, respectively, for Rib 1 and Rib 2. 167

Figure 4.15 Time variation of the volume of heavier fluid $M_{i,i+1}$ in between the crests or downstream faces of two successive obstacles for the LR-D15 and LR-R15 simulations.. 168

Figure 4.16 Mean flow and turbulence structure of the flow in the tail region after the quasi-steady regime is reached (LR-D15 simulation). a) concentration, C; b) velocity magnitude u_{mag}/U; c) mean out-of-plane vorticity, $\omega_z(H/U)$; d) turbulence kinetic energy, k/U^2; e) the primary Reynolds shear stress, $\overline{u'v'}/U^2$. The mean variables were averaged in the spanwsie direction and in time, after the quasi-steady state was reached. The comparison is done in the region situated around the second obstacle in the series... 169

Figure 4.17 Mean flow and turbulence structure of the flow in the tail region after the quasi-steady regime is reached (LR-R15 simulation). a) concentration, C; b) velocity magnitude u_{mag}/U; c) mean out-of-plane vorticity, $\omega_z(H/U)$; d) turbulence kinetic energy, k/U^2; e) the primary Reynolds shear stress, $\overline{u'v'}/U^2$. The mean variables were averaged in the spanwsie direction and in time, after the quasi-steady state was reached. The comparison is done in the region situated around the second obstacle in the series. The dashed and solid lines in frame a) correspond to the top of the layer of heavy fluid (C=0.8) and bottom of the layer of ambient fluid (C=0.1), respectively. The dashed line in frame b) corresponds to the top of the layer of high velocity magnitude.. 170

Figure 4.18 Mean flow and turbulence structure of the flow in the tail region after the quasi-steady regime is reached (HR-D15 simulation). a) concentration, C; b) velocity magnitude u_{mag}/U; c) mean out-of-plane vorticity, $\omega_z(H/U)$; d) turbulence kinetic energy, k/U^2; e) the primary Reynolds shear stress, $\overline{u'v'}/U^2$. The mean variables were averaged in the spanwsie direction and in time, after the quasi-steady state was reached. The comparison is done in the region situated around the second obstacle in the series... 171

Figure 4.19 Mean flow and turbulence structure of the flow in the tail region after the quasi-steady regime is reached (HR-R15 simulation). a) concentration, C; b) velocity magnitude u_{mag}/U; c) mean out-of-plane vorticity, $\omega_z(H/U)$; d) turbulence kinetic energy, k/U^2; e) the primary Reynolds shear stress, $\overline{u'v'}/U^2$. The mean variables were averaged in the spanwise direction and in time, after the quasi-steady state was reached. The comparison is done in the region situated around the second obstacle in the series... 172

Figure 4.20 Comparison of the vertical profiles of u_{mag}/U, C and k/U^2 at sections A to F in the tail region after the quasi-steady regime is reached. Results are shown for the low and high Reynolds number simulations with obstacles of height D=0.15H. The positions of sections A to F is shown in Figure 4.16a....... 173

Figure 4.21 Sketch of the flow structure within the tail region in the case dunes (a) or ribs (b) are present at the channel bottom at large distances behind the front of the gravity current. 174

Figure 4.22 Vertical profiles of the double-averaged streamwise velocity, $\hat{u}$ /U, concentration, $\hat{C}$, and turbulent kinetic energy, $\hat{k}/U^2$, in the LR-F and HR-F simulations....... 174

Figure 4.23 Vertical profiles of the double-averaged streamwise velocity, $\hat{u}$ /U, in the low and high Reynolds number simulations with flat bed and with obstacles of height D=0.15H. 175

Figure 4.24 Vertical profiles of the double-averaged concentration, $\hat{C}$, in the low and high Reynolds number simulations with flat bed and with obstacles of height D=0.15H. 176

Figure 4.25 Vertical profiles of the double-averaged turbulent kinetic energy, $\hat{k}/U^2$, in the low and high Reynolds number simulations with flat bed and with obstacles of height D=0.15H. 177

Figure 4.26 Time variation of the mean pressure difference between the upstream and downstream faces of the ribs, $\Delta P/\rho u_b^2$, in the LR-R15 (dashed line) and HR-R15 (solid line) simulations. 177

Figure 4.27 Time variation of the mean pressure difference between the upstream and downstream faces of the ribs, $\Delta P/\rho u_b^2$, in the LR-R30 simulation. 178

Figure 4.28 Time variation of the mean pressure difference between the upstream and downstream faces of the ribs, $\Delta P/\rho u_b^2$, in the LR-R15 simulation. The profiles were translated in time such that the impact stage starts at $t/t_0=0$ for all the five ribs. 178

Figure 4.29 Time variation of the mean pressure difference between the upstream and downstream faces of the ribs, $\Delta P/\rho u_b^2$, in the HR-R15 simulation. The profiles were translated in time such that the impact stage starts at $t/t_0=0$ for all the five ribs. 179

Figure 4.30 Time variations of the mean pressure on the upstream face of the ribs, $P^+/\rho u_b^2$, mean pressure on the downstream face of the ribs, $P^-/\rho u_b^2$, and mean pressure difference between the upstream and downstream faces of the ribs, $\Delta P/\rho u_b^2$, in the LR-R30 simulation. The arrows show the increase in P^- and the corresponding decrease in ΔP as a result of the passage of the hydraulic jump originating at Rib 2 over Rib 1. 180

Figure 4.32 Contour plots showing the concentration, C, (left) and pressure, $p/\rho u_b^2$, (right) distributions in a vertical x-y plane around Rib 2 in the LR-R30 simulation at representative time instants. Also shown are the 2-D streamline patterns of the flow around Rib 1. 182

Figure 4.33 Time variations of the mean pressure on the upstream face of the ribs, P$^+$/ ρu_b^2, mean pressure on the downstream face of the ribs, P$^-$/ ρu_b^2, and mean pressure difference between the upstream and downstream faces of the ribs, ΔP/ ρu_b^2, in the LR-R15 simulation. The arrows show the increase in P$^-$ and the corresponding decrease in ΔP as a result of the passage of the hydraulic jumps originating at Rib 2 and Rib 4 over Rib 1. 183

Figure 4.34 Contour plots showing the concentration, C, (left) and pressure, $p/\rho u_b^2$, (right) distributions in a vertical x-y plane around Rib 1 in the LR-R15 simulation at representative time instants. Also shown are the 2-D streamline patterns of the flow around Rib 1. 184

Figure 4.35 Contour plots showing the concentration, C, (left) and pressure, $p/\rho u_b^2$, (right) distributions in a vertical x-y plane around Rib 3 in the LR-R15 simulation at representative time instants. Also shown are the 2-D streamline patterns of the flow around Rib 3. 185

Figure 4.36 Variation of the potential energy, E_p, kinetic energy, E_k, and integral of the total dissipation, E_d, in the low Reynolds number simulations with flat bed and with obstacles of height D=0.15H. a) plotted versus time in linear-linear scale; b) plotted versus the front position in linear-linear scale; c) plotted versus time in log-log scale. All the terms are non-dimensionalized by the initial potential energy E_{p0}. The arrows in frame a) indicate the times when the current reaches a certain rib in the LR-R15 simulation. 186

Figure 4.37 Variation of the potential energy, E_p, kinetic energy, E_k, and integral of the total dissipation, E_d, in the low Reynolds number simulations with flat bed and with obstacles of height D=0.3H. a) plotted versus time in linear-linear scale; b) plotted versus the front position in linear-linear scale. All the terms are non-dimensionalized by the initial potential energy E_{p0}. The arrows in frame a) indicate the times when the current reaches a certain rib in the LR-R30 simulation. 187

Figure 4.38 Variation of the potential energy, E_p, kinetic energy, E_k, and integral of the total dissipation, E_d, in the high Reynolds number simulations with flat bed and with obstacles of height D=0.15H. a) plotted versus time in linear-linear scale; b) plotted versus the front position in linear-linear scale; c) plotted versus time in log-log scale. All the terms are non-dimensionalized by the initial potential energy E_{p0}. The arrows in frame a) indicate the times when the current reaches a certain rib in the HR-R15 simulation. 188

Figure 4.39 Variation of the potential energy, E_p, kinetic energy, E_k, and integral of the total dissipation, E_d, in the low and high Reynolds number simulations a) with flat bed (time variation); b) with ribs of height D=0.15H (time variation); c) with flat bed and with ribs of height D=0.15H (variation with the front position). All the terms are non-dimensionalized by the initial potential energy E_{p0}. 189

Figure 4.40 Time variation of the terms ($-dE_k/dt$, dE_p/dt and ε) in the differential equation of the mechanical energy in the low Reynolds number simulations with flat bed and with obstacles of height D=0.15H. All the terms are non-dimensionalized by $u_b^3 H^2$ 190

Figure 4.41 Time variation of the terms (*-dE$_k$/dt*, *dE$_p$/dt* and ε) in the differential equation of the mechanical energy in the high Reynolds number simulations with flat bed and with obstacles of height D=0.15H. All the terms are non-dimensionalized by $u_b^3 H^2$ 190

Figure 4.42 Time variation of the terms (*-dE$_k$/dt*, *dE$_p$/dt* and ε) in the differential equation of the mechanical energy in the low Reynolds number simulations with flat bed and with obstacles of height D=0.3H. All the terms are non-dimensionalized by $u_b^3 H^2$ 191

Figure 4.43 Spatial distributions of the non-dimensional spanwise-averaged local dissipation rate $\varepsilon_r/(u_b^3/H)$ in the low Reynolds number simulations with flat bed and ribs of height D=0.15H. a) $t/t_0=8$; b) $t/t_0=16$; c) $t/t_0=32$; d) $t/t_0=40$ (LR-F) and $t/t_0=48$ (LR-R15)... 192

Figure 4.44 Spatial distribution of the non-dimensional spanwise-averaged local dissipation rate $\varepsilon_r/(u_b^3/H)$ in the low Reynolds number simulations with dunes of height D=0.15H. a) $t/t_0=32$; b) $t/t_0=48$.. 193

Figure 4.45 Streamwise distributions of $\varepsilon^{23}(x_1)/(u_b^3 H)$ in the low Reynolds number simulations with flat bed and obstacles of height D=0.15H. a) $t/t_0=32$; b) $t/t_0=40$ (LR-F and LR-D15) and $t/t_0=48$ (LR-R15). 193

Figure 4.46 Spatial distributions of the non-dimensional spanwise-averaged local dissipation rate $\varepsilon_r/(u_b^3/H)$ in the high Reynolds number simulations with flat bed and obstacles of height D=0.15H. a) HR-F simulation at $t/t_0=38$; b) HR-D15 simulation at $t/t_0=40$; c) HR-R15 simulation at $t/t_0=40$........... 194

Figure 4.47 Streamwise distributions of $\varepsilon^{23}(x_1)/(u_b^3 H)$ showing the effect of increasing the Reynolds number. a) $t/t_0=40$ (HR-D15 and HR-R15) and $t/t_0=38$ (HR-F); b) $t/t_0=40$ (LR-F) and $t/t_0=38$ (HR-F); c) $t/t_0=40$ (LR-D15 and HR-D15). 195

Figure 4.48 Spatial distributions of the non-dimensional spanwise-averaged local dissipation rate $\varepsilon_r/(u_b^3/H)$ in the low Reynolds number simulations with obstacles of height D=0.3H. b) HR-D30 simulation at $t/t_0=32$; c) HR-R30 simulation at $t/t_0=32$. 195

Figure 4.49 Spatial distributions of the non-dimensional spanwise-averaged local dissipation rate $\varepsilon_r/(u_b^3/H)$ in the low Reynolds number simulations with obstacles of height D=0.3H. b) HR-D30 simulation at $t/t_0=40$; c) HR-R30 simulation at $t/t_0=40$. 196

Figure 4.50 Spatial distributions of the non-dimensional spanwise-averaged local dissipation rate $\varepsilon_r/(u_b^3/H)$ in the low Reynolds number simulations with obstacles of height D=0.3H. b) HR-D30 simulation at $t/t_0=56$; c) HR-R30 simulation at $t/t_0=56$. 196

Figure 4.51 Streamwise distributions of $\varepsilon^{23}(x_1)/(u_b^3 H)$ in the low Reynolds number simulations with flat bed and obstacles of height D=0.3H. a) $t/t_0=32$; b) $t/t_0=40$ (LR-F) and $t/t_0=56$ (LR-D30 and LR-R30). 197

Figure 4.52 Visualization of the flow structure in the vicinity of the channel bottom in the LR-D15 simulation at t/t_0=40. a) vertical vorticity contours on the bottom wall, the view is lateral and from below the bottom propagating current; b) streamwise velocity (u/u_b) contours showing the positions of the regions containing streaks of high and low streamwise velocity. The contours are shown in a surface situated at 0.006H from the deformed channel bottom surface; c) vertical vorticity contours ($\omega_y H/u_b$) on the bottom wall, the view is from below the bottom propagating current; d) spanwise-averaged concentration contours. The light and dark vorticity contours in frames a) and c) correspond to $\omega_y = 2u_b / H$ and $\omega_y = -2u_b / H$, respectively. The arrows in frame a) indicate the position of the crest of each dune. The aspect ratio is 1:2 in the x-y plots in frames b) to d). 198

Figure 4.53 Visualization of the flow structure in the vicinity of the channel bottom in the LR-R15 simulation at t/t_0=40. a) vertical vorticity contours on the bottom wall, the view is lateral and from below the bottom propagating current; b) streamwise velocity (u/u_b) contours showing the positions of the regions containing streaks of high and low streamwise velocity. The contours are shown in a surface situated at 0.006H from the deformed channel bottom surface; c) vertical vorticity contours ($\omega_y H/u_b$) on the bottom wall, the view is from below the bottom propagating current; d) spanwise-averaged concentration contours. The light and dark vorticity contours in frames a) and c) correspond to $\omega_y = 2u_b / H$ and $\omega_y = -2u_b / H$, respectively. The arrows in frame a) indicate the position of the center of each rib. The aspect ratio is 1:2 in the x-y plots in frames b) to d). 199

Figure 4.54 Spatial distribution of the bed friction velocity u_τ/u_b in the low Reynolds number simulations with a flat bed and with obstacles of height D=0.15H at time instances when the front of the bottom-propagating current is close to 18H. a) LR-F; b) LR-D15; c) LR-R15. Also shown are the concentration contours in an x-y section. The aspect ratio is 1:2 in the x-y plots. 200

Figure 4.55 Streamwise distribution of the spanwise-averaged bed friction velocity in the low Reynolds number simulations with a flat bed and with obstacles of height D=0.15H. a) t/t_0=8; b) t/t_0=16; c) t/t_0=32; d) t/t_0=40. Also shown are the non-dimensional entrainment bed-friction velocities for sand particles of different sizes. 201

Figure 4.56 Spatial distribution of the bed friction velocity u_τ/u_b in the low Reynolds number simulations with obstacles of height D=0.3H at time instances when the front of the bottom-propagating current is close to 19H. a) LR-D30; b) LR-R30. Also shown are the concentration contours in an x-y section. The aspect ratio is 1:2 in the x-y plots. 202

Figure 4.57 Streamwise distribution of the spanwise-averaged bed friction velocity in the low Reynolds number simulations with dunes of height D=0.15H and D=0.3H at t/t_0=40. Also shown are the non-dimensional entrainment bed-friction velocities for sand particles of different sizes. 202

Figure 4.58 Streamwise distribution of the spanwise-averaged bed friction velocity in the low Reynolds number simulations with ribs of height D=0.15H and D=0.3H at t/t_0=40. Also shown are the non-dimensional entrainment bed-friction velocities for sand particles of different sizes. 203

Figure 4.59 Effect of the passage of the backward propagating hydraulic jump on the bed friction velocity in the LR-R30 simulation. a) Spatial distribution of the bed friction velocity u_τ/u_b and concentration at representative time instants; b) Streamwise distribution of the spanwise-averaged bed friction velocity at the time instants shown in frame a). The arrow shows the position of the bore at a particular time instant. 204

Figure 4.60 Spatial distributions of the bed friction velocity u_τ/u_b in the high Reynolds number simulations with a flat bed and with obstacles of height D=0.15H at time instances when the front of the bottom-propagating current is close to 18H. a) HR-F; b) HR-D15; c) HR-R15. Also shown are the concentration contours in an x-y section. The aspect ratio is 1:2 in the x-y plots. 205

Figure 4.61 Streamwise distribution of the spanwise-averaged bed friction velocity in the high Reynolds number simulations with flat bed and obstacles of height D=0.15H at t/t_0=40. Also shown are the distributions of the spanwise-averaged bed friction velocity in the corresponding low Reynolds number simulations multiplied by a factor α=0.58. a) LR-F vs. HR-F; b) LR-D15 vs. HR-D15; c) LR-R15 vs. HR-R15. 206

Figure 4.62 Spatial distributions of the bed friction velocity u_τ/u_b in the LR-R15 simulation at representative time instances. Also shown at each time instant are the concentration distributions in an x-y section and the regions where sediment is entrained ($u_\tau > u_{\tau c}$) assuming $u_{\tau c}/u_b$=0.038. The concentration plots also show the integration domain A“ associated with each rib that is used to quantify the time variation of the amount of sediment entrained over a certain region of the bed. a) t/t_0=18; b) a) t/t_0=20; c) t/t_0=24; d) t/t_0=28; e) t/t_0=32; f) t/t_0=36. The aspect ratio is 1:2 in the x-y plots. 207

Figure 4.63 Time variation of I_2 calculated over the region associated with each of the ribs present in the LR-R15 simulation. I_2 characterizes the flux of sediment of a certain particle size entrained from the bed, assuming no sediment is entrained if $u_\tau < u_{\tau c}$ 208

Figure 4.64 Time variation of I_2 calculated over the region associated with each of the ribs present in the LR-R15 simulation. The distributions of I_2 for Rib 3 to Rib 5 were translated along the time axis by a multiple of the time it takes the current to propagate from one rib to the next one (~9t_0) and superimposed on the distribution for Rib 2. 209

Figure 4.65 Time variation of I_1 calculated over the region associated with each of the ribs present in the LR-R15 simulation. I1 characterizes the flux of sediment of a certain particle size entrained from the bed, assuming sediment is entrained at all values of uτ. The distributions of I1 for Rib 3 to Rib 5 were translated along the time axis by a multiple of the time it takes the current to propagate from one rib to the next one (~9t0) and superimposed on the distribution for Rib 2. 209

Figure 4.66 Time variation of I_2 calculated over the region associated with each of the dunes present in the LR-D15 simulation. The distributions of I_2 for Dune 3 to Dune 5 were translated along the time axis by a multiple of the time it takes the current to propagate from one rib to the next one (~$9t_0$) and superimposed on the distribution for Dune 2. 210

Figure 4.67 Time variation of I_1 calculated over the region associated with each of the dunes present in the LR-D15 simulation. The distributions of I_1 for Dune 3 to Dune 5 were translated along the time axis by a multiple of the time it takes the current to propagate from one rib to the next one and superimposed on the distribution for Dune 2. 210

Figure 4.68 Time variation of the non-dimensional flux of the sediment particles of a certain diameter *d* entrained from the bed per unit time and unit width over the whole length (x/H>0) of the bottom propagating current in the low Reynolds number simulations with flat bed and with obstacles of height D=0.15H and D=0.3H. The flux F(t) is calculated based on van Rijn (1984) formula for the pick up rate. a) d=14 μm; a) d=30 μm a) d=50 μm. 211

Figure 4.69 Time variation of the dimensional flux of the sediment particles of diameter *d*=14 μm entrained from the bed per unit time and unit width over the whole length (x/H>0) of the bottom propagating current in the low and high Reynolds number simulations with flat bed. The values for the LR-F simulation are multiplied by 100. 211

Figure 4.70 Visualization of the structure of the gravity current in case LR-R15-HD. a) concentration, C at $t=77t_0$; b) concentration, C at $t=108t_0$; c) out-of-plane vorticity, $\omega_z H/u_b$, $t=108t_0$. 212

Figure 4.71 Time variation of the non-dimensional position of the front, x_f/H, function of the nondimensional time, t/t_0, in the LR-R15-HD simulation (solid black line). The symbols show the $x_f(t)$ variation based on the times the front reaches the upstream face of each rib. The red lines shows a best fit of the form t^{α}. a) linear-linear plot; b) log-log plot. Also shown in frame c is the time variation of the discharge at the section x/H=0 where the lock gate is located. The regime in which $\alpha=0.72$ is established at about the time the discharge at the section x/H=0 becomes close to constant. 213

Figure 4.72 Variation of the potential energy, E_p, kinetic energy, E_k, and integral of the total dissipation, E_d, in the LR-F and LR-R15-HD simulations. a) plotted versus time in linear-linear scale; b) plotted versus the front position in linear-linear scale. All the terms are non-dimensionalized by the initial potential energy E_{p0}. The vertical line in frame a indicates the change in the slope of the linear variation for E_p and E_d in the LR-R15-HD simulation. 214

Figure 4.73 Distribution of the velocity magnitude, u_{mag}/u_b, at different stages of the propagation of the gravity current in case LR-R15-HD. a) $t=25t_0$; b) $t=65t_0$; c) $t=108t_0$. 215

Figure 4.74 Contour plots showing the concentration, C, (left) and out-of-plane vorticity, $\omega_z H/u_b$, (right) distributions in a vertical x-y plane as the gravity current overtakes Rib 23 and Rib 24 in the LR-R15-HD simulation at representative time instants. 216

Figure 4.75 Contour plots showing the concentration, C, distributions in a vertical x-y plane as the gravity current overtakes Rib 5 and Rib 6 in the LR-R15-HD simulation at representative time instants.. 217

Figure 5.1 Sketch of the flow during the slumping phase (a) and the buoyancy-inertia and turbulent drag-dominated phases (b) for the case of a lock-exchange flow with a small volume of release ($x_0/h=O(1)$). The top boundary is a slip horizontal wall. The bottom boundary is a no-slip horizontal wall. In some of the simulations an array of 2-D ribs or dunes are mounted on the bottom surface only. 297

Figure 5.2 Structure of the gravity current at a time when the front is situated close to $x_f/(H/2)=18$ in the SV-LR-F simulation. a) concentration, C; b) velocity magnitude, u_{mag}/u_b; c) streamwise velocity, u/u_b ; d) out-of-plane vorticity, $\omega_z (H/2)/u_b$. The aspect ratio is 1:2 in the x-y contour plots. 298

Figure 5.3 Structure of the gravity current at a time when the front is situated close to $x_f/(H/2)=18$ in the SV-LR-D15 simulation. a) concentration, C; b) velocity magnitude, u_{mag}/u_b; c) streamwise velocity, u/u_b ; d) out-of-plane vorticity, $\omega_z (H/2)/u_b$. The aspect ratio is 1:2 in the x-y contour plots... 299

Figure 5.4 Distribution of concentration, C, in the SV-LR-R15 simulation. a) $t=22t_0$; b) $t=34t_0$; c) $t=50t_0$; d) $t=87_0$. The aspect ratio is 1:2 in the x-y contour plots... 300

Figure 5.5 Distribution of velocity magnitude, u_{mag}/u_b, in the SV-LR-R15 simulation. a) $t=22t_0$; b) $t=34t_0$; c) $t=50t_0$; d) $t=87_0$. The aspect ratio is 1:2 in the x-y contour plots. 301

Figure 5.6 Distribution of streamwise velocity, u/u_b, in the SV-LR-R15 simulation. a) $t=22t_0$; b) $t=34t_0$; c) $t=50t_0$; d) $t=87_0$. The aspect ratio is 1:2 in the x-y contour plots. 302

Figure 5.7 Distribution of out-of-plane vorticity, $\omega_z (H/2)/u_b$, in the SV-LR-R15 simulation. a) $t=22t_0$; b) $t=34t_0$; c) $t=50t_0$; d) $t=87_0$. The aspect ratio is 1:2 in the x-y contour plots. 303

Figure 5.8 Streamwise distribution of the Froude number in the SV-LR-D15 simulation. The structure of the current is visualized in an x-y section using concentration contours. a) $x_f/(H/2)=9.5$ (buoyancy-inertia phase); b) $x_f/(H/2)=18.5$ (drag-dominated phase). 304

Figure 5.9 Streamwise distribution of the Froude number in the SV-LR-R15 simulation. The structure of the current is visualized in an x-y section using concentration contours. a) $x_f/(H/2)=10.5$ (buoyancy-inertia phase); b) $x_f/(H/2)=18.5$ (drag-dominated phase). 305

Figure 5.10 Streamwise variation of the depth-averaged concentration, $\overline{C}$ (non-dimensional height of the gravity current, $\overline{h}/(H/2)$), in the low Reynolds number simulations with a flat bed and with dunes and ribs of height D=0.15(H/2). a) $x_f/(H/2)$~4.8; b) $x_f/(H/2)$~10.0; c) $x_f/(H/2)$~15.5; d) $x_f/(H/2)$~18.5. 306

Figure 5.11 Comparison of the structure of the gravity current in the low (Re=48,000) and high (Re=10^6) Reynolds number simulations with a flat bed, with dunes and with ribs of height D=0.15H when the front is situated at $x_f/(H/2)$~18. a) concentration, C; b) out-of-plane vorticity, $\omega_z(H/2)/u_b$ 307

Figure 5.12 Streamwise variation of the depth-averaged concentration, $\overline{C}$ (non-dimensional height of the gravity current, $\overline{h}/(H/2)$), in the low and high Reynolds number simulations. a) flat bed, $x_f/(H/2)$~15; b) flat bed, $x_f/(H/2)$~17; c) dunes, D=0.15(H/2), $x_f/(H/2)$~15; b) dunes, D=0.15(H/2), $x_f/(H/2)$~18; e) ribs, D=0.15(H/2), $x_f/(H/2)$~15; f) ribs, D=0.15(H/2), $x_f/(H/2)$~18. 308

Figure 5.13 Distribution of concentration, C, in the SV-LR-R10 simulation. a) $t=22t_0$; b) $t=34t_0$; c) $t=50t_0$; d) $t=87_0$. The aspect ratio is 1:2 in the x-y contour plots. 309

Figure 5.14 Distribution of velocity magnitude, u_{mag}/u_b, in the SV-LR-R10 simulation. a) $t=22t_0$; b) $t=34t_0$; c) $t=50t_0$; d) $t=70_0$; e) $t=100t_0$. The aspect ratio is 1:2 in the x-y contour plots. 310

Figure 5.15 Distribution of streamwise velocity, u/u_b, in the SV-LR-R10 simulation. a) $t=22t_0$; b) $t=34t_0$; c) $t=50t_0$; d) $t=87_0$; e) $t=100t_0$. The aspect ratio is 1:2 in the x-y contour plots. 311

Figure 5.16 Distribution of out-of-plane vorticity, $\omega_z(H/2)/u_b$, in the SV-LR-R10 simulation. a) $t=22t_0$; b) $t=34t_0$; c) $t=50t_0$; d) $t=87_0$; e) $t=100t_0$. The aspect ratio is 1:2 in the x-y contour plots. 312

Figure 5.17 Streamwise variation of the depth-averaged concentration, $\overline{C}$ (non-dimensional height of the gravity current, $\overline{h}/(H/2)$), in the SV-LR-R10 simulation. a) $x_f/(H/2)$~5.2; b) $x_f/(H/2)$~10.5; c) $x_f/(H/2)$~15.5; d) $x_f/(H/2)$~23.5. 313

Figure 5.18 Streamwise distribution of the Froude number in the SV-LR-R10 simulation. The structure of the current is visualized in an x-y section using concentration contours. a) $x_f/(H/2)=9.5$ (buoyancy-inertia phase); b) $x_f/(H/2)=24$ (drag-dominated phase). 314

Figure 5.19 Visualization of the interface between the gravity current and the ambient fluid using a 3-D concentration isosurface (C=0.1) in the SV-LR-R15 simulation during the buoyancy-inertia phase. a) $t=16t_0$; b) $t=20t_0$; c) $t=22t_0$; d) $t=24_0$. 315

Figure 5.20 Visualization of the interface between the gravity current and the ambient fluid using a 3-D concentration isosurface (C=0.02) in the SV-LR-R15 simulation. a) $t=62t_0$; b) $t=72t_0$; c) $t=76t_0$; d) $t=86_0$; e) $t=62t_0$, view from above; f) $t=86_0$, view from above. 316

Figure 5.21 Visualization of the gravity current as it passes Rib5 in the SV-LR-R15 simulation using concentration (left) and out-of-plane vorticity (right) contours. a) t=65t_0; b) t=70t_0; c) t=75t_0; d) t=80$_0$; e) t=83t_0........................ 317

Figure 5.22 Visualization of the interface between the gravity current and the ambient fluid using a 3-D concentration isosurface (C=0.1) in the SV-LR-D15 simulation during the buoyancy-inertia phase. a) t=12t_0; b) t=14t_0; c) t=16t_0; d) t=20$_0$... 318

Figure 5.23 Visualization of the interface between the gravity current and the ambient fluid using a 3-D concentration isosurface (C=0.02) in the SV-LR-D15 simulation. a) t=46t_0; b) t=52t_0; c) t=56t_0; d) t=62$_0$; e) t=52t_0, view from above; f) t=62t_0, view from above. 319

Figure 5.24 Visualization of the gravity current as it passes Dune5 in the SV-LR-D15 simulation using concentration (left) and out-of-plane vorticity (right) contours. a) t=46t_0; b) t=50t_0; c) t=54t_0; d) t=61$_0$; e) t=63.5t_0.......... 320

Figure 5.25 Visualization of the interface between the gravity current and the ambient fluid using a 3-D concentration isosurface (C=0.02) in the SV-LR-R10 simulation. a) t=40t_0; b) t=48t_0; c) t=40t_0, view from above; d) t=48t_0, view from above. The dashed lines indicate the position and spanwise extent of the interfacial billows. 321

Figure 5.26 Visualization of the gravity current in the SV-LR-R10 simulation using concentration (left) and out-of-plane vorticity (right) contours as it passes Rib19. a) t=60t_0; b) t=61.5t_0; c) t=63t_0; d) t=66$_0$. 322

Figure 5.27 Time variation of the non-dimensional position of the front, (x_f-x_0)/x_0, function of the non-dimensional time, t/t_0, in the SV-LR-F, SV-LR-D05 and SV-LR-D15 simulations a)linear scale; b) log-log scale...................... 323

Figure 5.28 Time variation of the non-dimensional position of the front, (x_f-x_0)/x_0, function of the non-dimensional time, t/t_0, in the SV-LR-F, SV-LR-R10 and SV-LR-R15 simulations. a) linear scale; b) log-log scale. 324

Figure 5.29 Time variation of the non-dimensional position of the front, (x_f-x_0)/x_0, function of the non-dimensional time, t/t_0 (log-log scale) in the high Reynolds number simulations SV-HR-F, SV-HR-D15 and SV-HR-R15. .. 325

Figure 5.30 Evolution of the concentration with time along the x axis. The distance from the bottom wall is y/(H/2)=0.09. a) SV-LR-F simulation; b) SV-HR-F simulation. The dashed lines correspond to the forward propagating disturbances FD1 and FD2 and to the backward propagating disturbance BD1. After reflection BD1 is called FD1............................... 326

Figure 5.31 Visualization of the structure of the gravity current in the SV-LR-F simulation using concentration contours. The position and direction of propagation of the flow disturbances are shown using arrows. a) t=9t_0; b) t=11.5t_0; c) t=20.5t_0; d) t=26.5$_0$. The aspect ratio is 1:2 in the x-y contour plots.. 327

Figure 5.32 Visualization of the structure of the gravity current in the SV-HR-F simulation using concentration contours. The position and direction of propagation of the flow disturbances are shown using arrows. a) t=9t_0; b) t=11.5t_0; c) t=20.5t_0; d) t=26.5$_0$. The aspect ratio is 1:2 in the x-y contour plots. 328

Figure 5.33 Evolution of the concentration with time along the x axis in the SV-LR-R15 simulation. The distance from the bottom wall is y/(H/2)=0.09. The dashed lines visualize the main forward and backward propagating flow disturbances. S1, BD1, FD11 and FD12 form due to the collapse of a large interfacial billow on the channel bottom. S2 to S5 form due to the partial reflection of the gravity current fluid as the front passes Rib1 to Rib4, respectively. 329

Figure 5.34 Visualization of the structure of the current between the end wall and Rib1 in the SV-LR-R15 simulation using non-dimensional concentration contours (left) and streamwise velocity contours (right). Also shown are the position and direction of propagation of the main flow disturbances. a) t=12t_0; b) t=15t_0; c) t=21t_0; d) t=24$_0$; e) t=30t_0; f) t=40t_0. 330

Figure 5.35 Visualization of the structure of the current between Rib1 and Rib2 in the SV-LR-R15 simulation using non-dimensional concentration contours (left) and streamwise velocity contours (right). Also shown are the position and direction of propagation of the main flow disturbances. a) t=20t_0; b) t=26t_0; c) t=30t_0; d) t=38$_0$; e) t=39t_0; f) t=40t_0; g) t=41t_0. 331

Figure 5.36 Visualization of the structure of the current around Rib2 in the later stages of the SV-LR-R15 simulation using non-dimensional concentration contours (left) and streamwise velocity contours (right). Also shown are the position and direction of propagation of the main flow disturbances. a) t=52t_0; b) t=53t_0; c) t=55t_0; d) t=56$_0$; e) t=58t_0; f) t=60t_0; g) t=62t_0. 332

Figure 5.37 Evolution of the concentration with time along the x axis in the SV-HR-R15 simulation. The distance from the bottom wall is y/(H/2)=0.09. The dashed lines visualize the main forward and back propagating flow disturbances. S1 forms due to the collapse of a large interfacial billow on the channel bottom. S2 to S5 form due to the partial reflection of the gravity current fluid as the front passes Rib1 to Rib4, respectively. 333

Figure 5.38 Time variation of the total volumetric flux of heavier fluid $Q_i = (4/u_b H^2)\int CudA$ and of the volumetric flux of heavier fluid moving upstream $Q\text{-}_i = (1/u_b H^2)\int Cu\_dA$ at the streamwise locations corresponding to the center of the ribs in the SV-LR-R15 simulation. a) Q_i, $t/t_0<45$; b) $Q\text{-}_i$, $t/t_0<45$; c) Q_i, $30<t/t_0<75$. 334

Figure 5.39 Time variation of the total volumetric flux of heavier fluid $Q_i = (4/u_b H^2)\int CudA$ at the streamwise locations (x/(H/2)=5, 8, 11, and 14) corresponding to the center of the ribs and the crest of the dunes in the SV-LR-F, SV-LR-R15 and SV-LR-D15 simulations. 335

Figure 5.40 Time variation of the total volumetric flux of heavier fluid $Q_i = (4/u_b H^2)\int CudA$ at the streamwise locations (x/(H/2)=5, 7, 11, and 17) corresponding to the center of Rib3, Rib5, Rib9 and Rib15 in the SV-LR-R10 simulation. 336

Figure 5.41 Time variation of the volume of heavier fluid $M_{i\text{-}i+1}$ in between the crests or centers of two successive obstacles (i and i+1). a) SV-LR-D15 and SV-LR-R15 simulations; b) SV-LR-R15 and SV-HR-R15 simulations; c) SV-LR-D15 and SV-HR-D15 simulations; d) SV-LR-R10 simulation. 337

Figure 5.42 Time variation of the mean pressure difference between the upstream and downstream faces of Rib1, Rib2, Rib3, Rib4 and Rib5, $\Delta P/\rho u_b^2$, in the SV-LR-R15 and SV-HR-R15 simulations. 338

Figure 5.43 Time variation of the mean pressure difference between the upstream and downstream faces of Rib1, Rib2, Rib3, Rib4 and Rib5, $\Delta P/\rho u_b^2$. a) SV-LR-R15 simulation; b) SV-HR-R15 simulation. The profiles were translated in time such that the impact stage starts at $t/t_0=0$ for all the five ribs. 339

Figure 5.44 Time variation of the mean pressure difference between the upstream and downstream faces of Rib3, Rib5, Rib9, Rib15 and Rib19, $\Delta P/\rho u_b^2$, in the SV-LR-R10 simulation. 340

Figure 5.45 Time variation of the mean pressure difference between the upstream and downstream faces of Rib3, Rib5, Rib9, Rib15 and Rib19, $\Delta P/\rho u_b^2$, in the SV-LR-R10 simulation. The profiles were translated in time such that the impact stage starts at $t/t_0=0$ for all the five ribs. 340

Figure 5.46 Time variations of the mean pressure on the upstream face of the ribs, $P^+/\rho u_b^2$, mean pressure on the downstream face of the ribs, $P^-/\rho u_b^2$, and mean pressure difference between the upstream and downstream faces of the ribs, $\Delta P/\rho u_b^2$, in the SV-LR-R15 simulation. Results are shown for Rib1 and Rib4. 341

Figure 5.47 Contour plots showing the concentration, C, (left) and pressure, $p/\rho u_b^2$, (right) distributions in a vertical x-y plane around Rib1 in the SV-LR-R15 simulation at representative time instants. a) $t=9.1t_0$; b) $t=15.3t_0$; c) $t=22.9t_0$; d) $t=37.7_0$; e) $t=53.8t_0$. 342

Figure 5.48 Contour plots showing the concentration, C, (left) and pressure, $p/\rho u_b^2$, (right) distributions in a vertical x-y plane around Rib4 in the SV-LR-R15 simulation at representative time instants. a) $t=43.9t_0$; b) $t=46.7t_0$; c) $t=54.0t_0$; d) $t=64.5_0$; e) $t=82.6t_0$. 343

Figure 5.49 Time variations of the mean pressure on the upstream face of the ribs, $P^+/\rho u_b^2$, mean pressure on the downstream face of the ribs, $P^-/\rho u_b^2$, and mean pressure difference between the upstream and downstream faces of the ribs, $\Delta P/\rho u_b^2$, in the SV-LR-R10 simulation. Results are shown for Rib3 and Rib15. 344

Figure 5.50 Contour plots showing the concentration, C, (left) and pressure, $p/\rho u_b^2$, (right) distributions in a vertical x-y plane around Rib3 in the SV-LR-R10 simulation at representative time instants. a) t=7.1t$_0$; b) t=8.4t$_0$; c) t=10.8t$_0$; d) t=22.2$_0$; e) t=39.7t$_0$. 345

Figure 5.51 Contour plots showing the concentration, C, distribution in a vertical x-y plane around Rib15 in the SV-LR-R10 simulation at representative time instants. a) t=42.0t$_0$; b) t=43.8t$_0$; c) t=45.6t$_0$; d) t=54.3$_0$; e) t=67.2t$_0$.......... 346

Figure 5.52 Variation of the potential energy, E_p, kinetic energy, E_k, and integral of the total dissipation, E_d, in the SV-LR-F, SV-LR-D15 and SV-LR-R15 simulations. a) plotted versus time in linear-linear scale; b) plotted versus the front position in linear-linear scale. 347

Figure 5.53 Time variation of the terms ($-dE_k/dt$, dE_p/dt and ε) in the differential equation of the mechanical energy in the SV-LR-R15 simulation. All the terms are nondimensionalized by $u_b^3(H/2)^2$ 348

Figure 5.54 Variation of the potential energy, E_p, kinetic energy, E_k, and integral of the total dissipation, E_d, with the front position, x$_f$/(H/2) in the: a) SV-LR-F and SV-HR-F simulations; b) SV-LR-R15 and SV-HR-R15 simulations. 349

Figure 5.55 Variation of the potential energy, E_p (a), kinetic energy, E_k (b), and integral of the total dissipation, E_d (c), with the front position, x$_f$/(H/2), plotted in linear-log scale for the SV-LR-F, SV-LR-R15 and SV-LR-R10 simulations. The green arrows show the end of the slumping phase. The black arrows show the start of the buoyancy-inertia phase. The red arrows show the start of the drag-dominated phase. 350

Figure 5.56 Spatial distributions of the non-dimensional spanwise-averaged local dissipation rate $\varepsilon_r/(u_b^3/(H/2))$ in the SV-LR-R15 simulation. a) t/t$_0$=8; b) t/t$_0$=12; c) t/t$_0$=18; d) t/t$_0$=48; e) t/t$_0$=80. 351

Figure 5.57 Spatial distribution of the non-dimensional spanwise-averaged local dissipation rate $\varepsilon_r/(u_b^3/(H/2))$ in the SV-LR-F simulation at t/t$_0$=40. 351

Figure 5.58 Streamwise distributions of $\varepsilon^{23}(x_1)/(u_b^3(H/2))$ in the SV-LR-R15 simulation. a) t/t$_0$=8; b) t/t$_0$=12; d) t/t$_0$=18; b) t/t$_0$=48; e) t/t$_0$=80............... 352

Figure 5.59 Visualization of the flow structure in the vicinity of the channel bottom in the SV-LR-D15 simulation during the buoyancy-inertia phase when the front is situated x$_f$/(H/2)=7.7. a) vertical vorticity contours, the view is lateral and from above the bottom propagating current; b) vertical vorticity contours, $\omega_y(H/2)/u_b$, on the bottom wall, the view is from below the bottom propagating current; c) spanwise-averaged concentration contours; d) bed friction velocity, u_τ/u_b, contours showing the positions of the regions containing streaks of high and low streamwise velocity; e) concentration contours in a horizontal plane situated close to the channel bottom. The light and dark vorticity contours in frames a) and b) correspond to $\omega_y = 2u_b/(H/2)$ and $\omega_y = -2u_b/(H/2)$, respectively. The arrows in frame a) indicate the position of the crest of each rib. The aspect ratio is 1:2 in the x-y plots in frame c) and in the x-z plots in frames b) and d). 353

Figure 5.60 Visualization of the flow structure in the vicinity of the channel bottom in the SV-LR-D15 simulation during the drag-dominated phase when the front is situated $x_f/(H/2)=18.5$. a) vertical vorticity contours, the view is lateral and from above the bottom propagating current; b) vertical vorticity contours, $\omega_y(H/2)/u_b$, on the bottom wall, the view is from below the bottom propagating current; c) spanwise-averaged concentration contours; d) bed friction velocity, u_τ/u_b, contours showing the positions of the regions containing streaks of high and low streamwise velocity; e) concentration contours in a horizontal plane situated close to the channel bottom. The light and dark vorticity contours in frames a) and b) correspond to $\omega_y = 2u_b/(H/2)$ and $\omega_y = -2u_b/(H/2)$, respectively. The arrows in frame a) indicate the position of the crest of each rib. The aspect ratio is 1:2 in the x-y plots in frame c) and in the x-z plots in frames b) and d). 354

Figure 5.61 Spatial distribution of the bed friction velocity, u_τ/u_b, during the buoyancy-inertia phase when the front position is $x_f/(H/2)=8$. a) SV-LR-F simulation; b) SV-LR-D15 simulation; c) SV-LR-R15 simulation. Also shown are the concentration contours in an x-y section. The aspect ratio is 1:2 in the x-y plots. 355

Figure 5.62 Spatial distribution of the bed friction velocity, u_τ/u_b, during the drag-dominated phase (simulations with roughness elements only) when the front position is $x_f/(H/2)=16.5$. a) SV-LR-F simulation; b) SV-LR-D15 simulation; c) SV-LR-R15 simulation. Also shown are the concentration contours in an x-y section. The aspect ratio is 1:2 in the x-y plots. 356

Figure 5.63 Visualization of the structure of the gravity current in an x-y plane between $x/(H/2)=8$ and the front, in the SV-LR-D15 simulation, when the front position is $x_f/(H/2)=16.5$. a) concentration; b) streamwise velocity. The solid lines correspond to the concentration isosurface C=0.05... 357

Figure 5.64 Streamwise distribution of the spanwise-averaged bed friction velocity in the SV-LR-F, SV-LR-R15 and SV-LR-D15 simulations. a) $x_f/(H/2)\sim4.5$; b) $x_f/(H/2)=8.5$; c) $x_f/(H/2)=16.2$; d) $x_f/(H/2)=17$. The dotted line corresponds to $u_{\tau c}=0.014u_b$. 358

Figure 5.65 Spatial distribution of the bed friction velocity u_τ/u_b during the buoyancy-inertia phase when the front position is $x_f/(H/2)=9$. a) SV-LR-F simulation; b) SV-LR-R10 simulation; c) SV-LR-R15 simulation. Also shown are the concentration contours in an x-y section. The aspect ratio is 1:2 in the x-y plots. 359

Figure 5.66 Spatial distribution of the bed friction velocity u_τ/u_b during the transition to the drag-dominated phase when the front position is $x_f/(H/2)=16.5$ in the SV-LR-R10 simulation. Also shown are the concentration contours in an x-y section. The aspect ratio is 1:2 in the x-y plot............................ 360

Figure 5.67 Streamwise distribution of the spanwise-averaged bed friction velocity in the SV-LR-F, SV-LR-R15 and SV-LR-R10 simulations. a) $t/t_0=2.5$; b) $t/t_0=4$; c) $x_f/(H/2)\sim4.5$; d) $x_f/(H/2)\sim5.5$; e) $x_f/(H/2)=8.5-9.5$; f) $x_f/(H/2)=13.5-14.5$; g) $x_f/(H/2)=18-19.5$; h) $x_f/(H/2)=23.5$. The dotted line corresponds to $u_{\tau c}=0.014u_b$. The dashed line shows the region where the overall decay of the bed friction velocity in the SV-LR-R10 simulation is linear. The solid vertical lines show the position of the ribs in the SV-LR-R15 simulation. 361

Figure 5.68 Streamwise distribution of the spanwise-averaged bed friction velocity in the high Reynolds number simulations with flat bed and obstacles of height D=0.15H when the front position is $x_f/(H/2)=15.5-16.5$. Also shown are the distributions of the spanwise-averaged bed friction velocity in the corresponding low Reynolds number simulations multiplied by a factor $\alpha=0.43$. a) SV-LR-F vs. SV-HR-F; b) SV-LR-D15 vs. SV-HR-D15; c) SV-LR-R15 vs. SV-HR-R15. 362

Figure 5.69 Spatial distributions of the bed friction velocity, u_τ/u_b, in the SV-LR-R15 simulation at representative time instances. Also shown at each time instant are the concentration distributions in an x-y section and the regions where sediment is entrained ($u_\tau > u_{\tau c}$) assuming $u_{\tau c}/u_b=0.014$. The concentration plots also show the integration domain A" associated with each rib that is used to quantify the time variation of the amount of sediment entrained over a certain region of the bed. a) $t/t_0=40$; b) a) $t/t_0=46$; c) $t/t_0=52$; d) $t/t_0=58$; e) $t/t_0=64$; f) $t/t_0=70$. The aspect ratio is 1:2 in the x-y plots. 363

Figure 5.70 Time variation of I_2 calculated over the region associated with each of the ribs present in the SV-LR-R15 simulation. I_2 characterizes the flux of sediment of a certain particle size entrained from the bed, assuming no sediment is entrained if $u_\tau < u_{\tau c}$. 364

Figure 5.71 Time variation of I_2 calculated over the region associated with Rib2 to Rib5 in the SV-LR-R15 simulation. I_2 characterizes the flux of sediment of a certain particle size entrained from the bed, assuming sediment is entrained at all values of u_τ. The distributions for Rib2 to Rib5 were translated along the time axis such that I_2 becomes non zero at $t/t_0=0$........ 364

Figure 5.72 Time variation of I_1 calculated over the region associated with Rib2 to Rib5 in the SV-LR-R15 simulation. I_1 characterizes the flux of sediment of a certain particle size entrained from the bed, assuming sediment is entrained at all values of u_τ. The distributions for Rib2 to Rib5 were translated along the time axis such that I_1 becomes non zero at $t/t_0=0$........ 365

Figure 5.73 Spatial distributions of the bed friction velocity u_τ/u_b in the SV-LR-D15 simulation at representative time instances. Also shown at each time instant are the concentration distributions in an x-y section and the regions where sediment is entrained ($u_\tau > u_{\tau c}$) assuming $u_{\tau c}/u_b=0.014$. The concentration plots also show the integration domain A" associated with each dune that is used to quantify the time variation of the amount of sediment entrained over a certain region of the bed. a) $t/t_0=40$; b) a) $t/t_0=46$; c) $t/t_0=52$; d) $t/t_0=58$. The aspect ratio is 1:2 in the x-y plots. 366

Figure 5.74 Time variation of I_2 calculated over the region associated with each of the dunes present in the SV-LR-D15 simulation. I_2 characterizes the flux of sediment of a certain particle size entrained from the bed, assuming no sediment is entrained if $u_\tau < u_{\tau c}$. 367

Figure 5.75 Time variation of I_2 calculated over the region associated with Dune2 to Dune5 in the SV-LR-D15 simulation. I_2 characterizes the flux of sediment of a certain particle size entrained from the bed, assuming sediment is entrained at all values of u_τ. The distributions for Dune2 to Dune5 were translated along the time axis such that I_2 becomes non zero at $t/t_0=0$. 367

Figure 5.76 Time variation of I_1 calculated over the region associated with Dune2 to Dune5 in the SV-LR-D15 simulation. I_1 characterizes the flux of sediment of a certain particle size entrained from the bed, assuming sediment is entrained at all values of u_τ. The distributions for Dune2 to Dune5 were translated along the time axis such that I_1 becomes non zero at $t/t_0=0$. 368

Figure 5.77 Comparison of the capacity of the bottom propagating current to entrain sediment particles of diameter $d=0.14\ \mu m$ over its whole length during its propagation in the SV-LR-F, SV-LR-R15 and SV-LR-R15 simulations. a) non-dimensional flux of sediment particles entrained from the bed per unit time and unit width, F(t); b) non-dimensional mass of sediment particles entrained from the bed per unit width between the time the lock gate is released and the current time, $G(t) = \int_0^t F(t)dt$. The flux F(t) is calculated based on van Rijn (1984) formula for the pick-up rate. 369

Figure 6.1 Sketch of the computational domain used to study the interaction between a bottom propagating gravity current an obstacle (submerged dam). a) lock-exchange gravity current; b) constant-flux gravity current. 446

Figure 6.2 Sketch of the flow structure during a) the first type of quasi-steady regime (SS1) showing the main flow parameters upstream and downstream of the obstacle and the moving submerged hydraulic jump; b) the second type of quasi-steady regime (SS2) showing the main flow parameters upstream and downstream of the obstacle. The index "b" refers to the values of the variables during SS2. 447

Figure 6.3 Time variation of the non-dimensional discharges at the inlet section (q_g), at the section cutting through the crest of the obstacle (q_d) and at a section situated at about $5h_0$ downstream of the crest of the obstacle (q_3). a) D-LE-D034b; b) D-CF-D068; c) D-CF-D068-HR; d) D-CF-D137. The horizontal lines denote the mean values of q_g during the quasi-steady regimes. In the constant-flux current simulations, q_g is constant in time. ... 448

Figure 6.4 Comparison of the shape of the undular bores based on the distribution of the concentration contours near the interface. a) D-LE-D034b; b) D-LE-D068; c) D-CF-D068-HR. The vertical arrows indicate the crest of the first and second waves of the undular bore. 449

Figure 6.5 Comparison of the structure of the gravity current in the simulations with a triangular obstacle (D-CF-D068) and a Gaussian-shape obstacle of same height (D-CF-D068-G). a) $t=15t_0$; b) $t=29t_0$. 450

Figure 6.6 Comparison between the evolutions of the gravity current in the experiment (Lane Serff et al., 1995) and LES simulation for case D-LE-D034a. The arrow indicates the position of the front of the bore. The time scale is $t_0=0.28$ s. 451

Figure 6.7 Comparison between the evolutions of the gravity current in the experiment (Lane Serff et al., 1995) and LES simulation for case D-LE-D034b. The arrow indicates the position of the front of the bore. The time scale is $t_0=0.38$ s. 452

Figure 6.8 Contour plots given by Lane Serff et al. (1995) to predict the main parameters describing the evolution of the flow after the gravity current passes the obstacle. The theoretical model predictions apply during the first type of quasi-steady regime. a) the proportion of the incoming flux over the obstacle, q_d/q_0; b) the ratio of the hydraulic jump velocity to the velocity of the lower layer behind the head of the current, u_{b1}/u_0; c) the ratio of the height of the lower layer behind the hydraulic jump to the height of the undisturbed tail, d_{l1}/d_0. The rectangles correspond to the theoretical model predictions for cases D-LE-D034a (red), D-LE-D034b (green), D-LE-D068 (blue), D-CF-D068 and D-CF-D068-HR (black). 453

Figure 6.9 Variation of the relative depth of the gravity current, $z=H/d_0$ (red line) and the Froude number of the incoming current, $Fr_0 = u_0 / \sqrt{g' d_0}$ (blue line) based on the experimental data of Lane-Serff et al. (1995). The dashed lines correspond to the upper and lower bound of the variable based on the scatter of the experimental data. The LES predictions of z are shown using red triangles. The LES predictions of $Fr_0 = u_0 / \sqrt{g' d_0}$ are shown using hollow blue rectangles. The LES predictions of $Fr_{0f} = u_f / \sqrt{g' d_0}$ are shown using filled blue rectangles. 454

Figure 6.10 Contour plots given by Oehy (2003) to predict the main parameters describing the evolution of the flow after the gravity current passes the obstacle. The theoretical model predictions apply during the first type of quasi-steady regime. a) the proportion of the incoming flux over the obstacle, q_d/q_0; b) the ratio of the height of the lower layer behind the hydraulic jump to the height of the undisturbed tail, d_{l1}/d_0........................ 455

Figure 6.11 Comparison between the predictions given by the theoretical model of Gonzales-Juez and Meiburg (2009) and those of LES. a) nondimensional discharge of the downstream current $v_f d_f / \sqrt{g' d_0^3}$; b) non-dimensional front velocity of the downstream current, $v_f / \sqrt{g' d_0}$; c) non-dimensional height of the lower layer behind the front of the downstream current, d_f/d_0. 455

Figure 6.12 Distribution of the concentration, C, out-of-plane vorticity, $\omega_z h_0 / u_b$ and spanwise-averaged local dissipation rate, $\varepsilon_r/(u_b^3 / h_0)$ in the D-CF-D068 simulation. a) $t/t_0=8$; b) $t/t_0=16$; c) $t/t_0=28$; d) $t/t_0=36$; e) $t/t_0=80$. The vertical arrows indicate the position of the crest of the waves of the undular bore. 456

Figure 6.13 Distribution of the concentration, C, out-of-plane vorticity, $\omega_z h_0 / u_b$ and spanwise-averaged local dissipation rate, $\varepsilon_r/(u_b^3 / h_0)$ in the D-CF-D068-HR simulation. a) $t/t_0=8$; b) $t/t_0=16$; c) $t/t_0=20$; d) $t/t_0=30$; e) $t/t_0=36$; f) $t/t_0=80$. The vertical arrows indicate the position of the crest of the waves of the undular bore. 457

Figure 6.14 Distribution of the concentration, C, out-of-plane vorticity, $\omega_z h_0 / u_b$ and spanwise-averaged local dissipation rate, $\varepsilon_r/(u_b^3 / h_0)$ in the D-CF-D137 simulation. a) $t/t_0=8$; b) $t/t_0=16$; c) $t/t_0=28$; d) $t/t_0=36$; e) $t/t_0=48$; f) $t/t_0=60$; g) $t/t_0=90$. The vertical arrows indicate the position of the crest of the waves of the undular bore. 458

Figure 6.15 Streamwise distributions of $\varepsilon^{23}(x_1)/(u_b^3 h_0)$ in the D-CF-D068 (red line) and D-CF-D068-HR (blue line) simulations. B1 and B2 mark the regions of large dissipation induced by the passage of the waves of the undular bore. 459

Figure 6.16 Streamwise distributions of $\varepsilon^{23}(x_1)/(u_b^3 h_0)$ in the D-CF-D137 simulation. B1 and B2 mark the regions of large dissipation induced by the passage of the waves of the undular bore. a) $t/t_0=8$; b) $t/t_0=16$; c) $t/t_0=28$; d) $t/t_0=36$; e) $t/t_0=48$; f) $t/t_0=60$; g) $t/t_0=90$. 460

Figure 6.17 Comparison of the spatial distributions of the bed friction velocity u_τ/u_b after the current has passed the obstacle ($t=28t_0$) in the D-CF-D068 (a) and the D-CF-D068-HR (b) simulations during SS1. Also shown are the concentration contours in an x-y section. The aspect ratio is 1:2 in the x-y plot. Frame c shows the comparison of the streamwise distributions of the spanwise-averaged bed friction velocity in the two simulations at $t=28t_0$. 461

Figure 6.18 Comparison of the spatial distributions of the bed friction velocity u_τ/u_b after the current has passed the obstacle ($t=80t_0$) in the D-CF-D068 (a) and D-CF-D137 (b) simulations, during SS2. Also shown are the concentration contours in an x-y section. The aspect ratio is 1:2 in the x-y plot. Frame c shows the comparison of the streamwise distributions of the spanwise-averaged bed friction velocity in the two simulations at $t=80t_0$. 462

Figure 6.19 Time variation of the mean pressure difference (streamwise drag force divided by the obstacle height) between the upstream and downstream faces of the obstacle, $\Delta P/\rho u_b^2$. a) D-LE-D034a vs. D-LE-D034b; b) D-LE-D034b vs. D-LE-D068; c) D-CF-D068 vs. D-CF-D068-HR; d) D-CF-D137. 463

Figure 6.20 Time variations of the mean pressure on the upstream face of the obstacle, $P^+/\rho u_b^2$, mean pressure on the downstream face of the obstacle, $P^-/\rho u_b^2$, and mean pressure difference between the upstream and downstream faces of the obstacle, $\Delta P/\rho u_b^2$, in the D-CF-D068 simulation. 464

Figure 6.21 Contour plots showing the concentration, C, (left) and piezometric pressure, $p/\rho u_b^2$, (right) distributions in a vertical x-y plane around the obstacle in the D-CF-D068 simulation at representative time instants. a) $t=15.6t_0$; b) $t=18.6t_0$; c) $t=35.1t_0$; d) $t=55.5t_0$; e) $t=60t_0$; f) $t=68.8t_0$. 465

Figure 6.22 Time variations of the mean pressure on the upstream face of the obstacle, $P^{+}/\rho u_b^2$, mean pressure on the downstream face of the obstacle, $P^{-}/\rho u_b^2$, and mean pressure difference between the upstream and downstream faces of the obstacle, $\Delta P/\rho u_b^2$, in the D-CF-D137 simulation. 466

Figure 6.23 Contour plots showing the distribution of the concentration, C, (left) and piezometric pressure, $p/\rho u_b^2$, (right) in a vertical x-y plane around the obstacle in the D-CF-D137 simulation at representative time instants. a) $t=15.8t_0$; b) $t=27.5t_0$; c) $t=40.5t_0$; d) $t=47.2t_0$; e) $t=73.7t_0$; f) $t=78t_0$; g) $t=86.5t_0$. 467

Figure 6.24 Contour and line plots showing the structure of the mean flow around the obstacle during SS1 in the D-LE-D034b simulation. a) concentration, C; b) streamwise velocity, u_x/u_b; c) velocity magnitude, u_{mag}/u_b; d) piezometric pressure $p/\rho u_b^2$; e) turbulent kinetic energy k/u_b^2; f) depth of the lower layer, d/h_0; g) mean streamwise (with respect to the bottom surface) velocity in the lower layer, u_s/u_b; h) Froude number of the flow in the lower layer, Fr; i) bed friction velocity, $\bar{u}_\tau/u_b$. The dashed line in frame i corresponds to $\bar{u}_\tau/u_b=0.06$. 468

Figure 6.25 Contour and line plots showing the structure of the mean flow around the obstacle during SS1 in the D-CF-D068 simulation. a) concentration, C; b) streamwise velocity, u_x/u_b; c) velocity magnitude, u_{mag}/u_b; d) piezometric pressure $p/\rho u_b^2$; e) turbulent kinetic energy k/u_b^2; f) depth of the lower layer, d/h_0; g) mean streamwise (with respect to the bottom surface) velocity in the lower layer, u_s/u_b; h) Froude number of the flow in the lower layer, Fr; i) bed friction velocity, $\bar{u}_\tau/u_b$. The dashed line in frame i corresponds to $\bar{u}_\tau/u_b=0.06$. 469

Figure 6.26 Contour and line plots showing the structure of the mean flow around the obstacle during SS1 in the D-CF-D068-HR simulation. a) concentration, C; b) streamwise velocity, u_x/u_b; c) velocity magnitude, u_{mag}/u_b; d) piezometric pressure $p/\rho u_b^2$; e) turbulent kinetic energy k/u_b^2; f) depth of the lower layer, d/h_0; g) mean streamwise (with respect to the bottom surface) velocity in the lower layer, u_s/u_b; h) Froude number of the flow in the lower layer, Fr; i) bed friction velocity, $\bar{u}_\tau/u_b$. The dashed line in frame i corresponds to $\bar{u}_\tau/u_b=0.06$. 470

Figure 6.27 Contour and line plots showing the structure of the mean flow around the obstacle during SS2 in the D-CF-D068 simulation. a) concentration, C; b) streamwise velocity, u_x/u_b; c) velocity magnitude, u_{mag}/u_b; d) piezometric pressure $p/\rho u_b^2$; e) turbulent kinetic energy k/u_b^2; f) depth of the lower layer, d/h_0; g) mean streamwise (with respect to the bottom surface) velocity in the lower layer, u_s/u_b; h) Froude number of the flow in the lower layer, Fr; i) bed friction velocity, $\bar{u}_\tau/u_b$. The dashed line in frame i corresponds to $\bar{u}_\tau/u_b=0.06$. 471

Figure 6.28 Contour and line plots showing the structure of the mean flow around the obstacle during SS2 in the D-CF-D068-HR simulation. a) concentration, C; b) streamwise velocity, u_x/u_b; c) velocity magnitude, u_{mag}/u_b; d) piezometric pressure $p/\rho u_b^2$; e) turbulent kinetic energy k/u_b^2; f) depth of the lower layer, d/h_0; g) mean streamwise (with respect to the bottom surface) velocity in the lower layer, u_s/u_b; h) Froude number of the flow in the lower layer, Fr; i) bed friction velocity, $\bar{u}_\tau/u_b$. The dashed line in frame i corresponds to $\bar{u}_\tau/u_b$=0.06. 472

Figure 6.29 Contour and line plots showing the structure of the mean flow around the obstacle during SS2 in the D-CF-D137 simulation. a) concentration, C; b) streamwise velocity, u_x/u_b; c) velocity magnitude, u_{mag}/u_b; d) piezometric pressure $p/\rho u_b^2$; e) turbulent kinetic energy k/u_b^2; f) depth of the lower layer, d/h_0; g) mean streamwise (with respect to the bottom surface) velocity in the lower layer, u_s/u_b; h) Froude number of the flow in the lower layer, Fr; i) bed friction velocity, $\bar{u}_\tau/u_b$. The dashed line in frame i corresponds to $\bar{u}_\tau/u_b$=0.06. 473

Figure 6.30 Sketch showing the extent of the four zones over which the flux of sediment entrained from the bed surface over surface i, $F_i(t)$, is estimated using van Rijn‟s formula. 474

Figure 6.31 Comparison between the time variations of the flux of sediment particles of diameter $d=50\mu m$ ($u_{\tau c}/u_b = 0.06$) entrained from a certain zone in the D-LE-D034b and D-CF-D068 simulations. The time scale is t_0=0.32 s. a) Zone 1; b) Zone 2; c) Zone 3; d) Zone 4. 474

Figure 6.32 Comparison between the time variations of the flux of sediment particles of diameter $d=50\mu m$ ($u_{\tau c}/u_b = 0.06$) entrained from a certain zone in the D-CF-D068 and D-CF-D137 simulations. The time scale is t_0=0.32 s. a) Zone 1; b) Zone 2; c) Zone 3; d) Zone 4. 475

CHAPTER 1 INTRODUCTION

1.1 Background

Gravity currents are mainly horizontal flows moving under the influence of gravity and generated by density differences within a fluid or between two fluids. Gravity currents contain a front region usually called the head, a dissipative wake region in which Kelvin-Helmholtz billows are shed, and a tail (Figure 1.1). The last two regions form the body of the current. The motion of the fluid behind the head depends on the slope of the bed and can be approximated with a modified form of the Chezy equation describing flow in open channels using the reduced gravity. The buoyancy flux into the head increases with increasing slope.

Gravity currents occur widely in nature. Figure 1.2 shows several examples. The presence of density differences of only a few percent can be enough to induce a gravity current that travels over very long distances. Predicting the evolution of turbulent gravity currents is of great interest in many areas of geophysics and engineering, in particular due to their impact on the environment (e.g., see Fannelǿp, 1994 and Simpson, 1997).

For example, erosion by gravity currents is one of the main causes for formation of submarine canyons on continental slopes and plays a determinant role in transporting sediments from shallower to deeper regions in water environments. The propagation of a gravity current is often accompanied by disastrous damage. The result of the impact between a gravity current and a submarine structure (e.g., dams, porous screens, dikes, oil and gas pipelines, wellheads and submarine cables in deep environments) can result in an environmentally hazardous situation (Blanchette et al., 2005). This justifies the interest in studying the structure of these currents and their dynamic effects on various obstacles. To be able to predict the capacity of a turbulent gravity current propagating over a loose bed to entrain, carry, and deposit sediment requires a detailed understanding of its structure and the role played by the large-scale instabilities present in the flow.

Examples of gravity currents in the atmosphere include sea breezes, and other phenomena in which cold air intrusions form. Other examples include powder-snow avalanches in mountainous terrains. Even the propagation of lava of an erupting volcano and mudflows can be considered as gravity currents. The presence of dissolved substances that modify the fluid density (e.g., salt in water or hazardous materials) can also lead to the formation of intrusive or bottom propagating gravity currents. As fresh water from rivers or fjords comes into contact with marine water, gravity currents can form along the surface. Oil spillage on the sea surface, accidental release of dense industrial gases, and spreading of hot water discharge from power stations are other examples of gravity currents relevant for engineering and geosciences applications (Simpson and Britter, 1979).

Gravity currents can be classified as *continuous or discontinuous* depending if the source of heavier fluid is continuous or not. Depending on the stratification of the ambient fluid in which they propagate and of their density, they can propagate along the bottom of the channel (*bottom-propagating* currents) or as an intrusion at a certain distance from the bottom (*intrusive currents*). If the source of the density difference is the result of spatial heterogeneity of temperature, salinity or other fluid variable affecting the fluid density, then gravity currents are classified as *compositional*. When the formation of gravity currents is due to density differences resulting from differential particle loading (e.g., due to sediment particles, dust particles, snow flakes) then gravity currents are classified as *particulate or turbidity currents*.

Turbidity currents are often the main transport medium for suspended sediments in reservoirs. They largely contribute to the redistribution of the sediments within reservoirs by entraining sediment particles and carrying them to the deepest areas of the reservoir (Oehy, 2003). Though the present work considers only compositional Boussinesq gravity currents, some of the findings are also relevant for turbidity currents that can be modeled using the Boussinesq approximation. This is true especially for the case of low-concentration turbidity currents (particle concentrations lower than 5% by volume) which have low net exchange sediment rates with the bottom (loose) boundary and for many cases in which the interest is in quantifying the interaction (e.g., impact forces) between the gravity current and an obstacle.

For instance, in the operation of lock facilities in an estuarine environment, a salinity driven gravity current forms when the lock gate opens. Each time the facility is operated, a finite-volume of saline water is released. As the saline current propagates in the river, it entrains sediment. As a result, a turbidity current forms. The turbidity current can carry the entrained sediment over considerable distances from the entrainment location before it dissipates and sediment is redeposited.

Moreover, the loose bed surface over which the gravity current propagates in the environment is often not smooth or flat. Bed forms, typically in the form of ripples, dunes or anti-dunes are present at the seafloor or river bed. The presence of bed forms and topographic bumps or of a vegetation layer leads to an additional net drag force which slows down the gravity current (Hatcher et al., 2000). The presence of large-scale bedforms provides an additional mechanism for energy dissipation and can substantially modify the capacity of a compositional gravity current to entrain sediment with respect to the case of a flat bed. The lower values of the front velocity during the slumping phase and the faster decay of the front velocity during the turbulent-drag dominated regime reduces the overall capacity of the gravity current propagating over a rough surface to entrain sediment compared to the case of a current propagating over a smooth surface. Unfortunately, not much is known on the interaction of gravity currents with bed morphology. Quantifying the sediment entrainment capacity of the compositional gravity current as it propagates over the loose bed is a first step toward understanding the mechanisms for the formation of the turbidity current induced by the passage of the compositional gravity current and predicting the sediment transport and bed morphology changes downstream of lock facilities.

The interaction between a compositional or particulate gravity current and an array of obstacles is another class of important applications. Arrays of obstacles are often used as protective measures on the hilly terrains and on the skirts of the mountains to stop or slow down gravity currents in the form of powder-snow avalanches (Hopfinger, 1983). Such powder-snow avalanches were responsible for serious damage to a number of towns located at the foot of steep slopes (Johannesson et al., 1996). Even if they do not arrest the flow, the retarding obstacles reduce the impact of the avalanche with the buildings situated downstream of the obstacles. Similarly, defense structures such as baffle blocks are designed to slow down gravity currents in river environments (e.g., they can be used as buffers upstream of dams). Other relevant examples of gravity currents interacting with a rough surface or a porous layer include high Reynolds number gravity current flows in rough wall fractures, gravity currents propagating over a layer of vegetation (e.g., grass, marine plants, trees), and dense gas flows through wooded or built-up areas. The proper design of these flow-retarding structures requires detailed information on the maximum forces and moments as well as on their temporal evolution.

The interaction of gravity currents with isolated obstacles has many engineering and environmental applications. The presence of obstacles may act as flow control devices that can trigger a change in the flow regime within the current (e.g., from subcritical to supercritical depending on whether or not the speed of the current is greater or less than the speed of the gravity waves propagating along their interface with the ambient fluid). Moreover, for obstacles of arbitrary shapes, or situated at an oblique angle with the front of the incoming gravity current, the flow past and around the obstacle, and the reflected hydraulic jump can get very three-dimensional even if the on-going flow is two-dimensional. These situations arise often in estuarine mixing (Kneller et al., 1991).

One of the most popular ways to control the sediment depositing in reservoirs is the construction of obstacles such as submerged dams on the path of the gravity current (Oehy and Schleiss, 2007). Therefore, the effect of such obstacles on reservoir sedimentation due to gravity currents is an important area of research. As in most cases these submerged dams are built from erodible material, information on the dynamic loads and their time scales and on the shear stress distribution over the dam surface is important to properly design these structures. Barriers are also built to impede the propagation of gravity currents in situations when accidental emissions of heavy hazardous gases have to be contained over a short distance from the emission source (e.g., Rotmann et al., 1985). The interaction of sea breezes with hills and of turbidity currents with oil and gas pipes situated close to the seabed are other important examples of a gravity current interacting with an obstacle.

1.2 The Role of High-Resolution Eddy-Resolving Numerical Simulations

Studying gravity currents in the field is in most cases very difficult. Often, these currents develop in remote and hostile environments (e.g., in the deep part of large rivers, lakes and oceans). Gravity currents on the bottom of large rivers and oceans occur infrequently and monitoring equipments are hard to install and to protect from the impact with the current. Thus, most of the information on the structure and evolution of gravity currents comes from laboratory experiments conducted at much smaller Reynolds numbers (e.g., Stacey and Bowen, 1988, Kneller et al., 1998, Baas et al., 2005, Gray et al., 2006). It is not very clear how much of the information obtained from these laboratory experiments is applicable to gravity currents forming in large bodies of air and water (geophysical scale). Moreover, detailed measurements of the velocity and density fields within the gravity current are seldom available from laboratory and in situ studies. Basically, no such information is yet available for the case of gravity currents propagating over non-flat surfaces. Information on the turbulent structure of the current, in particular on the role of coherent structures in the entrainment of the sediment particles from the loose bed, is of great interest. Knowledge of the spatial and temporal distributions of the bed shear stress is essential to determine the amount of sediment entrained and carried by a compositional or turbidity current propagating over a loose bed. This kind of information can be used in simpler models that try to predict the sediment entrained by the current in an integral sense and to qualitatively understand the way the sediment is entrained. Unfortunately, measurements of the instantaneous bed shear stress distributions are nearly impossible to achieve experimentally.

High-resolution three-dimensional (3-D) simulations using the Direct Numerical Simulation (DNS) and Large Eddy Simulation (LES) techniques offer a way to obtain this information. Such simulations can accurately capture the temporal development of the lobe and cleft instability at the front, the formation and breaking of the interfacial billows into smaller 3-D eddies at the current interface, and the interaction among the near-wall turbulent structures that are present in high Reynolds number currents (e.g., see Figure 1.3). 3-D eddy-resolving numerical simulations have the advantage that allow a detailed visualization and understanding of the turbulent structure of the gravity current and obtaining the concentration and bed shear stress distributions during the evolution of the current. Finally, information on the global energy balance at different stages of the evolution of the current are quite difficult to obtain experimentally. High-resolution numerical simulations can provide this information.

The use of LES allows to study the physics of gravity currents at Reynolds numbers that are above the range at which most experimental studies are conducted ($Re=10^3-10^5$). The upper limit is mainly a result of the limitations in the physical length of the channels in which these currents develop and the properties of the fluids employed in the experiments. As such experiments most often use common fluids (water), it is generally not possible to maintain all the dimensionless parameters within ranges appropriate for modeling gravity current flows at field scale. Generally, some parameters are maintained within a critical range (e.g., experiments are conducted at Reynolds numbers that are large enough for the current to be turbulent) while others are relaxed (e.g., scaling of particle size and settling velocity in the case of turbidity currents, scaling of small-scale bedforms that increase the bed roughness). Though in LES simulations conducted at $Re>10^5$ the flow is not as well resolved as in simulations conducted at laboratory scale, these simulations can help to better understand the physics of finite-volume lock-release currents and their interactions with obstacles for flow conditions that are closer to the inviscid state that is often assumed in theoretical models, and to conditions encountered in practical applications in rivers, lakes and oceans.

The focus of this study is on highly turbulent gravity currents (Re>10^4). 3-D LES simulations can resolve the dynamically important eddies in the flow, similar to DNS, but are computationally much less expensive at high Reynolds numbers. A 3-D DNS simulation at Re~10^4 using a non-dissipative method would require an increase of the number of mesh points by at least one order of magnitude compared to the mesh used in an LES simulation. The difference in the computational resources needed to perform LES and DNS simulations increases even more at higher Reynolds numbers. For example, the mesh size needed to perform a DNS at Re=10^6 will be about three order of magnitude higher than the mesh size required by LES. The increase in the computational resources needed to perform such a DNS simulation will be even higher, as smaller time steps have to be used in DNS. Thus, such DNS simulations are outside the reach of today‟s supercomputers. 2-D DNS and LES simulations are about two orders of magnitude less expensive than the 3-D simulations in terms of computational resources, but their ability to accurately capture the structure of high-Reynolds-number gravity currents past the initial stages of the slumping phase is limited (Ooi et al., 2009).

As will be discussed in Chapter 3, the LES solver employed in the present work uses a non-dissipative method and a dynamic Smagorinsky subgrid-scale (SGS) model to account for the effect of the unresolved scales. The use of a dynamic procedure allows the estimation of the eddy viscosity and eddy diffusivity based on the flow physics (information from the smallest resolved scales) and to reduce to a minimum the dissipation added to the resolved scales. This means that the resolved scales can be computed accurately. Still, compared to well-resolved DNS, in which all the scales up to the dissipative range are resolved by the simulation, LES contains a certain amount of empiricism related to the use of a SGS model.

Use of Reynolds-Averaged Navier-Stokes (RANS) models would allow performing simulations on even coarser meshes but, due to the very dissipative nature of these models, the large-scale structures in particular in the near-bed region cannot be accurately resolved. Thus, LES with a dynamic SGS model offers one of the best alternatives for the study of the physics of high-Reynolds-number gravity currents using numerical simulations.

1.3 Description of Problems

This study mainly considers gravity currents in lock-exchange configurations in which the current is generated by the instantaneous removal of a vertical lock gate separating two fluids at rest and of different densities in a straight horizontal channel of rectangular section. A rear wall is present at one end of the channel. The heavier lock fluid initially occupies the volume between the rear wall and the lock gate (Figure 1.4). When the lock-gate is removed instantaneously, a bottom current containing heavier lock fluid (forward propagating in Figure 1.4) and a surface current containing lighter fluid (backward propagating in Figure 1.4) form.

This is a configuration that is directly relevant for the case of lock facilities in estuarine environments in which a finite volume of heavier lock fluid is released into the lighter ambient fluid each time the lock is opened. One should also mention that most of the fundamental understanding of the physics of gravity current flows came from the study of gravity currents in lock-exchange environments. This is why the present study focuses on this case.

However, especially in rivers, gravity currents propagate within the turbulent channel flow. This problem is more complex and adds several new parameters that can influence the evolution of the gravity current propagating over flat or rough surfaces (e.g., the ratio between the mean channel velocity and the buoyancy velocity, the shape of the mean velocity profile in the channel, the turbulence intensity of the channel flow, etc.). This case is not considered in the present study.

The focus of this study is on the case relevant for practical applications in river and ocean engineering in which the flow in the region behind the front of the gravity current is strongly turbulent. A gravity current is considered highly turbulent if velocity spectra contain a clear inertial range as the upstream part to the current is convected over streamwise locations situated at a sufficient distance from the lock gate. The threshold value in terms of the minimum value of the Reynolds number, Re, defined with the gravity current depth and buoyancy velocity for the inertial range to develop is around 10^4. Above this Reynolds number, the turbulence inside the near-bed region situated beneath the current head and part of the tail is similar to that in a fully turbulent boundary layer over a no-slip wall.

The lock-exchange flow is dominated by two instabilities: the predominantly 2-D Kelvin-Helmholtz instability at the interface between the heavier lock fluid and the lighter ambient fluid, and the 3-D lobe-and-cleft instability at the front (e.g., see Figure 1.3). This study considers only the case of small enough density differences between the two fluids such that the Boussinesq approximation is valid. For the Boussinesq case, the front speeds of the heavier and lighter currents forming once the lock-gate is removed are equal. In lock-exchange flows, most of the mixing takes place along the interface between the two fluids. The Kelvin-Helmholtz billows shed behind the head play a primary role in the mixing between the two fluids (Britter and Simpson, 1978).

A large number of experimental and theoretical studies were conducted to investigate the evolution of gravity currents propagating over a flat bed and to measure and predict the front velocity, the height of the head region and other integral quantities of interest (see discussion in Chapter 2.1.1). The present investigation focuses on the case in which large-scale roughness elements or isolated obstacles are present at the channel bottom. This study considers only two-dimensional flows in which the front of the incoming gravity current is parallel to the axes of the obstacles and large-scale roughness elements. Though the average flow is two-dimensional, fully 3-D simulations are performed to capture the large-scale instabilities and dynamics of turbulent structures.

In particular, the present study considers two distinct cases in which gravity currents interact with obstacles. The case in which the gravity current propagates over an array of dunes or ribs (Figure 1.5) is representative of cases in which the current propagates through a spatially extensive region containing obstacles (some refer to this region as a porous layer by analogy with the case in which the roughness elements or obstacles are arrays of cylinders mounted on the bed) such that, under certain conditions, the drag induced by the obstacles can dominate the dynamics of the evolution of the current. Of particular interest is the evolution of currents during the turbulent-drag dominated regime in which the decay of the front velocity is faster ($U_f \sim t^{-1/2}$) than that observed over the buoyancy-inertia regime ($U_f \sim t^{-1/3}$). Very little is known about the flow and turbulence structure during this regime.

Depending also on the form of the obstacles, the denser part of the flow is likely to behave more differently than the mixed layer above it and some of the denser fluid may get arrested in between the crests of two successive bedforms. In the case of relatively large obstacles compared to the height of the current, the hydraulic jumps generated close to the crest of each obstacle and moving upstream may strongly disturb the propagation of the flow inside the body of the current. It is possible that under certain conditions flow decoupling may occur, by this one means that the initial gravity current will break into a series of gravity currents.

The case in which the gravity current propagates over an isolated obstacle representative of a submerged dam is representative of cases in which the gravity current propagates past a localized porous barrier or region containing obstacles or a patch of large-scale roughness. In this case the presence of an obstacle of height comparable to that of the incoming current can partially arrest the flow. A fraction of the flow is convected over the barrier/obstacle (also through the barrier if the region containing the obstacles is porous, e.g., a localized patch of vertical cylinders) while the other part is blocked by the obstacle. This blockage induces the formation and upstream propagation of a weak hydraulic jump (Lane-Serff et al., 1995).

1.3.1 Gravity currents with a large volume of release propagating over an array of obstacles

In the first part of this study 3-D LES simulations of bottom propagating gravity currents are performed to understand how the presence of large-scale bedforms in the form of 2-D dunes and 2-D square ribs affect the physics of the flow with respect to the base case in which the gravity current propagates over a flat bed. The full-depth release case in which the initial height of the lock fluid, h, is equal to the channel height, H, is studied. This part of the study considers only on the case in which the initial aspect ratio of the lock fluid $R=h/x_0$ (x_0 is the distance between the rear wall and the lock gate) is much smaller than one (initial volume of release is very large) and the channel is long enough to avoid interactions of the gravity currents with the end walls during a large interval of time (Figure 1.4).

The evolution of the gravity current is investigated at relatively large Reynolds numbers during the short initial acceleration phase and during the slumping phase in which the front velocity of the current, U_f, can be considered approximately constant. The non-dimensional front velocity expressed as a Froude number $Fr_f=U_f/u_b$ ($u_b = \sqrt{g'h}$ is the buoyancy velocity and g' is the reduced gravity) is dependent on the Reynolds number (Re= $u_b h/\nu$, where ν is the molecular viscosity) which is related to the ratio of buoyancy forces to viscous forces. Experiments have shown that the non-dimensional front velocity of full-depth lock-release Boussinesq currents propagating over a flat smooth surface increases with the Reynolds number and eventually approaches the theoretical value corresponding to Benjamin‟s (1968) half-depth solution.

The range of Reynolds number considered in this study is 10^4 to 10^6. At Re~10^6, the current is relatively close to the inviscid state often assumed in theoretical models. The ratio of the maximum height of the roughness element, D, to their wavelength λ is equal to 0.05 (Figure 1.5). Two relative heights of the dunes and ribs (D=0.15H and D=0.3H) are considered in the study. The shape of the dunes is identical to the 2-D dunes used in the experiment of Mierlo and de Ruiter (1988). The simulations are conducted with no-slip boundary conditions at the bottom and top surfaces. The initial lock gate position is at x/H=0. To maintain the anti-symmetry of the solution, the obstacles are positioned on the bottom surface in the region with x/H>0 and on the top surface in the region with x/H<0.

The main variables governing the evolution of the gravity current for the configuration considered in this section are the height of the channel H, the height over which the lock gate is removed at the start of the lock exchange flow, h, the length of the initial volume of lock fluid, x_0, the fluid molecular viscosity, ν, the fluid molecular diffusivity, α, the density of the lock fluid, ρ_1, the density of the ambient fluid, ρ_0, the maximum height of the roughness element, D, the distance between two consecutive roughness elements or the wavelength, λ, and the shape of the roughness element, S. Using the height of the initial volume of lock fluid h as the length scale and the buoyancy velocity $u_b = \sqrt{g'h}$ ($g''=g(\rho_1-\rho_0)/\rho_0$) as the velocity scale, the main non-dimensional variables describing the evolution of the gravity current are the Reynolds number Re= $u_b h/\nu$, the Schmidt number, $Sc=\nu/\alpha$, h/H, x_0/h, D/λ and D/h. Assuming an unknown variable, F, is nondimensionalized using the same length and velocity scales, the non-dimensional quantity F'' can be expressed as:

$$F''=f(Re, Sc, h/H, x_0/h, D/\lambda, D/h, S) \qquad (1.1)$$

For the case of full depth release currents h=H, so h/H can be eliminated from (1.1). Also for currents with a large volume of release $x_0 >> h$, and x_0/h can also be eliminated from (1.1). For most practical applications $1<Sc<600$. Previous investigations together with simulation results discussed in Chapter 3.3 showed that over this range the effect of the Schmidt number on the evolution of the gravity current is not very significant. Thus, one can write

$$F''=f(Re, D/\lambda, D/H, S) \qquad (1.2)$$

For example, if the variable F is the front velocity during the slumping phase, U_f, then $F''= U_f / u_b= U_f/\sqrt{g'H}$, which is in fact the densimetric Froude number, Fr. The investigation reported in Chapter 4 focuses on the study of scale effects (Re) and of the relative height (D/H) and shape (S) of the large-scale obstacles on the evolution of the gravity current.

1.3.2 Gravity currents with a small volume of release propagating over an array of obstacles

In the second part of the study gravity currents generated by a small initial volume of release (R=O (1)) are considered. Most of the study concentrates on the partial-depth-release case is studied in which the initial height of the lock fluid, h, is smaller than the channel depth, H (Figure 1.6). The focus is on the evolution of the current containing heavier lock fluid after the lighter (backward propagating) current forming along the top of the channel starts interacting with the rear wall.

As the lighter current starts interacting with the rear wall, it reflects and forms a bore or a hydraulic jump (Figure 1.6b) that propagates in the same direction as the heavier current. The bore speed, U_{bore}, is nearly constant and slightly higher than the front velocity (U_f). Meanwhile, the head of the heavier current propagates with practically constant depth and constant velocity (U_f). For sufficiently high Reynolds numbers, once the bore catches the front (Figure 1.6c), the heavier current transitions to the buoyancy-inertia self-similar phase in which the motion of the current is determined by a balance between the inertial and gravitational (buoyancy) forces, and the front velocity decays with time following a power law ($U_f{\sim}t^{-1/3}$). If the channel is long enough such that viscous effects become dominant, the current will transition to the viscous-buoyancy self-similar phase in which the motion of the current is determined by a balance between the viscous and gravitational forces. The flow at the front decelerates faster as $U_f{\sim}t^{-4/5}$ (see Huppert, 1982, Rottman and Simpson, 1983). The buoyancy-inertia phase may not be present if the Reynolds number is sufficiently low (Rottman and Simpson, 1983, Cantero et al. 2007).

In the case in which the bed surface is rough or a porous layer (e.g., vegetation layer) is present close to the bed, the volume of release is sufficiently large, and the drag force acting on the gravity current as a result of the presence of a rough bed is significant, a buoyancy-turbulent drag flow regime can be present in between the buoyancy-inertia and the viscous-buoyancy self-similar phases (Hatcher et al., 2000). As the initial volume of release increases (R decreases), the time interval over which the drag-controlled regime is present increases. Over this regime the front speed decreases with time as $U_f \sim t^{-1/2}$. The faster decrease of the front velocity compared to the one expected over the buoyancy-inertia phase is due to the added action of the drag induced by the presence of a deformed surface, a rough bed or a porous layer.

The dimensional analysis undertaken for the case of currents with a large volume of release also applies for the case of currents with a small volume of release. Assuming again that Schmidt number effects can be neglected, any non-dimensional quantity F'' can be expressed as:

$$F''=f(\mathrm{Re}, H/h, x_0/h, D/\lambda, D/h, S) \qquad (1.3)$$

The range of Reynolds numbers considered in the numerical simulations is 10^4 to 10^6. In most of the simulations, the initial aspect ratio of the lock fluid is $R=h/x_0=1.78$. Large-scale roughness elements (bedforms) in the form of 2-D dunes and 2-D square ribs with an aspect ratio $D/\lambda=0.05$ are considered. One simulation is conducted with bedforms having an aspect ratio of 0.1. The height of the dunes and ribs is varied between $0.05(H/2)$ and $0.15(H/2)$. The investigation reported in Chapter 5 focuses on the study of scale effects (Re) and of the relative height (D/h)), spacing (D/λ) and shape (S) of the large-scale obstacles on the evolution of the gravity current.

1.3.3 Gravity currents propagating over an isolated obstacle (submerged dam)

The third part of the study concentrates on investigating the interaction between a bottom-mounted obstacle in the form of a submerged dam and a bottom-propagating gravity current. Both the case of a partial depth release lock-exchange current with a large volume of release (Figure 1.7) and the case of a constant flux current are considered.

The case of a partial blocked flow in which the height of the gravity current is comparable to that of the obstacle is the focus of the present study. In this case, when a gravity current hits the obstacle, part of the flow is convected over the obstacle and reattaches to the bottom wall. The ratio between the gravity current flow convected over the obstacle and the incoming gravity current flow depends on the ratio between the height of the structure, D, and the height of the undisturbed dense fluid layer (gravity current), the ratio between the height of the undisturbed layer and the channel depth and the Froude number of the undisturbed dense fluid layer. As the height of the obstacle relative to that of the incoming current increases, the flux of dense fluid over the obstacle decreases. At some point, depending also on the shape of the obstacle, especially at its upstream side, no dense fluid can pass the obstacle continuously. Part of the initial volume splash may still be convected over a tall obstacle over a finite amount of time. In most cases, the flux of dense fluid past the obstacle is zero if the height of the obstacle is larger than twice the height of the incoming current.

The remaining part of the flow containing denser fluid is reflected back (upstream) in the form of a hydraulic jump. The dense fluid still flows toward the obstacle in the region between the front of the hydraulic jump and the obstacle but with a lower speed compared to that in the gravity current before reaching the obstacle. The influence of the hydraulic jump on the solution is important especially in cases in which the height of the incoming gravity current is comparable to that of the obstacle height. Assuming a constant-flux incoming current or an incoming current with a very large volume of release and a partially blocked flow at the obstacle, the flow around the obstacle becomes quasi-steady after a sufficiently large amount of time. At quasi-steady state the hydraulic jump moves with approximately constant speed and the flux of dense fluid over the obstacle is close to constant.

The presence of the obstacle induces significant changes in the flow and sediment entrainment capacity around the obstacle. Also, in the case of turbidity currents, major changes in the distribution and orientation of the regions of sediment deposit around the obstacle were observed to occur in the case of a partially blocked flow (Alexander and Morris, 1994).

Information on the flow structure upstream and downstream of the obstacle, the proportion of the flow convected over the structure, the variation of the flow regime as the gravity current is convected over the obstacle (e.g., the flow can transition from subcritical on the upstream side of the triangular obstacle to supercritical on its downstream side), the speed of the reflected hydraulic jump and its characteristics (e.g., sharp vs. undular), the depth of the reflected flow, the generation of intensified mixing vortices around the obstacle, and the temporal evolution of the forces and moments on the obstacle are important to properly design these structures and to develop strategies for controlling the interaction of the gravity current with the obstacle. Additionally, information on the front speed of the gravity current that forms downstream of the obstacle is important when the objective of placing the obstacle is to reduce the speed of the incoming gravity current. This is the case when the goal is to protect submarine installations (impact forces are smaller for lower speed currents) or to reduce the erosion capacity of the current in a certain region.

Numerical simulations can be particularly helpful of obtaining relevant information that is difficult to measure experimentally. For example, a detailed characterization of the undular hydraulic jump, observed to form in many cases in which the flow is partially blocked, is still missing (e.g., in terms of the wavelengths). A detailed description of the behavior of the flow during the impact phase when the incoming gravity current slows down and the newly formed jump accelerates up to its final speed is not yet available. Same is true for the dynamics and mixing characteristics of the finite-volume splash forming during the initial impact of the current with the upstream face of the obstacle. This is of particular importance for cases when the obstacles are designed as barriers of currents containing pollutants or hazardous substances.

In most of the simulations a lock exchange configuration is considered (Figure 1.4). The dimensional analysis undertaken for the case of gravity currents propagating over an array of obstacles applies also for the case of an isolated obstacle. An additional variable is the distance between the lock gate and the center of the obstacle, L_0. Assuming again that Schmidt number effects can be neglected, any non-dimensional quantity F'' can be expressed as:

$$F''=f(Re, x_0/h, h/H, D/h, S, L_0/h) \tag{1.4}$$

The shapes of the obstacle considered in the present study are triangular or Gaussian, similar to the ones in the experimental investigations of Lane Serff et al. (1995) and Oehy and Schleiss (2007). If the base of the obstacle is B, then the shape factor S can be replaced by the ratio D/B or by the angle α (Figure 17) defined such that tg α=2D/B. Also, if the initial volume of lock fluid is relatively large (x_0>>h) such that the gravity current is in the slumping phase when it hits the obstacle, then the parameter L_0/h plays a minor role. Thus, in a good approximation one can write

$$F^{``}=f(Re, h/H, D/h, D/B) \tag{1.5}$$

The value of h/H is varied between 0.96 (close to a full-depth-release case) and 0.187 (partial-depth-release case). The base angle of the triangular obstacle, α, is varied between 32^0 and 51^0, corresponding to a doubling in the ratio between the height of the obstacle, D, and its base length, B. The ratio between the height of the obstacle, D, and the gate opening, h, is varied between 0.34 and 0.69. The height of the incoming current is close to *h*/2, thus the current height is close to the obstacle height. The range of Reynolds number considered is 10^4 to 10^6. The height of the obstacle is sufficiently small not to block the incoming current completely.

The case in which a constant flux of denser fluid is introduced at the position of the lock gate is also studied. In this case two additional parameters are the depth of the opening d_0 and the initial velocity of the lock fluid u_0 (Figure 1.7). As a lock release current with an opening of the lock gate of h produces a gravity current of height close to h/2, one can consider that d_0 and h are related quantities. In the case the gravity current is due to a constant flux of lock fluid introduced through an opening, any non-dimensional quantity $F^{``}$ can be expressed as:

$$F^{``}=f(Re, h/H, D/h, D/B, u_0/u_b) \tag{1.6}$$

The flow and geometrical parameters are similar to those considered in the case when the removal of a lock gate was used to induce the formation of the gravity current. Additionally, a simulation of a constant-flux gravity current whose height is significantly smaller than the obstacle (the flow is completely blocked during the initial impact) is run until the region between the inlet section and the obstacle is filled with denser fluid, up to a level situated close to the top of the obstacle. After some time, a quasi-steady flow establishes over the obstacle and some distance downstream of it. Such a regime can occur in practical applications when a constant flux gravity current is convected over a tall submerged structure over large periods of time (e.g., in case of flooding events lasting over large time intervals). Knowledge of the forces on the obstacle and information on the sediment entrainment capacity of the current around the position of the structure is essential to properly design the structure and evaluate the impact of the presence of the structure on sediment transport.

1.3 Research Objectives

The major research objectives of this study are:

- Developing insight into the flow physics of highly-turbulent Boussinesq compositional gravity currents in lock-exchange configuration propagating over an array of large-scale roughness elements or obstacles in the form of dunes and ribs. Comparing the changes that occur with respect to the case the gravity current propagates over a smooth flat bed. Study these changes for the case of currents with a large volume of release during the slumping phase and for the case of currents with a small volume of release for which the buoyancy-turbulent drag flow regime is reached. Studying the impact of the bed topography on sediment entrainment capacity due to the passage of a compositional gravity current.
- Understanding the flow physics at different stages of the interaction of a compositional gravity current with an isolated submerged obstacle representative of a submerged dam. Determining the characteristic times and magnitudes of the hydrodynamic impact forces

over the different flow regimes characterizing the impact of the current with the submerged obstacle.

- Understanding how the shape and the relative size of the large-scale roughness elements and of the submerged obstacle affect the structure of the current, the energy balance, the bed shear distributions and sediment entrainment capacity of the current as it propagates over a loose channel bottom.
- Understanding scale effects between Reynolds numbers at which most of the laboratory studies are conducted ($Re \sim 10^4$) and Reynolds numbers that are within the lower range of those encountered in the field ($Re=10^6$). At these higher Reynolds numbers the structure of the gravity current is thought to be relatively close to the one in an inviscid current.
- Describing the temporal evolution of the drag forces acting on the ribs and submerged dam. Understanding how this variation is related to the different flow structures that develop within the flow and the physical mechanisms behind the formation of such structures.

The outline of the thesis is as follows. The relevant theoretical models, experimental and numerical studies are summarized in Chapter 2. The numerical method is presented in Chapter 3. Previous validation studies of gravity current flows performed using the same flow solver are discussed. The same chapter discusses the effect of the Schmidt number and grid dependency studies. Chapter 4 presents the main results obtained for compositional gravity currents with a high volume of release propagating over a surface containing large-scale bedforms. Chapter 5 presents the main results obtained for compositional gravity current with a small volume of release propagating over a surface containing large-scale bedforms. Chapter 6 presents the main results obtained from cases of compositional gravity current – submerged dam interaction. The focus is on the effect of the shape and relative size of the obstacle and Reynolds number scale effects on the structure of the current, development of the flow instabilities, front velocity, energy budget, dissipation rate and bed shear stress distributions. Chapter 7 gives the conclusion of the study and suggests some future on the subject.

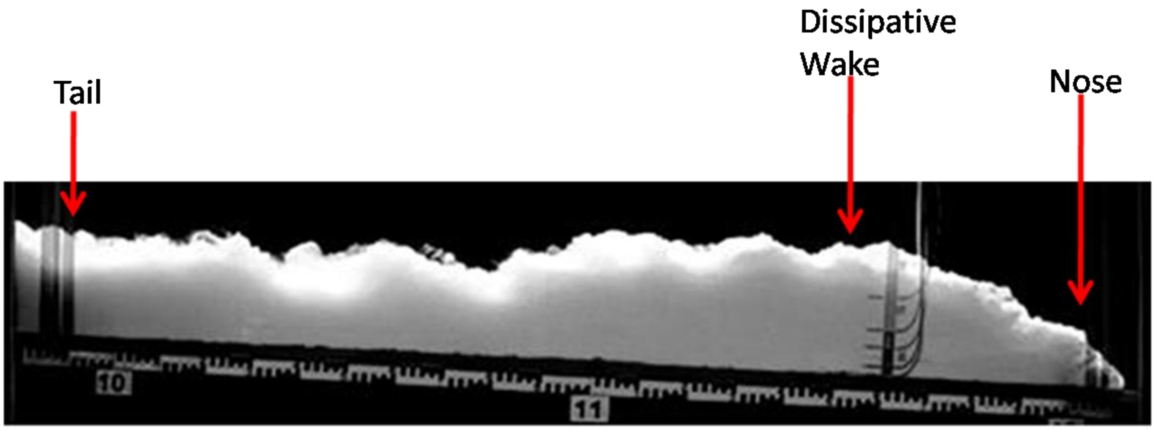

Figure 1.1. Picture of a gravity current showing the head, dissipative wake and tail regions from the experimental study of Sequeiros et al. (2009) on self-accelerating gravity currents in slightly tilted channels.

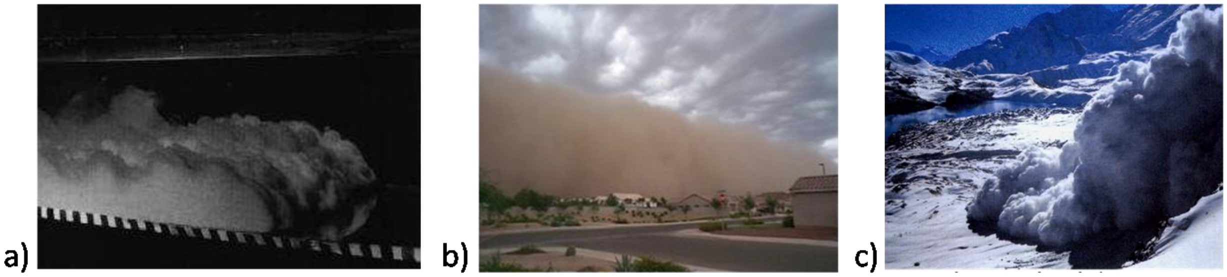

Figure 1.2. Visualization of gravity currents in the environment. a) salinity current (Simpson, 1987); b) morning glory phenomenon, an example of a temperature driven gravity current, c) snow-powder avalanche, an example of particle-laden gravity current.

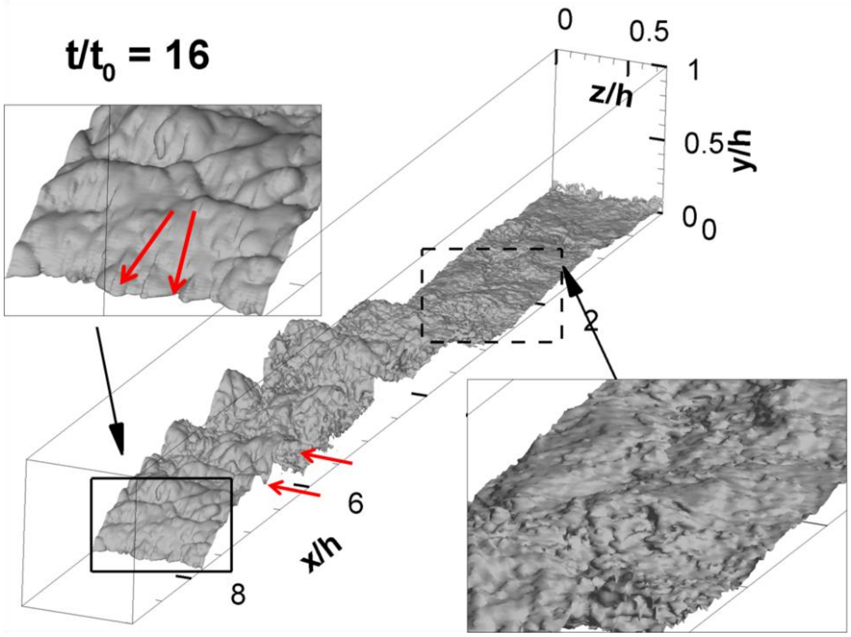

Figure 1.3. Visualization of the interface of a bottom propagating gravity current from the 3-D LES simulation (Re~47,750) of Ooi et al. (2009) using a concentration isosurface. The red arrows point toward the lobes and clefts at the front of the current and the interfacial Kelvin-Helmholtz billows forming behind the head.

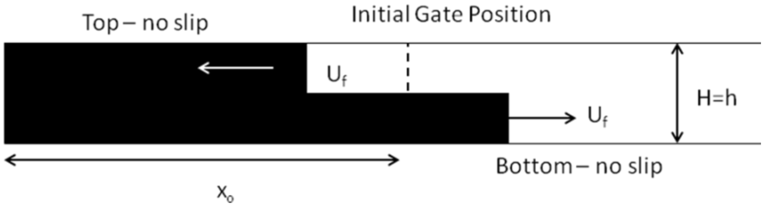
Top – no slip
Initial Gate Position
U_f
U_f
H=h
Bottom – no slip
x_o

Figure 1.4. Sketch of the flow during the slumping phase for the case of a full depth release lock-exchange flow. The gate is positioned far from the extremities of the channel ($x_0/H>>1$). The evolution of the forward and backward propagating Boussinesq gravity currents is anti-symmetric.

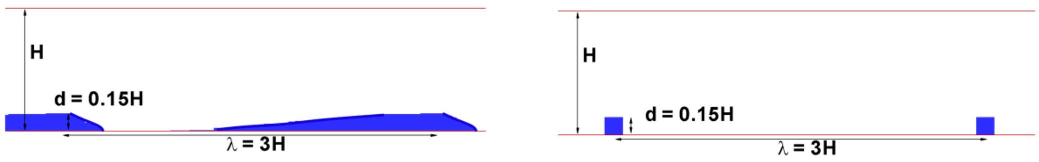
H
d = 0.15H
λ = 3H
H
d = 0.15H
λ = 3H

Figure 1.5. Sketch showing relative dimensions of the 2-D ribs and dunes used in the simulations.

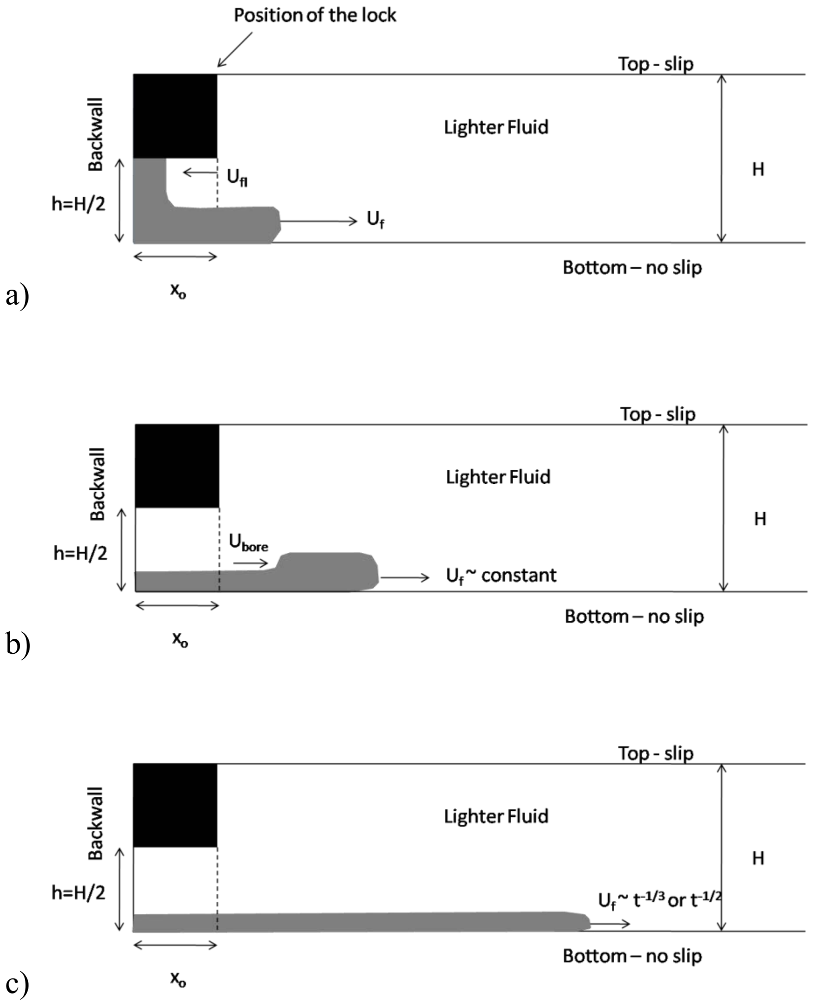
Position of the lock
Top - slip
Lighter Fluid
Backwall
U_{fl}
U_f
H
h=H/2
Bottom – no slip
x_o
a)
Top - slip
Lighter Fluid
Backwall
U_{bore}
U_f~ constant
H
h=H/2
Bottom – no slip
x_o
b)
Top - slip
Lighter Fluid
Backwall
H
h=H/2
U_f~ $t^{-1/3}$ or $t^{-1/2}$
Bottom – no slip
x_o
c)

Figure 1.6. Sketch of the computational domain and flow for the partial-depth lock-release cases. a) slumping phase before the backward propagating current starts interacting with the rear wall; b) slumping phase after bore formation; c) buoyancy-turbulent drag or buoyancy-inertia self-similar phase. The buoyancy-turbulent drag regime can be present only if the bottom boundary is rough.

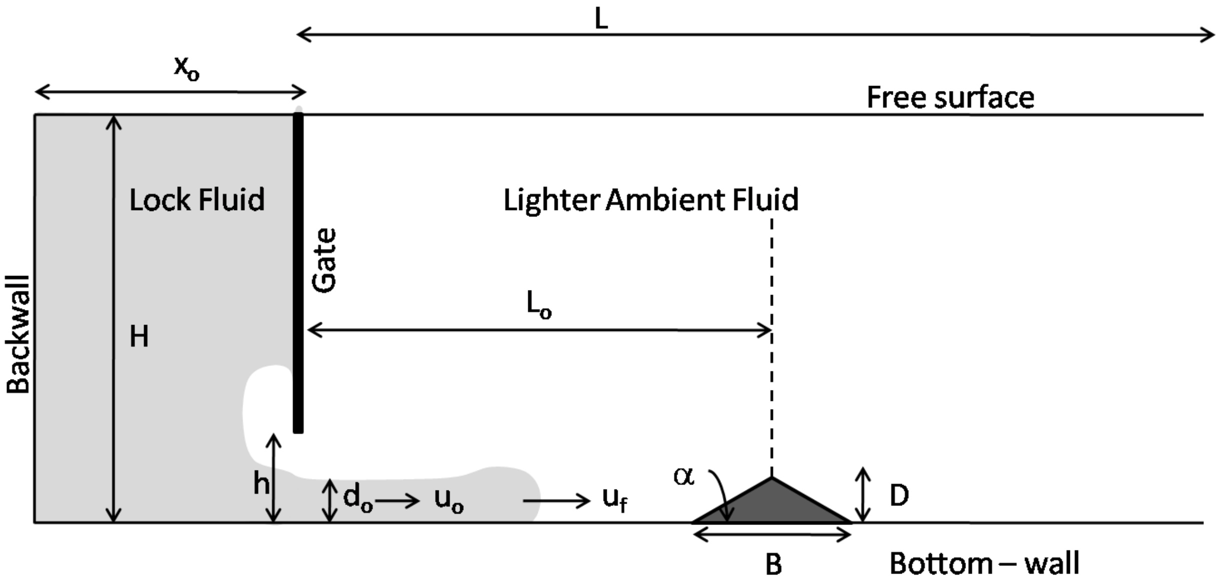
L
x_o
Free surface
Lock Fluid
Lighter Ambient Fluid
Gate
Backwall
L_o
H
h
d_o
u_o
u_f
α
D
B
Bottom – wall

Figure 1.7. Sketch of the computational domain for the case of a lock-release gravity current interacting with a bottom obstacle corresponding to a submerged dam.

CHAPTER 2 LITERATURE REVIEW

2.1 Theoretical and Experimental Studies

2.1.1 Gravity currents propagating over a flat surface

The first theoretical attempt to study these flows came from Von Kármán (1940) who used potential flow theory to describe the spreading of gravity currents. His study showed that the mean front velocity of a gravity current with density ρ_1 propagating into a lighter ambient fluid of density ρ_o is proportional to the square root of the reduced gravity, $g' = g(\rho_1 - \rho_o)/\rho_o$ and the front height h_F. Later, Benjamin (1968) deduced the proportionality factor for the case of an inviscid current propagating into a deep ambient.

A large number of experimental and theoretical studies were conducted to isolate the various mechanisms that drive gravity currents in lock-exchange flows and predict the temporal evolution of global parameters such as the front velocity, the height of the head region, etc. Most of these studies considered the case of low-density differences where the Boussinesq approximation is valid (e.g., Benjamin, 1968; Simpson, 1972; Britter and Simpson, 1978; Simpson and Britter, 1979; Huppert and Simpson, 1980; Huppert, 1982; Keller and Chyou, 1991; Hallworth et al., 1996; Shin et al., 2004).

The study of Simpson and Britter (1979) was one of the first to allow a detailed description on the motion behind the head of the gravity current. An apparatus that brought the gravity current to rest by using an opposing flow and a moving floor was used in their experiments (see Figure 2.1). The front velocity, the rate of mixing between the two fluids and the depth of the mixing layer region behind the head were estimated for a range of dimensionless gravity current heights. The height of the head region and the front velocity showed a strong dependence on Reynolds number for Re<$O(10^3)$. They found that that most of the mixing occurs along the interface between the two fluids.

Several other experimental studies also showed that the effects of the Reynolds number on the evolution of the gravity current can be important. For example, Parsons and Garcia (1998) found the entrainment of ambient fluid into the head region is dependent on the Reynolds number defined with the cube root of the buoyancy flux into the head. Ellison and Turner (1959) found that the entrainment into the body of the current is function of the Richardson number. Later, Parker et al. (1987) proposed an empirical relationship, based on experiments with turbidity currents, to estimate the mean entrainment velocity based on the value of the Richardson number. Linden and Simpson (1986) have shown that the mixing behind the head significantly affects the dynamics of the current. For example, in one of their experiments they demonstrated that the current is destroyed once the denser fluid is vertically mixed with the lighter ambient fluid through turbulence; the turbulence within the flow was added by bubbling air.

The vertical structure of gravity currents was investigated by Stacey and Bowen (1988). They found the structure of the mean streamwise velocity profile over the depth consists of an inner layer close to the bed in which the velocity gradient is positive and an outer layer, 5-10 times thicker than the inner layer, in which the velocity gradient is negative and the primary shear stress changes sign. The inner layer resembles a turbulent boundary layer while the outer layer can be described as a shear layer. Experimental investigations found that the turbulent kinetic energy (tke) decays to very small values at the vertical location corresponding to the maximum in the mean streamwise velocity profile. This indicates that shear associated with the vertical variation of the streamwise velocity profile is the main contributor to the total turbulence production.

Kneller et al. (1999) used 2D laser-Doppler anemometry to study the velocity and turbulence within lock exchange gravity currents. They observed the velocity maxima occurred at a distance from the bed equal to one fifth of the current height. They found that the velocity profile within the current can be approximated using the law of the wall up to the location of the maximum in the vertical profile of the mean streamwise velocity and a cumulative distribution above this level and up to the interface with the ambient fluid. Kneller et al. (1999) also found the regions of high turbulence amplification are determined by the location of the large eddies in the flow. These eddies scale with the flow thickness. They observed that the tke peaks in the interfacial layer at the top of the current and is at a minimum at the interface between the inner and the outer layer. The interface is situated close to the location of the maximum in the mean streamwise velocity profile.

Gray et al. (2006) studied the changes in the structure of saline and turbidity currents that initially propagate over a sloped bed (several bed slopes were considered) and then transition abruptly onto a horizontal bed. They found the presence of sediment particles significantly affect the distributions of the Reynolds stresses in the flow (e.g., Reynolds normal stresses are amplified independently of the gradients of the mean velocity) and enhance mixing with respect to the case of a saline current. They found the deceleration of the current on the horizontal bed is faster in the case of a saline current.

More complicated cases include the propagation of a lock-exchange compositional current into a linearly stratified fluid. This case was studied experimentally and numerically by Maxworthy et al. (2002). The non-Boussinesq case was investigated experimentally by Keller and Chyou (1991), Grobelbauer et al. (1993) and Lowe et al. (2005).

The experiments of Huppert and Simpson (1980) provide the non-dimensional front velocity for gravity currents in environments of finite depth, function of the ratio between the current thickness (front height) and the flow depth. Shin et al. (2004) extended Benjamin‟s model for shallow currents (e.g., produced by partial-depth releases). As discussed by Shin et al. (2004), full-depth lock-release experiments with high Reynolds number gravity currents showed that the front velocity during the slumping phase was consistent with Benjamin‟s half-depth solution.

The evolution of lock exchange gravity currents past the slumping phase was studied among others by Huppert and Simpson (1980), Huppert (1982), Rottman and Simpson (1983), Choi and Garcia (1995), Hacker et al. (1996) and Shin et al. (2004). Huppert and Simpson (1980) proposed a box model for finite-volume releases in which the main assumption is that the gravity current advances as a series of boxes of equal volume. Assuming the mass is conserved and neglecting entrainment of ambient fluid, this allows relating the position of the front to the height of the current. Using empirical relations and the conservation of mass, the position of the front and its velocity can be expressed function of time over both the slumping and buoyancy-inertia phases. The resulting expression for the front velocity during the slumping phase, however, predicted a small (power) decay with time instead of a constant value. The expression for the front velocity during the inviscid phase was consistent with the expected power law decay in time with an exponent of -1/3 as predicted by Hoult (1972). Hoult (1972) and Fannelop and Waldman (1972) proposed theories that predicted the evolution of the current during the buoyancy-inertia and viscous-buoyancy self-similar phases.

Several studies of gravity currents developing in horizontal or slightly tilted channels showed that the dynamics of the current can be explained using shallow-water theory if sufficiently accurate front conditions are prescribed for the non-hydrostatic flow at the head of the current. Rottman and Simpson (1983) were the first to propose a shallow water model for compositional gravity currents. Extensions for particulate currents are discussed by Bonnecaze et al. (1993). In these models, the viscous forces are neglected and the pressure is assumed to be hydrostatic. These models assume no mass exchange between the current and the ambient fluid at the top of the gravity current. The flow inside the gravity current is assumed to be well mixed such that the concentration does not depend on the vertical location within the gravity current. For the case of a deep ambient, the model (single-layer shallow water model) neglects the motion of the ambient fluid over the top of the gravity current. For the case of a shallow ambient, the model (two-layer shallow water model) accounts for the movement of the overlaying fluid layer. The system of governing equations in these models has to be closed by specifying an additional equation relating the front height, front velocity and the reduced gravity.

2.1.2 Interaction of gravity currents with obstacles

Greenspan and Young (1978) studied experimentally the impact of surging fluid in the form of a gravity current against a safety barrier. The experimental measurements of the fraction of the incoming gravity current flow that overruns the safety barrier, total spillage and fluid velocity after collision were compared with theory and numerical simulations. The study analyzed the relationship between the spillage and the inclination of the dyke. A simplified theoretical model allowed them to predict the relationship between the obstacle height and the overflow.

Rottman et al. (1985) studied the impact of a gravity current with a localized solid or porous barrier in the form of a surface-mounted obstacle. In their theoretical model they considered the case when the upper layer of ambient lighter fluid is infinitely deep and stationary. The model predicted the height of the flow behind the hydraulic jump function of the ratio between the height of the obstacle and the height of the incoming gravity current. The model applies for the case the flow is either partially blocked or completely blocked. Experiments were also conducted for the case of solid and porous barriers as well as for the case of a surface mounted cube with varying angle of attach relative to the incoming flow direction. For the case of a completely blocked flow, the model predicted the bulk of heavier fluid should rise to about twice the height of the current when it meets the obstacle (wall), in reasonably good agreement with experiment. They also provided a discussion of the conditions under which the gravity current encountering an isolated 3-D obstacle (cube) will be convected around the obstacle or over it.

Lane-Serff et al. (1995) proposed a shallow water model to predict the proportion of the flow that is convected over the obstacle, the speed of the reflected jump and the depth of the reflected flow for a gravity current propagating over an isolated obstacle, at large times after the impact. Two models were proposed using shallow water theory for the flow of a denser fluid under a lighter fluid past bottom topography (e.g., see discussion in Baines, 1995). Both models assume the energy dissipation is confined to the lower layer. The first model, called 1-1/2 model (the 1/2 signifies the equation of the interface is part of the model besides the equation of motions in the bottom layer), considers the case when the height of the undisturbed dense fluid to that of the lighter upper layer fluid is very small, such that the upper layer of light fluid can be assumed to be stationary. The second model, called 2-layer model, considers the case when the heights of the two layers are of the same order and the equations of motions for both layers have to be considered in the analysis. A variant called the 2-1/2 layer model considers the case in which the free surface above the upper layer of light fluid is accounted for. The model proposed by Lane-Serff et al. (1995) applies for the case in which the two layers of fluid flow in opposite directions such that there is no net flow across a vertical plane. Reference is made to the study by Armi and Farmer (1986) for counter-flowing layers with non-zero net flow and to Baines (1995) for co-flowing layers.

The model predictions were found to give reasonable agreement when compared to data from a set of experiments performed to validate the theoretical models. The experiments studied the propagation of partial depth release lock-exchange currents over a 2-D obstacle of triangular shape (see Figure 2.2). The triangular ridge ran over the whole width of the channel. For cases with total reflection (completely blocked flow) they observed the depth of the reflected bore was 2-3 times that of the incoming current, with a small initial “splash” reaching higher heights. In the case of a partial blocked flow with a relatively large height of the obstacle only the “splash” flow was convected past the obstacle. In all experiments they observed an undular bore to form. By contrast, their theoretical model assumed a sharp jump to form. The flow depth behind the upstream propagating front of the jump was changing slowly and a train of waves was observed at the interface behind the jump. For the partial blocked flow cases where part of the gravity current flow, besides the initial splash flow, was convected over the obstacle, they observed the formation of a high-speed thinner layer of dense fluid over the downstream side of the triangular obstacle followed by a hydraulic jump (similar to a single layer flow over a weir). This is followed by a gravity current propagating away from the obstacle. Experiments showed that when the upper layer is thinner then the return flow is faster. The height of the reflected bore decayed and its speed increased. Also, the flux of dense fluid over the obstacle decreased. The measured speed of the reflected jump was found to be generally smaller than the model prediction. The predictions of the flux of dense fluid over the obstacle were found to be in very good agreement with measurements.

Gonzalez-Juez and Meiburg (2009) extended the 1-1/2 steady shallow water model proposed by Lane-Serff et al. (1995) to investigate gravity currents propagating over surface mounted obstacles (square ridge) for the case of a deep ambient (current height much smaller than channel depth). The model assumes the current downstream of the obstacle as a constant-flux current. The value of the flux in the downstream current is equal to the flux of denser fluid that passes the obstacle. The model can predict the height and front speed of the current forming as a result of the flow being convected over the obstacle. The values of these two variables are function of the Froude number defined with the depth and velocity in the undisturbed tail of the current, upstream of the obstacle and outside the region overtaken by the hydraulic jump (for comparison purposes, the front speed was used instead of the velocity in the tail of the current), and the ratio of the obstacle height to the height of the incoming current before it reaches the obstacle. The model predictions were validated using data from DNS simulations. The model can also predict the maximum drag on the surface mounted square obstacle using information from numerical simulations that showed that the maximum drag is close to the pressure force on the upstream face of the square ridge during the quasi-steady state. The pressure force was estimated using the shallow water model. Model predictions were within 10% of the value obtained from DNS simulations for cases in which the obstacle height was much larger than the thickness of the boundary layer on the bottom wall at the location of the obstacle.

One important limitations of the theoretical models based on shallow water theory is that they cannot obtain a detailed description of the current structure during the impact stage and thus of the time-dependent forces on the obstacle during the times when the peak values are expected.

The temporal variation of the force on rectangular and circular obstacles as a result of their impact with an incoming gravity current was studies experimentally by Ermanyuk and

Gavrilov (2005a, 2005b). The study considered both obstacles mounted very close to the channel bottom and the case when a significant gap was present between the obstacle and the channel bottom. Their study found that the magnitude of the drag force increases exponentially toward a maximum value during the impact stage. Then, they found that the drag force variation goes through a transient phase before reaching a quasi-steady state. In some of the experiments, the ratio between the maximum value of the drag recorded during the impact stage and the value corresponding to the quasi-steady stage was close to two. The drag on the obstacle was found to be dependent on the degree of blocking induced by the obstacle. The experiments provide a comprehensive set of data on the front velocity function of the main flow and geometrical parameters.

The dynamics of salinity currents propagating in a straight channel with a sharp slope change in the channel bottom was studied experimentally by Pantin and Leeder (1987). The study showed a main flow feature is the formation of reflected solitary waves (solitons). Edwards (1993) investigated the formation of bore-like solitary waves that were reflected off laterally extensive ramps.

Alexander and Morris (1995) studied the effect of topographic obstacles on the spreading of high density turbidity currents in the laboratory. Both the case of wedge-shaped obstacles occupying the whole width of the tank and of obstacles of limited extent (e.g., wedge-shaped rectangular obstacles at different angles with the direction of the incoming current flow) was considered. In most of their experiments the width of the lock gate, and thus of the incoming gravity current flow, was smaller than that of the tank in which the obstacle was placed, so the current grew laterally as it was convected downstream. The heights of the obstacles were of the same order as the height of the incoming current. The study also provided information on the sediment deposits around the obstacles, in particular on the formation and characteristics of the thick ridge of deposited sediment in front of the obstacle. Stationary mixed vortices were observed to form upstream and downstream of the obstacle in the region where the current collides with the upstream face of the obstacle and in the region downstream of the obstacle where the flow resembles the one in a hydraulic jump. The variations in the thickness and velocity of the current around the obstacle caused large local variations in the sediment deposit. They observed that the shape of the bed containing sediment deposits around the obstacle was mainly controlled by the shape of the obstacle and the parameters of the incoming gravity current flow, and less by the grain size of the sediment in the turbidity current.

The effect of topographic obstacles on sedimentation patterns from turbidity currents was studied by Bursik and Woods (2000). They studied the changes in the sedimentation patterns induced by a local variation in the channel depth due to the presence of a surface mounted cross-flow ridge and to variations in the channel width (constrictions and sudden openings). They found that as long as the size of the obstacle was not large enough to partially block the flow of heavier particle-laden fluid and induce the formation of a hydraulic jump (bore), the topographic features did not cause a significant change from exponential deposit thinning, even when there was a transition in the flow regime from subcritical to supercritical caused by the topographic feature. The formation of a hydraulic jump and the reduction of the flux of particle-loaded flow over the ridge had a significant effect on sedimentation. For example, the deposit of sediment did not thin with the same gradient on both sides of the ridge. The additional sedimentation observed to occur upstream of the ridge was induced by the reflected part of the current whose sediment load was deposited upstream of the ridge. When a strong upstream propagating bore formed, then the deposit did not thin exponentially.

2.1.3 Gravity currents propagating over rough surfaces

Hopfinger (1983) and Johanneson et al. (1996) provide a discussion of dilute powder-snow avalanches and their interaction with an array of retarding mounds. Such mounds exert a drag force proportional to the square of the flow speed. Based on this finding, Hatcher et al. (2000) developed a theoretical model for gravity-driven flows past arrays of distributed obstacles in which the presence of the obstacles is modeled by a uniform drag force proportional to the square of the velocity and inversely proportional to the mean length scale of the obstacle. The model is based on depth-averaged single-layer shallow-water theory and considers the case of a gravity current propagating into an extensive region containing obstacles or roughness elements so that the turbulent drag induced by the presence of these obstacles can dominate the flow dynamics some time after the formation of the current.

Based on this model, Hatcher et al. (2000) developed a new class of similarity solutions to describe the motions of such planar and axisymmetric gravity currents following finite instantaneous and continuous releases of heavier fluid. In particular they found that for finite (constant) volume instantaneous releases, an intermediate buoyancy-turbulent drag flow regime may be present in between the buoyancy-inertia and viscous-buoyancy self-similar regimes. In this intermediate flow regime the main forces that drive the evolution of the current are the turbulent drag and the buoyancy forces. They found that during the turbulent drag dominated regime the decay of the front velocity is proportional with $t^{-1/2}$ rather than $t^{-1/3}$ as is the case for the buoyancy-inertia regime. They also predicted the approximate time when the gravity current with a finite volume of release was expected to transition to the buoyancy-turbulent drag flow regime and for the time when this regime will end as the current starts transitioning to the viscous-buoyancy regime. Their theory shows that for gravity currents with a relatively large volume of release the turbulent drag dominated regime may be present for a considerable amount of time. The model applies to gravity currents propagating over horizontal and sloped surfaces and is restricted to the case when the depth of the current is much smaller than the channel depth such that the return flow in the upper layer can be neglected.

Finally, they successfully tested their model against a series of laboratory experiments in which a lock-exchange gravity current with a finite volume of release propagated over an array of bed-mounted vertical cylinders (poles) occupying the whole channel depth. In principle the model assumes the volume fraction occupied by the cylinders is much smaller than one, but good agreement with experiment was found for cases when the volume fraction was smaller than 0.3. The model predictions of the nose and shape of the current were found to be in good agreement with experimental measurements.

Tanino et al. (2005) performed an experimental study of gravity currents in lock exchange configurations with a very large volume of release (the evolution of the current in the channel was studied at times before the forward and backward propagating currents start interacting with the lateral walls). The currents propagated through a random array of rigid emergent cylinders that represent a canopy of aquatic plants. The experiments were very similar to those conducted by Hatcher et al. (2000) in terms of the type of roughness elements. They found that the gravity current transitions from the slumping phase to a turbulent drag dominated regime in which the front velocity decreases with time and the shape of the interface changes from being roughly horizontal, before curving sharply in the front region, to a triangular shape (see Figure 2.3). As the drag was increased, the interface gradient at the lock-gate position increased, assuming the same position of the front of the current with respect to the lock gate. This is consistent with the results of Rottman et al. (1985) who observed that for steady gravity currents propagating through screens, the interface gradient at the screen position increased with the increase in the screen drag. As the current advanced, the interface rotated around the mid-depth at the position of the lock gate. In this regime the drag coefficient is essentially inversely proportional to the cylinder Reynolds number (linear drag regime). The transition between the slumping and the turbulent drag-dominated regime was classified function of the dimensionless drag of the array of cylinders. Based on experimental results, a criterion for the formation of a linear interface was proposed based on the values of the Reynolds number defined with the front velocity and the cylinder diameter, and the dimensionless array drag. A theoretical model was developed to predict the temporal variation of the front velocity during the turbulent drag dominated regime. Similar to Hatcher et al. (2000), the model assumes a quadratic drag law. Moreover, they assumed a constant streamwise slope of the interface position (self-similar interface). The decay of the front velocity during the buoyancy-turbulent drag regime predicted by their model was the same as the one predicted by Hatcher et al. (2000). Their experiments confirmed $U_f \sim t^{-1/2}$ during the buoyancy-turbulent drag regime.

Interestingly, Tanino et al. (2005) found an intermediate regime where the Reynolds number was sufficiently high that a nonlinear drag law applies (meaning the drag is not inversely proportional to the cylinder Reynolds number). The interface was at a slight angle to the bed similar to the shape observed in the high Reynolds number simulations of Ooi et al. (2009) for lock-exchange gravity currents with a high volume of release propagating over a flat bed during the slumping phase. This suggest the dissipation in high Reynolds number currents propagating over a flat smooth bed is not negligible as is the case of the classic full-depth-release lock exchange flow that has negligible dissipation, is inertia dominated, and for which the current depth is about half the channel depth. The difference is that in the experiments of Tanino et al. (1995) most of the dissipation is provided by the presence of the cylinders over the whole depth of the channel.

2.2 Numerical Studies

2.2.1 Integral and RANS Models

A larger number of numerical studies have been attempted to complement the information usually obtained from experimental studies. Many of the earlier computational studies (e.g., Jacobsen and Magnussen, 1987; Klemp et al. 1994) employed coarse computational grids and low-order dissipative numerical schemes, coupled with empirical models to predict the evolution of the gravity current. A review of numerical models based on integral models is available in Choi and Garcia (2002). Integral models require additional closure relationships for the bed resistance (e.g., shear stress) and entrainment.

The challenge related to the use of RANS models is that basically all these models are calibrated for fully developed turbulent flows and are not capable of accurately predicting transition and relaminarization, which is essential for simulating lock-exchange flows. They also tend to damp the energy in the interfacial billows and cannot capture the flow instabilities at the bed (e.g., formation of near-bed streaks of high and low streamwise velocity similar to constant density turbulent boundary layers) because of the dissipative character of RANS models.

RANS models were used to model lock-release flows by Chen and Lee (1999), plunging density currents by Bournet et al. (1999) and density currents on a slope by Choi and Garcia (2002). RANS models with a deformable bed were used to study turbidity currents propagating over a loose bed by Kassem and Imran (2004) and by Huang et al. (2005, 2007).

2.2.2 DNS and LES studies of gravity currents propagating over flat smooth surfaces

High-resolution numerical simulations of gravity currents using eddy-resolving techniques have only recently been attempted. Most of these studies are 2-D DNS and use the Boussinesq approximation.

The first 3-D highly-resolved numerical simulation of a Boussinesq gravity current was reported by Härtel et al. (2000a, 2000b), who performed DNS of a lock exchange flow with a large volume of release at a relatively low Grashof number (Re~1,000). The simulation successfully captured the formation of the lobe and cleft instability at the front of the gravity current (see Figure 2.4) and allowed a detailed investigation of the flow topology in the head region. The study highlighted the important role played by the lighter fluid present below the head, in the unstably stratified region between the foremost point and the stagnation point (in a reference system translating with the front velocity). Using stability analysis Hartel et al. (2000b) showed that this region is responsible for the development of the lobes and clefts at the front of the current. Previously (e.g., Simpson, 1972), it was thought that the main reason for the development of the lobe and cleft instability was the thin layer of light fluid pulled underneath the front. 2-D DNS simulations at Reynolds numbers up to 30,000 (Hartel et al., 2000a) showed that the topology of the flow in the head region remained similar to that observed in the 3-D DNS at Re~1,000.

Necker et al. (2002) used 3-D DNS to study several laboratory-scale flows in lock exchange configurations (Re~2,000). The focus of the study was on particle-driven gravity currents. The suspended phase was described in an Eulerian fashion, similar to the case of a compositional gravity current, using a convection-diffusion equation with an additional settling velocity term. While their simulations did not account for entrainment and resuspension of sediment particles at the bed, they found that the largest bed shear stresses are exerted in the initial phases of the propagation of the current by the large Kelvin-Helmholtz billows shed in the dissipative wake region. In the later stages, the largest bed shear stresses are recorded at the front of the current and correlate with the position of the lobes and clefts.

In a related study, Necker et al. (2005) studied the changes in the energy budgets and mixing behavior for lock-exchange currents developing in shallow and deep water environments at Re=O (10^3). Their study provides a detailed analysis of the energy budgets, dissipative losses, influence of initial level of turbulence inside the lock fluid and of the mixing between interstitial and ambient fluid for particle-driven gravity currents. One of their main conclusions was that the two components of dissipation in particle-driven flows, due to gradients in convective velocity field and due to microscopic Stokesian flow around particles, have comparable contributions to loss of overall mechanical energy.

More complex cases, such as eroding resuspending gravity currents on sloped surfaces, and particulate currents over slopes of varying angles were investigated using 2-D DNS simulations by Blanchette et al. (2006) and Blanchette et al. (2005), respectively. Although the governing equations were solved on a Cartesian mesh in a rectangular domain, the influence of the varying bottom slope was accounted for by introducing a spatially-varying gravity vector. The simulation results showed that the particles eroded over the length of the current were transferred gradually toward the head region. Once there, they can lead to an acceleration of the flow and thus induce higher bed shear stresses and create the conditions for the gravity current to become self-sustained. The conditions required to obtain a self-sustaining turbidity current were investigated as a function of slope angle, current height, particle size and particle concentration. The effect of the initial aspect ratio of the current was also studied. The re-suspension process was modeled based on empirical relations determined experimentally (García and Parker, 1993) by means of a diffusive-flux boundary condition for the particles at the bed. Particle-to-particle interactions which can alter the settling velocity and the viscosity of suspension were not taken into account.

Maxworthy et al. (2002) reported 2-D DNS simulations of gravity currents propagating into a stably stratified ambient fluid for Reynolds numbers up to 20,000. Non-Boussinesq lock exchange flows were studied recently using 2-D DNS by Birman et al. (2005) at Reynolds numbers up to 12,000. The simulations successfully captured the head height and the propagating velocity of the light and dense currents. Hallez and Magnaudet (2008) used DNS to investigate the role of confinement and channel geometry on the evolution of lock-exchange gravity current flows.

3-D DNS simulations of Boussinesq gravity currents at Grashof numbers up to three times higher than the one considered by Härtel et al. (2000a) were reported by Cantero et al. (2007) in planar and cylindrical configurations (e.g., see Figure 2.5). As the planform area of the current increases linearly in the case of a planar configuration, and quadratically in the case of a cylindrical configuration, fundamental differences were observed in the spreading rates of the currents in the two configurations. Several simulations with different sizes of the volume of release were conducted to study the evolution of the lock-release current during the initial acceleration phase, the slumping phase, the buoyancy-inertia and the viscous-buoyancy self-similar phases. They found that depending on the Reynolds number and the size of the release, the current may transition from the slumping phase to the buoyancy-inertia phase or to the viscous-buoyancy phase. Their simulations showed a significant increase in the flow three-dimensionality past the end of the slumping phase, and showed the interfacial billows strongly interact among themselves and with the channel bed in a chaotic manner. As a result the front speed can locally increase or decrease. The simulation results showed that the body of the current qualitatively resembles a turbulent boundary layer with quasi-streamwise and inclined hairpin vortices. These structures were observed to have a strong influence on the density field and the interface between the fluids. They also proposed a criterion for the critical Reynolds number needed for the current to transition from the slumping phase to the buoyancy-inertia phase.

Comparison of 2-D and 3-D simulation results showed an increased coherence of the interfacial vortices in the 2-D simulations and an underprediction of the front velocity. The increased coherence is due to the absence of the 3-D break up mechanism.

In another recent study, Cantero et al. (2008) simulated a 2-D current driven by inertial particles at Re~3,000. They assumed pure depositional flow without any resuspension. The migration of particles was quantified by tracing the core of the Kelvin-Helmholtz vortices shed behind the front. 2-D and 3-D simulations of gravity currents in planar and cylindrical configurations were also reported by Patterson et al. (2006) using implicit LES.

Ooi et al. (2007) used high-resolution 3-D LES to study the temporal evolution of symmetric lock-exchange intrusion currents at relatively high Reynolds numbers (Re~38,000) developing into a two-layer ambient fluid with a sharp interface. Two cases were studied in which the density of the lock fluid is equal to the depth-weighted mean of the densities inside the two layers of ambient fluid. In the first one (the so-called doubly-symmetric case) the depths of the two layers of ambient fluid were equal. In the second one the depths of the two layers were different. In both cases the evolution of the current and the quantities describing their propagation during the slumping phase were found to be close to the experimental results of Sutherland et al. (2004) and theory. Experimental observations showed the front continued to propagate for some time after the bore has caught the head region with the same constant velocity observed during the slumping phase. The simulations allowed explaining this phenomenon based on the fact that unmixed lock fluid is still left inside the head region at the end of the slumping phase. This is in contrast to the case of gravity currents propagating over no-slip surfaces. The LES simulations also confirmed that even after the end of the slumping phase the local dissipation rate inside the region of unmixed fluid present inside the head remains very small compared to typical values observed in the interfacial layers behind the head. However, the size of the head and the region of unmixed fluid inside the head and dissipative-wake continue to decrease after the end of the slumping phase. The growth of 3-D instabilities at the front of the intrusion current was observed to generate large-scale structures similar to the lobes observed in the case of gravity currents propagating over a no-slip surface. This confirmed the findings of McElwaine and Patterson (2004) that provide evidence that the instability mechanism responsible for the development of the lobes and clefts is not necessarily related to the presence of a no-slip surface if the Reynolds numbers are high enough. Simulation results showed the dominant wavelength present in the initial growth stages of the 3-D front instability in doubly-symmetric case is about half the one predicted by stability theory for a current propagating over a no-slip surface at the same Reynolds number. The length scales of the front structures during the slumping phase were found to be smaller than the ones observed for currents propagating over no-slip surfaces at the same Reynolds number.

More recently, Ooi et al. (2009) used the same LES solver to study compositional bottom-propagating gravity currents in lock-exchange configurations. The study considered the evolution of Boussinesq gravity currents with a large initial volume of the release ($R<<1$) and with a small initial volume of release (R=O (1)).

The effect of the Reynolds number on the evolution of gravity currents with $R<<1$ during the slumping phase was studied by comparing results from two simulations with Re=3,150, in the range of previous 3-D DNS simulations, and $Re \sim 10^5$, respectively. In the simulation at $Re \sim 10^5$ the flow was strongly turbulent in the regions behind the two fronts. Compared to the lower Reynolds number simulation, the interfacial billows lost their coherence much more rapidly. This resulted in a much faster decay of the large-scales content and turbulence intensity in the trailing regions of the flow. A slightly tilted, stably stratified interface layer developed away from the two fronts. Simulation results showed that the concentration profiles across this layer can be approximated by a hyperbolic tangent function. For the highly turbulent current, the energy budget showed that past the initial stages of the slumping phase the flow reaches a regime where the total dissipation rate and the rates of change of the total potential and kinetic energy are essentially constant in time.

The effect of the initial aspect ratio of the lock fluid on the transition of Boussinesq gravity currents with a small initial volume of the release (R=O (1)) to the buoyancy-inertia self similar phase was studied based on result of several simulations with $3\times10^4<Re<9\times10^4$. Additionally, a calculation at $Re=10^6$ was performed to understand the behavior of a bottom-propagating current closer to the inviscid limit. The LES simulations showed good agreement with the experimental data of Hacker et al. (1996) and correctly predicted a front speed decrease proportional to $t^{-\alpha}$ (the time t is measured from the release) over the buoyancy-inertia phase, with the constant α approaching the theoretical value of 1/3 as the current approached the inviscid limit. At $Re>3\times10^4$, the intensity of the turbulence in the near-wall region behind the front was large enough to induce the formation of a region containing streaks of low and high streamwise velocity (e.g., see Figure 2.6). The streaks were present well into the buoyancy-inertia phase before the speed of the front decayed below values at which the streaks can be sustained. Simulation results showed that the formation of the velocity streaks induced a streaky distribution of the bed friction velocity in the region immediately behind the front. Past the later stages of the transition to the buoyancy-inertia phase, the temporal variations of the potential energy, the kinetic energy, and the integral of the total dissipation rate were found to be logarithmic. Additional 2-D LES simulations of bottom propagating gravity currents in lock exchange configurations for Reynolds numbers up to 10^6 are discussed in Ooi et al. (2006).

The numerical studies of Ooi et al. (2006, 2007, 2009) showed the utility of high resolution LES simulations to study scale effects and the distributions of quantities that are hard to obtain experimentally (e.g., bed friction velocity, dissipation rate, kinetic and potential energy) for lock-exchange gravity currents.

2.2.3 Studies of interaction of gravity currents with obstacles or deformed bottom topography

The effect of the presence of large-scale bed deformations in the form of regular bumps of various shapes and forms on the propagation of a saline gravity current on a sloped surface and the sediment entrainment capacity of the current were studied by Ozgokmen et al. (2004) based on viscous 3-D Navier-Stokes simulations. The model assumed a constant ratio between the vertical and horizontal diffusivities and did not use any model to account for turbulence effects. The length and width of the computational domain were 10 km and 2 km, respectively. The water depth on the sloped surfaced varied from 400 to 1,000 m. The local entrainment rate was calculated empirically based on a modification of a model proposed by Turner (1986). Simulation results showed that a bumpy surface can lead to a significant enhancement of entrainment (30-100%) compared to a smooth surface. In some of the simulations containing bumps, a head region cannot be clearly identified anymore.

Gonzalez-Juez et al. (2009a) performed 2-D DNS simulations of the flow past circular cylinders mounted above a non-erodible channel bed. The study was motivated by the hazard associated with the impact of gravity currents on submarine installations. Consistent with previous experimental investigations (Ermanyuk and Gavrilov, 2005a), the temporal evolution of the drag and lift forces on the cylinder showed the presence of three regimes (impact, transient and quasi-steady). The numerical study allowed an in-depth discussion of the linking between the dynamics of the flow structures and the temporal variation of the lift and drag forces on the cylinder. The case of a partial-depth-release lock-exchange current was considered. 2-D simulations showed that during the quasi-steady regime Karman vortex shedding is present behind the cylinder for sufficiently large gaps between the cylinder and the channel bottom, and for sufficiently large ratios of the channel height and lock height. They also found the shedding frequency and the r.m.s. fluctuations of the lift are comparable to those seen in constant density flow past cylinders placed near a wall. A difference with the case of a constant density flow past a cylinder is the presence of a component of the mean lift due to buoyancy and one due to the deflection of the wake by the denser fluid flow. They also found that for sufficiently small ratios of the channel height and lock height the shear layer between the fluids is strong enough and close enough to the cylinder to cancel the roll up of vorticity of opposing sign on top of the cylinder. As a result, vortex shedding behind the cylinder was suppressed for these conditions.

The conditions under which the use of 2-D simulations is adequate to study gravity current flows past circular cylinders was investigated in a following study by Gonzalez-Juez et al. (2009c) who performed both 2-D and 3-D numerical simulations (2,000<Re<45,000). In their simulations the ratio of the channel height to the lock height was 2.5 and the ratio between the cylinder diameter and the lock height was 0.1. 2-D simulations were found to show good qualitative agreement for the spanwised-averaged force with 3-D results. They also were able to successfully capture the spanwise and time-averaged bed shear stress levels below the cylinder, as long as separated structures were no longer convected along the bottom wall. However, due to the absence of 3-D instabilities that can break the coherence of the interfacial vortices, 2-D simulations significantly overpredicted the amplitude of the force fluctuations and bed shear stress beneath the cylinder during the transient regime. Their study also found that the flow past the circular cylinder during the quasi-steady regime has many similarities with a constant density flow, provided that the values of the cylinder Reynolds number and the Reynolds number based on the gap distance and the front speed of the current are similar. In particular, the coherent structures in the wake and the values of the drag, vortex shedding frequency and bed shear stress beneath the cylinder were similar (within 20% for most of the cases). Thus, their study concluded that data from constant density flows past a cylinder situated near a bottom wall can be used to determine the main flow variables of interest during the quasi-steady regime observed in the case of a gravity current flow past a cylinder.

Gonzalez-Juez et al. (2009c) also considered the effect of the impact on the sediment entrainment capacity of the gravity current in the region situated around the cylinder. In particular, they studied the mechanisms that generate the bed shear stresses in the region situated around the cylinder and how the bed shear stress distributions vary in time function of the values of the main flow and geometrical parameters. The study found that the largest bed friction velocity occurred during the impact stage. This value is about 1.6 times larger than the value recorded during the quasi-steady regime and for constant density flows. This suggests the potential for scour is much larger in the case a gravity current impacts a cylinder. Results of 3-D simulations showed that the largest values of the bed shear stress during the impact regime occurred near the lobes. A relatively large amplification of the bed shear stress was also observed during the transient stage in the region where the current plunges downwards toward the bed past the cylinder. The vortex shedding in the cylinder wake is expected to induce erosion at the bed in the region situated behind the cylinder, in the case of a loose channel bed. The authors proposed a criterion for the onset of scour when a gravity current impacts a cylinder present close to the channel bottom. This information is relevant for the study of scour in gravity current flows.

Bottom-mounted square cylinders were studied using 2-D and 3-D DNS and LES simulations by Gonzalez-Juez et al. (2007, 2009b). The predictions were successfully validated using the experimental results of Ermanyuk and Gavrilov (2005b) (see Figure 2.8). Simulation results for partial depth release currents showed that the pressure variations on the upstream face of the square cylinder are the main factor controlling the temporal drag fluctuations. These pressure variations are associated with the existence of separated flow regions along the bottom wall that approach the cylinder from upstream. The separated flow regions are generated by the interfacial billows in the mixing layer. The pressure variations in the wake associated with the large-scale vortex shedding was a less significant factor. As a result, the frequency of the dominant drag fluctuations was that of the recirculation flow regions convected toward the cylinder. This frequency is function of the ratio between the current height and the channel height. These findings were confirmed by running simulations with a slip bottom wall in which these recirculation regions did not form. The drag and lift fluctuations were significantly less compared to the no-slip case. The study also showed that in the case of a full-depth-release (see Figure 2.7) current the amplitude of the drag fluctuations are smaller. This was explained based on the fact that the interfacial billows in the mixing layer present between the forward and backward propagating currents are nearly stationary. A parametric study of the effect of the ratio of cylinder height to current height showed that larger cylinders are subject to higher drag and stronger fluctuations as they are more exposed to the high momentum region of the incoming gravity current. The increase in the Reynolds number was found to generate more sustained drag and lift fluctuations due to the thinner boundary layer on the bottom wall and the larger strength of the recirculation regions in the flow upstream of the cylinder and in the wake (see Figure 2.9).

Comparison of 2-D and 3-D simulation results showed that while the temporal evolution of the force during the impact stage was similar, 2-D simulations significantly underpredict the force fluctuations after impact, in particular during the quasi-steady regime for Re>10,000. The underprediction is due to the formation of much stronger Kelvin-Helmholtz vortices in 2-D simulations. For full depth release currents the initial fluctuation of the drag during the transient regime predicted by 2-D simulations was found to be in good agreement with 3-D predictions.

3-D simulations showed the formation of an unsteady cellular flow structure upstream of the square cylinder, similar to that observed in the corresponding case of a constant density flow. This structure explained the spanwise variations of the drag (~20% compared to the mean value). The dominant length scale of these variations was close to the cylinder height. Compared to the case of a constant density flow, the hydrostatic drag component, absent in constant density flows, was found to be significant, especially at larger ratios of cylinder height to current depth. Also, the results showed the downward motion of the dense fluid after it is convected over the top of the cylinder can have a significant effect on the drag.

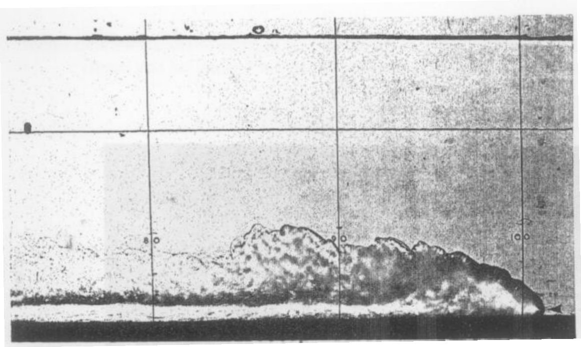

Figure 2.1. The shadowgraph of a gravity current head from the study of Simpson and Britter (1979).

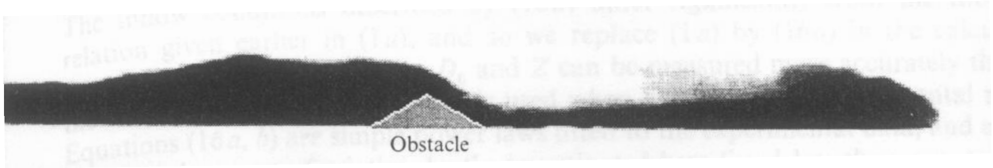

Figure 2.2. A typical image of the flow from the study of Lane-Serff et al. (1995) showing the reflected jump and the flow continuing over the triangular obstacle.

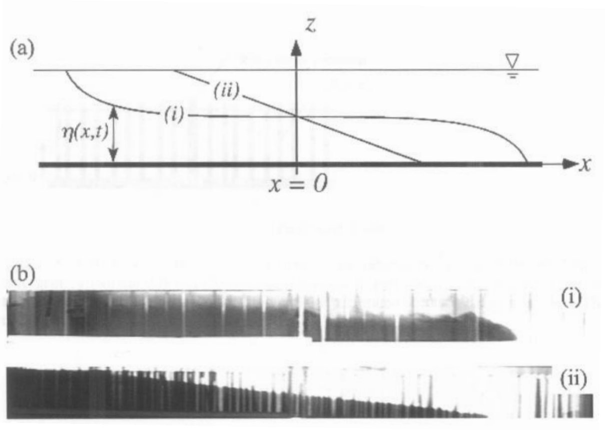

Figure 2.3. Comparison of the interface profile, η(x,t), from the study of Tanino et al. (2005). a) slumping phase for gravity currents propagating over smooth surfaces; b) buoyancy-turbulent drag regime for gravity currents propagating over a porous medium (array of vertical emerged cylinders).

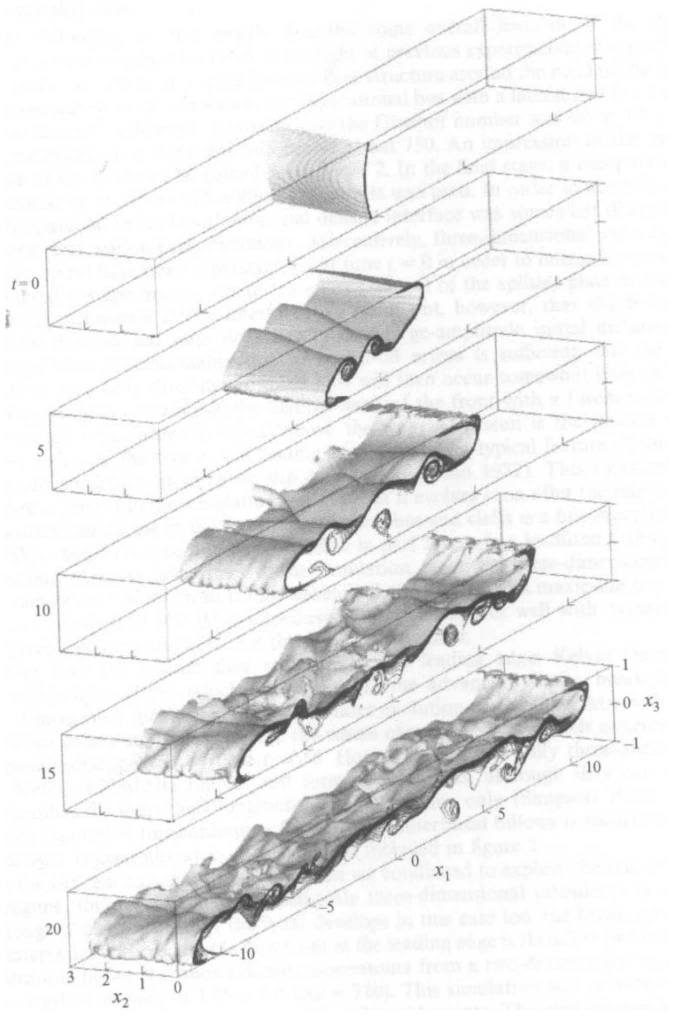
$t = 0$
5
10
15
20
1
0 x_3
−1
10
5
0
x_1
−5
−10
3
2
1
0
x_2

Figure 2.4. Evolution of a lock-exchange gravity current at Re~1,000 during the slumping phase from the 3-D DNS simulation performed by Härtel et al. (2000a)

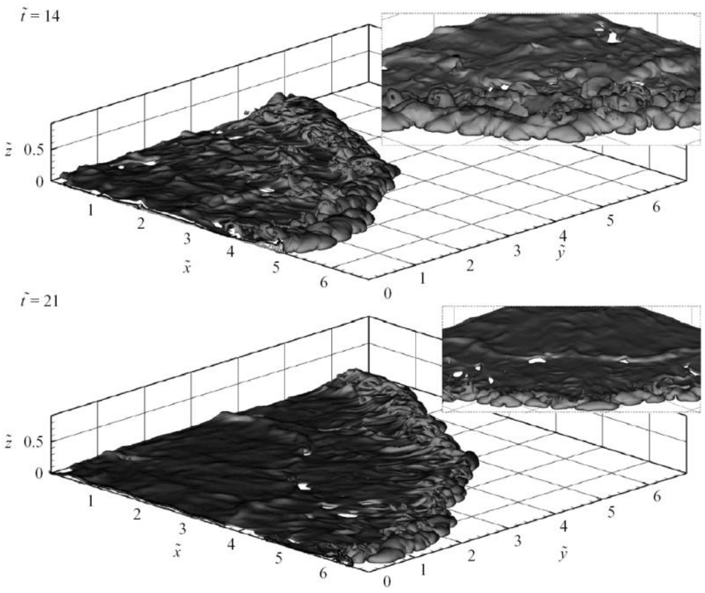

$\tilde{t}$ = 14
$\tilde{z}$
0.5
0
1
2
3
4
5
6
$\tilde{x}$
0
1
2
3
4
5
6
$\tilde{y}$
$\tilde{t}$ = 21
$\tilde{z}$
0.5
0
1
2
3
4
5
6
$\tilde{x}$
0
1
2
3
4
5
6
$\tilde{y}$

Figure 2.5. Visualization of interface of an axisymmetric gravity current in one quadrant of the computational domain in the 3-D DNS simulation (Re~3,000) of Cantero et al. (2007) using a concentration isosurface.

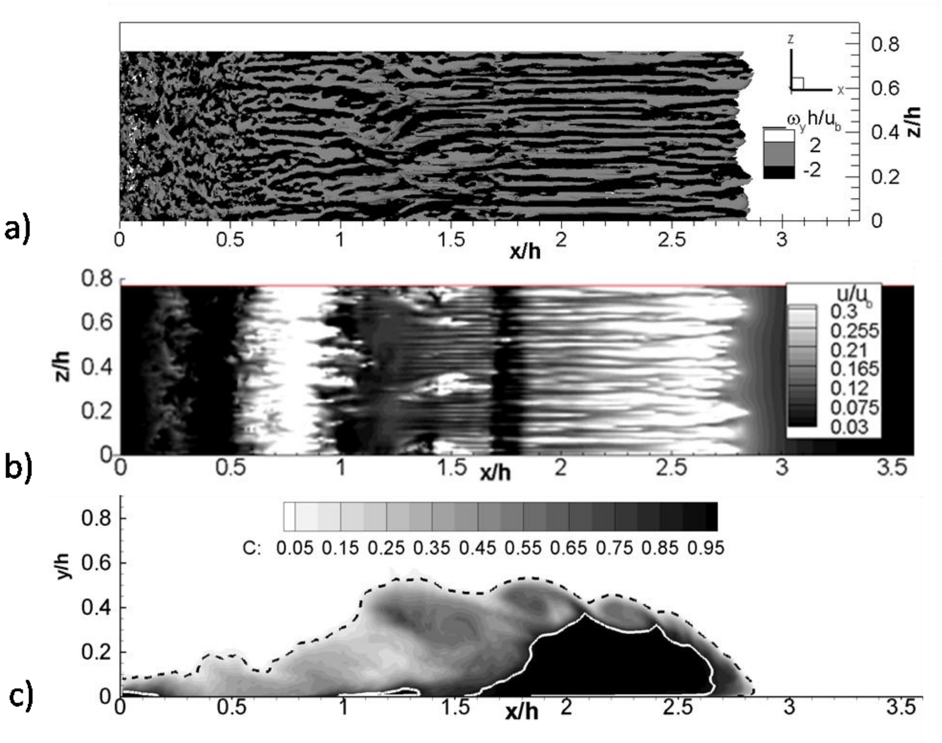

Figure 2.6. Visualization of the flow structure in the near wall region at t/t_0=5 from a 3-D LES simulation with R=1.0 and Re=47,750 performed by Ooi et al. (2009). a) vertical vorticity contours on the bottom wall; b) streamwise velocity contours showing the high and low streaks of streamwise velocity in a plane located at about 11 wall units from the bottom wall; c) spanwise-averaged concentration contours. The light and dark vorticity contours in frame a correspond to $\omega_y = 2u_b / h$ and $\omega_y = -2u_b / h$, respectively. The solid and dashed lines in frame c correspond to the C=0.9 and C=0.1 concentration levels, respectively.

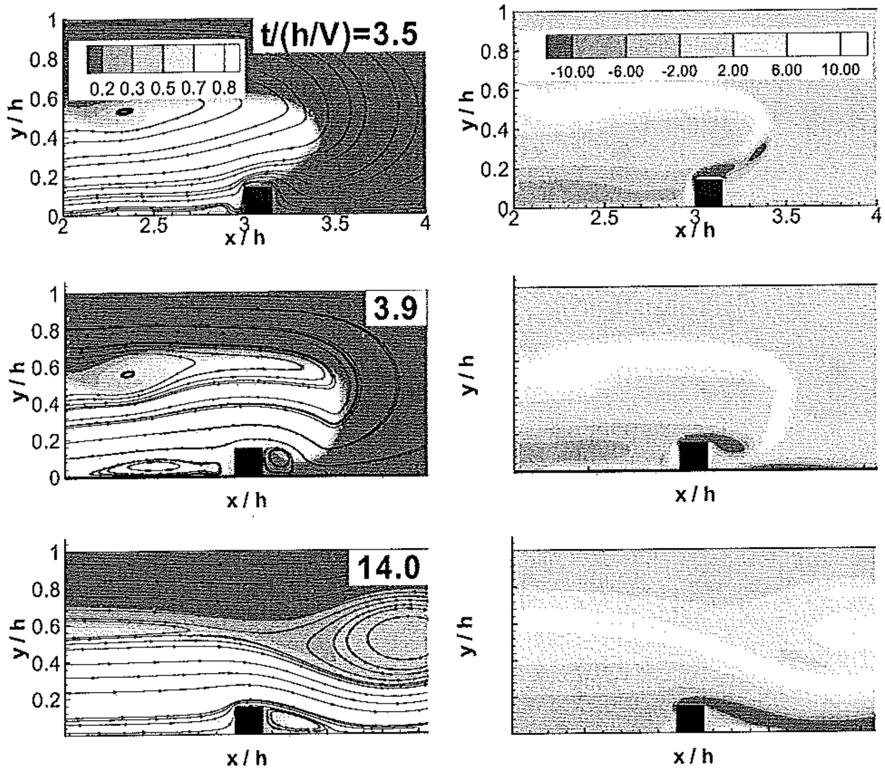

Figure 2.7. Evolution of the concentration, 2-D streamline patterns and vorticity fields during the impact stage for a gravity current propagating over a square cylinder mounted on the bottom wall of a channel. The simulation was conducted for a full depth release case by Gonzalez-Juez et al., (2009b).

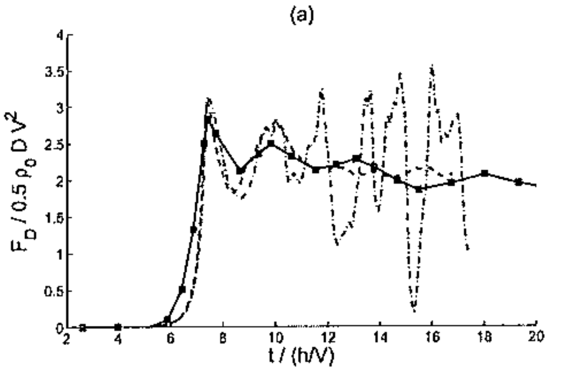

Figure 2.8 Temporal evolutions of drag (a) and lift (b) predicted by the 3-D simulation (dashed line) and 2-D simulation (dash-dotted line) of the flow past a bottom-mounted rectangular cylinder performed by Gonzalez-Juez et al. (2009b) are compared to the experiments of Ermanyuk and Gavrilov (2005b) (solid lines).

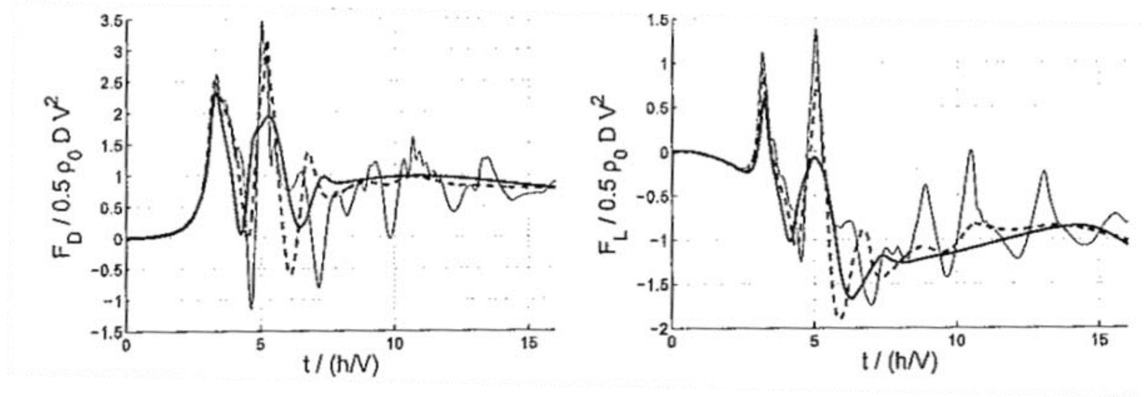

Figure 2.9 Effect of the Reynolds number on the drag (a) and lift (b) fluctuations from simulations (Gonzalez-Juez et al., 2009b) conducted with partial depth gravity currents (H/h=5): Re = 2,000 (thick solid line), Re = 4,000 (dashed line), Re = 10,000 (thin solid line).

CHAPTER 3 NUMERICAL METHOD

3.1 Description of Governing Equations, Subgrid-Scale Model and Numerical Algorithms

The numerical solver is a finite-volume DNS / LES code. A detailed description of the code and computational technique is available in Pierce and Moin (2001, 2004). The conservative form of the Navier-Stokes equations is integrated on non-uniform Cartesian meshes. A semi-implicit iterative method that employs a staggered conservative space-time discretization is used to advance the equations in time while ensuring second order accuracy in both space and time. A Poisson equation is solved for the pressure using multigrid. The algorithm discretely conserves energy, which allows obtaining solutions at high Reynolds numbers in the LES regime without artificial damping. A detailed discussion of discrete energy conserving non-dissipative schemes for DNS and LES calculations and their properties is provided by Mahesh et al. (2004). All operators are discretized using central discretizations, except the convective term in the advection-diffusion equation solved for the concentration for which the QUICK scheme is used. The code is parallelized using MPI.

In the present study the density differences between the lock fluid and the ambient fluid are kept small enough such that the Boussinesq approximation is valid. The filtered continuity and momentum equations and the advection-diffusion equation for the concentration $\overline{C}$ are made dimensionless using a characteristic length scale (in most cases, the height of the gate opening, h, or the channel half depth, H/2), *L*, and the buoyancy velocity, $u_b = \sqrt{g'L}$, ($g' = g(\overline{C}_{\max} - \overline{C}_{\min}) / \overline{C}_{\max}$, $\overline{C}_{\max}$ and $\overline{C}_{\min}$ are the maximum and minimum initial concentrations in the domain, *g* is the gravitational acceleration).

$$\frac{\partial u_i}{\partial x_i} = 0 \tag{3.1}$$

$$\frac{\partial u_i}{\partial t}+\frac{\partial (u_i u_k)}{\partial x_k}=-\frac{\partial p}{\partial x_i}+\frac{\partial}{\partial x_k}\left[\left(\frac{1}{\sqrt{Gr}}+\nu_{SGS}\right)\left(\frac{\partial u_i}{\partial x_k}+\frac{\partial u_k}{\partial x_i}\right)\right]-C\delta_{i2} \qquad (3.2)$$

$$\frac{\partial C}{\partial t}+\frac{\partial (Cu_k)}{\partial x_k}=\frac{\partial}{\partial x_k}\left(\left(\frac{1}{\sqrt{Gr\,Sc}}+\alpha_{SGS}\right)\frac{\partial C}{\partial x_k}\right) \qquad (3.3)$$

where p and u_i are the dimensionless pressure and Cartesian velocity component in the i direction. The dimensionless concentration is defined as $C=(\overline{C}-\overline{C}_{\min})/(\overline{C}_{\max}-\overline{C}_{\min})$ and is linearly related to the density ρ. The coordinates in the three directions are denoted either (x_1, x_2, x_3) in index notation, or (x, y, z). The vertical direction is y (i=2, in index notation). The time scale is $t_0=L/u_b$.

The Schmidt number, Sc, is the ratio of the molecular viscosity, ν, to the molecular diffusivity, κ. The expressions used to calculate the SGS viscosity (ν_{SGS}) and SGS diffusivity (α_{SGS}) in eqns. (3.2) and (3.3) can be found in Pierce and Moin (2001). No assumptions are needed on the value of the turbulent Schmidt number as the dynamic procedure (Germano et al., 1991) directly estimates the value of the SGS diffusivity based on the resolved velocity and concentration fields. The need to use empirical near-wall viscosity corrections (e.g., Van Driest damping functions) is avoided when the dynamic procedure is used and the governing equations are integrated through the viscous sub-layer ($\Delta n_1^+ \cong 1$ for the first point off the wall, where $n^+ = nu_\tau/\nu$, u_τ is the wall friction velocity and n is the normal distance from the wall). The simulations discussed in the present paper were conducted with a ratio of the test filter to the grid filter equal to two (Pierce and Moin, 2001). Preliminary tests showed the results were relatively insensitive to values of this ratio between 1.41 and 2.8.

In the simulations, the flow field was initialized with the fluid at rest. The time step was equal to $0.001t_0$. Based on the maximum velocity magnitude in the flow domain, the maximum value of the Courant number was below 0.5. The concentration field was initialized with a constant value of one in the region containing initially heavier (lock) fluid and a constant value of zero in the remaining part of the computational domain containing lighter (ambient) fluid. A small random disturbance was applied in the lock-gate region at the start of the simulations to accelerate the growth of 3-D instabilities.

A zero normal gradient boundary condition was assumed for the concentration at the boundaries at which no slip (wall surfaces) or slip (free surface) boundary conditions were used. A convective outflow boundary condition (Pierce and Moin, 2001) of the form $\partial F/\partial t + U_c \partial F/\partial x = 0$ (F is a velocity component or the concentration) was used at the open boundaries. The value of the convective velocity U_c was equal to the estimated front velocity when reaching the open boundary. Similar to the investigations of Härtel et al. (2000a), Necker et al. (2005), Cantero et al. (2007) and Ooi et al. (2007, 2009) the flow was assumed to be periodic in the spanwise direction in all the 3-D simulations. Thus, the present study considers only gravity currents of large relative width, which are particularly relevant for geosciences applications. The effect of the sidewalls was studied by Hallez and Magnaudet (2008).

The meshes employed in the 3D simulations contained between 20 and 50 million cells. The width of the computational domain was equal to the height of the lock-gate opening. This corresponds to a width roughly equal to two times the height of the gravity current during the slumping phase. This width was found to be sufficient for the turbulence structures to be uncorrelated in the spanwise direction for Re>10,000. In particular, the average number of lobes was larger than ten during the slumping phase. As the size of the lobes and of the other coherent structures decreases with the increase in the Reynolds number, assuring the correlation in the spanwise direction decays to zero over the width of the computational domain is less of a concern in the high Reynolds number simulations (Re=10^6).

The simulations were run on three different high-performance computers: a) IIHR‟s Xeon PC cluster with Myrinet (128 processors); b) the TRACC cluster of Argonne National Laboratories using LS-1 system from Linux Networx. The cluster has 512 processors (128 nodes, each with two dual-core AMD 2216 Opteron CPUs); and c) the IBM cluster of the National Center of High Performance Computing in Taiwan (2048 processors). The 3D simulations were run on 32 or 48 processors. The total CPU time needed to complete most of the simulations was between 10,000 and 40,000 hours.

3.2 Previous Validation Studies

Validation of the incompressible flow solver for canonical (e.g., channel flow) and complex turbulent flows (e.g., cold flow in a coaxial combustor) is discussed in Pierce and Moin (2001, 2004). Additionally, Chang et al. (2006) conducted a detailed validation study of the code for 3-D LES simulations of flow past a bottom-mounted rectangular cavity with an incoming fully turbulent channel flow. Chang et al. (2007) added a stratified flow module based on the Boussinesq approximation and studied the ejection of buoyant (heavier) pollutants from bottom channel cavities.

Ooi et al. (2007) studied the formation, evolution and structure of intrusive Boussinesq gravity currents propagating into a two-layer fluid with a sharp interface at $Re\sim10^4$. They found the front and the bore speeds and the head thickness during the slumping phase to be close to the values measured experimentally by Sutherland et al. (2004), Faust and Plate (1984), Lowe et al. (2002) and to theory. They also found the changes in the structure of the intrusive current were similar to those in the flow visualizations performed by Sutherland et al. (2004). In the doubly symmetric case, the experiments showed no significant leading interfacial waves and the front continues to propagate for some time after the bore has caught the head region with the same constant velocity observed during the slumping phase. The LES simulation correctly captured this phenomenon. The streamwise velocity distributions inside the head and wake regions were found to be qualitatively similar to the ones observed experimentally by Lowe et al. (2002).

The study of Ooi et al. (2009) reports additional validation for bottom-propagating lock-exchange compositional currents with high and small volume of release. In the case of lock-exchange currents with a high volume of release, the numerical simulations correctly captured the variation of the front velocity with the Reynolds number during the slumping phase observed in experiments (e.g., Keulegan, 1957, Keller and Chyou, 1991). The structure of the gravity current predicted in a simulation conducted at Re~10^3 was very close to the one predicted using 3-D DNS by Hartel et al. (2000). The changes in the average size of the lobes developing at the front of the current with the Reynolds number were found to be in good agreement with the correlations deduced by Simpson (1972) based on experiments. In the case of lock-exchange currents with a small volume of release (R=O (1)), LES correctly predicted the front and bore velocities during the slumping phase, and the non-dimensional streamwise length at which the bore overtakes the front (end of slumping phase). The simulations correctly predicted a front speed decrease proportional to $t^{-\alpha}$ (the time t is measured from the release) over the buoyancy-inertia phase, with the constant α approaching the theoretical value of 1/3 as the current approaches the inviscid limit (Re=O (10^6)). A simulation of a low Reynolds number current (Re=O (10^2)) predicted the correct front velocity decay with time ($U_f \sim t^{-4/5}$) during the viscous-buoyancy self similar phase. Finally, the structure of the gravity current predicted by the 3-D LES simulations from the time the lock gate was released and until the start of the buoyancy-inertia phase was found to be in good qualitative agreement with the experiments of Hacker et al. (1996). In particular, the 3-D simulations accurately captured the dimension of the region containing unmixed lock fluid behind the front and the overall shape of the gravity current. Unfortunately, the experiments of Hacker et al. (1996) did not report visualizations of the current after the end of the transition to the buoyancy-inertia phase.

3.3 Grid Dependency and Schmidt Number Sensitivity Study

Simulations in the present study assumed a Schmidt number of $Sc = 600$ which corresponds to the saline diffusion in water. Based mostly on 2-D simulations, Härtel et al. (2000), Necker et al. (2005), Cantero et al. (2007) and Ooi et al. (2009) did not find a significant effect of the Schmidt number on the solution if Sc>1.

To confirm this, two 3-D simulations of a lock-exchange current with a high volume of release propagating over a smooth free surface were conducted with Sc=1 and Sc=600, respectively. The size of the computational domain, the Reynolds number (Re=$u_b h/\nu$~50,000) and the mesh were identical. The size of the grid was 3072(x)×160(y)×48(z) and the spanwise length of the domain was equal to the channel height. Results showed the front speed was identical in the two high Reynolds number simulations, while the shape and structure of the gravity current behind the front were similar at all stages of the evolution of the current. The results in Figure 3.1 show that the shape and overall distribution of the concentration in the tail and head regions are largely unaffected by the value of the Schmidt number. In part, this is because, even for $Sc=1$, α_{SGS} is significantly larger than the molecular diffusivity in the regions of strong turbulence.

A grid dependency study was conducted to study the sensitivity of the solution to the number of grid points in the spanwise direction for simulations with Re~50,000. The finer mesh had 72 grid points in the spanwise direction while the coarser mesh had only 48 grid points. The size of the computational domain, the number of mesh points in the vertical and streamwise directions and the flow parameters were kept the same in the fine and coarse mesh simulations of a lock-exchange gravity current with a high volume of release propagating over a flat bed.

Comparison of the concentration distributions in vertical-streamwise sections at different stages of the evolution of the lock exchange flow shows the positions of the large-scale interfacial billows and of the front are similar. Figure 3.2a show this comparison at $t=10t_0$. Simulation results predicted an identical front velocity for the forward and backward propagating currents in the two simulations. Good qualitative agreement is also observed for the distribution of the bed friction velocity, u_τ. For example, the distributions of u_τ/u_b are compared in Figure 3.2b at $t=10t_0$. Observe the position of the spanwise bands of high and respectively low u_τ/u_b values in the region situated close to the lock gate (x/H<2) is very similar in the two simulations. Same is true for the mean values of u_τ/u_b within these spanwise bands.

Between x/H=2 and the front (x/H~4.5) streamwise streaks of high values of u_τ/u_b are observed in both simulations. Also important, the average number of streaks at a certain spanwise location is close in the two simulations. For example, just behind the front the number of streamwise streaks is 13 in the coarse mesh simulation and 15 in the fine mesh simulation at $t=10t_0$ (see Figure 3.2b). These streaks are the thinnest structures in the flow and are aligned with the streamwise direction, thus one expects they should show the highest sensitivity to the grid resolution in the spanwise direction.

As one of the main purposes of the present study is the accurate estimation of the capacity of the compositional gravity current to entrain sediment from the loose bed, one has to check that the flow resolution is sufficient to insure the spanwise-averaged distributions of u_τ/u_b at different stages of the evolution of the lock exchange flow are independent of the grid. The comparison of these distributions at $t=14t_0$ in Figure 3.3 proves this is the case. Overall, the comparison of the finer and coarser mesh results shows that using 48 points in the spanwise direction (domain width is H) is sufficient to accurately capture the large-scale features and integral quantities describing the evolution of the lock-exchange flow at $Re=O(10^4)$.

Another requirement is that the spanwise length of the domain is large enough such that the development of the lobes is not constrained significantly by the periodic boundary conditions. Previous studies have shown that the present numerical method can accurately capture the variation of the mean size of the lobes with the Reynolds number on grids of similar density for Reynolds numbers smaller than 10^5.

To be able to accurately resolve the large scale deformations of the free surface the spanwise length should be at least 3-4 times larger than the average dimension of the lobes at the Reynolds number of the simulation and each lobe of average should be resolved with at least 6-7 points. There requirements were satisfied in most of the simulations discussed in the result chapters where the spanwise length of the domain was equal to the channel depth.

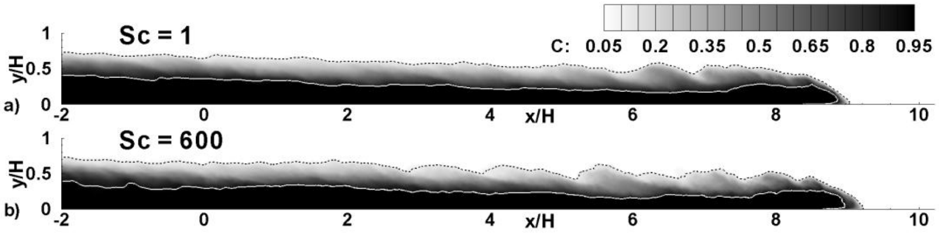

Figure 3.1. Concentration contours in a two dimensional (streamwise-vertical) plane during the later stages of the slumping phase for a lock exchange current with a high volume of release (R<<1). a) Sc=1; b) Sc=600.

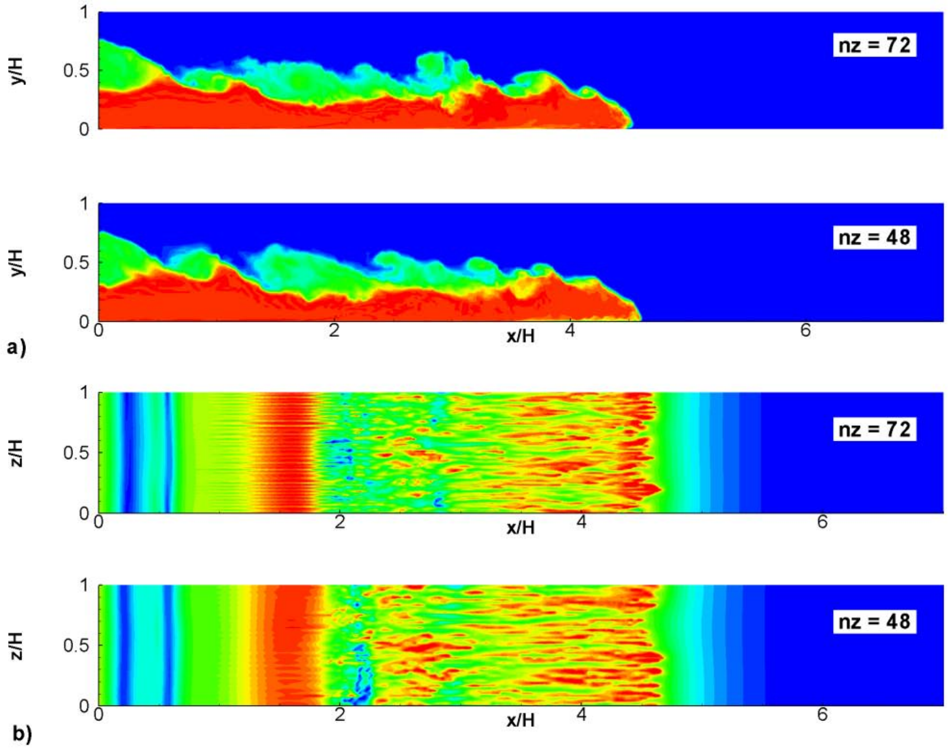

Figure 3.2. Visualization of the structure of the lock-exchange bottom propagating current and bed friction velocity at t = $10t_o$. a) Concentration distribution in a streamwise-vertical section; b) bed friction velocity distribution. The top frame shows the finer mesh results (nz=72). The bottom frame shows the coarser mesh results (nz=48).

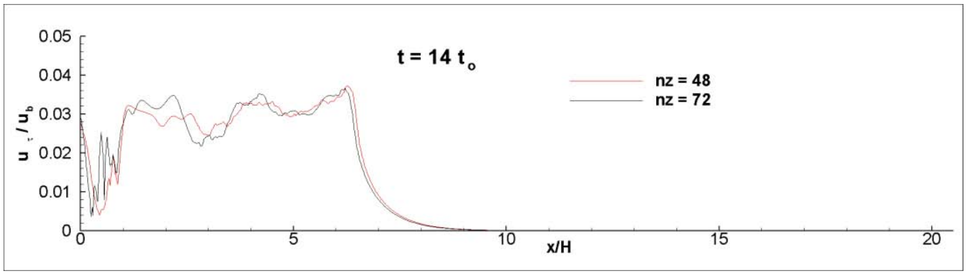

Figure 3.3 Comparison of the spanwise-averaged bed friction velocity distribution at $t=14t_0$.

CHAPTER 4 GRAVITY CURRENTS WITH A LARGE VOLUME OF RELEASE (R<<1) PROPAGATING OVER AN ARRAY OF 2-D OBSTACLES

4.1 Description of Test Cases

In this chapter, the case of full-depth release (h=H) lock-exchange compositional currents with a large volume of release is considered. The initial volume of release is large enough ($R=h/x_0<<1$) such that no interactions occur between the forward and backward propagating currents and the channel end walls during the simulation. The main goal of the present chapter is to study the physics of gravity currents propagating over an array of 2-D large-scale obstacles (roughness elements) during the slumping phase.

The height of the lock-gate opening, *h*, which is equal to the channel height, *H*, in the full-depth-release cases analyzed here, is used to scale the lengths. The buoyancy velocity $u_b = \sqrt{g'h}$ is used to scale the velocities. The time scale is $t_0=h/u_b$. The channel is long enough ($L_1/h=41$) to allow the study of the propagation of the currents during the slumping phase over a large amount of time ($t>40t_0$). Most of the simulations are conducted at a Reynolds number ($Re=u_bh/\nu$) of 47,800 which is high enough for the flow behind the front to be strongly turbulent and to induce the formation of regions of high and low velocity streaks at the bed similar to those observed in a constant density turbulent boundary layer (Ooi et al., 2009).

Two types of obstacles are considered (Figure 1.5). The 2-D dunes are representative of bedforms present at the bottom of rivers and oceans. The shape of the dunes is taken from the experiment of Mierlo and de Ruiter (1988) that focused on typical dunes observed in rivers. The ratio between the height, D, and the wavelength, λ, of the dune is 0.05, which is within the typical range observed for dunes in small and medium-size rivers.

The effect of the shape of the obstacles is studied based on differences observed in simulations conducted with dunes and ribs of equal height (D=0.15H) and equal wavelength (λ=3H, λ/D=20). This corresponds to the k-type roughness regime which is the relevant one for most practical applications in geosciences. The main difference between the two obstacles is the degree of bluntness of the obstacle given by the degree of inclination of the upslope face of the obstacle with the bed. In the case of ribs, the upslope face is perpendicular to the channel bed. The flow around the ribs resembles the flow past a surface mounted bluff body. This increases the impact force, induces flow separation upstream and downstream of each rib and increases the dissipation with respect to the case when the change in elevation between the lowest and highest levels of the obstacle is gradual (e.g., dunes). Additionally, the head of the current slows down considerably during the impact stage with the rib and the height of the splash region forming as a result of the impact of the current with the rib is large. In the case of dunes, the variation in the bed elevation between the lowest (trough) and highest (crest) level of the dune is gradual and continuous, thus the interaction between the current and the dune can be classified as a streamlined body case as opposed to a bluff body case for ribs. As a result, in the case dunes are present, the flow does not separate as it is convected toward the crest, no splash region is forming and the amount by which the front speed decreases as the current is convected from the trough to the crest of the dune is much smaller. On the other hand, the flow past the crest of the dune is expected to be relatively similar to that past the top of the rib.

The effect of the size of the obstacle is analyzed based on comparison of simulations conducted with dunes and ribs of height equal to 0.15H and 0.30H. As the height of the incoming gravity current is around 0.5H, the flow past the obstacles is partially blocked. The larger height simulation with dunes (D=0.3H) is representative of cases when large dunes are present at the river bottom, as the observed maximum height of dunes in open channels with loose bed is close to one third of the channel depth. The simulation in which ribs of height 0.3H are present at the bed is representative of cases in which retarding obstacles (baffle blocks) are used to slow down powder snow avalanches.

Scale effects are discussed based on comparison of simulations with flat bed, dunes and ribs conducted at Re=47,800 and Re=10^6. In the latter case, the Reynolds number is high enough for the current to approach the inviscid state. $Re=10^6$ is also within the lower part of the range of Reynolds numbers observed in the field (e.g., small rivers).

The simulations conducted at Re=47,800 are denoted LR. The ones conducted at $Re=10^6$ are denoted HR. The presence of a flat bed, 2-D dunes or 2-D ribs is indicated by the presence of an F, D or R in the name used for the simulation. Finally, the non-dimensional height of the dunes or ribs, D/H*100 is indicated by a number. For example LR-D15 refers to the simulation of the flow past an array of 2-D dunes of height 0.15H conducted at Re=47,800.

Some general characteristics of the flow and some of the main variables describing its evolution were discussed in Chapter 1.3.1. More details of the test cases and simulation set up are given below (see also Table 4.1). The initial lock gate position is at x/H=0. To maintain the anti-symmetry of the solution, the obstacles are positioned on the bottom surface in the region with x/H>0 and on the top surface in the region with x/H<0. The center of each rib is situated at the location of the crest of the corresponding dune. Their streamwise positions on the top and bottom walls are given in Table 4.1. As the channel geometry and boundary conditions are such that the propagation of the heavier and lighter currents is anti-symmetrical, the discussion of the results focuses on the evolution of the heavier (forward propagating current in Figure 4.1) current.

The grid size was 4232×48×152 in the streamwise (domain length L_1=41h), spanwise (domain width L_3=h), and vertical (domain height L_2=h) directions, respectively. Away from the walls, the grid spacing in the three directions was 0.01h-0.02h. To resolve the viscous sub-layer, the grid spacing in the vertical direction was reduced to 0.002h near the walls of the computational domain in the simulations conducted with Re=47,800. The maximum physical Reynolds number defined with the front velocity during the slumping phase and the current height is close to 11,000. A grid spacing of 0.002h in the wall normal direction corresponds to about one wall unit. This is sufficient to resolve the viscous sub-layer if the flow behind the front is assumed to be fully developed and, thus, to avoid the use of wall functions. In the simulations conducted at $Re=10^6$, the grid spacing in the wall normal direction was around 0.0007h.

No slip boundary conditions were used for the velocity at the top, bottom and end-wall boundaries. The Schmidt number was Sc=600. A zero normal gradient was imposed for the concentration at the top, bottom and end-wall boundaries. The flow field was initialized with fluid at rest. The time step was $0.001t_0$.

4.2 Structure of the gravity current in the head and dissipative wake regions

Figure 4.2 shows the distributions of the non-dimensional concentration C, velocity magnitude u_{mag}/u_b, and pressure $p/\rho u_b^2$ for the low Reynolds number simulations with flat bed and small obstacles of height D=0.15H in the later stages of the slumping phase when the front of the current is around $x_f/H=18.5$.

The largest difference in the head region between the three simulations is the lower values of the concentration / density in the simulations with obstacles at the bed compared to the flat bed simulation in which unmixed lock fluid is still present behind the head. The reason for the gradual decay of the concentration inside the head of the current is its interaction with the obstacles which induces more mixing. In the case of blunt obstacles (e.g., square ribs) the decay of the concentration in the head region is larger due to the additional mixing occurring during the impact of the front with the upstream face of the obstacles. This is why the decay of the concentration in the head region in Figure 4.2 is larger in the case ribs are present at the channel bottom. Still, the head maintain its compactness in the simulations with obstacles at the channel bottom.

The changes in the level of mixing inside the head and dissipative wake regions as the front propagates over a dune is illustrated in Figure 4.3. The presence of the dunes increases the mixing of the fluid inside the head with the surrounding lower density ambient fluid, especially after the front overtakes the crest of the dune. Once this happens, the flow remains attached but, as the nose plunges downwards, lower density fluid situated in the vicinity of the lee face is trapped into the head and mixes with the fluid inside the head of the current (Figure 4.3b).

During the time the head is convected downwards, the strength of the Kelvin-Helmholtz billows increases and so does the mixing in the dissipative wake region. Then, the front impacts the bed surface in the vicinity of the trough of the next dune (Figure 4.3c). During the impact stage the front decelerates. This interaction produces strong vortices in the impact region. As the flow at the front of the current changes direction and orients itself parallel to the upslope face of the next dune, mixing is again enhanced.

Once the head starts propagating over the upslope face of the next dune (Figure 4.3d) a region of highly accelerated and relatively high-density fluid develops over the leeside of the dune and the trough region of the next dune. This region has the form of a wall-attached jet-like flow and is going to be referred as the jet-like flow. For dunes of height of 0.15H, the flow becomes supercritical as the jet-like flow reaches the trough of the next dune. The Froude numbers in the supercritical flow region are less than 1.5 in the LR-D15 simulation. The length of the supercritical flow region is about 0.5H. A strong shear layer develops at the boundary between the jet-like flow and the surrounding fluid. As the jet-like flow reaches the trough region, it changes orientation. During the time the jet like flow is established, the front propagates over an inclined surface with negative slope and decelerates. The flow in the head region is subcritical. As a result a hydraulic jump forms. Besides increasing mixing at the back of the head, the hydraulic jump creates the conditions for the formation of a large vortex at the back of the head region. As this vortex forms and becomes more coherent, the core of high-speed fluid within the jet-like flow situated beneath the vortex is slightly diverted away from the bed. The position of the vortex is close to stationary after it attains maximum size. The vortex is situated at about 1.5H from the crest of the dune that induced its formation. Such intensified mixing vortices were also observed experimentally by Alexander and Morris (1994) in the flow past an isolated ridge of a form similar to that of a dune. These vortices are very dissipative due to the small scale turbulent structures created by the hydraulic jump and entrained into the cores of the intensifying mixing vortices.

The presence of larger dunes of height (D=0.3H) comparable to that of the head of the incoming current does not changes the dynamics of the flow in the head region as the front propagates over the obstacles. The jet-like flow is stronger with respect to the case when dunes of smaller height (D=0.15H) are present. The maximum Froude number in the supercritical flow region is around 3. The length of the supercritical flow region is about 1H. The formation of the mixing vortex at the back of the head of the current is illustrated using a 3-D concentration iso-surface (C=0.1) in Figure 4.4a-d. The view is from the side. The large mixing occurring as the front reaches the through region (Figures 4.4a and 4.4e) is also suggested by the complex shape of the interface in that region. The jet like flow and the intensified mixing vortex start forming in Figure 4.4b. The vortex attains its maximum size in Figure 4.4c after which its intensity (circulation) starts to decay slowly.

The propagation of the front over the smaller dunes does not affect significantly the dynamics of the lobe and cleft structures at the front. However, in the case the front propagates over the larger dunes there appears to be a correlation between the degree of irregularity of the interface in the front region and the position of the front. Figures 4.4e and 4.4f show the surface of the front interface immediately after the impact of the front with the through region (Figure 4.4a) and before the front reaches the crest (Figure 4.4d), respectively. As a result of the strong acceleration of the front as it is convected on the leeside of the dune and its subsequent impact with the bed surface, large-scale cleft regions that contain several well-developed lobes develop. It is likely that the strong flow acceleration increases the differences in the propagation velocity of the different parts of the front region. As the flow is convected on the upslope face of the next dune, the magnitude of the large-scale clefts diminishes such that when the front is close to the top the lobes are relatively well aligned in the spanwise direction. Once the head of the current gets away from the intensified mixing vortex, the deformations of the interface behind the front are relatively two-dimensional and their characteristic length-scale is larger. By contrast, the deformations are much more three-dimensional and their length-scale is smaller in the region where the intensified mixing vortex is present.

In the case ribs of height D=0.15H rather than dunes of identical height are present at the channel bottom, the mixing at the head of the current is even stronger. Analysis of the concentration distributions in Figure 4.5 allows understanding how the changes in the flow structure, as the head propagates over the rib; increase the mixing in the head region. In the LR-R15 simulation, the height of the head before the current starts interacting with the ribs is 2 to 2.5 times that of the obstacle. As the front impacts the upstream face of a rib (Figure 4.5d), the head is projected upwards. The deformations of the front as it is convected past the top of the rib are much higher compared to the case when dunes of identical height are present at the bed (e.g., compare Figure 4.5d with 4.3b). The sudden change in the flow direction as a result of the impact creates strong turbulent eddies. This increases mixing around the front of the current. Then, as the heavy fluid inside the front reattaches to the bed (Figure 4.5a), a patch of low density ambient fluid is caught in between the downstream face of the rib and the higher concentration fluid from the head, as the head reattaches to the horizontal part of the bed surface. The trapped low-density fluid mixes with the head fluid. The size of this patch is larger in the case ribs rather than dunes are present at the channel bottom. Then, similar to the case dunes are present at the bed, a strong jet like flow develops (Figure 4.5b). A hydraulic jump forms as the flow transitions from supercritical in the upstream part of the jet-like flow to subcritical in the head region. The interaction of the newly formed jet-like flow with the back of the head induces the formation of an intensified mixing vortex. Its center is initially situated at about 0.5H from the rib in Figure 4.5b. Until the head reaches the next rib (Figure 4.5c), the vortex is pushed slowly away from the rib that induced its formation (from 0.5H to about 1.0H). Then, the position of the vortex does not change in time.

The formation of the jet-like flow and of the intensified mixing vortex is also illustrated using a 3-D concentration iso-surface (C=0.1) in Figures 4.6a to 4.6d. Observed the presence of a region of very low-density fluid trapped downstream of the second rib (R2) in Figure 4.6b. The jet-like flow starts forming in Figure 4.6c. The intensified mixing vortex is strongly coherent and starts separating from the back of the head in Figure 4.6d. Examination of the intensified mixing vortex forming downstream of the first rib (R1) in Figures 4.6a to 4.6d illustrate the evolution of the vortex after the front passes the next rib. The vortex is stretched in the streamwise direction and diffuses slowly.

The 3-D concentration iso-surface and the lob and cleft structure at the front are visualized in Figure 4.6e and 4.6f during the time the front is projected downwards toward the bed (Figure 4.6a) and before it starts interacting with the next rib in the series (Figure 4.6d). As a result of the impact with the upstream face of the rib, the large-scale lobe and cleft structure disappears. Meanwhile, their presence at the front of the current during the impact stage was shown by Gonzalez-Juez et al. (2009) to induce significant oscillations of the pressure drag force in the spanwise direction. Figure 4.6e shows that small-scale deformations are still present, but they are much smaller than the typical sizes expected for the lobes during the propagation over the flat part of the bed surface. After the head of the current reattaches and regains its normal shape, the lobe and cleft structures at the front develop rapidly. Figure 4.6f provides a representative view of these structures when the front is situated at distances larger than 1H from the rib. This behavior of the lobe and cleft structures is somewhat opposite to the one observed in the case dunes where present at the bed. In that case, the lobe and cleft structures where observed at all stages of the propagation of the current over the dune. Additionally, the amplification of the spanwise non-uniformity of the front velocity in the region where the front impacted the trough of the next dune induced the formation of larger structures containing several lobes of regular size.

The concentration distributions in Figures 4.7a to 4.7d illustrate the interaction between the head and a large rib obstacle of height D=0.3H. An increase in the size of the ribs such that their height becomes comparable to that of the head of the incoming current induces changes mostly during the impact stage, when a large splash of heavy fluid forms (Figure 4.7b). The fluid at the front is strongly decelerated as it is convected over the top of the large rib. As a result, the decelerated flow in the head plunges downwards at a small angle to the downstream face of the large rib (Figure 4.7c). Then, the jet-like flow forms as more heavy fluid accumulates in the vicinity of the downstream face of the rib. Its angle is very close to that observed in the flow past large dunes (Figure 4.7e) where it is parallel to the lee face of the dune (Figure 4.7d). A recirculation region forms in between the jet-like flow and the bed. The characteristics of the intensified mixing vortex are also very similar in the simulations with large ribs (Figure 4.7d) and large dunes at the bottom (Figure 4.7e).

The simulations conducted at $Re=10^6$ do not show any significant changes in the dynamics of the flow in the head region as the head is convected over dunes or ribs of same height with respect to the lower Reynolds number simulations.

4.3 Front velocity

The front velocity can be calculated by differentiating the front position from the spanwise-averaged frames over time. Alternatively, the front velocity can also be inferred from the slope of the front trajectory with respect to the time axis. Figure 4.8 shows the temporal evolution of the front position $x_f/H(t/t_0)$ for the heavier, forward-propagating current in the simulations conducted in the simulations conducted with a flat bed and with obstacles of height $D=0.15H$ at the channel bottom, at $Re=47{,}800$ and $Re=10^6$. Figure 4.9 compares the front trajectories in the simulations with obstacles of height $D=0.15H$ and $D=0.3H$ conducted at $Re=47{,}800$ ($Re_f=10{,}800$). Simulation results showed that in all the cases the temporal evolution of the lighter current propagating along the top surface was nearly identical to that observed for the heavier current. This is expected for Boussinesq currents (e.g., see Shin et al., 2004).

Analysis of the flat bed simulations show that for $t/t_0>3.5$, after the end of the initial accelerating phase, the front trajectory can be very well approximated by a line of constant slope until the current starts interacting with the end wall (the front is situated at less than 2H from the end wall). This means the front velocity is nearly constant (slumping phase). The corresponding Froude numbers ($Fr_f=U_f/u_b$) are 0.45 and 0.49 for LR-F and HR-F, respectively. These values are in very good agreement with those inferred from experiments of high-Reynolds-number currents propagating over a flat smooth bed (e.g., Keulegan, 1957, Keller and Chyou, 1991, Shin et al., 2004). These experiments showed that the non-dimensional front velocity during the slumping phase increases with the Reynolds number and, eventually, approaches a value of 0.5. For example, Keulegan (1958) found Fr_f=0.48 for currents with front Reynolds numbers around 150,000. The front velocity in the HR-F simulation (Re=10^6), in which the front Reynolds number, Re_f, is 248,000, is very close to the theoretical value of 0.5 (half-depth solution) obtained by Benjamin (1968) for an energy-conserving inviscid current.

As expected, the presence of ribs or dunes slows down the advancement of the front of the current compared to the flat-bed case. In Figure 4.8 and Figure 4.9, the front trajectories are very close until the front approaches the first obstacle in the simulations in which obstacles are present at the bed. Then, the trajectories start diverging for $t>10t_0$. Still, in the simulations with small obstacles (D=0.15H) the mean slope of the trajectory can be considered, in a good approximation, constant for $t/t_0>16$, after the current passed the first obstacle in the series. This means that a slumping phase in which the front velocity is approximately constant is also present for gravity currents propagating over a surface containing a series of identical 2-D dunes or 2-D ribs, at least for obstacles whose height is less than half that of the incoming current. The mean value of the front velocity during the slumping phase is smaller than that in the corresponding flat-bed cases. This is obviously a consequence of the additional form drag induced by the presence of large-scale obstacles at the bed. The obstacles increase significantly the dissipation over the body of the current (e.g., see Figures 4.36 and 4.37). The smaller value of the mean front velocity predicted during the slumping phase in the simulation in which obstacles are present at the bed is fully consistent with the fact that once the current passes the first obstacle in the series, the total kinetic energy of the flow at a given time, or at a given front position, is smaller than the value predicted in the flat-bed case.

In the simulations in which dunes and, especially, ribs are present at the bed, the slope of the front trajectory is subject to larger temporal variations compared to the flat-bed simulations. The amplitude of the temporal variations around the straight line describing the front trajectory in the case of a constant front velocity increases with the size of the obstacles. This is mainly because the front is decelerating as it propagates toward the crest of each dune or as it approaches the upstream face of each rib due to the adverse pressure gradients induced by the inclined upstream surface of the obstacle. During this time, the potential energy increases, as the head rises above the top of the obstacle, at the expense of the head losing some of its kinetic energy. In the case of large ribs, there is an additional increase in the potential energy due to the splash of high density fluid that is projected upwards and reaches heights that are about 2.5 times larger than the rib height. Then, the front velocity increases above the mean value during the time the head is projected downwards as it passes the crest of the dune or the top surface of the rib. The increase in the amplitude of these temporal variations is much larger in the case the flow around the upstream face of the obstacle resembles the flow past a surface-mounted bluff body. In fact, in the LR-R30 simulation the slope of the front trajectory is close to zero around $t=15t_0$, $32t_0$ and $50t_0$ when the front of the current hits the three large ribs. The local changes in the slope of the front trajectory in Figure 4.8 are much less severe if the obstacles are of smaller size (D=0.15H) or if the shape of the obstacle does not resemble a bluff body (dunes).

The mean front velocity, U_f/u_b, is 0.4 and 0.34 in the simulations (Re=47,800) in which dunes and ribs of height D=0.15H are present at the bed, respectively. The mean value obtained from the front trajectory is in very good agreement with estimations of the mean front velocity based on the time it takes the current to advance between the crests of two successive dunes or between the upstream faces of two successive ribs. The mean front velocity inferred from the time of travel between two successive obstacles is close to independent of the rank of the obstacle in the series, and oscillates around the mean value inferred from the front trajectory. The mean front velocity in the LR-D15 and LR-R15 simulations is 12% and, respectively, 24% lower than the value ($U_f/u_b=0.45$) predicted for the flat bed case. The difference is explained by the fact that ribs induce higher form drag due to their larger degree of bluntness when the height of the head is larger than that of the obstacle.

When the height of the obstacles approaches that of the head of the current, the degree of bluntness appears to play a smaller role, as the mean front velocities are very similar in the simulations with large (D=0.3H) dunes (U_f/u_b=0.316) and ribs (U_f/u_b=0.30). These values were calculated based on the time it takes the front to advance between the second and the third (last) obstacle in the series. The mean front velocities are slightly higher if calculated based on the time the front advances between the first two obstacles. This is somewhat expected for large obstacles, because the flow is expected to change dramatically as the current reaches the first obstacle in the series. Unfortunately, the computational domain contained only three large obstacles in these simulations. This did not allow establishing clearly if the mean front velocity becomes independent of the rank of the obstacle for the higher-rank obstacles.

Once the jet like flow attaches on the flat part of the bed surface between two ribs and the current starts advancing toward the next rib, the front speed in the simulation with ribs (LR-R30) is close to constant (U_f/u_b~0.4) and slightly larger than that in the simulation with dunes (LR-D30) in the region in which the current moves on an inclined surface with a negative slope, which slows down the current. In fact, animations show that at times the front in the simulation with ribs is situated slightly ahead of the front in the simulation with dunes. However, the front speed decreases substantially during the impact stage between the current and the upstream face of the rib. Such a phenomenon is absent in the case dunes are present at the bed. In the end, the average front velocity is only slightly larger (0.5%) in the LR-D30 simulation.

As opposed to the flat bed simulations in which there is an increase of about 10% in the front velocity between Re=47,800 and Re=10^6, the mean front velocity is relatively insensitive to the Reynolds number, within the same range, if obstacles of height less than half the height of the incoming current are present at the bed. This is true for both types of obstacles with high and low bluntness. In fact, in the case of dune obstacles no variation is observed in the value of the front velocity (U_f/u_b=0.397) between the LR-D15 and HR-D15 simulations. For ribs, a small increase of the front velocity is observed between the LR-R15 (U_f/u_b=0.34) and HR-R15 (U_f/u_b=0.36) simulations. Thus, scale effects are relatively minor in terms of the temporal evolution of the front position for gravity currents propagating over series of dunes and ribs. In conclusion, as opposed to the flat bed case, experiments conducted with Re_f~10,000 should be representative of field conditions, at least as far as the front velocity is concerned.

4.4 Structure of the tail of the gravity current

The structure of the tail in the low Reynolds number simulations with a flat bed and with small obstacles at the bed is compared in Figure 4.10 at times when the front is situated at x~18.5H in all the three simulations. Important qualitative differences are observed between the case the heavier current propagates over a flat bed and the case it propagates over an array of obstacles.

Consistent with the findings of Ooi et al. (2009), the concentration distribution in Figure 4.10a shows that in the flat bed case a stably stratified interface, depleted of large-scale eddies, develops between the heavier current and the lighter fluid, starting at the position of the lock gate. In the later stages of the slumping phase ($x_f/H>10$), the interface ends at about 5H behind the front. The Kelvin-Helmholtz billows forming at the back of the head lose their coherence over a distance of about 4.5H. The stably stratified interface is slightly tilted toward the front region. The height of the high-density layer of fluid reaches a minimum at the end of the interface. It remains fairly constant in the dissipative wake region before increasing again in the head region.

As a result of the presence of the tilted interface, the streamwise velocity inside the current peaks at the end of the tilted interface and over the upstream part of the dissipative wake region ($u\sim0.7u_b$). The velocity decreases gradually as the front ($U_f\sim0.45u_b$) is approached. The velocity magnitude is close to zero within the tilted interface layer containing mixed fluid (Figure 4.10d). The thickness of the region of small velocity magnitude increases slightly in the dissipative wake region due to the presence of large-scale interfacial billows.

The structure of the current is very different in the case dunes or ribs are present at the bed. A layer of varying height containing mixed fluid develops between the regions containing heavier fluid and ambient fluid. The top of this layer is close to horizontal in the simulations with obstacles at the bed. The bottom of this layer undergoes quasi-regular deformations with the same wavelength at that of the obstacles (λ=3H in the present simulations). The velocity magnitude inside this layer is very small (Figure 4.10d). The reason for the formation of this layer is related to the formation of the jet-like flow and of the upstream propagating hydraulic jump as the front overtakes the obstacle. The extent of the jet-like flow corresponds to the regions of high velocity in Figure 4.10c and 4.10d. As already discussed, the formation of the jet-like flow containing mostly higher-density fluid induces a strong shear layer on its outer side (toward the ambient fluid). Once they form, the jet like flow and the associated shear layer are permanent features of the flow around the obstacle (Figure 4.10b). The downstream extent of the shear layer past the crest or downstream face of the obstacle is larger in the case ribs are present (2.25H vs. 1.5H). The only temporal change is that, after the front gets sufficiently far from the obstacle, the jet-like flow remains subcritical over its whole length. For obstacles of height D=0.15H, this happens starting with the second dune behind the front and, respectively, with the third rib behind the front.

The formation of the backward propagating hydraulic jump amplifies the strength of the upstream part of the shear layer associated with the jet-like flow. As the hydraulic jump propagates, the shear layer extends further upstream and becomes more horizontal. The shear later separates the layer of mixed fluid carried behind the jump with the ambient fluid above it (e.g., see also sketch in Figure 4.21). As the hydraulic jump reaches the obstacle situated behind the one where it originated, and propagates over this obstacle, the shear layer continues to expand upstream. At those locations two shear layers containing vorticity of the same sign can be observed. As time passes, these shear layers merge and the interface with the top layer of ambient fluid becomes closer to horizontal. Thus, the variable height layer containing low-velocity mixed fluid is a result of the interaction of the backward propagating hydraulic jumps with the obstacle situated upstream from the one the jump originated and the jet-like flow over the upstream obstacles. The process of formation and temporal evolution of the shear layer are very similar in the case of dunes and ribs of height D=0.15H.

In the case ribs are present at the bed; a strong shear layer of vorticity of opposite sign to the one in the shear layer forming on the outer side of the jet-like flow is also present. On the other hand, in the case of dune obstacles, a near-bed region of small velocity magnitude is present at about the middle of the leeside of the dune (e.g., around x/H=10, x/H=13 and x/H=16 in Figure 4.10d). It is due to the fact that the core of high-velocity fluid within the jet-like flow is slightly diverted away from the dune surface. The flow does not separate but a shear layer forms.

The above discussed mechanisms are similar for the case of obstacles of height D=0.3H. The differences are mostly of a quantitative nature, as can be seen from comparison of the concentration, out-of-plane vorticity and velocity magnitude distributions in Figures 4.10 and 4.11. For example, in the LR-D30 simulation, the velocity magnitude distributions show that the intensity of the jet-like flow downstream of obstacles situated at large distances from the front decreases much faster compared to the intensity of the jet-like flow downstream of the first obstacle behind the front. This also explains why the streamwise distribution of the Froude number in the LR-D30 simulation (Figure 4.12) shows the Froude number is less than 0.6 in the jet-like flow region around the second dune behind the front, despite being as high as 2.5 in the jet-like flow region around the first dune behind the front. In the LR-R30 simulation, the flow is slightly supercritical downstream of the second rib behind the front. The height $\bar{h}$ and streamwise velocity $\bar{u}$ used to calculate the Froude number ($\bar{u}/\sqrt{g\bar{h}}$) at a certain streamwise location are estimated as $\bar{h}=\int_0^H C dy$ and $\bar{u}=\int_0^H uC dy / \int_0^H C dy$.

In the case of obstacles of height D=0.3H, the vorticity amplification in the vorticity sheet forming as the hydraulic jumps propagate upstream is significantly faster in the case dunes are present at the bed (e.g., compare the extent and strength of the vorticity sheet forming upstream of the second and third obstacles in Figure 4.11b). This is because, in the case of large ribs, the splash of fluid generated during the impact sets up a region containing large-scale highly 3-D vortical eddies upstream of the obstacle. This induces additional jittering of the shear layer eddies in the region where the shear layer tries to extend upstream of the obstacle. However, at sufficiently large times, the vorticity levels in the horizontal part of the shear layer are again very similar in the LR-D30 and LR-R30 simulations.

Analysis of the distributions of the same variables in the simulations conducted at Re=10^6 shows scale effects are insignificant over this range of Reynolds numbers.

Figure 4.13 shows the instantaneous concentration distribution in a cross-flow section (x/h=10.5) cutting through the tail of the current in the LR-D15 simulation. The top interface between the layer of mixed fluid and the ambient fluid is close to horizontal. In contrast, the bottom interface with the layer of high-density fluid contains large-scale deformations with average amplitude of 0.1H. Analysis of the instantaneous flow fields at other time instances shows that this is a general characteristic of the flow in the tail region.

4.5 Analysis of the time variation of the mass fluxes and mass balance for the heavier lock fluid

The temporal variation of the total volumetric flux of heavier fluid $Q_i = (1/u_b H^2)\int CudA$ at selected streamwise locations is plotted in Figures 4.14a and 4.14c for the LR-D15 and LR-R15 simulations, respectively. The streamwise locations correspond to the initial position of the lock gate (x/H=0, i=0) and the crest or the downstream face of the five obstacles (i=1 to 5). Figures 4.14b and 4.14d show the time history of the flux of heavier fluid moving upstream $Q\text{-}_i = (1/u_b H^2)\int Cu\_dA$, at the location of the first two obstacles (i=1 and i=2), where $u_- = 0.5(u - |u|)$. A large part of this negative contribution to the total flux at a certain streamwise location is induced by the passage of the upstream propagating hydraulic jumps through that location. Figure 4.15 shows the time history of the volume of heavier fluid $M_{i,i+1}$ in between the crests or downstream faces of two successive obstacles. From continuity, one can write

$$M_{i,i+1} = (u_b / H)\int (Q_{i+1} - Q_i)dt \qquad (4.1)$$

The time history of Q_0 shows that the flux does not reach a constant value at the end of the acceleration phase (t~3.5t_0). Rather, a slow non-monotonic decrease is observed until t~35t_0 when Q_0 starts oscillating around an average value corresponding to the quasi-steady regime Q_s

($Q_s=0.105\,u_b H^2$ for the LR-D15 simulation and $Q_s=0.11\,u_b H^2$ for the LR-R15 simulation). This shows that the lock exchange set up used in the present investigation to induce the formation of the heavier current is not totally equivalent to the case when a constant flux gravity current is introduced at the position of the gate (x/H=0). In both simulations, the ratio between the peak value and the average value observed in the later stages of the propagation of the current is slightly higher than two.

The shapes of the Q_i plots at the location of the obstacles are qualitatively similar to that of Q_0. The ratio between the peak value and the average value observed after the quasi-steady regime is reached is less than 1.4 for Q_1 and Q_2. Starting with i=3, Q_i remains smaller than Q_s during the transient to the quasi-steady regime. This is because by the time the current reaches the third obstacle, there is a significant streamwise decay of the average value of the concentration inside the heavier current.

One important question is what is the time needed for the quasi-steady regime to be established between two successive obstacles ($M_{i,i+1}(t)$=constant). One will answer this question using i=1 as an example, for which the length of the computational domain was sufficient for the quasi-steady regime to be reached. For $M_{i,i+1}$ to become constant one needs both Q_i and Q_{i+1} to be constant in time. One expects Q_i to become close to constant after the hydraulic jump propagating from the i+1 obstacle reached section i. Though at later times the hydraulic jumps forming at the higher-rank obstacles (i+2, i+3, etc.) will reach section i, one expects the changes in Q_i to be of the order of those induced by the unsteadiness associated with the turbulence inside the gravity current (e.g., streamwise changes in the iso-concentration contours within the body of the current).

The average velocity of the backward propagating jumps in the LR-D15 simulation is $U_j=0.286\ u_b$, about 28% smaller than the front velocity ($U_f=0.397\ u_b$). This value is basically insensitive to the rank of the dune in the series. The average velocity of the jumps in the LR-R15 simulation is $U_j=0.25u_b$, about 26% smaller than the front velocity ($U_f=0.34\ u_b$). A small decrease of U_j with the rank of the rib was observed (e.g., the values of U_j/u_b were 0.27, 0.25 and

0.23 for the jump originating at the second, third and fourth rib, respectively). In the LR-R30 simulation U_j=0.25 u_b, while U_f=0.3 u_b.

Analysis of the simulation results shows that for the LR-D15 simulation the hydraulic jump forming as the current reaches the second dune (t=18.5t_0) passes the crest of the first dune at t=29_0, while the hydraulic jump forming as the current reaches the third dune (t=26t_0) passes the crest of the second dune at t=37t_0. Thus, one expects the quasi-steady regime to be reached a short time after t=37t_0 for the flow between Dune 1 and Dune 2. A similar analysis shows that the quasi-steady regime is expected to be reached after t=44t_0 for the flow between Dune 2 and Dune 3. In the case of ribs, the times at which M_{12} and M_{23} are expected to reach the quasi-steady regime are 40t_0 and 50t_0, respectively. These values are larger because of the lower velocities of the front and backward propagating hydraulic jumps in the simulation in which ribs are present at the bed. The time histories of Q_1 and Q_2 in Figures 4.14a and 4.14c and of M_{12} in Figure 4.15 support this analysis.

The backward propagating jumps play an important role in the analysis of the temporal variation of the fluxes. Indeed, the variations in time of Q_{-1} and Q_{-2} in Figure 4.14b show that the largest peaks occur at t=29t_0 and t=37t_0 when the jumps originating at the second and third dune reach the first and the second dune, respectively. The time at which the hydraulic jump passes over an obstacle is defined as the time when the interface between the mixed fluid region convected with the jump and the top layer of ambient fluid becomes horizontal above the top/crest of the obstacle. The occurrence of these events is relatively easy to infer from animations showing the concentration field. The passage of the hydraulic jump induces strong non-uniform variations in the values of Q_-. In the LR-D15 simulation, Q_- starts increasing from zero about 7t_0 before the peak value (~0.01 $u_b H^2$ for both Q_{-1} and Q_{-2}) is reached and then decreases during the next 4t_0. After some time Q_- starts oscillating about a non-zero value (about -0.003 $u_b H^2$). This is in part because these jumps are not sharp and their passage strongly disturbs the turbulent flow around the crest/top of the obstacle. As expected, in the simulation in which ribs are present at the channel bottom, the transient is shorter. In particular, the peak value is reached much faster, over about 2-3t_0. After the transient associated with the hydraulic jump passage, Q_{-1} and Q_{-2} oscillate around -0.003$u_b H^2$.

As the average value of the concentration in the heavier current decays with x, the mass of heavier fluid between two successive obstacles $M_{i,i+1}$ is expected to decay with i, once the quasi-steady regime was reached. The results in Figure 4.15 confirm this. For example, the ratio of $M_{1,2}$ to $M_{2,3}$ is around 1.15 in the LR-R15 simulation after the quasi-steady regime is reached. For a given i, $M_{i,i+1}$ is slightly larger in the LR-R15 simulation, mainly because the ribs occupy a smaller volume compared to the dunes.

The temporal variations of $M_{i,i+1}$ show the presence of an initial regime starting when the front of the current reaches the obstacle of rank i and ending when the front reaches the next obstacle. During this initial regime, the growth of $M_{i,i+1}$ is close to linear (Q_i>0 and Q_{i+1}=0). At the end of the initial regime, the region between the two obstacles contains about 70% of the total volume of heavier fluid present during the quasi-steady state. Once a backward propagating jump forms at the obstacle of rank i+1, a regime of logarithmic growth is reached. This regime lasts until a short time after the hydraulic jump forming at the obstacle of rank i+2 reaches the obstacle of rank i+1. At this point, the quasi-steady regime is reached (Q_i~Q_{i+1}). Because the front velocity is smaller in the simulation in which ribs are present at the channel bottom, the initial regime lasts longer in the LR-R15 simulation.

4.6 Mean flow and turbulence structure in between two successive obstacles situated at a large distance behind the front

The mean flow and turbulence structure in a region situated away from the head of the gravity current is analyzed after the flow reaches the quasi-steady regime in that region. Though the mean flow and turbulence statistics around an obstacle are somewhat dependent on the rank of the obstacle after the quasi-steady regime is reached, qualitatively these distributions remain very similar. Also, a direct comparison of the distributions of the relevant variables predicted by the low and high Reynolds number simulations with obstacles of height D=0.15H around the second obstacle allows understanding in a quantitative way the effect of the shape of the obstacle and of the Reynolds number on the flow and turbulence structure in the region where the quasi-steady regime is reached. For gravity currents with a large volume of release ($R<<1$), if the current propagates in the slumping phase over a large number of obstacles, most of the sediment may be entrained from the bed beneath the tail of the current. Finally, these distributions allow understanding what are the similarities and differences in the flow and turbulence structure between the case of a stratified flow (gravity current) over a surface containing large-scale roughness and the widely studied case of a constant density flow propagating over the same large-scale roughness elements.

4.6.1. Analysis of the 2-D flow and turbulence structure

The non-dimensional distributions of the mean (spanwise and time-averaged) concentration, C, mean velocity magnitude, u_{mag}, mean out-of-plane vorticity, ω_z, turbulent kinetic energy, k, and primary Reynolds shear stress, $\overline{u'v'}$, are compared in Figures 4.16 to 4.19 for the low and high Reynolds number simulations in which ribs and dunes of height D=0.15H are present at the bed. The comparison is done in the region situated around the second obstacle in the series. The length of this region is equal to the distance between the obstacles (λ=3H). In Figures 4.16 to 4.19 the streamwise coordinate has the origin ($x/\lambda=0$) at the center of the rib or at the crest of the dune. The domain shown in Figures 4.16 to 4.19 extends between $x=-0.33\lambda$ (-H) and $x=0.67\lambda$ (2H) in the streamwise direction. Figure 4.20 shows a comparison of the vertical profiles of these quantities at 6 stations.

The discussion bellow focuses on comparison of the low Reynolds number simulations. Reynolds number scale effects are discussed only when these effects are relevant.

The mean concentration contours in Figures 4.16a and 4.17a allow comparing the shape of the interface with the ambient (lighter) fluid in the simulations with ribs and dunes. The definition of the interface position is somewhat arbitrary. In the discussion below the interface is defined as the position of the iso-concentration contour C=0.1. In both simulations the interface is situated at y/H~0.57 at x/λ=-0.33. In the case dunes are present at the bed, the elevation of the interface decreases fairly linearly until the crest (x/λ=0). The decrease continues until close to the location of the trough (x/λ~0.1) where y/H~0.52. Then, the elevation starts increasing. The maximum value (y/H~0.6) is reached at x/λ~0.5. The relative positions of the maximum and minimum of the interface elevation are in very good agreement with those measured by Mierlo and de Ruiter (1988) for a constant density channel flow over an array of identical dunes (channel Reynolds number was close to 20,000) and with the RANS predictions of the same flow by Yoon and Patel (1996). In their experiments the mean depth of the open channel flow was close to 0.6H which is close to the average position of the interface in the present gravity current simulations. The maximum relative difference in the interface position was $\Delta y_{max}/H$~0.01. As expected, this value is much smaller than the one recorded for the gravity current case ($\Delta y_{max}/H=0.08$) for which the relative density difference between the two fluids on the two sides of the interface, and thus the reduced gravity, is much smaller.

In the case ribs are present at the channel bottom, the interface elevation is close to constant (y/H~0.57) between x/λ=-0.33 and x/λ=-0.05. This region of constant elevation is followed by a region in which there is a sharp decay of the interface elevation ($-0.05<x/\lambda<0.13$). The minimum elevation is y/H~0.5. The flow over the rib resembles the channel flow over a weir. Between x/λ=0.13 and x/λ=0.6 the interface elevation increases monotonically before reaching a plateau value around y/H=0.57. Though experimental data are not available for the case of a constant density flow over an array of ribs of identical size and spacing to the present gravity current simulation to compare the variation of the free surface elevation, one can suspect the constant density flow case will show a similar trend in terms of the positions of the regions where the free surface elevation is increasing or decreasing.

For both types of obstacles, no significant changes in the interface position are observed as a result of increasing the Reynolds number (compare Figure 4.16a to Figure 4.18a and Figure 4.17a to Figure 4.19a).

Comparison of Figures 4.17 and 4.19 allows a better understanding of the changes in the structure of the tail region of a gravity current propagating over large-scale roughness elements as a result of the shape and degree of bluntness of the roughness elements. A general sketch of the flow structure within the tail region in the case dunes or ribs are present at the channel bottom is given in Figures 4.21a and 4.21b, respectively. The sketch shows the position of the shear layers and the top interface of the high density fluid layer ($C>0.8$) present above the bed surface.

Though for both types of roughness elements, a layer of high concentration fluid ($C>0.8$) is present in the bottom part of the domain, as shown in Figures 4.16a and 4.17a, the height of this layer in the LR-D15 and LR-R15 simulations is different in several regions situated at an equal distance from $x/\lambda=0$. The comparison below starts at $x/\lambda=-0.33$ where the height of this layer is close in the two simulations (0.26H for dunes vs. 0.27H for ribs).

In the case dunes are present at the channel bottom, the height of the layer of high concentration fluid monotonically decreases as the crest is approached and then remains approximately constant (~0.15H) over the leeside of the dune and the trough region. Past $x/\lambda=0.33$ the thickness of this layer starts increasing again. It reaches a value close to 0.26H at $x/\lambda=0.67$. Thus, the maximum variation in the height of the layer of heavier fluid is only 0.11H. In contrast to this, the layer of mixed, lower concentration, fluid ($0.05<C<0.3$), in between the layer of heavier fluid and the layer of ambient fluid propagating in opposite direction, is subject to much larger height variations in the same region ($-0.33<x/\lambda<0.67$).

The presence of ribs with a blunt upstream face induces a gradual increase of the height of the layer of heavier fluid as the rib is approached. The height increases from 0.27H to 0.35H just upstream of the rib. The height of this layer over the rib is about 0.2H. Past the rib the height decreases sharply up to $x/\lambda=0.2$, where it reaches a value of 0.13H. The height of the layer of heavier fluid in this region is very close to the one in the simulation with dunes in the same region. Also, similar to the simulation with dunes, the height of the layer remains approximately constant for a certain distance (until $x/\lambda=0.45$ compared to $x/\lambda=0.33$ for dunes), after which it starts increasing again. Thus, most of the differences between the height of this layer in the LR-D15 and LR-R15 simulations occur in the region $-0.25<x/\lambda<0.2$. The differences will be much smaller if the height of this layer is defined such that it contains only heavier fluid that is convected in the streamwise direction. In other words, the height of the heavier fluid part of the recirculation regions forming upstream and downstream of the rib is not counted.

Indeed this is clearly seen from the comparison of the streamwise variation of the height of the layer of high velocity magnitude ($u_{mag}>0.2u_b$) in the simulations with dunes (Figure 4.16b) and ribs (Figure 4.17b). In both simulations, the top side of this layer is situated slightly above the upper interface of the layer of heavier fluid ($C>0.8$) over the whole length of the domain. The streamwise variation of the two interfaces is similar. In the case ribs are present at the channel bottom; the height of this layer is approximately constant over the whole length of the domain, including the regions situated upstream and downstream of the rib. The average height of this layer of high velocity fluid propagating over the bed surface is about 0.3H.

In the case dunes are present at the channel bottom, the height of the layer of high velocity fluid varies between 0.5H at $x/\lambda=-0.33$ and 0.3H close to the crest and in the trough region. The top interfaces of the layers of high velocity fluid and of high concentration fluid are roughly parallel, with the interface of the layer of high velocity fluid situated slightly above the interface of the layer of high concentration fluid. While in the case dunes are present at the channel bottom, the bottom interface of the layer of high velocity fluid is situated in the immediate vicinity of the bed at all streamwise locations, in the case ribs are present at the channel bottom, the bottom interface corresponds to the location of the separated shear layers forming upstream and downstream of the rib.

In both simulations the region situated downstream of the top of the roughness element, where the jet-like flow is forming, contains mostly high concentration fluid ($C>0.8$). Thus, in both simulations the role of the layer of high velocity fluid is to advect mostly high concentration fluid over the deformed bed surface. Observe also that the core of very large velocity magnitude ($u_{mag}>0.2u_b$) associated with the formation of the jet-like flow, as the heavier fluid is convected past the top of the roughness element, extends further downstream in the simulation with ribs. In other words, the penetration distance in the streamwise direction is larger in the case ribs are present at the channel bottom. This is also the reason the height of the layer of high velocity and high concentration fluid remains approximately constant for a longer distance downstream of $x/\lambda=0$ in the case ribs are present at the channel bottom.

The distribution of the out-of-plane vorticity ω_z in Figures 4.16c and 4.17c show the presence of a strong shear layer of positive vorticity that covers the whole length of the domain. As already discussed, this shear layer starts forming downstream of the crest/top of the roughness element on the outer boundary of the jet-like flow. Consistent with the different penetration length of the core of large velocity magnitude in Figures 4.16b and 4.17b, the streamwise decay of vorticity in the shear layer is significantly sharper in the case dunes are present at the channel bottom (e.g., the tongue of high vorticity extends up to $x=0.5\lambda$ in the simulation with dunes and up to $x=0.67\lambda$ in the simulation with ribs). In the region with $0<x/\lambda<0.67$ the shape of the shear layer follows the one of the top interface of the layers of high velocity fluid and high concentration fluid. However, this is not the case in the regions situated at $-0.33<x/\lambda<0.0$ in Figures 4.16b and 4.17b. Though a weak shear layer is still observed in both cases in the vicinity of the top interface of the layer of high concentration fluid (the vorticity is quite diffused in the simulation with ribs and much more concentrated in the simulation with dunes), the main region of high positive vorticity is situated at higher elevations. As already discussed, this region of high positive vorticity forms gradually in time as the shear layer forming on the outer side of the jet-like flow penetrates more and more in the upstream direction until it reaches equilibrium.

The distributions of ω_z in Figures 4.16c and 4.17c correspond to this equilibrium regime. The upstream extension of the shear layer is a result of the interaction of the current of lighter fluid with the region containing mixed fluid and with the downstream part of the shear layer forming on the outer side of the jet like flow. At equilibrium, this tongue of positive vorticity can be observed starting at $x/\lambda=-0.33$. In both simulations it extends upstream for another 0.33λ. The tongue of vorticity around y/H=0.6 present between x=0.33λ and x=0.67λ correspond to this segment of the shear layer forming over the next roughness element. Thus, the shear layer extends up to -0.67λ for the roughness elements analyzed in Figures 4.16c and 4.17c. While in both simulations the shear layers are close to horizontal and situated at an elevation of about 0.6H at their upstream part (-0.67<x/λ<-0.33 or equivalently 0.33<x/λ<0.67 according to Figures 4.16c and 4.17c) some differences are observed for -0.33<x/λ<0.0. While in the LR-R15 simulation the shear layer is still horizontal, in the LR-D15 simulation the shear layer becomes inclined, with a close to constant slope, as it connects the horizontal upstream part of the shear layer with the part situated close to the crest of the dune. In this region the position of the shear layer follows that of the top interface of the layer of large velocity fluid rather than that of the layer of high concentration fluid. The overall strength of the part of the main shear layer situated upstream of the crest/top of the roughness element (-0.67<x/λ<0.0) is larger in the LR-D15 simulation. As already mentioned, a secondary shear layer is present in this region at the location of the top interface of the layer of high concentration fluid.

The high turbulence production due to the shear present in the shear layers forming on the two sides of the jet-like flow induces high Reynolds stresses. The distribution of k in Figure 4.16d shows that in the simulation in which dunes are present at the channel bottom two regions of high tke develop downstream of the crest of the dunes. The tke levels inside the shear layer forming in the near-bed region as a result of the jet-like flow being deflected slightly away from the bed starting at x/λ~0.33 are similar to those inside the shear layer on the outer side of the jet-like flow. The tke amplification on the leeside of the dune is comparatively very small, as the flow remains attached. This is a main difference with the case of a constant density flow over a dune where a recirculation region and a strong separated shear layer form downstream of the crest. The tke levels inside the core of large velocity magnitude inside the turbulent jet-like flow are much smaller than those in the shear layers.

In the case ribs are present at the channel bottom; a similar region of high tke values is present inside the shear layer on the outer side of the jet-like flow (see Figure 4.17d). The non-dimensional values of tke are about 30% smaller compared to the simulation in which dunes are present at the channel bottom and its streamwise extent is larger (0.66λ for the ribs case compared to 0.45λ for the dunes case), which is consistent with the relative position and size of the core of large velocity magnitude inside the jet-like flow in the two simulations. The second region of high tke values corresponds to the separated shear layer forming at the upstream top corner of the rib. The tke levels remain relatively high even after the separated shear layer attaches to the horizontal part of the channel bottom. The tke levels are comparable to those in the shear layer forming on the outer side of the jet-like flow.

The distribution of the primary shear stress $\overline{u'v'}$ in Figure 4.16e confirms once again that turbulence production by shear is the main mechanism for the amplification of the Reynolds stresses in the tail of a gravity current propagating over dunes. A region of high positive values of $\overline{u'v'}$ forms on the outer part of the jet-like flow. Its position and size are fairly close to those of the region of high the values in Figure 4.16d. Interestingly, the magnitude of $\overline{u'v'}$ remains low inside the shear layer forming close to the bed, despite the high tke amplification observed in Figure 4.16d. Rather, a region of large negative values of $\overline{u'v'}$ is present on the leeside of the dune until the trough.

In the case ribs are present at the channel bottom, the positions and sizes of the regions of high tke values and those of high magnitude of the primary shear stress $\overline{u'v'}$ are similar.

In the case dunes are present at the channel bottom, the only significant difference in the non-dimensional distributions of the variables analyzed in Figures 4.16 and 4.18 as a result of the increase in the Reynolds number is the decrease in the size of the region of high tke values forming in the shear layer on the outer part of the jet-like flow, and the increase of the tke inside the region situated close to the leeside of the dune.

In the case ribs are present at the channel bottom, the increase in the Reynolds number produces a significant increase in the length of the core of high velocity magnitude inside the jet-like flow (e.g., see Figures 4.17b and 4.19b). The jet-like flow penetrates closer to the next rib. This also affects the thickness of the regions of high k and $\overline{u'v'}$ present at the location of the shear layer forming on the outer side of the jet-like flow, and the amplification levels of the turbulent Reynolds stresses within these regions (e.g., compare Figures 4.17d and 4.17e with Figures 4.19d and 4.19e).

Compared to the case of a constant density flow over ribs and dunes, the distribution of the Reynolds stresses is very different. In the case of constant density flow, a large recirculation region develops downstream of the leeside of the roughness elements. For k-type roughness its length is roughly equal to three times the height of the roughness element. The highest levels of amplification of the Reynolds stresses and of the tke are observed over the upstream part of the separated shear layer forming in between the main flow and this recirculation region. In fact, for the case ribs are present at the bed, the region of high tke is situated slightly above the level corresponding to the top of the ribs. The mean elevation of the upstream part of the detached shear layer is close to that of the top of the rib (e.g., see Cui et al., 2000, 2003) or crest of the dune (e.g., see Stoesser et al., 2008). Though such a region is also present in the case of a gravity current propagating over ribs, the amplification of the Reynolds stresses and tke is large not only over the upstream region of the separated shear layer but also over the downstream region where the shear layer reattaches. In the case of constant density channel flow past roughness elements no jet-like flow develops, thus all the regions of turbulence amplification associated with the presence of this flow feature in the case of a stratified flow are absent.

These differences can be analyzed in a more quantitative way by comparing the vertical profiles of the non-dimensional velocity magnitude, concentration and tke plotted in Figure 4.20.

4.6.2. Analysis of the 1-D flow and turbulence structure

4.6.2.1 Double-averaging procedure

In the case of constant density periodic channel flow, the flow is homogeneous in the spanwise and streamwise directions, so the mean flow and turbulence properties are function only of the vertical coordinate, y. In the case of constant density flow over an array of identical large-scale roughness elements, the flow in between two roughness elements is still periodic in the streamwise direction but not homogeneous. The period is equal to the spacing (the wavelength λ) between two successive roughness elements. Thus:

$$\bar{f}(x,y,z) = \bar{f}(x+\lambda,y,z)) \tag{4.2}$$

where $\bar{f}$ is the time-averaged value of an arbitrary variable f.

A 2-D spatial averaging procedure can still be employed to better understand the global changes in the flow and turbulence structure with the size / shape of the roughness elements and, in particular, with respect to the case of the flow over a smooth bed. The averaging is performed over the homogeneous direction and over the streamwise direction. At vertical locations situated below the crest of the large-scale roughness elements, the streamwise averaging includes only grid points situated inside the flow domain. Thus, for an arbitrary variable f:

$$\hat{f}(y) = \int\limits_{x}\int\limits_{z} \bar{f}(x',y,z)dx'dz \Big/ \int\limits_{x}\int\limits_{z} dx'dz \tag{4.3}$$

where x“ is a subset of x and does not contain the region situated in the interior of the roughness elements. This allows characterizing the global changes in the mean flow and turbulence structure in the case of a rough bed surface with respect to the base case when the bed surface is smooth based essentially on a 1-D analysis. This method (e.g., Nikora et al., 2001, 2004) is widely employed to study constant density flow past large-scale roughness elements, in particular past dunes.

For the case of a gravity current flow over a rough bed, a similar procedure can be used to characterize the global changes with respect to the base case (flow over a smooth bed) in the region situated far from the head where the flow over a large-scale bed roughness element is quasi-steady. The average in the streamwise direction is performed over the wavelength λ. The gravity current flow over a smooth (flat) bed is not exactly periodic in the streamwise direction, mainly because of the formation of the stably stratified tilted mixing layer in the tail. Also, the flow past the large-scale roughness elements in the quasi-steady region is weakly dependent on the rank of the obstacle, which again means the flow cannot be considered to be exactly periodic in the streamwise direction. However, comparing the flow and turbulence variables obtained using the double-averaging procedure is still relevant, especially if the comparison is made over the same region (e.g, the rank of the roughness element in the series is the same and the flow over the flat bed is analyzed in the region situated at the same distance from the initial lock gate position as the one considered in the simulations in which roughness elements are present at the bed).

The double-averaged streamwise velocity, $\hat{u}$, concentration, $\hat{C}$, and turbulence kinetic energy, $\hat{k}$, profiles from the low and high Reynolds number simulations are compared in Figures 4.22 to 4.25. The double-averaging procedure was applied over the flow domain used to analyze the 2-D flow past dunes and ribs in Figures 4.16 to 4.19.

4.6.2.2 Flat-bed cases

Figure 4.22 compares the non-dimensional distributions of $\hat{u}$ and $\hat{k}$ for the flat bed simulations. In both simulations the interface between the forward and the backward propagating current (C=0.5) is situated around y/H=0.38. At the same position, $\hat{u}$ ~0. A relative minimum is observed in the distribution of $\hat{k}$ at this position.

As one moves toward the bottom wall, $\hat{u}$ increases and then decreases back to zero to satisfy the no-slip condition at the bottom surface. As discussed in the literature review, the region between the bottom and the elevation at which $\hat{u}$ reaches a maximum (e.g., 0<y/H<0.18 in the LR-F case and 0<y/H<0.11 in the HR-F case) is called the inner layer (e.g., Stacey and Bowen, 1988), while the region above it ending at the edge of the bottom propagating gravity current (y/H~0.38 in the two simulations) is called the outer layer. The flow inside the outer layer resembles that in a shear layer while that in the inner layer resembles a turbulent boundary layer. As the Reynolds number increases, the boundary between the inner layer and the outer layer moves closer to the bottom wall. Consistent with the fact that the front velocity is larger in the HR-F simulation, $\hat{u}$ is larger in the HR-F case compared to the LR-F case. Most of the differences between the two velocity profiles occur in the lower half of the bottom-propagating current (y/H<0.19). They are due to the fact that the velocity gradient close to the bottom wall is much higher in the HR-F simulation, which is of course expected to happen as the Reynolds number increases in a turbulent boundary layer. The larger peak value of $\hat{u}$ is a secondary reason for the larger values of the velocity gradient at the wall observed in the HR-F simulation. In the top half of the bottom propagating current, the streamwise velocity is slightly higher in the LR-F simulation beneath the interface with the tilted mixing layer. The velocity profiles in the two simulations are close to identical within the tilted layer.

On the lighter fluid side, the profile of $\hat{u}$ is quite different. Reynolds number effects are felt only close to the top wall inside the thin attached boundary layer (1>y/H>0.96 in the LR-H simulation). The velocity decay inside the tilted mixing layer is close to identical. A plateau region is observed to form in both simulations some distance from the edge of the tilted layer. In both simulations the value of $\hat{u}$ within the plateau region is close to -0.3u_b. The only difference occurs neat the top wall. In the HR-F case, the plateau region extends closer to the top wall (0.99H compared to 0.93H in the LR-F case), consistent with the presence of a much higher vertical gradient of $\hat{u}$ at the top wall. This means the flux of lighter fluid moving in the opposite direction to the bottom propagating current is higher in the HR-F case, consistent with the observed variation of the flux of heavier fluid with the Reynolds number in the bottom part of the channel.

Two peaks are observed in the vertical variation of $\hat{k}$ at the boundaries between the tilted layer containing mixed fluid and the regions containing unmixed fluid present on the two sides of this layer. As a result of the larger thickness of the tilted layer in the high Reynolds number simulation, the peaks are situated farther away from the interface compared to the low Reynolds number simulation. The difference on both sides is close to 0.05H. Interestingly, while the peak value of $\hat{k}$ at the edge of the stably stratified tilted layer with the heavier current is relatively insensitive to the Reynolds number ($\hat{k}/u_b^2$=0.00145 and $\hat{k}/u_b^2$=0.00155 for the LR-F and HR-F simulations, respectively), the peak value on the lighter current side increases significantly with the Reynolds number from $\hat{k}/u_b^2$=0.0019 to $\hat{k}/u_b^2$=0.0029. The fact that $\hat{k}$ peaks at the interface between the tilted mixing layer and the heavier current in the present simulations is consistent with the measurements of Kneller et al. (1999).

On the lighter fluid side, this is followed by a monotonic decay of $\hat{k}$ with increasing y until very close to the top flat surface. Due to the presence of the thin attached boundary layer at the top surface (its thickness is about 0.04H for the LR-F case), a secondary peak is observed around the middle of this boundary layer (e.g., at y/H~0.98 for the LR-F case). However, the value of $\hat{k}$ at that location is very close to the values of $\hat{k}$ immediately outside the boundary layer. In the HR-F case the secondary peak can hardly be distinguished because of the very small thickness of the attached boundary layer.

On the heavier fluid side corresponding to the gravity current propagating over the bottom wall, $\hat{k}$ decays monotonically from the edge of the tilted layer until y/H=0.18 in the LR-F case and until y/H=0.11H in the HR-F case. The minimum values ($\hat{k}/u_b^2$ ~0.0001) are comparable to those on the lighter fluid side. In both simulations, the position of the minimum values is that of the maximum in $\hat{u}$. In other words the minimum in $\hat{k}$ occurs at the interface between the inner and the outer layer. This is fully consistent with the measurements of Kneller et al. (1999) and Stacey and Bowen (1988).

However, rather than remaining close to those minimum values, $\hat{k}$ starts increasing sharply as one moves toward the bottom wall. It peaks close to the wall, inside the boundary layer forming on the bottom wall beneath the gravity current, at y/H=0.025 in the LR-F case and at y/H=0.005 in the HR-F case. In both simulations, the peak values are around $\hat{k}/u_b^2$=0.0024 and are about 70% larger than the peak values at the edge of the tilted layer on the heavier current side.

The reason for the very different distribution of $\hat{u}$ on the two sides of the tilted layer is due to the shape of the mean velocity profile. Assuming most of the turbulence production is due to the presence of shear associated with a vertically non-uniform streamwise velocity profile, one expects the turbulence production and the tke to peak at locations where the gradient of the streamwise velocity is the largest. On the lighter fluid side $\hat{u}$ is close to constant until the edge of the thin attached boundary layer on the top wall, once one moves away from the tilted layer. This explains the very small values of $\hat{k}$ in this region (e.g., for 0.7<y/H<0.96 for the LR-F case). In contrast to this, on the heavier current side the vertical profile of $\hat{u}$ does not contain a plateau region. As a result, the turbulence production by shear in this region is significant and is the reason for the gradual increase of $\hat{k}$ starting at the boundary between the inner and outer layers and ending within the thin attached boundary later present at the bottom wall.

4.6.2.3 Effect of the bed deformation

The focus of the following discussion is on the changes in the vertical distributions of $\hat{u}$, $\hat{C}$ and $\hat{k}$ within the tail of the bottom propagating current as a result of the presence of ribs or dunes at the bottom surface.

The distributions of $\hat{u}$ (Figure 4.23) and $\hat{C}$ (Figure 4.24) in the layer of lighter fluid above the bottom propagating current are largely unaffected by the shape of the roughness elements (dunes vs. ribs of equal height) and the Reynolds number. In particular, this means the mean (integrated over the wavelength) velocity in the upper current of lighter fluid around a certain location situated above the tail of the bottom-propagating current is the same, regardless of the shape of the roughness elements. Meanwhile, the front velocity and the mean (integrated over the wavelength) streamwise velocity at certain location situated in the tail of the bottom propagating current are function of the shape of the roughness elements. The distributions of $\hat{k}$ (Figure 4.25) in the low-Reynolds number simulations with ribs and dunes at the channel bottom are similar only within the region where the streamwise velocity is close to constant ($0.65<y/H<0.93$). In the case when ribs are present at the channel bottom, the values of $\hat{k}$ inside the layer of lighter fluid show a significant increase with the Reynolds number. Scale effects are much less significant for the case dunes are present at the channel bottom.

The presence of large-scale roughness elements of height D=0.15H increases the height of the bottom-propagating current with respect to the flat bed case. As shown in Figure 4.23, the position of the interface between the two currents, defined as the elevation at which $\hat{u}=0$, increases from 0.38H in the LR-F and HR-F cases to 0.523H in the LR-D15, LR-R15, HR-D15 and HR-R15 cases.

In the case ribs are present at the channel bottom the distribution of $\hat{u}$ within the bottom propagating current is qualitatively similar to that in the flat bed case. The velocity increases monotonically to a peak value of $0.4u_b$ in case LR-R15 and $0.45u_b$ in case HR-R30. This is followed by a monotonic decay up to the channel bottom. Similar to the flat bed case, the elevation at which the peak $\hat{u}$ value is reached decreases with the increase in the Reynolds number from y=0.13H to y=0.08H. Both values are situated below the top of the ribs. The high $\hat{u}$ values are due to the presence of the downstream part of the jet-like flow, where the core of the high velocity is parallel to the bed (see Figure 4.17b). The increase in the Reynolds number induces an increase in $\hat{u}$ only below the top of the ribs (y=0.15D). As a result, the mean streamwise velocity $\hat{u}$ and the flux of fluid convected inside the tail of the bottom propagating current increase with the Reynolds number. This is consistent with the observed increase of the front velocity from $0.34u_b$ in the LR-R15 simulation to $0.36u_b$ in the HR-R15 simulation.

One qualitative difference with the flat bed case is the very mild increase of $\hat{u}$ between the interface (y/H=0.52) and y/H~0.35. By contrast, in the case dunes are present at the channel bottom, the increase of $\hat{u}$ in the same region is much more similar to that observed in the flat bed cases. The difference can be explained by comparison of the velocity distributions in Figures 4.16b and 4.17b. In the simulation with ribs, the region of large velocities between $y/\lambda=-0.33$ and $y/\lambda=-0.1$ and between $y/\lambda=-0.1$ and $y/\lambda=0.67$ is situated below y/H=0.3. It is only around the rib that large velocities are observed up to y/H=0.5, as the heavier fluid inside the tail is convected over the rib. The velocity magnitude above this region of large velocities remains very small until the interface (y/H~0.52) with the lighter current over the whole distance between two successive ribs. This explains the small increase in $\hat{u}$ values between 0.52H and 0.35H. By contrast, in the case of dunes the position of the upper interface of the region of high velocity fluid varies between y/H=0.5 and y/H=0.27. In fact the thickness of this region (0.35H to 0.4H) does not vary significantly with the streamwise position. Thus, at least over a significant part of the total length of the dune, large velocities are present between y=0.52H and y=0.35H.

Comparison of the profiles of $\hat{u}$ in the simulations with ribs and with dunes shows that most of the differences occur in between the top of the bottom propagating current (y/H=0.52) and the top/crest of the roughness element (y/H=0.15). Over this region $\hat{u}$ is larger in the case dunes are present at the channel bottom. As a result, the flux of fluid in the bottom gravity current is larger in the case dunes are present at the channel bottom. This is again consistent with the fact that at both Reynolds numbers the front velocity is higher in the simulations in which dunes are present at the channel bottom.

Reynolds number effects are insignificant in the case dunes are present at the channel bottom. This is consistent with the fact that the front velocity of the bottom current is basically the same in the LR-D15 and HR-D15 simulations ($U_f \sim 0.4u_b$). The profiles of $\hat{u}$ contain a plateau region starting some small distance below the top of the dune (y~0.12H) and ending at about 0.05H. The formation of this region is a consequence of the relative position of the region of high velocity fluid with respect to the dune surface (see Figure 4.16b). Such a plateau region is not observed in the case ribs are present at the channel bottom. In the case dunes are present at the channel bottom, the peak value of $\hat{u}$ occurs slightly above the crest of the dune. This was not the case when ribs were present at the channel bottom. Also, when the Reynolds number is increased, the position of the peak value moves away from the channel bottom rather than closer to it, as was the case for ribs.

Due also to the fact that the peak value is quite close to the value of $\hat{u}$ in the plateau region, one can argue a definition of the inner and outer layers based on the position of the peak value of $\hat{u}$ is not as appropriate in the case dunes are present at the channel bottom. Based on the distributions of $\hat{k}$ one will argue that the position of the dune crest, where $\hat{k}$ reaches its minimum within the core region of the bottom current, can be chosen to delimitate between the inner layer and the outer layer. Still, the velocity distribution within the inner layer is obviously different from the one expected in a turbulent boundary layer. On the other hand, the velocity profile within the outer layer is similar to the one observed for currents propagating over a flat channel bottom. In the case of ribs, the usual definition of the interface between the inner and outer layers appears to be appropriate, as the maximum in $\hat{u}$ is reached at about the same level with the minimum in $\hat{k}$ (see corresponding profiles in Figures 4.23 and 4.25).

The comparison of the vertical profiles of $\hat{C}$ in Figure 4.24 shows that below y~0.45H the concentration is larger in the simulation in which dunes are present at the bottom. The difference can be easily explained based on the spatial distributions of C in between two ribs or dunes (compare Figures 4.16a and 4.17a). For example, let us consider the region where y~0.15H, corresponding to the top of the dune or rib. The double-averaging procedure averages through all the cells situated at the same level. The iso-concentration lines with C>0.8 are roughly parallel to the deformed bed surface with the exception of the region situated close to the rib. Also in the region of high concentration, C increases as the distance to the bed decreases. Thus, in the simulations with dunes the average performed at y=0.15H will contain regions with very high values of C especially in between x=-0.33λ and x=0.05λ and for x>0.5λ, where y=0.15H is situated relatively close to the bed surface. In the case of ribs, with the exception of the short region corresponding to the streamwise extent of the top surface of the rib, the line y=0.15H is situated at 0.15H from the bottom. At that distance the values of the concentration are significantly smaller than those present in the simulations with dunes.

An important observation is that at the streamwise locations at which the structure of the bottom propagating current is analyzed in Figures 4.16 to 4.19, the concentration is smaller than one even close to the bed surface. This means some level of mixing is present over the whole height of the tail of the bottom propagating current. It may be induced by the significant amount of lighter fluid that is trapped near the bed as the head of the current propagates over the crest of the dunes or the top of the ribs. As the gravity current advances this lighter fluid in the leeside of the roughness elements mixes with the surrounding heavier current. As a result, over most of the length of the current the fluid near the bottom contains some small amount of lighter (ambient) fluid. Thus, no plateau region with $\hat{C}$=1, similar to the flat bed simulations (see Figure 4.24), is present in the simulations in which roughness elements are present at the channel bottom. The maximum value of $\hat{C}$ is close to 0.96 in the simulation in which dunes are present at the bed.

While in the flat bed simulations the mean value of $\hat{C}$ =0.5 is reached exactly at the interface between the two currents (y/H=0.38), that is not the case in the simulations in which roughness elements are present. The value of $\hat{C}$ =0.5 is recorded at y/H~0.47, which is situated below the interface (y/H~0.52).

Regarding the distributions of $\hat{k}$ in Figure 4.25, one has already commented on the correspondence between the position of the relative minimum value of $\hat{k}$ and the position of the interface between the inner layer and the outer layer. Similar to the flat bed cases, $\hat{k}$ increases sharply as one goes from the interface toward the bed, and reaches a peak at y/H=0.01-0.02 before sharply decaying to zero at y/H=0. Despite these similarities, the main reason for the strong amplification of $\hat{k}$ close to the bed is not the tke amplification within the thin attached boundary layer forming near the bed surface in the regions where the flow does not separate, but rather the formation of strong shear layer regions close to y/H=0. Obviously, these shear layer regions are absent in the flat bed simulations. In the simulations with dunes (Figures 4.16d and 4.18d), the shear layer on the inner side of the jet-like flow forming around x/λ~0.3 is the one mostly responsible for the amplification of $\hat{k}$. In the simulations with ribs (Figures 4.17d and 4.19d), it is the downstream part (0.1<x/λ<0.25) of the shear layer situated in between the jet-like flow and the recirculation region present downstream of the rib that is mostly responsible for the amplification of $\hat{k}$ near y/H=0. Consistent with these observations, the peak values of $\hat{k}$ are several times larger in the simulations containing roughness elements compared to the values observed in the flat bed simulations.

In all the simulations containing roughness elements a relative maximum is present in the vertical profile of $\hat{k}$ within the outer layer region. The peak values are reached in between 0.2H and 0.27H. A similar trend was observed in the flat bed simulations, where the peak corresponded to the location of the interface between the tilted mixing layer and the heavier fluid within the bottom propagating current. Around this interface the streamwise velocity gradient is high, which explains the high tke values. Despite these similarities, the origin of the peak in the vertical profile of $\hat{k}$ within the outer layer region is different in the case roughness elements are present. The peak in $\hat{k}$ is mainly a consequence of the strong tke amplification within the shear layer forming on the outer side of the jet-like flow (e.g., see tke distributions in Figures 4.16d and 4.17d). The peak values of $\hat{k}$ are smaller and the decay of $\hat{k}$ away from the peak value is milder in the simulations in which dunes are present at the channel bottom compared to the ones containing ribs. This is just a consequence of the relative size and position of the shear layer and degree of tke amplification within it in the simulations containing dunes and ribs, respectively. Finally, $\hat{k}$ decreases monotonically until close to the interface (y/H=0.52) between the bottom propagating current and the lighter current above it. In the case ribs are present at the bottom wall, a relative minimum is present close to the interface in the profiles of $\hat{k}$. This is similar to the variation observed in the flat bed cases. However, such a minimum is not present in the profiles predicted in the simulations containing dunes at the channel bottom.

4.7 Drag force on the ribs

The temporal history of the difference between the mean pressure on the upstream (P^+) and downstream (P^-) faces of the ribs, $\Delta P=P^+-P^-$, are shown in Figure 4.26 for the LR-R15 and HR-R15 cases and in Figure 4.27 for the LR-R30 case. The drag force F_d on the rib can be calculated as

$$F_d=A*\Delta P \qquad (4.4)$$

where A is the frontal area of the rib. The ratio of the frontal areas in the simulations with large ribs and in the simulations with small ribs is equal to the ratio of the heights of the ribs (0.3H/0.15H), which is equal to 2. Thus, the ΔP plots give direct information on the variation of the pressure component of the drag force. As was shown by Gonzalez-Juez et al. (2009b), the viscous component of the drag force on surface-mounted rectangular cylinders can be neglected, especially at high Reynolds numbers. Similar to previous investigations of flow past isolated obstacles (e.g., Gonzalez-Juez et al., 2009b, 2009c), ΔP, or equivalently F_d, increases exponentially due to the pressure increase on the upstream side, as the approaching gravity current decelerates, until it reaches a maximum. The time at which the first maximum occurs is taken as the end of the impact stage and the beginning of the transient stage during which ΔP is subject to large-scale temporal variations. Eventually, the value of ΔP becomes close to constant (quasi-steady stage). The transition to the final quasi-steady state is more complex in the case an array of obstacles is present at the bed compared to the case of an isolated obstacle. One obvious reason is the interactions of the reversed hydraulic jumps with the obstacles situated upstream of the one where the hydraulic jump is originating.

The variation of the drag with time in the simulation ribs of height D=0.3H, shown in Figure D1 for the first two ribs in the series, presents many similarities to the one observed for isolated ribs (e.g., see Figure 4.5 in Gonzalez-Juez et al., 2009b). For the first rib in the series, the impact stage ends at $t=15.4t_0$ when ΔP reaches a maximum. During the transient stage, ΔP first decays and then increases again to reach a second maximum at $t=19.5t_0$. Notice, this value of ΔP is about 15% larger than the value of ΔP at the end of the impact stage. The drag variation for the second rib (Rib 2 in Figure 4.27) shows an identical behavior. Starting at $t\sim24t_0$, ΔP oscillates around a mean value ($0.28\,\rho u_b^2$) which is only slightly smaller than the value at the end of the impact stage ($0.33\,\rho u_b^2$). In the case of an isolated obstacle, ΔP is expected to remain constant for currents with a very large volume of release. Thus, starting around $t=24t_0$, a first quasi-steady regime is reached. However, the presence of the backward propagating hydraulic jumps induces further variations in ΔP. The hydraulic jump originating at the second ribs starts interacting with the first rib around $t=48t_0$. The interaction ends at $t\sim56t_0$. During this time ΔP decreases abruptly by about 20%. The interaction of the first rib with the hydraulic jump originating at the higher rank ribs in the series is expected to produce further decay in the mean level around which ΔP oscillates. However, quantitatively the further reduction in ΔP is expected to be much less.

Interestingly, the time variation of ΔP for the second rib is qualitatively very similar to that observed for the first rib in the series. For both ribs, the absolute maximum occurs about $4t_0$ after the end of the impact stage and the ratio between this maximum value and the relatively constant value reached by ΔP before the arrival of the backward propagating hydraulic jump originating at Rib 3 is close to 1.4. Unfortunately, the computational domain was not long enough to investigate the evolution of ΔP after the hydraulic jump originating at Rib 3 reached Rib 2.

The temporal variation of ΔP is somewhat more complex in the case ribs that are small (less than half) compared to the height of the incoming gravity current are present at the channel bottom. Similar to the simulation with ribs of height D=0.3H, following the end of the impact stage, ΔP first decreases and then increases to reach a second maximum. Then, it decreases again. However, rather than reaching a regime in which ΔP is close to constant, large-scale oscillations in the variations of ΔP are still present for a long time. There are two reasons why the variation of ΔP shows much larger oscillations. The first is that the upper interface of the layer of higher concentration fluid is itself subject to relatively large-scale oscillations. The second one, which is the main reason, is the formation of the backward propagating hydraulic jumps.

A close inspection of the curves in Figure 4.26 shows that the regions of sharp decay in ΔP are in fact associated with the interaction of these hydraulic jumps with ribs situated upstream of the rib where they originated. For example, in the case of Rib 1 (LR-R15 case)) the jump originating at Rib 2 is responsible for the sharp decay of ΔP between $26t_0$ and $28t_0$. Though the jump originating at Rib 3 does not induce a very noticeable decay of ΔP around $37t_0$, probably because of the way it interacts with the large-scale deformations present at the upper interface of the layer of high concentration fluid in the vicinity of Rib 1, the jump originating at Rib4 induces a clear decay of ΔP between $44t_0$ and $46t_0$. As a result of the interaction of the hydraulic jumps with the obstacle, the overall shape of the temporal variation of ΔP is closer to a slow exponential decay toward a quasi-steady value rather than to a stair-step variation (from a constant value to a lower constant value after the passage of each hydraulic jump). This decay is characterized by a wider range of oscillations around the mean value. For Rib 1, the quasi-steady regime appears to be reached only after the passage of the jump originating at Rib 4 ($t>48t_0$).

The reason why for a certain rank of the rib the plots showing ΔP as a function of time for the high Reynolds number simulations are situated to the right of the plots showing ΔP(t) for the low Reynolds number simulation is the slightly larger front velocity in the HR-R15 simulation.

The next question is how the temporal history of ΔP varies with the rank of the rib and with the Reynolds number. To answer this question, the curves in Figure 4.26 were plotted in Figure 4.28 for the LR-R15 case and in Figure 4.29 for the HR-R15 case, such that the start of the impact stage occurs at the origin of the time axis for all the ribs in the series.

In the LR-R15 simulation, starting with Rib 3 a significant decay is observed in the maximum value of ΔP at the end of the impact phase. This is because, as a result of the interaction of the head of the current with the first two ribs, the fluid in the head region mixes with the ambient fluid. The decay of the mean concentration in the head region results in a smaller force during the impact stage. Starting with Rib 3, the maximum value of ΔP at the end of the impact phase decays monotonically with the rank of the rib. For all the ribs, the duration of the impact stage is close to $4t_0$ and ΔP decays after the end of the impact stage. Then, ΔP starts increasing again and a second peak is observed between $9.5t_0$ (Rib 1) and $10.5t_0$ (Rib 5). The increase and decrease in the values of ΔP before and after the second peak is reached is much milder compared to the ones observed around the first peak. Starting with Rib 4, the values of ΔP corresponding to the first and second peak are very close. For all the ribs, large-scale variations in the values of ΔP are observed past the second peak ($t>10.5t_0$). As already discussed, some of the regions of large decay are due to the passage of the reflected hydraulic jumps over the rib. For $t>10.5t_0$, the values of ΔP at a certain time from the moment the current starts interacting with the rib are comparable for all the five ribs. An envelope curve following an exponential decay toward a constant value can be used to represent the average decay of ΔP past the second peak.

Some similarities and some interesting differences are observed in the higher Reynolds number simulation. The maximum non-dimensional values of ΔP at the end of the impact phase for the first two ribs are similar and basically equal to the values observed in the LR-R15 simulation. The decay of this value with the rank of the rib is more uniform in the HR-R15 simulation. Still, the non-dimensional value of ΔP at the end of the impact stage for Rib 5 is the same in the two simulations. The main difference occurs after the minimum value of ΔP is reached at about $6t_0$ from the start of the interaction between the gravity current and the rib. For Rib 1 and Rib 2 the second peak value is comparable to that of the first peak value and is recorded at about $10.5t_0$ from the start of the interaction between the current and the rib. This is similar to the trend observed for Rib 1 in the LR-R15 simulation. Starting with Rib 3, the second peak value is slightly lower than the first peak value. However, no clear second peak can be distinguished for Rib 5. These two values remained close for all the ribs in the LR-R15 simulation. Moreover, starting with Rib 3 values of ΔP comparable to the second peak value are observed at later times.

The analysis below provides an explanation for some of the important features observed in the temporal variations of ΔP in the LR-R30 simulation. Figure 4.30 shows the time history of ΔP for Rib 1 and Rib 2 together with those of the mean pressure on the upstream and downstream faces of the rib, P^+ and P^-. Figure 4.31 shows the distributions of the concentration and the pressure around Rib 1 in a vertical section at representative moments. 2D streamlines superimposed on the concentration plots were used to visualize the main eddies at these time moments. Figure 4.31 shows similar information for Rib 2. The information in Figures 31 and 4.32 allows relating the temporal variation in the mean pressure to the flow physics.

The temporal variation of P^+ for both Rib 1 and Rib 2 is qualitatively similar. The pressure increases rapidly during the impact stage and then remains approximately constant for about $20t_0$ after the end of the impact stage (e.g., $t\sim31t_0$ for Rib1). Then, P^+ increases rather sharply due to an increase of elevation of the upper interface of the layer of higher concentration fluid close to Rib 1. As this raise of the interface induces a similar increase in P^- a very short time afterwards, the net effect on ΔP is negligible. Then, P^+ remains close to constant until the end of the simulation time.

The concentration contours in Figure 4.31a shows the maximum in P^+ occurs when the head impacts the upstream face of the rib and the loss of kinetic energy results into an increase of the pressure on the upstream face, consistent with Bernoulli‟s equation. This is immediately followed (Figure 4.31b) by the formation of a large splash of decelerating fluid from the head. The velocities inside the splash containing heavier fluid are fairly small. Observe also the formation of a strong vortex on the top of the rib that is detaching from the rib and is projected upwards with the splash. During the impact stage the pressure field on the downstream face of the rib is unaffected by the interaction between the head of the current and the upstream face of the rib (Figure 4.30).

Past the impact stage, the variation of ΔP is mainly related to that of P^-. Thus, the discussion will concentrate on the flow and concentration distribution behind Rib1. The decrease in $P^{\square}$ between $18t_0$ and $19.5t_0$ is mainly due to the fact that, as the higher concentration fluid starts moving past the top of the rib, a vortex forms behind the rib close to the top corner (Figure 4.31c). This vortex is bordered by the intrusion of high concentration fluid that moves toward the bed and increases its vertical velocity as it approaches the bed. As most of the high concentration fluid near the front of this intrusion originated in the splash, the fluid near the front has very little streamwise momentum. So, the trajectory of the particles situated at the front makes a low angle with the vertical. Observe that the pressure in between the front and the bed starts increasing in Figure 4.31c.

At a certain point ($t \sim 19t_0$, see Figure 4.31d) the front starts reaching the horizontal bed. As shown by the pressure contours in Figure 4.31d, the strength of the recirculating vortex in between the intrusion and the rib is large enough to reduce the pressure in that region to values comparable to those in the flow outside the gravity current. As shown in Figure 4.30, P^- reaches a minimum and ΔP reaches the second peak shortly afterwards, at $t=19.5t_0$. Then P^- starts increasing sharply until $21t_0$. To explain this increase, one has to analyze the changes in the flow as a result of the front of high concentration fluid reaching the bed.

In Figure 4.31d the flow resembles a jet of high concentration fluid reaching a flat surface at a high angle of attack. Consequently, a significant part of the high concentration fluid that increased its vertical velocity as it approached the channel bottom is diverted toward the downstream face of the rib. During the impact with the horizontal surface, the high concentration fluid loses its vertical momentum and acquires streamwise momentum. Thus, the high concentration fluid moving toward the rib close to the bed has a significant streamwise momentum. When this high concentration fluid reaches the lower part of the downstream face of the rib, it decelerates and P^- increases. The increase stops at around $21t_0$. What happens is that the structure of the high concentration flow convected over the top of the rib changes. This fluid acquires more streamwise momentum as the jet-like flow starts forming. As a result, the angle between the axis of the jet like flow and the vertical increases considerably compared to the angle observed during the initial stages of the interaction between the bed and the intrusion containing mostly high concentration fluid from the initial splash. The amount of high concentration flow convected from the jet like flow toward the rib decreases. Then, P^- is close to constant until $t \sim 31t_0$. The concentration contours in Figure 4.31e show the change in the orientation of the core of high concentration fluid convected over the rib as a result of the formation of the jet-like flow together with the accumulation of a layer of high concentration fluid at the bottom part of the recirculation region behind the rib. The pressure contours show a large increase of the pressure in the impact region between the jet-like flow and the bed. A noticeable increase of the pressure levels is also observed in the bottom part of the recirculation eddy that accumulates higher concentration fluid as the time passes.

P^- increases sharply around $t \sim 31t_0$ (Figure 4.30) due to an increase of the elevation of the upper interface of the layer of higher concentration fluid. As this increase is accompanied by a similar one for P^+, the change in ΔP is negligible. A comparison of the pressure distributions at $t=23.9t_0$ (Figure 4.31e) and $t=40t_0$ (Figure 4.31f) shows a general increase of the pressure levels on the upstream and downstream faces of the rib, consistent with the general increase of the elevation of top of the layer of higher concentration fluid. The position of the impact point between the jet-like flow and the bed is unchanged. The mean velocities inside the recirculation region that is filled with higher concentration fluid at $t=40t_0$ are much smaller than at $t=23.9t_0$. The pressure distribution on the downstream face of the rib becomes close to hydrostatic. Observe also an increase of the pressure on the top surface of the rib as the thickness of the layer of high concentration fluid over the top of the rib has increased.

Finally, comparison of the concentration distributions at $t=46.0t_0$ (Figure 4.31g) and $t=51.0t_0$ (Figure 4.31h) allows understanding the reason for the sudden increase of P^- around $t=51t_0$. At $t=46t_0$, the hydraulic jump propagating toward Rib1 is situated at x/H~8.5. The region situated on the outer side of the jet-like flow contains low concentration ambient fluid. At $t=51t_0$, the hydraulic jump has reached Rib 1 and a layer of mixed fluid is present on top of the jet-like flow. The top interface between this layer of mixed fluid and the layer of lighter ambient fluid, in the region situated downstream of Rib 1, is now horizontal and situated at the same level with that of the interface upstream of Rib 1. As a result, the pressure in the region situated immediately downstream of the rib increases within the whole water column below this interface. This produces the observed sharp increase in P^-. Meanwhile the increase in P^+ is negligible, as the interface with the lighter layer of ambient fluid does not change as a result of the passage of the hydraulic jump.

The pressure and concentration distributions are shown in the six frames of Figure 4.32 for Rib 2 at equivalent times to those at which the distributions are shown in Figures 4.31a to 4.31e for Rib 1. Comparison of these frames shows that the dynamics of the flow as the current reaches and is convected over Rib 2 is qualitatively very similar to that described for Rib 1. This includes the formation of the initial splash, the formation and growth of a vortex close to the downstream corner of the top of the rib, the convection of high concentration fluid from the splash toward the channel bottom at a small angle with the vertical and the increase of this angle as the jet-like flow forms, the large increase of the pressure near the impact point between the jet-like flow and the horizontal bed and the initial convection of high-speed high-concentration fluid toward the lower part of the downstream face of the rib followed by the accumulation of high concentration fluid in the recirculation region. The main difference is the fact that the mean concentration levels in the head of the gravity current impacting Rib2 are significantly lower than those in the head of the same current when it impacts Rib1. This is why, at equivalent times, the pressure levels upstream and downstream of the rib are lower for Rib2 compared to those for Rib1, but the distributions remain similar.

A similar analysis can be done for the LR-R15 simulation. Figure 4.33 shows the time histories of ΔP, P^+ and P^- for Rib 1 and Rib 3. Figure 4.34 shows the concentration and pressure distributions together with the 2D streamline patterns around Rib 1 in a vertical section at relevant time instants. Figure 4.35 shows similar information for Rib 3.

Compared to the LR-R30 simulation, in which P^+ remained constant after the end of the impact stage with the exception of the sudden increases produced by the passage of the backward propagating jumps, in the LR-R15 simulation P^+ increases with time over the simulated period. The overall trend can be approximated as being linear with a slope that is similar for Rib 1 and Rib 3. For both ribs, the temporal variation of P^+ after the end of the impact stage is subject to large-scale oscillations. The linear increase is expected to cease when the quasi-steady regime is reached. This increase is produced by the fact that it takes a lot of time for the top interface of the layer of high concentration fluid, and especially for the concentration distribution within this layer, to reach quasi-equilibrium.

The time behavior of P^- is also similar for Rib 1 and Rib 3, so one will focus on Rib 1 for which P^- is available over a longer time interval. A short time after the end of the impact stage, P^- starts increasing and reaches a maximum at about $3t_0$ after the end of the impact stage. Then, P^- decreases and reaches a minimum at about $6t_0$ after the end of the impact phase. Finally, P^- increases back to a value close to the one observed when the first maximum is reached (~$8.5t_0$ after the end of the impact stage) and then remains constant until the arrival of the hydraulic jump originating at the rib situated immediately downstream of the rib where the time variation of P^- is analyzed (~$17t_0$ after the end of the impact stage). The passage of the hydraulic jump produces a noticeable increase in P^-. This behavior of P^- is very similar to the one observed in the

LR-R30 simulation. Differences occur after the passage of the first reflected jump over the rib. Similar to the time history of P^+, P^- increases in a non-monotonic fashion. Again, the overall trend is linear but the mean slope is slightly larger than that for P^+. This explains the observed mild (linear or exponential) decay of ΔP for $t>17t_0$ after the end of the impact stage. Whether or not the difference in the average slopes is due to a faster increase in P^- at all times or it is related to the passage of the hydraulic jumps originating at the higher-rank embayments in the series is not entirely clear. One favors the former explanation, as one expects that as the rank increases the increase produced by the propagation of these jumps over the lower-ranked ribs will decrease and, at a certain point, ΔP should become constant in time (quasi-steady state is reached). For example, an increase in P^- at Rib 1 due to the passage of the hydraulic jump originating at Rib 4 is clearly distinguishable in the time variation of P^- around $t=45t_0$.

The concentration and pressure distributions around Rib 1 in Figure 4.34 for case LR-R15 show that the changes in the flow structure responsible for the aforementioned features of the temporal variations of P^-, P^+ and ΔP past the impact stage have many similarities to changes in the flow structure observed in case LR-R30. However, some differences are also present.

Figure 4.34a shows the structure of the current at the end of the impact stage, just before the splash starts forming around Rib 1. Similar to Figure 4.31a, a vortex forms on top of the rib. This vortex is convected away from the rib as the slash forms. The splash contains low-speed higher concentration fluid that is first convected upwards and then downwards as it passes the rib. Until the higher concentration fluid from the splash does not move below the top of the rib in the region situated downstream of the rib, the pressure in this region increases (see pressure distribution in Figure 4.31c). This produces the observed increase in P^- between $11.7t_0$ and $13.9t_0$.

As more higher-concentration fluid is convected past the top of the rib, the jet-like flow forms (Figure 4.31d). During this time, the angle between the jet-like flow and the vertical increases significantly and the recirculation region becomes very elongated and weak. In fact, at $t=16.7t_0$ the jet-like flow is close to parallel to the bed in the region situated immediately downstream of the rib. High concentration fluid already present into the lower part of the recirculation region is drawn back into the strong jet-like flow. This explains why P^- decreases behind the downstream face of the rib (compare the direction of the arrows on the 2D streamlines in the recirculation region in Figures 4.34c and 4.34d). This produces the minimum in P^- and the maximum in ΔP around $t=16.7t_0$.

As the shape of the top interface of the layer of high concentration fluid convected over the rib starts changing, the angle of the jet-like flow with the vertical starts decreasing (compare Figures 4.34d and 4.34e). The recirculation region recovers its usual shape and starts accumulating higher concentration fluid from the inner part of the jet-like flow. At this point, the pressure distribution upstream of the rib can be considered hydrostatic. Downstream of the rib, the largest pressures are observed in the region where the jet-like flow impacts the horizontal bed. As the flow velocities in the recirculation regions containing higher concentration fluid are relatively low, the pressure levels downstream of the rib reflect the presence of the layer of higher concentration fluid. This explains the increase in P^- and the decrease in ΔP that reaches a minimum around $t=20t_0$ (Figure 4.34e).

The concentration field at $t=24t_0$ (Figure 4.34f), just before the backward propagating jump starts interacting with Rib 1, resembles the one observed at $t=20t_0$. The only change occurs in the pressure field downstream of the rib. As the angle of the jet-like flow with the horizontal increases slightly, the size of the recirculation eddy increases too, and the pressure amplification in the impact region decreases. However, the pressure distribution close to the downstream face of the rib is not affected significantly. This is why P^-, P^+ and ΔP remain close to constant for $20t_0<t<24t_0$. Similar to what was observed in the LR-R30 case, the passage of the hydraulic jumps fills with mixed fluid most of the region situated above the jet-like flow downstream of the rib. The interface between the layer of mixed fluid above the jet-like flow and the top layer of unmixed ambient fluid becomes close to horizontal and is situated at about the same level as the interface with the layer of unmixed fluid upstream of the rib. Indeed, at $t=40t_0$ (Figure 4.34g) after the hydraulic jump has passed, the lines of constant pressure are close to horizontal both upstream and downstream of the rib. This mean the pressure distribution is close to hydrostatic on both sides of the rib. At a given level, the pressure values on the two faces of the rib are not equal. This is because the layer of mixed fluid above the jet-like flow is thicker downstream of the rib.

The concentration and pressure fields in Figures 4.35a to 4.35e show that the main mechanisms responsible for the variation of ΔP on Rib 3 are similar to the ones analyzed for Rib 1.

4.8 Energy budget and dissipation rate

Gravity currents are flows driven by the conversion of potential energy into kinetic energy, which is then dissipated by viscous friction. The local dissipation rate ε_r integrated over the computational domain Ω at a certain moment in time is denoted ε. For LES simulations, in which the model can directly calculate only the gradients in the resolved velocity field, the total dissipation rate has two components. One is the viscous dissipation, ε_0, and the other is the sub-grid scale (SGS) dissipation, ε_t, due to velocity gradients at the unresolved scales

$$\varepsilon = \int^{L_1}\int^{L_2}\int^{L_3} \varepsilon_r(x_1, x_2, x_3, t)dV = \int_{\Omega} \varepsilon_r dV = \int_{\Omega} u_i \frac{\partial}{\partial x_k}\left[\left(\frac{1}{\sqrt{Gr}} + \nu_{SGS}\right)\left(\frac{\partial u_i}{\partial x_k} + \frac{\partial u_k}{\partial x_i}\right)\right] dV = \varepsilon_0 + \varepsilon_t \qquad (4.5)$$

The total potential energy over the flow domain is:

$$E_p(t) = \int_{\Omega} C x_2 \, dV \qquad (4.6)$$

The total kinetic energy over the flow domain is:

$$E_k = \int_{\Omega} 0.5 u_i u_i dV \qquad (4.7)$$

Following Necker et al. (2005), in the case of compositional gravity currents a differential equation relating the rates of change of the potential and kinetic energy can be obtained if the velocity components are assumed to be equal to zero on all the non-periodic boundaries and the effects of diffusion in the transport equation solved for the concentration field are neglected:

$$\frac{dE_k}{dt} = -\varepsilon - \int_{\Omega} C u_2 \, dV = -\varepsilon - \frac{dE_p}{dt} \tag{4.8}$$

Integrating equation (4.8) with respect to time gives an integral balance equation for the mechanical energy:

$$E_k + E_p + E_d = const. = E_{k0} + E_{p0} \tag{4.9}$$

where E_{k0} and E_{p0} are the total initial kinetic energy and potential energy. The present simulations are started from rest so $E_{k0}=0$. The term, E_d, represents the time integral of the total dissipation rate.

$$E_d(t) = \int_0^t \varepsilon(\tau) \quad d\tau \tag{4.10}$$

The time evolution of the terms in equation (4.9) is plotted in Figure 4.36 for the simulations conducted at Re=47,800 with flat bed and obstacles of height D=0.15H. All three terms are non-dimensionalized by E_{p0}. A first regime characterized by the conversion of potential energy into kinetic energy is present at the start of all the simulations. This region roughly corresponds to the duration of the acceleration phase ($t<3.5t_0$). The process is essentially inviscid, as not much dissipation takes place during this regime ($E_d(t=3.5t_0)/E_{p0}\sim 0$).

In the flat bed case, the growths of E_k and E_d become linear for $t>18t_0$. This can be observed from the log-log plot in Figure 4.36c, where the variations of these two variables can be approximated by a straight line with the slope of 1. The linear regime is observed until the end of the simulation ($t\sim 40t_0$). The magnitude of the total dissipation rate peaks at $t\sim 10t_0$ ($x_f/h \cong 5$), and then decreases slowly until $t\sim 18t_0$ ($x_f/h \cong 9.5$), after which it oscillates around a constant value ($-0.035 u_b^3 h^2$). During the linear regime, the ratio of ε to dE_p/dt is 0.32 and that of $-dE_k/dt$ to dE_p/dt is 0.68.

As shown by the results in Figure 4.39a, A and B, the time variations of E_k, E_p and E_d and their time derivatives are qualitatively similar in the simulations with a flat bed. The effect of increasing the Reynolds number from 47,800 to 10^6 is mainly to enhance the temporal rate of growth of E_k during the linear regime from $0.07 u_b^3 h^2$ to $0.085 u_b^3 h^2$. This increase is mainly due to a reduction of the magnitude of ε from $0.035 u_b^3 h^2$ to $0.025 u_b^3 h^2$ and to a very small increase (from $0.105\,u_b^3 h^2$ to $0.11\,u_b^3 h^2$) in the magnitude of the rate of decay of E_p. During the linear regime the ratio of ε to dE_p/dt is 0.22 and that of $-dE_k/dt$ to dE_p/dt is 0.73 in the HR-F simulation. The increase in the Reynolds number causes a reduction in the value of the total dissipation rate over the linear regime of about 33%. The reduction in the values of ε during the linear regime in the high Reynolds number simulation is expected, as the viscous component of the dissipation rate is proportional to 1/Re and the increase of ν_{SGS}/ν with the Reynolds number in the regions where velocity gradients are present is, in average, not as fast as Re (less than linear).

The presence of obstacles induces significant qualitative and quantitative changes in the energy balance after the current overtakes the first obstacle. As will be analyzed below in greater detail, the combined effect of the smaller decay rate of E_p and higher dissipation rates within the body of the gravity current observed in the case in which obstacles are present at the channel bottom causes a decrease of E_k with respect to the flat bed case. This also partially explains the decrease of the front velocity compared to the case the bed is flat.

The rate of decay of E_p decreases with respect to the flat bed case after the front passes the first obstacle. Interestingly, at least for obstacles with D=0.15H, the temporal decay rate of E_p is independent of the shape of the obstacle, if one neglects the large-scale oscillations around the mean decay.

The most important qualitative change with respect to the flat bed case is observed in the variation of E_k. After the current passes the first obstacle, the rate of increase of E_k decreases substantially and, once it overtakes the second obstacle (x_f>9h), a regime in which E_k increases proportional to $t^{1/3}$ ($dE_k/dt \sim t^{-2/3}$) is maintained until the end of the simulation for both types of obstacles (see Figures 4.36c and 4.40). Some large-scale oscillations around the mean decay are observed in Figures 4.36 and 4.40. They are induced by the successive acceleration and deceleration of the flow in head region due to its interaction with the obstacles. The amplitude of the oscillations is larger in the case ribs are present at the channel bottom. In fact, the anti-symmetric character of the temporal variations of dEk/dt and dEp/dt and the absence of such oscillations in the variation of ε in Figure 4.40 show that the large-scale oscillations in dE_k/dt are just a consequence of the vertical movement of the heavier fluid in the head of the current induced by the large-scale bed deformations.

Some time after E_k starts increasing proportional to $t^{1/3}$, the total dissipation rate $\varepsilon=dE_d/dt$ in the simulations containing obstacles becomes larger than the one observed in the flat bed case. The log-log plot in Figure 4.36c shows that after a small time interval over which E_d increases faster in the case dunes are present at the bed, E_d increases proportional to $t^{1.63}$ for both types of obstacles. As shown in Figure 4.36, in the regime in which $E_d\sim t^{1.63}$, the values of E_d are slightly larger in the case in which dunes are present at the channel bottom. This may look surprising as one expects the regions of strong flow separation upstream and downstream of the square ribs and the separated shear layer forming close to the top of each rib will increase the dissipation rate with respect to the case dunes are present. The reason is that the length of the region of high dissipation values is larger in the simulation with dunes as the current propagates faster.

So, a more physically meaningful way is to look at the variation of the components of the energy budget with the front position, x_f. This is shown in Figure 4.36b. The magnitudes of the decay rates of E_p for ribs and dunes are not anymore identical. The simulation with ribs shows the smallest rate of decay. As expected, for $x_f>9H$ E_d increases faster in the simulation with ribs compared to the simulation with dunes. The variation of E_k with the front position remains independent of the shape of the obstacle for $x_f>9H$.

In contrast to the results for the flat bed case, as the Reynolds number is increased from 47,800 to 10^6, the temporal evolution of the terms in the energy budget is very similar both quantitatively and qualitatively and continues to be independent of the shape of the obstacle (see Figures 4.38a and 4.41). For example, the comparison of the energy budget in the LR-R15 and HR-R15 simulations (Figures 4.38c and 4.39b) shows the rate of increase of E_d is slightly lower as $E_d\sim t^{1.45}$ rather than $t^{1.63}$ and the average level of E_k in the region where $E_k\sim t^{1/3}$ is slightly higher in the HR-R15 simulation. This is consistent with the slightly larger front velocity observed in the higher Reynolds number simulation ($0.36u_b$ vs. $0.34u_b$). Scale effects are even less significant when the simulations with dunes (LR-D15 and HR-D15) are compared. In these simulations the front velocity is the same (U_f=0.397u_b). Scale effects are also negligible in the simulations in which obstacles are present at the bed when the variations of E_k, E_p and E_d are plotted function of the front position (compare Figures 4.36b and 4.38b). In fact the variations of E_p and E_d with x_f in the HR-D15 and HR-R15 simulations are even closer, as the average front velocities in the two higher Reynolds number simulations are closer compared to those observed in the lower Reynolds number simulations.

The presence of dunes and ribs with a height of D=0.3H, that is relatively close to that of the head of the current, induces significant changes in the variation of E_k compared with the cases in which smaller obstacles of height D=0.15H are present at the bed.

As shown in Figure 4.37b, in the case of larger obstacles E_k reaches a plateau around x_f/H=9. Rather than remaining constant, E_k starts to slowly decay in a non-monotonic fashion. The average value of E_k/E_{p0} in the plateau region is 0.13 in the LR-R30 simulation and 0.10 in the LR-D30 simulation. These values are close to value of E_k/E_{p0} (~0.13) at the start of the region where $E_k \sim t^{1/3}$ in the simulations with smaller obstacles (e.g., see Figure 4.36a). E_k is also expected to start decaying in the simulations with smaller ribs if a sufficiently long channel and a large number of ribs will be present such that the current starts transitioning to a turbulent drag dominated regime.

Moreover, despite the fact that the average front velocities in the two simulations are very close, for x_f>6H E_k is smaller in the LR-D30 simulation compared to the LR-H30 simulation. This is because the velocity distributions within the body of the current are not similar in the two simulations. As shown in Figure 4.11, the streamwise extent of the region of high velocity magnitude forming in the downstream part of the jet-like flow past each obstacle is much larger in the case ribs are present at the channel bottom. In the LR-R30 simulation, the current advances over a flat bed for a relatively long distance (~5H) as it propagates between two successive ribs. This results in relatively low streamwise decay rates for the large velocities present in the region the jet-like flow attaches to the bed. This explains why the current propagating over ribs has a higher kinetic energy than the current propagating over dunes despite the average front velocity being slightly smaller.

The variations of E_p and E_d in the simulations with obstacles of height D=0.3H (Figure 4.37a) are qualitatively similar to those observed in the simulations with smaller obstacles (D=0.15H). In the case of the obstacles of height D=0.3H, the rate of the decay of E_p is smaller compared to the case of obstacles of height D=0.15H. This difference is mainly compensated by the fact that starting from comparable levels in the plateau region, E_k decreases with x_f in the simulations with larger obstacles while it increases proportional to $t^{1/3}$ in the simulations with smaller obstacles. The smaller rate of decay of E_p is due to the fact that, as the current propagates over larger obstacles, larger regions of high density fluid are present at larger distances from the y/H=0 level.

Consistent with the results for the simulations with obstacles of height D=0.15H, when plotted function of the front position (Figure 4.37b), the rate of increase of E_d is slightly larger in the case dunes, rather than ribs, are present at the bed. After the front overtakes the first obstacle, the average rate of decay of E_p is the highest for the case of a flat bed and the smallest for the case dunes are present at the channel bottom.

Similar to the results for the case obstacles of height D=0.15H are present at the bed, the large scale oscillations of dE_p/dt and dE_k/dt (Figure 4.42) are out-of-phase in the simulations with obstacles of height D=0.3H.

4.9. Total dissipation rate

Analysis of the distribution of the spanwise-averaged local dissipation rate $\varepsilon_r(x_1,x_2,x_3,t)$ allows to better understand the changes in the structure of a gravity current as a result of the additional form drag induced by the presence of a series of obstacles that play the role of large-scale roughness elements. To study the distribution of the dissipative losses along the channel, the local dissipation rate ε_r is integrated over the spanwise and vertical directions. This leads to a variable ε^{23} which is a function only of the streamwise position.

$$\varepsilon^{23}(x_1) = -\int^{L_3}\int^{L_2} u_i \frac{\partial}{\partial x_k}\left[\left(\frac{1}{\sqrt{Gr}} + \nu_{SGS}\right)\left(\frac{\partial u_i}{\partial x_k} + \frac{\partial u_k}{\partial x_i}\right)\right] dx_3 dx_2 \tag{4.11}$$

Information on the spatial and temporal distribution of the local dissipation rate is also useful for developing theoretical models of these flows (e.g., see Huppert & Simpson, 1980), which incorporate the effect of the dissipation, and for determining the parameters in these models. As the dissipation cannot be estimated directly in these simplified models, one possible solution is to calibrate these parameters using the distributions of the local dissipation rate determined from numerical simulations. Moreover, the separate contributions of the head and tail regions of the current, or the contribution of the interface region to the total dissipation rate, can be calculated and modeled independently.

Figure 4.43 compares the distributions of ε_r for the case the bed is flat (LR-F) and for the case ribs of height D=0.15H are present at the channel bottom (LR-R15). Before the front starts interacting with the first rib in the series (e.g., see distributions at $t/t_0=8$ in Figure 4.43a) the distributions of ε_r in the two simulations are identical. Most of the dissipation takes place in the large-scale interfacial billows shed in the dissipative wake region. In some cases these billows are strong enough to interact with the bed surface and to induce detachment of vortical eddies from the attached boundary layer in the near-bed region (e.g., at x/H~2 in Figure 4.43a). The dissipation inside these eddies is comparable to the one inside the interfacial billows.

After the head passes the first rib, the distributions of ε_r in the two simulations (Figure 4.43b) start showing important qualitative differences. At $t/t_0=16$ (Figure 4.43b) the regions where the dissipation is the highest in the LR-R15 simulation correspond to the shear layer forming in between the jet-like flow and the separated region downstream of the rib originating at the upstream corner of the top rib surface, and to the shear layer on the outer side of the jet-like flow. In Figure 4.43b this second shear layer is basically indistinguishable from the region of high dissipation associated with the interfacial billows present immediately downstream of the rib. However, at later times (e.g., see Figure 4.43c and 4.43d), the region of high dissipation rate within this shear layer is distinct from the one associated with the interface region, especially after the reflected hydraulic jump has propagated over the distance separating two successive ribs. The dissipation levels are also relatively high in the core of the intensified mixing vortex. As the head propagates away from the vortex, the dissipation inside its core decreases quite fast.

A secondary region of high dissipation rate is present upstream of the rib. It corresponds to the recirculation region and shear layer that separates from the incoming boundary layer on the bottom of the channel. The dissipation levels within this region are comparable to the ones in the shear layers on the outer and inner side of the jet like flow.

Each time the current impacts a new rib, the amount of mixing in the head region increases. This is why, compared to the flat bed case, the degree of coherence of the interfacial billows shed behind the head is smaller. In the flat bed case, the length of the interfacial region behind the head in which the local dissipation rate is relatively high ($\varepsilon_r > 0.005 u_b^3 / h$) is close to constant (~3H) for $t/t_0 > 15$. In contrast to this, in the case ribs are present at the bed the length of this region continues to decrease in time (e.g., its length is about H at $t/t_0 = 16$). For $t/t_0 > 40$ the values of ε_r in this region are only slightly larger than the ones within the body of the current at the same streamwise positions and significantly lower than the average levels observed in the flat bed case.

In Figure 4.45 the distribution of ε^{23} is plotted at several non-dimensional times which are representative of the evolution of the current during the slumping phase in the low Reynolds number simulations with flat bed and obstacles of height D=0.15H.

In the later stages of the propagation of the current over the ribs ($t/t_0 > 35$), most of the dissipation takes place in the shear layers forming on the two sides of the jet-like flow past each rib. As inferred from the distributions of ε^{23} at $t > 32t_0$ in Figure 4.45, the average values of ε^{23} in the head and dissipative wake are slightly less than those recorded in between the first two ribs behind the front. Consistent with this, the total dissipation in the head and dissipative wake regions is about three times lower than the dissipation in between the first two ribs situated behind the front.

For example, at $t=48t_0$, the dissipation in the head and dissipative wake region account only for 9% of the total dissipation in the region with x/H>0. The dissipation in between two successive ribs decreases with the distance between the front and the ribs. The ratios between the total dissipation in these regions, starting with the one situated closest to the front, and the total dissipation in the region with x/H>0 are 13%, 20%, 24% and 31%, respectively. By contrast, in the flat bed case the average levels of ε[23] in these two regions are more than twice larger than the ones observed in the downstream part of the tail.

In the case dunes are present at the bed (LR-D15 simulation) the distributions of the local dissipation rate show many qualitative similarities with those observed in the case ribs are present at the bed. For example, the distributions of ε_r in the simulation with ribs (LR-R15) at $t=32t_0$ and $t=48t_0$ in Figures 4.43c and 4.43d are compared with the ones in the simulation with dunes (LR-D15) in Figures 4.44a and 4.44b. In the later stages of the propagation of the current most of the dissipation takes place over the body of the current. However, because the higher density flow does not separate as it is convected past the crest of each dune, there is no shear layer in between the core of high-velocity and high-density fluid and the bed (this is true only for sufficiently dense flows propagating over dunes, as the constant density turbulent flow past the dunes considered in the present study separates). Thus, immediately past the crest of the dune, most of the dissipation takes place in the shear layer forming on the outer side of the jet-like flow. Compared to the case ribs are present at the bed, the overall decay of the dissipation rate inside this shear layer is much faster as one moves to obstacles situated farther from the front. For example, at $t=48t_0$ the shear layer region on the outer side of the jet-like flow is hardly recognizable around the first two dunes in the series. This is not the case if ribs are present at the bed. The upstream propagation of the fluid with the successive hydraulic jumps forming at the crest of the obstacles provides an important mechanism which strengthens the vorticity and dissipation inside this shear layer. The hydraulic jumps are sharper and their strength is larger in the case of bluff obstacles like ribs.

The presence of dunes induces another qualitative modification in the flow structure past the crest of the dune. The strong spanwise vorticity component of the intensified mixing vortex induces a change in the orientation of the core of high-speed fluid within the jet-like flow. The core is diverted slightly away from the bed in the region situated beneath the eddy. This is also why a region of high dissipation develops close to the bed, starting at a short distance from the trough of the dune (e.g, around x=12.5H in Figure 4.44a). Such a region of high dissipation does not form in the case ribs are present at the bed. The dissipation inside this region and inside the core of the intensified mixing vortex remains high even after the front propagates over the next one or two dunes in the series (e.g., see Figure 4.44a).

In the case ribs are present at the channel bottom, ε^{23} peaks in front of each rib. It remains high until the dissipation starts decaying in the separated shear layers forming on the two sides of the jet-like flow. Then, it starts to decay as the next rib is approached. In the case dunes are present at the bed, large values of ε^{23} are observed immediately downstream of the crest of each dune and toward the middle of the upslope face where a region of high dissipation rate develops at the bed. Finally, ε^{23} decreases as the flow approaches the crest of the next dune.

Comparison of the distributions of ε^{23} in the simulation with dunes ($t=40t_0$) and ribs ($t=48t_0$) shows that, at a given moment in time, the total dissipation in the region between two successive dunes or ribs situated at the same distance from the front, is comparable. The different times at which the two distributions are plotted in Figure 4.45b were chosen such that the front positions are relatively close. The average levels are slightly higher in the case ribs are present at the bed, consistent with the fact that the total dissipation rate is slightly higher for ribs when ε is plotted function of the front position.

The distributions of ε_r are shown in Figure 4.46 at $t=38t_0$ for the HR-F simulation and at $t=40t_0$ for the HR-D15 and HR-R15 simulations.

For the flat bed case, the main effect of increasing the Reynolds number from Re=47,800 to $Re=10^6$ is the decay in the dissipation levels over the tail of the current. This can be observed from comparison of the distributions of ε_r at $t=40t_0$ in Figure 4.43d and at $t=38t_0$ in Figure 4.46a, when the front of the current is situated at the same position, $x_f/H\sim18.5$. The distributions of ε^{23} are compared in Figure 4.47b. In the LR-F simulation, the values of ε^{23} in the tail region are 50-100% larger at most streamwise locations. This is consistent with the fact the total dissipation rate over the whole length of the current ($x/H>0$) is close to 30% larger in the LR-F simulation, once the regime where ε becomes close to constant is reached in both simulations ($x_f/H>10$).

Scale effects are much less significant in the simulations containing ribs or dunes. For example, the streamwise variations of ε^{23} at $t=40t_0$ are compared in Figure 4.47c for the simulations in which dunes are present at the channel bottom. As the front velocity is the same, the distributions are compared at the same time instant. The distributions are qualitatively and quantitatively similar over the whole length of the current. The difference in the values of ε between the low and high Reynolds number simulations is less than 4% in the later stages of the evolution of the current once $\varepsilon_d\sim t^{\alpha}$. This means that for Re>50,000 the flow is controlled to a large degree by the turbulent form drag induced by the presence of the obstacles rather than by viscosity.

The presence of obstacle of height comparable to that of the head of the current induces significant modifications in the distributions of ε_r and ε^{23}. The distributions of ε_r in the LR-D30 and LR-R30 are compared at $t=32t_0$, $t=40t_0$ and $t=56t_0$ in Figure 45, 46 and 47. The distributions of ε^{23} at $t=32t_0$ and $t=56t_0$ are compared in Figure 4.48.

In the case ribs are present at the channel bottom, ε_r is strongly amplified over the lower part of the splash (e.g., see Figure 4.48b). This amplification is not present in the simulation with smaller ribs. A corresponding region is not present in the case of obstacles of low bluntness like dunes (see Figure 4.48a). However, once the front is convected past the top of the rib or the crest of the dune, the flow past large dunes and ribs, and the corresponding distributions of ε_r, are fairly similar. The flow past large obstacles presents more similarities with the flow past small dunes rather than small ribs. This is because the heavier fluid convected past the top of the large ribs does not have enough momentum to induce the formation of a large separation eddy downstream of the rib and of a strongly dissipative shear layer in between the jet-like flow and the bed. Rather, the core of high concentration fluid plunges toward the bed at an angle that is close to that of the fluid convected past the leeside of the large dunes. This explains the formation in the simulations with large dunes and ribs of only one region of high ε_r corresponding to the strong shear layer forming on the outer side of the jet-like flow. The dissipation is also amplified in the core of the intensified mixing vortex. The vortex is situated at x/H~14.5 in Figures 4.49a and 4.49b. The vortex can still be observed at $t/t_0=56$ in Figures 4.50a and 4.50b. Its dissipation is greatly reduced once the hydraulic jump propagating in the upstream direction overtakes it.

For obstacles of height D=0.3H, the overall amount of dissipation between the obstacle and the head is comparable until the head reaches the next obstacle (e.g., see Figures 4.51a and 4.51b). However, there is a difference between the distributions of the dissipation rate in the simulations with large dunes and with large ribs at the channel bottom. In the case dunes are present at the channel bed, the dissipation decays much faster in the two regions of high local dissipation rate, associated with the shear layer on the outer side of the jet-like flow and the region where the jet-like flow decelerates. This can be observed in the by comparing the distributions of ε_r in Figure 4.50 and ε^{23} in Figure 4.51b at $t=56t_0$ in between the first two obstacles (7<x/H<13) with those in between the second and the third obstacle (13<x/H<19). This also explains why, once the front has passed the second obstacle, the magnitude of the total dissipation rate in Figure 4.42 is larger in the LR-R30 simulation compared to the LR-D30 simulation.

4.10 Near-wall flow structure

Ooi et al. (2009) analyzed the near-wall flow structure for high Reynolds number gravity currents propagating over a flat horizontal surface. They showed that after the initial stages of current development, in the regions where the turbulence is strong, the near-wall flow contains the usual coherent structures associated with a turbulent wall boundary layer developing in a constant density flow over a no-slip surface. In particular, they showed that high and low streamwise velocity streaks are present in the vicinity of the bed behind the front. The presence of these streamwise velocity streaks in turbulent wall boundary layers is associated with the legs of the hairpin like vortices that form over the near-wall region.

The present flat-bed simulations (LR-F, HR-F) that were run over a longer time than the simulations performed by Ooi et al. (2009) allowed investigating in more details the temporal evolution and extent of the regions over which streaks are forming. The sizes of these regions vary as the current with R<<1 propagates over the horizontal bed. The streaks extend over the whole width of the current for a certain distance behind the front. After the stably stratified tilted layer has formed, the region containing streaks over the whole width of the current extends from the front until, at least, the downstream end of the stably stratified mixing layer. Then, a transitional region is present where areas of limited width not containing streaks are present beneath the tail of the current. The position and size of these areas changes in time. Finally, even in the cases with R<<1, the streaks disappear in the most upstream regions of the tail (x/H<0) where fluid is being accelerated from rest and the turbulence is not strong enough to induce the formation of the streaks in the near-bed region.

The discussion bellow concentrates on the near wall flow structure for the case when dunes or ribs are present at the channel bottom. The instantaneous vertical vorticity contours at the bed surface are shown in Figure 4.52a for the LR-D15 simulation at t/t_0=48 and in Figure 4.53a for the LR-D15 simulation at t/t_0=54.

Similar to the flat bed case, in the case roughness elements are present streamwise streaks of positive and negative vertical vorticity are observed over most of the length of the bottom surface in the region with x/H>0. These vertical vorticity streaks correspond to the streamwise velocity streaks situated at a short distance above the wall. Figures 4.52b and 4.53b show a top view of the distribution of u/u_b over a surface situated at a small distance from the deformed bed surface (0.006H). Figures 4.52c and 4.53c show a top view of the vertical vorticity contours at the bed to make possible a direct comparison with the velocity streaks visualized in Figures 4.52b and 4.53b.

The streamwise velocity contours show the presence of streaks only in the regions where the jet-like flow moves at a high speed parallel to the channel bottom. This happens downstream of the crest of the dunes and the downstream face of the ribs (see Figures 4.52d and 4.53d). However, this is just a consequence of the scale used to represent the streamwise velocity contours. In the case the bed surface has large-scale deformations, the average values of the streamwise velocity change significantly in the streamwise direction. Depending on the scale chosen, streaks can be visualized in one region or another. The vertical vorticity has the advantage that is less sensitive to the relatively uniform increase or decrease in mean values of the streamwise velocity in the streamwise direction. Thus, the discussion of the instability associated with the formation of streamwise streaks in the near-bed region will focus on the analysis of the vertical vorticity contours.

In the case dunes are present at the bed, the vorticity streaks cover the whole width of the channel past the first dune in the series. The streaks have a larger coherence beneath the region where the high-speed jet-like flow past the crest of the dune is strong. The average width of the streaks is 0.025H. Their coherence decreases as the crest of the next dune is approached. The fact that the vorticity streaks are still present above the highly inclined leeside of the dunes (e.g., see the inset in Figure 4.52a showing the vorticity distribution around the second dune behind the front) is not quite surprising as the heavier fluid convected close to the dune surface does not separate. Despite the fact that a recirculation region similar to the one observed for constant density flow over dunes does not form, the flow over the leeside of the dunes is close to separation. The loss in coherence over the downstream part of the upslope face of the dunes is due to the decay in the strength of the jet-like flow and the formation of the shear layer on the inner side of the jet like flow. Recall, this shear layer is induced the change in the direction of the core of high velocities inside the jet-like flow from being parallel to the deformed dune surface to being oriented slightly away from it. As a result, one expects the vorticity streaks start being lifted from the dune surface and the loss of coherence is smaller than the one suggested by Figure 4.52a that shows a view of the vertical vorticity contours at the bed.

The case in which ribs are present at the bed is even more interesting, as recirculation regions are present both upstream and downstream of the ribs. The streaks are highly coherent over the horizontal part of the bed where the flow is attached. A region of higher disturbance is observed over the top of the ribs and over the separated regions. However, many of the streaks present just before the flow separates, upstream of the rib, appear to have a correspondent in the flow downstream of the position where the flow reattaches, after it passes the rib. The experimental study of Djenidy et al. (1999) of flow past an array of bottom mounted cavities and the numerical study of Chang et al. (2006) of the flow past a 2D channel cavity with a length over depth ratio of 2 have shown that the streaks forming in a turbulent flow over a flat surface continue to be present over regions of flow separation, provided that the length of the separated region is not very high. In fact, for an array of cavities with an aspect ratio close to one, Djenidy et al. (1999) observed the formation of streamwise velocity streaks in a horizontal plane situated slightly above the tops of the cavities. Chang et al. (2006) observed that most of the incoming streaks maintained their coherence over the first half of the bottom cavity with a length to depth ratio of 2. The streaks were situated just above the shear layer forming on top of the cavity. At times, some of the streaks extended over the whole length of the cavity.

A similar phenomenon is present in the case of ribs. The velocity and vorticity streaks forming on the horizontal part of the channel bottom are lifted over the separated shear layers forming on top of the recirculation regions upstream and downstream of the rib and on top of the rib. Over this region the streaks lose some of their coherence. However, as the length of the region in which the streaks are lifted from the bed is less than 20% of the wavelength (3H), the loss of coherence, at least for some of the streaks, is not very large. After the flow reattaches downstream of the rib, the presence of a flat surface provides the energy needed for this instability to grow again and to form strongly coherent streaks. Additionally, the presence of the streaks above the recirculation regions can provide a mechanism for the mass exchange between the fluid convected above the recirculation regions and within the recirculation region (Chang et al., 2006).

4.11 Bed friction velocity

The bed friction velocity distributions are needed to estimate the amount of sediment entrained from the bed by a compositional current propagating over a loose bed. This is because most sediment entrainment formulae predict the entrainment rate function of the difference between the actual bed friction velocity and the critical bed friction velocity obtained from Shields" diagram for a given particle sediment size.

The number of mesh points in the spanwise direction in the lower Reynolds number simulations (LR) was sufficient to accurately resolve the streamwise velocity streaks. This was not the case in the high Reynolds number simulations (HR) where the streaks are expected to have a thickness that is smaller than the spanwise grid spacing used in the simulations. Still, the distributions of the spanwise averaged values of u_τ/u_b are expected to be reasonably well predicted, as these distributions are determined to a large extent by the large-scale flow features present in the flow (e.g., recirculation regions, presence of a jet-like flow in the vicinity of the bed, interfacial vortices, etc.).

The friction velocity is defined as $u_\tau = \sqrt{\tau_b / \rho}$. As the viscous sub-layer is resolved in the present simulations, the modulus of the wall shear stress vector, τ_b, is calculated from $\tau_b = \nu \cdot (\partial u_{mag} / \partial x_2)_{wall}$, where u_{mag} is the modulus of the velocity vector.

The instantaneous distribution of the non-dimensional bed-friction velocity contours, u_τ/u_b, is shown in Figure 4.54 for the LR-F, LR-D15 and LR-R15 simulations at a time when the front is close to x=18H. The spanwise-averaged distributions of u_τ/u_b for the three simulations are compared in Figure 4.55 at relevant time instants. Figures 4.56 and 4.57 provide similar information for the simulations with larger ribs and dunes (LR-D30 and LR-R30).

One obvious feature of the distribution of u_τ/u_b in the flat-bed simulation (Figure 4.54a) is the streaky structure present between x/H=0 and the front. The length of the compact zone behind the front in which the distribution of u_τ is streaky over the whole width of the current is about 7H. However, regions containing streaks are observed at all streamwise locations between the front and x/H=0. The size of the streaks forming in these regions is, in average, larger. In the later stages of the slumping phase ($t>20t_0$), after the stably stratified tilted layer has formed, the spanwise coherence of the billows shed in the dissipative wake region is not strong enough to induce significant variations in the distribution of the spanwise-averaged bed friction velocity in Figure 4.54a. This happens because the billows are strongly disturbed in the formation region, in part due to their interactions with the lobes and the clefts present at the front of the current. By contrast, in simulations of gravity currents with $R<<1$ conducted at much lower Reynolds numbers ($Re \sim 1,000$, see Ooi et al., 2009) large spanwise bands of high and low u_{τ} value were present behind the front at all stages of the evolution of the current during the slumping phase, as a result of the presence of highly-coherent interfacial billows.

The spanwise averaged distributions of u_{τ} in Figures 4.55a and 4.55b show that during the initial stages of the slumping phase ($t<20t_0$, roughly corresponding to the time when front overtakes the top/crest of the third roughness element in the series), the streamwise variation of u_{τ} behind the front is characterized by the presence of large amplitude oscillations. Analysis of the concentration and bed friction velocity fields at these time instants show that the oscillations are due to the formation of strongly coherent quasi two-dimensional interfacial billows behind the head. However, in the later stages of the slumping phase ($t>20t_0$), the amplitude of the large scale oscillations of u_{τ} in the streamwise direction becomes very small. The line plots in Figures 4.54c and 4.54d show that the initial rapid growth of u_{τ} at the front is followed by a mild non-monotonic decay until $x/H=0$. The absence of large-amplitude oscillations over the whole length of the current is a result of the low spanwise coherence of the interfacial billows shed behind the head and the absence of large-scale eddies in the tilted stably stratified mixing layer present above the tail. For $t>20t_0$, the maximum value of u_{τ} behind the front and the slope of the relatively linear decay of u_{τ} observed behind the front are close to constant in time.

The presence of large-scale roughness elements changes dramatically the distributions of u_{τ} once the current overtakes the first roughness element in the series. The distributions of u_{τ} in the streamwise direction are strongly modulated by the presence of the array of identical roughness elements and by the shape and length of these elements. Observe that in the later stages of the slumping phase, the distributions of u_τ between two successive roughness elements in Figures 4.54b and 4.54c are fairly independent of the rank of the roughness elements after a certain time from the time the front passed the downstream element. This is confirmed in a more quantitative way by the analysis of the distributions of the spanwise averaged values of u_τ in Figures 4.55c and 4.55d. This time interval is roughly equal to the time the hydraulic jump forming at the downstream element needs to reach the upstream element (close to $11t_0$ for the LR-D15 and LR-R15 simulations). The effect of the passage of the hydraulic jump on the bed friction velocity distributions will be analyzed later (see discussion of Figure 4.58). Thus, to characterize the distribution of u_τ beneath a gravity current with $R<<1$ propagating over a large array of roughness elements during the slumping phase, it is largely sufficient to analyze the details of the streamwise and temporal variations of u_τ between two successive roughness elements situated at a sufficiently large distance behind the front.

In the case dunes are present at the channel bottom, u_τ is strongly amplified close to the crest of each dune. Then, u_τ decreases sharply on the strongly inclined leeside of the dune where the flow is close to separating (e.g., observe the minimum value of u_τ in this region is very close to zero). A short distance after the trough of the dune, u_τ increases sharply due to the high-velocity and high-concentration jet-like flow impacting the dune surface at a high angle of attack. The formation of a short shear layer at the upslope side of the dune, as the core of high velocities inside the jet-like flow starts changing directions and orients itself slightly away from the dune surface, produces a significant decrease in u_τ over the distance the shear layer is present. Then, u_τ starts increasing again in a non-monotonic fashion, as the layer of heavier fluid is advancing against the slope of the dune toward the crest.

In the case ribs are present at the channel bottom, u_τ first increases and then decreases within the recirculation region situated downstream of the rib, as the reattachment point is approached. Then, the strongest increase is observed in the region where the jet-like flow reaches the flat horizontal bottom surface and changes direction to become parallel to it. The peak value is observed at a distance of about 0.3λ from the center of the rib. This is followed by a region of relatively slow non-monotonic decay (its length is close to 0.6λ), until the start of the small recirculation region forming just upstream of the next rib.

As opposed to the flat bed case, in the cases in which roughness elements are present, past the initial stages of the slumping phase the largest values of u_τ do not generally occur close to the front (e.g., see Figures 4.55c and 4.55d). This is because as a result of the interaction between the front and the roughness elements, the mixing in the head region is very high (e.g., compare concentration contours for the three simulations in Figure 4.54) and the mean concentration in the head region is smaller than the one in the layer of high concentration fluid behind the head. In Figures 4.55c and 4.55d, the maximum values of $u_\square$ in the front region are about 20% lower than the peak values observed in between two successive roughness elements situated beneath the tail of the current. A comparison of the distributions of u_τ at $t=32t_0$ and $t=40t_0$ shows that the distributions remain similar. A very mild decay of $u_\square$ in time is observed to occur in between two successive roughness elements situated at large distances behind the front, as the flow in that region approaches the quasi-steady state.

Though the average level of u_τ in the tail of the current is higher by 15-20% in the flat bed simulation compared to the simulations containing roughness elements, the presence of regions containing values of u_τ that are significantly larger (typically by about 30% for roughness elements of height $D=0.15H$) than the maximum values present in the flat bed case, including at the head of the current, means the capacity of a current propagating over roughness elements to entrain coarser sediment particles, for which $u_{\tau cr}$ is around or above the maximum value of u_τ in the flat bed case simulation, is much larger compared to the case the current propagates over a flat surface. Also, in the case large-scale roughness elements are present, most of the sediment is not going to be entrained beneath the head and dissipative wake regions but rather in the successive regions situated between consecutive roughness elements where the plunging jet-like flow reaches the lower part of the bed surface. On the other hand, the capacity of the current to entrain fine sediments is expected to be higher in the case the current propagates over a flat surface. The shape of the roughness has an influence on the peak values of u_τ. Past the initial stages of the slumping phase (e.g., see Figures 4.55c and 4.55d), the peak u_τ values in the simulation with dunes are larger by 10-15% than the ones in the simulation with ribs.

The distributions of u_τ in the simulations with larger roughness elements (D=0.3H) in Figure 4.56 do not show significant qualitative differences compared to those predicted in the simulations with smaller roughness elements having the same shape (see Figure 4.54). The comparison of the spanwise-averaged u_τ distributions at $t=40t_0$ in the simulations with dunes (Figure 4.57) shows the peak u_τ values are basically the same in the two simulations ($u_\tau \sim 0.05u_b$). Meanwhile, the comparison of the average values of u_τ and of the streamwise distributions between the crest of the first dune and the front suggests the capacity of the gravity current to entrain sediment is larger in the simulation with smaller dunes. In the case of roughness elements in the form of ribs, the peak u_τ values increase by about 20% as a result of the increase in the height of the ribs from 0.15H to 0.3H. The average values of u_τ in between the first rib and the front is also slightly larger in the simulation with large ribs. So, as opposed to the case in which dunes are present at the bed, one expects the capacity of the gravity current to entrain sediment will be larger in the simulation with larger ribs.

Figure 4.59a visualizes the changes in the distributions of u_τ between the first two ribs situated behind the front as a result of the passage of the backward propagating hydraulic jump in the LR-R30 simulation. As the hydraulic jump advances there is a clear decay in the levels of u_τ behind the jump. The concentration fields in a vertical plane in Figure 4.59a are used to infer the position of the jump. Comparison of the spanwise-averaged values of u_τ in Figure 4.59b allows a more quantitative analysis of the effect of the passage of the hydraulic jump on the bed friction velocity. When the hydraulic jump traveled about one third of the distance between the two ribs ($t=40t_0$), the u_τ values in the region situated behind the jump are up to 50% lower than the values present before the passage of the jump (e.g., see line plot at $t=34t_0$). The decay of $u_{\square}$ behind the jump is much less important during the time interval ($40t_0<t<46t_0$) the jump travels another $\lambda/3$. During the time interval the jump travels the last third of the distance to the next rib, u_τ decreases over the whole distance between the two ribs with the exception of the recirculation regions. The decay is of the order of 25% from the values recorded at $t=46t_0$. The effect of the passage of the backward propagating hydraulic jumps on the u_τ distributions is similar in the other simulations in which roughness elements are present. The hydraulic jump continues to propagate upstream after it has reached the crest of the first roughness element behind the one at which it formed. However, as it propagates further upstream, the effect on the bed friction velocity distributions is negligible.

Figure 4.60 shows the distributions of u_τ/u_b for the HR-F, HR-D15 and HR-R15 simulations. Comparison of Figures 4.54 and 4.60 allows understanding how the bed friction velocity distributions change as the current gets closer to the inviscid limit and to conditions present in practical applications of interest in geosciences and environmental engineering. Despite the larger velocity gradients at the bed, the values of u_τ/u_b are smaller in the higher Reynolds number (HR) simulations. This is mainly because u_τ is proportional to the square root of the molecular viscosity, so u_τ scales with $Re^{-1/2}$.

Qualitatively, a very good agreement is observed between the distributions of u_τ/u_b at the two Reynolds numbers both in the simulations with a flat bed and with a deformed bed. This is mainly due to the fact that the structure of the gravity current in the low and high Reynolds number simulations analyzed here is similar. If the Reynolds number in the LR simulations would not have been high enough for the flow in the head region to be strongly turbulent (Re_f>10,000), the u_τ/u_b distributions are expected to be subject to much larger Reynolds number induced scale effects. Besides the expected general decrease in the size of the streaks as a result of the increase in the Reynolds number, the only noticeable difference occurs for the flat bed simulations. The extent of the region situated behind the front and containing well defined streaks over the whole width of the current in the u_τ/u_b field increases from 7H in the LR-F simulation to about 13H in the HR-F simulation. Still, a large region not containing streaks in present close to x/H=0 in the HR-F simulation.

The spanwise averaged distributions of u_τ/u_b are plotted in Figures 4.61a, 4.61b and 4.61c for the HR simulations with a flat bed, with small dunes and with small ribs, respectively. The distributions are plotted at a time instant when the front is close to x/H=17. In the same figures, the distributions obtained in the corresponding LR simulations multiplied by a factor α=0.58 are shown. To allow a direct comparison, the distributions of u_τ/u_b in the LR simulations are also plotted at time instants when the front position is very close to the one in the corresponding HR simulation. The value of α was determined such that the best agreement between the distributions of u_τ/u_b is obtained in the flat bed simulations. The comparison shows that, in a very good approximation, the HR distribution of u_τ/u_b over the whole length of the current can be obtained by simply multiplying the LR distribution by a constant factor.

The same factor was then used in Figures 4.61b and 4.61c to scale the LR distributions of u_τ/u_b in the simulations containing roughness elements. Remarkably, the quantitative agreement between the scaled LR distributions and the HR distributions remained very good, especially in the simulations in which ribs are present at the channel bottom. Larger disagreements are observed only upstream of the position of the first rib or the crest of the first dune in the series. In the case dunes are present at the channel bottom, the comparison of the two line plots in Figure 4.61b suggests a slightly higher value of α (by 10-15%) would have produced a better agreement for the distributions of u_τ/u_b between successive dunes. Observe also, the length of the region of high bed friction velocity amplification present around the streamwise location where the jet-like flow impinges on the dune surface is slightly longer in the LR-D15 simulation. This can also be seen by comparing the distributions of u_τ/u_b in Figures 4.54b and 4.60b. Still, the overall agreement remains very satisfactory.

This finding has important consequences for experimental studies conducted to understand the behavior and sediment entrainment capacity of gravity currents at field conditions in rivers, lakes and oceans. The results in Figure 4.61 suggest that information collected from experiments conducted at much lower Reynolds numbers can be used towards quantifying the capacity to entrain sediment of gravity currents at field conditions, provided the Reynolds number in the laboratory experiments is high enough for the flow at the head of the current is highly turbulent. A related question is whether or not one can determine the value of the multiplication factor α. One possible way to try to theoretically determine the value of α is to assume the turbulence in the head region of the current propagating over a flat horizontal smooth surface is similar to that in a fully developed turbulent channel or pipe flow, and then to use the Moody diagram. The physical Reynolds number calculated with the average height of the head (~H/2) and the front velocity is close to 11,000 in the LR-F simulation and close to 250,000 in the HR-F simulation. Using the Moody diagram for the hydraulically smooth regime, the values of the friction factors are 0.028 and 0.015, and those of u_τ/u_b are 0.027 and 0.021, for the LR-F and HR-F simulations, respectively. The value predicted for the higher Reynolds number case is very close to the one (u_τ/u_b=0.02) predicted at the front in the HR-F simulation. However, the value predicted for the lower Reynolds number is smaller than the one (u_τ/u_b =0.036) predicted in the LR-F simulation. This explains the difference between the predicted (α=0.74) and observed value (α=0.58) of the multiplication factor.

Finally, one should point out that the bed friction velocity distributions in Figure 4.55 show that the mean level of u_τ/u_b behind the front of the current is similar in the flat bed (LR-F) and rough bed (LR-D15 and LR-R15) simulations. The comparison is always done for the same position of the front. However, as the front velocity is different in these simulations, the mean level of u_τ/U_f is larger in the simulations containing ribs and dunes. In particular, for the case when dunes are present at the channel bed, the skin friction component of the total drag is larger than the one predicted for the flat bed case. Of course, the presence of the roughness elements induces an additional drag form component to the total drag which increases with the relative size of the elements and their degree of bluntness.

4.12 Sediment entrainment capacity

The bed friction velocity distributions are needed to estimate the amount of sediment entrained from the bed by a compositional gravity current propagating over a loose bed. In most theoretical approaches, the flux of sediment entrained from the bed by the overflow at a certain time instant is also function of the critical entrainment velocity, $u_{\tau c}$. The critical bed friction velocity is function of the size of the sediment particle and is generally obtained using Shields" diagram, if the bed is assumed to contain uniform cohesionless sediment.

The distributions of u_τ/u_b were analyzed in the previous section. Figures 4.55, 4.57 and 4.58 contain horizontal lines corresponding to u_τ/u_b=0.048, 0.038 and 0.028. Let us assume the fluid is water, and the ratio between the density difference between the heavier lock and the ambient fluid and the ambient density, $\Delta\rho/\rho_o$, is 2% in the LR and HR simulations.

Then, for the LR simulations (Re=48,000) one obtains H=0.23 m and $u_b = \sqrt{g'H}$ =0.21 m/s. The time scale is t_0=1.1 s. Using Shields diagram, one can show that u_τ/u_b=0.048, 0.038 and 0.028 are the non-dimensional critical values of the bed friction velocity, $u_{\tau c}$, for sediment particles with a diameter of 50, 30 and 14 microns, respectively. For the HR simulations, one obtains H=1.72 m and $u_b = \sqrt{g'H}$ =0.58 m/s. The time scale is t_0~2.8 s. The values of $u_{\tau c}/u_b$ for sediment particles with a diameter of 50, 30 and 14 microns are 0.01, 0.008 and 0.006, respectively.

Most semi-empirical approaches used to estimate sediment entrainment assume either that the bed-load flux of sediment is proportional to u_τ^φ or to $(u_\tau^2 - u_{\tau c}^2)^{\varphi/2}$, where the former are typically used for live-bed scour conditions (e.g., φ=3 in the Meyer-Peter Muller formula, φ=5 in the Engelund and Hansen formula), while the later (e.g., φ=4.2 in the van Rijn formula to predict the equilibrium) are used mostly for clearwater scour conditions when contributions to the flux of sediment occur only at locations where $u_\tau > u_{\tau c}$ and are proportional to the excess bed shear stress.

A similar approach, not directly related to a formula for the bed-load flux of sediment, was proposed by van Rijn (1984). In this approach the local pick up rate, P, is estimated first.

$$P = 0.00033\left(\frac{u_\tau^2 - u_{\tau c}^2}{u_{\tau c}^2}\right)^{1.5} \frac{(s-1)^{0.6} g^{0.6} d^{0.8}}{\nu^{0.2}} \qquad \text{if } u_\tau > u_{\tau c} \qquad (4.12)$$

where d is the diameter of the sediment particle, g is the gravitational acceleration, ν is the molecular viscosity and s is the ratio between the density of the sediment particle and that of the carrying fluid. The pick-up rate P is expressed in units of volumetric flux per unit area per unit time. If at a certain location $u_\tau<u_{\tau c}$, then the local sediment entrainment is equal to zero (P=0). Once P is known, the flux of the sediment particles of diameter d entrained from the bed per unit time and unit width F(t) can be calculated as

$$F(t)=\frac{1}{W}\int_{A} P\,dA \tag{4.13}$$

where W (=H in the present simulations) is the width of the channel and A is the area of the channel bottom behind the front. For a given size of the sediment particles, P and F are proportional to $(u_\tau^2-u_{\tau c}^2)^{\varphi/2}$ with $\varphi=3$. Finally, the total amount of sediment entrained by the gravity current at a time T after the release of the lock gate can be obtained by integrating F(t) between t=0 and t=T.

Based on the above discussion, it is relevant to analyze the temporal variation of two non-dimensional variables characterizing the flux of sediment entrained by the gravity current over a certain distance. Assuming a certain size of the sediment particles at the channel bottom, most formulas predict the flux of sediment to be proportional either to I_1 or I_2 where:

$$I_1=\frac{1}{H^2u_b^3}\int_{A'} u_\tau^3\,dA' \tag{4.14}$$

$$I_2=\frac{1}{H^2u_b^3}\int_{A',u_\tau>u_{\tau c}} (u_\tau^2-u_{\tau c}^2)^{3/2}\,dA' \tag{4.15}$$

where A‟ is a certain region of the channel bottom. Moreover, in the simulations containing roughness elements, one can take the integration domain A‟ to be the bed region corresponding to one dune or to one rib. In this case, the time variations of I_1 and I_2 allow analyzing how the flux of sediment entrained at the bed in the region corresponding to a certain roughness element changes with the rank of the roughness element. As the quasi-steady state is approached, at large times after the passage of the front over a certain group of roughness element, one expects the values of I_1 and I_2 to become independent of the rank of the roughness element in that group. Moreover, past the first couple of roughness elements in the series, one expects the time variation of I_1 and I_2 for different roughness elements in the series to be similar if the variables are plotted such that the origin of the time axis is taken at the moment when the front starts moving over the integration domain A" that was defined for a certain roughness element.

Such an analysis was undertaken for the LR-R15 and LR-D15 simulations. In both simulations the extent of A" in the spanwise direction is equal to the channel width. In the simulation with ribs, the extent of A" in the streamwise direction for the rib of rank n was from $x=-\lambda$ ($x=-3H$) to $x=0$ where the center of the rib of rank n is situated at $x=0$ in a local system of coordinates. In the simulation with dunes, the extent of A" in the streamwise direction for the dune of rank n was from $x=-0.66\lambda$ ($x=-2H$) to $x=0.33\lambda$ ($x=H$). The crest of the dune of rank n is situated at $x=0$ in a local system of coordinates.

Figure 4.62 shows a visualization of the gravity current using the concentration fields together with the instantaneous distributions of u_τ/u_b downstream of the first rib ($x/H>5$) at representative time instants during the propagation of the current. Also shown are the regions where $u_\tau>u_{\tau c}$. An arbitrary value $u_{\tau c}/u_b=0.038$ was used to define the threshold for sediment entrainment in Figure 4.62. As previously discussed, for the LR simulations, this threshold value corresponds to sediment particles with a diameter of 30 microns. The regions with $u_\tau>0$ and with $u_\tau>u_{\tau c}$ within the integration domain A" associated with a certain roughness element are the ones which contribute to the I_1 and I_2 variables, respectively, calculated for the same roughness element. The threshold value $u_{\tau c}/u_b=0.038$ is large enough such that, as the flow approaches the quasi-steady regime in a certain region of the tail, $u_\tau<u_{\tau c}$ over the whole region. For example, at $t=40t_0$ the distributions of u_τ/u_b in Figure 4.55d show that $u_\tau<u_{\tau c}$ over the whole integration domain associated with Rib 2 ($5<x/H<8$). For Rib 3 a short region where u_τ is slightly larger than $u_{\tau c}$ is present within the integration domain ($8<x/H<11$) at $t=40t_0$. This small region is situated close to the location where the jet-like flow reaches the channel bottom ($x/H\sim8.5$). This short region disappears for $t>46t_0$. Thus, at large times after the front passage one expects I_1 will start oscillating around a non-zero value, while I_2 will be close to and slightly larger than zero. If the threshold value for sediment entrainment is such that at quasi-steady state $u_\tau>u_{\tau c}$ over some part of the integration domain associated with a certain dune or rib, then one expects I_2 will start oscillating around a non-zero value that is smaller than the corresponding one for I_1.

At $t=18t_0$ (Figure 4.62a), for $x/H>5$ the streamwise locations where $u_{\tau}>u_{\tau c}$ and $u_{\tau}>0$ are situated within the integration domain associated with Rib 2 ($5<x/H<8$). Though not shown, $u_{\tau}>0$ within the integration domain associated with Rib 1 ($2<x/H<5$). However, $u_{\tau}<u_{\tau c}$ over the same region so $I_2(t=18t_0)$ is expected to be equal to zero for Rib 1. At $t=20t_0$ (Figure 4.62b) the region where $u_{\tau}>u_{\tau c}$ is still located within the integration domain associated with Rib 2, but this area is much more compact and shorter. As the maximum values of u_{τ} are significantly larger compared to those observed at $t=18t_0$, $I_2(t=20t_0)> I_2(t=18t_0)$ for Rib 2. Meanwhile, as at both $t=18t_0$ and $t=20t_0$, $u_{\tau}<u_{\tau c}$ for $8<x/H<11$, $I_2(t=20t_0)= I_2(t=18t_0)=0$ for Rib 3. At $t=24t_0$ (Figure 4.62c), the size of the regions where $u_{\tau}>u_{\tau c}$ and the values of u_{τ} within these regions are comparable in the integration domains associated with Rib 2 and Rib 3. So, one expects the values of $I_2(t=24t_0)$ to be comparable for Rib 2 and Rib 3. At $t=28t_0$ (Figure 4.62d), the current is just overtaking Rib 3. The size of the regions where $u_{\tau}>u_{\tau c}$ is clearly larger in the integration domain associated with Rib 3 than in the one associated with Rib 2. Thus, $I_2(t=28t_0)$ for Rib 3 will be larger than $I_2(t=28t_0)$ for Rib 2. Meanwhile, similar to what was observed within the integration domain for Rib 2 between $t=18t_0$ and $t=20t_0$, the region where $u_{\tau}>u_{\tau c}$ within the integration domain associated with Rib 3 becomes more compact, shorter and the values of u_{τ} increase significantly (e.g., compare distributions of u_{τ}□at $t=24t_0$ and $t=28t_0$). At $t=32t_0$ (Figure 4.62e) the gravity current passed Rib 3. The total size of the regions where $u_{\tau}>u_{\tau c}$ is the largest within the integration domain associated with Rib 3. Smaller regions where $u_{\tau}>u_{\tau c}$ are present within the integration domains associated with Rib 2 and Rib 4. Finally, at $t=36t_0$ (Figure 4.62f) the gravity current is close to reaching Rib 4. The total size of the regions where $u_{\tau}>u_{\tau c}$ is larger in the integration domain associated with Rib 4 than the one associated with Rib 3. Meanwhile, the total size of the region within the integration domain associated with Rib 2 is very small. Thus, one expects $I_2(t=36t_0)$ to be close to zero for Rib 2.

The temporal variation of I_2 for the five ribs is plotted in Figure 4.63. The calculated values of I_2 confirm the qualitative analysis of the variation of I_2 for Rib 2 and Rib 3, which was based on comparisons of the bed friction velocity distributions at the time instants shown in Figure 4.62. The temporal variation of I_2 for Rib 1 is qualitatively and quantitatively different than the one observed for the other ribs. This is expected as the flow within the integration domain associated with Rib 1 is similar to the one of a current propagating over a flat surface that approaches an obstacle rather than to the one between two obstacles in a series. The distributions of I_2 for the other ribs are much more similar. This can be seen more clearly in Figure 4.64 where the distributions of I_2 for Rib 3 to Rib 5 were translated along the time axis by a multiple of the time it takes the current to propagate from one rib to the next one (~$9t_0$) and superimposed on the distribution for Rib 2. The current reaches the start of the integration domain for the rib of rank n (n>1) at around $t=10t_0$. The start of the integration domain is situated at the center of the rib of rank n-1. The maximum value of I_2 for the rib of rank n occurs around $t=20.5t_0$, a short time after current overtakes the rib of rank n. The average rate of decay for $t>20.5t_0$ is only slightly milder than the average rate of increase of I_2 between $10t_0$ and $20.5t_0$. A significant decay of the peak values of $I_2(t)$ with the rank of the rib is observed.

Figure 4.65 shows the time variations of $I_1(t)$ for the ribs of rank higher than 1 in a format similar to that used in Figure 4.64 for I_2. The maximum value of I_1 for the rib of rank n occurs when the current reaches the rib of rank n ($t=19t_0$), a little bit earlier than the time when the maximum value for I_2 was reached. For $t>19t_0$, I_1 starts decreasing slowly toward a constant value corresponding to the reach of the quasi-steady regime. The decay of the peak values of $I_1(t)$ with the rank of the rib is much smaller than the one observed for I_2.

Figures 4.66 and 4.67 show the time variation of $I_2(t)$ and $I_1(t)$ in a similar format to the one used in Figure 4.64 and 4.65. Similar to the case when ribs are present at the channel bottom, $I_2(t)$ peaks around $t=19t_0$. The only exception is for Dune 2, for which I_2 peaks earlier at $t\sim17t_0$. With the exception of the curve for Dune 2, the other three curves are quite close at all times and no significant decay in the peak value is observed starting with the dune of rank 3. Though the peak values for $I_2(t)$ are slightly smaller in the simulation with dunes, the decay of $I_2(t)$ toward zero after the peak is reached is much milder. This explains why the area beneath $I_2(t)$ is larger in the simulation with dunes. This means that a gravity current propagating over dunes will entrain more coarse sediment (such that $u_\tau<u_{\tau c}$ once the quasi-steady regime is reached in a certain region) in between two consecutive roughness elements than a current propagating over ribs of the same height. Most of the differences will occur after the front current reaches the crest/top of the downstream roughness element.

Similar to the time variation of I_1 plotted in Figure 4.65 for the simulation with ribs, the curves showing $I_1(t)$ for Dune 2 to Dune 5 are very close and the decay of the peak values of $I_1(t)$ with the rank of the dune is small. All the curves show a maximum at $t\sim20t_0$, immediately after the crest of the next dune is reached. This is followed by a region of very mild decay toward the constant value expected to be reached once the quasi-steady regime is established. The larger values of $I_1(t)$ observed for $t>20t_0$ in the simulation with dunes, means that the capacity of the current to entrain sediment in between the crests of two consecutive dunes after the front passed the crest of the second dune is larger than the one of the same current propagating over ribs of equal height in the same region. This is in particular true once the quasi-steady regime is reached. Of course, the present simulations allow to draw these conclusions only for roughness elements with $D/\lambda=0.05$ (k-type roughness) and for the case the height of the high Reynolds number gravity current is larger (by about two times) than the height of the roughness elements.

Figure 4.68 shows the non-dimensional distributions of the flux of sediment entrained at the bed per unit width $F(t)$ calculated using Van Rijn‟n (1984) formula (equations 4.12 and 4.13) for the LR simulations with a flat bed and with roughness elements of height $D=0.15H$ and $D=0.30H$. This quantity is similar to $I_2(t)$. However, the integration is done over the whole length of the current ($x/H>0$). The results are shown for three values of $u_{\square c}$ corresponding to mean sediment particle diameters of 14, 30 and 50 microns. One should mention that even for $d=50$ μm, the values of $u_{\tau c}$ are relatively high compared to the values of u_τ beneath the current at all stages of the evolution of the current in the LR simulations (see Figures 4.55, 4.57 and 4.58).

The results in Figures 4.68a and 4.68b confirm the qualitative trends describing the variation of the sediment entrainment capacity that were inferred just based on the comparison of the distributions of u_τ at different stages of the propagation of the gravity current in the LR-F, LR-D15 and LR-R15 simulations. They show that once the current propagates over the first roughness element in the series ($t>10t_0$), the flux of sediment entrained at the bed by the current propagating over dunes is higher than the flux induced by the current propagating over ribs of equal height. The flux is the lowest for the case the current propagates over a flat surface. This flux is negligible in the LR-F simulation for particles with $d \geq 30$ μm (Figure 4.68b). However, as already pointed out, one expects that for much smaller particles ($d<<14$ μm), the flux of sediment entrained at the bed will be the highest for the current propagating over a flat bed. F(t) is negligible in the LR-R15 simulation for particles with $d \geq 50$ μm. Non-zero values are observed in the LR-D15 simulation only over part of the simulation time.

Consistent with the distributions of u_τ in Figure 4.57, the effect of increasing the size of the dunes is to slightly decrease the values of F(t) for particles with $d<30$ μm after the current passes the first dune (see Figures 4.68a and 4.68b). By contrast, the effect of increasing the size of the ribs is to significantly increase the values of F(t) for particles with $d<30$ μm (see Figures 4.68a and 4.68b). These results are consistent with the distributions of u_τ in Figure 4.58.

Finally, Figure 4.69 compares the dimensional distributions of F(t) in the low and high Reynolds number flat-bed simulations for particles with $d=14$ μm. Recall, that one has assumed $\Delta\rho/\rho_o=0.02$ in both simulations. As a result $H=1.72$ m, $u_b=0.21$ m/s, $t_0=1.1$ s in the LR-F simulation and $H=1.72$ m, $u_b=0.21$ m/s, $t_0=2.8$ s in the HR-F simulation. The difference between the dimensional values of F(t) after the initial stages of the slumping phase is between 2 and 3 orders of magnitude.

4.13 The case of a gravity current propagating over an array of closely-spaced 2D ribs

The simulations with ribs and dunes of height D=0.15H have shown the presence of a slumping phase in which the front velocity is constant and smaller than the front velocity observed for the flat bed case. The computational domain in the simulations with obstacles of height D=0.3H was too short to clearly establish the presence of a constant velocity slumping phase. In the present section the case of a gravity current propagating over more densely spaced ribs of height D=0.15H is considered. The spacing between the ribs is only λ=H, compared to λ=3H, in the LR-R15 and LR-D15 simulations. The smaller spacing means the effect of the drag force on the current will be larger over the same streamwise distance. The simulation with a higher drag for which λ=H is denoted LR-R15-HD. The Reynolds number is the same (47,800) and the number of ribs on each side of the lock is equal to 22, compared to only 5 in the LR-R15 case. In the LR-R15-HD case, the first rib is located at 5H from the lock position (x/H=0).

In the case of constant density flows, the ratio between the rib spacing and the rib height in the LR-R15-HD simulation corresponds to a d-type roughness regime. However, in the case of a gravity current, the higher density fluid splashed as a result of the impact with the rib plunges down and reattaches on the bottom of the channel way upstream of the next rib. Also, the front regains its usual shape before starting interacting with the next rib (e.g., see discussion of Figure 4.74). Thus, in the case of gravity currents, the conditions considered in the additional simulation with λ=H correspond to k-type roughness, similar to that in the LR-R15 and LR-D15 simulations.

The larger drag force per unit length is expected to slow down the current with respect to the LR-R15 simulation. However, two important questions are whether or not the slumping phase will be present and if for a gravity current with a large volume of release (R<<1) this slumping phase will be followed by a turbulent-drag dominated regime in which the front velocity decays in time. The results in chapter 5 for currents with a small (finite) volume of release (R=O(1)) will show that for sufficiently large obstacles and for long domains, the current transitions from the slumping phase to the inertia-buoyancy phase and then to the turbulent-drag dominated regime. Over this last regime, the simulations confirmed that $U_f \sim t^{-1/2}$ which agrees with theory (Hatcher et al, 2000).

Obviously, for the case of currents with a very large volume of release, the buoyancy-inertia phase is not present. However, as the experiments of Tanino et al. (2005) and Jamali et al. (2008) have shown, gravity currents with a large volume of release (no interaction of the lighter current with the endwall) propagating in a porous medium transition from the slumping phase to the drag-dominated regime. Their experiments showed that for sufficiently low cylinder Reynolds numbers ($Re_d<35$) and relatively large porosities (interaction among the wakes of neighboring cylinders is small), such that the drag coefficient for the cylinders in the canopy $C_d \sim 1/Re_d$ (linear drag regime), $U_f \sim t^{-1/2}$ and $x_f \sim t^{1/2}$ over the drag-dominated regime. Over this regime, the interface height varies linearly with the streamwise distance until very close to the front position. For very high Reynolds numbers and relatively large porosities, $C_d \sim 1+10.0Re_d^{-2/3}$ is expected to be only slightly dependent on the Reynolds number. If the value of C_d is assumed to be constant, one can show that the model of Tanino et al. (2005) predicts $U_f \sim x_f^{-1/2} \sim t^{-1/3}$ and $x_f \sim t^{2/3}$. The experiments of Tanino et al. (2005) showed that outside the linear drag regime, the shape of the interface is linear up to some distance from the front. This basically means that in their model one assumes $U_f \sim x_f^{-1/2}$. Over some distance behind the front the shape of the current interface was similar to the one observed for gravity currents propagating in an open channel (no obstacles). Another relevant result was obtained by Hatcher et al. (2000) for high Reynolds number gravity currents ($C_d \sim$constant) with a total volume of lock fluid that increases linearly with time. The similarity solution indicates that $x_f \sim t^{3/4}$ over the drag dominated regime. No assumptions were made about the variation of the interface over the length of the gravity current.

The presence of closely spaced vertical cylinders extending over the whole depth of the channel in the experiments of Tanino et al. (2005), Jamali et al. (2008) and Hatcher et al. (2000) is a much more effective way to increase the drag force acting on the gravity current over a certain streamwise distance compared to the present case when the drag is induced only by roughness elements present at the bed.

Finally, the LR-R15-HD simulation (λ=H) should provide a more clear description of the variation of the terms in the energy equation for the case of a larger drag force per unit length acting on the gravity current. For example, the LR-D15 and LR-R15 simulations showed that the kinetic energy increases slightly with time ($E_k \sim t^{1/3}$), after the slumping phase is established for the gravity current propagating over the roughness elements. If in the new test case E_k starts decaying monotonically in time past the initial stages of the propagation of the current over the ribs, this will be an indication that the front velocity will also reach a regime in which it decays with time.

Figure 4.70 shows the structure of the current in the LR-R15-HD simulation at $t=77t_0$ and $t=108t_0$, after the front has overtaken the 15th ($x_f/H \sim 19.5$) and 21st ($x_f/H \sim 25.5$) rib in the series, respectively. The concentration distribution in Figure 4.70a is many respects qualitatively similar to the one for the LR-R15 case shown in Figure 4.10a. In particular, between the lock gate and the fourth rib behind the front the interface between the layer of mixed fluid and the layer of ambient fluid above it is very close to horizontal. As expected, for the same position of the front, the average value of the concentration in the head region is smaller in the LR-R15-HD simulation compared to the LR-R15 simulation. For example, when $x_f/H=19.5$, $C \sim 0.55$ in the LR-R15 simulation and $C \sim 0.45$ in the LR-R15-HD simulation. As the current continues to propagate, the concentration in the head region decreases monotonically. At $t=108t_0$ (Figure 4.70b), the concentration in the head region is close to 0.3. Also, the distance between the front and the region containing fluid with a concentration ($C>0.9$) close to that of the lock fluid increases monotonically in time (e.g., from about 7H at $t=77t_0$ to 10H at $t=108t_0$). However, the structure of the current remains similar.

The interface between the layer of heavier fluid and the layer of mixed fluid has a wavy shape in the LR-R15 case (Figure 4.10a). This waviness is also present in the LR-R15-HD case around the first couple of ribs situated behind the front (Figures 4.70a and 4.70b). However, the waviness is very reduced around the ribs situated at large distances behind the front (e.g., for x/H<14 in Figure 4.70b, or starting with the 10th rib behind the front). Over this region, the interface between the heavier layer of fluid and the mixed layer of fluid can be considered flat. However, this interface is slightly tilted such that the thickness of the layer of mixed fluid increases with x. This region corresponds to the one over which the vorticity sheet forming at the interface between the layer of heavier fluid and the layer of mixed fluid is close to continuous (see Figure 4.70c). At locations situated closer to the front (14<x/H<25 in Figure 4.70c), this vorticity sheet is oriented at much larger angles ($\sim 30^0$) with the horizontal, due to the orientation of the jet-like flow forming over the ribs situated closer to the front. The downstream part of the shear layer present at the outer side of the jet-like flow forming over a rib does not connect to the upstream part of the same shear layer forming over the next rib in the series. Also, in the region where the vorticity sheet is flat, the vorticity levels beneath it are relatively small (Figure 4.70c). This means no large disturbances of the sheet of vorticity are expected to occur. The interactions with the vortical eddies beneath it containing vorticity of opposite sign are not significant. As one moves closer to the front, these interactions become more and more important.

The small number of ribs present in the LR-R15 simulation did not allow to study whether the shear layers between the layer of heavier fluid and the layer of mixed fluid will become relatively flat over the ribs situated at very large distances from the front.

The temporal evolution of the front position is shown in Figure 4.71. The current transitions to the slumping phase ($U_f=0.45u_b$) before it starts interacting with the first rib in the series ($t\sim 10t_0$). After the current overtakes the first couple of ribs, the front velocity is close to $0.28u_b$, which is significantly smaller than the front velocity ($0.34u_b$) observed during the slumping phase in case LR-R15. However, the velocity never reaches a regime where it is constant over time. Rather, the time interval it takes the current to travel to the next rib in the series and the associated front velocity decay in a non-monotonic fashion over the whole duration of the simulation. For example, at $t\sim 50t_0$ the average front velocity is close to $0.22u_b$, while at $t\sim 90t_0$ the front velocity is $0.19u_b$.

The log-log plot in Figure 4.71b shows that, after the current overtakes the first couple of ribs in the series ($t>20t_0$), $x_f(t)\sim t^{\alpha}$ with $\alpha\sim0.72$. This value is close to the value ($\alpha=2/3=0.67$) predicted by the model of Tanino et al. (2005) assuming a constant drag coefficient for the high Reynolds number flow past the obstacles. Even more relevant, the predicted value of α is also close to the value ($\alpha=0.75$) given by the analytical model of Hatcher et al. (2000). The comparison with the analytical model of Hatcher et al. (2000) for gravity currents with a volume of lock fluid increasing linearly in time is justified, as the discharge of lock fluid at the lock-gate position is close to constant for $20<t/t_0<100$ (see Figure 4.71c). This means that the increase of the volume of lock fluid in the region with $x/H>0$ is close to linear. The presence of a regime in which $x_f(t)\sim t^{\alpha}$ with $\alpha<1$ suggests that a drag-dominated (non-linear) regime is present in case LR-R15-HD. In contrast to the experiments of Tanino et al. (2005), the shape of the interface away from the front was not linear. However, this is expected as the linear shape of the interface in the experiments of Tanino et al. (2005) is due to the presence of uniformly distributed obstacles over the whole height of the channel. The drag force induced by the surface mounted obstacles in the LR-R15-HD case acts only over the bottom part of the gravity current.

Figure 4.72 shows the temporal variation of E_k, E_p and E_d in the LR-R15-HD simulation. Also shown in Figure 4.72b are the results for the flat bed case (LR-F simulation) at the same Reynolds number. Compared to the LR-R15 simulation (Figure 4.36), the variation of E_p is qualitatively similar. After the current overtakes the first couple of ribs in the series ($x_f/H>9$), the decay of E_p with x_f (Figure 4.72b) is close to linear and has a constant slope until the end of the simulation. Meanwhile, the decay rate is significantly slower than the one observed for the flat bed case. At about the same time, the increase of E_d with x_f becomes close to linear, too. When plotted against time (Figure 4.72a), small changes in the slopes of the linear variations of $E_d(t)$ and $E_p(t)$ are observed around $65t_0$ ($x_f/H\sim15.5$). The rate of increase of E_d is significantly higher compared to the flat bed case due to the additional dissipation generated by the interaction of the gravity current with the ribs over its whole length. The evolution of E_d is case LR-R15 is qualitatively similar, with the exception of the fact that the increase of E_d with x_f was larger than linear in the later stages of the slumping phase (Figure 4.36b).

The most important differences are observed for E_k. In the LR-R15 simulation the current reaches the slumping phase around $t=22t_0$ ($x_f/H>9$). Its front velocity remains approximately constant until the end of the simulation ($t/t_0\sim50$). As time increases, a larger volume of fluid is set into motion. As the front velocity is constant, the kinetic energy should continue to increase with time. Indeed, the variation of E_k in Figure 4.36c shows that E_k increases with time, proportional to $t^{1/3}$. This increase is smaller than the one observed in the flat bed case where E_k increases linearly with time. By contrast, after the gravity current overtakes the third rib ($x_f/H\sim7$), E_k starts decaying in the LR-R15-HD simulation.

In a good approximation, the decay of E_k with both x_f and t is close to linear until the end of the simulation ($t\sim110t_0$). In contrast to the time variation of E_p and E_d, no change in the slope of the linear decay is observed for $E_k(t)$ at $t\sim60t_0$. The linear decay of E_k for $t>22t_0$ is consistent with the observed decay of the front velocity with time (Figure 4.71). The time variation of E_k suggests it is unlikely the front velocity will reach a regime where U_f is constant, corresponding to a slumping phase of the current propagating over the ribs. For that to happen, E_k should start increasing in time. The trends observed in Figure 4.72 for the three terms of the energy balance do not suggest this will be the case. Thus, a regime in which the drag force effects on the evolution of the gravity current are significant is present in the LR-R15-HD simulation. This regime is characterized by the decay in time of the front velocity and kinetic energy. In this regard, results of the LR-R15-HD simulation are consistent with the finding of Tanino et al. (2005) and Jamali et al. (2008) that a gravity current with a large volume of release can reach a drag dominated regime in which the front velocity decreases in time. However, for the conditions considered in the LR-R15-HD, the shape of the current interface is still very different than the one (Figure 2.3) observed in the experiments of Tanino et al. (2005) and Jamali et al. (2008). This is because of the important differences in the relative size, position and density of the roughness elements in the channel in the present simulation and in the experiments of Tanino et al. (2005) and Jamali et al. (2008).

Figure 4.73 shows the distribution of the velocity magnitude along the current at three representative times after E_k started decaying with time. Comparison of the distributions at $t=25t_0$, $65t_0$ and $108t_0$ shows that the decay of the kinetic energy in time takes place in a relatively uniform way over the whole length of the bottom-propagating gravity current. The same is true for the layer above the gravity current containing ambient fluid moving in opposite direction. The region of low velocity magnitude corresponds to the interface between the forward bottom propagating current and the layer of ambient fluid over it.

Figure 4.74 provides more details of the interaction between the gravity current and the ribs (Rib 20 and Rib 21) in the later stages of the propagation of the current in the LR-R15-HD simulation. The vorticity contours in Figure 4.74a show that the front recovers its compact shape at about 0.66H from the center of the rib that was overtaken by the gravity current. Thus, despite the smaller distance between the ribs in the LR-R15-HD case, the vorticity sheet at the front is relatively strong and continuous, and the shape of the front as it approaches the next rib in the series is similar to the one observed in case LR-R15. This confirms that the ribs in case LR-R15-HD still act as k-type roughness.

The evolution of the fluid at the head of the current as it interacts with a new rib is qualitatively similar in the two simulations (e.g., see also Figures 4.5, 4.34 and 4.35 for case LR-R15). Even before the front touches the upstream face of the next rib, a strong vortex starts forming on the top face of the rib. This vortex is then lifted away from the rib by the approaching front (Figures 4.74b and 4.74c). The sheet of vorticity at the front contains vorticity of opposite sign to the one inside the core of this vortex. Meanwhile, as a result of the interaction between the lower part of the front and the upstream wall of the rib, the denser fluid propagating parallel to the channel bottom is deflected upward. This higher density fluid moving upward interacts with the lower density fluid convected in the upper part of the gravity current. The result is the formation of a large splash containing relatively high density fluid originating from both the lower and upper parts of the head region. The fluid inside the splash looses rapidly its kinetic energy as it moves away from the channel bottom and past the rib (Figure 4.74d). Then, the fluid inside the splash plunges back toward the channel bottom and increases its predominantly vertical velocity as it approaches the channel bottom (Figures 4.74e). As the impact direction is close to vertical, a large part of the plunging heavier fluid is convected toward the downstream face of the rib that was overtaken by the gravity current (Figures 4.74f and 4.74g). The other part starts propagating toward the next rib.

As the lower part of the front of the current is destroyed as it reaches the upstream face of the next rib and the splash region is populated by a wide range of energetic eddies, a large part of the vorticity sheet normally present at the front of the current is destroyed as a result of the impact with the rib. However, the vorticity sheet at the front becomes compact again a short time after the impact of the splashed fluid with the channel bottom and the partial deflection of this fluid toward the next rib (Figure 4.74g). The mixing is particularly strong due to the trapped ambient fluid behind the rib overtaken by the fluid. This ambient fluid is pushed into the heavier fluid convected over the rib by the splash fluid moving toward the downstream wall of the rib after the impact with the channel bottom (Figures 4.74f to 4.74g).

As the current propagates between two successive ribs, the front velocity or, more precisely, the velocity of the interface between the heavier fluid originating in the gravity current and the ambient fluid is strongly non-uniform. The largest velocity is observed immediately after the vorticity sheet at the front becomes again compact (Figures 4.74f and 4.74g). As the upstream face of the next rib is approached, the velocity decays strongly. The velocity remains small during the time the splash is forming and also during the time the fluid within the splash plunges downwards toward the channel bottom.

Figure 4.75 visualizes the interaction between the gravity current and the third rib in the series. Comparison of Figures 4.74 and 4.75 shows that the interaction of the front of the current with the ribs is qualitatively similar for the lower and higher rank ribs in the series.

4.14 Summary and Conclusions

The present investigations focused on the changes in the flow physics and parameters characterizing the structure of highly-turbulent bottom-propagating Boussinesq gravity currents (Re>40,000) and the capacity of these currents to entrain sediment at different stages of their evolution, as a result of the presence of an array of 2D identical obstacles of different sizes and shapes at the channel bottom. This chapter considered only the case of full-depth currents with a large volume of release (R<<1). The focus of the investigation was on currents propagating over large-scale roughness elements for cases in which the shape and height of the elements was such that a relatively long slumping phase was present. Additionally, the study analyzed scale effects induced by an increase in the Reynolds number toward values ($Re=10^6$) that are within the lower range of those encountered in practical applications (e.g., gravity currents forming at the bottom of rivers, lakes and oceans), where the structure of the current is closer to the one expected for inviscid currents.

The structure of the gravity current in the head and dissipative wake regions was found to change dramatically as a result of the presence of large-scale roughness elements compared to the case the current propagates over a horizontal flat surface. In particular, the mixing occurring in the head region as a result of the interaction of the current with the roughness elements resulted in an additional drag force acting on the current and in the decay of the front velocity in the simulations in which obstacles in the form of roughness elements were present at the bed. In the case of roughness elements that resemble a bluff body (e.g., ribs), the mixing at the head was further amplified due to the formation of a splash of high concentration fluid as a result of the initial interaction between the head of the incoming current and the upstream face of the roughness element. A strong jet-like flow was observed to form downstream the top or crest of a certain roughness element at a short time after the front started getting away from the obstacle. The flow was observed to become supercritical in the region of strong flow acceleration in which the high-concentration fluid inside the jet-like flow plunges toward the lower regions of the bed, at least for the roughness elements situated close to the front at a certain time.

The front velocity during the slumping phase in the flat bed high Reynolds number simulation was found to be very close to the analytical value ($U_f/u_b=0.5$) expected for energy-conserving inviscid gravity currents propagating over horizontal surfaces. A slumping phase in which the front velocity is approximately constant was also present in the simulations with roughness elements of height D=0.15H and wavelength λ=3H for both streamlined (e.g., dunes) and bluff (e.g., ribs) obstacles. In these simulations, the height of the obstacles was less than half that of the incoming current. In the lower Reynolds number simulations (Re=48,000) the mean front velocity during the slumping phase was 12% and, respectively, 24% lower than the value ($U_f/u_b=0.45$) predicted for the flat bed case. The larger reduction observed for the case ribs were present at the channel bottom is because ribs induce a higher form drag due to their larger degree of bluntness. The finite length of the computational domain in the simulations in which the height of the obstacles (D=0.3H) and that of the current were comparable did not allow to clearly establish the presence of a slumping phase during which the mean front velocity based on the time of travel between two consecutive obstacles is constant (independent of the rank of the obstacle). Analysis of the simulation results also showed that, as opposed to the flat bed simulations in which there is an increase of about 10% in the front velocity between Re=47,800 and $Re=10^6$, the mean front velocity is relatively insensitive to the Reynolds number, within the same range, if obstacles of height D=0.15H are present at the bed. Thus, as opposed to the flat bed case, experiments conducted with Re_f~10,000 (Re=48,000) should be representative of field conditions, at least as far as the front velocity is concerned.

Consistent with the findings of Ooi et al. (2009) a stably stratified tilted interface, depleted of large-scale eddies, developed between the heavier current and the lighter fluid, starting at the position of the lock gate in the flat bed simulations at both Reynolds numbers. As a result, in the flat bed simulations the streamwise velocity inside the current peaked at the end of the tilted interface and over the upstream part of the dissipative wake region. The structure of the tail of the current was very different in the simulations with roughness elements at the bed. A layer of varying height containing mixed fluid developed between the regions containing heavier fluid and lighter ambient fluid. The top of the layer of mixed fluid is close to horizontal at large distances behind the front. The bottom of this layer undergoes quasi-regular deformations with the same wavelength at that of the roughness elements. The structure of the tail was similar in the simulations with small and large obstacles and was not subject to Reynolds induced scale effects for Re>48,000.

The temporal variation of the total volumetric flux of heavier fluid $Q_i = (1/u_b H^2)\int CudA$ at selected streamwise locations and of the volume of heavier fluid between two consecutive obstacles ($M_{i,i+1}$) showed that a quasi-steady regime is reached in between two consecutive obstacles (i and i+1) at sufficiently large times after the passage of the front and after the hydraulic jumps forming at the downstream obstacles (i+1 and i+2) passed the obstacle situated upstream of it (i and i+1, respectively). The average velocity of these hydraulic jumps in the simulations with Re=48,000 and obstacles of height D=0.15H is about 27% smaller than the front velocity. The volume of heavier fluid between two consecutive obstacles was found to decay with i, once the quasi-steady regime was reached. The time variations of $M_{i,i+1}$ showed the presence of an initial linear-growth regime starting when the front reaches the obstacle of rank i and ending when the front reaches the next obstacle. Once the backward propagating jump forms at the obstacle of rank i+1, a logarithmic growth regimes was present. This regime lasted until a short time after the jump forming at the obstacle of rank i+2 reaches the obstacle of rank i+1. At that point the quasi-steady regime was reached.

The mean flow and turbulence structure was then analyzed for the simulations with obstacles of height D=0.15H in a region situated away from the head of the gravity current, after the flow reaches the quasi-steady regime in that region. This is important because for gravity currents with a large volume of release, if the current propagates in the slumping phase over a large number of obstacles, most of the sediment may be entrained from the bed beneath regions of the tail where the quasi-steady regime was reached. The non-dimensional distributions of the concentration, velocity magnitude and Reynolds stresses were found to be dependent on the shape of the roughness elements but relatively independent of the Reynolds number. The largest amplification of the turbulence was observed in the shear layer region forming on the outer part of the jet-like flow. In the case ribs were present at the channel bed, a second region of high turbulence corresponded to the detached shear layer forming at the edge of the recirculation region downstream of the rib.

The double-averaging procedure was then applied over the tail region between two consecutive obstacles situated in the domain where the quasi-steady regime was reached. This allowed characterizing the global changes in the mean flow and turbulence structure in the case of a rough bed surface with respect to the base case when the bed surface is smooth, based essentially on a 1-D analysis. For the flat bed cases, the present simulations confirmed previous experimental results that showed that the turbulent kinetic energy peaks at the interface between the mixing layer and the heavier bottom propagating current. Then tke monotonically decayed from the edge of the tilted layer until $y/H=0.18$ in the LR-F case and $y/H=0.11H$ in the HR-F case. Consistent with previous experimental investigations, the position of the minimum tke was that of the maximum in the streamwise velocity, which also defines the interface between the outer layer and the inner layer of the bottom propagating current.

The present simulations showed that the streamwise velocity profile on the lighter current side contained a region of uniform velocity. In this region the tke values were very small. Such a region was not present on the side containing the heavier current. The high correlation between the regions of high tke and those of high streamwise velocity gradient showed that most of the turbulence production was due to shear. The presence of the obstacles induced significant differences in the 1-D profiles of the concentration, streamwise velocity and tke over the height of the heavier current. For example, the overall amplification of the tke was close to five times as a result of the presence of roughness elements with a height of 0.3H. Interestingly, the tke profiles looked qualitatively similar to those observed in the simulations with a flat bed. However, the quantitative differences were mostly due to the large turbulence amplification in the shear layer forming on the outer side of the jet-like flow. The jet-like flow has no equivalent in the case the gravity current propagates over a flat bed. As expected, comparison of the 1-D profiles of the concentration, streamwise velocity and tke showed that scale effects were much less significant in the simulations in which roughness elements were present at the bed.

The analysis of the temporal evolution of the drag force, or equivalently of the mean pressure difference between the upstream and the downstream faces of the rib, on the ribs showed that the important role played by the backward propagating hydraulic jumps. For example, the passage of the hydraulic jump originating at the first rib downstream of the one where the drag force is analyzed can induce a reduction of up to 20% of the drag force on the rib. This explains way the transition to the final quasi-steady state is more complex in the case an array of obstacles is present at the channel bottom compared to the case of an isolated obstacle. Significant qualitative differences were observed between the simulations with small (D=0.15H) and large (D=0.3H) ribs after the end of the impact stage. The temporal evolutions of the drag force on the ribs in the series were found to be qualitatively and qualitatively similar. The temporal evolutions showed an increase dependence on the rank of the rib in the higher Reynolds number simulations ($Re=10^6$, D=0.15H). The LES simulations allowed a detailed analysis of the link between the flow structure around the ribs (e.g, strength and orientation of the jet-like flow, level of the layer of high concentration fluid, presence of an approaching hydraulic jump, etc.) and the increase or decrease of the pressure force on the upstream and downstream faces of the ribs.

Analysis of the energy balance in the flat bed simulations showed that at both Reynolds numbers the growths of the total kinetic energy E_k, the potential energy, E_p, and the time integral of the dissipation rate from the start of the lock exchange flow, E_d, reach eventually a linear regime. During the linear regime, the ratio of the dissipation ε to dE_p/dt is 0.32 in the simulation at Re=48,000. The same ratio decreases to 0.22 in the simulation at $Re=10^6$.

The presence of the obstacles induced significant qualitative and quantitative changes in the energy balance after the current overtakes the first obstacle. The combined effect of the smaller decay rate of E_p and higher dissipation rates within the body of the current observed in the case in which obstacles were present at the channel bottom caused a faster temporal decrease of E_k with respect to the flat bed case. For example, once the current overtakes the second obstacle (x_f>9H), a regime in which E_k increases proportional to $t^{1/3}$ ($dE_k/dt \sim t^{-2/3}$) was maintained until the end of the simulation for both types of obstacles with D=0.15H. The variation of E_k with the front position for x_f>9H remained independent of the shape of the obstacle. The increase in the Reynolds number had a minimal effect on the energy balance. The presence of larger obstacles (D=0.3H) induced some significant differences in the temporal evolutions of the terms in the energy balance equation.

Analysis of the spatial distributions of the total dissipation rate, ε, in the later stages of the evolution of the gravity current during the slumping phase in the simulations containing obstacles showed that most of the dissipation takes places over the tail of the current. In the simulations containing ribs, the regions of high values of ε correspond to the shear layer forming in between the jet-like flow and the separated region downstream of the rib, and to the shear layer on the other outer side of the jet-like flow. In the case dunes are present at the bed, most of the dissipation takes place in the shear layer forming on the outer side of the jet-like flow and in the short shear layer region forming on the upslope face of the dunes, where the core of high velocity within the jet-like flow starts getting away from the bed surface. By contrast, in the flat bed simulations most of the dissipation occured in the dissipative wake region (up to 3H behind the front) at the interface between the current and the ambient fluid. Scale effects were found to be minimal in the simulations containing obstacles at the bed.

The near-wall flow structure showed the presence of high and low velocity streaks in the vicinity of the bed surface. The average size of the streaks decayed with the increase in the Reynolds number. In the simulations with obstacles the streaks were clearly seen in the region downstream of the location where the jet-like flow reaches the bed surface. In this region, streaks were present over the whole width of the channel. However, some evidence was given that the streaks maintain to a certain degree their coherence over most of the region where the flow in the tail of the current remains strongly turbulent. For example, the streaks detach from the bed surface and are convected over the separated shear layer that forms over the recirculation regions present upstream and downstream of each rib in the series. Due to the presence of the velocity streaks just above the bed, the distributions of the bed friction velocity at the bed surface showed a similar streaky structure.

In the later stages of the propagation of the current, after the formation of the tilted stably stratified interface, the distribution of the bed-friction velocity in the flat bed simulations reached a maximum at the front of the current and then decayed smoothly over most of the tail region. By contrast, in the simulations in which ribs or dunes were present at the bed, the largest values of $u_{\square}$ were observed in the regions where the jet-like flow reattaches to the bed surface and over the crest of the dunes. The distribution of u_τ between two consecutive roughness elements was found to be relatively independent of the rank of the obstacle, for obstacles situated at large distances behind the front. The overall levels of u_τ between two consecutive roughness elements were larger at small times after the front left that region. Then, a mild temporal decay was observed as the quasi-steady regime was approached in that region. The presence of larger ribs with D=0.3H induced a clear increase in the levels of u_τ between two consecutive roughness elements with respect to the case in which ribs with D=0.15H were present at the bed. In the case of dunes, the effect of the increase of the dune height was much smaller, and resulted in a small decay of the overall levels of u_τ. The passage of the backward propagating hydraulic jump was found to result in a significant decay of u_τ between the crest/top of the roughness element where the jump forms and the next roughness element situated upstream of it.

The increase of the Reynolds number in the flat bed simulations resulted in a large decay of the overall levels of u_τ. However, the two distributions remained qualitatively similar. For example, the ratio between the bed friction velocity in the HR-F and LR-F simulations was close to 0.58 over the whole length of the current. More important, the same ratio can be used to successfully scale the low and high Reynolds number simulations in which ribs or dunes were present at the channel bottom. This means that the shape of the bed shear stress distributions is basically independent of the Reynolds number at Reynolds numbers that are high enough for the flow at the head of the current to be strongly turbulent. This result has also important consequences in terms of the relevance of laboratory experiments and simulations performed at lower Reynolds numbers for the study of the capacity of a gravity current to entrain sediment at field conditions.

The numerical simulations allowed a detailed analysis of the time variation of the flux of sediment entrained by the current in specific regions of the flow. The analysis was performed for the case of obstacles of height D=0.15H for which a long slumping phase was present in the evolution of the bottom propagating gravity current. The simulation results showed that the time variations of the flux of sediment entrained between the centers or crests of two consecutive roughness elements in the series were similar stating with the second roughness element. In these distributions, the flux of sediment peaked around the time when front reached the downstream roughness element or its crest. This was followed by a relatively mild decay toward the value corresponding to the establishment of the quasi-steady regime. The decay rates in the simulation with ribs were faster than the ones in the simulation with dunes. Finally, the study provided an analysis of the temporal variations of the flux of sediment entrained by the whole current function of the sediment particle diameter and the shape of the bed surface.

Finally, a simulation with small ribs (D=0.15H) spaced at a much smaller interval (λ=H) showed that the drag force was large enough to induce the decay of the front velocity and of the kinetic energy within the lock exchange flow with time, after the current propagated past the first couple of ribs in the series. For the conditions considered in this simulation, the current propagating over the ribs did not reach a slumping phase. Rather, the current transitioned directly to a regime where drag effects due to the presence of the large-scale roughness elements are significant and the front velocity decays proportional with t^{α} with $\alpha \sim 0.72$.

Table. 4.1. Main parameters of the simulations and computational domain for the full depth gravity current simulations with a large volume of release.

Simulation	Re	Obstacle Type	Height of the obstacle	Position of the obstacle
LR-F	47,800	-	-	-
LR-D15	47,800	Dune	0.15H	x/H = ±5,8,11,14,17
LR-R15	47,800	Rib	0.15H	x/H = ±5,8,11,14,17
LR-D30	47,800	Dune	0.30H	x/H = ±7,13,19
LR-R30	47,800	Rib	0.30H	x/H = ±7,13,19
HR-F	1,000,000	-	-	-
HR-D15	1,000,000	Dune	0.15H	x/H = ±5,8,11,14,17
HR-R15	1,000,000	Rib	0.15H	x/H = ±5,8,11,14,17
LR-R15-HD	47,800	Rib	0.15H (λ/H=1)	x/H= ±5, 6, 7, 8….26

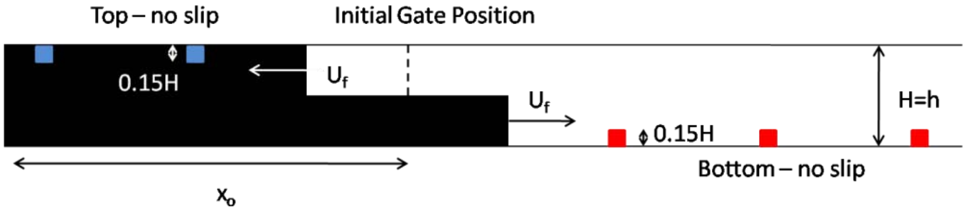

Figure 4.1 Sketch of the flow during the slumping phase for the case of a full depth release lock-exchange flow. The gate is positioned far from the extremities of the channel ($x_0/H>>1$). The top and bottom no-slip walls are horizontal.

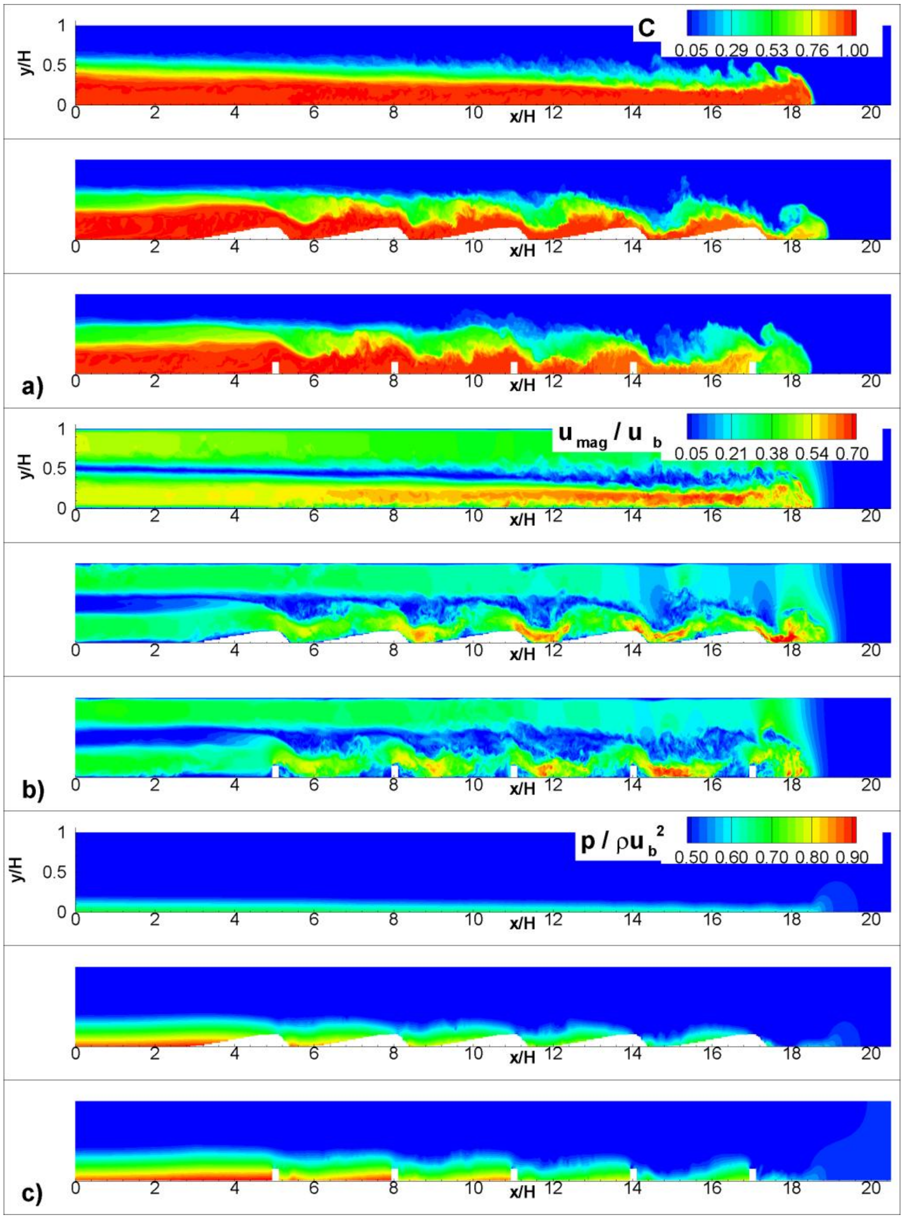

Figure 4.2 Structure of the gravity current at a time when the front is situated close to x/H=19 in the low Reynolds number simulations with flat bed and with obstacles of height D=0.15H. a) concentration, C; b) velocity magnitude, u_{mag}/u_b; c) pressure, $p/\rho u_b^2$. The aspect ratio is 1:2 in the x-y contour plots.

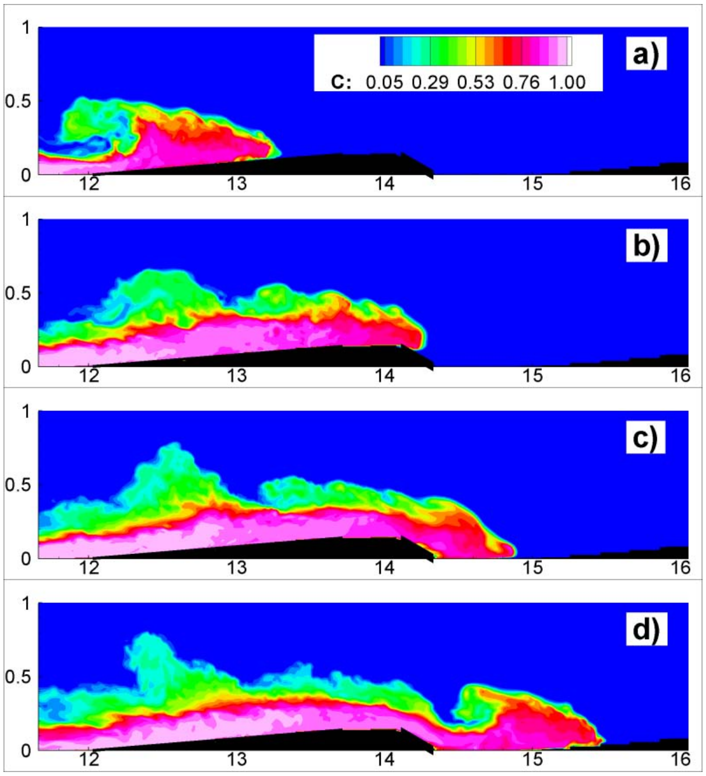

Figure 4.3 Visualization of the changes in the structure of the gravity as the current overtakes the fourth dune in the LR-D15 simulation. The concentration field is shown.

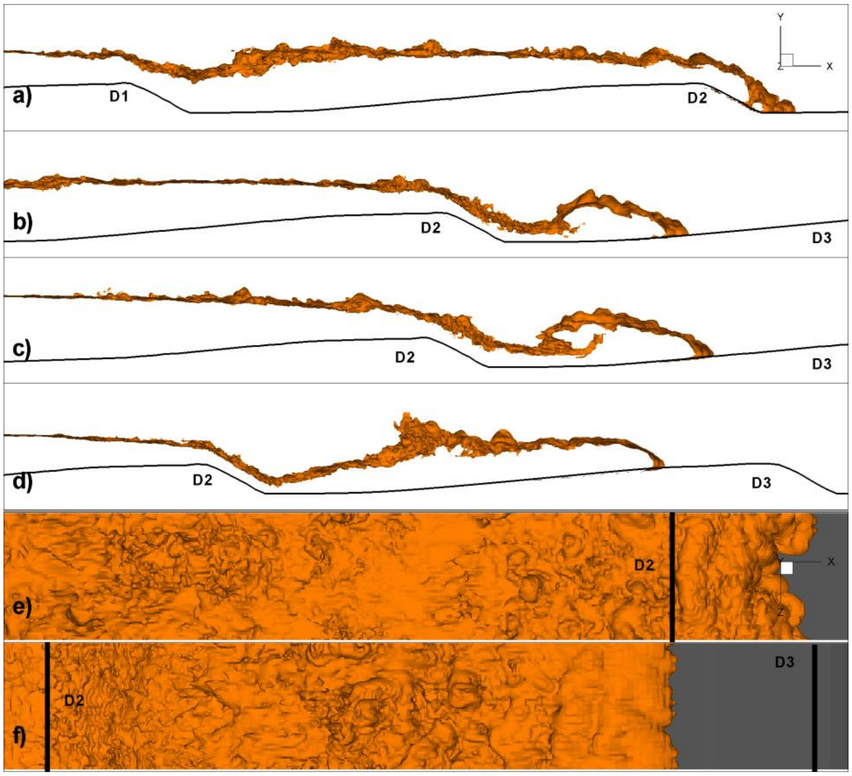
a)
D1
D2
Y
X
Z
b)
D2
D3
c)
D2
D3
d)
D2
D3
e)
D2
X
Z
f)
D2
D3

Figure 4.4 Visualization of the interface between the gravity current and the lighter ambient current using a 3-D concentration iso-surface (C=0.1) in the LR-D30 simulation. a) $t=36t_0$; b) $t=40t_0$; c) $t=42t_0$; d) $t=48_0$; e) $t=36t_0$, view from above; d) $t=48_0$, view from above.

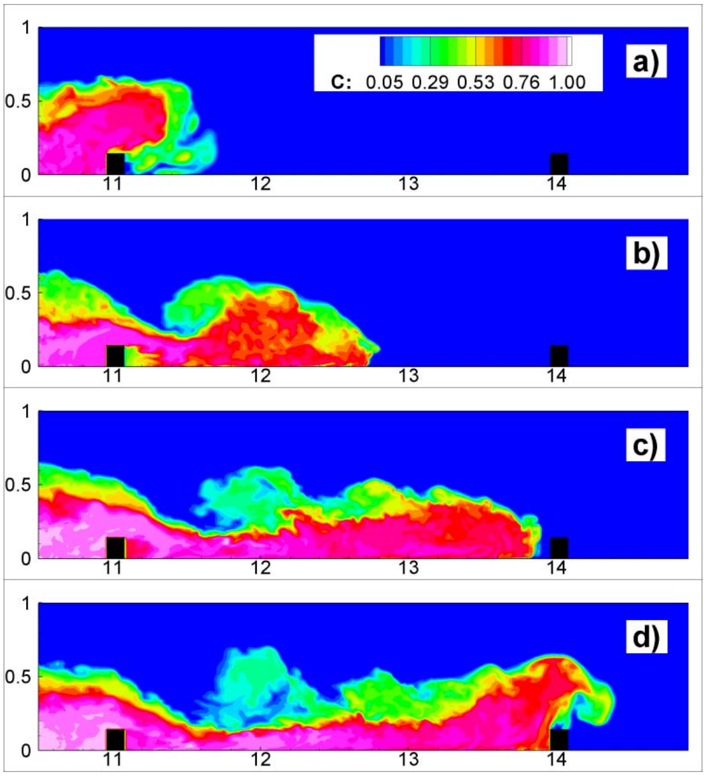

Figure 4.5 Visualization of the changes in the structure of the gravity as the current propagates between the third and the fourth rib in the LR-R15 simulation. The concentration field is shown.

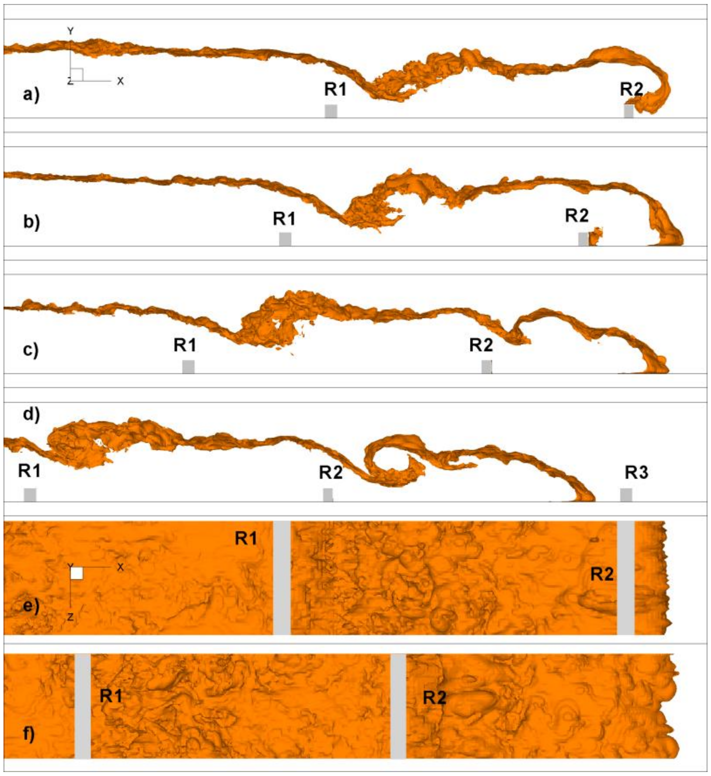
a)
R1
R2
b)
R1
R2
c)
R1
R2
d)
R1
R2
R3
R1
R2
e)
R1
R2
f)
Y
X
Z

Figure 4.6 Visualization of the interface between the gravity current and the lighter ambient current using a 3-D concentration iso-surface (C=0.1) in the LR-R15 simulation. a) t=20t$_0$; b) t=22t$_0$; c) t=24$_0$; d) t=26$_0$; e) t=20t$_0$, view from above; d) t=26$_0$, view from above.

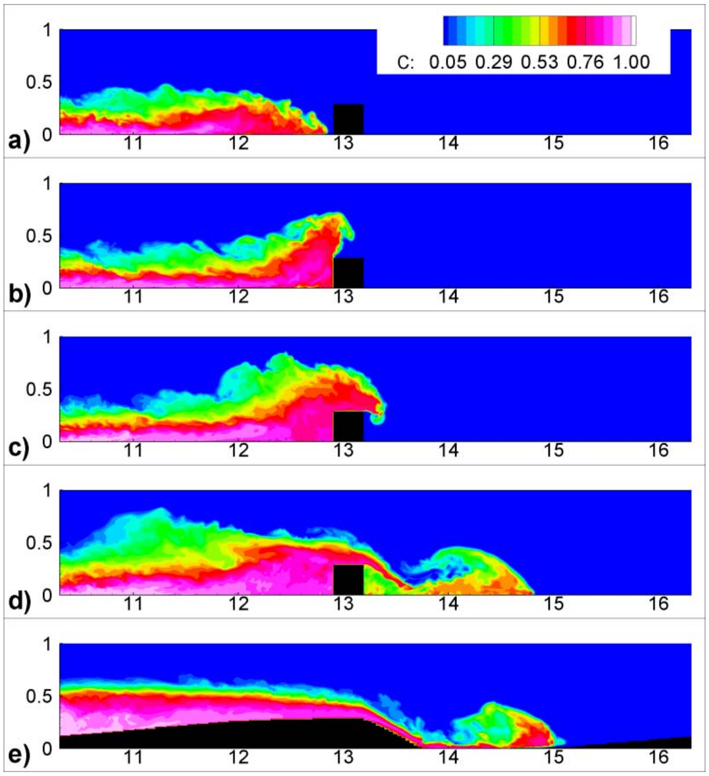

Figure 4.7 Visualization of the changes in the structure of the gravity as the current overtakes the second rib in the LR-D30 simulation (a-d). Also shown in frame e) is the structure of the current in the LR-R30 simulation when the front is situated at the same position as in frame d). The concentration field is shown.

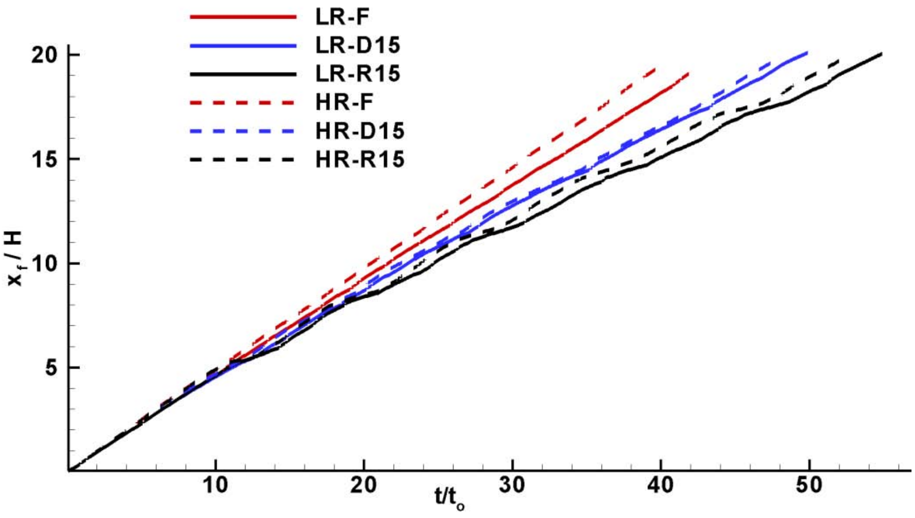

Figure 4.8 Time variation of the non-dimensional position of the front, x_f/H, function of the non-dimensional time, t/t_0 in the low and high Reynolds number simulations with flat bed and with obstacles of height D=0.15H.

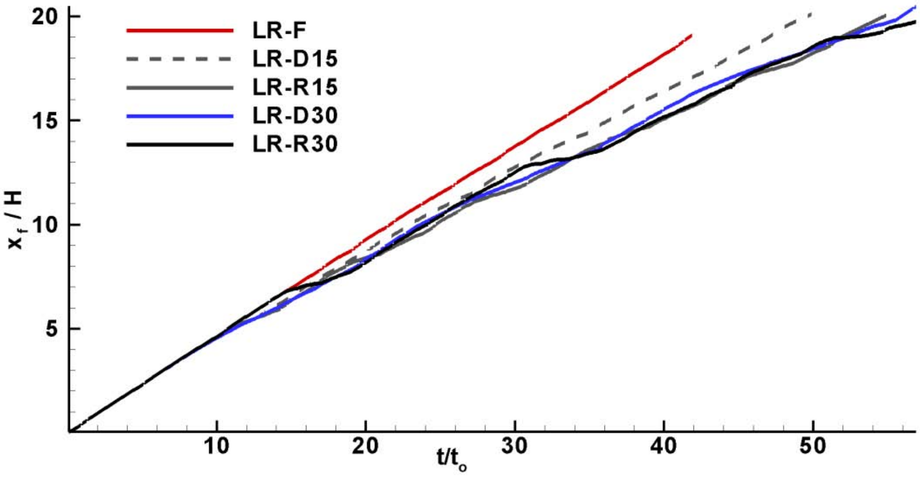

Figure 4.9 Time variation of the non-dimensional position of the front, x_f/H, function of the non-dimensional time, t/t_0 in the low Reynolds number simulations with flat bed and with obstacles of height D=0.15H and D=0.3H.

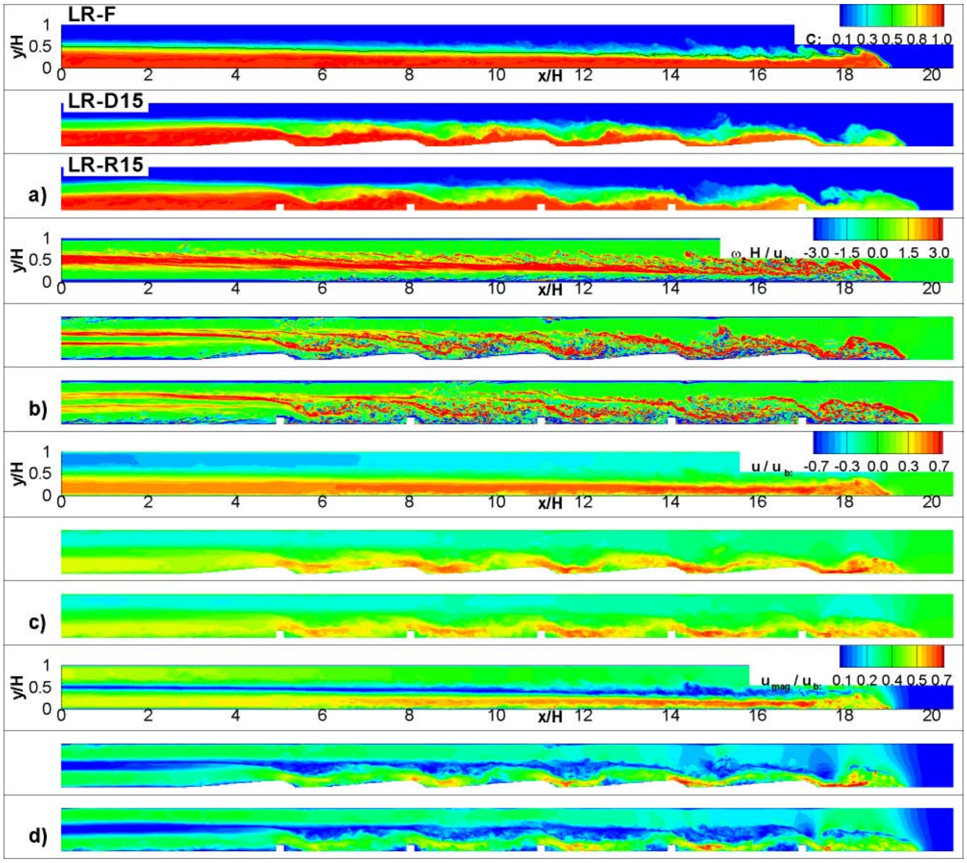

Figure 4.10 Visualization of the structure of the tail in the low Reynolds number simulations with a flat bed and with obstacles of height D=0.15H at times when the front is situated close to x/H=18.5. a) concentration, C; b) out-of-plane vorticity, $\omega_z H / u_b$; c) streamwise velocity, u/u_b; d) velocity magnitude, u_{mag}/u_b.

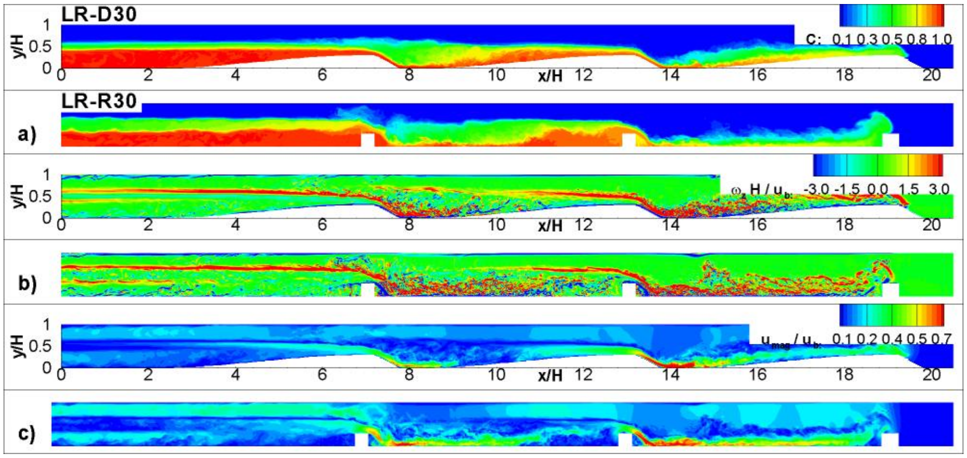

Figure 4.11 Visualization of the structure of the tail in the low Reynolds number simulations with obstacles of height D=0.3H at times when the front is situated close to x/H=18.5. a) concentration, C; b) out-of-plane vorticity, $\omega_z H/u_b$; c) velocity magnitude, u_{mag}/u_b.

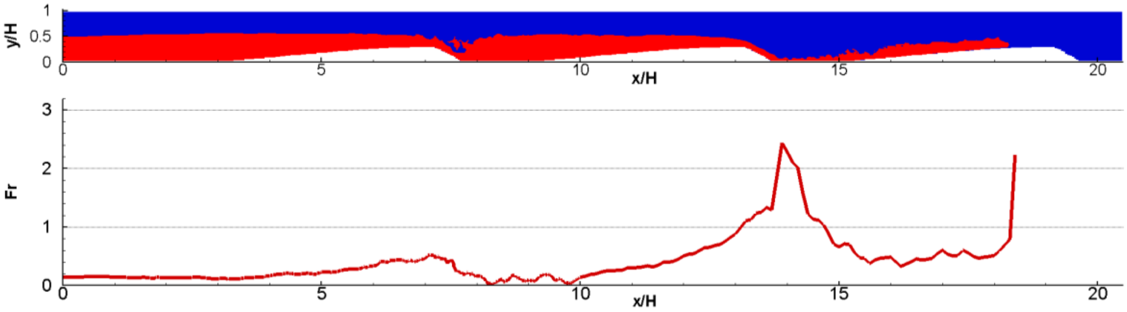

Figure 4.12 Distribution of the Froude number along the gravity current in the LR-D30 simulation at the time instant when x_f/H=18.5. Also shown is the iso-concentration contour C=0.5 in a vertical plane at the same time instant.

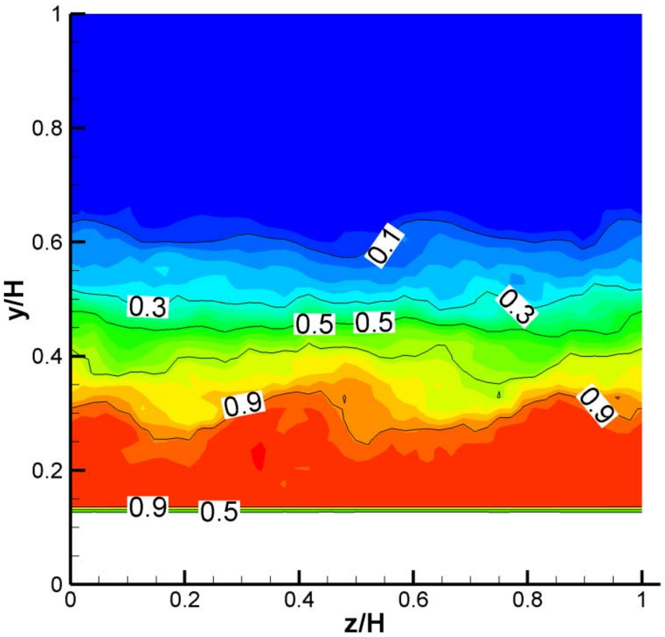

Figure 4.13 Concentration distribution in a cross-flow (y-z) section (x/H=10.5) cutting through the tail of the current in the LR-D15 simulation.

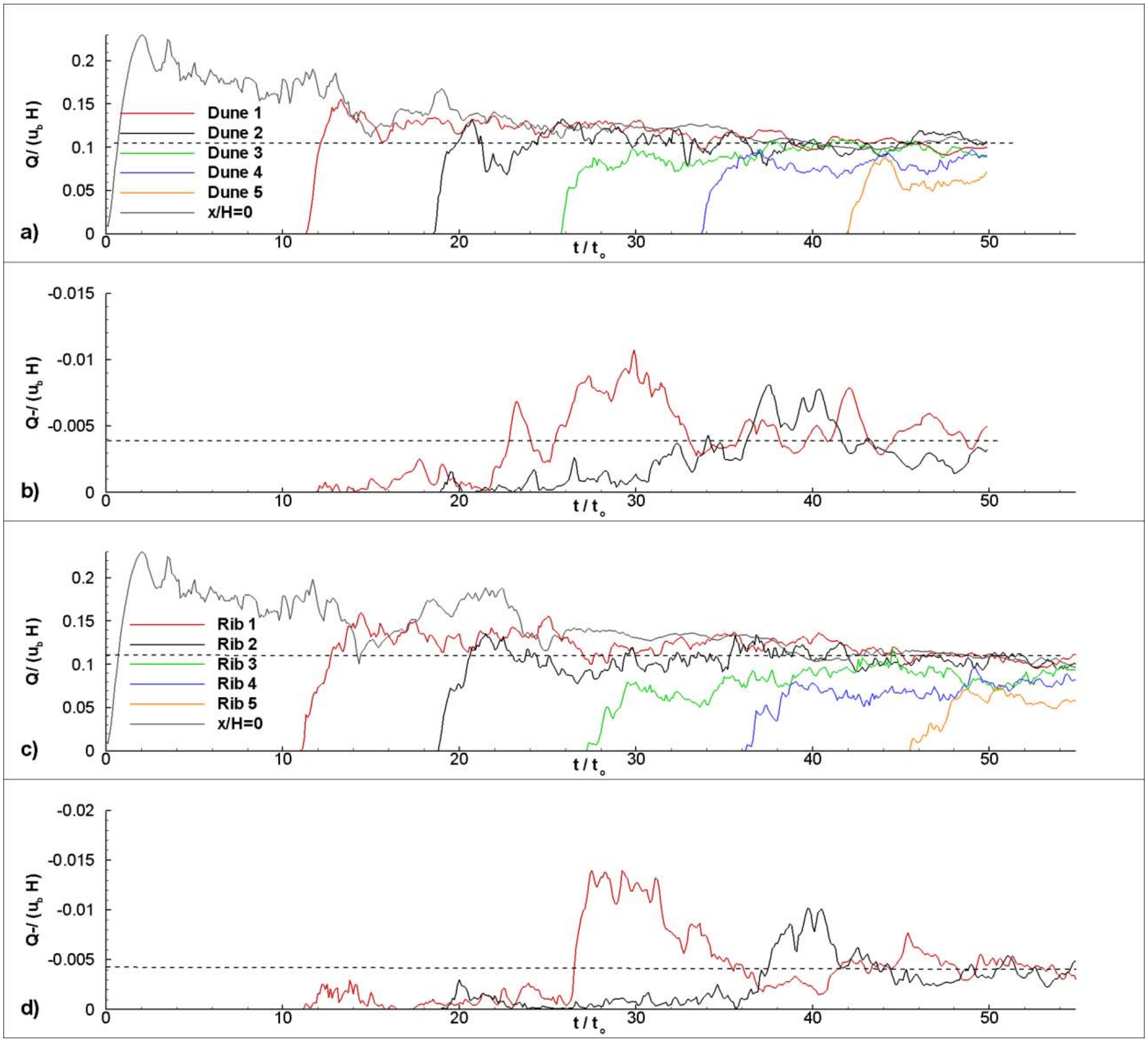

Figure 4.14 Time variation of the total volumetric flux of heavier fluid $Q_i = (1/u_b H^2)\int CudA$ and of the volumetric flux of heavier fluid moving upstream $Q\text{-}_i = (1/u_b H^2)\int Cu\_dA$ a) Q_i, LR-D15; b) $Q\text{-}_i$, LR-D15; c) Q_i, LR-R15; d) $Q\text{-}_i$, LR-R15. The flux Q_i in frames a) and c) is plotted at x/H=0 and at the sections cutting through the crests of Dune 1 to Dune 5 or the downstream faces of Rib 1 to Rib 5. The flux $Q\text{-}_i$ in frames b) and c) is plotted for Dune 1 and Dune 2 and, respectively, for Rib 1 and Rib 2.

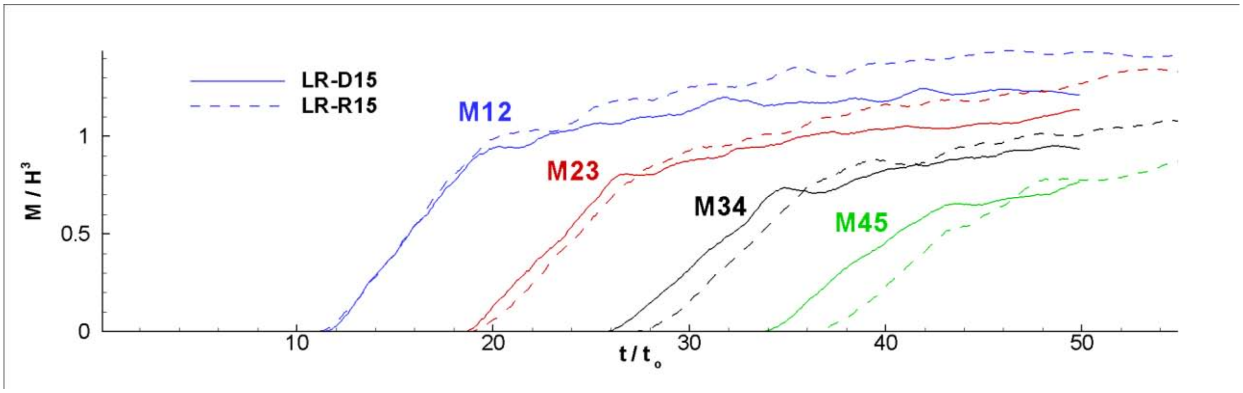

Figure 4.15 Time variation of the volume of heavier fluid $M_{i,i+1}$ in between the crests or downstream faces of two successive obstacles for the LR-D15 and LR-R15 simulations.

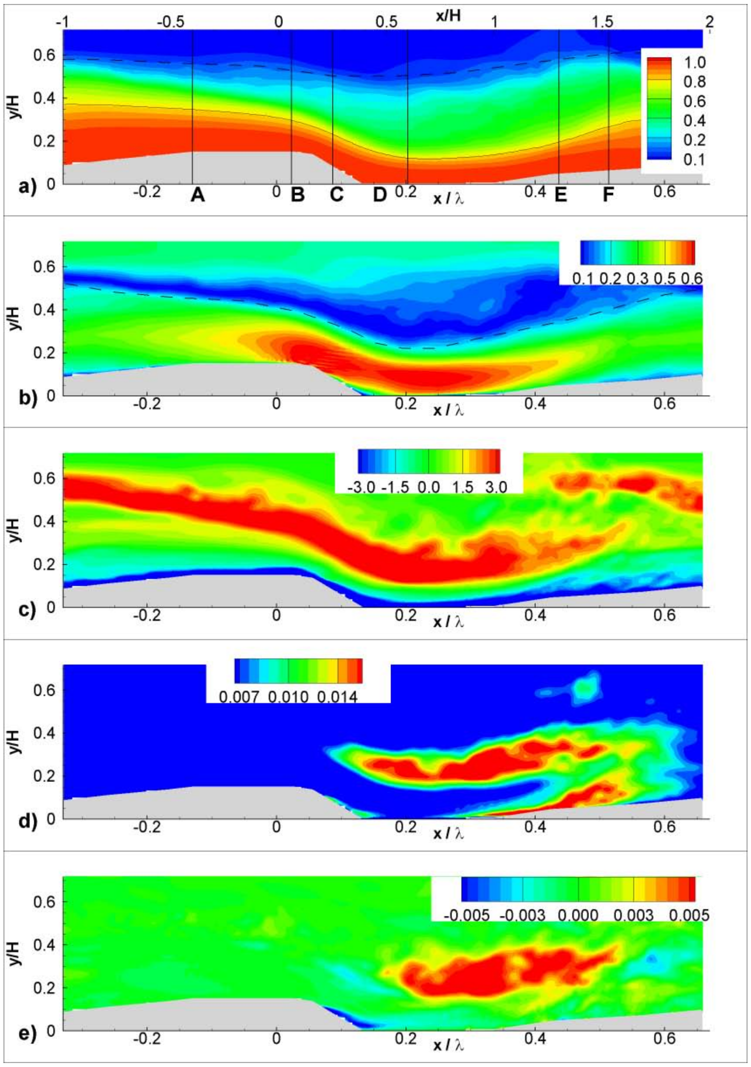

Figure 4.16 Mean flow and turbulence structure of the flow in the tail region after the quasi-steady regime is reached (LR-D15 simulation). a) concentration, C; b) velocity magnitude u_{mag}/U; c) mean out-of-plane vorticity, ω_z(H/U); d) turbulence kinetic energy, k/U^2; e) the primary Reynolds shear stress, $\overline{u'v'}$/U^2. The mean variables were averaged in the spanwsie direction and in time, after the quasi-steady state was reached. The comparison is done in the region situated around the second obstacle in the series.

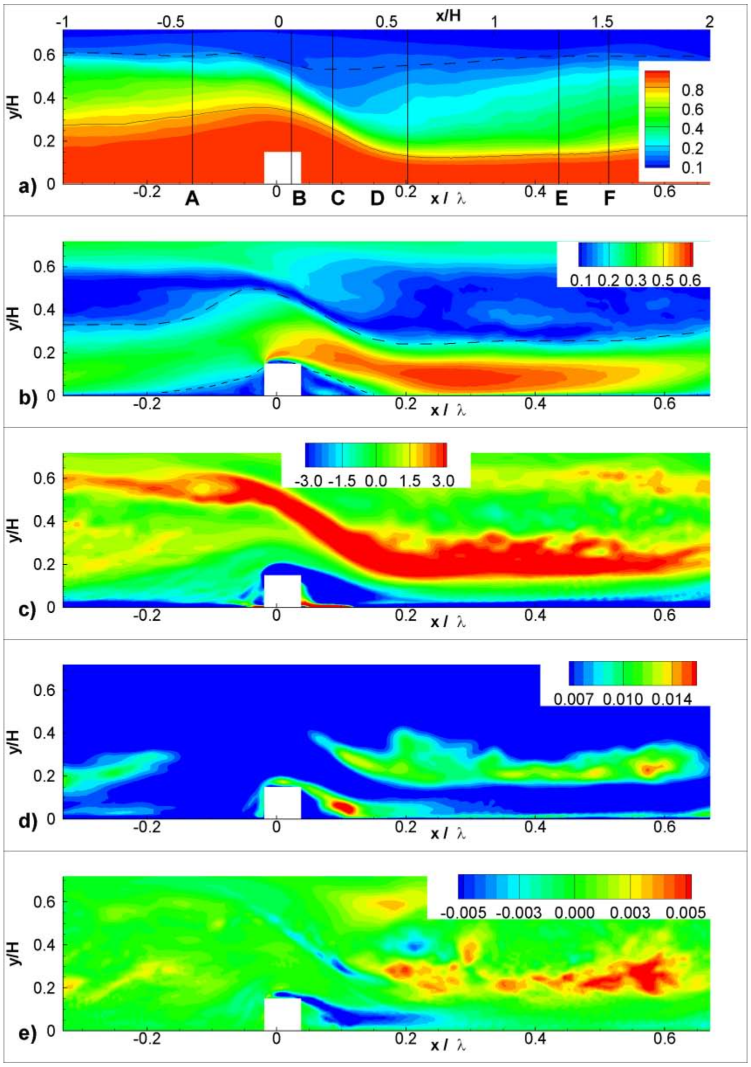

Figure 4.17 Mean flow and turbulence structure of the flow in the tail region after the quasi-steady regime is reached (LR-R15 simulation). a) concentration, C; b) velocity magnitude u_{mag}/U; c) mean out-of-plane vorticity, ω_z(H/U); d) turbulence kinetic energy, k/U^2; e) the primary Reynolds shear stress, $\overline{u'v'}$/U^2. The mean variables were averaged in the spanwsie direction and in time, after the quasi-steady state was reached. The comparison is done in the region situated around the second obstacle in the series. The dashed and solid lines in frame a) correspond to the top of the layer of heavy fluid (C=0.8) and bottom of the layer of ambient fluid (C=0.1), respectively. The dashed line in frame b) corresponds to the top of the layer of high velocity magnitude.

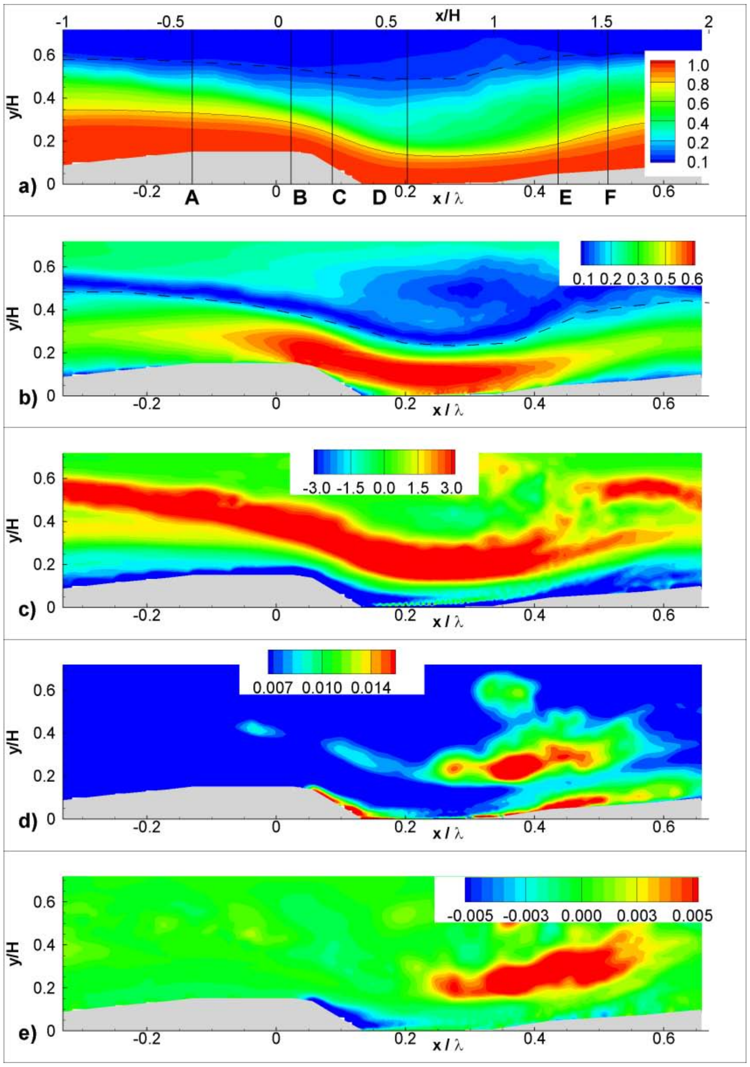

Figure 4.18 Mean flow and turbulence structure of the flow in the tail region after the quasi-steady regime is reached (HR-D15 simulation). a) concentration, C; b) velocity magnitude u_{mag}/U; c) mean out-of-plane vorticity, ω_z(H/U); d) turbulence kinetic energy, k/U^2; e) the primary Reynolds shear stress, $\overline{u'v'}$/U^2. The mean variables were averaged in the spanwsie direction and in time, after the quasi-steady state was reached. The comparison is done in the region situated around the second obstacle in the series.

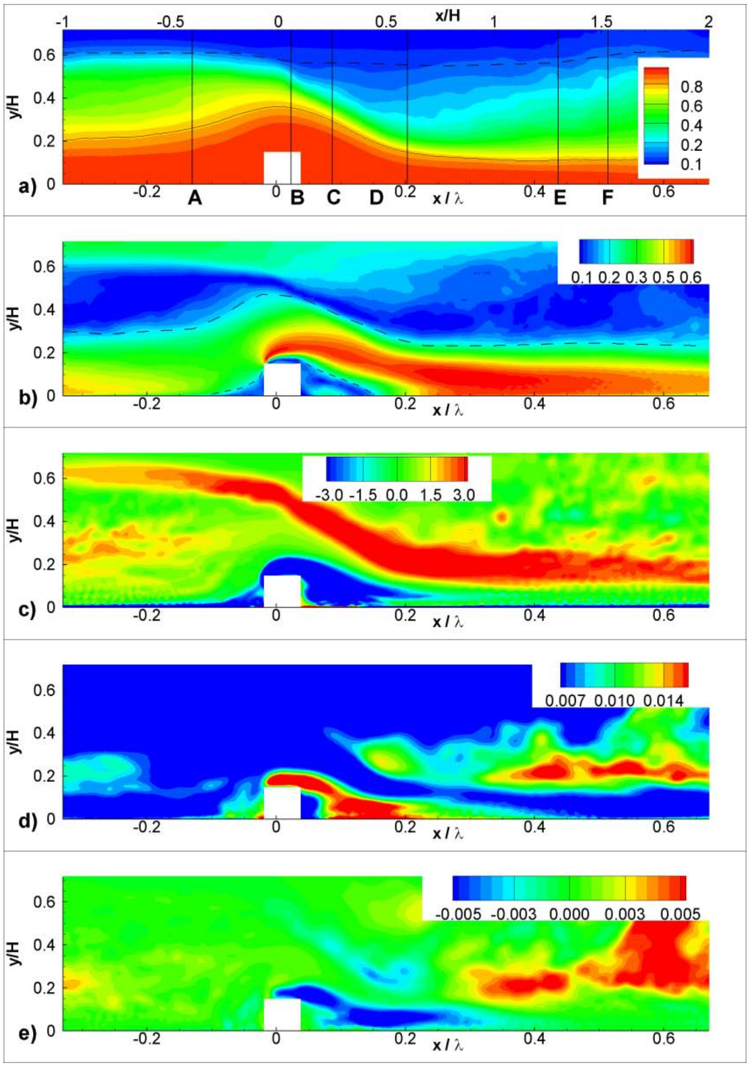

Figure 4.19 Mean flow and turbulence structure of the flow in the tail region after the quasi-steady regime is reached (HR-R15 simulation). a) concentration, C; b) velocity magnitude u_{mag}/U; c) mean out-of-plane vorticity, ω_z(H/U); d) turbulence kinetic energy, k/U^2; e) the primary Reynolds shear stress, $\overline{u'v'}/U^2$. The mean variables were averaged in the spanwise direction and in time, after the quasi-steady state was reached. The comparison is done in the region situated around the second obstacle in the series.

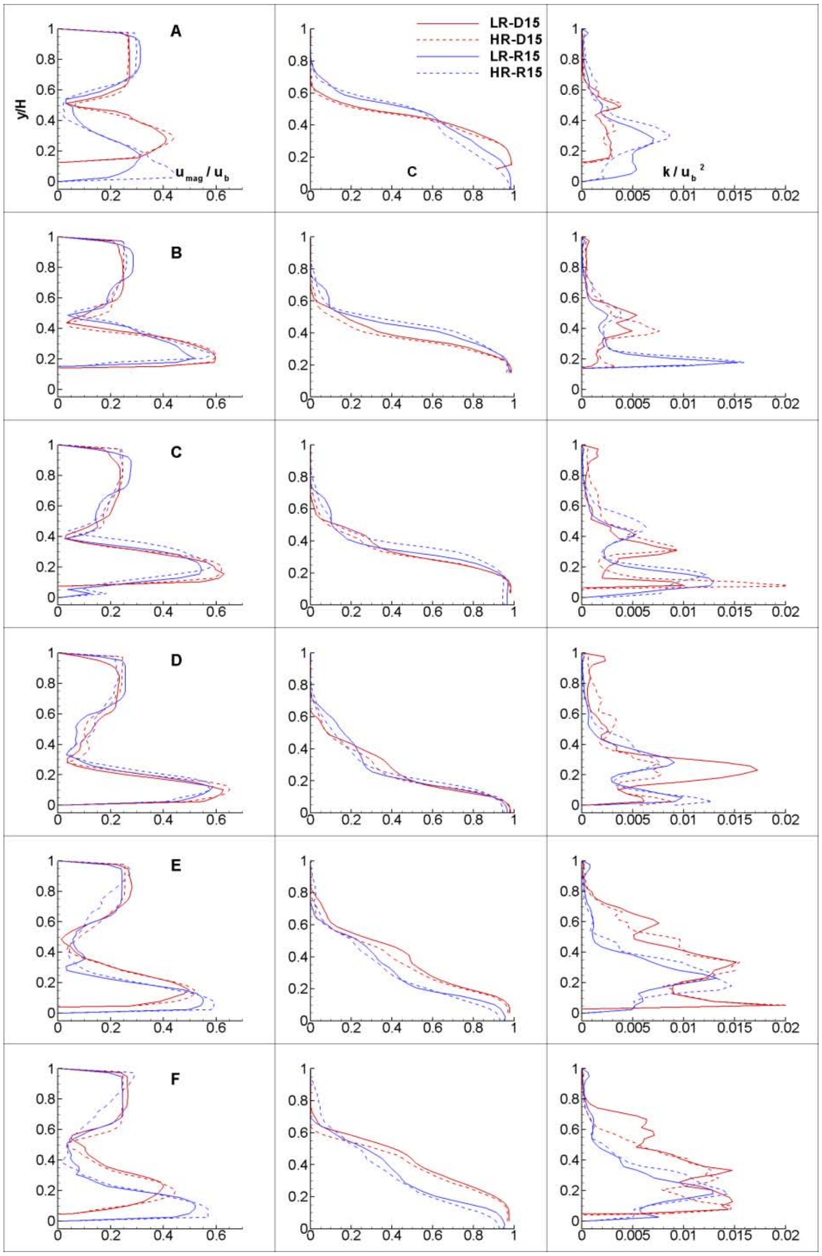

Figure 4.20 Comparison of the vertical profiles of u_{mag}/U, C and k/U^2 at sections A to F in the tail region after the quasi-steady regime is reached. Results are shown for the low and high Reynolds number simulations with obstacles of height D=0.15H. The positions of sections A to F is shown in Figure 4.16a.

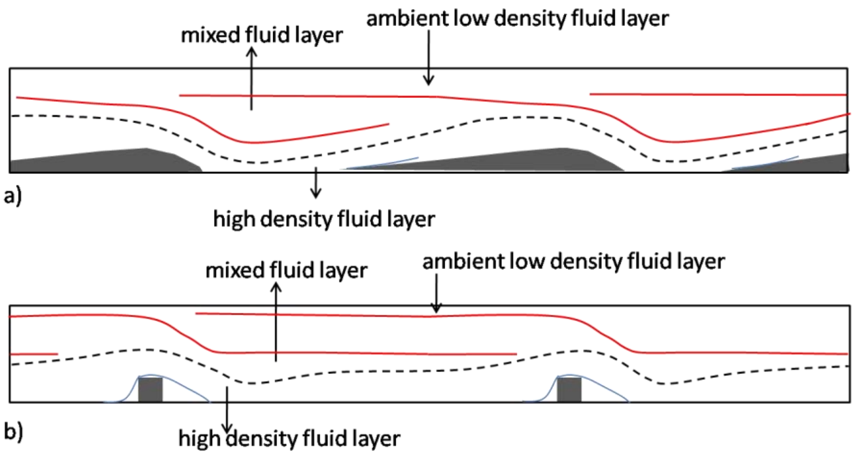
mixed fluid layer
ambient low density fluid layer
a)
high density fluid layer
mixed fluid layer
ambient low density fluid layer
b)
high density fluid layer

Figure 4.21 Sketch of the flow structure within the tail region in the case dunes (a) or ribs (b) are present at the channel bottom at large distances behind the front of the gravity current.

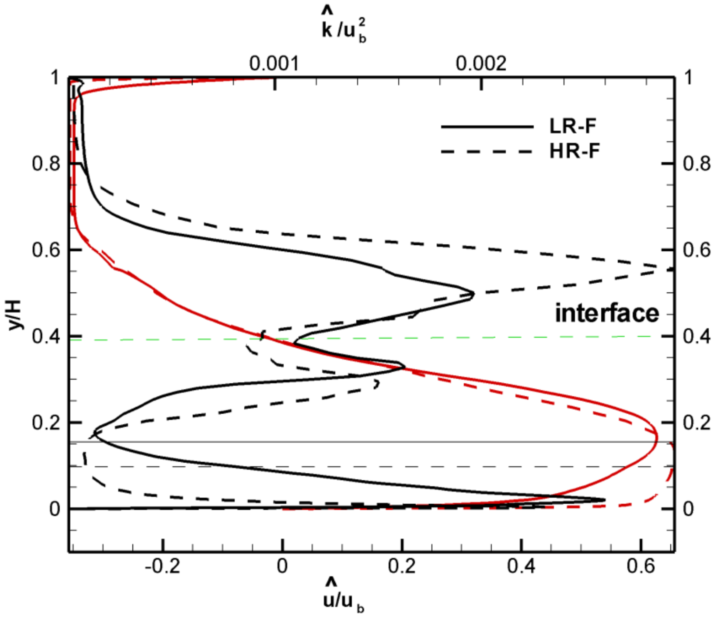

Figure 4.22 Vertical profiles of the double-averaged streamwise velocity, $\hat{u}$ /U, concentration, $\hat{C}$, and turbulent kinetic energy, $\hat{k}$ /U^2, in the LR-F and HR-F simulations.

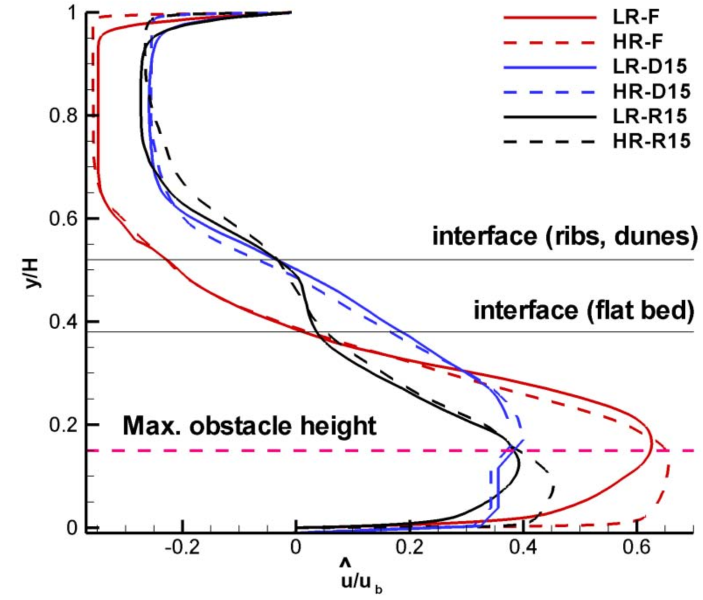

Figure 4.23 Vertical profiles of the double-averaged streamwise velocity, $\hat{u}$/U, in the low and high Reynolds number simulations with flat bed and with obstacles of height D=0.15H.

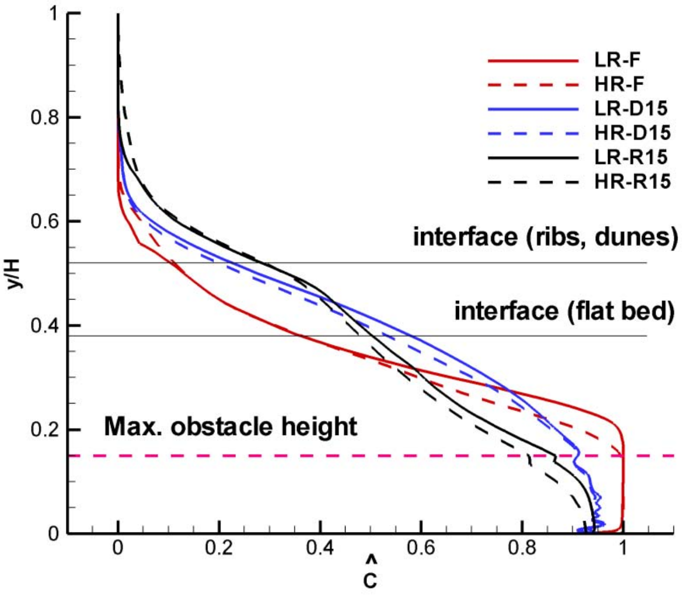

Figure 4.24 Vertical profiles of the double-averaged concentration, $\hat{C}$, in the low and high Reynolds number simulations with flat bed and with obstacles of height D=0.15H.

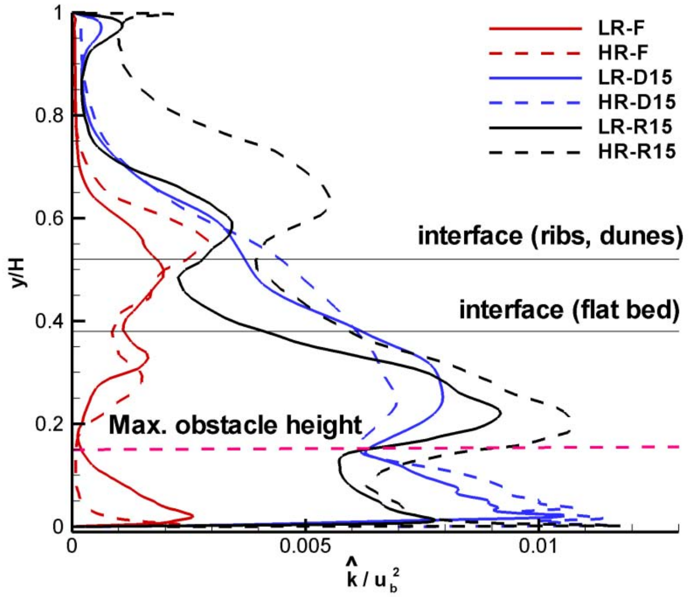

Figure 4.25 Vertical profiles of the double-averaged turbulent kinetic energy, $\hat{k}$/U^2, in the low and high Reynolds number simulations with flat bed and with obstacles of height D=0.15H.

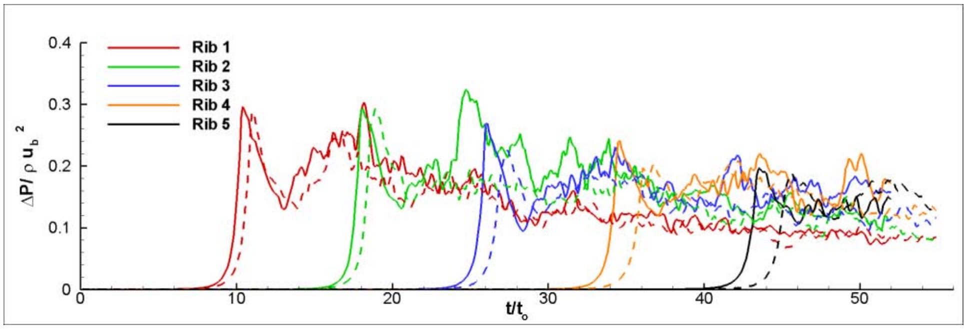

Figure 4.26 Time variation of the mean pressure difference between the upstream and downstream faces of the ribs, $\Delta P / \rho u_b^2$, in the LR-R15 (dashed line) and HR-R15 (solid line) simulations.

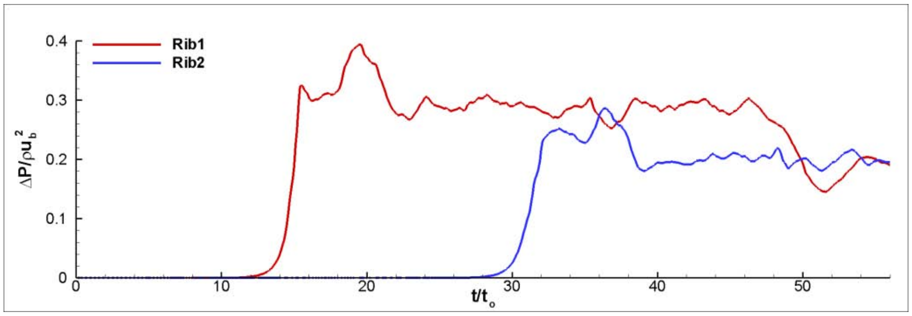

Figure 4.27 Time variation of the mean pressure difference between the upstream and downstream faces of the ribs, $\Delta P/\rho u_b^2$, in the LR-R30 simulation.

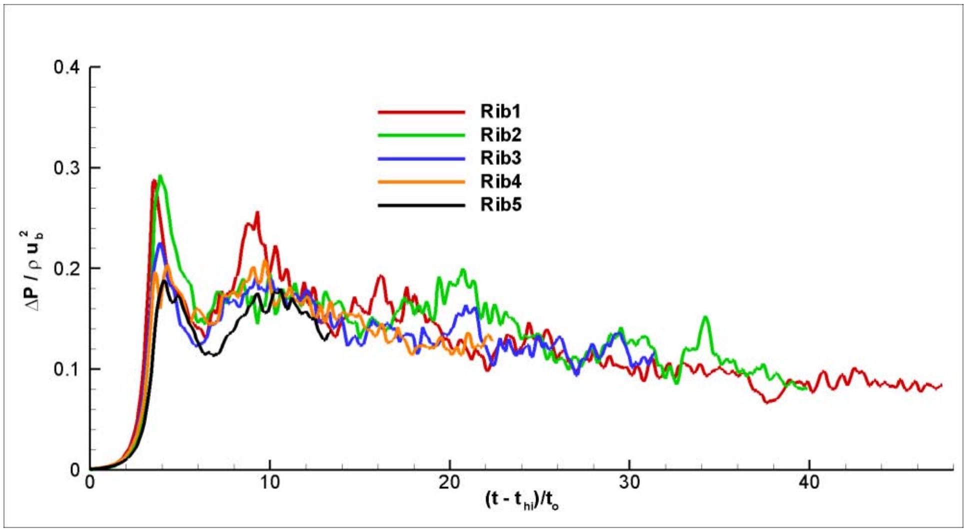

Figure 4.28 Time variation of the mean pressure difference between the upstream and downstream faces of the ribs, $\Delta P/\rho u_b^2$, in the LR-R15 simulation. The profiles were translated in time such that the impact stage starts at $t/t_0=0$ for all the five ribs.

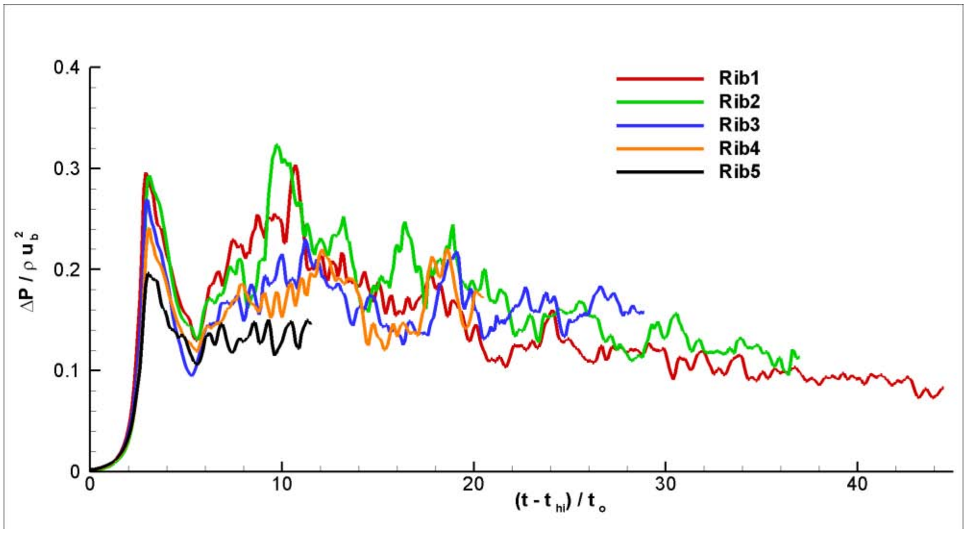

Figure 4.29 Time variation of the mean pressure difference between the upstream and downstream faces of the ribs, ΔP/ ρu_b^2, in the HR-R15 simulation. The profiles were translated in time such that the impact stage starts at t/t$_0$=0 for all the five ribs.

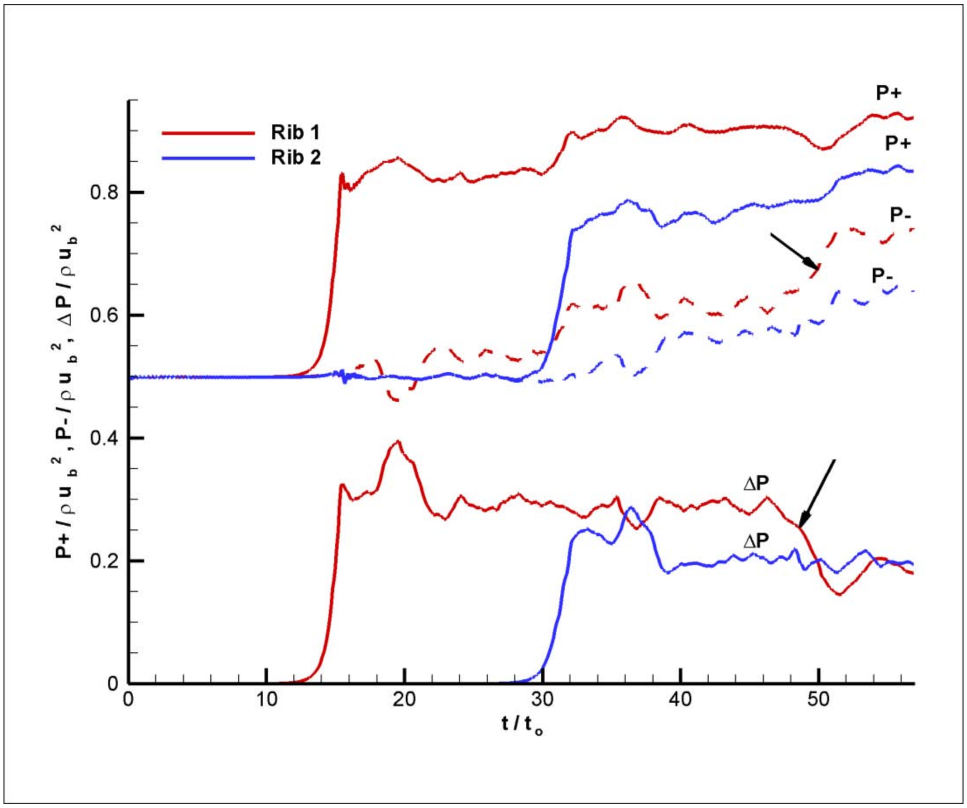

Figure 4.30 Time variations of the mean pressure on the upstream face of the ribs, $P^+/\rho u_b^2$, mean pressure on the downstream face of the ribs, $P^-/\rho u_b^2$, and mean pressure difference between the upstream and downstream faces of the ribs, $\Delta P/\rho u_b^2$, in the LR-R30 simulation. The arrows show the increase in P^- and the corresponding decrease in ΔP as a result of the passage of the hydraulic jump originating at Rib 2 over Rib 1.

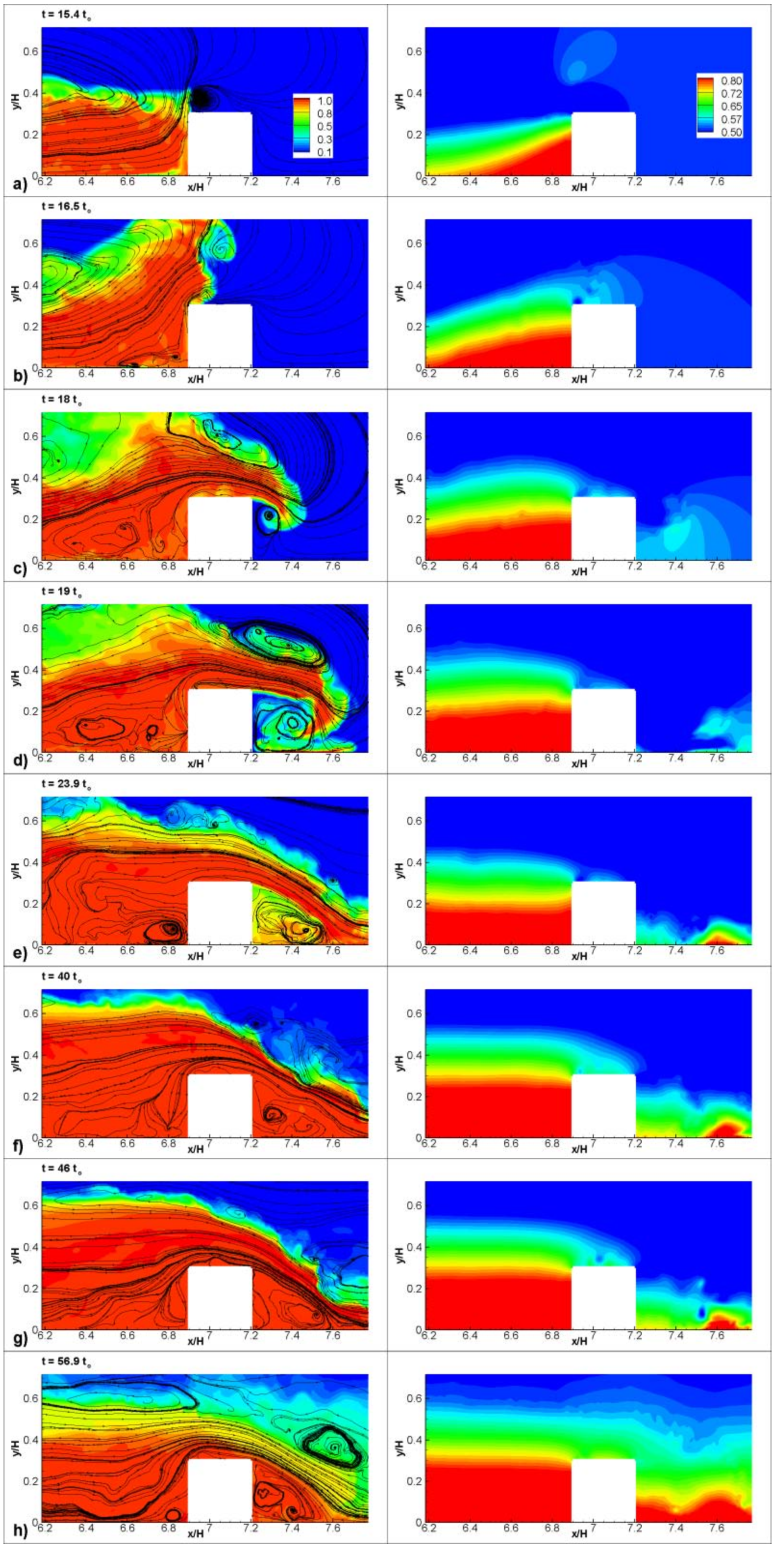

Figure 4.31 Contour plots showing the concentration, C, (left) and pressure, $p/\rho u_b^2$, (right) distributions in a vertical x-y plane around Rib 1 in the LR-R30 simulation at representative time instants. Also shown are the 2-D streamline patterns of the flow around Rib 1.

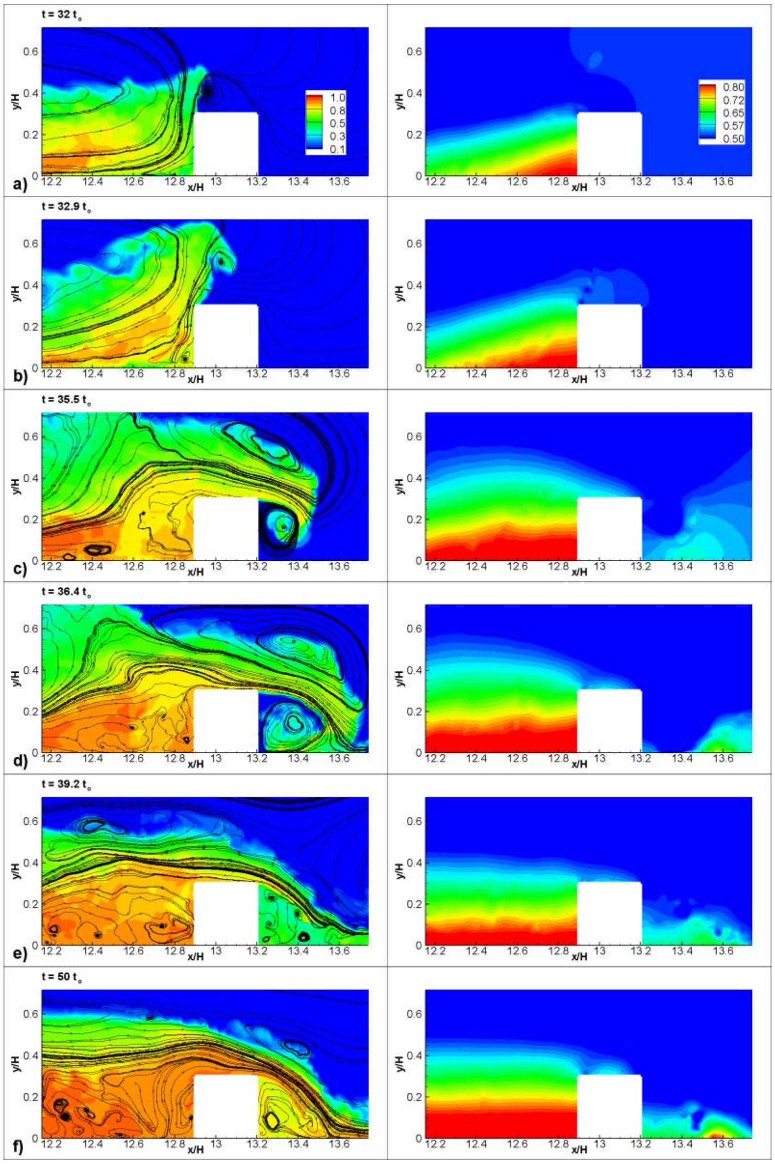

Figure 4.32 Contour plots showing the concentration, C, (left) and pressure, $p/\rho u_b^2$, (right) distributions in a vertical x-y plane around Rib 2 in the LR-R30 simulation at representative time instants. Also shown are the 2-D streamline patterns of the flow around Rib 1.

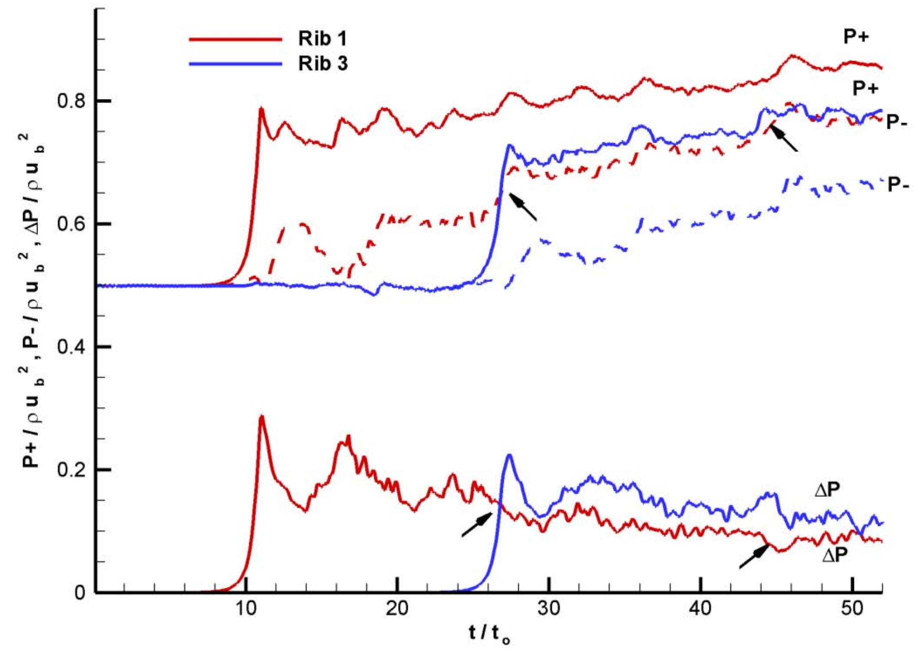

Figure 4.33 Time variations of the mean pressure on the upstream face of the ribs, $P^+/\rho u_b^2$, mean pressure on the downstream face of the ribs, $P^-/\rho u_b^2$, and mean pressure difference between the upstream and downstream faces of the ribs, $\Delta P/\rho u_b^2$, in the LR-R15 simulation. The arrows show the increase in P^- and the corresponding decrease in ΔP as a result of the passage of the hydraulic jumps originating at Rib 2 and Rib 4 over Rib 1.

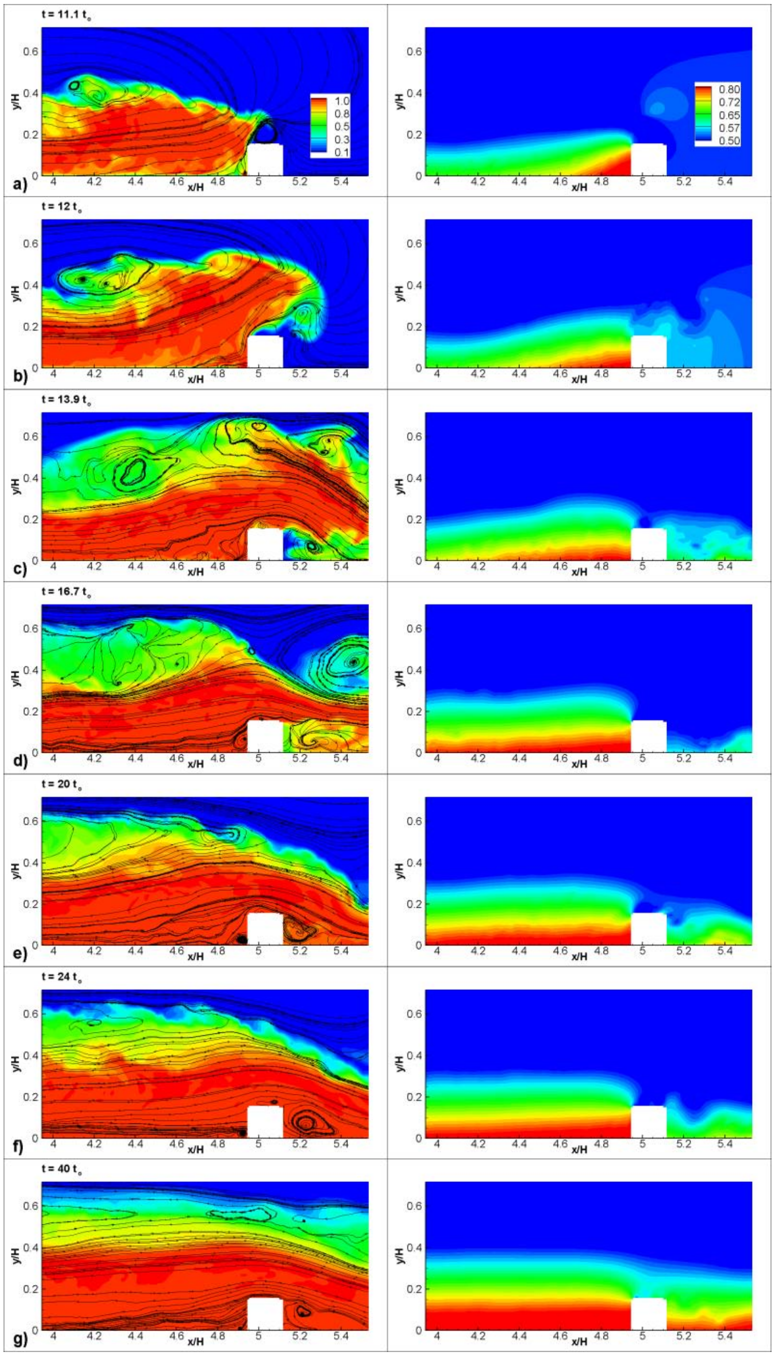

Figure 4.34 Contour plots showing the concentration, C, (left) and pressure, $p/\rho u_b^2$, (right) distributions in a vertical x-y plane around Rib 1 in the LR-R15 simulation at representative time instants. Also shown are the 2-D streamline patterns of the flow around Rib 1.

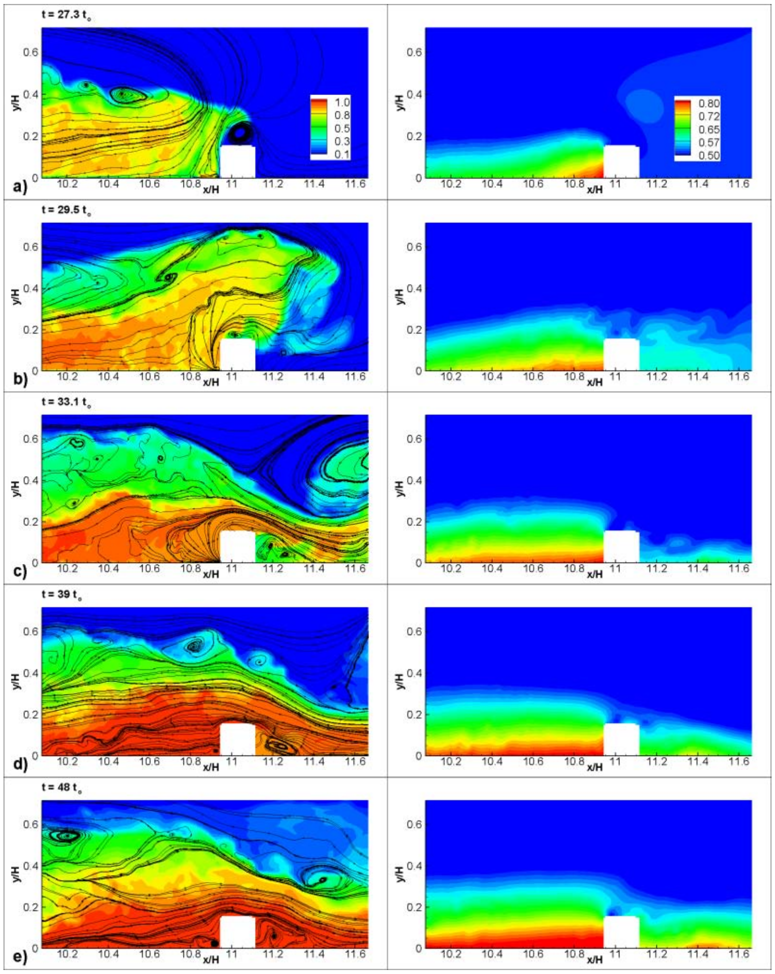

Figure 4.35 Contour plots showing the concentration, C, (left) and pressure, $p/\rho u_b^2$, (right) distributions in a vertical x-y plane around Rib 3 in the LR-R15 simulation at representative time instants. Also shown are the 2-D streamline patterns of the flow around Rib 3.

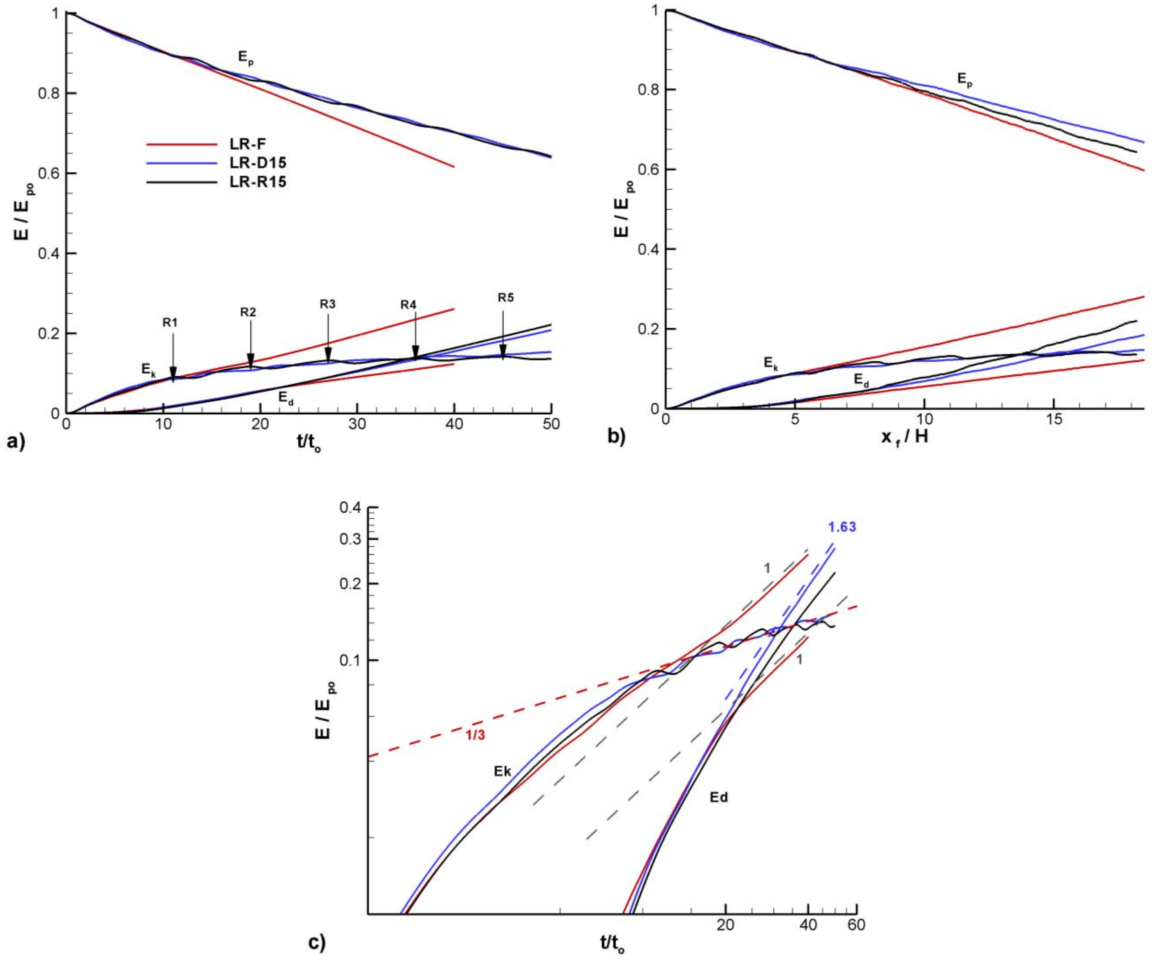

Figure 4.36 Variation of the potential energy, E_p, kinetic energy, E_k, and integral of the total dissipation, E_d, in the low Reynolds number simulations with flat bed and with obstacles of height D=0.15H. a) plotted versus time in linear-linear scale; b) plotted versus the front position in linear-linear scale; c) plotted versus time in log-log scale. All the terms are non-dimensionalized by the initial potential energy E_{p0}. The arrows in frame a) indicate the times when the current reaches a certain rib in the LR-R15 simulation.

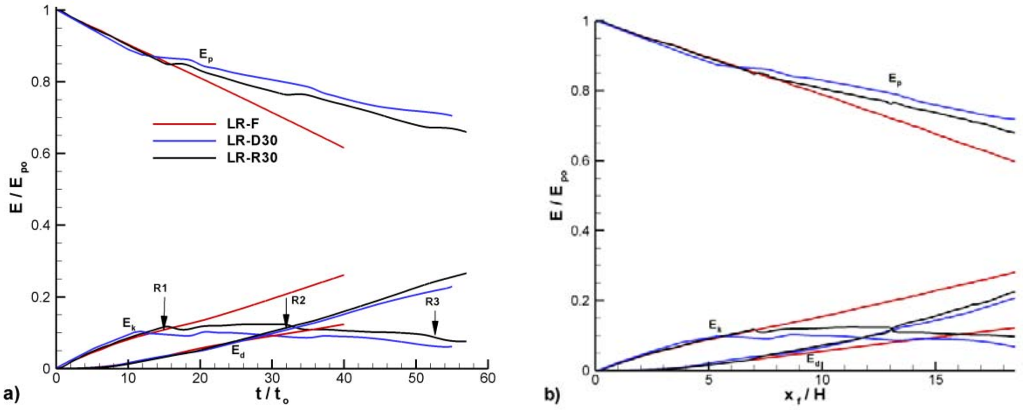

Figure 4.37 Variation of the potential energy, E_p, kinetic energy, E_k, and integral of the total dissipation, E_d, in the low Reynolds number simulations with flat bed and with obstacles of height D=0.3H. a) plotted versus time in linear-linear scale; b) plotted versus the front position in linear-linear scale. All the terms are non-dimensionalized by the initial potential energy E_{p0}. The arrows in frame a) indicate the times when the current reaches a certain rib in the LR-R30 simulation.

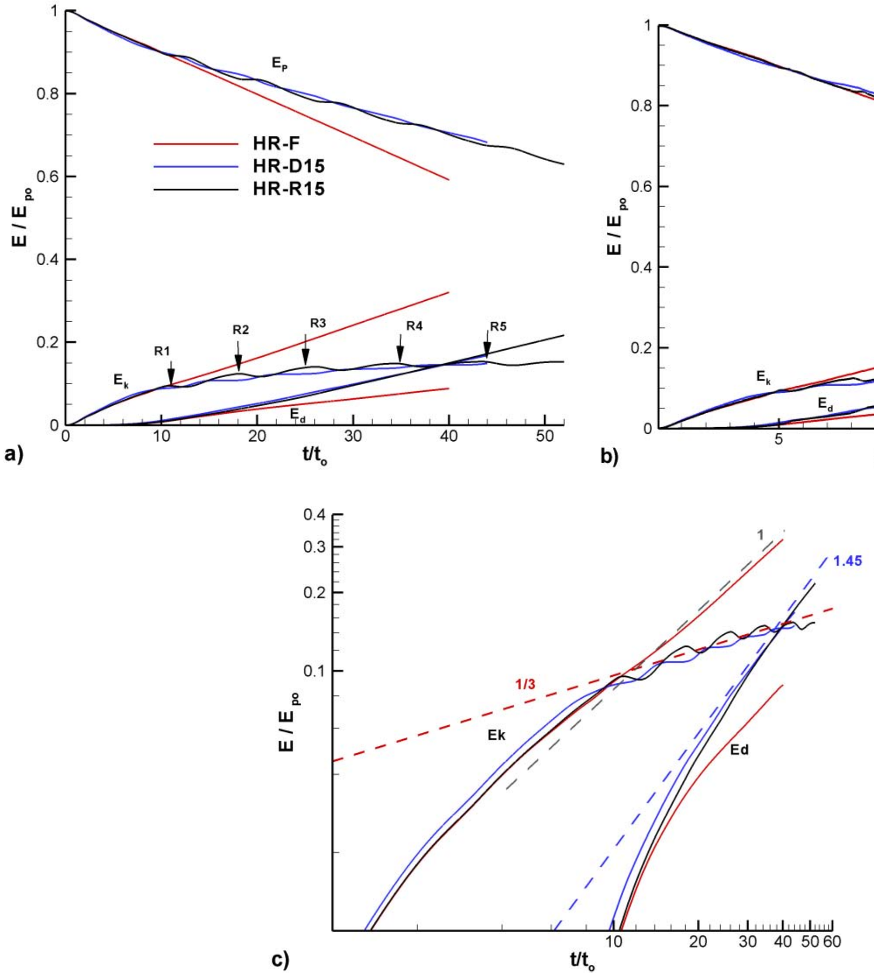

Figure 4.38 Variation of the potential energy, E_p, kinetic energy, E_k, and integral of the total dissipation, E_d, in the high Reynolds number simulations with flat bed and with obstacles of height D=0.15H. a) plotted versus time in linear-linear scale; b) plotted versus the front position in linear-linear scale; c) plotted versus time in log-log scale. All the terms are non-dimensionalized by the initial potential energy E_{p0}. The arrows in frame a) indicate the times when the current reaches a certain rib in the HR-R15 simulation.

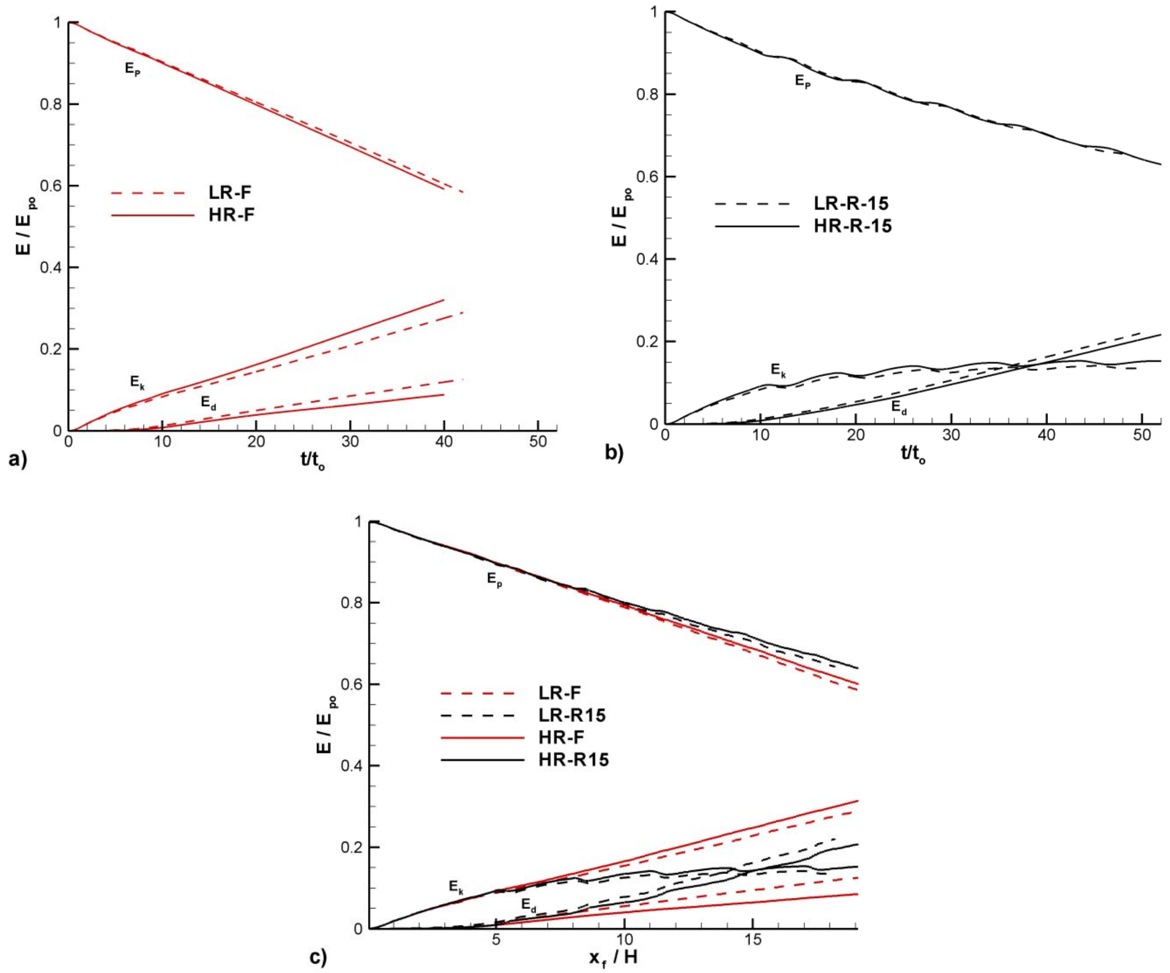

Figure 4.39 Variation of the potential energy, E_p, kinetic energy, E_k, and integral of the total dissipation, E_d, in the low and high Reynolds number simulations a) with flat bed (time variation); b) with ribs of height D=0.15H (time variation); c) with flat bed and with ribs of height D=0.15H (variation with the front position). All the terms are non-dimensionalized by the initial potential energy E_{p0}.

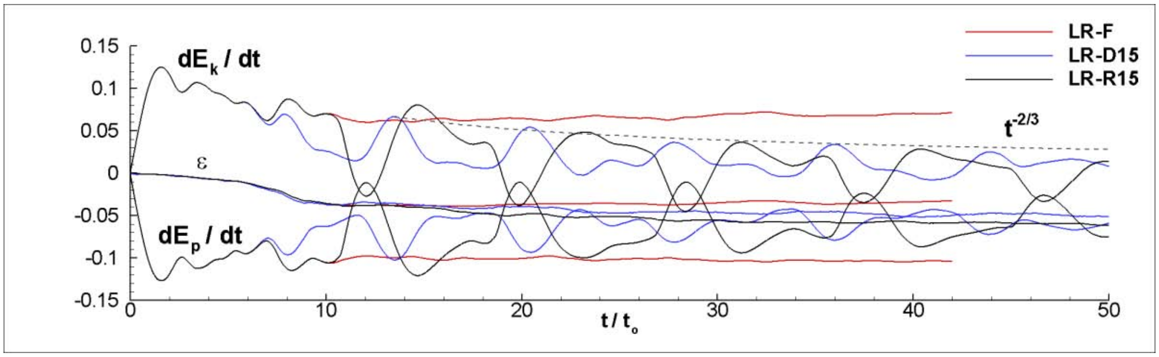

Figure 4.40 Time variation of the terms (-*dE$_k$/dt*, *dE$_p$/dt* and ε) in the differential equation of the mechanical energy in the low Reynolds number simulations with flat bed and with obstacles of height D=0.15H. All the terms are non-dimensionalized by $u_b^3 H^2$.

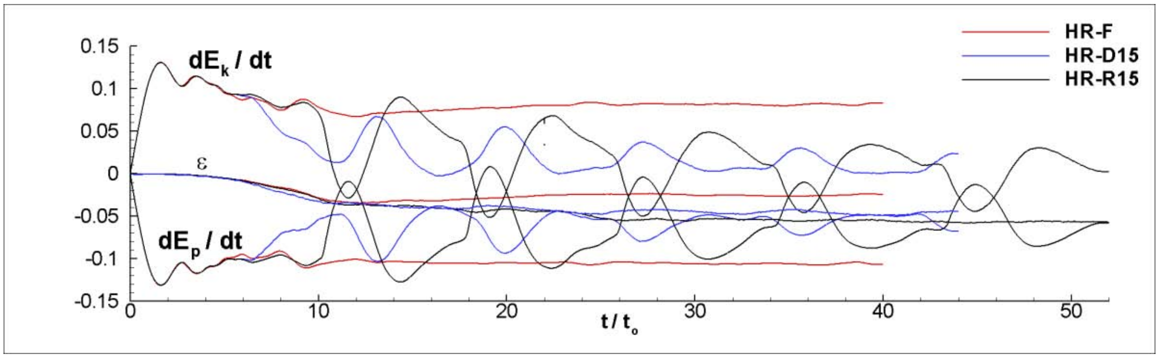

Figure 4.41 Time variation of the terms (-*dE$_k$/dt*, *dE$_p$/dt* and ε) in the differential equation of the mechanical energy in the high Reynolds number simulations with flat bed and with obstacles of height D=0.15H. All the terms are non-dimensionalized by $u_b^3 H^2$.

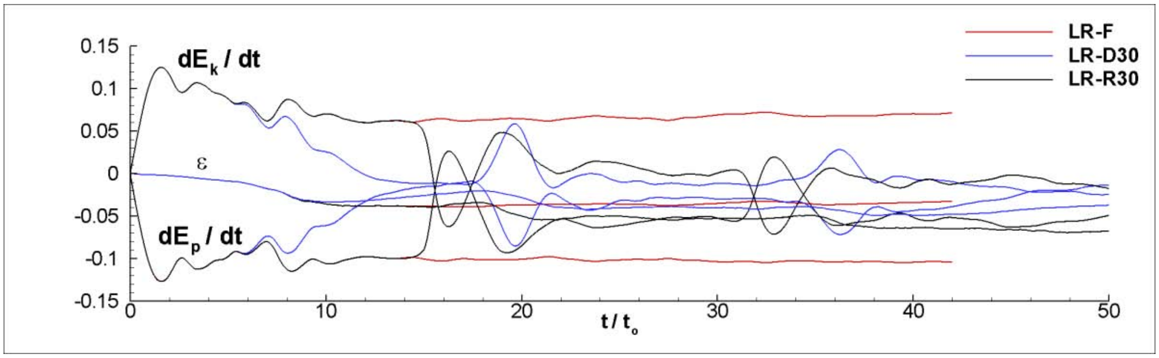

Figure 4.42 Time variation of the terms (-dE_k/dt, dE_p/dt and ε) in the differential equation of the mechanical energy in the low Reynolds number simulations with flat bed and with obstacles of height D=0.3H. All the terms are non-dimensionalized by $u_b^3 H^2$.

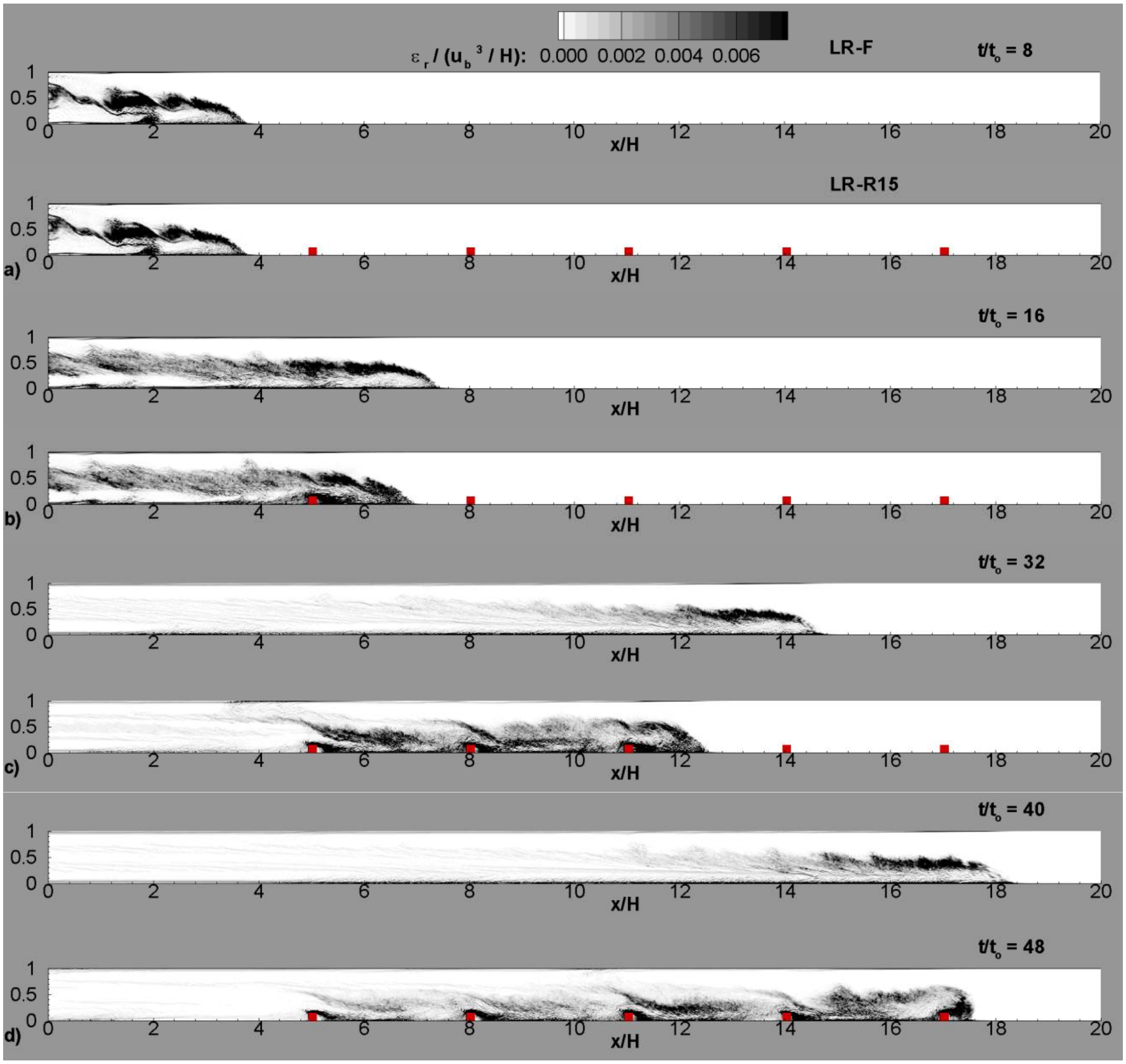

Figure 4.43 Spatial distributions of the non-dimensional spanwise-averaged local dissipation rate $\varepsilon_r/(u_b^3/H)$ in the low Reynolds number simulations with flat bed and ribs of height D=0.15H. a) $t/t_0=8$; b) $t/t_0=16$; c) $t/t_0=32$; d) $t/t_0=40$ (LR-F) and $t/t_0=48$ (LR-R15).

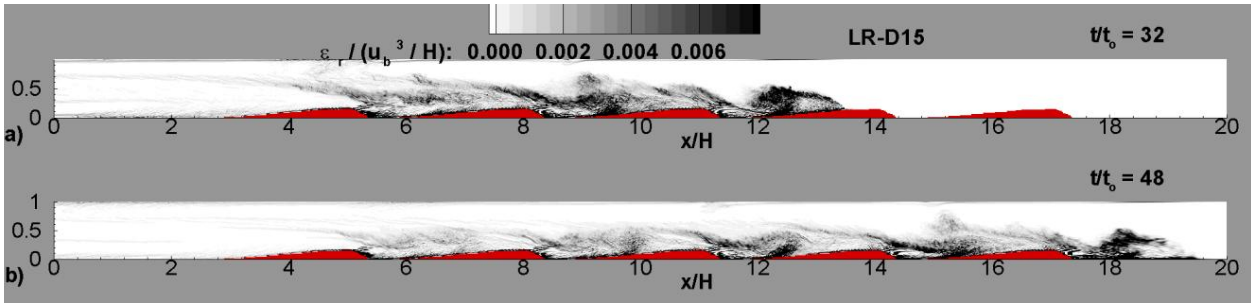

Figure 4.44 Spatial distribution of the non-dimensional spanwise-averaged local dissipation rate $\varepsilon_r/(u_b^3/H)$ in the low Reynolds number simulations with dunes of height D=0.15H. a) $t/t_0=32$; b) $t/t_0=48$.

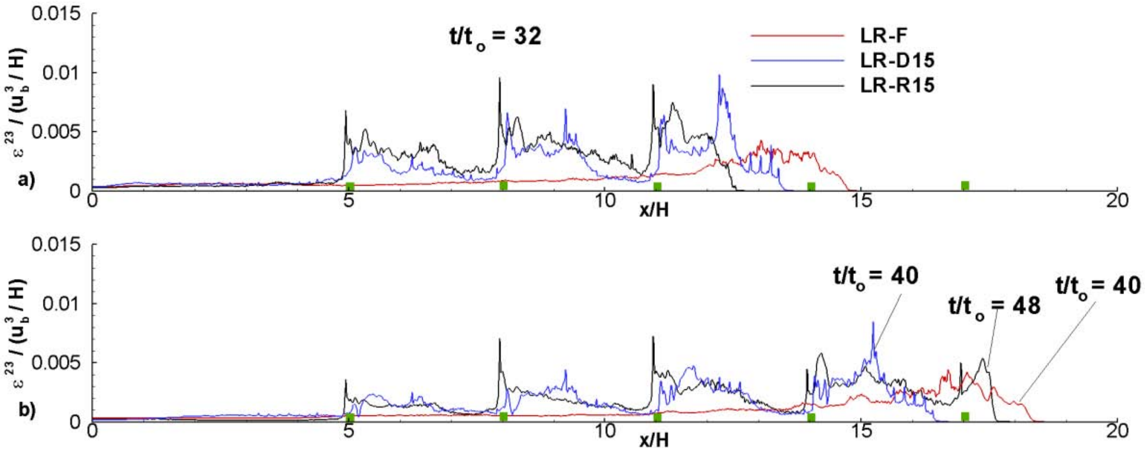

Figure 4.45 Streamwise distributions of $\varepsilon^{23}(x_1)/(u_b^3 H)$ in the low Reynolds number simulations with flat bed and obstacles of height D=0.15H. a) $t/t_0=32$; b) $t/t_0=40$ (LR-F and LR-D15) and $t/t_0=48$ (LR-R15).

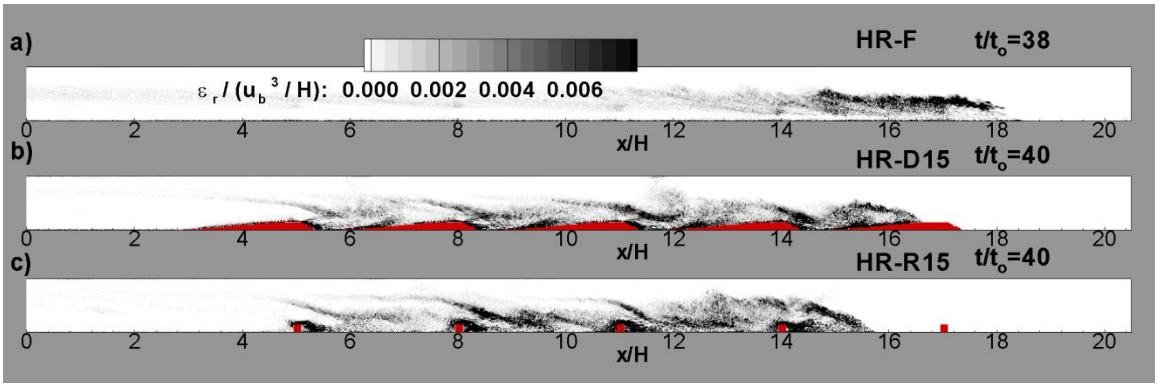

Figure 4.46 Spatial distributions of the non-dimensional spanwise-averaged local dissipation rate $\varepsilon_r/(u_b^3/H)$ in the high Reynolds number simulations with flat bed and obstacles of height D=0.15H. a) HR-F simulation at $t/t_0=38$; b) HR-D15 simulation at $t/t_0=40$; c) HR-R15 simulation at $t/t_0=40$.

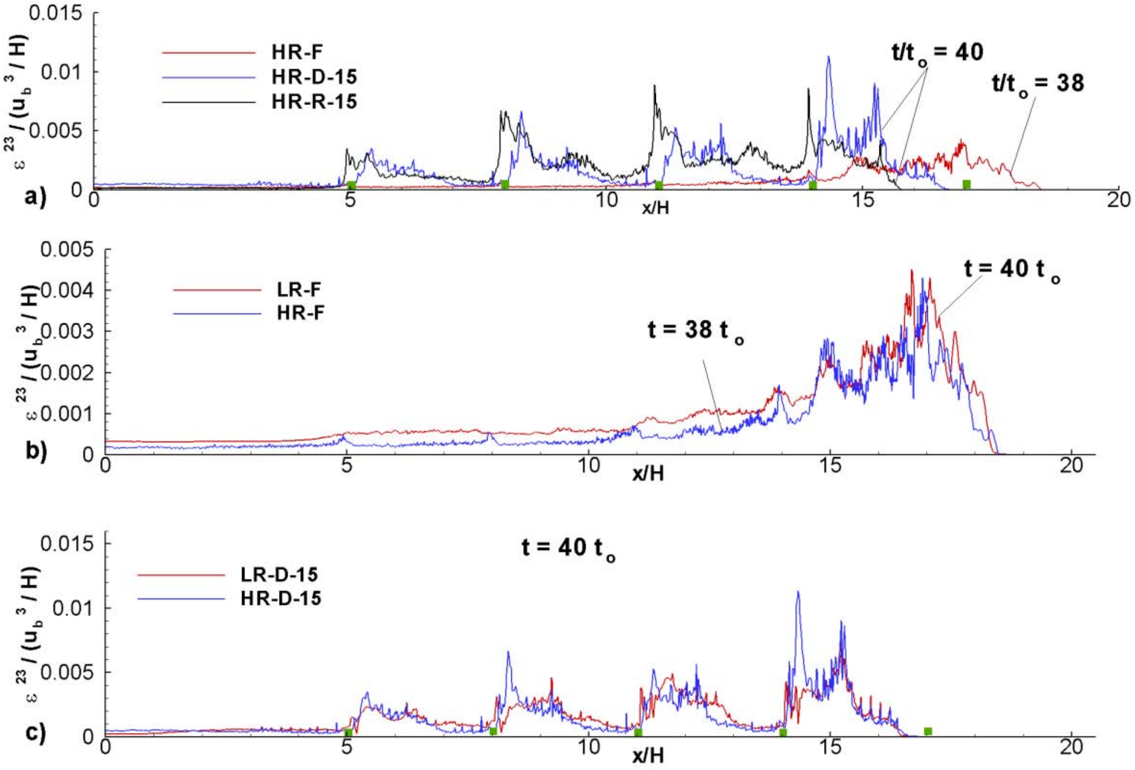

Figure 4.47 Streamwise distributions of $\varepsilon^{23}(x_1)/(u_b^3 H)$ showing the effect of increasing the Reynolds number. a) t/t$_0$=40 (HR-D15 and HR-R15) and t/t$_0$=38 (HR-F); b) t/t$_0$=40 (LR-F) and t/t$_0$=38 (HR-F); c) t/t$_0$=40 (LR-D15 and HR-D15).

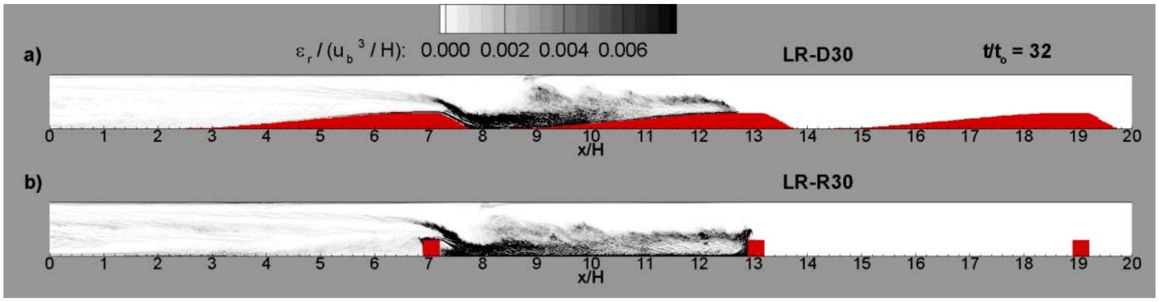

Figure 4.48 Spatial distributions of the non-dimensional spanwise-averaged local dissipation rate ε$_r$/(u_b^3 / H) in the low Reynolds number simulations with obstacles of height D=0.3H. b) HR-D30 simulation at t/t$_0$=32; c) HR-R30 simulation at t/t$_0$=32.

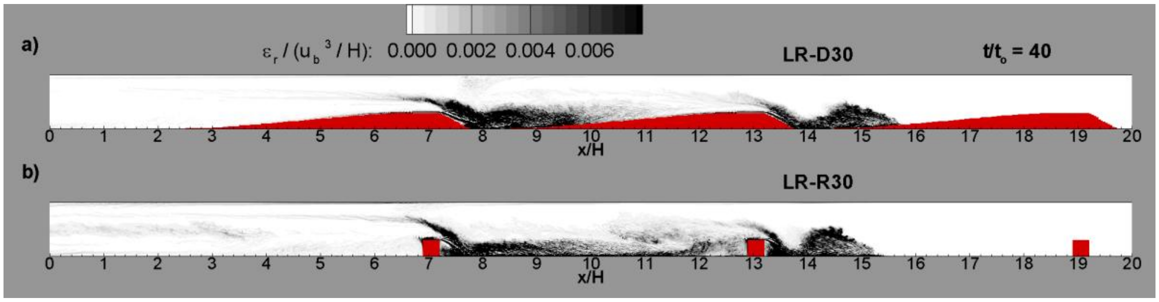

Figure 4.49 Spatial distributions of the non-dimensional spanwise-averaged local dissipation rate $\varepsilon_r/(u_b^3/H)$ in the low Reynolds number simulations with obstacles of height D=0.3H. b) HR-D30 simulation at t/t_0=40; c) HR-R30 simulation at t/t_0=40.

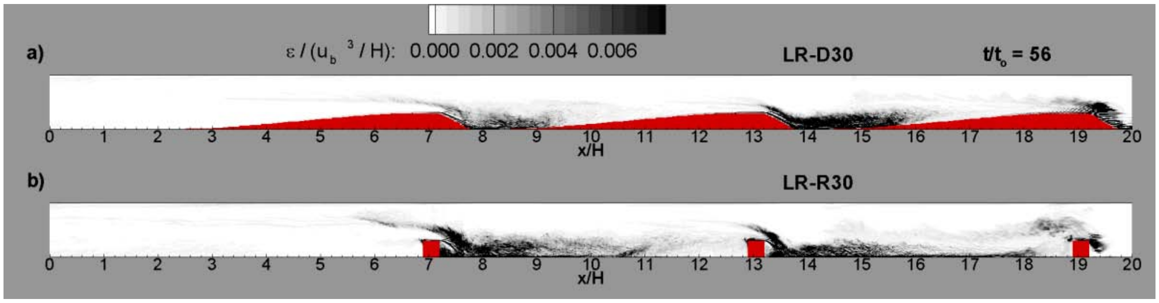

Figure 4.50 Spatial distributions of the non-dimensional spanwise-averaged local dissipation rate $\varepsilon_r/(u_b^3/H)$ in the low Reynolds number simulations with obstacles of height D=0.3H. b) HR-D30 simulation at t/t_0=56; c) HR-R30 simulation at t/t_0=56.

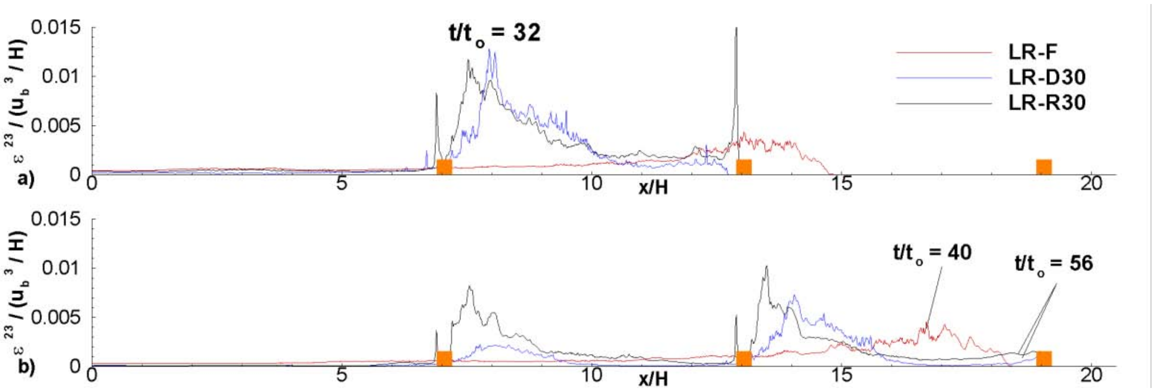

Figure 4.51 Streamwise distributions of $\varepsilon^{23}(x_1)/(u_b^3 H)$ in the low Reynolds number simulations with flat bed and obstacles of height D=0.3H. a) t/t$_0$=32; b) t/t$_0$=40 (LR-F) and t/t$_0$=56 (LR-D30 and LR-R30).

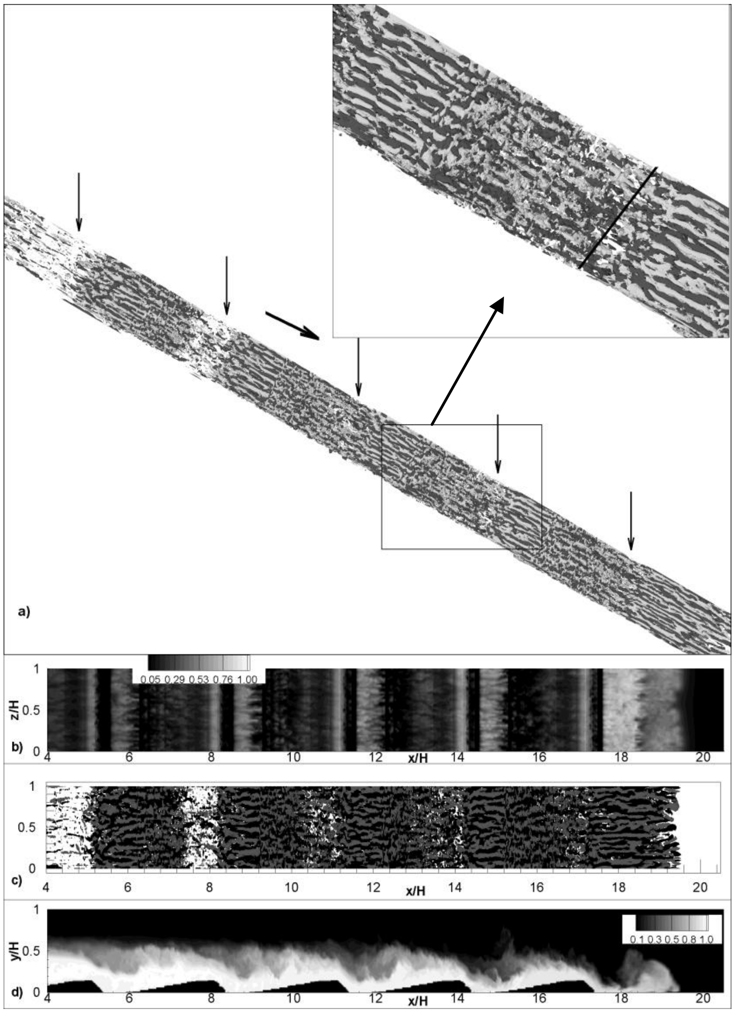

Figure 4.52 Visualization of the flow structure in the vicinity of the channel bottom in the LR-D15 simulation at t/t_0=40. a) vertical vorticity contours on the bottom wall, the view is lateral and from below the bottom propagating current; b) streamwise velocity (u/u_b) contours showing the positions of the regions containing streaks of high and low streamwise velocity. The contours are shown in a surface situated at 0.006H from the deformed channel bottom surface; c) vertical vorticity contours ($\omega_y H/u_b$) on the bottom wall, the view is from below the bottom propagating current; d) spanwise-averaged concentration contours. The light and dark vorticity contours in frames a) and c) correspond to $\omega_y = 2u_b / H$ and $\omega_y = -2u_b / H$, respectively. The arrows in frame a) indicate the position of the crest of each dune. The aspect ratio is 1:2 in the x-y plots in frames b) to d).

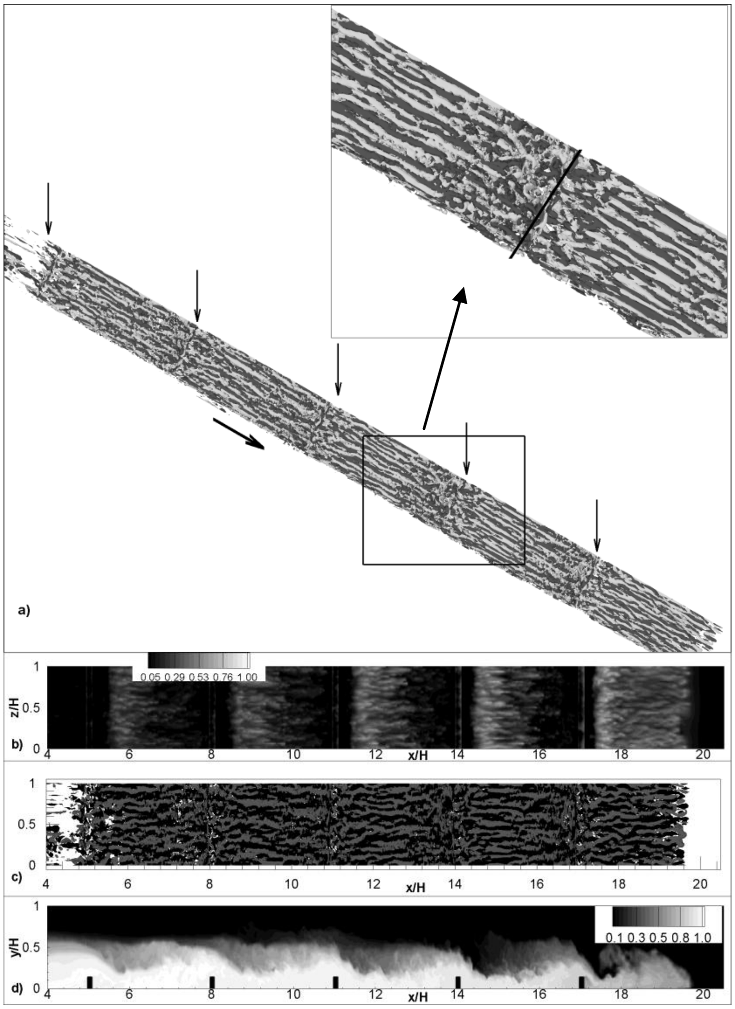

Figure 4.53 Visualization of the flow structure in the vicinity of the channel bottom in the LR-R15 simulation at t/t_0=40. a) vertical vorticity contours on the bottom wall, the view is lateral and from below the bottom propagating current; b) streamwise velocity (u/u_b) contours showing the positions of the regions containing streaks of high and low streamwise velocity. The contours are shown in a surface situated at 0.006H from the deformed channel bottom surface; c) vertical vorticity contours ($\omega_y H/u_b$) on the bottom wall, the view is from below the bottom propagating current; d) spanwise-averaged concentration contours. The light and dark vorticity contours in frames a) and c) correspond to $\omega_y = 2u_b / H$ and $\omega_y = -2u_b / H$, respectively. The arrows in frame a) indicate the position of the center of each rib. The aspect ratio is 1:2 in the x-y plots in frames b) to d).

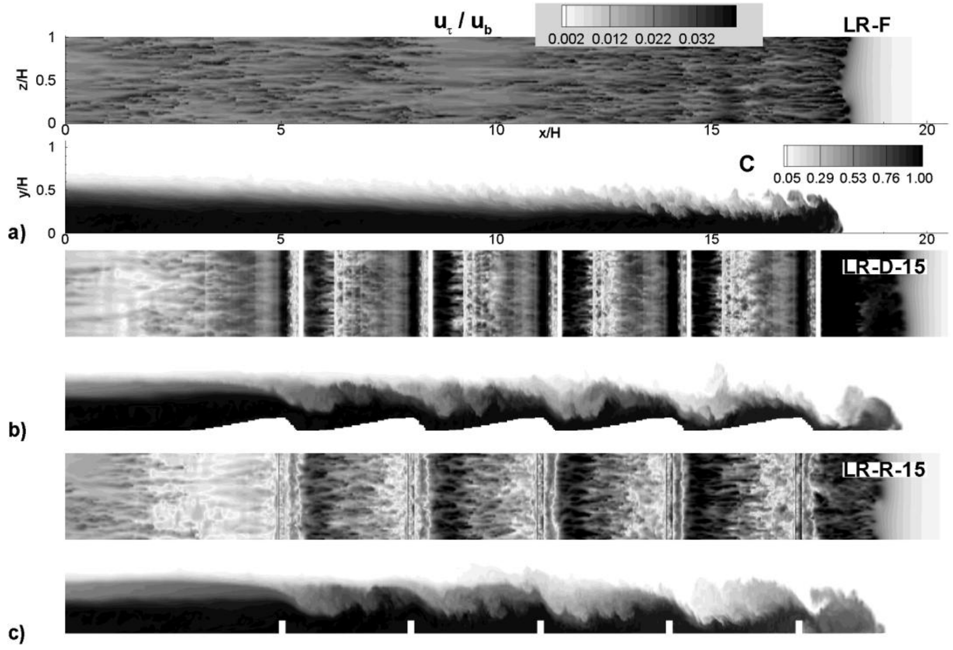

Figure 4.54 Spatial distribution of the bed friction velocity u_τ/u_b in the low Reynolds number simulations with a flat bed and with obstacles of height D=0.15H at time instances when the front of the bottom-propagating current is close to 18H. a) LR-F; b) LR-D15; c) LR-R15. Also shown are the concentration contours in an x-y section. The aspect ratio is 1:2 in the x-y plots.

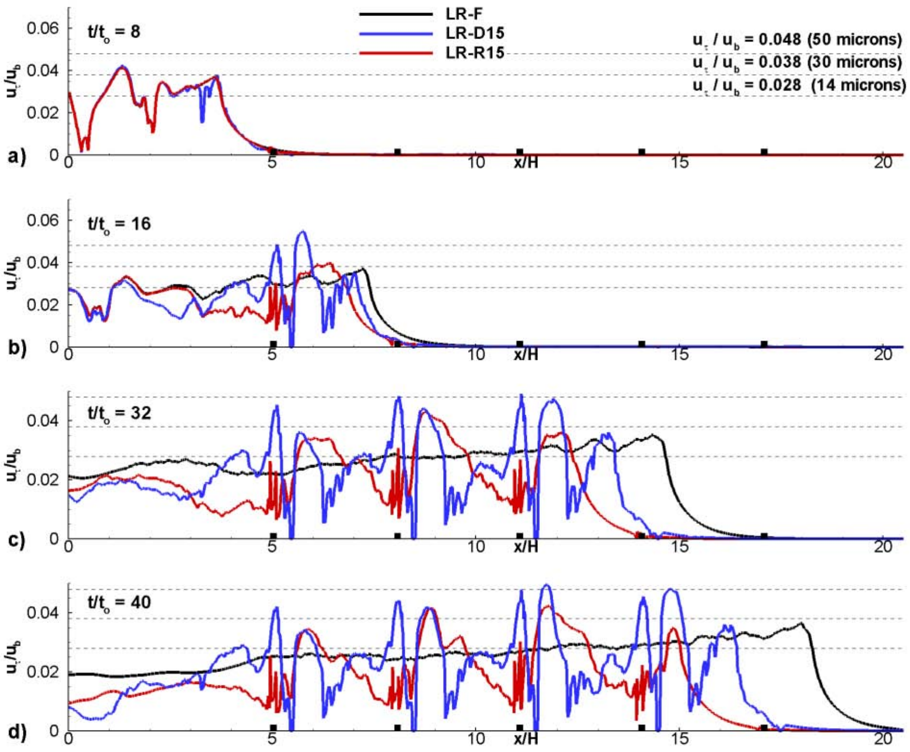

Figure 4.55 Streamwise distribution of the spanwise-averaged bed friction velocity in the low Reynolds number simulations with a flat bed and with obstacles of height D=0.15H. a) $t/t_0=8$; b) $t/t_0=16$; c) $t/t_0=32$; d) $t/t_0=40$. Also shown are the non-dimensional entrainment bed-friction velocities for sand particles of different sizes.

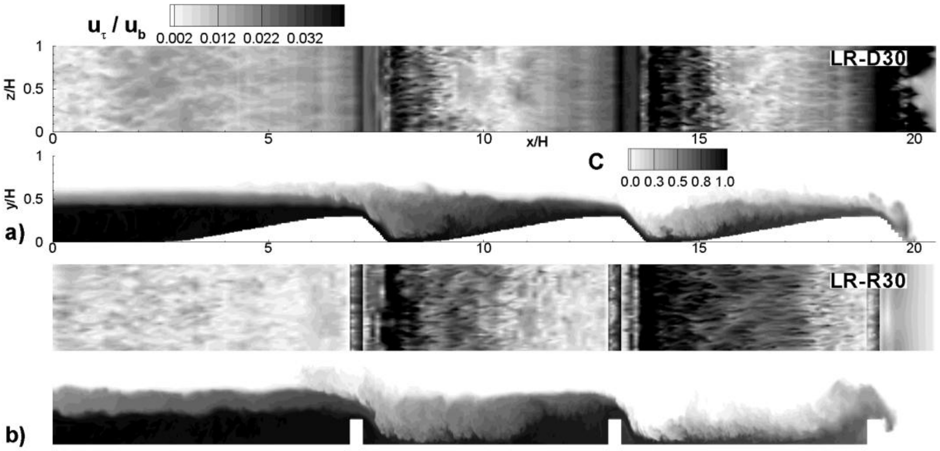

Figure 4.56 Spatial distribution of the bed friction velocity u_τ/u_b in the low Reynolds number simulations with obstacles of height D=0.3H at time instances when the front of the bottom-propagating current is close to 19H. a) LR-D30; b) LR-R30. Also shown are the concentration contours in an x-y section. The aspect ratio is 1:2 in the x-y plots.

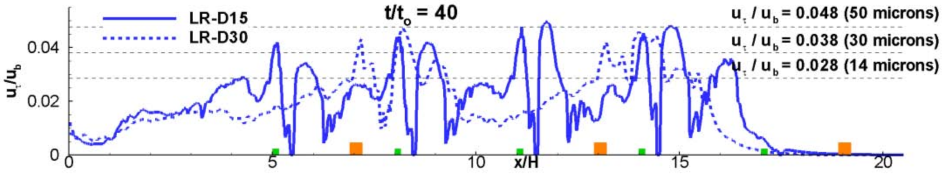

Figure 4.57 Streamwise distribution of the spanwise-averaged bed friction velocity in the low Reynolds number simulations with dunes of height D=0.15H and D=0.3H at t/t_0=40. Also shown are the non-dimensional entrainment bed-friction velocities for sand particles of different sizes.

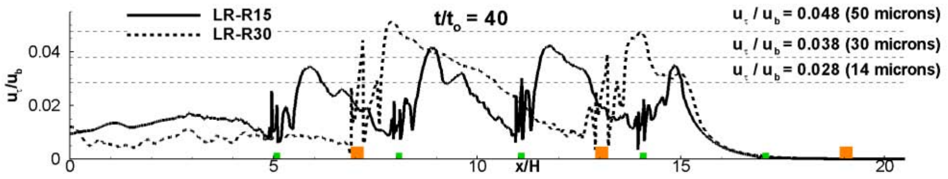

Figure 4.58 Streamwise distribution of the spanwise-averaged bed friction velocity in the low Reynolds number simulations with ribs of height D=0.15H and D=0.3H at t/t_0=40. Also shown are the non-dimensional entrainment bed-friction velocities for sand particles of different sizes.

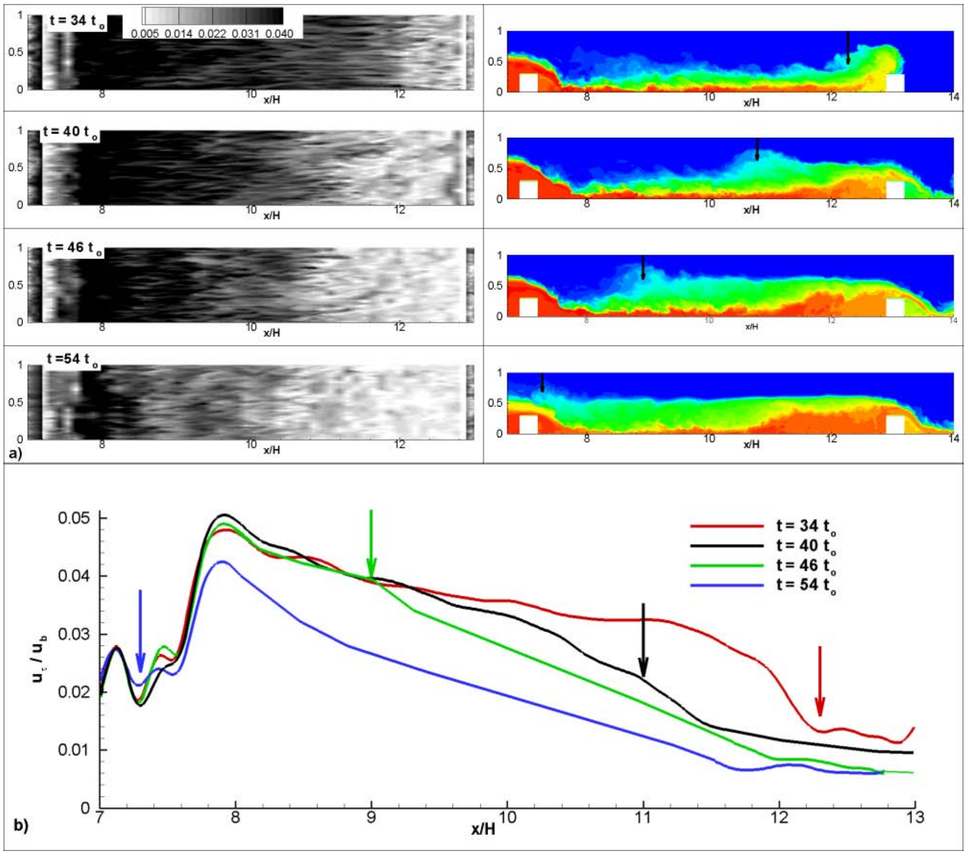

Figure 4.59 Effect of the passage of the backward propagating hydraulic jump on the bed friction velocity in the LR-R30 simulation. a) Spatial distribution of the bed friction velocity u_τ/u_b and concentration at representative time instants; b) Streamwise distribution of the spanwise-averaged bed friction velocity at the time instants shown in frame a). The arrow shows the position of the bore at a particular time instant.

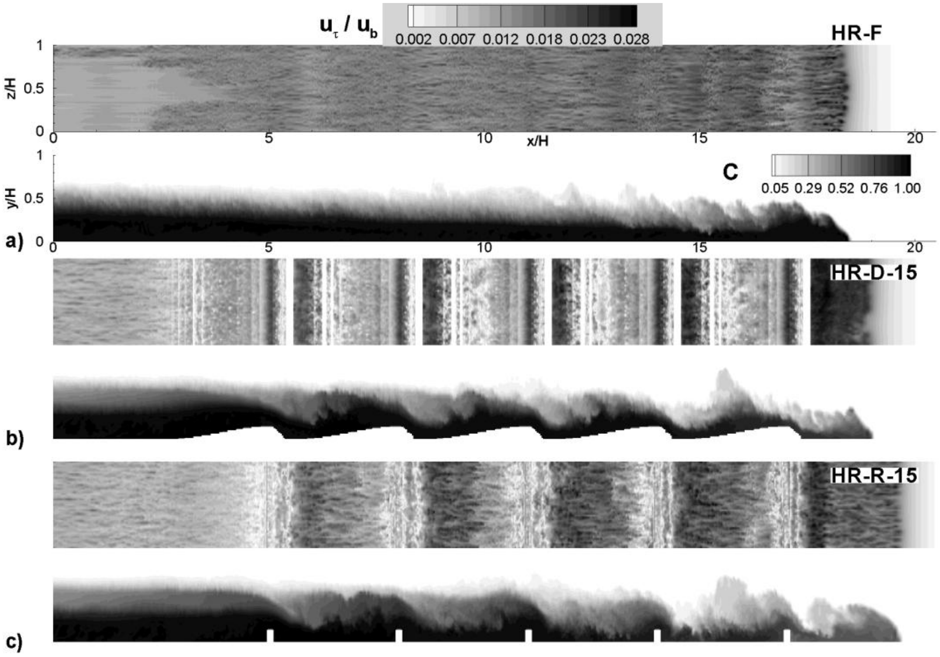

Figure 4.60 Spatial distributions of the bed friction velocity u_τ/u_b in the high Reynolds number simulations with a flat bed and with obstacles of height D=0.15H at time instances when the front of the bottom-propagating current is close to 18H. a) HR-F; b) HR-D15; c) HR-R15. Also shown are the concentration contours in an x-y section. The aspect ratio is 1:2 in the x-y plots.

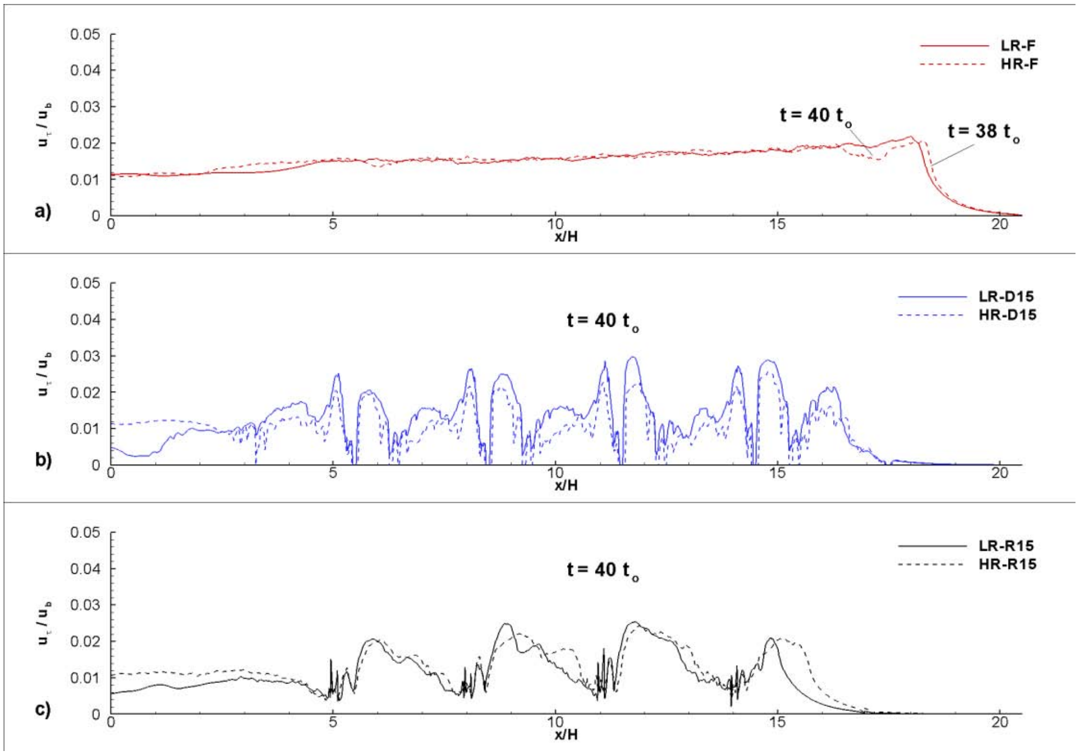

Figure 4.61 Streamwise distribution of the spanwise-averaged bed friction velocity in the high Reynolds number simulations with flat bed and obstacles of height D=0.15H at $t/t_0=40$. Also shown are the distributions of the spanwise-averaged bed friction velocity in the corresponding low Reynolds number simulations multiplied by a factor $\alpha=0.58$. a) LR-F vs. HR-F; b) LR-D15 vs. HR-D15; c) LR-R15 vs. HR-R15.

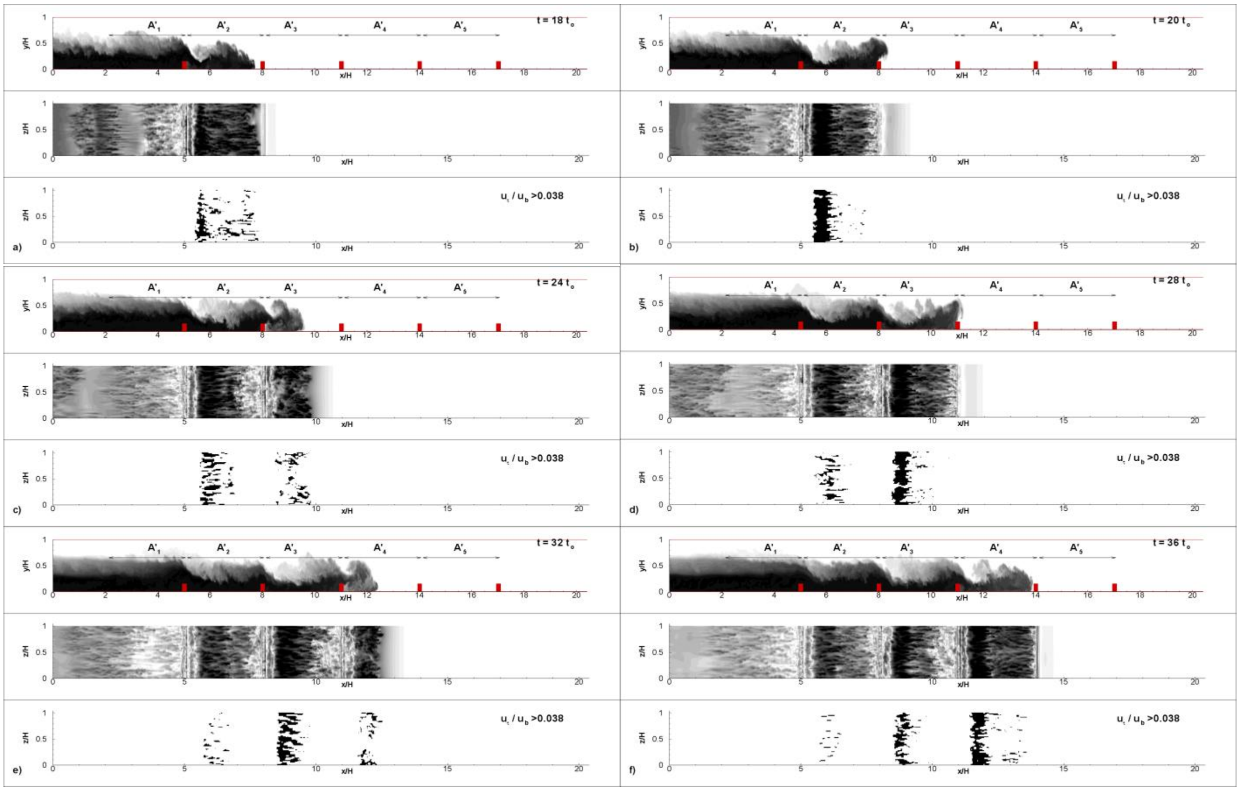

Figure 4.62 Spatial distributions of the bed friction velocity u_τ/u_b in the LR-R15 simulation at representative time instances. Also shown at each time instant are the concentration distributions in an x-y section and the regions where sediment is entrained ($u_\tau > u_{\tau c}$) assuming $u_{\tau c}/u_b$=0.038. The concentration plots also show the integration domain A" associated with each rib that is used to quantify the time variation of the amount of sediment entrained over a certain region of the bed. a) t/t_0=18; b) a) t/t_0=20; c) t/t_0=24; d) t/t_0=28; e) t/t_0=32; f) t/t_0=36. The aspect ratio is 1:2 in the x-y plots.

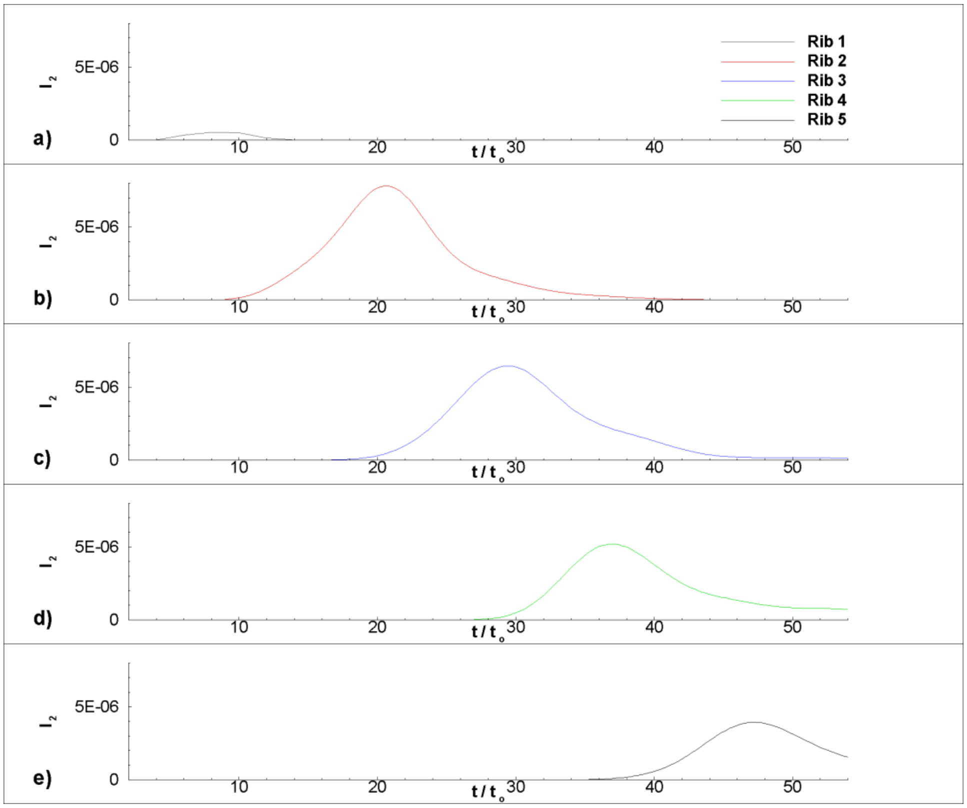

Figure 4.63 Time variation of I_2 calculated over the region associated with each of the ribs present in the LR-R15 simulation. I_2 characterizes the flux of sediment of a certain particle size entrained from the bed, assuming no sediment is entrained if $u_\tau < u_{\tau c}$.

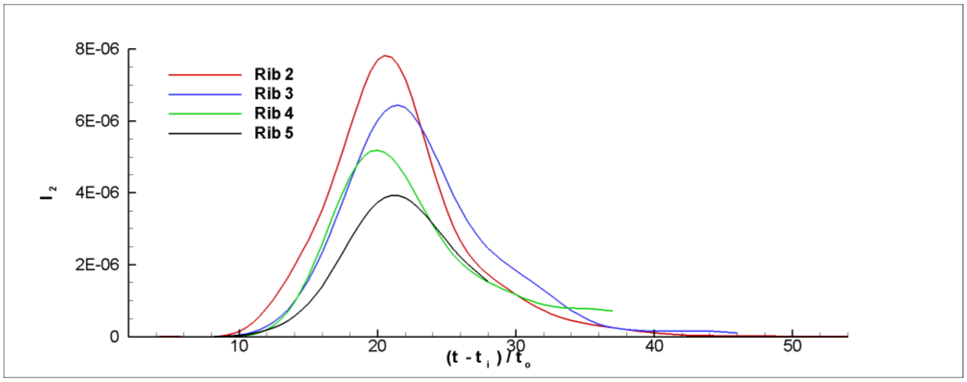

Figure 4.64 Time variation of I_2 calculated over the region associated with each of the ribs present in the LR-R15 simulation. The distributions of I_2 for Rib 3 to Rib 5 were translated along the time axis by a multiple of the time it takes the current to propagate from one rib to the next one (~9t_0) and superimposed on the distribution for Rib 2.

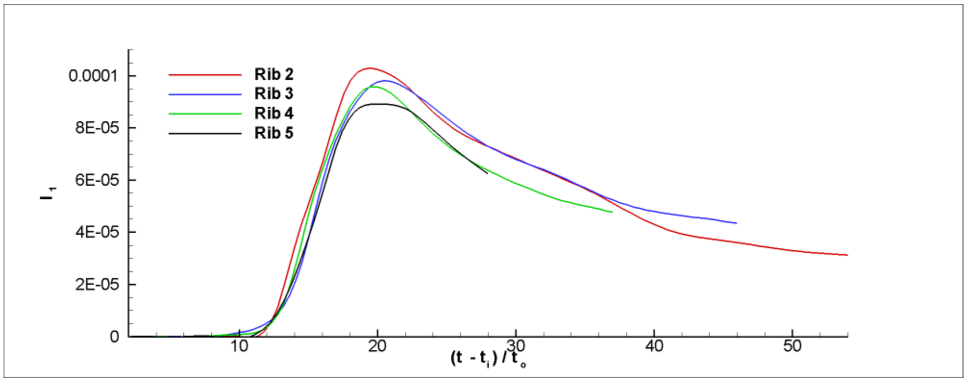

Figure 4.65 Time variation of I_1 calculated over the region associated with each of the ribs present in the LR-R15 simulation. I1 characterizes the flux of sediment of a certain particle size entrained from the bed, assuming sediment is entrained at all values of uτ. The distributions of I1 for Rib 3 to Rib 5 were translated along the time axis by a multiple of the time it takes the current to propagate from one rib to the next one (~9t0) and superimposed on the distribution for Rib 2.

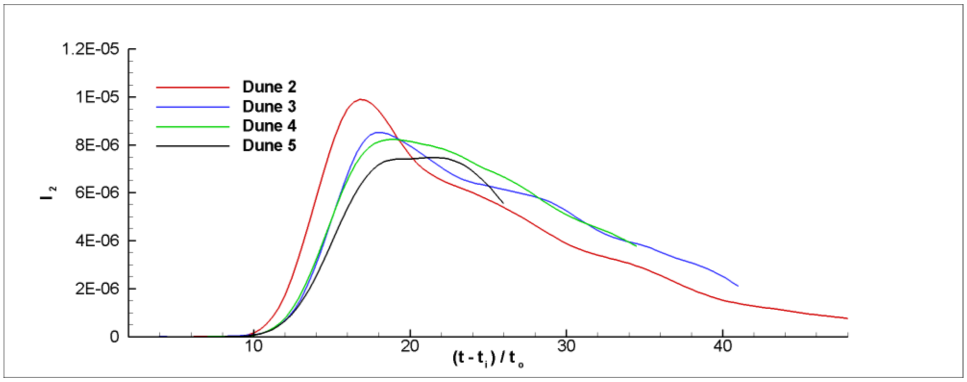

Figure 4.66 Time variation of I_2 calculated over the region associated with each of the dunes present in the LR-D15 simulation. The distributions of I_2 for Dune 3 to Dune 5 were translated along the time axis by a multiple of the time it takes the current to propagate from one rib to the next one (~$9t_0$) and superimposed on the distribution for Dune 2.

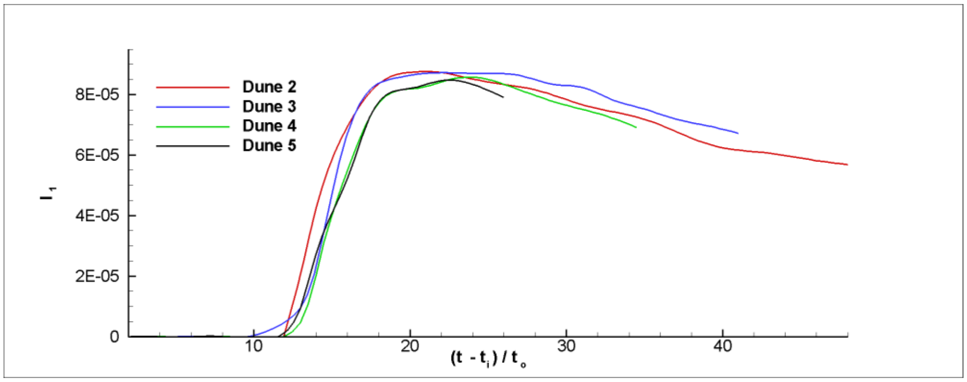

Figure 4.67 Time variation of I_1 calculated over the region associated with each of the dunes present in the LR-D15 simulation. The distributions of I_1 for Dune 3 to Dune 5 were translated along the time axis by a multiple of the time it takes the current to propagate from one rib to the next one and superimposed on the distribution for Dune 2.

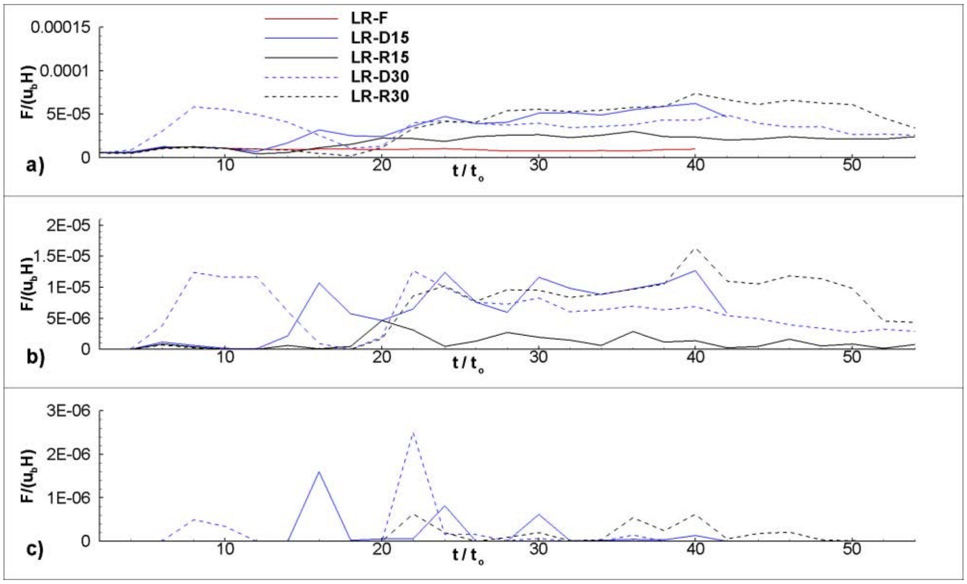

Figure 4.68 Time variation of the non-dimensional flux of the sediment particles of a certain diameter *d* entrained from the bed per unit time and unit width over the whole length (x/H>0) of the bottom propagating current in the low Reynolds number simulations with flat bed and with obstacles of height D=0.15H and D=0.3H. The flux F(t) is calculated based on van Rijn (1984) formula for the pick up rate. a) d=14 μm; a) d=30 μm a) d=50 μm.

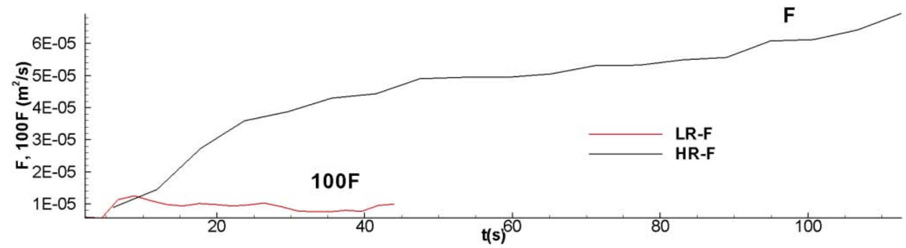

Figure 4.69 Time variation of the dimensional flux of the sediment particles of diameter *d*=14 μm entrained from the bed per unit time and unit width over the whole length (x/H>0) of the bottom propagating current in the low and high Reynolds number simulations with flat bed. The values for the LR-F simulation are multiplied by 100.

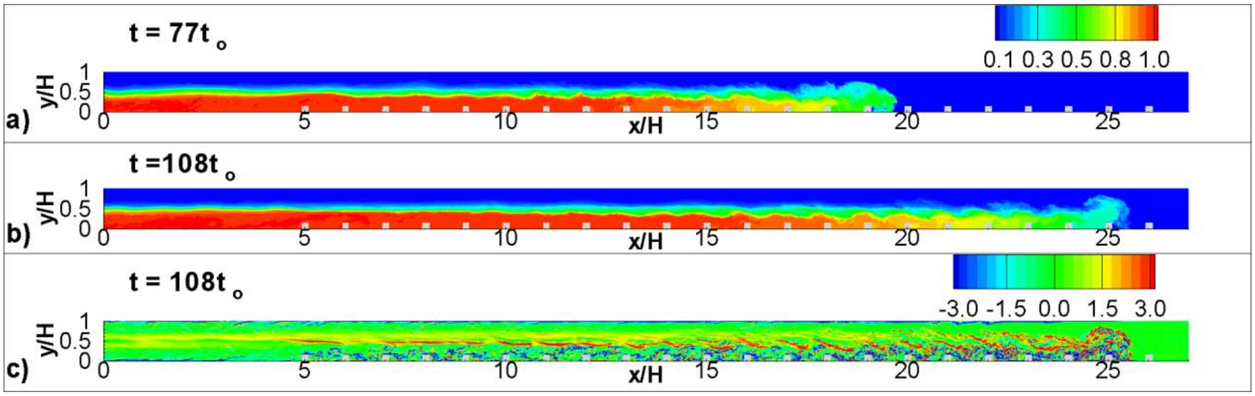

Figure 4.70 Visualization of the structure of the gravity current in case LR-R15-HD. a) concentration, C at $t=77t_0$; b) concentration, C at $t=108t_0$; c) out-of-plane vorticity, $\omega_z H/u_b$, $t=108t_0$.

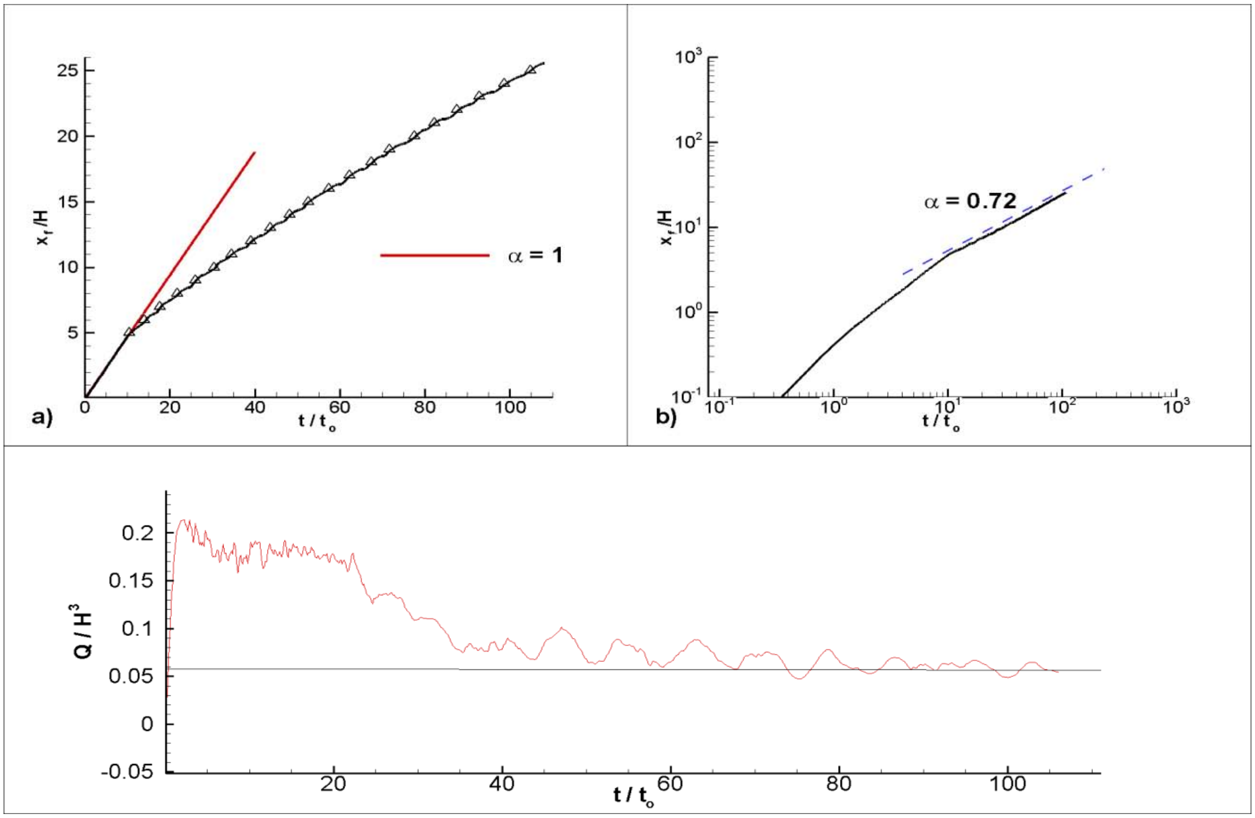

Figure 4.71 Time variation of the non-dimensional position of the front, x_f/H, function of the nondimensional time, t/t_0, in the LR-R15-HD simulation (solid black line). The symbols show the $x_f(t)$ variation based on the times the front reaches the upstream face of each rib. The red lines shows a best fit of the form t^{α}. a) linear-linear plot; b) log-log plot. Also shown in frame c is the time variation of the discharge at the section x/H=0 where the lock gate is located. The regime in which $\alpha=0.72$ is established at about the time the discharge at the section x/H=0 becomes close to constant.

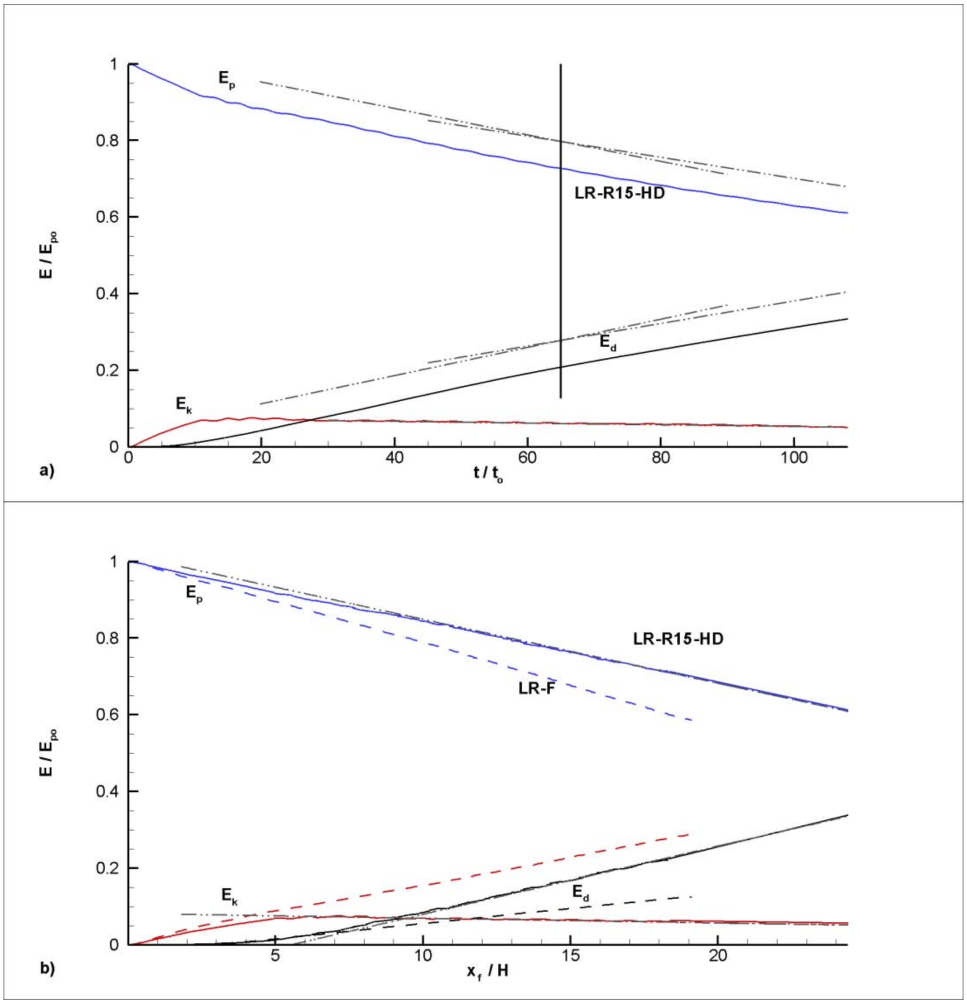

Figure 4.72 Variation of the potential energy, E_p, kinetic energy, E_k, and integral of the total dissipation, E_d, in the LR-F and LR-R15-HD simulations. a) plotted versus time in linear-linear scale; b) plotted versus the front position in linear-linear scale. All the terms are non-dimensionalized by the initial potential energy E_{p0}. The vertical line in frame a indicates the change in the slope of the linear variation for E_p and E_d in the LR-R15-HD simulation.

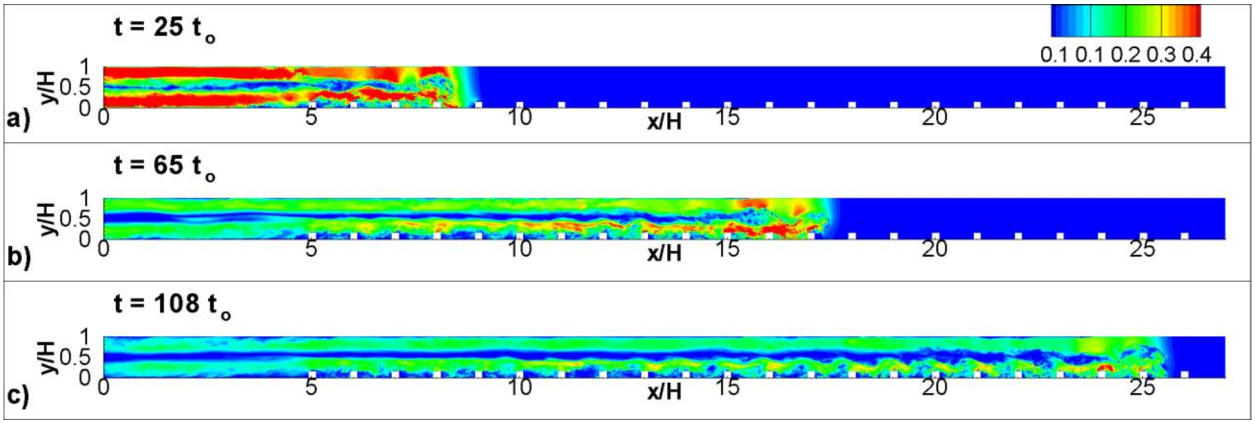

Figure 4.73 Distribution of the velocity magnitude, u_{mag}/u_b, at different stages of the propagation of the gravity current in case LR-R15-HD. a) $t=25t_0$; b) $t=65t_0$; c) $t=108t_0$.

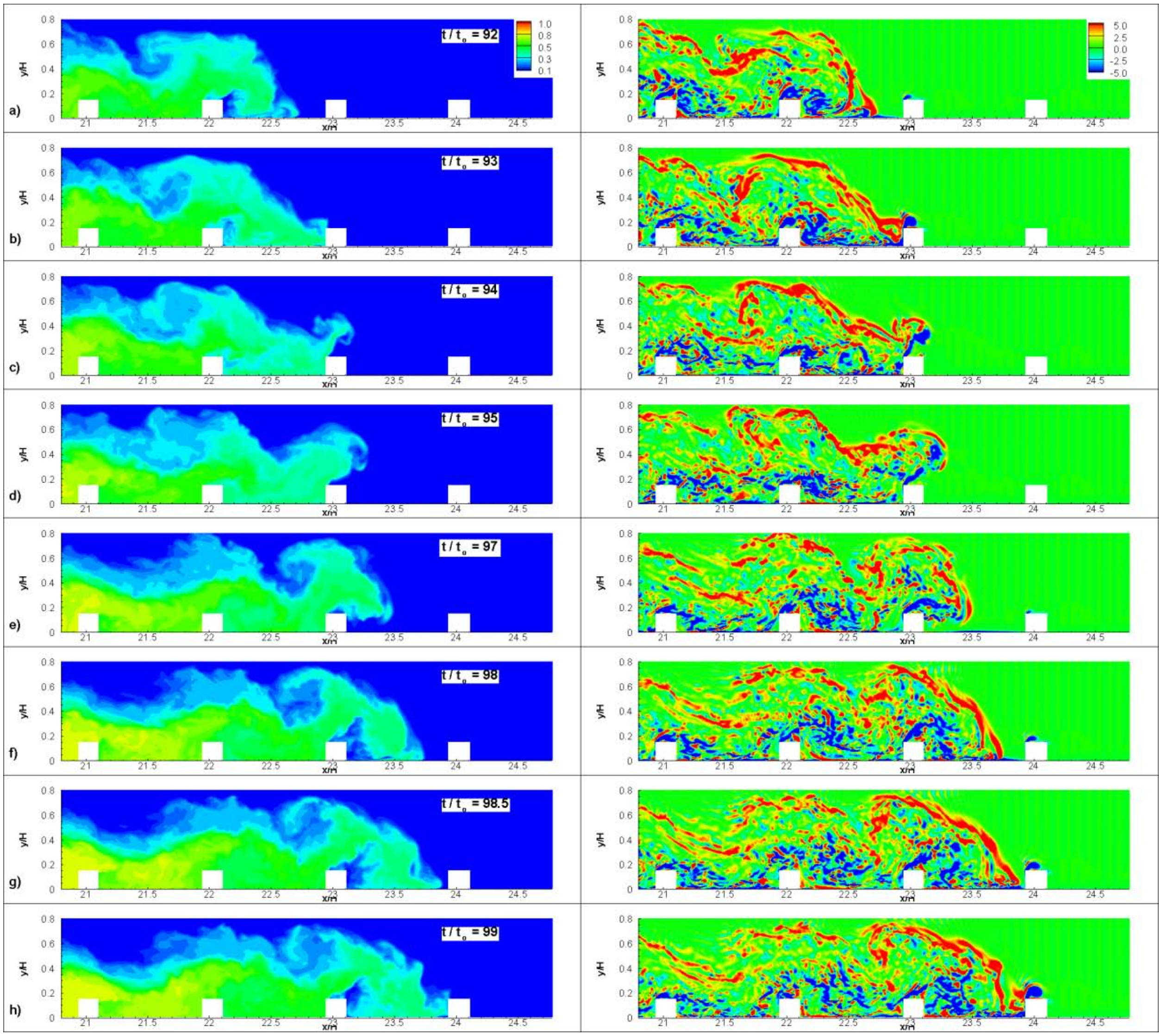

Figure 4.74 Contour plots showing the concentration, C, (left) and out-of-plane vorticity, $\omega_z H/u_b$, (right) distributions in a vertical x-y plane as the gravity current overtakes Rib 23 and Rib 24 in the LR-R15-HD simulation at representative time instants.

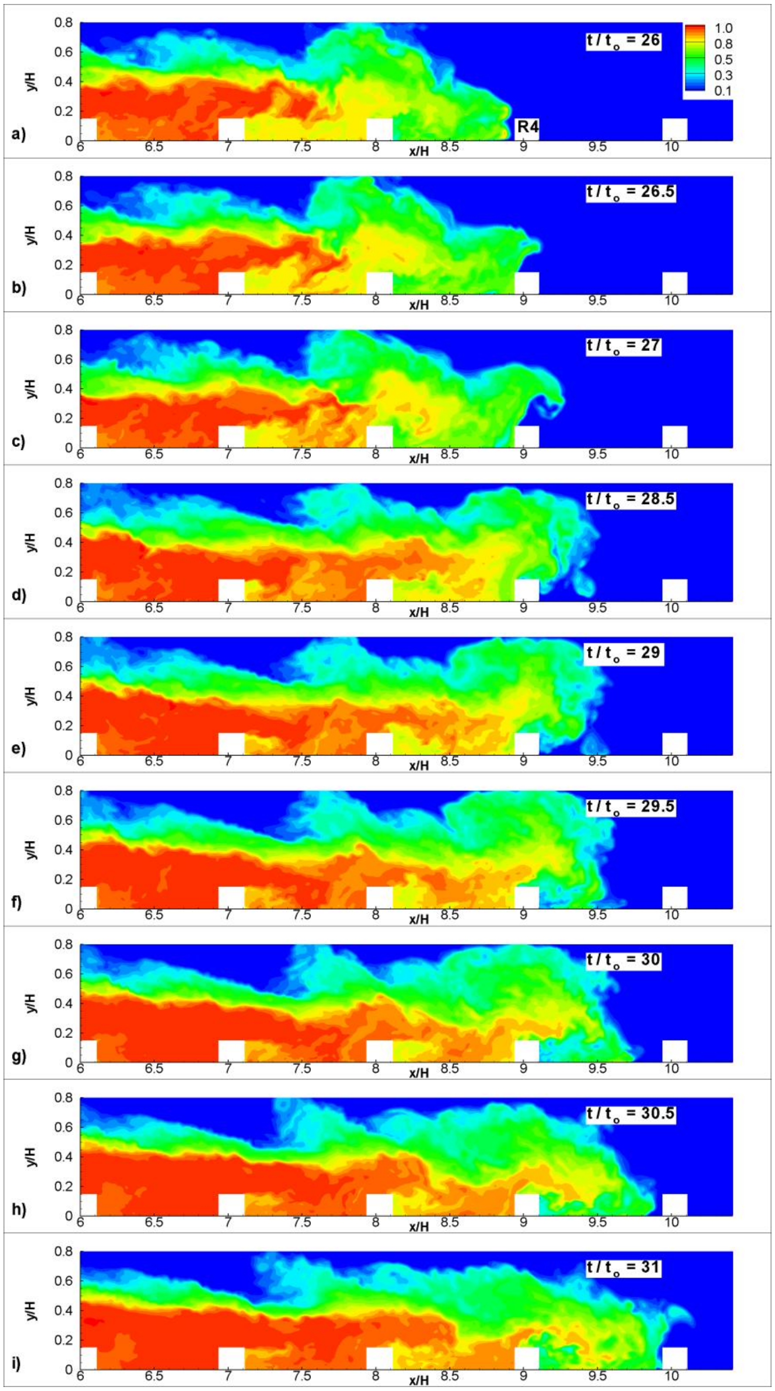

Figure 4.75 Contour plots showing the concentration, C, distributions in a vertical x-y plane as the gravity current overtakes Rib 5 and Rib 6 in the LR-R15-HD simulation at representative time instants.

CHAPTER 5 GRAVITY CURRENTS WITH VOLUME OF RELEASE (*R*=O(1)) PROPAGATING OVER AN ARRAY OF 2-D OBSTACLES

5.1 Description of Test Cases

In this chapter, the case of lock-exchange compositional currents with R=O(1) is considered (see Figure 5.1). The physical Reynolds number during the slumping phase is high enough (Re_f>10,000) such that the flow is strongly turbulent in the head region and the current transitions to the buoyancy-inertia self-similar phase in which the front velocity, U_f, decays proportional to $t^{-1/3}$, where t is the time measured after the removal of the lock gate. The initial volume of release is relatively small ($x_0/(H/2)$=0.56-0.8, H is the channel depth) such that the backward propagating current starts interacting with the rear end-wall a short time after the removal of the lock gate. Most of the simulations consider partial-depth release ($h=H/2$) lock exchange currents in which the top interface of the gravity current is situated well beneath the free surface. Only one full-depth release case ($h=H$) is considered. The focus is on the evolution of the heavier gravity current after the forward propagating disturbance (bore) forms, which signifies the start of the transition to the buoyancy-inertia regime.

As discussed in Chapter 1.3.3, in the case when an array of obstacles is present at the bed, the current is expected to transition from the buoyancy-inertia phase to the turbulent drag-controlled phase in which the flow is determined by the balance between the buoyancy and turbulent drag forces and U_f decays faster, proportional to $t^{-1/2}$. The time at which the current transitions to the drag dominated phase is expected to be earlier as the maximum relative height of the obstacles, D/h, is increased and their spacing (λ/h) is decreased. Both geometrical modifications result in a larger drag force per unit (streamwise) length acting on the bottom propagating gravity current.

At very large times, the gravity current is expected to transition to the viscous-buoyancy phase in which $U_f \sim t^{-4/5}$. In all the simulations discussed in this chapter, the length of the channel was not sufficient for the transition to the viscous-buoyancy regime to happen.

Some general characteristics of the lock exchange flows with a small volume of release and some of the main variables describing its evolution were discussed in Chapter 1.3.2. More details of the test cases and simulation set up are given below (see also Figure 5.1). The channel half depth, $H/2$, is used to scale the lengths. The buoyancy velocity $u_b = \sqrt{g'(H/2)}$ is used to scale the velocities. The time scale is $t_0=(H/2)/u_b$. The center of each rib is situated at the location of the crest of the corresponding dune. In most of the simulations the center/crest of the first obstacle was situated at $x/(H/2)=5$.

Consistent with the notation adopted in Chapter 4, the simulations conducted at Re=47,800 are denoted LR. The ones conducted at $Re=10^6$ are denoted HR. The presence of a flat bed, 2-D dunes or 2-D ribs is indicated by an F, D or R in the notation. Finally, the non-dimensional height of the dunes or ribs, $D/(H/2)*100$ is indicated by a number. For example SV-LR-D15 refers to the simulation of a gravity current with a small volume of release (SV) past an array of 2-D dunes of height 0.15(H/2) conducted at Re=47,800. The main parameters of the simulations discussed in this chapter are summarized in Table 5.1.

The main goal of the present chapter is to study the changes in the flow physics for gravity currents propagating over an array of 2-D large-scale obstacles (roughness elements) during the buoyancy-inertia and drag-controlled phases. In most of the simulations, the channel is long enough ($L_1/(H/2)=20.5$) to allow the study of the propagation of the current after the transition to the drag-controlled regime is completed. Most of the simulations are conducted at a Reynolds number defined with the buoyancy velocity and the channel half depth ($Re=u_b(H/2)/\nu$) of 47,800.

Two types of obstacles are considered. The 2-D dunes have a ratio between their height, D, and their wavelength, λ, of 0.05. Similar to the case of full-depth release currents (Chapter 4), the shape of the dunes is taken from the experiment of Mierlo and de Ruiter (1988).

The effect of the shape of the obstacles is studied based on the differences observed in simulations conducted with dunes and ribs of equal height (D=0.15(H/2)) and equal wavelength (λ=3(H/2), λ/D=20). The total number of obstacles in these simulations was equal to five. The ratio λ/D=20 corresponds to the *k*-type roughness regime, which is the relevant one for most practical applications in geosciences. The ribs have a high degree of bluntness, as the upslope face is perpendicular to the channel bed. The dunes have a much lower degree of bluntness, as the variation in the bed elevation between the lowest (trough) and the highest (crest) level of the dune surface is gradual and continuous. Thus, for the same height of the obstacles of different shapes, the drag force per unit length is higher in the case ribs are present at the channel bottom.

The effect of the size of the obstacles is analyzed based on comparison with the simulations conducted with dunes and ribs of height equal to 0.15(H/2) for which λ/D=20 (base case). Two additional simulations were performed. In the SV-LR-D05 simulation, dunes of height D=0.05(H/2) and wavelength λ=1.0(H/2) (λ/D=20) were present at the channel bottom. The number of dunes was equal to 17. As will be discussed later, in this simulation the size of the obstacles was not large enough to induce transition to the drag-controlled regime over the length of the computational domain (L_1/(H/2)=20.5). In the SV-LR-R10 simulation, densely spaced ribs of height D=0.1(H/2) and wavelength λ=1.0(H/2) (λ/D=10) were present at the channel bottom. The number of ribs was equal to 25 and the domain length was larger (L_1/(H/2)=32). This simulation allowed the study of a full-depth release (h=H) gravity current of relatively large height compared to the one of the ribs during the drag-dominated phase.

Scale effects are discussed based on comparison of simulations with flat bed, dunes and ribs conducted at Re=47,800 and Re=10^6. The simulations conducted with Re=10^6 allow to better understand the physics of lock-exchange gravity currents with a small volume of release for flow conditions that are closer to the inviscid state that is often assumed in theoretical models, and to conditions encountered in practical applications.

In most of the simulations, the grid size was 3000×64×188 in the streamwise (domain length L_1=21.5*(H/2)*), spanwise (domain width L_3=*(H/2)*), and vertical (domain height L_2=*H*) directions, respectively. Away from the walls, the grid spacing in the three directions was 0.01*(H/2)*-0.02*(H/2)*. To resolve the viscous sub-layer in the simulations conducted with Re=47,800, the grid spacing in the vertical direction was reduced to 0.002*(H/2)* near the walls of the computational domain. The maximum physical Reynolds number defined with the front velocity during the slumping phase and the current height was close to 11,000. A grid spacing of 0.002*(H/2)* in the wall normal direction corresponds to about one wall unit. This is sufficient to resolve the viscous sub-layer if the flow behind the front is assumed to be fully developed and, thus, to avoid the use of wall functions. In the simulations conducted at $Re=10^6$, the grid spacing in the wall normal direction was further reduced to insure the first point off the wall was situated within the viscous sub-layer.

The simulations are conducted with no-slip boundary conditions at the bottom surface. To mimic the presence of a free surface at the top boundary in real applications, the top surface of the channel was treated as a non-deformable slip boundary (zero shear stress in the horizontal directions and zero vertical velocity) rather than as a no-slip wall, as was done in the simulations with $R<<1$ (Chapter 4). This is justified if the Froude number $U_f/\sqrt{g(H/2)}$ is much smaller than 0.5, which indicates negligible free-surface deformations. A convective outflow boundary condition was used at the right extremity of the computational domain. The value of the convective velocity U_c was equal to the estimated front velocity of the current when reaching the right end boundary. The Schmidt number was $Sc=600$. The flow field was initialized with fluid at rest. The flow was assumed to be periodic in the spanwise direction.

A zero normal gradient was imposed for the concentration at the top, bottom and end-wall boundaries. The non-dimensional concentration field was initialized with a constant value of one in the region containing the lock fluid and a constant value of zero in the rest of the computational domain. The time step was $0.001t_0$. For most simulations, the total simulation time was around $70t_0$. The total simulation time in the SV-HR-R10 simulation was $113t_0$.

5.2 Structure of the gravity current with a small volume of release

Figures 5.2 and 5.3 show the distributions of the non-dimensional concentration C, velocity magnitude u_{mag}/u_b, streamwise velocity u/u_b and out-of-plane vorticity $\omega_z(H/2)/u_b$ for the low Reynolds number simulation with a flat bed (SV-LR-F) and with dunes of height $D=0.15(H/2)=0.15h$ (SV-LR-D15) when $x_f/(H/2)\sim18$, well after the end of the slumping phase (Table 5.1). Compared to the case of a large volume of release (e.g., Figure 4.10 shows the distributions of these variables in the LR-F and LR-D15 simulations when $x_f/H\sim19$), the distributions of these variables along the gravity current with a small volume of release are quite different.

The shapes of the head region in the SV-LR-F and LR-F simulations are similar. Similar to case LR-F, a strong shear layer forms at the interface between the head and the ambient fluid (Figure 5.2d). The vorticity remains high over the head and dissipative wake, not only over the interfacial region but also within the body of the current. However, the concentration levels behind the front are much smaller in the SV-LR-F simulation once the transition to the buoyancy-inertia phase starts ($x_f/(H/2)\sim6$). The height of the region of high concentration fluid decays sharply over the dissipative wake region. Similar to case LR-F, the billows shed behind the head mix the high concentration fluid ejected from the head with the surrounding ambient fluid. This results into the presence of a region of mixed fluid, of concentration slightly higher than zero, for some distance behind the head. Over the dissipative wake ($15<x/(H/2)<17$), the thickness of the region containing mixed fluid is larger than the one observed in the LR-F simulation. This is because in the SV-LR-F simulation the billows maintain their coherence for longer times. The distribution of the patches of larger concentration in this region correlates well with the position of these interfacial billows.

Compared to case LR-F, the thickness of the tail region and the concentration levels averaged over the height of the tail are much smaller at all streamwise positions. This is a consequence of the small volume of lock fluid released in the SV-LR-F simulation. By contrast, in the LR-F simulation, the flux of incoming lock fluid at the lock gate position was close to constant in the later stages of the propagation of the current. The smaller volume of release means that a smaller amount of initial potential energy is available to transport the lock fluid at large distances from the lock gate.

Over the downstream part of the tail region ($10<x/(H/2)<15$), the velocity decrease with the distance from the front is close to monotonic (see Figures 5.2b and 5.2c). As one moves away from the dissipative wake region, the coherence of the billows reduces gradually and a layer of mixed fluid develops (Figure 5.2a). The thickness of this layer decreases, in average, with the distance from the front. As also shown by the vorticity distribution in Figure 5.2d, the decay in the coherence of the interfacial billows is accompanied by an overall decay of the strength of the turbulent eddies within the body of the current and the interfacial region. This decay is mainly due to the strong deceleration of the flow and increase in the importance of viscous effects. The decay of the coherence of the large-scale eddies happens because the physical Reynolds number at those streamwise locations decays below values at which turbulence can be sustained over large periods of time.

In the SV-LR-F simulation, the streamwise velocity is close to zero over the upstream part of the tail region, $x/(H/2)<10$ (Figure 5.2c). No shear layer depleted of large-scale eddies forms at the interface between the tail and the surrounding ambient fluid (Figure 5.2d). The flow velocities are very small (Figures 5.2b and 5.2c) and the flow tries to relaminarize. In the vertical direction, the transition in the concentration levels between the higher density fluid inside the tail and the low density ambient fluid above it is much sharper compared to that observed over the downstream part of the tail region (Figure 5.2a).

The presence of large-scale roughness elements at the bed induces important quantitative changes in the structure of the gravity current with a small volume of release compared to the flat bed case. However, at a qualitative level, the structure of the gravity current, at large times after the lock-fluid was released, is not very different. Most of the kinetic energy is concentrated in the head and dissipative wake regions. Of course, the presence of the obstacles induces modulations in the overall decay of the kinetic energy with the front position depending on the position of the front relative to the obstacle. For example, in the case of dunes (Figures 5.3b and 5.3c) the flow in the head accelerates as it propagates over the lee side of the dune. However, the shape and structure of the flow in the head region remains similar at equivalent stages of the propagation of the gravity current. This is particularly true during the time the front is propagating over the upslope side of the dune or over the horizontal part of the bed in between two ribs.

Similar to the case of a gravity current with a large volume of release (e.g., see case LR-D15 in Figure 4.10), a region of high velocity magnitude is present past the crest of the first dune behind the front. However, the amplification of the velocity past the crest of the dunes situated at large distances from the front is negligible. This is in contrast to case LR-D15 where the flow structure and velocity amplification past each of the dunes overtaken by the current was similar, both qualitatively and even quantitatively. The additional drag induced by the presence of the dunes reduces the velocity over the whole length of the current. This is why, when cases SV-LR-F and SV-LR-D15 are compared at times when the front is situated at the same streamwise location, the length of the downstream part of the tail over which the velocity magnitude is not negligible is smaller (e.g., by about 20% at $x_f/(H/2)=18$ according to Figures 5.2b and 5.3b).

With respect to the flat bed case, SV-LR-F, the largest difference is observed in the distribution of the concentration within the tail region. For example, in the case dunes are present at the channel bottom (Figure 5.3a), the top interface of the tail is situated at a higher level compared to the one predicted in the SV-LR-F simulation. This is mainly a consequence of the fact that high-density low-velocity fluid from the tail is trapped in between the crests of two consecutive dunes. At large distances behind the front, most of the higher-density fluid does not have enough momentum to go over the crest of the downstream dune. Over this region, only the passage of flow disturbances (see discussion of Figure 5.33) can convect, from time to time, a small quantity of the higher density fluid situated in the region between two consecutive obstacles to an adjacent one. Observe also the fact that even in the region corresponding to the first two dunes behind the front, the layer of high velocity magnitude fluid does not penetrate until close to the dune surface (Figure 5.3b). Rather, it is situated above the regions of higher-density fluid occupying the trough region between the crests of two consecutive dunes.

The early trapping of higher-density fluid in between the crests of two consecutive dunes is another reason the gravity current with a small volume of release slows down faster than the one propagating over a flat bed. As for the case of a gravity current with a high volume of release, the additional mixing occurring as the gravity current plunges downwards, as it passes the crest of each dune, decreases the mean density inside the head of the current compared to the flat bed case (e.g., compare concentration distributions in Figures 5.2a and 5.3a).

Finally, a relatively horizontal interfacial mixing layer starts forming behind the head and dissipative wake in the SV-LR-D15 simulation. It is observable in Figure 5.3d, past the second dune and over the downstream part of the third dune behind the front. However, at larger distances behind the front the decay of the kinetic energy and turbulence is fast enough, such that this interfacial shear layer disappears gradually. The flow structure between the front region and the second dune behind the front is similar to the one observed in the LR-D15 simulation. The jet like flow is present (e.g., see Figure 5.3d) and the temporal dynamics of the shear layer on the outer side of the jet-like flow is similar. However, compared to case LR-D15, the relative acceleration of the flow on the lee side of the dunes decays much faster with the rank of the dune relative to the front of the current.

Figures 5.4 to 5.7 show the distributions of the non-dimensional concentration C, velocity magnitude u_{mag}/u_b, streamwise velocity u/u_b and out-of-plane vorticity $\omega_z(H/2)/u_b$ for the low Reynolds number simulation with ribs of height D=0.15(H/2)=0.15h (SV-LR-R15) at $t = 22t_0$, which corresponds to a time instant in buoyancy-inertia phase, at $t = 34t_0$, which corresponds to a time instant when the flow transitions from buoyancy-inertia phase to turbulent drag-dominated phase, and at $t = 50t_0$ and $87t_0$, both of which corresponds to the turbulent drag-dominated phase in the simulation.

Figure 5.4 shows that as the current propagates in time some of the lock-fluid gets trapped between the consecutive ribs. The amount of higher-density fluid trapped in between two consecutive ribs decays with the rank of the ribs. The highest amount of trapping occurs in between the rear end-wall of the domain and the first rib. The trapped fluid is subject to successive reflections as it encounters the upstream and the downstream ribs. The first couple of these reflections can result in some of the higher density fluid being convected over the upstream or the downstream rib. In Figure 5.4a, disturbance, S1, is observed to propagate towards first rib while another disturbance S2, travels towards the rear end-wall of the domain. Similarly, due to the impact of the current to the second rib a backward propagating disturbance, S3 is formed between first and second rib. In Figure 5.4c, this time the disturbance S2, which got reflected from end-wall, is observed to travel towards first rib and disturbance S3 travelling between Rib1 and Rib2 has already reached and reflected back from first rib and travels towards second one. At the same instance disturbance S3 meets backward travelling disturbance, S1. Disturbance S1 has originated due to the collapse of a large billow at a very early stage of the simulation near the end-wall, started propagating toward Rib1, reached and passed over Rib1 and carried some higher-density fluid from the region between rear end-wall and first rib to the region between first and second rib. As the current propagates further in the domain with each current-rib interaction a new backward propagating disturbance forms such as S4 formed between second and third rib and S5 formed between third and fourth rib.

The presence of roughness elements enhances the mixing. However, compared to the SV-LR-D15 simulation, in the SV-LR-R15 simulation the mixing in the head and dissipative wake is larger and the mean concentration levels are lower due to the more blunt shape of ribs.

Similar to the simulation SV-LR-D15, the jet-like flow is clearly observed only over the first one to two ribs behind the front (see Figures 5.5 and 5.6). After the end of the slumping phase, most of the kinetic energy of the current is contained within the head and dissipative wake regions. The shape of the head of the current maintained its compactness similar to the one observed in simulation SV-LR-F however the values of the concentration are much lower. Out-of-plane vorticity values decay over the time and eddies in the dissipative wake region behind the head of the current lose their coherence as the current slows down.

The streamwise distributions of the Froude number in the SV-LR-D15 and SV-LR-R15 simulations are shown in Figures 5.8 and 5.9, respectively. The height, $\bar{h}$, and the streamwise velocity, $\bar{u}$, used to calculate the Froude number ($\bar{u}/\sqrt{g\bar{h}}$) at a certain streamwise location are estimated as $\bar{h} = \int_0^H Cdy$ and $\bar{u} = \int_0^H uCdy / \int_0^H Cdy$.

In the case of dunes, the flow goes supercritical (maximum Froude number is Fr=1.5-2) in the jet-like flow forming over the lee side of the first and second dunes, when the current overtakes the second obstacle in the series as shown in Figure 5.8a. The fact that Fr>1 over the crest of Dune1 are due to the very small depth of the layer of higher density fluid over the crest of the first dune. Figure 5.8b shows that in later stages of the simulation similar phenomenon is observed for higher rank of dunes. As the flow passes the fifth dune in the domain the Froude number increases at the crest of both Dune4 and Dune5. Another increase in the Froude number is observed around the crest and upslope of Dune3 due to the passage of a backward propagating disturbance. The passage of the disturbance propagating upstream, which carries small amount of heavier fluid, causes an increase in the depth and the velocity of the current over that region. Increase in velocity is more effective than the increase in height of the current at passage of these disturbances, therefore a relative increase in the Froude number in that region is observed.

Though the flow is clearly supercritical downstream of the crest of Dune5 in Figure 5.8b, the maximum value of the Froude number is smaller than that recorded as the front passed Dune2 in Figure 5.8a. Over the head of the current Froude number is close to unity at all stages of the flow (e.g., during the drag-dominated phase in Figure 5.8b).

The structure of the current in the SV-LR-R15 simulation is, in many regards, similar. The Froude numbers in the head region (see Figure 5.9) are very close to unity during the buoyancy inertia and the drag dominated phases. The Froude number becomes close to zero at a small distance behind the dissipative wake (7.5(H/2) in Figure 5.9a and 16(H/2) in Figure 5.9b), such that the length of the compact region of higher-density fluid propagating downstream is less than one wavelength. Also, the flow past the second rib behind the front is supercritical or gets close to critical over a very short distance. Similar to the simulation with dunes, this is mostly due to the very small depth of the relatively high-speed higher-density fluid convected over the top of the rib by flow disturbances propagating downstream. These disturbances can entrain some of the higher density fluid already trapped in the cavity region between two consecutive ribs.

Figure 5.12 compares the streamwise distributions of the depth averaged concentration $\overline{C} = 1/(H/2)\int_0^H C dy$ in the low Reynolds number simulations with a flat bed, dunes and ribs (D=0.15(H/2)) at different stages of the evolution of the current ($x_f/(H/2)$~5, 10, 15). The same definition applies to the non-dimensional height of the current at a streamwise location ($\overline{h}/(H/2) = 1/(H/2)\int_0^H C dy$). As expected, the distributions shown in Figure 5.12a are similar until the front reaches the location of the first obstacle in the series ($x_f/(H/2)$~5).

When the front is situated in between the second and the third obstacle (Figure 5.12b), the main difference in the values of $\overline{C}$ among the three simulations is due to the fact that in the simulations with obstacles higher concentration fluid gets trapped in between the left end-wall and the first obstacle. Consequently, at most locations between x=0 and x=5(H/2), $\overline{C}$ is smaller in the SV-LR-F simulation compared to the simulations with obstacles. As the total volume of lock fluid is the same in all the three simulations, the opposite is true in the region with x>5(H/2). The differences are the largest at the head of the current. This is also partly because, as already discussed, the mixing in the head is larger in the simulations with obstacles at the channel bottom. The relatively large decay of $\overline{C}$ around the positions of the ribs and of the crests of the dunes, is due to the fact that the high concentration fluid situated very close to the channel bottom in between two consecutive ribs or in the through region between the crests of two consecutive dunes is trapped and only the gravity current fluid situated above a certain vertical level will be convected over the rib or the crest of the dune.

These qualitative differences are also observed in the later stages of the evolution of the current, when the front is situated at $x_f/(H/2)$~15 (Figure 5.12c) and at $x_f/(H/2)$~18 (Figure

5.12d). The values of $\overline{C}$ are larger over the downstream part of the tail in the SV-LR-F simulation compared to the simulations in which obstacles are present. The trend becomes reversed in the downstream part of the tail and the head. As the flow in the tail of the current loses its kinetic energy, the distribution of $\overline{C}$ in the SV-LR-F simulation becomes close to uniform (e.g., see Figure 5.12d for x/(H/2)<15).

In all the three simulations, $\overline{C}$ decreases over the head and dissipative wake as the front advances. When $x_f/(H/2)\sim5$ (Figure 5.12a), the maximum values of $\overline{C}$ are around 0.32 and are recorded inside the head region. When $x_f/(H/2)\sim10$ (Figure 5.12b), the decrease in the peak value is the largest for the case ribs are present at the channel bottom (e.g., the maximum values of $\overline{C}$ in the SV-LR-F, SV-LR-D15 and SV-LR-R15 are 0.14, 0.14 and 0.1, respectively). This is because the mixing in the head region is the largest in the SV-LR-R15 simulation. The mixing in the head region is larger in the SV-LR-D15 simulation compared to the flat bed case. However, a substantial amount of mixed fluid is present inside the billows shed in the dissipative wake. This explains why the maximum values of $\overline{C}$ in the SV-LR-F and SV-LR-D15 simulations are very close.

When $x_f/(H/2)\sim15$ (Figure 5.12c), the maximum values of $\overline{C}$ are 0.08 in the SV-LR-F simulation and about 0.06 in the SV-LR-D15 and SV-LR-R15 simulations. Again, the largest values observed in the SV-LR-F simulation are mainly due to the lower amount of mixing behind the front in the case obstacles are not present at the channel bottom. Though when $x_f/(H/2)\sim15$ the average values of the concentration in the head region are smaller in the SV-LR-R15 simulation compared to the SV-LR-D15 simulation, the values of $\overline{C}$ are close to identical because the area occupied by the higher concentration fluid just convected over the top of the rib, that corresponds to the head of the current, is larger in the SV-LR-R15 simulation (e.g., compare the concentration distributions for the two simulations in Figure 5.10a at an equivalent position of the front relative to the rib, $x_f/(H/2)\sim18$). The trends remain similar in Figure 5.10d. The only change is the fact that the difference between the values of $\overline{C}$ in head of the current the SV-LR-F simulation and in the simulations with ribs and dunes grows significantly (0.05 compared to 0.025).

Comparison of the concentration distributions in Figure 5.11a and out-of-plane vorticity distributions in Figure 5.11b for the low and high Reynolds number simulations with flat bed, dunes and ribs allows understanding the role of scale effects for gravity currents with a small volume of release. In all the simulations the vorticity and concentration distributions are compared when the front position is close to 18(H/2). More quantitative information on scale effects on the streamwise variation of $\overline{C}$ at different stages of the propagation of the current are given in Figure 5.12.

Past the start of the buoyancy-inertia phase, the vertical extent of the gravity current in the head and dissipative wake is slightly larger in the SV-LR-F simulation compared to the SV-HR-F simulation. However, the values of $\overline{C}$, especially at the head of the current, are smaller in the SV-LR-F simulation. This happens because the mixing in the head region is stronger in the SV-LR-F simulation. By compassion (Figure 5.11a), the size of the head is smaller and the concentration levels higher and more uniform in the SV-HR-F simulation. The differences in the values of $\overline{C}$ and in the streamwise extent of the region where these differences are non-negligible increase during the later stages of the buoyancy-inertia phase (e.g., compare Figures 5.12a and 5.12b). In the high Reynolds number simulation, the vorticity is more uniformly distributed over the whole height of the current, the size of the turbulent eddies is smaller and their degree of three-dimensionality is larger (see Figure 5.11b). This is true especially over the head region and explains the more uniform distribution of the concentration over the height of the current in the head of the current.

Figures 5.12c and 5.12d shows scale effects on the streamwise distribution of $\overline{C}$ over the whole length of the current are negligible at all stages of the evolution of the current in the simulations with dunes of height D=0.15(H/2). However, the concentration distribution within the head of the current is somewhat different. Similar to the flat bed case, the size of the head is larger and the decay of the concentration with the distance from the bed is sharper in the low

Reynolds number simulation (see Figure 5.11a). These two trends explain why no significant differences in the levels of $\overline{C}$ are observed in the head region. In the case of ribs, scale effects on the streamwise distribution of $\overline{C}$ are negligible until the later stages of the evolution of the current during the buoyancy-inertia phase (e.g., see Figure 5.12e). However, for $x_f/(H/2)>16$, the values of $\overline{C}$ over the head region become larger in the high Reynolds number simulation (e.g., by about 35% when $x_f/(H/2)=18$). The 2D distributions of C in Figure 5.11a show the size of the head is similar in the simulations with ribs, but the values of C within the head of the current are larger in the SV-LR-R15 simulation.

Simulations SV-LR-R15 and SV-LR-R10 allow comparing the evolution of gravity currents with a small volume of release for which the height of the obstacle is comparable to the head height and, respectively, significantly lower than the height of the head. One should point out that even if the height of the ribs is only 30% smaller in the SV-LR-R10 simulation, the height of the head of the current is much larger than the one of the current forming in the SV-LR-R15 simulation. This is because simulation SV-LR-R10 considers the case of a full-depth-release current in which the volume of release is 2.85 times larger than the one in the SV-LR-R15 simulation. As a result, the ribs in the SV-LR-R10 simulation interact only with the lower layer of the downstream part of the gravity current. Interestingly, the front speeds of the gravity current in the two simulations remain close during all the stages of the propagation of the current.

Due to the much smaller ratio between the height of the head and the height of the rib, the changes in the head structure associated with the formation of the initial splash of higher density fluid, its convection over the top of the rib and the plunging of the higher density fluid toward the channel bottom, downstream of the rib, are not very large in the SV-LR-R10 simulation. This is because the higher density fluid pushed upward, as the lower part of the front starts interacting with the upstream face of the rib, is convected into a region that already contains relatively high density fluid from the upper part of the head region.

In Figures 5.13, 5.14, 5.15 and 5.16, the distribution of concentration, C, u_{mag}/u_b, streamwise velocity u/u_b and out-of-plane vorticity $\omega_z(H/2)/u_b$ in SV-LR-R10 simulation is shown at $t=22t_0$, $34t_0$,$50t_0$, and $87t_0$.

In contrast to the ones observed in SV-LR-R15 simulation the initial splash of the high-density fluid is smaller in SV-LR-R10 simulation. In Figure 5.4, it is observed that the initial splash of the high-density fluid when current impacts the rib, reaches almost three times the height of the obstacle from the channel bottom in earlier stages of the simulation and it reaches to a height of 1.5-2 times the obstacle height from the channel bottom in the later stages. Figure 5.13 shows that most of the current-obstacle interaction takes place near the lower layer of the gravity current in simulation SV-LR-R10. As opposed to the ones observed in SV-LR-R15 simulation, a clear splashing of high-density fluid which consists of initial splash of higher density fluid, its convection over the top of the rib and the plunging of the higher density fluid toward the channel bottom, downstream of the rib, is almost non-existent in SV-LR-R10 simulation. The presence of ribs situated with smaller wavelength over the channel bottom does not allow current to clearly interact with each rib but rather causes the high-density high-velocity top layer of the current to glide over them especially in the earlier stages of the simulation. Similar to the SV-LR-R15 simulation, the high-density fluid gets trapped in between the ribs as the current propagates further in SV-LR-R10. The time evolution of the concentration distribution in the SV-LR-R10 simulation (Figure 5.13) shows that the height of the tail of the current remains larger than that of the ribs even in the later stages of the propagation of the current. Most of the high density fluid gets trapped before $x/(H/2) = 20$. In the later stages of the evolution as the current transition to the turbulent-drag dominated phase ($x_f/(H/2)>19$), the height of the head decreases noticeably such that, when $x_f/(H/2)\sim26$ (Figure 5.13e), the height of the head is only slightly larger than that of the tail of the current. The distribution of the concentration inside the head of the current is close to uniform for $x_f/(H/2)>19$. Furthermore, in Figures 5.13d and 5.13e, the dissipative wake region is not visible compared to the earlier stages of the simulation where vortex-shedding wake region could clearly be observed behind the head of the current.

As expected the streamwise velocity and velocity magnitude inside the current and at the head of the current decreases in time (Figures 5.14 and Figure 5.15). The high velocity region within the head, dissipative wake and, especially, within the downstream part of the tail does not penetrate up to the channel bottom (e.g., see Figures 5.14d and 5.14e), as was the case in the SV-LR-R15 simulation (e.g., see Figures 5.5c and 5.5d) where a strong jet-like flow formed in the vicinity of the bed, downstream of each rib overtaken by the current. In simulation SV-LR-R10, there is no formation of jet-like flow region on the lee side of the ribs behind the head of the current. This is due to the fact that the wavelength between ribs and the height of the ribs are so small that the high-density high-velocity top layer of the current remains horizontal, i.e., does not get affected by the presence of the ribs and changes its direction but rather has a strong streamwise velocity component at all times of the simulation and rather passes over the ribs without getting affected by the presence of them. Only a small part of the lower layer of the current circulates and fills the space in between ribs with high-density fluid.

The decay of the velocity in the upstream part of the tail is more rapid in the SV-LR-R10 simulation in the later stages of the turbulent drag-dominated regime. The intensity of the vortices also diminishes faster as the current propagates further in the domain (Figure 5.16).

The temporal evolution of the streamwise distribution of $\overline{C}$ in the SV-LR-R10 simulation (Figure 5.17) resembles more the one observed in the flat bed simulation (SV-LR-F) rather than the one in the SV-LR-R15 simulation (see Figure 5.12). As in the flat bed case, most of the high concentration fluid is situated within the head and dissipative wake regions until the start of the buoyancy-inertia phase ($x_f/(H/2)\sim7$). The values of $\overline{C}$ in the tail start increasing during the buoyancy inertia phase (e.g., see Figure 5.17b), but remain much smaller than the ones recorded over the head and dissipative wake regions. During the initial stages of the turbulent drag-dominated regime (e.g., see distribution for $x_f/(H/2)\sim7$ in Fig 5.17c), the distribution of $\overline{C}$ over the tail region, starting at the rear end-wall, becomes close to uniform ($\overline{C}\sim0.1$). The average levels of $\overline{C}$ in the tail remain lower than those in the head. For example, the values of $\overline{C}$ are around 0.2 in the head of the current, when $x_f/(H/2)$~7. The distribution is qualitatively very similar to those observed in the later stages of the buoyancy-inertia phase in the SV-LR-F simulation (e.g., see Figures 5.12b and 5.12c). In the later stages of the turbulent drag-dominated phase (e.g., see distribution for $x_f/(H/2)$~23.5 in Fig 5.17d), the levels $\overline{C}$ in the upstream part of the tail (e.g., $x_f/(H/2)<10$ in Figure 5.17d) remain close to constant (the average value of $\overline{C}$ decays only from 0.1 to about 0.09 in the region with $x_f/(H/2)<10$), suggesting that the kinetic energy of the flow is small in that region. This is confirmed by the velocity distributions in Figures 5.14d and 5.15d. Meanwhile, compared to Figure 5.17c, there is a mild decay of $\overline{C}$ within the downstream part of the tail ($10< x_f/(H/2)<10$ in Figure 5.17d) and a much more significant decay of $\overline{C}$ within the head and dissipative wake, such that the values of $\overline{C}$ over these three regions become comparable ($\overline{C}$ ~0.065) and smaller than the ones observed over the upstream part of the tail region where $\overline{C}$ ~0.09.

The distributions of the velocity magnitude and streamwise velocity in Figures 5.14 and 5.15, respectively, show two interesting qualitative differences with the corresponding distributions (see Figures 5.5 and 5.6) in the SV-LR-R15 simulation.

The first one is that the decay of the velocity in the upstream part of the tail is more rapid in the SV-LR-R10 simulation in the later stages of the turbulent drag-dominated regime. This is also confirmed by examination of the streamwise variation of the Froude number in Figure 5.18b ($x_f/(H/2)$~24) that shows that Fr is close to zero over the whole upstream part of the tail region ($x/(H/2)<12$). Also interesting, the Froude number increases close to monotonically over the downstream part of the tail and the dissipative wake regions ($12<x/(H/2)$~24). Over these two regions, the streamwise modulations in the values of the Froude number associated with the presence of a rib are rather small. This is in contrast to the variation of the Froude number in Figure 5.9b, where the presence of the jet-like flow induced a noticeable increase in the Froude number for some distance downstream of the first two ribs behind the front. In fact, the Froude number was close to constant (Fr~1) in between the front and the start of the jet-like flow

developing downstream of the first rib behind the front. By contrast, in the SV-LR-R10 simulation, even during the buoyancy-inertia phase (Figure 5.18a), the Froude number over the downstream part of the tail and dissipative wake oscillates around a value smaller than one (Fr~0.7). Over this region, no significant amplification of the Froude number is observed close to the location of the ribs. This is because the ribs are much smaller than the current height.

The other qualitative difference with the SV-LR-R15 simulation is that the high velocity region within the head, dissipative wake and, especially, within the downstream part of the tail does not penetrate up to the channel bottom (e.g., see Figures 5.14d and 5.14e), as was the case in the SV-LR-R15 simulation (e.g., see Figures 5.5c and 5.5d) where a strong jet-like flow formed in the vicinity of the bed, downstream of each rib overtaken by the current. In the SV-LR-R10 simulation, the lower boundary of the core of high-speed velocities is close to horizontal and situated at a small distance from the top of the ribs. Though the presence of the ribs induces the formation of strong separated shear layers (e.g., see Figure 5.16), the vortical structures originating at the ribs do not interact with the much stronger eddies present at the interface between the current and the ambient fluid, and their effect on the flow structure within the gravity current is rather secondary. Their main effect is to decrease the flow velocity of the heavier fluid situated very close to the channel bottom faster compared to the case of a current propagating over a smooth surface.

Streamwise distribution of the Froude number in the SV-LR-R10 simulation is given in Figure 5.18 at $x_f/(H/2)=9.5$ (buoyancy-inertia phase) and at $x_f/(H/2)=24$ (drag-dominated phase). The structure of the current is visualized in an x-y section using concentration contours. The Froude number increases close to monotonically over the downstream part of the tail and the dissipative wake regions ($12<x/(H/2)\sim24$) in Figure 5.18b.

In contrast to the variation of the Froude number in Figure 5.9b, where the presence of the jet-like flow induced a noticeable increase in the Froude number for some distance downstream of the first two ribs behind the front, in presence of many small ribs there is no jet-like flow formation downstream of the ribs behind the head but rather due to the fact that the height of the current becomes smaller over the top of the rib, a local relative increase in Froude number is observed in that region (see the small spikes in the Figure 5.18b). However these local increases are not as strong as the one observed in the presence of jet-like flow in simulation SV-LR-R15.

In Figure 5.18a, Froude number right behind the head of the current, in the dissipative wake region and over the downstream part of the tail during buoyancy-inertia phase has smaller values (Fr ~ 0.7) compared to the close-to-critical values observed in simulation SV-LR-R15.

The distribution of the Froude number during the buoyancy-inertia phase shows that though the values of the Froude number in the head and dissipative wake are below 0.7, the flow past the first rib in the series becomes supercritical for a very short distance. This is due to the presence of a backward propagating disturbance passing over the first couple of ribs travelling towards the rear end-wall of the domain, which increases the velocity in that region at that instant in the simulation SV-LR-R10.

5.3 Interaction of the head region with the bottom-mounted obstacles

In the LR-R15 simulation, the interaction of the front of the current with each rib in the series resulted in the formation of a strongly coherent intensified mixing vortex (IMF). Once formed, the position of the IMF changed very little as the front of the current got away from the vortex. In time, the IMF got stretched in the streamwise direction and diffused slowly.

In the SV-LR-R15 simulation, the large-scale interfacial vortices present behind the front are not always associated with the formation of an IMF. This is true not only during the turbulent drag-dominated phase but also during the buoyancy-inertia phase. The largest and most coherent interfacial vortices are shed from the dissipative wake in a way similar to that observed in the case of a current propagating over a flat bed (e.g., case SV-LR-F). However, the presence of the ribs strongly affects the dynamics of these interfacial vortices.

For example, Figure 5.19 visualize the temporal evolution of the current interface (C=0.1 isocontour) in an x-y plane as the current overtakes Rib2. The current is in the buoyancy-inertia phase. The first three frames in Figure 5.19 show the gradual merging of two interfacial vortices denoted A and B. The merging is induced by the strong deceleration of vortex B as the front interacts with the second rib. The formation of the splash of higher density fluid over the rib strongly decelerates the fluid within the upper layer of the dissipative wake region and, in particular, vortex B. The streamwise momentum of vortex A is strong enough to approach vortex B and to start merging with it. In Figure 5.19d, the merging of the two vortices and their interaction with the highly 3D eddies present within the interface region behind the rib result in the gradual loss of their coherence. Meanwhile, a small IMF vortex denoted C (Figure 5.19c) starts forming, as the higher density fluid from the tail is convected over the first rib.

During the turbulent drag-dominated phase, the dynamics of the large-scale interfacial billows is similar. For example, the first four frames in Figure 5. 20 visualize the current interface (C=0.02 isocontour) in an x-y plane as the front propagates over Rib5. The concentration and out-of-plane vorticity contours in Figure 5.21 give additional information on the changes in the structure of the current as in passes Rib5. In Figure 5.20a, vortex D is being convected over the top of Rib4, while a large vortex E is present behind the head of the current (see also Figure 5.21a). As the front approaches Rib5, vortex E decelerates and vortex D approaches vortex E. The two vortices get close to each other and start interacting in Figure 5.20c (see also Figures 5.21c and 5.21e). The merging is basically complete in Figure 5.20d (see also Figure 5.21e).

Meanwhile, two new interfacial vortices F and G start forming behind the head. Vortex F originates in the fluid splashed upwards, as the front started interacting with Rib5 (see Figures 5.21d and 5.21e), while vortex G is an interfacial vortex shed from behind the head of the current just after it has passed Rib5. Observe also the formation in Figures 5.21d and 5.21e of a triangular region upstream of Rib5 containing relatively high density fluid. This heavier fluid decelerates rapidly as it interacts with the upstream face of Rib5. Meanwhile, lower density fluid from the interfacial region is convected at a relatively high speed over it and then over the top of Rib5. This triggers the formation of a strong shear layer containing negative vorticity at the interface between the layer of small-velocity and relatively high-density fluid and the layer of mixed fluid convected at a relatively large speed over it (see vorticity distribution in Figures 5.21d and 5.21e).

Thus, past the end of the slumping phase, the presence of the ribs facilitates the interaction, and in some cases the merging, of successively shed large-scale interfacial vortices.

The x-z plane views of the current interface at two time instances when the front approaches Rib5 but does not interact with it yet (Figure 5.20e) and a short time after the current reattached to the channel bottom after it passed Rib5 (Figure 5.20f) show that the presence of the ribs affects the size of the lobes and clefts at the front of the current. The average size of the lobes is the smallest immediately after the higher-density fluid reaches the channel bottom, downstream of each rib. The reason is similar to the one for gravity currents with a large volume of release. Most of the lobe and cleft structures are destroyed as the front starts interacting with the upstream face of the rib. The height of the ribs is large enough such that the high density fluid inside the splash moves initially mostly away from the bed. Most of the higher density fluid convected initially over the rib, which is going to form the new head of the current, originates in the splash. Consequently, after the front regains its usual shape, couple of rib heights downstream of the rib, the average size of the lobes is small, as most of the lobes started forming downstream of the region where the plunging heavier fluid reattaches to the channel bottom. The lobes and clefts continue to grow until the front gets close to the next rib and starts interacting with it.

Figure 5.20f shows a strong decay of the coherence of the interfacial eddies taking place behind the dissipative wake region. Large-scale disturbances are propagating over the downstream part of the tail region where the flow starts re-laminarizing gradually.

In the case dunes are present at the channel bottom (case SV-LR-D15), most of the large interfacial eddies originate in the dissipative wake region. However, the presence of the dunes impedes to a lesser degree the streamwise convection of the billows compared to the case ribs are present at the channel bottom. As previously discussed, the presence of the obstacles facilitates the interaction and merging of large-scale neighboring interfacial vortices. In the case of dunes, these events are much more seldom.

For example, Figure 5.22 visualizes the current interface (C=0.1 isocontour) as the front overtakes Dune2. Similar to Figure 5.19, the current is during the buoyancy-inertia phase. What is particular to dunes is that the head is not destroyed to a large degree as the front is convected over the crest of a dune. Moreover, similar to the case of a gravity current with a large volume of release, an interfacial vortex forms behind the head and over the lee side of the dune where the jet-like flow starts forming. Though somewhat similar to the mechanism responsible for the formation of the IMF in the LR-D15 simulation, vortex B forming over Dune1 (Figure 5.22a) and vortex D forming over Dune2 (Figure 5.22d) are not stationary. Rather, they are convected in the streamwise direction (e.g., follow the position of vortex B in Figure 5.22), similar to the other billows shed behind the head as the vortex propagates over the upslope side of the dune (e.g., vortex C that forms in Figure 5.22d). In contrast to what was observed in the case of ribs, a billow approaching the crest of a dune (e.g., vortex A in Figure 5.22a) is convected over it without the core of the billow being strongly disturbed, and especially without a significant reduction in its streamwise convective velocity. Though close to vortex B, vortex A remains independent and gets away of vortex B as the two vortices travel downstream.

During the turbulent drag-dominated phase, the dynamics of the large-scale interfacial billows is similar. The first four frames of Figure 5.23 visualizes the interface between the gravity current and the ambient fluid using a 3-D concentration isosurface (C=0.02) in the SV-LR-D15 simulation during turbulent-drag dominated phase at $t=46t_0$, $52t_0$, $56t_0$ and $62t_0$. Similarly in Figure 5.24 the gravity current is visualized using concentration, C, and out-of-plane vorticity, $\omega_z(H/2)/u_b$, contours during the turbulent-drag dominated phase at $t=46t_0$, $50t_0$, $54t_0$, $61t_0$ and $63.5t_0$.

Similar to what was observed during the buoyancy-inertia phase, when the back of the head is situated over the lee side of Dune5, a new interfacial billow forms (e.g., vortex F over Dune4 and vortex G over Dune5). In the drag dominated phase, the time over which the interfacial vortices maintain their coherence is much smaller compared to the buoyancy-inertia phase. The vortex E observed in Figures 5.23a, 5.23b and 5.24c disappears in Figure 5.23d in contrast to a similar vortex in buoyancy-inertia phase denoted A which maintains its coherence and is clearly present over all the frames of Figure 5.22.

Figures 5.23e and 5.23f show top view of the lobe and cleft structures using a 3-D concentration isosurface (C=0.02) in the SV-LR-D15 simulation during turbulent-drag dominated phase at the head of the current at $t=52t_0$ and $62t_0$. The average size of the lobes is comparable at all stages of the propagation of the current over the dunes. An increase in the average size of the clefts is noticeable a short distance after the front passes the trough of the dune. This is due to an increase in the spanwise non-uniformity of the front velocity in the region as the current impacted the trough of the dune.

Figures 5.25a and 5.25b visualize the interface between the gravity current and the ambient fluid using a 3-D concentration isosurface (C=0.02) in the SV-LR-R10 simulation at $t=40t_0$ and $48t_0$. The presence of ribs in the SV-LR-R10 simulation does not affect significantly the dynamics of the interfacial vortices shed behind the head. This is due to the smaller height of the obstacles and the undisturbed propagation of the top layer of the current over these obstacles rather than interacting with each of them separately as in simulation SV-LR-R15. Only the lower layers of the current are in active interaction with the ribs therefore the vortices in the dissipative wake region do not sense the presence of ribs significantly and no interactions between the interfacial billows and the ribs are observed for $x/(H/2)>9$.

Gravity current in the SV-LR-R10 simulation is shown in Figure 5.26 using concentration and out-of-plane vorticity contours as it passes Rib1 at $t=60t_0$, $61.5t_0$, $63t_0$ and $66t_0$. The rib disturbs only locally the sheet of positive vorticity associated with the front, as the front passes the rib. In out-of-plane vorticity contours of Figures 5.26a and 5.26d, formation of negative vorticity over the top surface of the rib is observed as the current takes over Rib19 and Rib20, respectively.

The layer of higher concentration fluid inside the head and dissipative wake continuously propagates forward as the current reaches Rib19. Figure 5.26a shows that lot of ambient fluid gets trapped inside the gap between Rib18 and Rib19 below the top level of the ribs, while the top layer of the current remains fairly undisturbed.

In Figures 5.25c and 5.25d shows the top view of the interface between the gravity current and the ambient fluid using a 3-D concentration isosurface (C=0.02) in the SV-LR-R10 simulation at $t=40t_0$ and $48t_0$. The dashed lines indicate the position and spanwise extent of the interfacial billows. In both figures, the size of the lobes and clefts are much smaller than those in the SV-LR-R15 simulation. This is due to the fact that the wavelength between the ribs in simulation SV-LR-R10 is so small that current does not have enough space to re-establish itself as in simulation SV-LR-R15. Therefore the lobe and cleft structures observed over the flat part of the channel bottom are much smaller since the front of the current experience the deceleration due to presence of the next rib immediately after the current reattaches the flat part of the channel bottom.

Another qualitative difference with the SV-LR-R15 simulation is the fact that the spanwise extent of the main interfacial billows is much larger in the SV-LR-R10 simulation (e.g., compare Figures 5.25c-d and 5.20e-f). This is again due to the fact that the height of the ribs in simulation SV-LR-R10 are smaller and they are more closely spaced compared to the SV-LR-R15 which causes top layer of the current to stay unaffected while the current in simulation SV-LR-R15 continuously interacts with each rib in the series and due to their bigger size they affect even the interfacial layer between the high-density current and the lower density ambient fluid causing billows to break down. Hence, the presence of ribs with a relatively large height is an efficient mechanism for breaking the spanwise coherence of the interfacial billows. This is particularly the case for the billows situated within or close to the dissipative wake.

5.4 Front velocity

Due to the small volume of release present in the simulations discussed in this chapter, the current propagates over a relatively small distance during the slumping phase. Taking into account the finite size of the channel in the simulations, the small duration of the slumping phase allows to study the evolution of the gravity current over the buoyancy-inertia and, if large-scale roughness elements are present, over the turbulent drag-dominated regime, which is the main goal of the present chapter.

In the simulations with a flat bed, the main reason the front velocity starts decaying are the frictional losses at the channel bottom and the losses from mixing at the current interface. As expected, the presence of ribs or dunes slows down the advancement of the front of the current compared to the flat-bed case due to the additional drag induced by the roughness elements. In the simulations with obstacles of same height, as the ribs have a higher degree of bluntness than dunes, the drag form component is higher. Consequently, the distance traveled by the front at a certain non-dimensional time in the simulation with ribs is smaller. Larger obstacles induce a larger drag force per unit length and reduce the distance traveled by the front at a given time compared to the case of smaller obstacles of same shape. This is the case for all the phases of the evolution of the gravity current with a small volume of release.

Figure 5.27 shows the temporal evolution of the non-dimensional front position $(x_f-x_0)/x_0$ vs. (t/t_0) in linear and log-log scale for the low Reynolds number simulations conducted with a flat bed and with dunes of height D=0.05(H/2) and D=0.15(H/2). Figure 5.28 shows the same information for the low Reynolds number simulations conducted with a flat bed and with ribs of height D=0.1(H/2) and D=0.15(H/2). The results for the high Reynolds number simulations ($Re=10^6$) with flat bed and obstacles of height D=0.15(H/2) are presented in Figure 5.29.

In all these simulations, after the end of the initial accelerating phase, the front trajectory, when plotted in linear-linear scale (Figures 5.27a and 5.28a) , can be well approximated by a line of constant slope before the trajectory starts curving toward the time axis. This means that the front velocity is nearly constant. Thus, a slumping phase is present both in the simulations with a flat bed and in the simulations in which obstacles are present at the channel bottom. When plotted in log-log scale, the slope of the front trajectory over the slumping phase is equal to one. The curving of the trajectory toward the time axis after the end of the slumping phase indicates the start of the decay of the front speed with time. Linear-linear plots of front trajectory clearly show the slowing effect of the obstacles on the front speed.

The non-dimensional front velocity expressed as a Froude numbers ($Fr_f=U_f/u_b$) for the SV-LR-F (Re=48,000) simulation is 0.53. Shin et al. (2004) proposed an analytical formula to calculate the front velocity during the slumping phase for partial depth release currents. The value of the Froude number is $Fr = \frac{\sqrt{2}}{2}\sqrt{\frac{h}{H}(2-\frac{h}{H})}$. As in the two simulations h=H/2, the value predicted by the analytical model of Shin et al. (2004) is Fr=0.61. The model neglects viscous effects. The value predicted by the SV-LR-F simulation is about 12% smaller that the value predicted by the theoretical model. However, in most of the experiments performed by Shin et al. (2004) the measured value of Fr was up to 10% smaller than the value predicted by theory. Thus, the agreement can be considered satisfactory. A reduction of the theoretical value by about 10% for full depth release gravity currents with Re_f~10,000 is also consistent with the difference between the theoretical value of Fr= $\sqrt{2}/2$=0.71 and the values inferred from experiments and the numerical simulations performed in Chapter 4 (Fr~0.63). Note that the differences in the values of the Froude number reported in Chapter 5 and Chapter 4 are due to the fact that the channel depth, rather than the channel half depth, was used as the length scale in Chapter 4.

Once the backward propagating disturbance encounters the rear end-wall, it reflects. The end of the slumping phase corresponds to the moment when the reflected disturbance reaches the front of the current. Table 5.2 summarizes the non-dimensional times and front positions corresponding to the end of the slumping phase. The end of the slumping phase in the SV-LR-F simulation occurs when $x_f/(H/2)$~5.9. This corresponds to about 10 lock lengths ($(x_f-x_0)/x_0$~9.5). This is very similar to the value expected for full-depth-release currents. As the size of the obstacles increases, the non-dimensional front position at which the end of the slumping phase is reached, $(x_f\text{-}x_0)/x_0$, decays. In the simulations with large obstacles (D=0.15(H/2)), the end of the slumping phase occurs around the time when the front passes the first obstacle ($x_f/(H/2)\sim5.0$). No clear slumping phase was identified in the SV-LR-R10 simulation. The initial flat part of the channel bottom ($x/(H/2)<3$) is too short for the current to finish the transition from the acceleration phase to the slumping phase. Once the front starts interacting with the ribs, the current slows down because of the additional drag induced by the ribs. The disturbance reaches the head while the front of the current is still decelerating as it tries to adjust to the presence of the ribs. The front position increases in a non-linear way with time, such that no clear slumping phase can be identified in the SV-LR-R10 simulation.

The slope of the front trajectory in the SV-LR-F and SV-LR-D05 simulations (Figure 5.27), when plotted in log-log scale, starts decaying past the end of the slumping phase, until it reaches a new constant value. This value is very close to 2/3 and corresponds to the buoyancy-inertia phase. The nondimensional times (t/t_0=25 vs. 22) and streamwise locations ($x_f/(H/2)\sim10.8$ vs. 9.7, $(x_f\text{-}x_0)/x_0\sim18.3$ vs. 16.3) corresponding to the start of the buoyancy-inertia phase in the two simulations are close. The trajectory follows the 2/3 slope curve until the end of the simulations. This is fully expected for the SV-LR-F simulation, at least until the front velocity is small enough for the transition to the viscous-buoyancy phase to start. In the SV-LR-D05, it is expected that the gravity current will start transitioning first to the turbulent drag dominated phase, in which $x_f\sim t^{1/2}$. This does not happen because the drag force added by the dunes is not large enough to force transition to the drag dominated phase before the front reaches the downstream end of the channel (~20(H/2)) in the simulation. However, it is expected the current will eventually transition to the drag dominated phase, except if the conditions for the transition to the viscous-buoyancy phase are not reached first.

By contrast, the slope of the trajectory in the SV-LR-D15 simulation decreases gradually from a value of 1 to a value close to 1/2 and then, for $t/t_0>32$ ($x_f/(H/2)>12.3$), remains approximately constant until the end of the simulation. The slope is close to 2/3 over a time interval, in between the end of the slumping phase and the start of the drag dominated phase.

This means that the current transitions first to the buoyancy-inertia phase and then to the drag-dominated phase. The transition to the drag-dominated phase happens at about the time the front propagates over Dune3.

The results for the SV-LR-R15 simulation are qualitatively very similar. The turbulent drag dominated phase is reached slightly earlier ($x_f/(H/2)\sim 11$, $t/t_0>30$). This is expected, as the ribs are blunter than dunes, and the drag force per unit (streamwise) length is larger. Thus, the transition to the drag-dominated phase is expected to happen when the front is situated closer to the initial position of the lock gate.

The results for the SV-LR-R10 simulation also show the current reaches the drag-dominated phase. Moreover, the domain was long enough to allow the current to propagate for a relatively long time in the drag-dominated regime, before reaching the end of the computational domain. As the ratio between the rib height and the current height was much smaller in the SV-LR-R10 simulation compared to the SV-LR-R15 simulation, the x_f vs. t curve does not contain any noticeable oscillations associated with the successive acceleration and deceleration of the front as it interacts with successive ribs. The slope of 1/2 is clearly present, starting somewhere in between $t/t_0=48$ and $t/t_0=60$. The simulation was run until $t/t_0=113$. The value of $x_f/(H/2)$ corresponding to the start of the drag dominated phase is significantly larger than the one in the SV-LR-R15 simulation. One should point out that a quantitative comparison of the two simulations is quite difficult because of the differences in the ratio h/H and the volume of release. Also, though in the SV-LR-R10 simulation the ribs have smaller height, they are disposed in a denser way as the ratio D/λ is larger. The non-dimensional times and front positions corresponding to the start of these two phases are summarized in Table 5.2.

The finding that a drag dominated regime in which $x_f\sim t^{1/2}$ is present for gravity currents propagating in a channel containing large-scale roughness elements is an important contribution of the present study. The theoretical study of Hatcher et al. (2000) and their experiments showed that a finite-lock release gravity current with a sufficiently high volume of release propagating into a porous medium can transition from the buoyancy-inertia phase to a turbulent drag dominated regime in which x_f~$t^{1/2}$. One assumption was that the drag coefficient was close to constant. This assumption is largely satisfied in the present high Reynolds number simulations. The effect of the porosity is accounted for in the model proposed by Hatcher et al. (2000) by making the drag force proportional to the volume fraction ϕ occupied by the obstacles. In the case of a medium of uniform porosity, the drag acts relatively uniformly over the whole height of the current at all stages of its propagation, so ϕ is a constant that is easy to calculate.

In the case of a gravity current propagating over large-scale roughness elements, the drag acts only over the bottom part of the current. If a turbulent-drag dominated regime will be present for gravity currents propagating over large-scale roughness elements, one expects that for the same flow conditions, the transition to the drag dominated regime will start later compared to the case in which the current propagates into a porous medium which porosity is close to that of the bottom layer containing the roughness elements. It is also not evident that during this regime x_f should increase proportional to $t^{1/2}$ for gravity currents propagating over large-scale roughness elements. The fact that even in case SV-LR-R10, in which the ratio between the height of the ribs and the current height is quite low, the current reaches the drag dominated regime and x_f~$t^{1/2}$ shows that gravity currents propagating in an environment containing obstacles that induce a significant drag force on the current have a similar evolution to that of gravity currents propagating into a porous medium of uniform porosity. Of course, in the case of gravity currents propagating over large-scale roughness elements it is not possible to define in a straightforward way an equivalent volume fraction accounting for the presence of the large-scale roughness elements (e.g., as the current advances, its height reduces; so the "equivalent volume fraction" increases rather than being a constant; thus, it is very difficult to propose a "mean" value), the analytical model proposed by Hatcher et al. (2000) to estimate the times the current transitions to the buoyancy-inertia phase and to the drag-dominated phase, as well as the shape of the current during these regimes does not apply.

The temporal evolution of the front position in the high Reynolds number simulations with a flat bed and with large obstacles shown in Figure 5.29 is qualitatively similar to the one observed in the low Reynolds number simulations.

In the flat bed simulations, the current transitions only to the buoyancy-inertia phase and remains in this phase till the end of the simulation time. In both simulations, the end of the slumping phase occurs at about 9.5 non-dimensional lock lengths, $(x_f-x_0)/x_0$.

In the low and high Reynolds number simulations with ribs and dunes of height 0.15(H/2), the current transitions first to the buoyancy-inertia phase and then to the turbulent drag-dominated phase. The start of the buoyancy-inertia phase occurs at about 14 lock lengths in the high Reynolds number simulations with ribs and dunes, compared to about 13 lock length in the corresponding low Reynolds number simulations. The start of the drag dominated phase in the high Reynolds number simulations is relatively independent of the shape of the obstacles. It occurs at about $41t_0$, when the front traveled about 25 lock lengths.

5.5 Dynamics of flow disturbances propagating within the gravity current

Figure 5.30 shows a plot of the concentration C(x,t) as it evolves in time on a line situated at a small distance ($y/(H/2)$=0.09) from the channel bottom in the SV-LR-F and SV-HR-F simulations. The front trajectory corresponds to the boundary between the white region containing only ambient fluid and the darker region. The slope is approximately constant up to x/(H/2)~6. This is consistent with the fact that the front velocity is constant until the end of the slumping phase ($x_f/(H/2)$=5.9, see also Table 5.2), when the reflected disturbance overtakes the front. Unfortunately, the trajectory of the reflected disturbance is not very clear in Figure 5.30. The short length of the initial volume of lock fluid in the simulations means that the lighter current moving toward the rear end-wall interacts with it a short time after the release of the lock fluid. Animations confirmed that the velocity of the front of the heavier current and that of the front of the disturbance propagating toward the end-wall are equal until the disturbance starts interacting with the rear end-wall. For partial depth release currents with h/H<0.76, Shin et al. (2004) have shown that the disturbance traveling toward the rear end-wall takes the form of a wave of rarefraction propagating on the interface between the lock fluid and the ambient fluid. The small distance between the lock and the rear end-wall did not allow to clearly visualize the form of the disturbance (bore like or rarefaction wave) in the simulations.

At a certain time, the front trajectory in Figure 5.30 starts curving toward the time axis. This means the slope of the front trajectory decreases with time. In other words, the front velocity starts decaying with time in a non-linear way, as analyzed in Figures 5.27 and 5.29.

Besides showing the front position, Figure 5.30 gives much more information on the dynamics of the flow within the current. For example, an array of relatively dark streaks is present close to the front (e.g., see arrows in Figure 5.30). These streaks trace the trajectory of the large interfacial billows being shed behind the head of the current. These billows have initially a velocity close to that of the front, but then decelerate and gradually reduce their velocity. Before they dissipate (the streaks in Figure 5.30 disappear after some time), the angle of the streak with the time axis becomes quite small, indicating that these billows move downstream with a very small velocity at large times after their formation.

Figure 5.30 also shows the presence of three streaks of darker fluid whose shapes are close to straight lines. They are denoted BD1, FD1 and FD2. They correspond to the trajectories of several disturbances that propagate within the gravity current. BD1 and FD1 originate at a common point in Figure 5.30, situated around ($4t_0$, H/2) in the SV-LR-F simulation and ($6t_0$, 1.3(H/2)) in the SV-HR-F simulation. In both simulations, a dark streak corresponding to a large billows separating from the dissipative wake passes through that point in the C(x,t) plot. Animations of the gravity current after the removal of the lock gate show that the core of the billow starts moving toward the bed as it is convected downstream with a very small velocity. As a result of its interaction with the channel bottom, some of the higher density fluid contained within the billow starts moving downstream creating the forward-moving disturbance front FD2. Meanwhile, the remaining higher-density fluid starts moving upstream toward the rear end-wall and gives raise to the backward-moving disturbance front BD1. As BD1 approaches the rear end-wall, it interacts with the wall ($t/t_0 \sim 10$) and reflects as a forward moving disturbance, FD1.

The velocity magnitudes of BD1 and FD1 are very close. The trajectories of BD1, FD1 and FD2 are close to straight lines. This means the velocities with which they propagate within the body of the current are constant. The corresponding front velocities of the BD1, FD1 and FD2 disturbances in the SV-LR-F simulation are $0.14u_b$, $0.145u_b$ and $0.25u_b$, respectively. Though the front velocity is higher in the SV-HR-F simulation, the velocities at which the disturbances propagate are slightly lower ($0.13u_b$, $0.14u_b$ and $0.21u_b$ for the BD1, FD1 and FD2 disturbances). This explains why FD2 gets much closer to the front in the later stages of the buoyancy inertia case in the SV-LR-F simulation compared to the SV-HR-F simulation. In fact, as the front velocity continues to decay, FD2 will eventually catch the front of the current.

In Figures 5.31 and 5.32, the structure of the gravity currents in the SV-LR-F and SV-HR-F simulations are visualized using concentration contours. The position and direction of propagation of the flow disturbances are shown using arrows at $t=9t_0$, $11.5t_0$, $20.5t_0$ and 26.5_0.

Figures 5.31a and 5.32a shows the backward propagating disturbance BD1 and forward propagating disturbance FD2, both of which have irregular shapes. When BD1 reaches and reflects from the rear end-wall at $t = 10t_0$, it is denoted as FD1 which is shown in Figure 5.31b and 5.32b. In the later stages of the evolution of the current, both disturbances have a smooth Gaussian wave-like shape that does not change as they propagate through the shallower or the deeper parts of the tail of the gravity current (e.g., see the shape of the disturbance FD1 and FD2 in Figures 5.31d and 5.32d). These propagating waves give rise to local perturbations of the current depth and concentration. The disturbances can transfer energy and momentum along the interface. The forward propagating disturbances transfer energy toward the current front. It is expected these disturbances will eventually reach the front that decelerates continuously.

Figure 5.33 shows C(x,t) at $y/(H/2)=0.09$ in the SV-LR-R15 simulation. Figure 5.34 visualizes the distributions of the concentration and streamwise velocity in between the rear end-wall and Rib1 for $12t_0<t<40t_0$. The pattern of streaks containing higher-density fluid is much more complex compared to the one observed in the flat bed simulation (Figure 5.30a). Similar to the SV-LR-F simulation, a large billow containing high density lock fluid separates from the dissipative region when $x_f/(H/2)\sim1$. As the billow reaches the channel bottom, it gives rise to a stronger forward-propagating disturbance, S1, and to a weaker backward-propagating disturbance, BD1. BD1 reaches the rear end-wall when $t\sim12t_0$ (Figure 5.34a) and then reflects as a forward-propagating disturbance, FD12 (Figure 5.34b). Another-forward propagating disturbance, FD11, forms when BD1 encounters a patch of higher density fluid that separated earlier from the back of the current and that moves downstream. However, the strengths of both FD11 and FD12 are much smaller than that of S1 or than the strength of the disturbance S2 corresponding to the backward-propagating hydraulic jump that forms as the front of the current starts interacting with Rib1 at $t\sim10t_0$.

The velocity of the disturbance S1 as it propagates toward Rib1 is close to $0.25u_b$, which is about half of the front velocity of the gravity current during the slumping phase. The velocity of S1 after reflection at Rib1 (Figures 5.34d and 5.34e) is about $0.24u_b$. The velocity of S2 as it propagates from Rib1 toward the end wall is slightly higher ($0.27u_b$). The subsequent reflections of S1 and S2 (e.g., see Figure 5.34e for S2) at the rear end-wall are accompanied by a noticeable loss in the velocity of the disturbance (e.g., from $0.27u_b$ to $0.19u_b$ for S2). By contrast, the subsequent reflections as S1 and S2 encounter Rib1 do not result in a noticeable drop of the disturbance velocity (e.g., the velocity of S2 after it reflects at $t=55t_0$ is still close to $0.19u_b$).

Both S1 and S2 have the form of a rarefraction wave with a mildly inclined interface forming behind the two disturbances (e.g., see Figure 5.34c and 5.34d). The concentration and streamwise velocity fields in Figure 5.34 allow to better understand how two disturbances propagating in opposite directions pass each other. For example, in Figure 5.34b S1 moves downstream while S2 moves upstream. As they start interacting S1, that contains lower density fluid compared to S2, moves over S2. After S1 has passed over S2, its center approaches again the channel bottom, as shown by the position of the region of high positive streamwise velocity associated with S1 in Figure 5.34c. The phenomenon repeats itself in Figure 5.34c when S2 moves underneath the disturbance FD11 that propagates downstream. S2 reflects at the rear end-wall in Figure 5.34e and then overpasses S1 that moves toward the end wall (Figure 5.34f). Notice that, as S1 approaches Rib1, the positive streamwise velocity over Rib1 increases. During this time, the heavier fluid moves past Rib1 and starts propagating toward Rib2. However, once S1 reflects and starts moving upstream (Figure 5.34d), the patch of positive streamwise velocities over Rib1 is reduced considerably. Some time later, as S1 moves fast away from Rib1 (Figure 5.34e), there is no flow of higher-density fluid over Rib1. In fact, the flow close to the upstream face of Rib2 is close to steady. Even the arrival of the forward propagating disturbance S2 around $t=55t_0$ is not able to sufficiently accelerate the higher-density fluid situated close to the channel bottom, to overpass Rib1. However, the arrival of S3 that propagates from Rib2 toward Rib1 in Figure 5.34e will force some of the higher-density fluid situated downstream of Rib1 to pass over Rib1 for a short period of time. Though S3 has just reflected in Figure 5.34f, the flow over the top of the rib still contains a small streak of negative streamwise velocities corresponding to the end of the convection of a small patch of higher density fluid past Rib1 (see also concentration distribution around the upstream top corner of Rib1 in Figure 5.34f).

In Figures 5.35 and 5.36 the structure of the current between Rib1 and Rib2 and around Rib2 in the SV-LR-R15 simulation are shown, respectively, using non-dimensional concentration contours and streamwise velocity contours together with the position and direction of propagation of the main flow disturbances. The dynamics of the disturbances is qualitatively similar for the ribs of higher rank. Each time the front reaches a rib, it gives rise to a backward propagating hydraulic jump (S3 for Rib2, S4 for Rib3 and S5 for Rib4). As the backward propagating disturbance reaches the rib situated upstream of it (e.g., see Figures 5.35c and 5.35d showing S3 before and after reflection at Rib1), it reflects and starts moving forward with a smaller velocity. S3 forms at around $t \sim 23t_0$ as the front of the current interacts with Rib2. S3 has the velocity of $0.24u_b$ as it first forms, it reaches Rib1 at $t = 37t_0$. In Figure 5.35d as S3 reaches Rib1, some of the high-density fluid is carried with the disturbance and pushed over Rib1, spilling to the space between rear end-wall and Rib1. S3 gets reflected and starts propagating toward Rib2 as soon as it interacts with Rib1 in Figure 5.35e. Similar to the spillage observed due to S3, when S1 reaches Rib1 at t~23t$_0$, part of the high concentration fluid is pushed over Rib1 to the space between Rib1 and Rib2 (see Figure 5.35a). While S1 gets reflected from Rib1, the high concentration fluid spilt over the rib continues to propagate in the same direction as original S1 toward Rib2 as shown in Figure 5.35b.

Another interesting situation occurs around t=56t$_0$ around Rib2 in Figure 5.36d, when the forward propagating disturbance S3 and the backward propagating disturbance S4 reach Rib2 at about the same time. Both disturbances have enough momentum to carry higher-density fluid from the vicinity of the rib past its top. In Figure 5.36e the high-density fluid from both sides of the Rib2 are observed to be pushed to the upper surface of the rib. The net amount of higher density fluid convected over the top of the rib is very small.

Evolution of the concentration with time along the x axis in the SV-HR-R15 simulation at a distance of y/(H/2)=0.09 from the bottom wall is shown in Figure 5.37 to better understand the scale effects on the dynamics of the disturbances propagating inside the body of the current. The dashed lines visualize the main forward and back propagating flow disturbances. S1 forms due to the collapse of a large interfacial billow on the channel bottom. S2 to S5 form due to the partial reflection of the gravity current fluid as the front passes Rib1 to Rib4, respectively. The trajectories of these disturbances are qualitatively very similar to the ones observed in SV-LR-R15 simulation. Their propagation speeds are also comparable with those observed in Figure 5.33.

5.6 Analysis of the time variation of the mass fluxes and mass balance for the heavier lock fluid

The temporal variation of the total volumetric flux of heavier fluid $Q_i=(4/u_b H^2)\int CudA$ at streamwise locations corresponding to the upstream face of the first four ribs in the series is plotted in Figures 5.38a and 5.38c for the SV-LR-R15 simulation. Figure 5.38b shows the time history of the flux of heavier fluid moving upstream, $Q\text{-}_i = (4/u_b H^2)\int Cu\_dA$, at the same streamwise locations, where $u_{-} = 0.5(u - |u|)$. Figures 5.34 to 5.36 help understanding the temporal variations of Q_i and Q_{-i} plotted in Figure 5.38.

As the front reaches one of the ribs, the total volumetric flux at the location of the rib starts increasing. The increase is very sharp until the higher density fluid contained within the initial splash moves over the top of the rib. Then, the flux decays in a milder way, as most of the remaining fluid contained within the head and dissipative wake of the incoming current is convected over the top of the rib. In some cases (e.g., first couple of obstacles in the series, small height obstacles, or obstacles with a low degree of bluntness), some of the lower-density fluid from within the downstream part of the tail of the current is convected over the top of the obstacle (e.g., see discussion of Figure 5.39). However, this contribution is negligible in the SV-LR-R15 simulation. Concomitantly with the formation of the splash containing relatively high-density and low-momentum fluid, a backward-propagating disturbance forms when the front reaches the upstream face of the rib. As the disturbance starts moving away from the upstream face of the rib, it entrains a small part of the higher-density fluid from within the splash. This is the reason why the values of Q_{-i} in Figure 5.38b are non-zero around the time the initial splash is convected over the top of the rib.

For example, the front of the current reaches the upstream face of Rib1 at $9t_0$. Most of the fluid from within the initial splash is convected over the streamwise location corresponding to the upstream face of Rib1 until $11t_0$. Most of the fluid from within the dissipative wake is convected past the same location by $15t_0$. Then, Q_1 is very close to zero until $19t_0$. During this time interval, a negligible amount of fluid from the downstream part of the tail of the current is convected over Rib1. For $t>19t_0$, Q_1 increases slightly for about 4-5t_0, as the forward moving disturbance S1 approaches Rib1 and reflects away from it. The interaction of S1 with Rib1 before it reflects is responsible for the small temporary increase in Q_1. The effect of the formation of the backward propagating disturbance S2 is to entrain with it a small part of the fluid contained within the splash. The values of Q_{-1} are at all times less than 10% of the net flux Q_1. The percentage is even smaller for Rib2 and Rib3 (see Figures 5.38a and 5.38b).

The other times when Q_{-i} is different from zero are when a disturbance moving backwards has enough momentum to advect with it some of the higher-density fluid located downstream of the rib, before it reflects away from the rib. For example, for Rib1 this happens around $t=37t_0$, when S3 reaches the face of Rib1 (e.g., see Figures 5.34e and 5.34f showing S3 before and after reflection). Before S3 reaches Rib1, there is no transfer of heavier fluid over Rib1, not only Q_{-1} but also Q_1 is equal to zero. During the time interval ($37<t/t_0<40$) some small amount of fluid is convected over the top of the rib, Q_1 is negative and equal to Q_{-1} (see Figures 5.38b and 5.38c).

Figures 5.38a and 5.38c show that the temporal variation of Q_i during the time the current passes each rib has a triangular shape. A regime characterized by a sharp linear increase in Q_i is followed by a second regime in which the decrease in Q_i is also linear but the magnitude of the rate of decrease is smaller compared to the rate of increase observed during the first regime. The first regime corresponds to the convection of the heavier fluid from within the initial splash. The second regime corresponds to the convection of the heavier fluid from the head and dissipative wake. Because the mixing within these regions increases fairly sharply as the current moves over the higher-rank ribs, the maximum values of Q_i decrease with i. Because the slumping phase ends around the time the front overtakes the first rib, and the front velocity decreases substantially as the front advances, the lengths of the time intervals needed to convect the heavier fluid from within the splash, the head and dissipative wake over the higher-rank ribs increase monotonically. This explains the changes in the size of the triangular region with the rank of the rib in Figures 5.38a and 5.38c.

Temporal variation of the total volumetric flux of heavier fluid $Q_i = (4/u_b H^2)\int CudA$ at the streamwise locations ($x/(H/2)=5$, 8, 11, and 14) corresponding to the center of the ribs and the crest of the dunes in the SV-LR-F, SV-LR-R15 and SV-LR-D15 simulations are shown in Figure 5.39.

The temporal variation of Q_1 at $x/(H/2)=5$ is qualitatively and quantitatively similar in all the three simulations. The tail on the descending part of the Q_1 curve ($t>15t_0$) is larger in the simulations with dunes and with flat bed. This is due to the blunt and more compact shape of the ribs which causes a larger part of the high-density fluid get trapped behind Rib1 compared to Dune1. The streamlined shape of dunes allows smoother passage of current compared to ribs. Similarly when no obstacles exist on the channel bottom it takes longer time for tail of the current to become stationary at the considered location due to the continuous (unblocked) propagation inside the body of the current on the flat bed.

The distributions of Q_2 and Q_3 are qualitatively similar in the SV-LR-F and SV-LR-D15 simulations. The only difference is that a plateau region is present, a short time after the discharge peaks in the SV-LR-F simulation. This is because the head of the current in SV-LR-F simulation is longer with less mixed fluid in its dissipative wake region compared to the head of the current in SV-LR-D15 simulation with more mixed fluid. Therefore until the end of passage of the head region from the zone of interest, the flux in SV-LR-F simulation remains unchanged while higher levels of mixing causes SV-LR-D15 to have changes in the flux more rapidly.

Consistent with the smaller front velocity in the SV-LR-R15 simulation after the current overtakes the first rib, the peaks in $Q_2(t)$ and $Q_3(t)$ occur at a later time compared to the other two simulations. Also the peak values of $Q_2(t)$ and $Q_3(t)$ are substantially lower in the SV-LR-R15 simulation. This is due to the fact that mixing is more vigorous in the presence of ribs compared to dunes. This causes higher reduction in the concentration levels at the head and dissipative wake region of the current. Also the blunt shape of the ribs introduces more form drag to the system compared to the dunes. Additional form drag slows down the front of the current further.

In the SV-LR-R15 simulation, the peak value of $Q_4(t)$ is about two times smaller than that in the SV-LR-F simulation and occurs about $16t_0$ later. Thus, compared to the flat bed case, the presence of blunt obstacles has a much larger effect, compared to that of streamlined obstacles (e.g., dunes), on the temporal evolutions of the fluxes of lock fluid at streamwise locations situated far from the initial position of the lock gate.

The temporal variation of flux at stations of interest in small volume of release simulations is very different from the ones observed in large volume of release. In large volume of release simulations the flux over the first three obstacles in the series reaches a non-zero steady state value as the front of the current long passes these obstacles , the obstacles ranked 4 and 5 also reaches non-zero steady state values which are little lower than the previous one (see Figures 4.14a and 4.14c). While in small volume of release simulations as the current progress further the flux over the obstacles and over the tail of the current becomes zero.

In Figure 5.40 temporal variation of the total volumetric flux of heavier fluid $Q_i = (4/u_b H^2)\int CudA$ at the streamwise locations (x/(H/2)=5, 7, 11, and 17) corresponding to the center of Rib3, Rib5, Rib9 and Rib15 in the SV-LR-R10 simulation is shown. The triangular shape observed in the previous simulations is also present in the Q_i plots of SV-LR-R10 simulation. The average concentration remains approximately constant over most of the dissipative wake region. It starts decaying mildly over the downstream part of the tail. For instance, $Q_4(t)$ for Rib15 shows a fast increase with the impact of current to rib at around t~42t_0 similar to the ones observed for previous ribs. After the maximum flux is reached at around t~44t_0, there exists a plateau region in $Q_4(t)$ which extends for about 4t_0. This plateau of almost constant flux corresponds to the passage of decelerated dissipative wake region of the current with approximately constant average concentration over the rib. After this plateau region the flux starts decaying mildly in time until t~90t_0.

Figure 5.41 shows the time histories of the volume of heavier fluid $M_{i-i+1} = (u_b/(H/2))\int(Q_{i+1} - Q_i)dt$ in between the crests or upstream faces of two successive obstacles i and i+1 in the SV-LR-R15 and SV-LR-D15 simulations. For a given i, the M_{i-i+1} curves in the two simulations are qualitatively and quantitatively similar. This is even more evident if one accounts for the differences in the front speed of the current, which result in M_{i-i+1} starting increasing from zero at slightly later times in the SV-LR-R15 simulation. Thus, it is enough to discuss in detail the time variation of M_{i-i+1} in the SV-LR-R15 simulation for which the time variation of the fluxes Q_i and Q_{i+1} is shown in Figures 5.38a and 5.38c.

If one neglects the small amount of heavier fluid that is convected past the top of a rib as a result of the interaction between the forward and backward propagating disturbances with that rib, the volume of lock fluid accumulated between the streamwise locations at which the two ribs are located is, in a good approximation, equal to the difference between the volume of lock fluid convected through section i and that convected through section i+1 between the time the front reaches the rib of rank i (Q_i becomes larger than zero) and the current time. Q_{i+1} becomes zero after the dissipative wake has passed section i+1. At that time, Q_i is already equal or very close to zero. Thus, once the dissipative wake has past section i+1, the total volume of lock fluid between the two ribs is close to constant. A "quasi-steady state" regime is reached.

The results in Figure 5.41a confirm this. For example, M_{1-2} start increasing from zero at $t=9t_0$ when the front reaches Rib1 and becomes constant around $27t_0$ when Q_2 becomes close to zero. Similarly, M_{2-3} start increasing at $t=18t_0$ when the front reaches Rib2 and becomes constant around $40t_0$ when Q_3 becomes close to zero. M_{i-i+1} first peaks when the front reaches the rib of rank i+1 and then decays proportional to the increase of Q_{i+1} in time until it reaches the "steady state" regime. For i=4, the SV-LR-R15 simulation was stopped before the front reached the rib of rank i+1. This is why M_{4-5} increases monotonically until the end of the simulation time ($73t_0$). By contrast, in the SV-LR-D15, in which the front speed is larger, the front passes the crest of Dune5 at $t\sim59t_0$. Then, M_{4-5} decays toward the "quasi-steady state" value that is reached around $t=71t_0$.

The "quasi-steady state" value of M_{i-i+1} decreases with i. This is because the concentration of the fluid inside the head and dissipative wake decreases substantially each time the current passes a new rib. Also, the head and dissipative wake shrink due to the heavier fluid lost with the billows separating from the dissipative wake. This heavier fluid becomes part of the tail and is eventually trapped in the cavity-like region between two consecutive ribs.

As already mentioned, once the "quasi-steady state" regime is reached, M_{i-i+1} can increase or decrease only due to the heavier fluid convected over the obstacles by the forward and backward propagating disturbances. For example, the forward propagating disturbance S1 reaches Rib1 around $t=38t_0$ and some small amount of fluid is convected past the top of Rib1. As a result, Q1 becomes positive for about $4t_0$. However, the volume of fluid convected over Rib1 over this time interval is very small compared to that convected during the time the front and dissipative wake passed Rib1.

As already discussed, the mixing in the head region is smaller in the case dunes, rather than ribs, are present at the channel bottom. Thus, for a given i, both the peak and the “quasi-steady state” values of M_{i-i+1} are slightly smaller in the simulation with ribs (see Figure 5.41a). Consistent with the fact that in the simulation with ribs of height D=0.15(H/2) the mixing at the head is smaller and the front velocity is slightly larger in the high Reynolds number simulation, the peak values of M_{i-i+1} are slightly larger and occur earlier in the SV-HR-R15 simulation compared to the SV-LR-R15 simulation (see Figure 5.41b). As shown by the comparison of M_{i-i+1} in the SV-LR-D15 and SV-HR-D15 simulations (Figure 5.41c), scale effects are negligible in the case in which dunes are present at the channel bottom.

In the case of the SV-LR-R10 simulation (Figure 5.41d), the variation of M_{i-i+1} with time is rather similar. One qualitative difference with the simulations in which the height of the gravity current was closer to that of the obstacles is that, once the front reaches the rib of rank i+1, M_{i-i+1} either continues to increase for a small amount of time, or remains close to the peak value for a certain amount of time, before it starts decreasing. This is because the part of the head and dissipative wake regions containing fluid with relatively close values of the height-averaged concentration can be longer than the distance between two ribs. Similar to the previous simulations, a “quasi-steady” state regime is reached once the dissipative wake is convected past the rib of rank i+1.

5.7 Drag force on the ribs

The temporal histories of the difference between the mean pressure on the upstream (P^+) and downstream (P^-) faces of selected ribs in the seires, $\Delta P=P^+-P^-$, are shown in Figure 5.42 for the SV-LR-R15 and SV-HR-R15 simulations and in Figure 5.44 for the SV-LR-R10 simulation. In Figure 5.43 the profiles of ΔP in the SV-LR-R15 and SV-HR-R15 simulations were plotted such that the start of the impact stage occurs at the origin of the time axis for all the ribs in the series. Figure 5.45 shows the time histories of ΔP for the SV-LR-R10 simulation, plotted in a similar way. The drag force, F_d, on the rib can be calculated as F_d=A*ΔP, where A is the frontal area of the obstacle.

Similar to the case of a gravity current with a high volume of release, ΔP increases exponentially as the front starts interacting with the upstream face of each rib in the series. The end of the impact phase corresponds to the time when ΔP reaches its maximum value. One important difference is that in the simulations with a small volume of release, the peak values of ΔP at the end of the impact stage are decreasing much faster with the rank of the rib. For example, for the flow and geometrical conditions considered in both the SV-LR-R15 (Figure 5.43a) and the SV-HR-R15 (Figure 5.43b) simulations, the peak value is reduced by a factor close to two between two consecutive ribs (e.g., the maximum values of ΔP acting on Rib1, Rib2, Rib3, Rib4 and Rib5 in the SV-LR-R15 simulation are, respectively, 0.3 ρu_b^2, 0.15 ρu_b^2, 0.075 ρu_b^2, 0.04 ρu_b^2 and 0.025 ρu_b^2). By comparison, in the corresponding simulation with a high volume of release (LR-R15), the maximum values of ΔP acting on Rib1, Rib2, Rib3, Rib4 and Rib5 were 0.3 ρu_b^2, 0.3 ρu_b^2, 0.22 ρu_b^2, 0.2 ρu_b^2 and 0.19 ρu_b^2. Thus, though the maximum pressure force on the first rib is basically the same, the decay of the maximum force with the rank of the rib is much more important in the simulation with a small volume of release.

Even though the variation of ΔP during the impact stage on Rib1 is close to identical in the simulations with a large and with a small volume of release, the variation of ΔP during the transient stage is different. This is because the length of the head and dissipative wake region is much smaller in the SV-LR-R15 simulation. Because the discharge of heavier fluid past Rib1 is close to zero after the dissipative wake has passed the streamwise location at which the rib is situated, ΔP goes back to zero at t~15t_0 (see Figures 5.38a and 5.42). By contrast, in the LR-R15 simulation, the transient was longer and the value of ΔP at the end of the transient stage was different from zero. This is because heavier fluid from the tail was continuously convected over the rib in the simulation with a large volume of release. The variation of ΔP during the quasi-steady stage in the LR-R15 simulation was modulated by the passage of the backward propagating disturbances originating at the ribs situated downstream of Rib1. In the SV-LR-R15, the variation of ΔP around zero during the quasi-steady stage is modulated by the impact of the forward and backward moving disturbances with Rib1. For example, ΔP acting on Rib1 increases above zero around $t=22t_0$, when the forward moving disturbance S1 reaches Rib1 (see Figures 5.33 and 5.34c-d), decreases below zero when the backward moving disturbance S3 reaches Rib1 around $t=38t_0$ (see Figures 5.33 and 5.34e-f), and then increases again over zero around $t=53t_0$ when the reflected forward disturbance S2 reaches Rib1 (Figure 5.33).

The temporal variation of ΔP on the ribs of higher rank is qualitatively similar to that discussed for Rib1. The impact stage ends when the front reaches the upstream face of the rib and a splash of heavier fluid starts forming. The transient stage ends when the upstream end of the dissipative wake passes the rib. At that time, the discharge of heavier fluid convected over the rib is basically equal to zero (e.g., at $t=28t_0$ for Rib2 and $t=40t_0$ for Rib3 in Figures 5.38a and 5.38c). Consequently, ΔP=0 at the end of the transient stage. During the quasi-steady stage, ΔP can increase or decrease below zero for some limited amount of time, as a result of disturbances reaching the upstream or the downstream face of the rib. For example, a noticeable increase in ΔP acting on Rib2 is present around $t=40t_0$, when the forward propagating disturbance S1 containing fluid convected over Rib1 reaches the upstream face of Rib2 (see Figures 5.33 and 5.38d-e).

The effect of increasing the Reynolds number from Re=48,000 to $Re=10^6$ is that the maximum value of ΔP acting on the ribs at the end of the impact stage increases by 15-20%. This is due to the higher front velocity of the current in high Reynolds number simulation. The buoyancy inertia phase starts at a later $x_f/(H/2)$ in SV-HR-F simulation compared to SV-LR-F simulation as shown in Table 5.2. Therefore the front velocity of the current in SV-LR-F simulation starts decaying proportional to $t^{-1/3}$ earlier while the current in SV-HR-F is still transitioning from slumping phase to buoyancy-inertia phase. This creates further time lag between the ends of the impact stage in the two simulations as the rank of the rib increases.

The temporal variations of ΔP in the SV-LR-R10 simulation are, in most respects, qualitatively similar to the ones predicted in the SV-LR-R15 simulation. For example, Rib3 and Rib5 of SV-LR-R10 simulation situated at similar locations with Rib1 and Rib2 of SV-LR-R15 show similar trends of ΔP in time. There is a clear increase in ΔP with the impact and a decay toward zero values which occur in the „steady-state regime". Similar to SV-LR-R15 simulation the interaction of backward and forward propagating disturbances with the rib create oscillations around ΔP=0. However, there is an important difference between the SV-LR-R10 and SV-LR-R15 simulations that is ΔP plots in SV-LR-R10 simulation have a second peak that follows the first one associated with the impact stage. The maximum value of ΔP does not always occur at the end of the impact stage. This is observed only for the first couple of ribs in SV-LR-R10 simulation. For the higher rank ribs (e.g., Rib9, Rib15 and Rib19), the value of ΔP corresponding to second peak, reached during the transient stage, is larger than the value of ΔP at the end of the impact stage.

Figure 5.46 shows the time variations of the mean pressure on the upstream face of the ribs, $P^+/\rho u_b^2$, mean pressure on the downstream face of the ribs, $P^-/\rho u_b^2$, and mean pressure difference between the upstream and downstream faces of the ribs, $\Delta P/\rho u_b^2$, for Rib1 and Rib4 in the SV-LR-R15 simulation. To better understand the changes in the pressure during the current-rib interaction, contour plots showing the concentration, C, and pressure, $p/\rho u_b^2$, distributions in a vertical x-y plane around Rib1 and Rib4 at representative time instants are given in Figures 5.47 and 5.48, respectively.

The end of the impact stage corresponds to the moment when the front reached the upstream face of the rib and the splash starts forming near the top upstream corner of the rib as shown in Figure 5.47a for Rib1 and Figure 5.48b for Rib4. Most of the increase in ΔP during the impact stage is due to the increase of P^+ values at the front face of the rib. After the impact stage P^+ value starts decaying toward a quasi-steady state. On the other hand, the pressure values on the back face of the ribs, P^-, have small depression at the impact which follows by an increase in the values close to quasi-steady state observed for P^+. However due to the passage of disturbances, oscillations are observed around this quasi-steady state value for both P^+ and P^-. For example, at around $t\sim15.3t_0$, Rib1 has almost equal P^+ and P^- values. This is in accordance with the contour plots shown in Figure 5.47b which indicates that height of the current and the pressure on the front and back faces of Rib1 is similar at that instance of the simulation. This results in $\Delta P=0$ on the line plots given in Figure 5.46. In contrast, at around $t\sim23t_0$, there is an increase in the P^+ value for Rib1 which results in a net increase in ΔP value. This is due to the fact that at that moment in simulation, disturbance S1 reaches Rib1 and increases the pressure on the front face (See Figure 5.47c). Later in the simulation, a depression in net pressure is observed around $t=38t_0$. This is when the backward propagating disturbance S3 reaches Rib1 and increases the P^- value on the back face of the rib which is shown in Figure 5.47d. Similarly, interaction of forward propagating S2 in Figure 5.47e with Rib1 causes an increase in P^+ which results in a net increase in total pressure on this rib. Likewise, Rib4 experience an increase in P^+ and ΔP with the impact and pressure values decay slowly to a steady-state. Around $t=82t_0$, the disturbance S4 reaches the front face of Rib4 increasing P^+ which increases the net pressure on the rib. Due to the facts that some of the high-concentration fluid is trapped in between lower ranked ribs, the concentration levels decrease in the current due to the mixing, and the current slows down in time, the pressure values observed for Rib4 are almost 6 times smaller than the ones observed for Rib1.

Similar to the Figures 5.46, 5.47 and 5.48 showing Rib1 and Rib4 of SV-LR-R15, Figure 5.49 shows time variations of the mean pressure in the SV-LR-R10 simulation for Rib3 and Rib15 and Figures 5.50 and 5.51 show the concentration and pressure contours at the representative instances for these ribs.

The main difference of SV-LR-R10 simulation with the time history of ΔP in the simulations in which the height of the current is comparable to the rib height is the presence of a second peak of large ΔP values during the transient stage as mentioned earlier. For Rib3 the first peak in ΔP occurs with the impact at around $t\sim7.1t_0$ which follows shortly by a depression at $t\sim8.4t_0$ as soon as the current front hits the region between Rib3 and Rib4 as shown in Figure

5.50. When current reaches this region, P^- on the back face of Rib3 increases causing a decrease in the net pressure. At around $t \sim 10.8t_0$, ΔP peaks again due to an increase in the P+ at the front face of Rib 3. This is due to the passage of a large vortex, B1, over Rib3 which formed behind the head of the current as shown in Figure 5.50c. At around $t \sim 22t_0$ the front of the current reaches a region between Rib6 and Rib7 where vortex B1 collapses and pushes some amount of high-density fluid inside the current backward causing an overall increase in the P- for Rib3, Rib4 and Rib5 which results in a net decrease in ΔP values which is shown for Rib3 in Figure 5.49. A disturbance S2 reflected from Rib1 at $t \sim 7t_0$ reaches rear-end wall at $t \sim 20t_0$ passed over Rib1 at $t \sim 30t_0$ and over Rib2 at $t \sim 35t_0$ reaches Rib3 around $t \sim 39.7t_0$ as shown in Figure 5.50e and increases P+ and therefore ΔP values for Rib3. After $t > 46t_0$ net pressure over Rib3 stays around zero steady-state value till the end of the simulation time.

For Rib15 the first peak is observed when the current impacts the rib at $t \sim 42t_0$ (See Figure 5.51a). There is a small decrease in the ΔP until the front of the current starts interacting with Rib16. When the current reaches the region between Rib15 and Rib16, another peak is observed at $t \sim 45.6t_0$ due to the passage of billows in the dissipative wake region of the current over Rib15. Passage of dissipative wake increases the height of the current over the rib causing an increase in the pressure on the front face. Different from Rib3 the second peak in net pressure over Rib15 is comparable to the first one. After the second peak the ΔP value drops quickly as the passage of the wake region similarly increases the P^- value on the back face of the rib. Until the passage of the dissipative wake is complete, the net pressure ΔP remains constant between $50 < t/t_0 < 55$. Later the ΔP decreases to zero steady-state value which it remains at until the end of the simulation time.

5.8 Energy budget and dissipation rate

The time evolutions of the kinetic energy E_k, potential energy E_p and integral of the total dissipation rate, E_d (4.10) are plotted in Figure 5.52a for the simulations conducted at Re=47,800 with flat bed and with obstacles of height D=0.15(*H/2*). The three terms are nondimensionalized by E_{p0}. A first regime characterized by the conversion of potential energy into kinetic energy is present at the start of all the simulations. This region roughly corresponds to the duration of the acceleration phase ($t<2.5t_0$, $x_f/(H/2)<1.7$). The process is essentially inviscid, as not much dissipation takes place during this regime ($\varepsilon<<dE_k/dt$). By this time around 55% of the initial potential energy has been converted into kinetic energy and the dissipative losses are very small (<4%).

During the time the current propagates over the initial flat part of the channel bottom and does not feel the presence of the first obstacle, the temporal variation of the three terms is identical in all the three simulations. The current starts interacting with the first obstacle around $t=5t_0$, during the slumping phase, when $x_f/(H/2)\sim3$. As expected, in the simulations with obstacles, once the current starts interacting with the first obstacle, the decay of the kinetic energy is faster compared to the flat bed case because of the additional obstacle-induced drag force acting on the body of the current. Conversely, the decay of E_p with time is slower.

The variation of E_d with time is close to identical in the SV-LR-F and SV-LR-R15 simulations. This can be surprising at first, as once expects a gravity current propagating over obstacles to be more dissipative. However, the current in the SV-LR-F simulation propagates faster. Thus, its length is larger at a given non-dimensional time. To make the comparison more meaningful, the variations of E_k, E_p and E_d are plotted function of the front position, $x_f/(H/2)$, in Figure 5.52b. When plotted with the front position, E_d increases faster in the simulation with ribs. A close inspection of the variations of E_d, shows that the slope of E_d is larger in the SV-LR-R15 simulation over three intervals of length 1(H/2) that start at the location of the first three ribs in the series ($5<x_f/(H/2)<6$, $8<x_f/(H/2)<9$ and $11<x_f/(H/2)<12$). Thus, during the interaction of the front with a new rib, the formation of the splash of heavier fluid, its convection over the top of the rib and its interaction with the channel bottom, the dissipation rate $\varepsilon=dE_d/dt$ is larger in the simulation with ribs. The dissipation rates in the two simulations become roughly equal once the front of the current regains its usual shape after the current has passed a new rib in the SV-LR-R15 simulation. This happens in the SV-LR-R15 simulation when the front is situated at a distance of about 1(H/2) from the rib. The differences are relatively smaller when the front overtakes Rib4 and Rib5. In the later stages of the propagation of the gravity current (x_f/(H/2)>12), E_d is about 8% larger in the SV-LR-R15 simulation compared to the SV-LR-F simulation.

The decay of E_k with x_f is significantly faster in the simulation with ribs compared to the flat bed case. The larger decay of E_k is accompanied by a smaller decay of E_p and, as was previously discussed, by a faster increase of E_d. In the case dunes are present at the channel bottom, the decay of E_k with x_f is very similar to the one predicted in the SV-LR-R15 simulation. However, the decay of E_p with x_f is not as fast as in the SV-LR-R15 simulation because of the fact that the increase of E_d with x_f is slower. This is expected, as dunes of equal height to that of the ribs and disposed with the same spacing are expected to induce a smaller drag force per unit length compared to the ribs.

Similar to the case of gravity currents with a large volume of release (e.g., see Figures 4.36 and 4.40), the variations of E_k and E_p with time and with x_f in the SV-LR-R15 and SV-LR-D15 simulations are subject to large-scale modulations induced by the interaction of the current with the obstacles. The explanation is similar. As the front approaches the obstacle, the head starts decelerating and the kinetic energy starts decreasing in that region. As the splash forms, the downstream part of the current containing heavier fluid raises and the potential energy in the front region increases. The kinetic energy increases again after the splash was convected over the obstacle and the head regains its usual shape. During this time, the heavier fluid convected over the top of the rib plunges toward the channel bottom and reduces its potential energy. Thus, an increase in E_p is associated with a decrease in E_k. This is clearly demonstrated by the analysis of the time variations of the rates of increase of E_p and E_k. Figure 5.53 shows that the two variations are out of phase. A maximum in dE_k/dt is associated with a minimum in dE_p/dt.

For example, the evolution of these two terms around the time the current interacts with Rib1 is shown in Figure 5.53b. Between $9t_0$ and $9.5t_0$, the fluid at the head of the current is strongly decelerating as the front interacts with the upstream face of Rib1. dE_k/dt is negative and its magnitude increases sharply. Then, dE_k/dt remains negative until $11t_0$, when the fluid from the splash that was convected over the front reaches the channel bottom. Once this happens, the jet-like flow starts forming and the fluid at the front starts accelerating. dE_k/dt becomes positive again and its magnitude peaks around $12.5t_0$, when the front regains its usual shape, as it propagates toward Rib2. Comparison of Figures 5.53b (Rib1) and 5.53c (Rib3) show that the time variations of dE_k/dt and dE_p/dt remain qualitatively similar as the current passes the ribs of higher rank.

By contrast, the time variations of E_d (Figure 5.52) and ε (Figure 5.53) are not subject to large-scale oscillations during the time the front overtakes an obstacle. In both simulations, ε increases rather fast, in a non-monotonic way, until $x_f/(H/2)\sim4$. Then, is starts decreasing in a non-monotonic way. The variation of ε with x_f is close to exponential for $x/(H/2)>4$.

The plots in Figure 5.54 show the effect of increasing the Reynolds number, from Re=48,000 to Re=10^6, on the variation with x_f of the terms in the energy equation is fairly small in the simulations with flat bed and with ribs. E_d increases at a slower rate in the low Reynolds number simulations. This is expected, as the dissipation rate is proportional to 1/Re. In the flat bed case, the smaller increase of E_d is mainly compensated by the larger values of E_k when the fronts are situated at the same location in the two simulations. This is consistent with the fact that the front velocity is higher in the SV-HR-F simulation compared to the SV-LR-F simulation. Similar to the scale effects observed in the simulations with a large volume of release (Figure 4.39), the variation of E_p with x_f is close to identical in the two simulations, at least until the start of the buoyancy-inertia regime, when E_p becomes slightly larger in the SV-HR-F simulation. In the simulations with ribs, after the start of the buoyancy-inertia phase ($x_f/(H/2)\sim8.5$), the smaller values of E_d in the high Reynolds number simulation are compensated by the larger values of E_k and of E_p. The larger values of E_k are consistent with the larger front velocity in the SV-HR-R15 simulation compared to the SV-LR-R15 simulation. The larger values of E_p for a certain value of x_f are consistent with results in Figure 5.11a that show the thickness of the layer containing fluid of higher density than that of the ambient fluid is slightly larger in the SV-HR-R15 simulation, especially in between the head and the second rib behind the front.

In the flat bed simulation, when E_p, E_k and E_d are plotted vs. time or x_f in log-linear scale, the curves show a variation which is close to linear past the end of the slumping phase (e.g., see Figure 5.55). This is consistent with the findings of Ooi et al. (2009) for full-depth release gravity currents with a small volume of lock fluid.

When plotted vs. x_f, a similar regime, in which the variations of E_p, E_k and E_d are close to logarithmic (e.g., $E_p/E_{p0}=a+b*\ln(x_f/(H/2))$, etc.), is present in the simulations with ribs. The identification of the logarithmic regime and of its extent are easier to do for the SV-LR-R10 simulation, in which the ribs are relatively small and the large-scale modulations in the variation of E_p and E_k associated with the head overtaking a rib are quite small. For the energy terms, the logarithmic regime starts during the buoyancy-inertia phase, when the front is situated around $x_f/(H/2)=10$. The logarithmic regime continues even after the current transitions to the drag-dominated phase, when $x_f/(H/2)\sim20$.

A logarithmic region is also observed in the variation of E_d with x_f in the SV-LR-R15 simulation. The logarithmic region starts around the same front position at which the transition to the buoyancy-inertia phase is over (~7.5(H/2)) and continues during the evolution of the current during the drag-dominated phase. The logarithmic variations of E_p and E_k are not so obvious because of the large-scale oscillations induced by the presence of the ribs. However, if one eliminates these oscillations, the decays of E_k and E_p appear to be logarithmic, past the end of the transition to the buoyancy-inertia phase. This is more clearly seen in Figure 5.55a where the troughs of the $E_p(x_f)$ curve in the SV-LR-R15 simulation are situated on top of the $E_p(x_f)$ curve for the SV-LR-F simulation. As already commented, the $E_p(x_f)$ curve in the SV-LR-F simulation is very close to a straight line when plotted in linear-log scale.

The spatial distributions of the non-dimensional spanwise-averaged local dissipation rate $\varepsilon_r/(u_b^3/(H/2))$ in the SV-LR-R15 simulation at representative time instances are given in Figure 5.56. In order to show the difference between flat bed case from the case in which obstacles are present, Figure 5.57 shows the local dissipation rate, $\varepsilon_r/(u_b^3/(H/2))$ for SV-LR-F at one instance toward the end of the simulation time. Figure 5.58 shows the streamwise distributions of depth integrated local dissipation rate, $\varepsilon^{23}(x_1)/(u_b^3(H/2))$ in the SV-LR-R15 simulation are given at same time instances as in Figure 5.56.

Before the current interacts with the rib most of the dissipation occurs at the head region of the current. As the current interacts with the first rib as shown in Figure 5.56b, the dissipation is largest in the region situated in between the front and the first rib. This is because the impact of the current with the rib, the formation of the splash of high-density fluid and its interaction with the channel bottom after its convection past the top of the rib result in high velocity gradients and increased dissipation. This is also observed in the line plots in Figure 5.58b where most of the dissipation is around $5<x_f/(H/2)<6$ where the current re-attaches with the flat part of the channel. Figure 5.56c shows a comparison between SV-LR-F and SV-LR-R15 simulation. The gravity current on the flat bed has a dissipative wake region longer than the one propagating over ribs. Most of the dissipation occurs for both simulations around the head of the current. Different from the flat bed case, the part of the current that got trapped behind Rib1 in simulation SV-LR-R15 has a disturbance propagating toward the rear-end wall which causes additional dissipation at the tail of the gravity current. At later stages of the simulation most of the dissipation still takes place around the head of the current and resembles qualitatively the earlier stages (compare the head region of the current in Figures 5.56b and 5.56e), however the dissipation values in the current depletes significantly as the current propagates in time. Very little local dissipation is observed as the current impacts the rib at later stages of the simulation (see Figure 5.56d). The dissipation observed over the top surface of the Rib4 in Figure 5.56d does not contribute significantly to the total dissipation in the current. Almost no dissipation is observed around lower ranked ribs in the simulation SV-LR-R15. This is in contrast with the large volume of release case for which the dissipation around all the obstacles behind the head of the current is as high as the front of the current due to the jet-like flow feature in these simulations. However, in small volume of release simulations the lack of jet-like flow feature around the lower ranked obstacles well behind the front of the current and much lower velocities at the tail of the current causes almost no dissipation at these regions. Similarly no dissipation values are observed at the tail of the current in SV-LR-F simulation in Figure 5.57.

Finally, Figure 5.57 shows the distribution of ε_r at t=40t$_0$ (x$_f$/(H/2)=14.8) in the SV-LR-F simulation. The regions of strong amplification of ε_r correspond to the dissipative wake and the cores of the large-scale billows situated behind it. Though in Figure 5.56d the front already started interacting with Rib4, the differences in the distribution of ε_r between Figure 5.56d and Figure 5.57 are representative of the ones observed between currents propagating over ribs and a flat bed. For example, the distance behind the front over which the interfacial billows maintain their coherence is, in average, about 30% larger than the one observed in the SV-LR-R15 simulation, for the same position of the front. One should mention that in the SV-LR-R15 simulation this distance varies rather significantly with the relative position of the front to the closest rib. The shape of the head in the SV-LR-R15 simulation is similar to the one observed in the flat bed simulation, when the front is situated between 1.5(H/2) and 2.7(H/2) from the last rib it passed.

5.9 Bed friction velocity

As in the simulations with a large volume of release, the number of mesh points in the spanwise direction in the low Reynolds number simulations with a small volume of release (SV-LR) was sufficient to accurately resolve the streamwise velocity streaks. This was not the case in the high Reynolds number simulations (SV-HR), in which the streaks are expected to have a thickness that is smaller than the spanwise grid spacing used in the simulations. Still, the distributions of the spanwise averaged values of u_τ/u_b are expected to be reasonably well predicted, as these distributions are determined, to a large extent, by the large-scale flow features present in the flow.

The changes in the distributions of the bed friction velocity for currents with a small volume of release propagating over a flat bed were analyzed by Ooi et al. (2009). They found that a region containing high and low streamwise velocity and vertical vorticity streaks forms beneath the head and dissipative wake during the slumping phase. The tail does not contain well-defined streaks. The length of the region containing streaks increases until the bore overtakes the front. Then, as the current transitions to the buoyancy-inertia phase, the length of the streaky region remains approximately constant. Past the initial stages of the buoyancy-inertia phase, the length of the region containing streaks starts decaying slowly. Ooi et al. (2009) also found that for currents with $Re=10^4-10^5$, the average width of the streaks behind the front was about 40 non-dimensional wall units and their length was around 1000 wall units. Compared to the case of gravity currents with a large volume of release, the interfacial billows are much more coherent and play a larger role in modulating the increase and decrease of the bed friction velocity in the streamwise direction. As, in most cases, the billows extend over the whole width of the domain, large spanwise bands of low and high u_τ are observed over the dissipative wake and the downstream part of the tail.

The present section focuses on describing the changes in the bed-friction velocity distributions between the buoyancy-inertia phase and the drag dominated phase for currents with a small volume of release propagating over large-scale roughness elements. Due to the small volume of release, the slumping phase is very short. Thus, in all the simulations discussed in this chapter most of the sediment is entrained after the transition to the buoyancy-inertia phase has started. The effect of the shape of the obstacles is investigated by comparing the distributions in the SV-LR-R15 and SV-LR-D15 simulations. The effect of the relative size between the head of the current and the roughness elements is investigated by comparing the distributions of u_τ in the SV-LR-R15 and SV-LR-R10 simulations. In both cases, these distributions are compared to those obtained for a current propagating a flat surface (SV-LR-F). Finally, scale effects are investigated by comparing the results of the low (SV-LR) and high (SV-HR) Reynolds number simulations with flat bed and with dunes and ribs of height $D=0.15(H/2)$.

The near-wall flow structure for the case when roughness elements in the form of dunes are present at the channel bottom is visualized in Figure 5.59 at the start of the buoyancy-inertia phase ($x_f/(H/2)=7.7$). The instantaneous vertical vorticity contours at the bed surface are shown in Figures 5.59a and 5.59b. The view is lateral and from above the current in Figure 5.59a. The view is from below the current in Figure 5.59b. The gravity current is visualized using concentration contours in Figure 5.59c. The bed friction velocity distribution is shown in Figure 5.59d. The gravity current is visualized from above on an x-z plane using concentration contours in Figure 5.59e. Figure 5.60 shows similar information when the current propagates during the turbulent drag-dominated phase ($x_f/(H/2)=18.2$). The front velocity is close to three time smaller when $x_f/(H/2)=18.2$ compared to when $x_f/(H/2)=7.7$.

Similar to the case of gravity currents with a large volume of release propagating over ribs and dunes, streamwise-oriented streaks of positive and negative vertical vorticity are present in the near bed region, starting at the front. These vertical vorticity streaks are induced by the streaks of high and low streamwise velocity present at a small distance above the channel bottom. The length of the region containing streaks is much smaller in the case of currents with a small volume of release. Both during the buoyancy-inertia (Figure 5.59b) and the drag-dominated phase (Figure 5.60b), well-defined streaks are forming only beneath the head and dissipative wake regions. This is why the extent of the region containing well-defined streaks decays slowly in time, as the dissipative wake and head regions shrink progressively. The shrinkage is mainly due to the loss of high-density fluid with the large-scale billows shed behind the head. However, the distributions of the vertical vorticity at the channel bottom and of the bed shear stress remain qualitatively similar during the buoyancy-inertia phase (Figure 5.59) and drag dominated phase (Figure 5.60). At all stages of the propagation of the current, the positions of the streaks of high streamwise velocity situated immediately behind the front correlate well with those of the primary and secondary lobes forming at the front. This correlation is observed clearly from the comparison of the concentration contours in Figures 5.59e and 5.60e to the bed friction velocity distribution in Figures 5.59d and 5.60d, respectively.

Another important observation is that less well-defined streaks of high and low vertical vorticity extend over a longer region, at least during the buoyancy-inertia phase. The region where streaks can be observed covers the downstream part of the tail containing fluid that continues to move downstream with a streamwise velocity that is high enough to maintain the streaks. For example, streaks can be detected starting at the crest of the first dune (x/(H/2=5)), where a thin layer of higher concentration fluid is moving over the lee side of the dune with a high velocity. Most of the heavier fluid moving on the upslope side of Dune1 has decelerated to levels where streaks cannot be sustained. That fluid is trapped between the rear end-wall and the crest of Dune1. Still, the magnitude of the vertical vorticity remains relatively high, suggesting that the flow trapped in between the rear end-wall and the crest of Dune1 is still turbulent. By contrast, in Figure 5.60 the vertical vorticity is close to zero in the three cavity-like regions present upstream of the crest of Dune3. This indicates that the turbulence intensity is much lower. However, the trapped fluid is not steady. Its movement is relatively uniform in the spanwise direction and is associated with the passage of the forward and backward propagating disturbances on the interface and with the general oscillatory movement of the fluid trapped within the cavity-like region. Due to these motions, spanwise bands of moderately high values of the bed shear stress are observed in the tail (Figure 5.60d). The near-bed turbulence is stronger in the cavity-like region between the crests of Dune3 and Dune4. However, no streaks are detected.

The presence of the streaks of high and low streamwise velocity in the vicinity of the bed surface, beneath the head and the dissipative wake, is also the reason why streamwise-oriented streaks are present in the bed-friction velocity distributions over the same regions. As discussed for the case of gravity currents with a large volume of release propagating over large-scale roughness elements, the length of the region containing bed-friction velocity streaks behind the front appears to be in many cases shorter than the one containing vertical vorticity streaks. This is mainly a consequence of the scale used to represent the bed friction velocity contours. In fact, the bed friction velocity streaks are still present, but the presence of a large billow or the large amplification of the bed friction velocity on the lee side of the dunes are the reason why the bed friction velocity streaks appear to extend over shorter distances behind the front. The vertical vorticity has the advantage that is less sensitive to the relatively uniform increase or decrease in mean values of the streamwise velocity in the streamwise direction.

Spatial distribution of bed friction velocity is very important in estimating the sediment entrainment from the channel bed. Figures 5.61 and 5.62 show spatial distribution of the bed friction velocity, u_τ/u_b, during the buoyancy-inertia phase when the front position is $x_f/(H/2)=8$ and during the turbulent drag-dominated phase when the front position is $x_f/(H/2)=16.5$, respectively, for SV-LR-F, SV-LR-D15 and SV-LR-R15 simulations. In order to understand the position and shape of the current better, the concentration contour plots on x-y plane accompanies the bed shear velocity distribution.

At a given time (front position), the distributions of u_τ in the simulations with a flat bed and with ribs are close to identical until the front starts interacting with the first rib in the SV-LR-R15 simulation. For example, the streamwise distribution of the spanwise-averaged bed friction velocity in the SV-LR-F, SV-LR-R15 and SV-LR-D15 simulations given in Figure 5.64a shows that the bed friction velocity for SV-LR-F and SV-LR-R15 are very similar at around $t=8t_0$.

The front velocity in slumping phase in the partial depth release simulation with a flat bed is $Fr_f=U_f/u_b \sim 0.53$. The maximum bed friction velocity is around $0.04u_b$. By comparison, in the LR-F simulation with a full depth of release the front velocity during the slumping phase was $0.45\sqrt{2}=0.63$ and the maximum value of u_τ was $0.04\sqrt{2}=0.056$ (Figure 4.55a) (the factor of $\sqrt{2}$ is introduced due to the fact that in this chapter the length scale is H/2 rather than H). The ratio between the front velocities in the LR-F and the SV-LR-F simulations is 1.19, while that of the maximum values of u_τ is close to 1.4.

Comparison of Figures 5.61a and 5.61c shows that the distribution of u_τ over the head and dissipative wake is qualitatively and quantitatively similar in the simulations with a flat bed and with ribs, at time instants when the front is situated at more than (H/2) from the last rib it passed but has not start interacting with the next rib.

However, the distribution of u_τ behind the dissipative wake, and in particular the position of the spanwise bands of high u_τ values, is quite different in the three simulations. This is because the positions and the strengths of the disturbances propagating on the interface of the gravity current are different. The direction of propagation of the bands of high u_τ values is very difficult to infer from the concentration contours. This is in contrast to case of the simulations with a large volume of release where the flow in the tail propagates in general downstream. For example, the band of high u_τ values centered around x/(H/2)=3 in the SV-LR-R15 simulation in Figure 5.61c is due to the passage of the backward propagating disturbance S2.

There is an important observation to be made in Figure 5.64 that u_τ decreases close to linear over the head and dissipative wake, starting at the front, in the SV-LR-F simulation in which the current transitions to the buoyancy inertia phase. For instance, in Figure 5.64b the decay of u_τ starting from the front of the current situated at x/(H/2) ~ 8.5 to the end of the dissipative wake region, which is around x/(H/2) ~ 5, is close to linear. For x/(H/2)<5 u_τ over the tail of the current is almost horizontal with some oscillation around the mean. The streamwise distributions of u_τ in the SV-LR-F simulation remain qualitatively similar as the current advances during the buoyancy-inertia phase. Similar phenomena are observed at later stages such as in Figure 5.64c. The bed friction velocity peaks at the front and then decays, close to linear, until x/(H/2)~8. The decay is non-monotonic due to the presence of interfacial billows (e.g., at x/(H/2)=15.3) and flow disturbances (e.g., FD2 which is responsible for the amplification of u_τ around x/(H/2)=12.5 and FD1 which is responsible for the amplification of u_τ around x/(H/2)=6, see also Figure 5.30a).

In the presence of dunes over the channel bottom, the values of u_τ peak immediately in the trough region, where the flow is strongly accelerated and transitions to supercritical as well as at the head of the current as shown in Figure 5.61b at around x/(H/2) ~ 5.1. The u_τ values decrease over the upslope of the next dune because the incoming heavier fluid has a significant amount of streamwise momentum and tries to separate.

In the SV-LR-D15 simulation, the streamwise variation of u_τ is much more complex. The current is propagating in the drag dominated phase. This is mainly due to the presence of strong flow disturbances propagating in between the crests of the dunes. Figure 5.63 visualizes the distribution of the concentration and streamwise velocity in between the front and the crest of the second dune, when $x_f/(H/2)=16.2$. The interface with the ambient fluid is superimposed on the contours of the streamwise velocity. Similar to the case of currents with a large volume of release propagating over dunes (e.g., see Figure 4.10c and 4.10d), the decay of the velocity around $x/(H/2)=15.2$ is due to the change in the direction of the jet-like flow forming past the lee side of Dune4 after it reaches the trough region. The jet like-flow is oriented slightly away from the bed surface around $x/(H/2)=15.2$. However, the near bed flow does not separate and the streamwise velocity remains positive. This explains the strong decay of u_τ around $x/(H/2)=15.2$ in Figure 5.64c. The variation of u_τ in between the crest of Dune4 ($x/(H/2)=14$) and the region where the jet-like flow plunging toward the trough reaches the bed surface and changes direction ($x/(H/2)=14.8$) is similar to the one observed in Figure 5.64b when the front passed Dune2. As the heavier fluid convected past the crest tries to detach, the bed friction velocity decays on the lee side of the dune. Interestingly, the values of u_τ at the front are slightly smaller than the two peaks situated close to the crest and trough of Dune3. However, all these values are smaller than the peak values observed in Figure 5.64b ($x_f/(H/2)=8.6$) at a time when the current was still in the buoyancy-inertia phase. This decay is consistent with the continuous decay of the front velocity with the front position and with time past the end of the slumping phase.

As shown in Figure 5.63, the streamwise velocity is negative in between the crest of Dune4 and the downstream end of the lee side of Dune3 ($x/(H/2)=11.4$). This coincides with the position of the disturbance S5 that originated due to reflection of some of the heavier fluid reaching the crest of Dune4. The flow past the crest of Dune3 is oriented in the positive streamwise direction. However, in between $x/(H/2)=10.4$ and $x/(H/2)=9.4$ the flow close to the bed propagates toward the rear end-wall due to partial reflection at the crest of Dune3 of the S1 disturbance that originated close to the end-wall and passed Dune1 and Dune2. The near-bed flow is oriented again in the positive streamwise direction between x/(H/2)=8.6 and x/(H/2)=9.4 because of the passage of the forward propagating disturbance S4 that originated at the crest of Dune3, propagated backward and partially reflected as it encountered the crest of Dune4. The flow changes again direction on the downstream part of the lee side of Dune2. The flow is oriented in the positive streamwise direction over the crest of Dune2. This is because past the crest of Dune2, the layer of mixed fluid close to the interface with the ambient fluid is moving downstream, while the heavier fluid at the bottom (if one ignores the small patch of heavier fluid moving downstream with S4) tries to move downstream and to climb the lee side of Dune2 until the point where it loses its momentum. As for Dune3 and Dune4, the values of u_τ are strongly amplified over the crest region before the flow detaches. The levels of u_τ close to the crest of the first three dunes behind the front are similar.

The streamwise variation of u_τ continues to be very complex as the streamwise velocity close to the bed changes sign several times over the upstream part of the tail. However, as the levels of u_τ are overall smaller, one expects a relatively small amount of sediment will be entrained from the bed over this region. Meanwhile, the values of u_τ at a certain streamwise location vary very little in the spanwise direction (e.g., see Figure 5.62b for x/(H/2)<8), suggesting the flow movement is mostly due to the passage of the flow disturbances and the turbulence is weak.

The main difference between the distributions of u_τ during the drag-dominated regime in the SV-LR-D15 and SV-LR-R15 (the comparison is done for the same position of the front) is the significantly smaller amplification of u_τ at the downstream of the crest of the first roughness element behind the front (e.g., compare the two distributions in Figures 5.64b-c). The smaller value of u_τ behind the front is due to the smaller velocity at the lee side of the Rib4 in the SV-LR-R15 simulation compared to the accelerated jet-like flow in the trough of Dune4 in SV-LR-D15 simulation. This is due to the larger drag force per unit length induced by the ribs. The front of the current slows down significantly in the presence of rib compared to the one propagating over dunes. The overall values of u_τ in the simulations with dunes and ribs of same height become much more comparable over the upstream part of the current, up to the crest of the second roughness element behind the front. This is because the velocity over the tail region for both simulations is very low, causing a reduction in the shear velocity over the bed at this region. The local Reynolds number of the current is so low that there are no high and low velocity streaks formed which indicates that the tail region of the current has almost no turbulence. Only the continuous reflection of disturbances formed due to the presence of roughness elements causes high shear velocity bands over the tail of the current over very short distances. Most of these disturbances are stronger in the SV-LR-R15 simulation compared to the ones in SV-LR-D15 simulation. This is because of the larger bluntness of the ribs causes more reflection compared to the streamlined shape of dunes which allows easier passage of the current.

Next, the focus is on the bed friction velocity distribution in the SV-LR-R10 simulation in which the height of the current is much larger than that of the ribs. So, one expects the distributions of u_τ will shear some common features with those observed for a current propagating over a flat bed and some with those for a current propagating over ribs of much larger relative height.

The instantaneous distributions of the non-dimensional bed-friction velocity contours, u_τ/u_b, are shown in Figure 5.65 for the SV-LR-F, SV-LR-R10 and SV-LR-R15 simulations at a time when the front position is close to x_f=9(H/2). The current is at the start of the buoyancy-inertia regime in the three simulations. Figures 5.66 (SV-LR-R10), 5.62a (SV-LR-F) and 5.62c (SV-LR-R15) compare the distributions of u_τ/u_b for the three simulations when x_f~16.5(H/2). The current is in the drag-dominated phase in the SV-LR-R15 simulation, but still in the buoyancy-inertia phase in the SV-LR-F and started its transition toward the drag-dominated regime in the SV-LR-R10 simulation.

Qualitatively, the largest differences in the distributions of u_τ occur behind the front. The smaller spacing of the ribs in the SV-LR-R10 simulation does not allow a sufficient distance for the streaks to develop after the nose of the current reattaches and the near-bed flow behind the front resembles again that in a current propagating over a flat surface. The absence of well defined streaks behind the front (e.g., see Figures 5.65b and 5.66) is a general characteristic of the gravity current flow in the SV-LR-R10 simulations at all stages of its evolution, including during the drag-dominated phase.

One interesting observation, is that the backward propagating disturbance S2 situated at x/(H/2)~1.8 in Figure 5.65c is so strong that it induces the formation of streaks behind it, similar to those forming behind the front of the current, when the front is situated at a sufficient distance downstream of the last rib that has passed. For example, similar to the SV-LR-R10 simulation, streaks are not present behind the front in the SV-LR-R15 simulation in Figure 5.65c, where the flow at the head is still strongly disturbed as a result of its interaction with Rib2. However, as expected, the near-bed flow is strongly turbulent in the SV-LR-R10 and SV-LR-R15 simulations over the head and dissipative wake, as shown by the high variability of u_τ in the spanwise direction. In fact, the level of turbulence is higher in the SV-LR-R10 simulation, as the small ribs induce the formation of separated shear layers on the top of the ribs, inside which small, but very energetic, turbulent eddies are shed at a high frequency. The situation is similar during the transition to the drag-dominated phase, as shown by the distribution of u_τ in Figure5.65. The region of high turbulence extends not only beneath the head and dissipative wake, but also over the downstream part of the tail. The distribution of u_τ becomes more uniform in the spanwise direction for x/(H/2)<8. Similar to the SV-LR-R15 simulation (Figure 5.62c), the passage of the flow disturbances can induce large values of u_τ on the bed (e.g., around x/(H/2)=1.5 and 3.5 in Figure 5.65), comparable to those beneath the head.

Figure 5.67 shows the distributions of the spanwise-averaged values of u_τ/u_b in the SV-LR-R10 simulation at representative moments during the evolution of the gravity current, from the end of the acceleration phase to the drag-dominated phase. In some cases, comparison with the distributions of u_τ/u_b in the other two simulations is provided.

Figure 5.67a shows that, during the acceleration phase, u_τ/u_b reaches a larger value (~0.055) just behind the front in the SV-LR-R10 simulation with a full depth of release compared to the other two simulations with a partial depth of release. This is not surprising, as the front velocity is expected to be larger for gravity currents with a full depth of release (e.g., see Shin et al., 2004). The value u_τ/u_b~0.055 is very close to the one observed during the slumping phase in the LR-F simulation with a large volume of release conducted at a comparable Reynolds number in Chapter 4 (u_τ/u_b~$0.04\sqrt{2}=0.056$ in Figure 4.55a), for which the front velocity during the slumping phase is expected to be close. The current is still in the acceleration phase when the front reaches the first rib (x/(H/2)=3) in the SV-LR-R10 simulation. Once the first rib is reached, the front velocity starts decaying. This is the reason why u_τ/u_b at the front decays pretty rapidly to values close to 0.025, at times when the front recovers its usual shape in the near bed region (e.g., see Figures 5.67e, 5.67f). However, during the times when the front overtakes a new rib, or is situated at a small distance downstream of it, the values of u_τ/u_b at the front can be considerably lower (e.g., around 0.02 in Figures 5.67b and 5.67c).

Especially during the initial stages of the propagation of the current after reflection of the bore at the endwall, regions of large amplification of u_τ/u_b can form behind the front as a result of the formation of large-scale billows and the passage of the reflected bore (e.g., at x/(H/2)~0.8 in Figure 5.67b and at x/(H/2)~1.7 in Figure 5.67c).

There is also an overall reduction of the values of u_τ/u_b over the whole length of the current and, in particular, at the front. This reduction is due to the decay of the front velocity and kinetic energy during the later stages of the buoyancy-inertia phase and during the drag dominated phase. The decay is clearly observed in Figure 5.67 for x_f/(H/2)>14.

If one discards the local variation of u_τ/u_b around each rib and the temporary amplification associated with the passage of a flow disturbance, the results in Figures 5.67e to 5.67h show that, past the start of the buoyancy inertia phase (t~10t_0), the values of u_τ/u_b over the upstream part of the tail are relatively constant. The distributions of u_τ/u_b in the same figures show that, starting at the front, the decay of the bed friction velocity is close to linear (see dashed lines in Figure 5.67) over the head, dissipative wake and the downstream part of the tail region. The slope decreases slowly as the current advances due to the large dilution of the fluid contained inside the head and dissipative wake regions (Figure 5.13) and the associated decay of the front velocity.

The spanwise averaged distributions of u_τ/u_b are plotted in Figures 5.68a, 5.68b and 5.68c for the high Reynolds number simulations with a flat bed and with dunes and ribs of height D=0.15(H/2). The distributions are plotted at a time instant when the front is close to x/(H/2)=17. The gravity current is within the buoyancy-inertia phase in the simulations with a flat bed and within the drag dominated phase in the simulations with ribs and dunes. In the same figures, the distributions obtained in the corresponding LR simulations multiplied by a factor α=0.43 are also shown. To allow a direct comparison, the distributions of u_τ/u_b in the LR simulations are plotted at time instants when the front position is very close to x/(H/2)=17. Table 5.3 gives the value of the front velocity when $x_f/(H/2)$=17. Despite the larger velocity gradients at the bed, the values of u_τ/u_b are smaller in the higher Reynolds number (HR) simulations. This is mainly because the bed friction velocity is proportional to the square root of the molecular viscosity, so u_τ scales with $Re^{-1/2}$. Qualitatively, a good agreement is observed between the distributions of u_τ/u_b at the two Reynolds numbers. This is true for both the simulations with a flat bed and with a deformed bed.

The value of α was determined such that the best agreement between the distributions of u_τ/u_b is obtained in the two simulations with a flat bed (SV-LR-F and SV-HR-F). The comparison shows that, in a very good approximation, the HR distribution of u_τ/u_b over the whole length of the current can be obtained by simply multiplying the LR distribution by a constant factor. Most of the differences are due to the different positions of the disturbances propagating over the body of the current.

The value of α=0.43 is smaller than the one predicted in the simulations with a high volume of release (α=0.58). This is somewhat expected, as the Reynolds numbers defined with the front velocities (u_f=0.22u_b, Re_f~5,000 in SV-LR-F and u_f=0.32u_b, Re_f=150,000 in SV-HR-F, see Table 5.3) and the height of the head of the current are smaller than those in the LR-F

(Re_f~11,000) and HR-F (Re_f~250,000) simulations. The bed friction factor variation with the Reynolds number over the hydraulically smooth regime is larger at lower Reynolds numbers.

Figures 5.68b and 5.68c show that, when nondimensionalized using the buoyancy velocity and after the distributions in the LR simulations are multiplied by the same value of α determined based on comparison of the u_τ/u_b distributions in the flat bed simulations, the bed friction velocity distributions in the simulations with ribs and dunes are qualitatively and quantitatively similar. One should also point out the front velocity is relatively close in the low and high Reynolds number simulations with dunes or ribs.

Finally, past the initial stages of the buoyancy inertia phase, similar to the SV-LR-R10 simulation, the distribution of u_τ/u_b can be considered to be close to linear for a certain distance behind the front. The length of the region of relatively linear decay of u_τ/u_b increases with the Reynolds number (e.g., from about 9(H/2) in the SV-LR-F simulation to about 10.5(H/2) in the SV-HR-F simulation when $x_f/(H./2)=17$). The effect of the Reynolds number of the distributions of u_τ/u_b in the simulations with relatively large ribs and dunes is less clear. In the simulations with dunes, after multiplication with α of the SV-LR-D15 distribution, the levels of u_τ/u_b at the head of the current are similar in the low and high Reynolds number simulations. However, the levels of u_τ/u_b tend to be larger over the downstream part of the tail in the high Reynolds number simulation. In the case of ribs scale effects are negligible.

The good qualitative similarity between the distributions of u_τ/u_b in the simulations with a flat bed and with roughness elements and the scaling of these distributions with Re, means that experimental and numerical investigations of gravity currents with a small volume of release conducted at lower Reynolds numbers (Re_f~10^4 during the slumping phase) can be used to understand the behavior and sediment entrainment capacity of gravity currents at much higher Reynolds numbers, that are within the range encountered in the field. Unfortunately, an a priori accurate estimation of the value of α was not possible.

5.10 Sediment entrainment capacity

The distributions of u_τ/u_b were analyzed in the previous section. Figure 5.64 contains the horizontal line corresponding to $u_\tau/u_b=0.014$. Assuming the fluid is water, and the ratio between the density difference between the heavier lock fluid and the ambient fluid, and the density of the ambient fluid, $\Delta\rho/\rho_o$, is 16.7% in the simulations conducted at Re=48,000, one obtains H/2=0.11 m and $u_b=\sqrt{g'(H/2}$ =0.43 m/s. The time scale is t_0=0.26 s. Using Shields‟ diagram, one can show that $u_\tau/u_b=0.014$ is the nondimensional critical value of the bed friction velocity, $u_{\tau c}$, for sediment particles with a diameter of 14 microns.

Similar to the analysis done in Chapter 4.12 for gravity currents with a large volume of release, the temporal variation of the two non-dimensional variables I_1 (eqn. 4.14) and I_2 (eqn. 4.15) characterizing the flux of sediment entrained by the gravity current per unit width over a certain distance is analyzed for the simulations with ribs and with dunes of height D=0.15(H/2). Assuming a certain size of the sediment particles at the channel bottom, most formulas predict the flux of sediment to be proportional either to I_1 or I_2. The two variables are calculated over the area, A‟, corresponding to each roughness element. In the simulation with roughness elements, the extent of A‟ in the streamwise direction for the obstacle of rank n was from $x=-\lambda$ ($x=-3(H/2)$) to x=0 where the center/crest of the rib/dune of rank n is situated at x=0 in a local system of coordinates.

Figure 5.69 shows the distribution of u_τ/u_b at representative time instants during the propagation of the current during the drag-dominated regime ($t>32t_0$), together with the distribution of the concentration in a vertical plane, that serves to visualize the current. Also shown are the regions where $u_\tau>u_{\tau c}$. A value $u_{\tau c}/u_b=0.014$ corresponding to sediment particles with a diameter of 14 μm was used to define the threshold for sediment entrainment. The regions with $u_\tau>0$ and with $u_\tau>u_{\tau c}$ within the integration domain A‟ associated with a certain roughness element are the ones which contribute to the I_1 and I_2 variables, respectively. The threshold value $u_{\tau c}/u_b=0.014$ is large enough such that, in the later stages of the drag-dominated regime (e.g., $t>70t_0$ in the SV-LR-R15 simulation), $u_\tau<u_{\tau c}$ over basically the whole region. At that point, I_2 is

equal to zero for all the surfaces associated with the five roughness elements. This means that after a certain finite amount of time, the current with a small volume of release does not have enough energy to entrain particles with a diameter larger than 14 μm.

The distributions of u_τ/u_b in Figure 5.69a-f are also useful to understand how the capacity of the current to entrain sediment changes as the gravity current propagates over Rib4 and Rib5.

For example, at $t=40t_0$ (Figure 5.69a), $u_\tau>u_{\tau c}$ beneath the head and dissipative regions, which are both situated entirely over the surface A''_4 associated with Rib4. The front is situated slightly downstream of the mid-distance point between Rib3 and Rib4 ($x/(H/2)=12.5$). Observe that I_2 for Rib4 reaches a maximum around $t=40t_0$ (see Figure 5.70), when most of the fluid within the dissipative wake region has been convected over Rib3. Examination of the temporal distributions of I_2 for the other ribs shows that I_2 for Rib2 to Rib5 reaches the maximum around the time the back of the dissipative wake was just convected over the rib. This happens after the front has traveled more than half of the distance separating two consecutive ribs. At $t=40t_0$, the value of I_2 for Rib1 and Rib2 are small, but not exactly equal to zero, because of the presence of small regions in the form of spanwise bands where $u_\tau>u_{\tau c}$. The amplification of the bed friction velocity is due the passage of the forward propagating disturbances S2 and FD11 and of the backward propagating disturbance S1 in the region associated with A''_1, and of the forward propagating disturbance S3 in the region associated with A''_2 (see also Figure 5.33 and 5.34f).

At $t=46t_0$ (Figure 5.69b), the front is close to reaching Rib4. Though the surface between Rib3 and Rib4 where $u_\tau>u_{\tau c}$ has increased compared to $t=40t_0$, the levels of u_τ are only slightly larger than $u_{\tau c}$. This explains the decrease of I_2 for Rib4 in Figure 5.70a. By the time the front overpasses Rib4 and the heavier fluid splashed as a result of the impact with Rib4 reaches the bed ($t=52t_0$, Figure 5.70c), $u_\tau<u_{\tau c}$ over A''_4 and, consequently, I_2 for Rib4 is equal to zero in Figure 5.70. Notice also that before the splashed fluid reaches the bed downstream of Rib4, I_2 for Rib5 is also equal to zero. I_2 for Rib5 reaches its maximum around $t=58t_0$ (Figure 5.70d) when the front is situated about mid-distance between Rib 4 and Rib5 (Figure 5.70). As the front continues to approach Rib5 (e.g., see Figure 5.69e when $t=64t_0$), the surface over which $u_\tau>u_{\tau c}$

increases, but this is accompanied by an overall decrease in the values of u_τ. As a result, I_2 for Rib5 decreases significantly at $t=64t_0$ compared to $t=58t_0$. By the time the front reaches Rib5 and the splash of heavier fluid starts forming, $u_\tau<u_{\tau c}$ over the whole A''_5 surface and I_2 for Rib5 is very close to zero.

The temporal variations of I_2 for Rib3, Rib4 and Rib5 are similar and contain only one peak. The peak value is reached when the head and dissipative wake passed over the upstream rib. This happens after the front passed the mid distance separating the upstream and downstream ribs. The temporal variations of I_2 for Rib1 and Rib2 are more complex. The largest peak value of I_2 for Rib1 and Rib2 is reached when the back of the dissipative wake region enters A''_1 and $A''2$, respectively. However, several smaller peaks are observed. For example, in the case of Rib2, I_2 contains two smallest peaks at $t=25.5t_0$ and $34.0t_0$. The first one is induced during the passage of the forward propagating disturbance S1 over Rib1 (Figure 5.33), which induces the temporary formation of a strong jet-like flow, a short distance downstream of Rib1. The second peak at $t=34t_0$ is mostly associated with the backward propagating disturbance S3 which moves from Rib3 toward Rib2. I_2 for Rib2 becomes equal to zero when S3 reaches Rib1 ($t\sim40t_0$).

In Figure 5.71, the distribution of I_2 in time is shown for Rib2 to Rib5. The distributions were translated along the time axis such that I_2 becomes non zero at $t/t_0=0$. The I_2 values decrease significantly with the rank of the rib, for example the entrainment associated with Rib5 is 18 times smaller than that associated with Rib2. This is in contrast with the large volume of release cases for which the decay of I_2 with the rank of the rib is much less, for instance the peak value of I_2 for Rib2 is only 2 times higher than the I_2 value of Rib5 in LR-R15 (see Figure 4.64).

In Figure 5.72 time variation of I_1 calculated over the region associated with Rib2 to Rib5 in the SV-LR-R15 simulation. I_1 characterizes the flux of sediment of a certain particle size entrained from the bed, assuming sediment is entrained at all values of u_τ. The distributions for Rib2 to Rib5 were translated along the time axis such that I_1 becomes non zero at $t/t_0=0$. The overall shape of curves of $I_1(t)$ is different than that of $I_2(t)$. The main differences occur after the peak value is reached. A larger "tail" region is present due to the fact that I_1 assumes sediment is entrained as long as $u_\tau>0$. Therefore at all stages of the simulation non-zero entrainment is observed in the simulation domain in contrast to the zero entrainment values of I_2 for $(t-t_i)/t_0>40$. In contrast with the large volume of release simulation, the value of I_1 decreases with the rank of the rib due to high levels of mixing and reduced front velocity in SV-LR-R15 while I_1 values are very similar for all ribs in simulation LR-R15 (see Figure 4.65). It is important to make the observation that the distributions of I_1 are slightly non-symmetrical and the peak moves toward the right as the rank of the rib increases. This is because the front velocity decreases with time, so the time interval it takes the head and dissipative wake regions to be convected over a rib increases slightly with the rank of the rib.

The comparison of the bed friction velocity distributions in Figures 5.69 and 5.73 allow explaining why the gravity current propagating over dunes has a higher capacity to entrain sediment compared to the gravity current propagating over ribs of equal height and placed at the bed with the same spacing.

A main reason is the fact that the decay of the bed friction velocity levels after the passage of the front is much slower in the SV-LR-D15 simulation. For example, the results in Figure 5.69 showed that during the drag-dominated regime, u_τ is larger than $u_{\tau c}$ in the region between two ribs only for a short time after the front passes the downstream rib associated with a certain entrainment surface (e.g., up to $50t_0$ for A''_4 and $70t_0$ for A''_5 as shown in Figures 5.69c and 5.69f). In the case of dunes, regions where $u_\tau>u_{\tau c}$ are still observed within A''_4, a long time after the front passed the lee side of Rib4 ($t\sim42t_0$). These regions are situated over the upstream part of the upslope face of Rib4, where the jet-like flow impinges into the bed surface, and around the crest of Rib4 (e.g., see Figures 5.73b and 5.73c). As the values of u_τ over these two regions start decaying, a region containing relatively high vales of u_τ starts forming over the lee side of Rib4 (e.g., at $t=52t_0$ in Figure 5.73d). This is because the heavier fluid from the tail convected over the crest of Rib4 has relatively little streamwise momentum. Thus, this heavier fluid flows over the lee side of Rib4 without trying to detach, as was the case at earlier times. The tail fluid is strongly accelerated as it moves over the lee side of Rib4 and induces relatively large values of u_τ that persist for a relatively long time. For example, the band of high values of u_τ over the lee side of Rib4 is still present at $t=58t_0$ in Figure 5.73d, when the front passed the crest of Rib5. The other reason is that, after the end of the slumping phase, the values of u_τ behind the front are, at most times, larger in the SV-LR-D15 simulation compared to the SV-LR-R15 simulation (e.g., see Figure 5.64).

The afore-mentioned differences in the distributions of u_τ explain the differences in the distributions of I_1 and I_2 between the two simulations.

The distribution of I_2 for the dunes of rank higher or equal to 2 (Figure 5.75) is characterized by a much lower degree of symmetry compared to the case ribs are present at the channel bottom (Figure 5.71). For example in the case of Dune3, $I_2(t)$ peaks when the front is situated close to the middle of the upslope face of Dune3 ($t\sim23t_0$). After it passes that location, I_2 starts decreasing mostly because of the strong deceleration of the head that is advancing over a surface of negative slope. The decay stops around $t=28\text{-}29t_0$, when the decelerating front reaches the crest and starts propagating over the lee side of Dune3. The smallest second peak in $I_2(t)$ around $21t_0$ is due to the strong increase in u_τ close to the crest of Dune3 after the back of the dissipative wake was convected over the crest. Then, u_τ starts decreasing again over the downstream part of the upslope face of Dune3, as the streamwise momentum of the tail fluid decreases.

On the other hand, as shown in Figures 5.74 and 5.75, the temporal evolution of $I_2(t)$ for Dune1, Dune2 and Dune3 are qualitatively and quantitatively very similar. This is different of the results for the SV-LR-R15 simulation in which the overall levels of $I_2(t)$ decayed strongly with the rank of the rib, starting with Rib1. A similar decay of $I_2(t)$ is observed in the SV-LR-D15 simulation only starting with Dune4 (Figure 5.75).

Figure 5.76 shows the temporal variation of I_1 for dunes ranked 2 or higher in simulation SV-LR-D15. Comparison of Figures 5.75 and 5.76 shows that the distributions of $I_1(t)$ are qualitatively similar to those predicted for $I_2(t)$ for all the five dunes. Of course, in the case of $I_1(t)$ the temporal decay is milder and takes longer time compared to $I_2(t)$, as entrainment is predicted for $u_\tau>0$. For a given dune, the quantitative differences between $I_1(t)$ and $I_2(t)$ are much less important compared to the ones observed in the simulation with ribs.

The results in Figure 5.77 confirms the qualitative trends describing the variation of the sediment entrainment capacity that were inferred just based on the comparison of the distributions of u_τ at different stages of the propagation of the gravity current in the SV-LR-F, SV-LR-D15 and SV-LR-R15 simulations (e.g., see Figure 5.64). They show that once the current propagates over the first roughness element in the series ($t>12t_0\sim3$ s), the flux of sediment entrained at the bed by the current propagating over dunes is, at most times, higher than the flux induced by the current propagating over ribs of equal height, or by the current propagating over a flat bed. Most of the differences are recorded between the end of the slumping phase and the start of the drag-dominated regime ($t\sim32t_0=8$ s). During this time interval, the interaction of the head of the current with the roughness elements induces large-scale oscillations in the variation of F(t). The main reasons for the larger values of F(t) in the simulation with dunes compared to the simulation with ribs (see Figure 5.64), are:

1) the formation of a region of high bed-friction velocity downstream of the lee side of the first two dunes behind the front, close to the crest of the dune and around the location where the jet-like flow reaches the lowest past of the bed surface and changes direction.
2) the larger values of the bed friction velocity behind the front. At a given streamwise position of the front, the mixing inside the head is larger and the front velocity is smaller in the SV-LR-R15 simulation. Also, the heavier fluid at the head convected over the top of the rib has very little streamwise momentum when it reaches the bed surface.

The mass of sediment particles of diameter d=14 μm entrained from the bed per unit width between the start of the lock exchange flow and a certain time t can be calculated as $G(t)=\int_0^t F(t)dt$. As in the SV-LR-R15 and SV-LR-D15 simulations, F(t) becomes very close to zero for t>T, where T~52t_0 (13 s) for the SV-LR-R15 simulation and T~60t_0 (15 s) for the SV-LR-D15 simulation. Thus, G(t) becomes approximately constant for t>T and represents the total mass of sediment per unit width entrained by the gravity current during its propagation. The results in Figure 5.77b show that the total mass of sediment entrained in the simulation with dunes is about 40% larger than the one entrained in the simulations with a flat bed or with ribs. The results also show that the amount of sediment entrained during the drag dominated regime ($t/t_0>32$ or t>8.5s) in the simulations with roughness elements is less than 15% of the total amount of sediment entrained by the current.

Thus, gravity currents with a small volume of release propagating over dunes are expected to entrain a substantially larger amount of sediment compared to gravity currents propagating over a flat bed. The trend is similar to that observed in Chapter 4 (see Figure 4.68) for gravity currents with a large volume of release.

5.11 Summary and Conclusions

The changes in the flow physics and parameters characterizing the structure of bottom-propagating Boussinesq gravity currents with a small volume of release and the capacity of these currents to entrain sediment at different stages of their evolution was investigated using high-resolution LES simulations. In particular, the study focused on the changes between the case the gravity current propagates over a flat smooth bed and the case the gravity current propagates over an array of 2D identical roughness elements of different sizes and shapes (ribs, dunes). This chapter considered the case of full-depth and partial-depth currents with R=O(1).

As a result of the small volume of release, the slumping phase was very short. Thus, the investigation focused on the study of the flow physics after the start of the transition to the buoyancy-inertia phase. The role and dynamics of the forward and backward propagating flow disturbances was discussed in detail. The simulations showed that if the domain was long enough, the presence of large-scale roughness elements at the channel bottom resulted in the current transitioning from the buoyancy-inertia phase, in which the front velocity decays proportionally with $t^{-1/3}$, to a turbulent drag-dominated regime in which the front velocity decays faster, as a result of the additional drag force acting on the gravity current.

The present investigation showed that gravity currents with a small volume of release propagating over large-scale roughness elements reach a regime in which the front velocity decays proportional to $t^{-1/2}$, similar to the case of gravity currents propagating into a porous medium. In the case of current propagating into a porous medium, the drag acts over the whole height of the current rather than only over the bottom layer of the gravity current. Though the establishment of a regime in which the flow evolution is mainly determined by the balance between the turbulent drag and the buoyancy force driving the flow was expected to happen (the actual way in which the drag force acts on the gravity current is not essential), the fact that the law of decay of the front velocity with time is identical for gravity currents propagating over roughness elements and in a porous medium of uniform porosity is not obvious. For that to happen, one condition is that the shapes of the current propagating over roughness elements and that of the current propagating within a porous medium have to be similar. This is not always the case. For example, the work of Tanino et al. (2005) has shown that the shape of gravity currents with a large volume of release propagating in a porous medium (the shape of the current is close to triangular) is not similar to that of gravity currents propagating over a smooth surface (interface is close to horizontal until close to the head).

Moreover the present simulations showed that the decay of the front velocity with $t^{-1/2}$ during the turbulent drag-dominated regime is independent of the relative height of the current compared to the height of the roughness elements. However, there are some differences. For example, while in the case of currents of height comparable to that of the obstacles, the Froude number over the head and dissipative wake is close to unity (critical flow), in the case of currents of much larger height that that of the roughness elements, the Froude number decays linearly starting at the head, where the Froude number is close to one, until the start of the upstream part of the tail where the Froude number is close to zero.

The simulations with a partial depth of release predicted a front velocity during the slumping phase that was in good agreement with theory and experiment (Shin et al., 2004). Similar to the case of gravity currents with a high volume of release, the ribs were more efficient in slowing down the gravity current. The differences in the front position between the simulations with dunes and ribs of same height increased significantly during the drag-dominated phase.

The present simulations allowed a detailed investigation of the changes in the structure of gravity currents propagating over large-scale roughness elements between the case of a current with a large volume of release and the case of a current with a small volume of release. For example, the spanwise extent and coherence of the interfacial billows was significantly larger in the case of gravity currents with a small volume of release. Though in the case of gravity currents with a small volume of release the presence of large-scale roughness elements at the bed was found to induce some significant quantitative changes, at a qualitative level, the structure of the gravity current, at large times after the lock-fluid was released, was not very different in the simulations with roughness elements and in the one with a flat bed. In all the simulations, the head and dissipative wake contained most of the kinetic energy of the current. While a region of high velocity magnitude was present past the crest/top of the first roughness element behind the front, similar to the case of gravity currents with a high volume of release, the amplification of the velocity past the crest/top of the roughness elements situated at large distances from the front was relatively small compared to the one observed for currents with a large volume of release.

The simulations demonstrated the important role played by the backward propagating disturbances forming at the crest/top of the roughness elements and by their reflections in transferring momentum and energy between the upstream and the downstream part of the current. Simulation results also showed the presence of a second mechanism that can result in the formation of strong disturbances, in which the disturbance was triggered by the collapse of an interfacial billow, containing higher-density fluid, on the channel bottom. The interaction of a forward or backward propagating disturbance with a roughness element could result into a finite amount of higher density fluid being convected past the top/crest of the obstacle. This was the main mechanism responsible for mass exchange in the longitudinal direction over the tail of gravity currents with a small volume of release.

The temporal variation of the total volumetric flux of heavier fluid $Q_i = (4/u_b H^2)\int CudA$ at streamwise locations corresponding to the position of the top/crest of a roughness element had a triangular shape. For example, in the simulations with ribs, the flux increases sharply until the higher density fluid contained within the initial splash moved over the top of the rib. Then, the flux decreases in a milder way, as the heavier fluid from the head and dissipative wake was convected over the top of the rib. In the simulations with dunes, a small region in which the discharge is close to constant was present a small time after the discharge reached the peak value.

The volume of lock fluid accumulated between the streamwise locations at which the crest/top of two consecutive roughness elements are located was found to increase sharply as the front was convected past the top/crest of the upstream obstacle. Once the back of the dissipative wake passed the crest/top of the downstream obstacle, the total volume of lock fluid between the two obstacles was close to constant. That time corresponds to the establishment of a “quasi-steady state” regime. During this regime, the volume of heavier fluid accumulated between the top/crest of the two consecutive roughness elements can increase or decrease only due to the convection of heavier fluid by the forward and backward propagating disturbances.

The analysis of the temporal evolution of the mean pressure difference between the upstream and the downstream faces of the rib showed that, similar to the case of a gravity current with a high volume of release, ΔP increases exponentially as the front starts interacting with the upstream face of each of the ribs in the series. However, in the simulations with a small volume of release, the peak values of ΔP at the end of the impact stage decreased much faster with the rank of the rib. The temporal variations of ΔP for all the ribs in the series were qualitatively similar in the simulation in which the height of the current and that of the ribs were comparable.

In the simulation in which the height of the current was much larger than the rib height, a second peak was present during the transient stage.

Similar to the case of gravity currents with a large volume of release, the variations of E_k and E_p with time and with x_f were subject to large-scale modulations induced by the interaction of the current with the obstacles. Analysis of the energy balance in the simulations with a flat bed and with roughness elements showed that the variations of the total kinetic energy, total potential energy, and the integral of the total dissipation rate with the front position are logarithmic after the end of the transition to the buoyancy-inertia phase.

Details of the distribution of the bed friction velocity, u_τ, were investigated at different stages of the evolution of gravity currents with a small volume of release. Scale effects were considered by comparing the distributions of u_τ from simulations with a flat bed and with obstacles in which the only difference was the value of the Reynolds number (Re=48000 vs. Re=10^6). Similar to the case of gravity currents with a large volume of release, at a given position of the front, the distributions of u_τ/u_b remained qualitatively similar in the simulations with a low and a high Reynolds number. Moreover, the scaling ratio deduced for the flat bed simulations also applied for the simulations in which roughness elements were present at the channel bottom. This means results from experiments and numerical simulations conducted at Reynolds numbers around 10^4-10^5 are relevant to understand the bed shear stress distributions, and thus the capacity of the sediment to entrain sediment, at much larger Reynolds numbers, that are typically encountered in the field. In the simulations of gravity currents with a small volume of release, the streamwise bed shear stress was positive at all times only beneath the head and dissipative wake. The passage of the forward and backward propagating flow disturbances was found to control the distribution of the bed shear stress magnitude and its sign over the tail of gravity currents with a small volume of release.

The presence of dunes was found to induce higher bed shear stresses over the head, dissipative wake, and downstream part of the tail compared to the case ribs of same height were present at the channel bottom. In part, this was due to the larger front velocity, at a given front position, in the simulation with dunes. However, most of the difference was due to the formation of two regions of high bed-friction velocity downstream of the lee side of the first two dunes behind the front, close to the crest of the dune and around the location where the jet-like flow reaches the lowest past of the bed surface and changes direction. By comparison, the heavier fluid convected over the top of the rib by currents with a small volume of release has a much lower amount of streamwise momentum when it reaches the bed surface.

The numerical simulations allowed a detailed analysis of the time variation of the flux of sediment entrained by the current in specific regions of the current. The analysis was performed for the case of obstacles of height D=0.15H. Some important qualitative differences were observed between the temporal distributions of the flux of sediment entrained at the bed over the distance between two consecutive roughness elements, in the simulations with ribs and with dunes. The flux of sediment entrained between the top/crest of two consecutive obstacles decayed to zero much faster in the simulations with ribs. Also, the overall variation of the flux with the relative position of the front of the current was different.

One of the main results was that for particles with a relatively high critical friction velocity (of about 50% of the average bed friction velocity induced by the current during the slumping phase), the mass of sediment entrained from the bed by the current after its release is by about 40% larger in the simulation with dunes compared to the simulation with ribs or with a flat bed. Most of the difference built during the buoyancy-inertia phase and the transition to the drag-dominated phase. For the sediment size that was analyzed, the mass of sediment entrained during the drag-dominated regime in the simulations with roughness elements of height D=0.15H was less than 15% of the total amount of sediment entrained by the current. The higher capacity of gravity currents with a small volume of release propagating over dunes to entrain sediment is consistent with the result obtained for gravity currents with a large volume of release propagating during the slumping phase.

Table 5.1 Main parameters of the simulations and computational domain for the simulations of gravity currents with a small volume of release.

Simulation	**Re**	**Obstacle Type**	**$x_o/(H/2)$**	**h/H**	**Obstacle Height**	**Wavelength**	**Number of Obstacles**
SV-LR-F	47,800	-	0.56	0.5	-	-	-
SV-LR-R15	47,800	Rib	0.56	0.5	0.15h	3	5
SV-LR-D15	47,800	Dune	0.56	0.5	0.15h	3	5
SV-LR-D05	47,800	Dune	0.56	0.5	0.05h	1	17
SV-LR-R10	47,800	Rib	0.80	1	0.10h	1	25
SV-HR-F	1,000,000	-	0.56	0.5	-	-	-
SV-HR-R15	1,000,000	Rib	0.56	0.5	0.15h	3	5
SV-HR-D15	1,000,000	Dune	0.56	0.5	0.15h	3	5

Table 5.2 Comparison of the non-dimensional times and front positions corresponding to the end of the slumping phase, the start of the buoyancy-inertia phase and the start of the drag-dominated phase in the simulations of gravity currents with a small volume of release.

	Slumping Phase			**Buoyancy-Inertia Phase**			**Drag Dominated Phase**		
	t/t_o	**$(x_f-x_o)/x_o$**	**$x_f/(H/2)$**	**t/t_o**	**$(x_f-x_o)/x_o$**	**$x_f/(H/2)$**	**t/t_o**	**$(x_f-x_o)/x_o$**	**$x_f/(H/2)$**
SV-LR-F	11	9.5	5.9	25	18.3	10.8	-	-	-
SV-LR-D05	10	8.5	5.3	22	16.3	9.7	-	-	-
SV-LR-D15	9	7.7	4.9	17.3	13.6	8.2	32	21	12.3
SV-LR-R10	-	-	-	10	8.2	7.4	51.3	24	20
SV-LR-R15	9	7.8	4.9	16.5	12.4	7.5	30	18.5	11
SV-HR-F	9	9.6	5.9	25	22	12.9	-	-	-
SV-HR-D15	7.5	8	5	16.6	14.8	8.8	40	25.8	15
SV-HR-R15	7.5	8	5	15.5	13.7	8.2	42	24.9	14.5

Table 5.3 Summary of non-dimensional times and front velocities when the front is situated at $x_f/(H/2)=17$ in the low and high Reynolds number simulations of gravity currents with a small volume of release.

Simulation	**t / t_o**	**u_f/u_b**
SV-LR-F	48	0.22
SV-LR-D15	48	0.19
SV-LR-R15	60	0.15
SV-HR-F	39.7	0.32
SV-HR-D15	48	0.17
SV-HR-R15	58	0.16

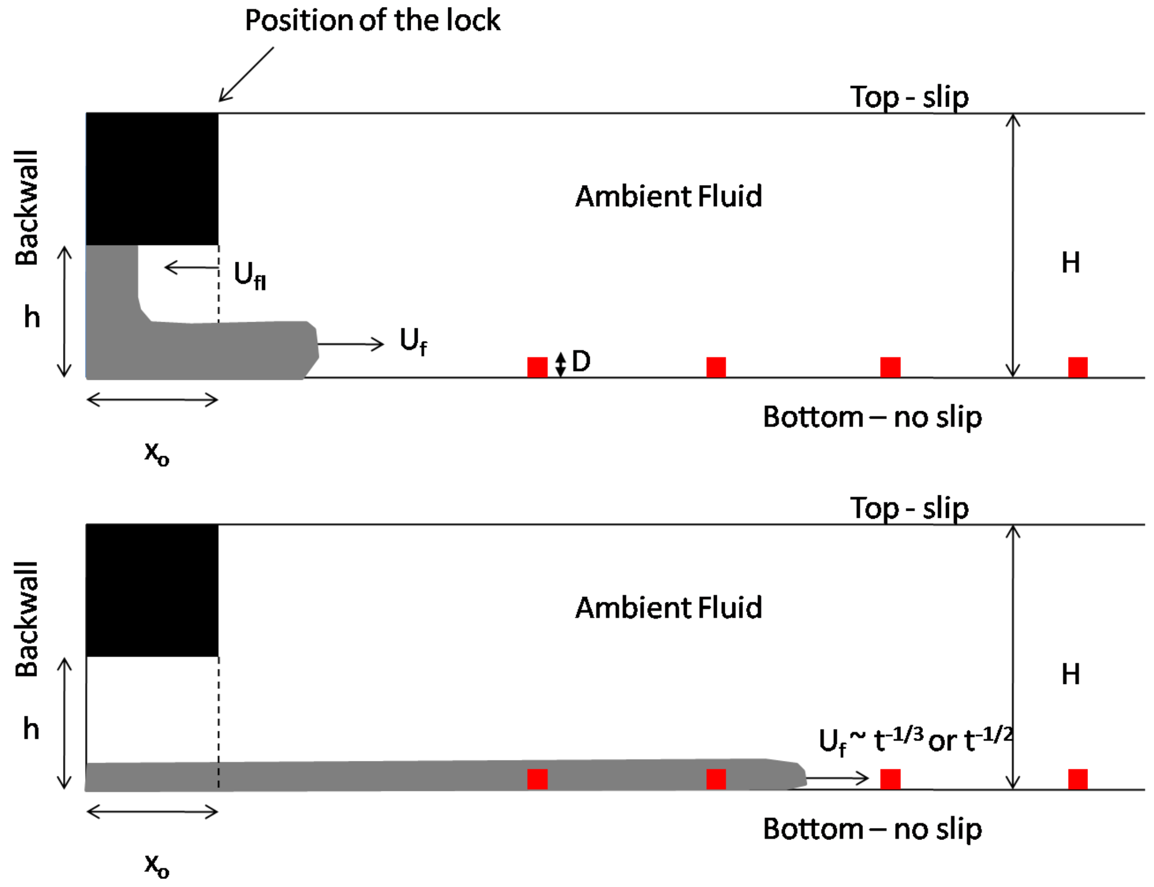
Position of the lock
Top - slip
Ambient Fluid
Backwall
h
U_{fl}
U_f
D
H
Bottom – no slip
x_o
Top - slip
Ambient Fluid
Backwall
h
H
$U_f \sim t^{-1/3}$ or $t^{-1/2}$
Bottom – no slip
x_o

Figure 5.1 Sketch of the flow during the slumping phase (a) and the buoyancy-inertia and turbulent drag-dominated phases (b) for the case of a lock-exchange flow with a small volume of release ($x_0/h=O(1)$). The top boundary is a slip horizontal wall. The bottom boundary is a no-slip horizontal wall. In some of the simulations an array of 2-D ribs or dunes are mounted on the bottom surface only.

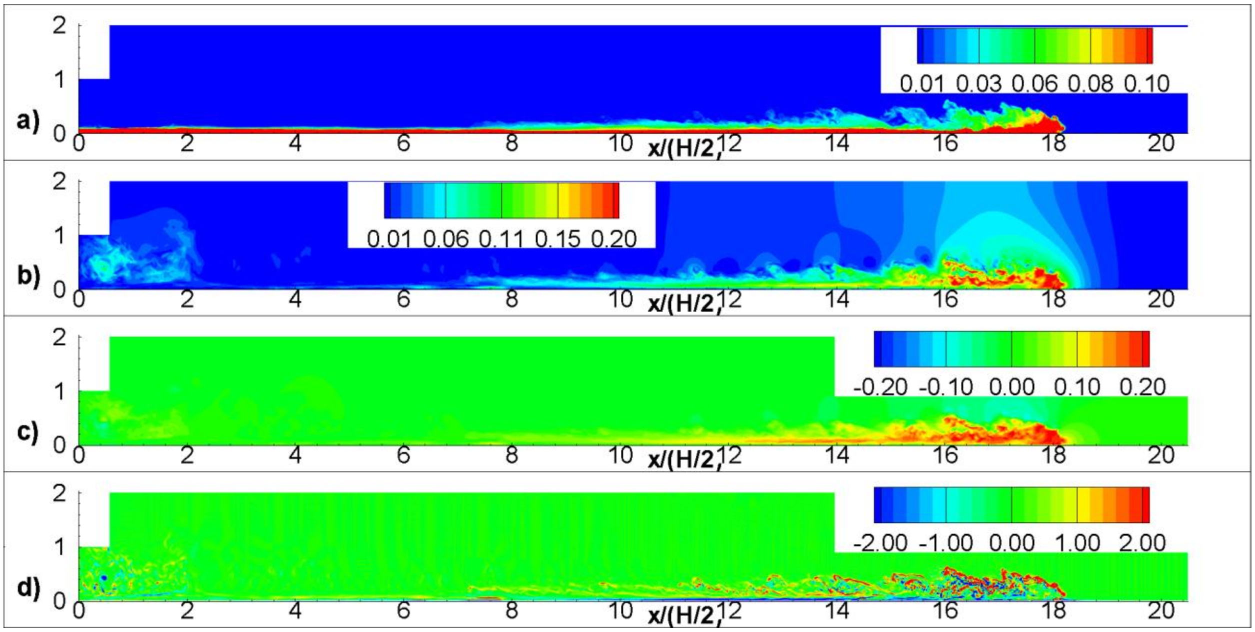

Figure 5.2 Structure of the gravity current at a time when the front is situated close to $x_f/(H/2)=18$ in the SV-LR-F simulation. a) concentration, C; b) velocity magnitude, u_{mag}/u_b; c) streamwise velocity, u/u_b; d) out-of-plane vorticity, $\omega_z(H/2)/u_b$. The aspect ratio is 1:2 in the x-y contour plots.

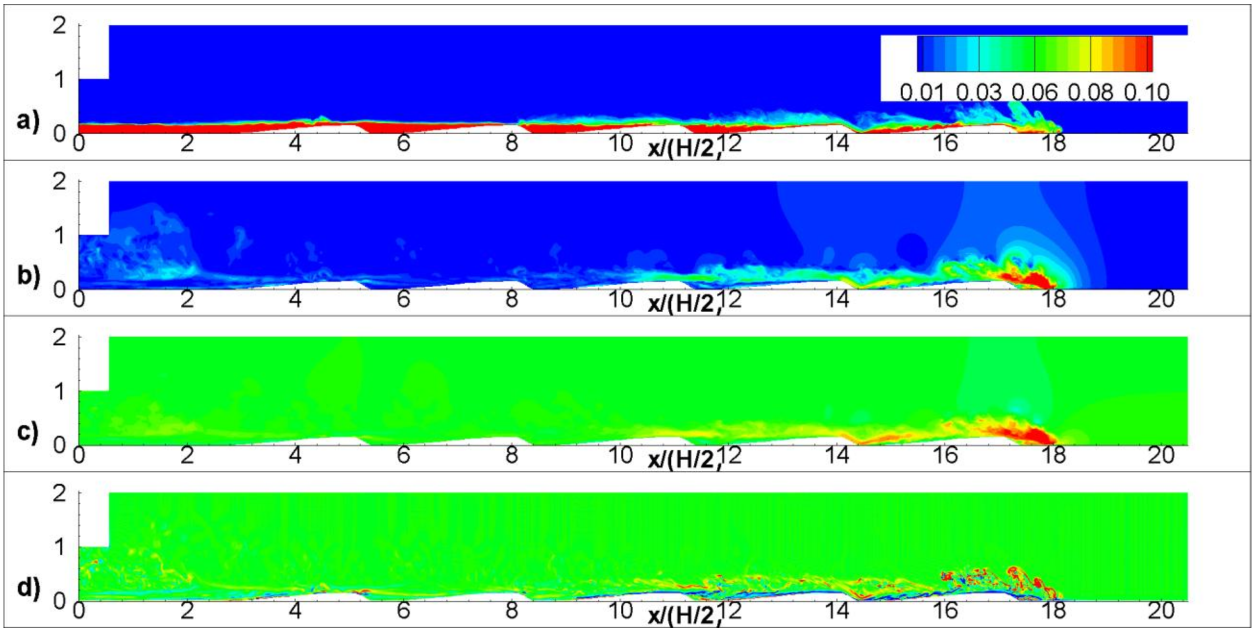

Figure 5.3 Structure of the gravity current at a time when the front is situated close to $x_f/(H/2)=18$ in the SV-LR-D15 simulation. a) concentration, C; b) velocity magnitude, u_{mag}/u_b; c) streamwise velocity, u/u_b; d) out-of-plane vorticity, $\omega_z(H/2)/u_b$. The aspect ratio is 1:2 in the x-y contour plots.

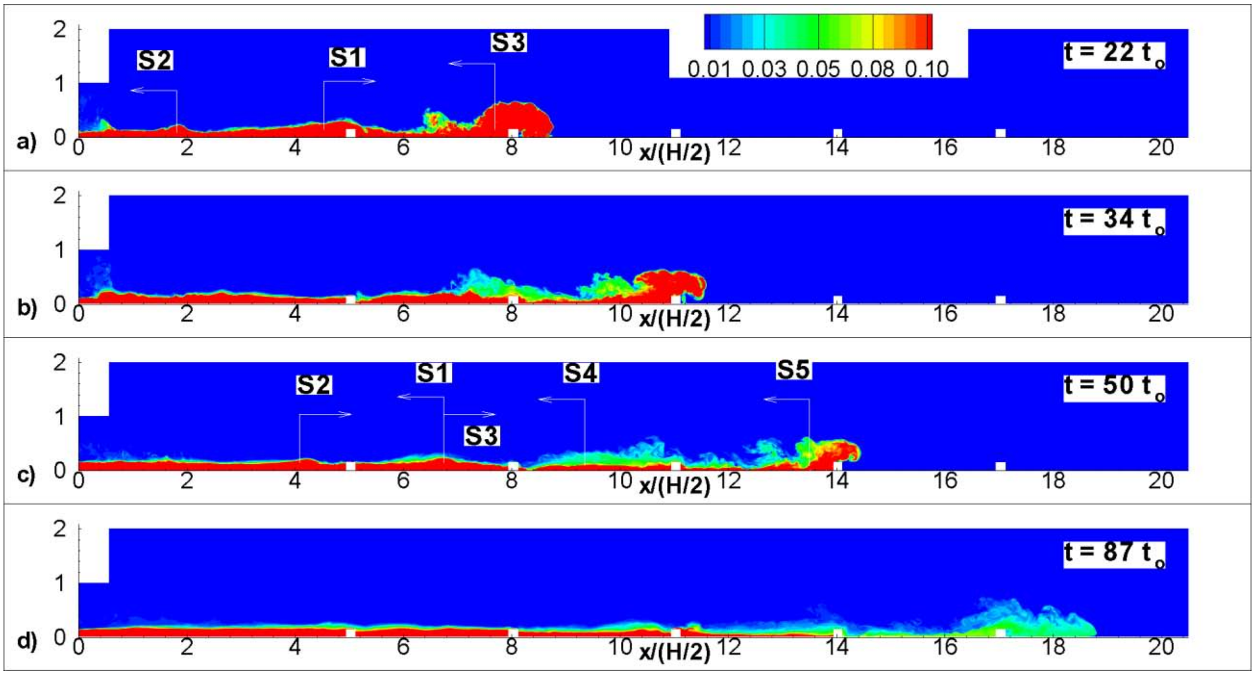

Figure 5.4 Distribution of concentration, C, in the SV-LR-R15 simulation. a) t=22t$_0$; b) t=34t$_0$; c) t=50t$_0$; d) t=87$_0$. The aspect ratio is 1:2 in the x-y contour plots.

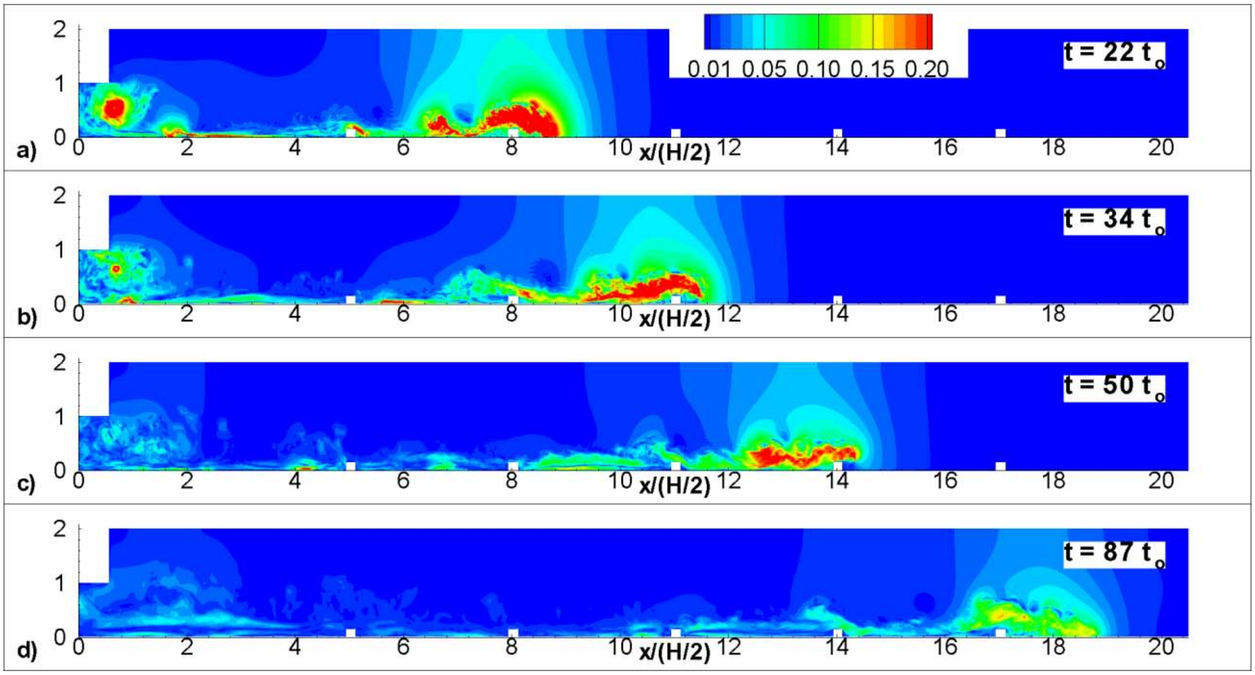

Figure 5.5 Distribution of velocity magnitude, u_{mag}/u_b, in the SV-LR-R15 simulation. a) $t=22t_0$; b) $t=34t_0$; c) $t=50t_0$; d) $t=87_0$. The aspect ratio is 1:2 in the x-y contour plots.

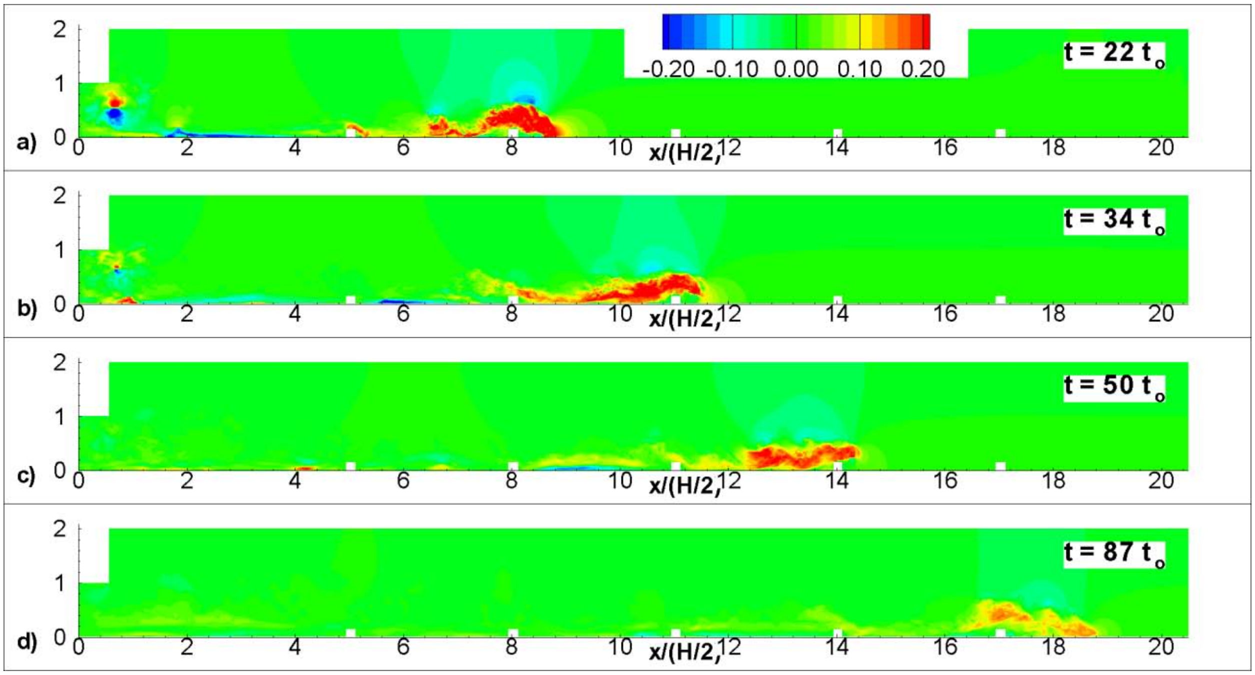

Figure 5.6 Distribution of streamwise velocity, u/u_b, in the SV-LR-R15 simulation. a) t=22t$_0$; b) t=34t$_0$; c) t=50t$_0$; d) t=87$_0$. The aspect ratio is 1:2 in the x-y contour plots.

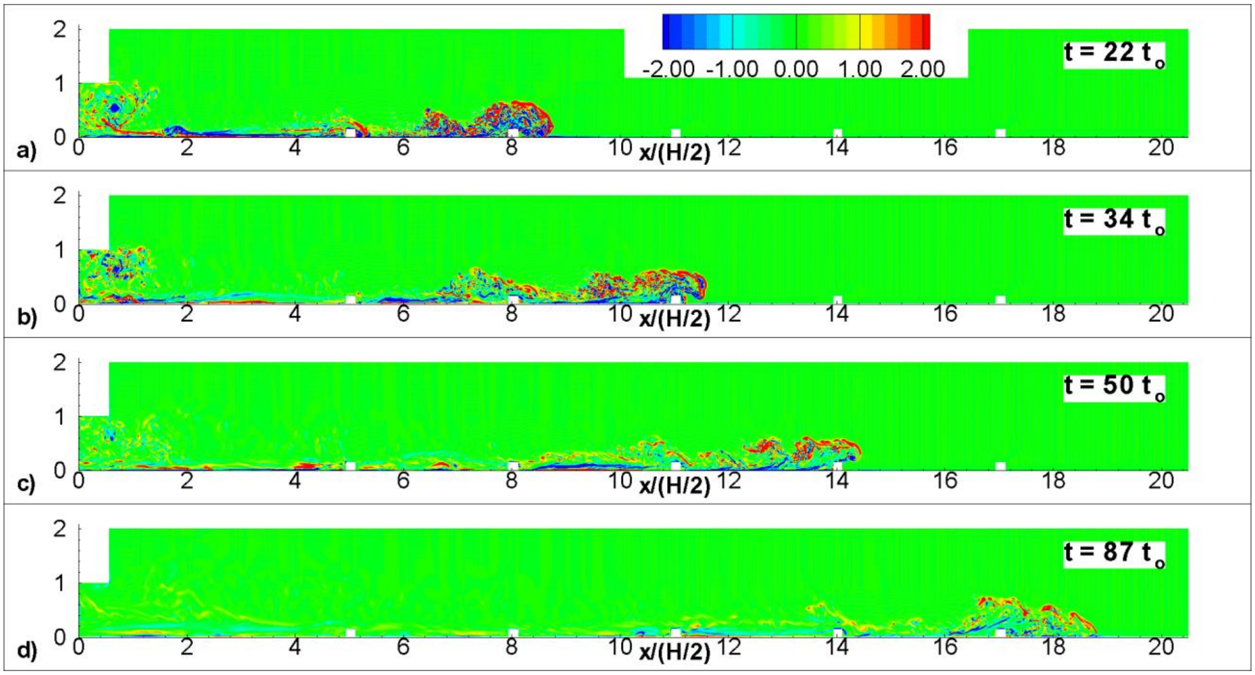

Figure 5.7 Distribution of out-of-plane vorticity, $\omega_z(H/2)/u_b$, in the SV-LR-R15 simulation. a) t=22t$_0$; b) t=34t$_0$; c) t=50t$_0$; d) t=87$_0$. The aspect ratio is 1:2 in the x-y contour plots.

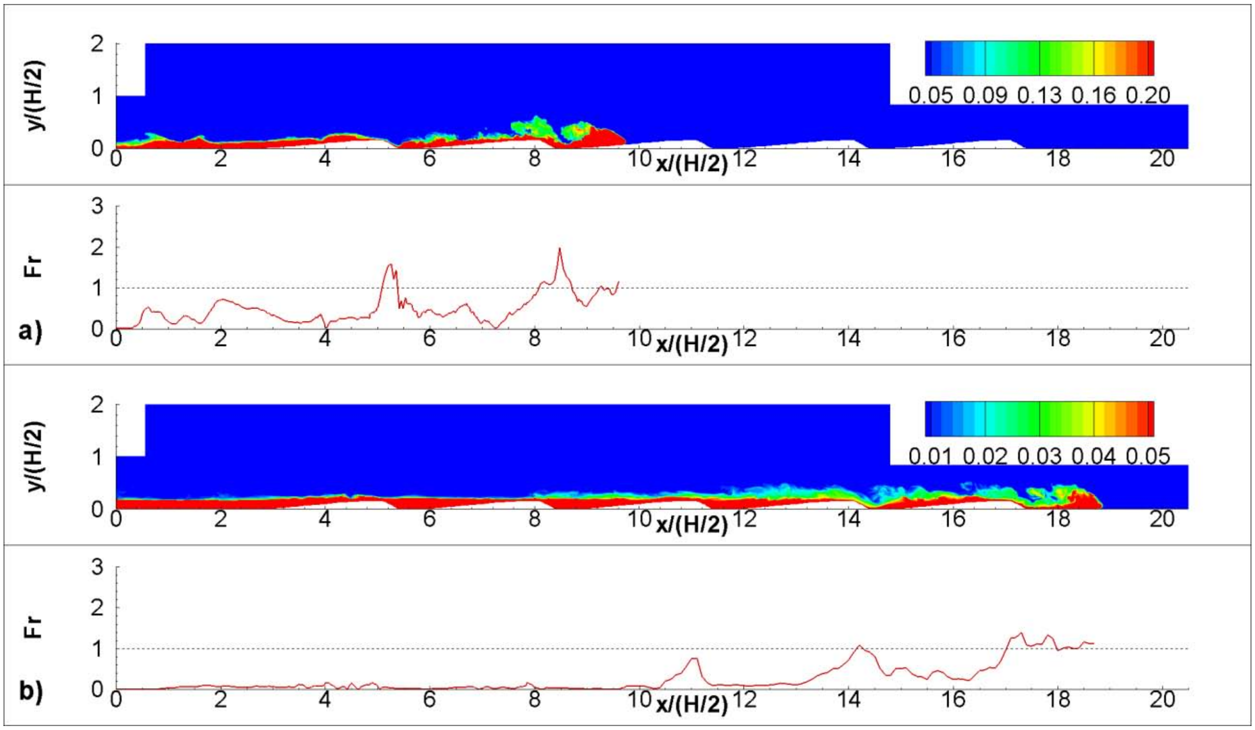

Figure 5.8 Streamwise distribution of the Froude number in the SV-LR-D15 simulation. The structure of the current is visualized in an x-y section using concentration contours. a) $x_f/(H/2)=9.5$ (buoyancy-inertia phase); b) $x_f/(H/2)=18.5$ (drag-dominated phase).

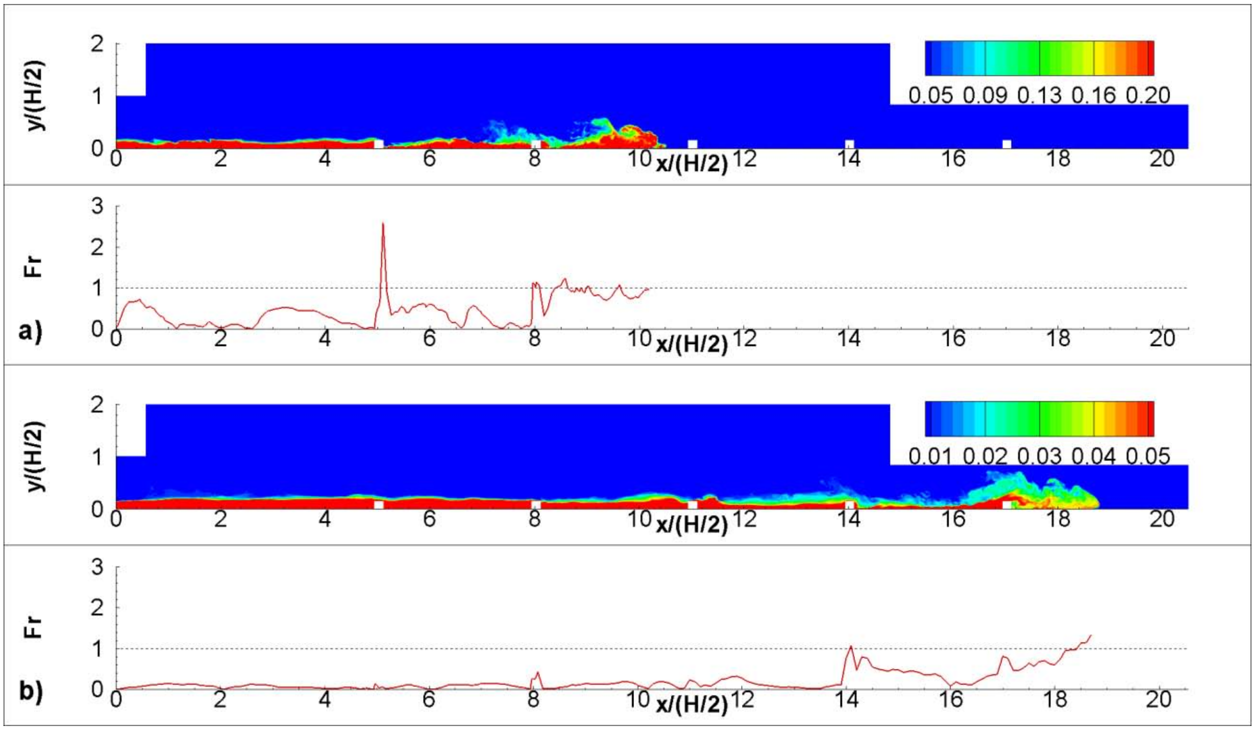

Figure 5.9 Streamwise distribution of the Froude number in the SV-LR-R15 simulation. The structure of the current is visualized in an x-y section using concentration contours. a) $x_f/(H/2)=10.5$ (buoyancy-inertia phase); b) $x_f/(H/2)=18.5$ (drag-dominated phase).

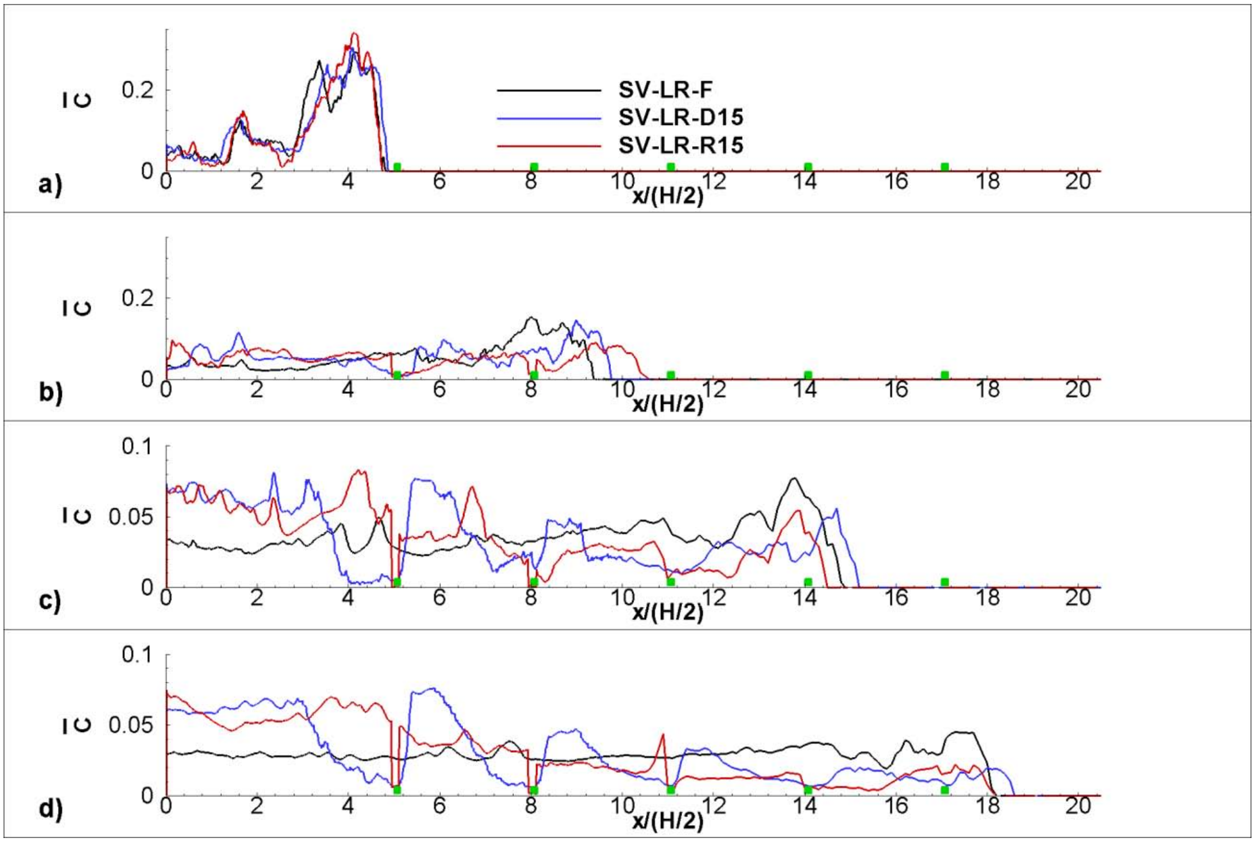

Figure 5.10 Streamwise variation of the depth-averaged concentration, $\overline{C}$ (non-dimensional height of the gravity current, $\bar{h}/(H/2)$), in the low Reynolds number simulations with a flat bed and with dunes and ribs of height D=0.15(H/2). a) x_f/(H/2)~4.8; b) x_f/(H/2)~10.0; c) x_f/(H/2)~15.5; d) x_f/(H/2)~18.5.

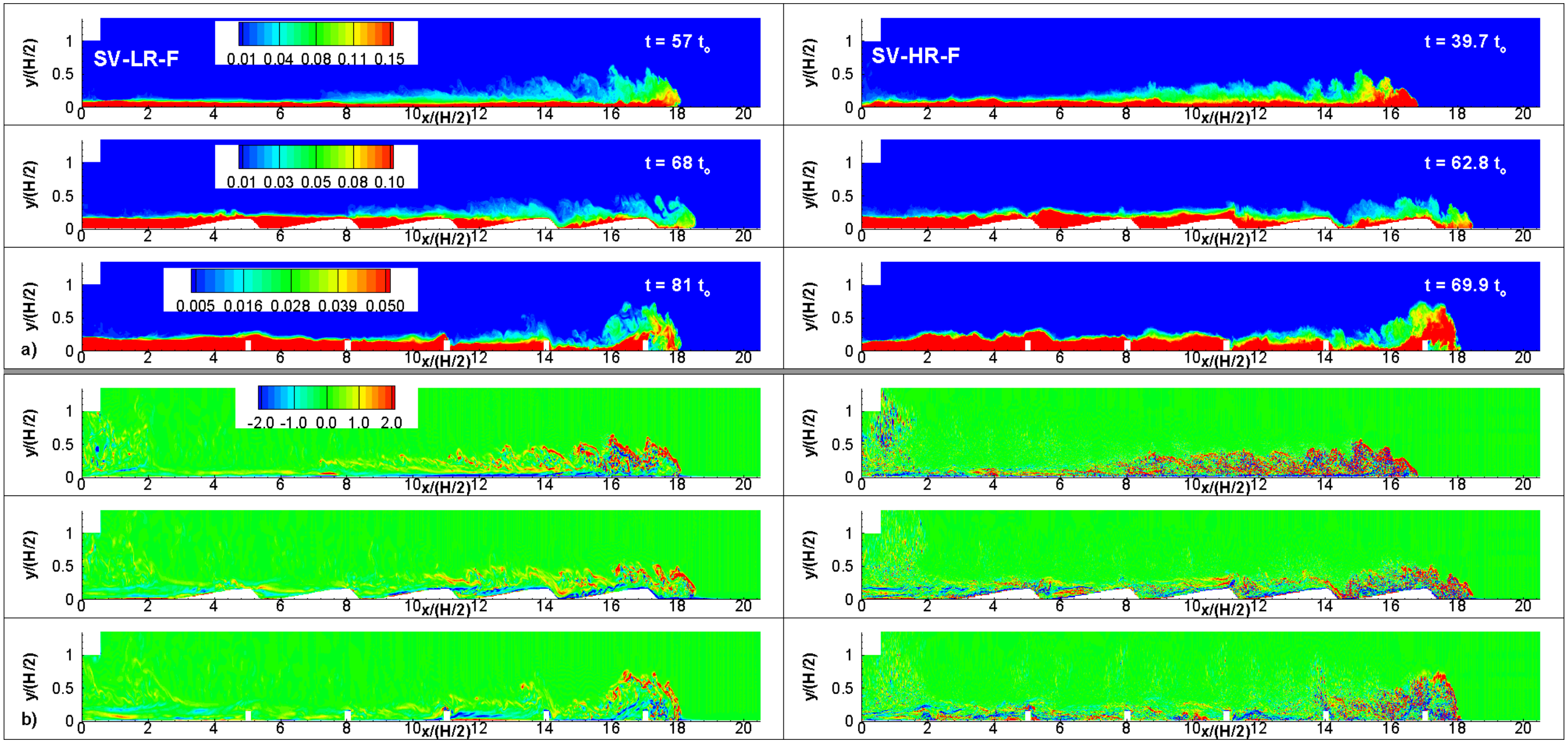

Figure 5.11 Comparison of the structure of the gravity current in the low (Re=48,000) and high (Re=10^6) Reynolds number simulations with a flat bed, with dunes and with ribs of height D=0.15H when the front is situated at $x_f/(H/2)\sim 18$. a) concentration, C; b) out-of-plane vorticity, $\omega_z (H/2)/u_b$.

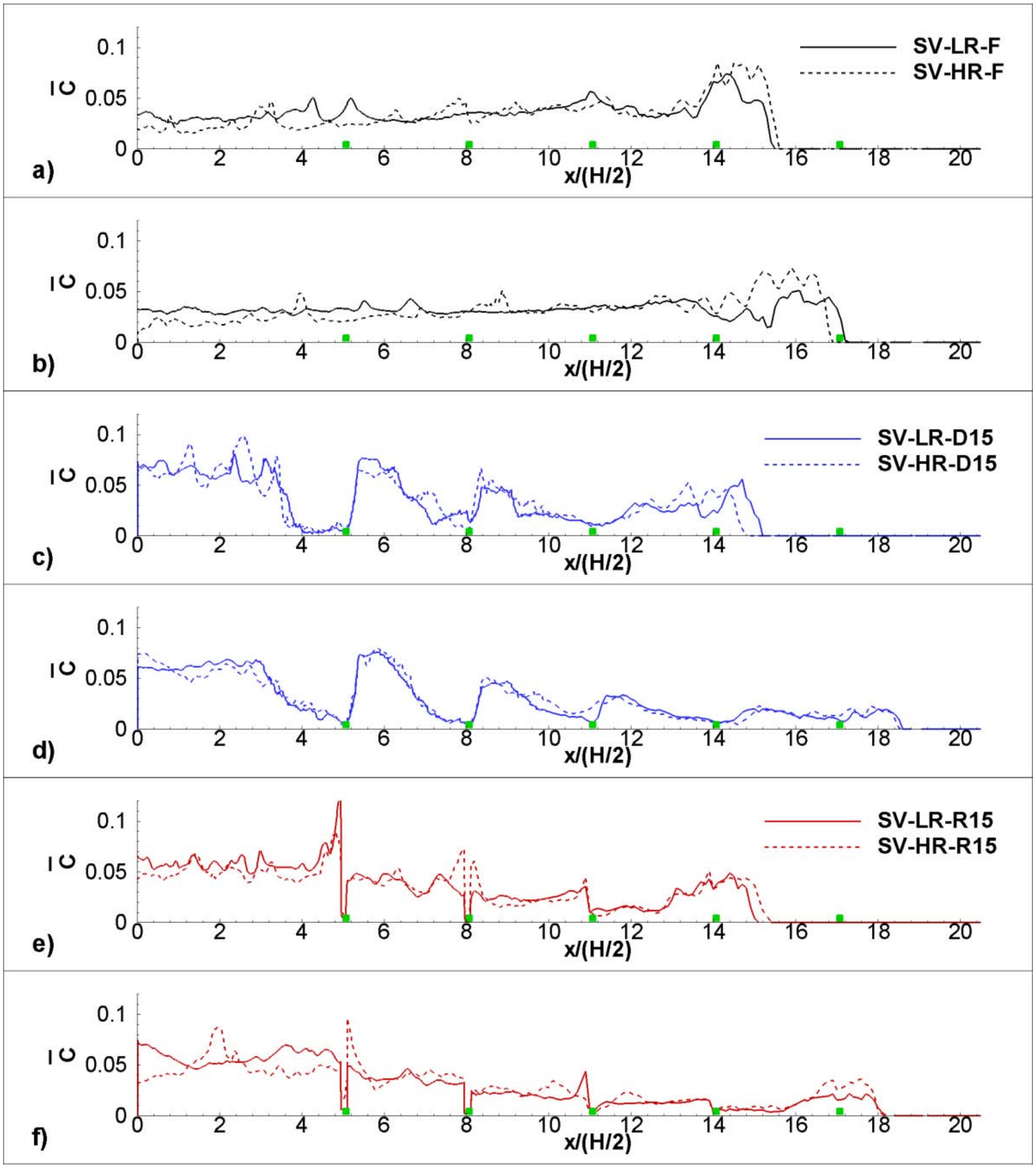

Figure 5.12 Streamwise variation of the depth-averaged concentration, $\overline{C}$ (non-dimensional height of the gravity current, $\overline{h}/(H/2)$), in the low and high Reynolds number simulations. a) flat bed, $x_f/(H/2)$~15; b) flat bed, $x_f/(H/2)$~17; c) dunes, D=0.15(H/2), $x_f/(H/2)$~15; b) dunes, D=0.15(H/2), $x_f/(H/2)$~18; e) ribs, D=0.15(H/2), $x_f/(H/2)$~15; f) ribs, D=0.15(H/2), $x_f/(H/2)$~18.

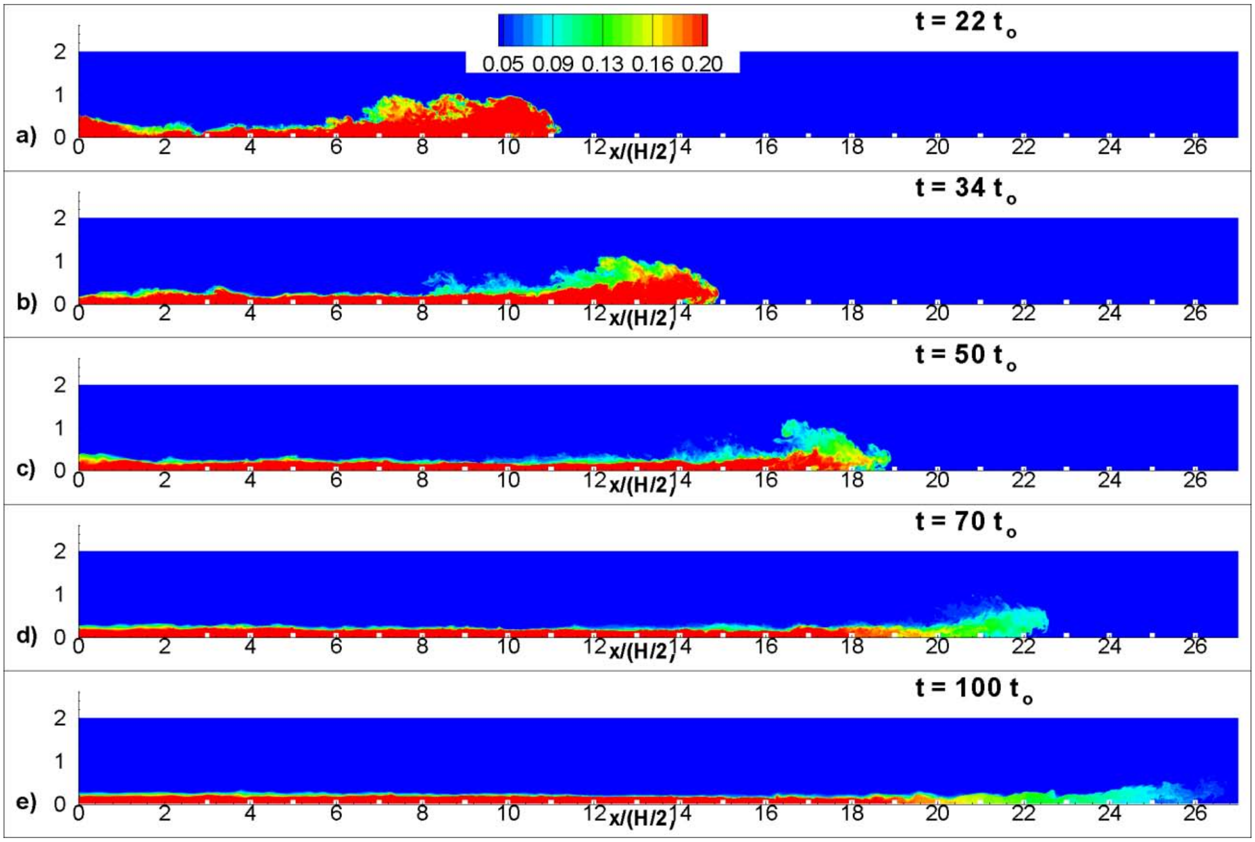

Figure 5.13 Distribution of concentration, C, in the SV-LR-R10 simulation. a) $t=22t_0$; b) $t=34t_0$; c) $t=50t_0$; d) $t=87_0$. The aspect ratio is 1:2 in the x-y contour plots.

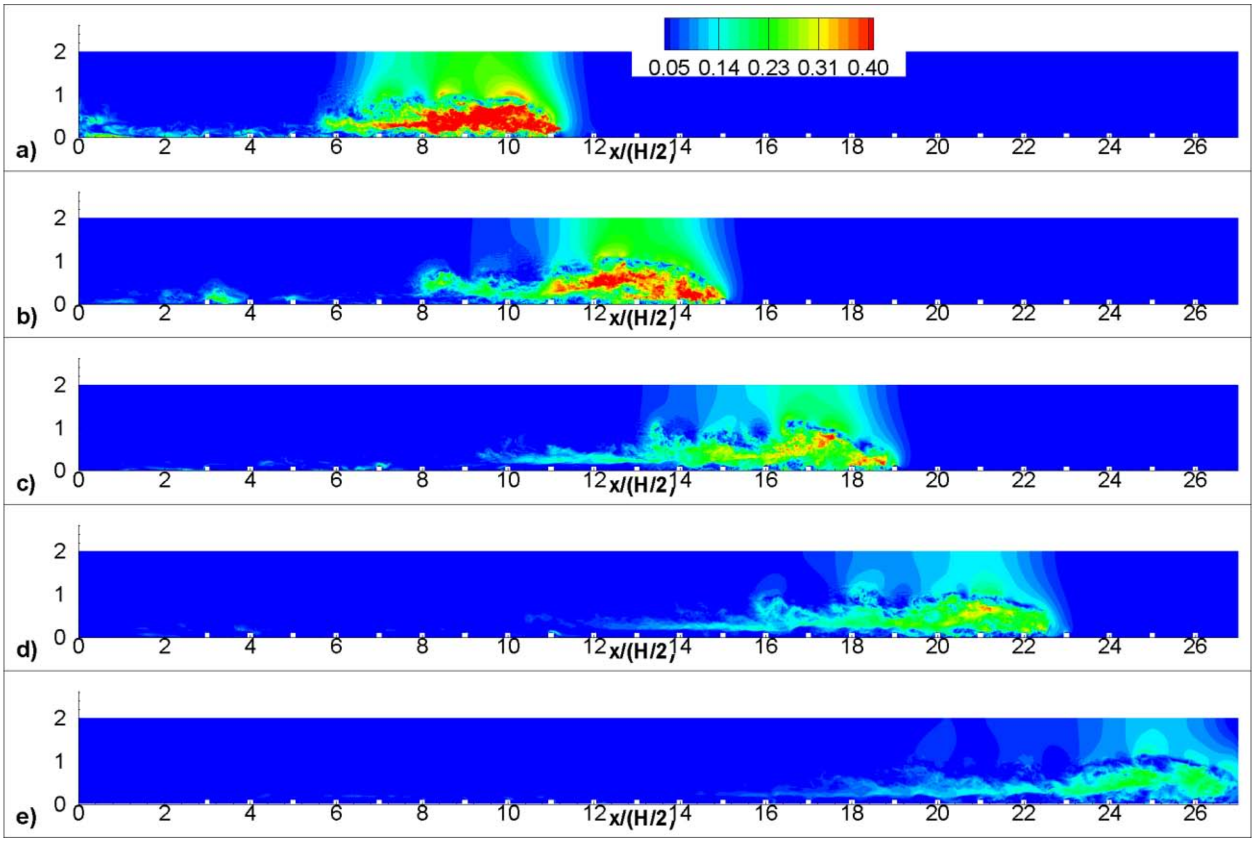

Figure 5.14 Distribution of velocity magnitude, u_{mag}/u_b, in the SV-LR-R10 simulation. a) $t=22t_0$; b) $t=34t_0$; c) $t=50t_0$; d) $t=70_0$; e) $t=100t_0$. The aspect ratio is 1:2 in the x-y contour plots.

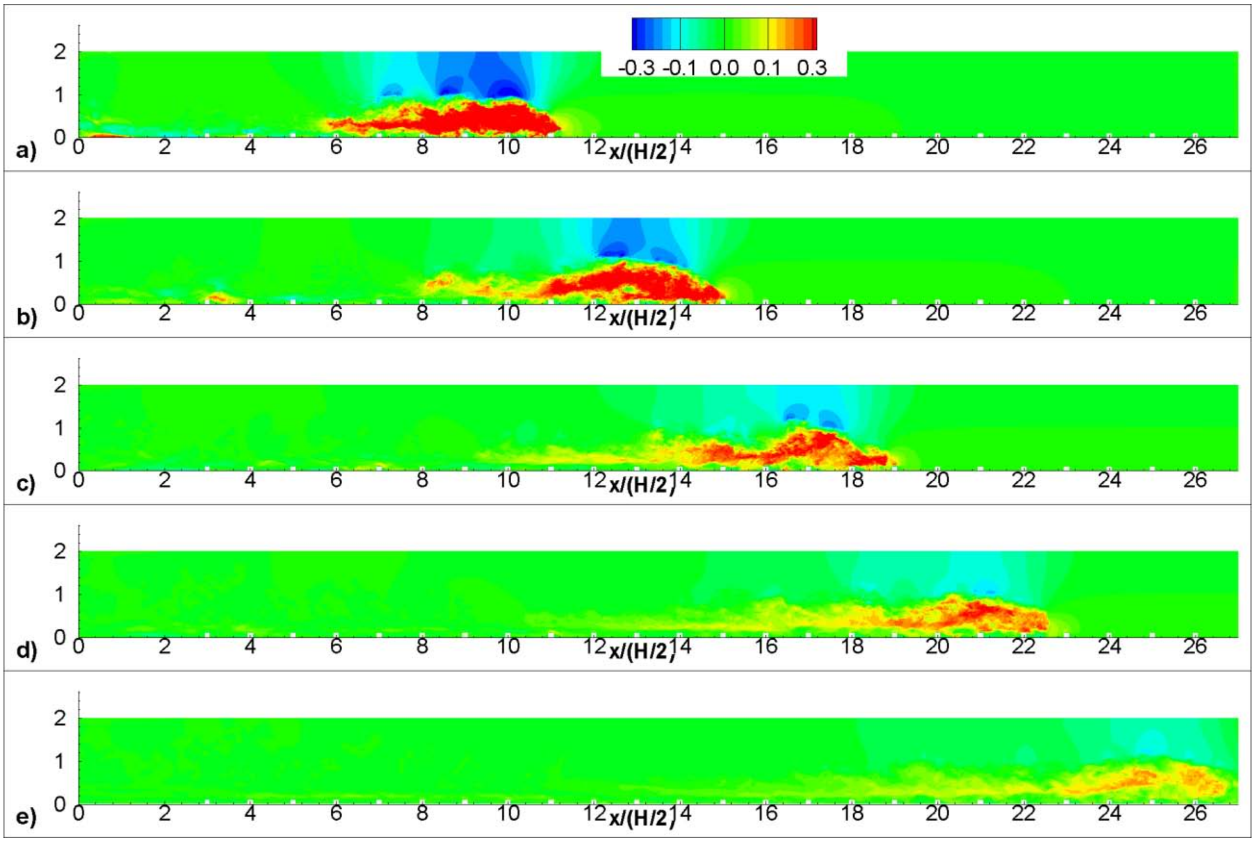

Figure 5.15 Distribution of streamwise velocity, u/u_b, in the SV-LR-R10 simulation. a) t=22t$_0$; b) t=34t$_0$; c) t=50t$_0$; d) t=87$_0$; e) t=100t$_0$. The aspect ratio is 1:2 in the x-y contour plots.

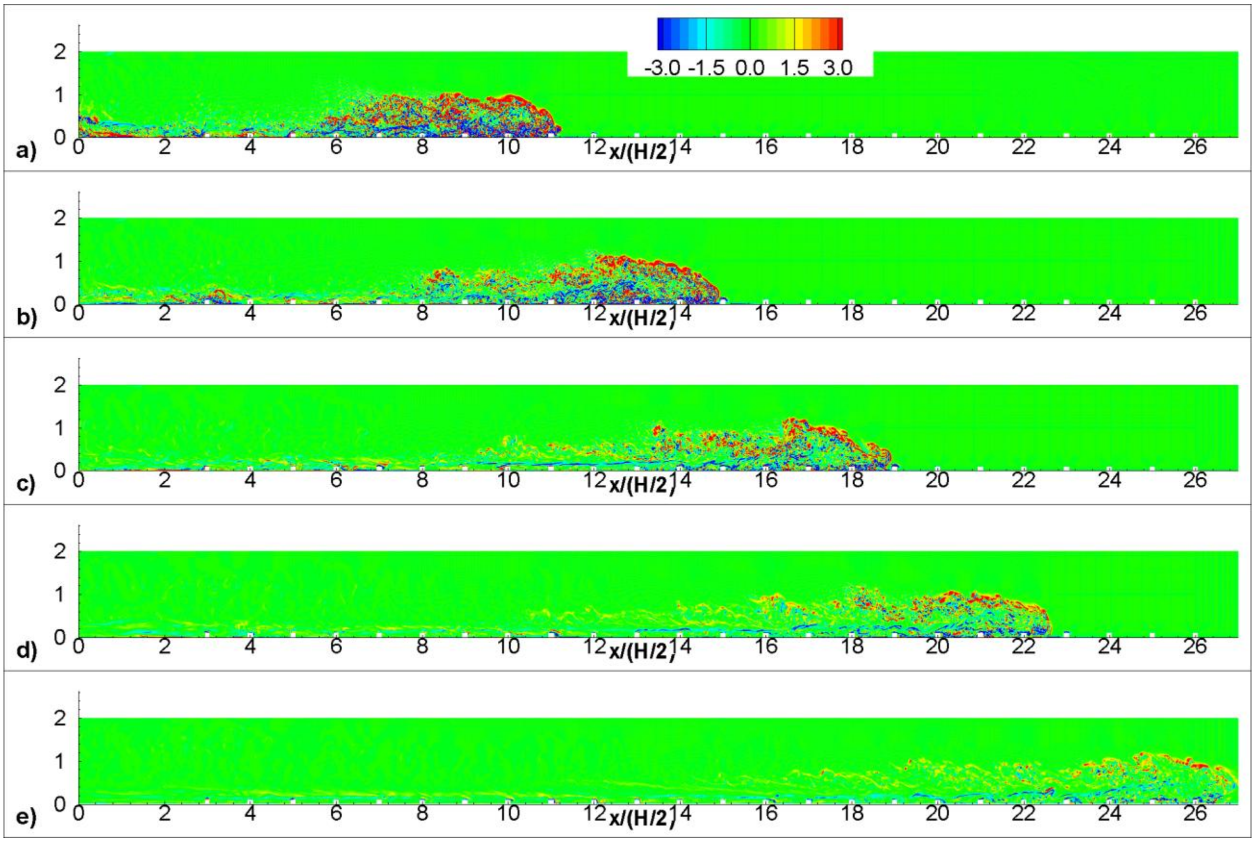

Figure 5.16 Distribution of out-of-plane vorticity, $\omega_z(H/2)/u_b$, in the SV-LR-R10 simulation. a) t=22t$_0$; b) t=34t$_0$; c) t=50t$_0$; d) t=87$_0$; e) t=100t$_0$. The aspect ratio is 1:2 in the x-y contour plots.

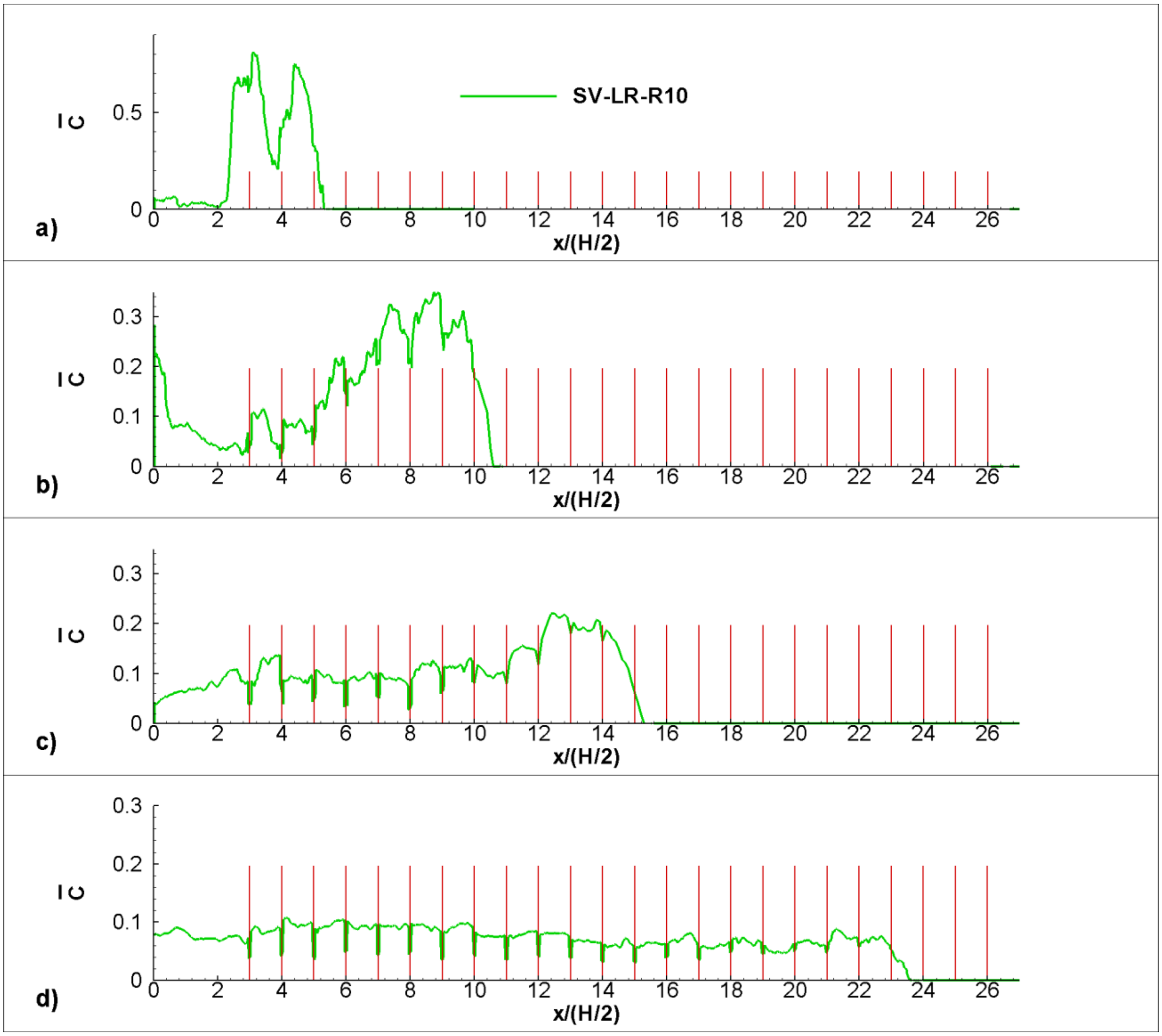

Figure 5.17 Streamwise variation of the depth-averaged concentration, $\overline{C}$ (non-dimensional height of the gravity current, $\overline{h}/(H/2)$), in the SV-LR-R10 simulation. a) $x_f/(H/2)\sim5.2$; b) $x_f/(H/2)\sim10.5$; c) $x_f/(H/2)\sim15.5$; d) $x_f/(H/2)\sim23.5$.

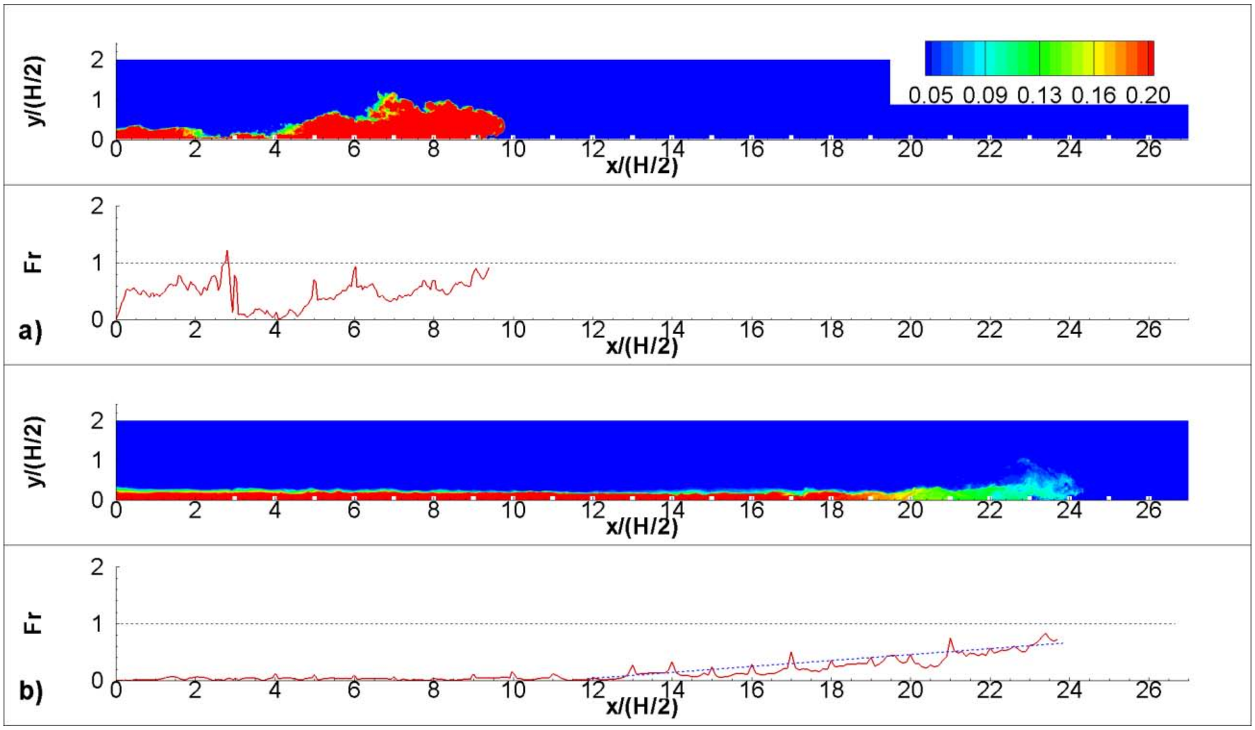

Figure 5.18 Streamwise distribution of the Froude number in the SV-LR-R10 simulation. The structure of the current is visualized in an x-y section using concentration contours. a) $x_f/(H/2)=9.5$ (buoyancy-inertia phase); b) $x_f/(H/2)=24$ (drag-dominated phase).

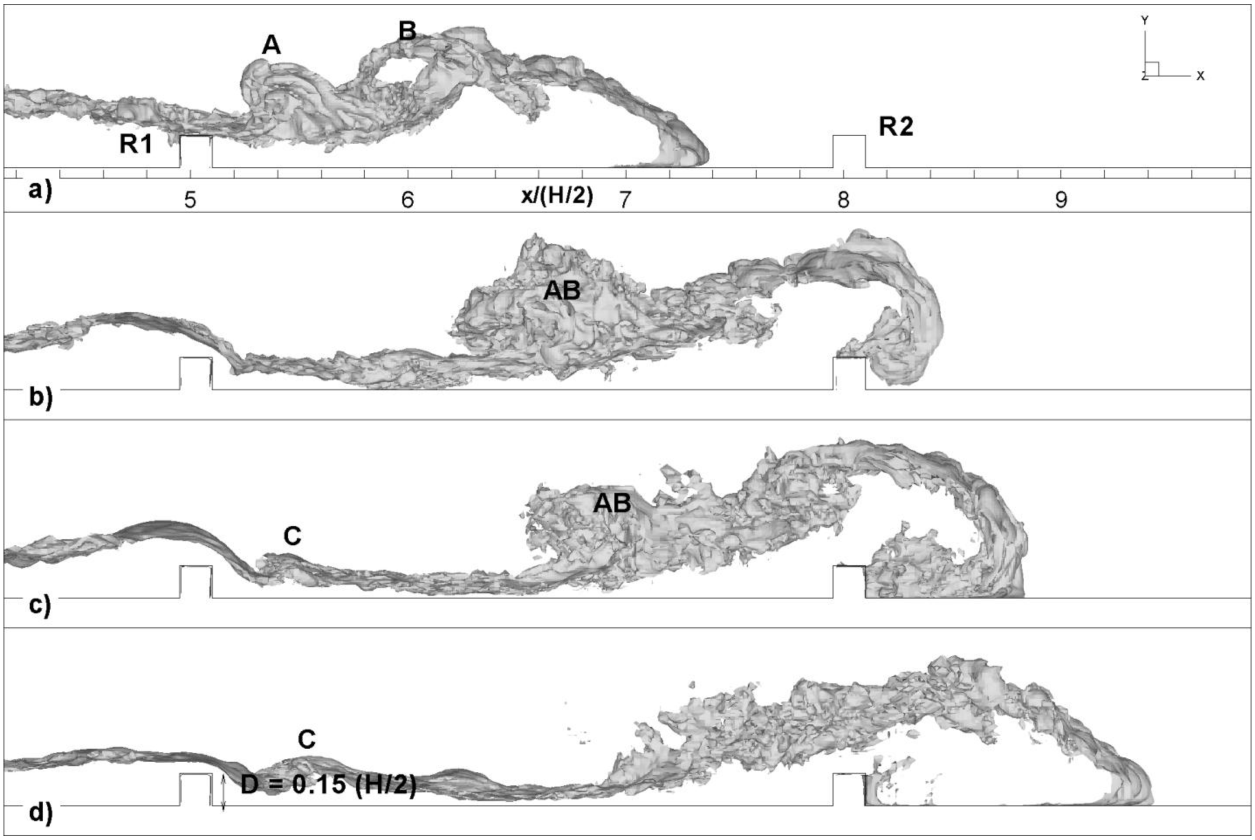
A
B
R1
R2
Y
X
Z
a)
5
6
x/(H/2)
7
8
9
AB
b)
AB
C
c)
C
D = 0.15 (H/2)
d)

Figure 5.19 Visualization of the interface between the gravity current and the ambient fluid using a 3-D concentration isosurface (C=0.1) in the SV-LR-R15 simulation during the buoyancy-inertia phase. a) $t=16t_0$; b) $t=20t_0$; c) $t=22t_0$; d) $t=24_0$.

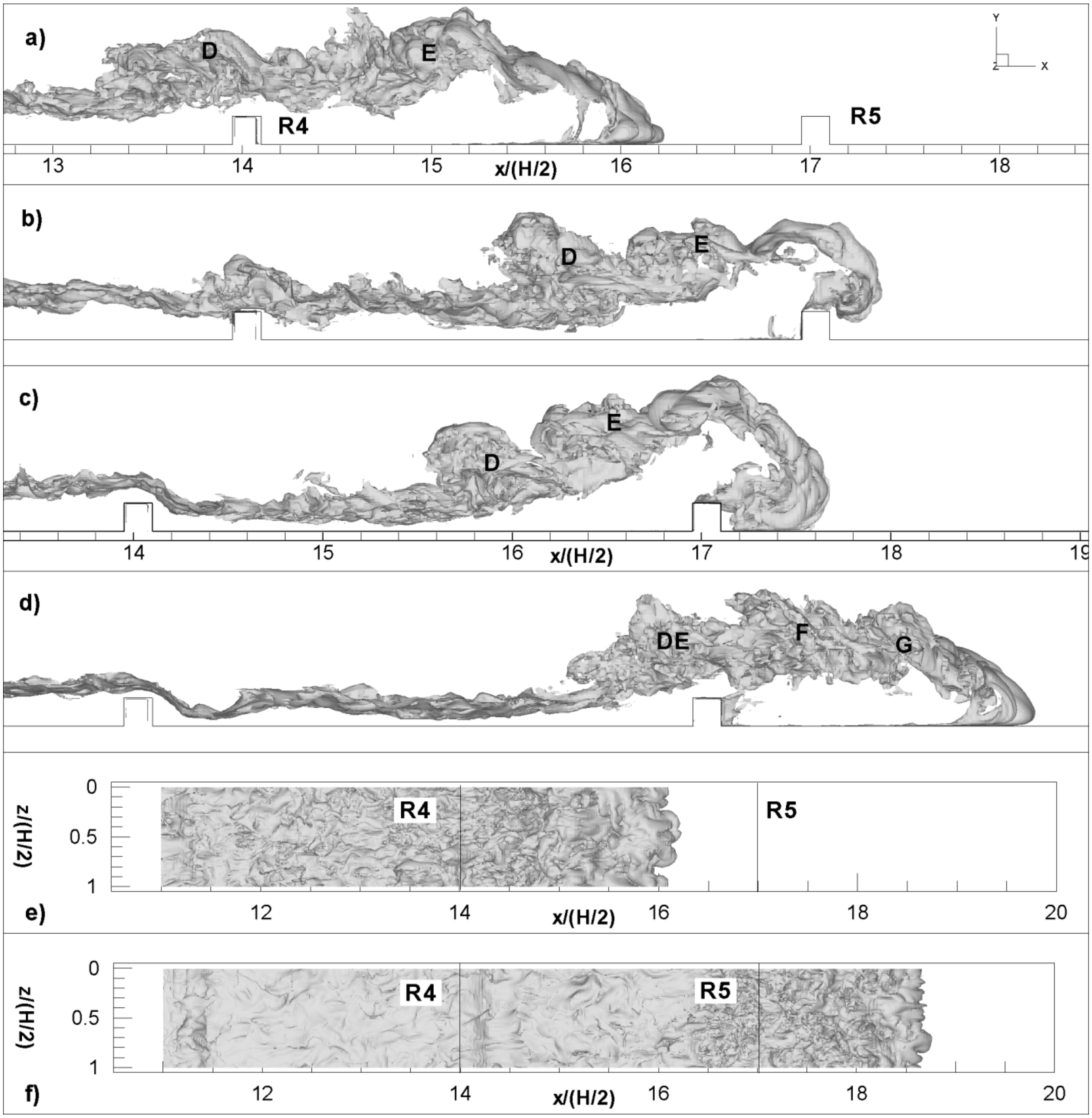
a)
D
E
R4
R5
13
14
15
x/(H/2)
16
17
18
b)
D
E
c)
E
D
14
15
16
x/(H/2)
17
18
19
d)
DE
F
G
0
0.5
1
z/(H/2)
R4
R5
e)
12
14
x/(H/2)
16
18
20
0
0.5
1
z/(H/2)
R4
R5
f)
12
14
x/(H/2)
16
18
20

Figure 5.20 Visualization of the interface between the gravity current and the ambient fluid using a 3-D concentration isosurface (C=0.02) in the SV-LR-R15 simulation. a) t=62t$_0$; b) t=72t$_0$; c) t=76t$_0$; d) t=86$_0$; e) t=62t$_0$, view from above; f) t=86$_0$, view from above.

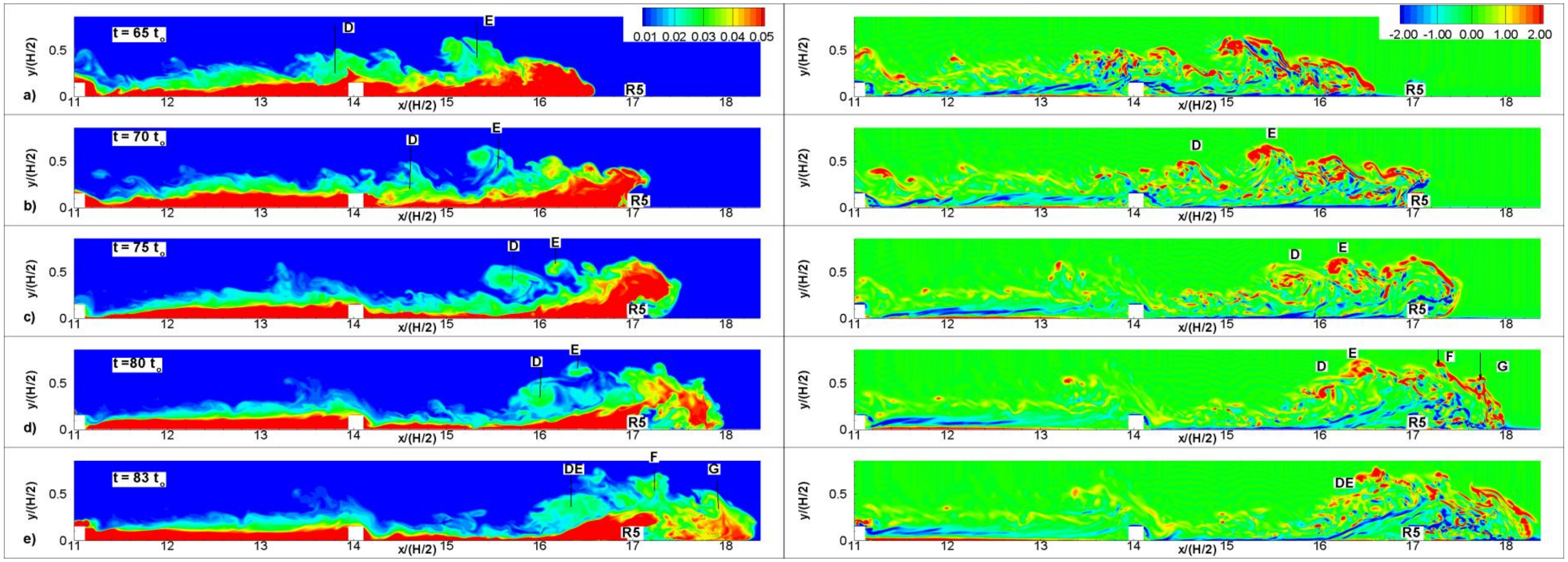

Figure 5.21 Visualization of the gravity current as it passes Rib5 in the SV-LR-R15 simulation using concentration (left) and out-of-plane vorticity (right) contours. a) t=65t$_0$; b) t=70t$_0$; c) t=75t$_0$; d) t=80$_0$; e) t=83t$_0$.

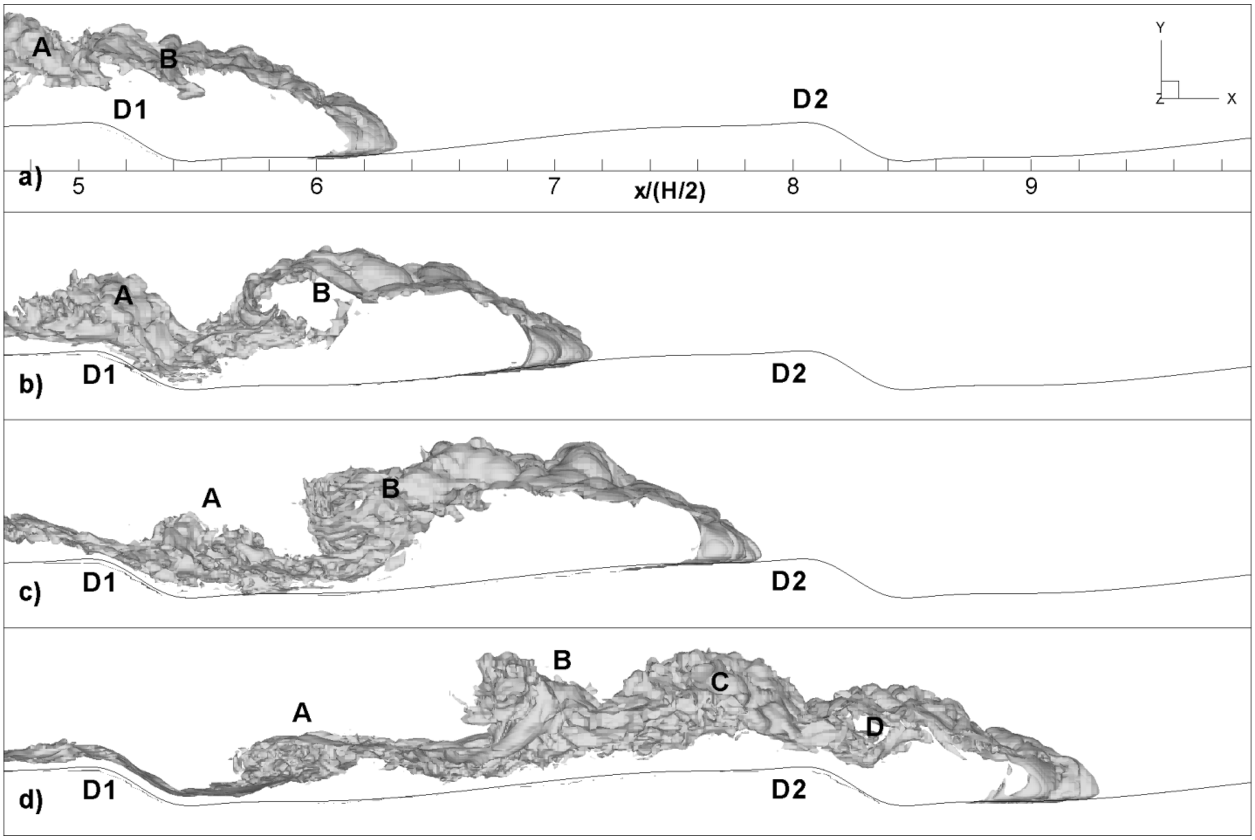
Y
Z
X
A
B
D1
D2
a)
5
6
7
x/(H/2)
8
9
A
B
b)
D1
D2
A
B
c)
D1
D2
B
C
A
D
d)
D1
D2

Figure 5.22 Visualization of the interface between the gravity current and the ambient fluid using a 3-D concentration isosurface (C=0.1) in the SV-LR-D15 simulation during the buoyancy-inertia phase. a) $t=12t_0$; b) $t=14t_0$; c) $t=16t_0$; d) $t=20_0$.

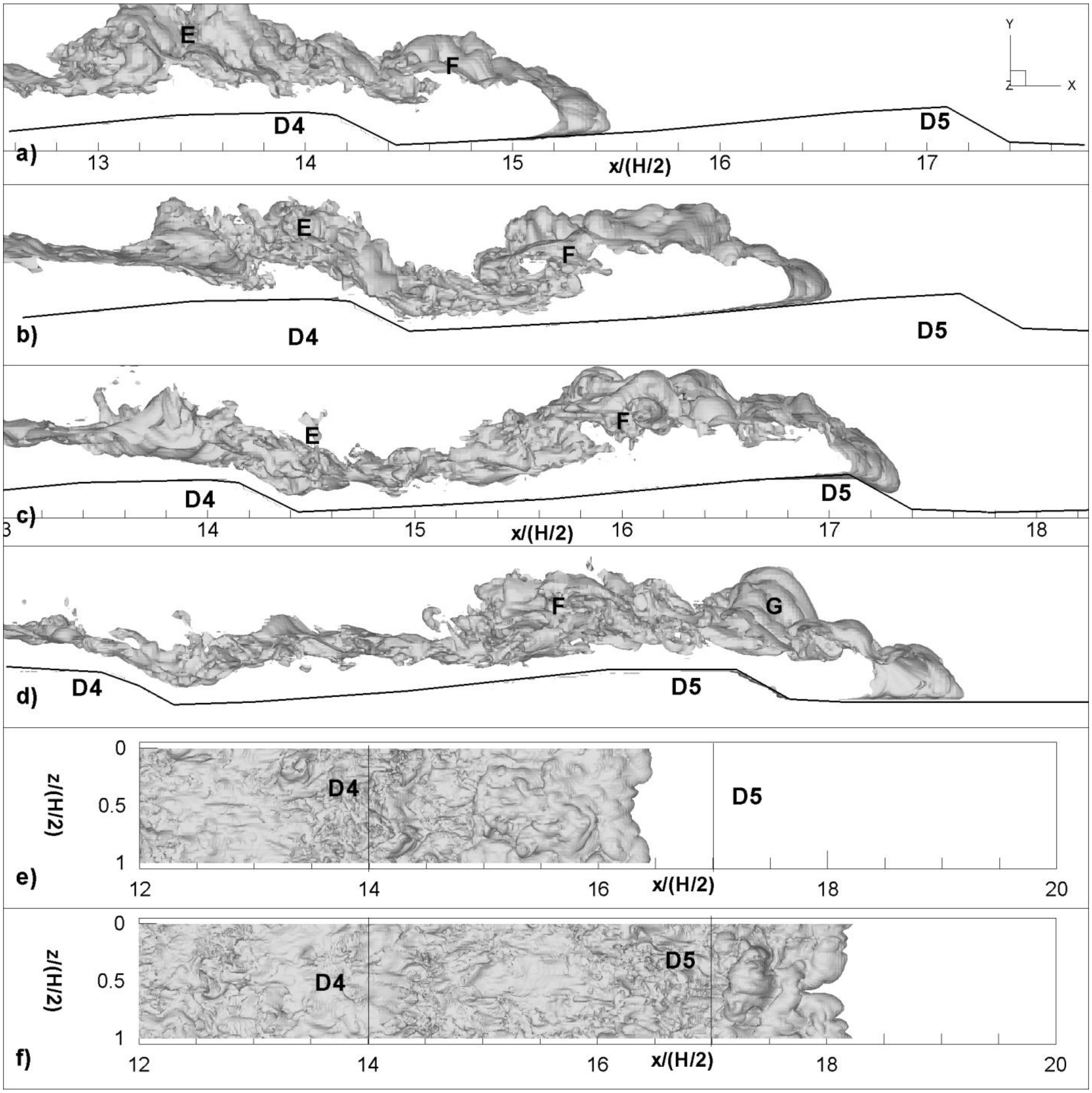
Y
Z
X
E
F
D4
D5
a)
13
14
15
x/(H/2)
16
17
E
F
b)
D4
D5
E
F
D4
D5
c)
13
14
15
x/(H/2)
16
17
18
F
G
d)
D4
D5
0
z/(H/2)
0.5
1
D4
D5
e)
12
14
16
x/(H/2)
18
20
0
z/(H/2)
0.5
1
D5
D4
f)
12
14
16
x/(H/2)
18
20

Figure 5.23 Visualization of the interface between the gravity current and the ambient fluid using a 3-D concentration isosurface (C=0.02) in the SV-LR-D15 simulation. a) t=46t$_0$; b) t=52t$_0$; c) t=56t$_0$; d) t=62$_0$; e) t=52t$_0$, view from above; f) t=62t$_0$, view from above.

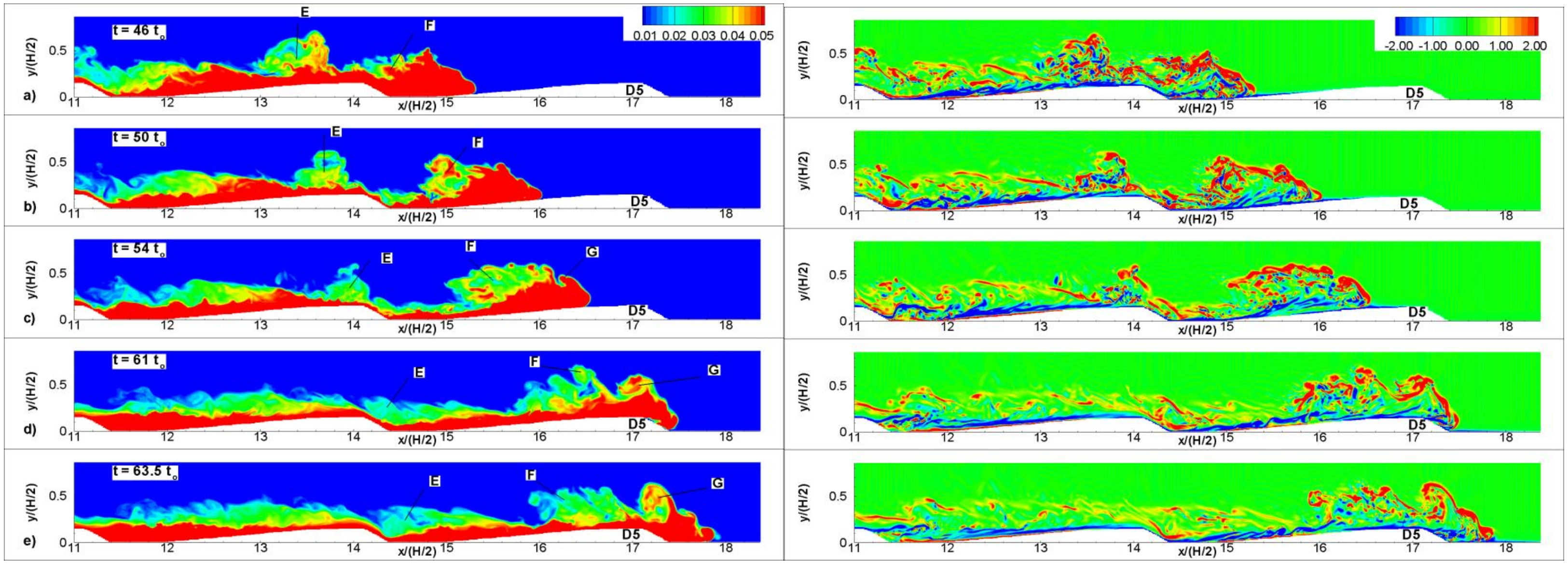

Figure 5.24 Visualization of the gravity current as it passes Dune5 in the SV-LR-D15 simulation using concentration (left) and out-of-plane vorticity (right) contours. a) t=46t$_0$; b) t=50t$_0$; c) t=54t$_0$; d) t=61$_0$; e) t=63.5t$_0$.

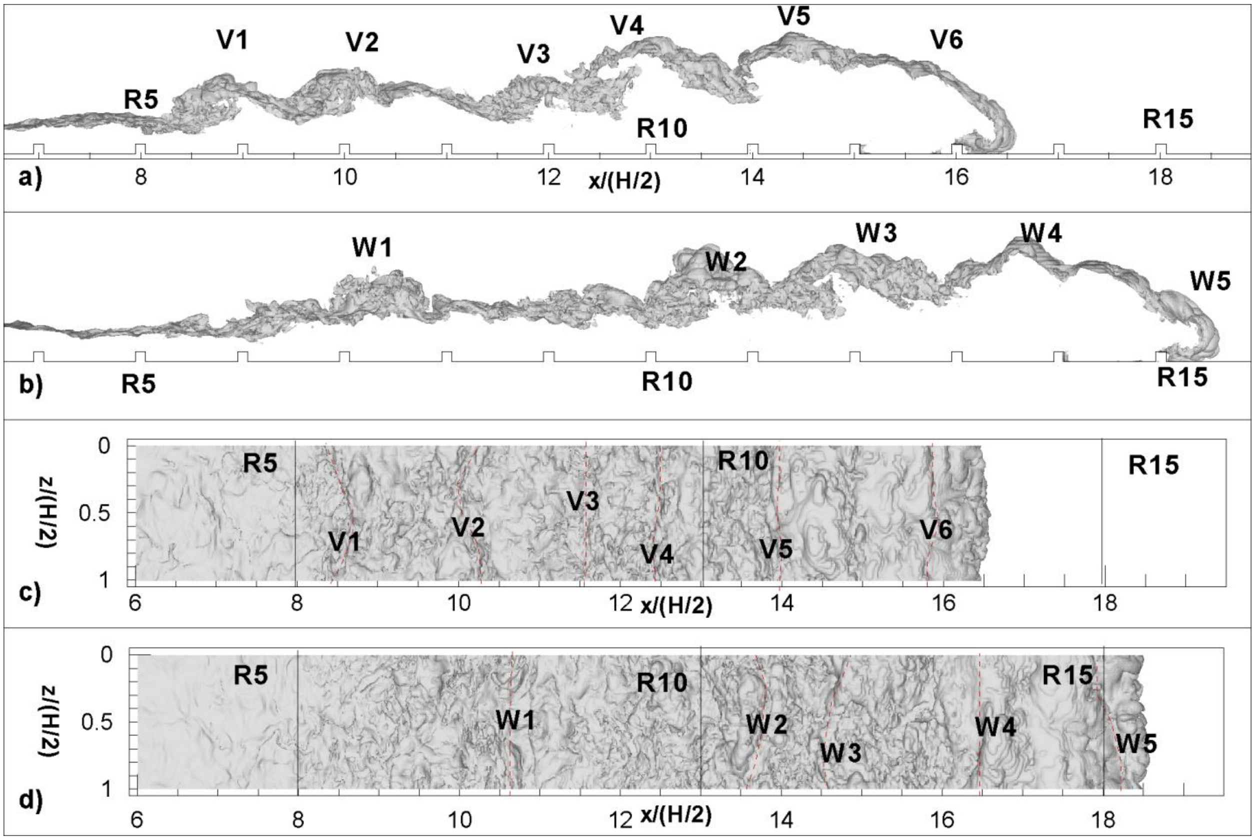
V1
V2
V3
V4
V5
V6
R5
R10
R15
a)
8
10
12
x/(H/2)
14
16
18
W1
W2
W3
W4
W5
b)
R5
R10
R15
c)
z/(H/2)
0
0.5
1
R5
R10
R15
V1
V2
V3
V4
V5
V6
6
8
10
12
x/(H/2)
14
16
18
d)
z/(H/2)
0
0.5
1
R5
R10
R15
W1
W2
W3
W4
W5
6
8
10
12
x/(H/2)
14
16
18

Figure 5.25 Visualization of the interface between the gravity current and the ambient fluid using a 3-D concentration isosurface (C=0.02) in the SV-LR-R10 simulation. a) $t=40t_0$; b) $t=48t_0$; c) $t=40t_0$, view from above; d) $t=48t_0$, view from above. The dashed lines indicate the position and spanwise extent of the interfacial billows.

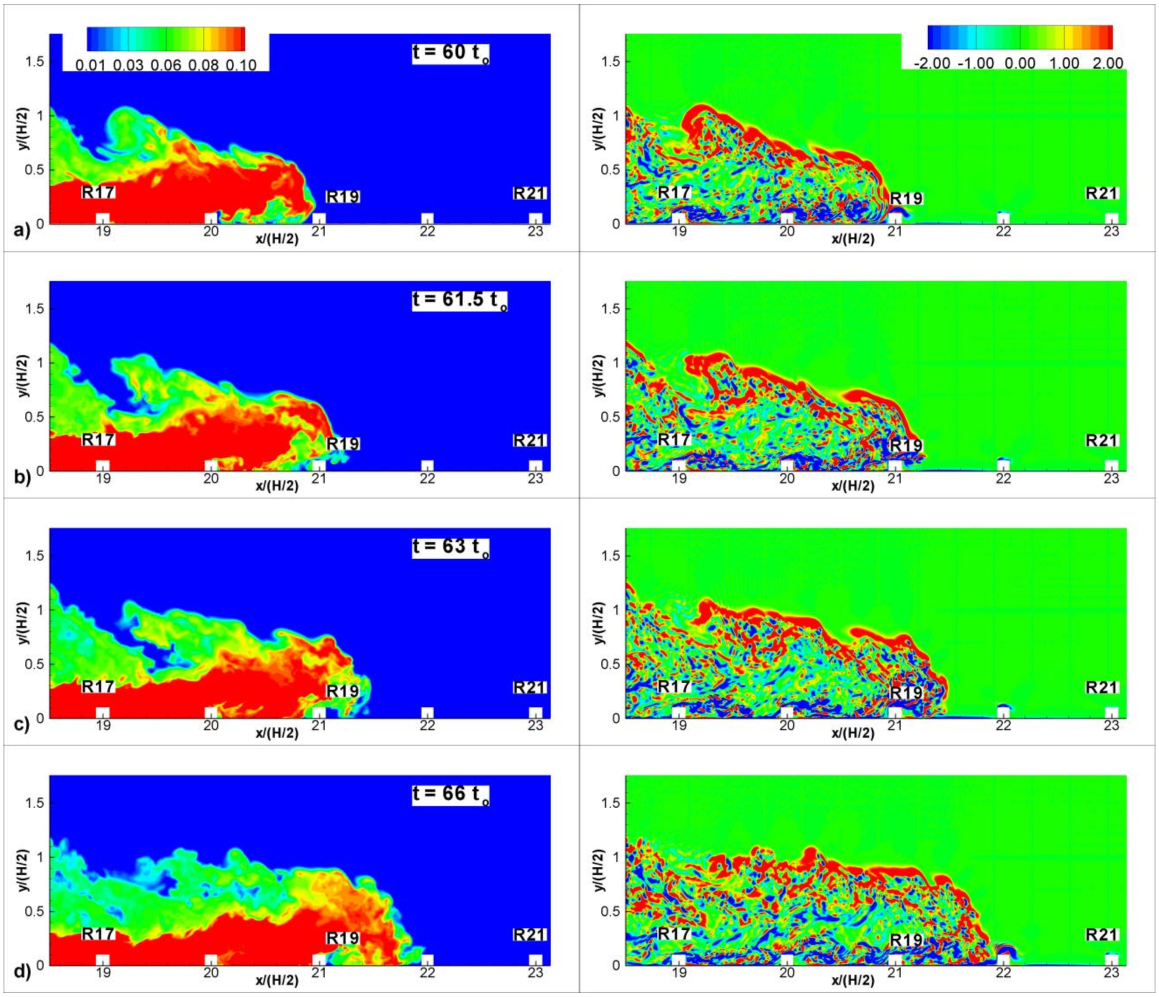

Figure 5.26 Visualization of the gravity current in the SV-LR-R10 simulation using concentration (left) and out-of-plane vorticity (right) contours as it passes Rib19. a) t=60t$_0$; b) t=61.5t$_0$; c) t=63t$_0$; d) t=66$_0$.

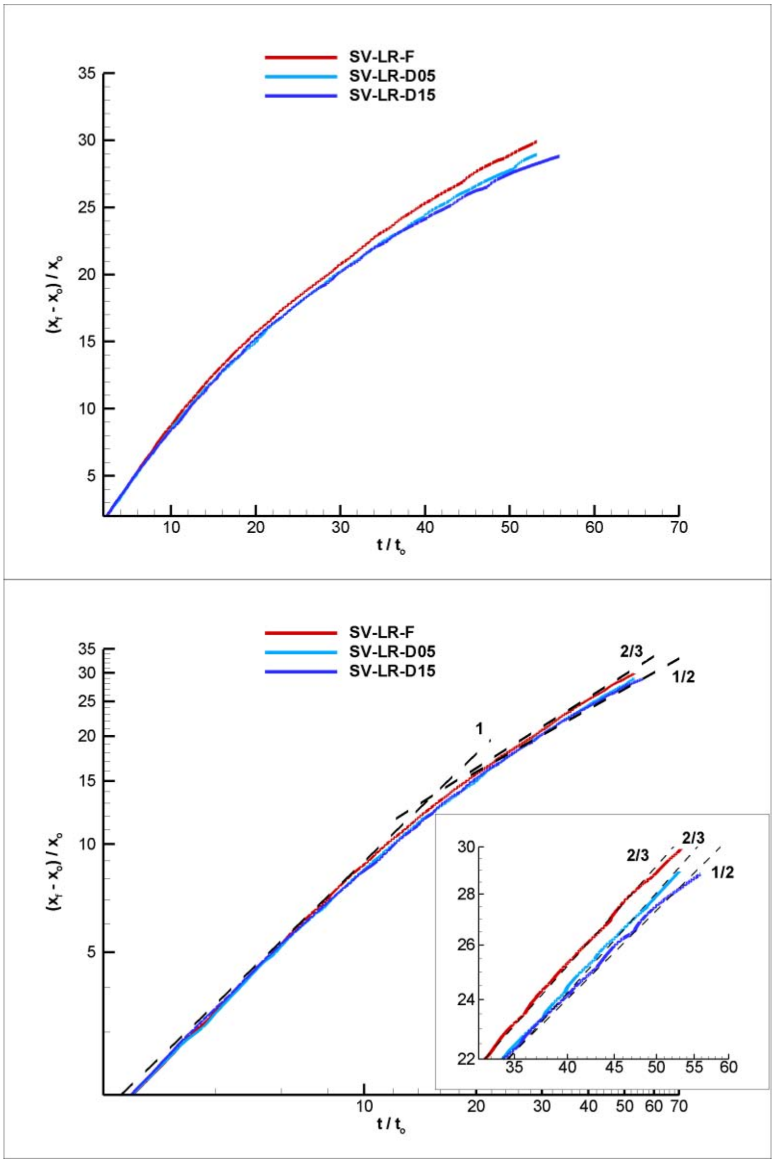

a)

b)

Figure 5.27 Time variation of the non-dimensional position of the front, $(x_f-x_0)/x_0$, function of the non-dimensional time, t/t_0, in the SV-LR-F, SV-LR-D05 and SV-LR-D15 simulations a)linear scale; b) log-log scale.

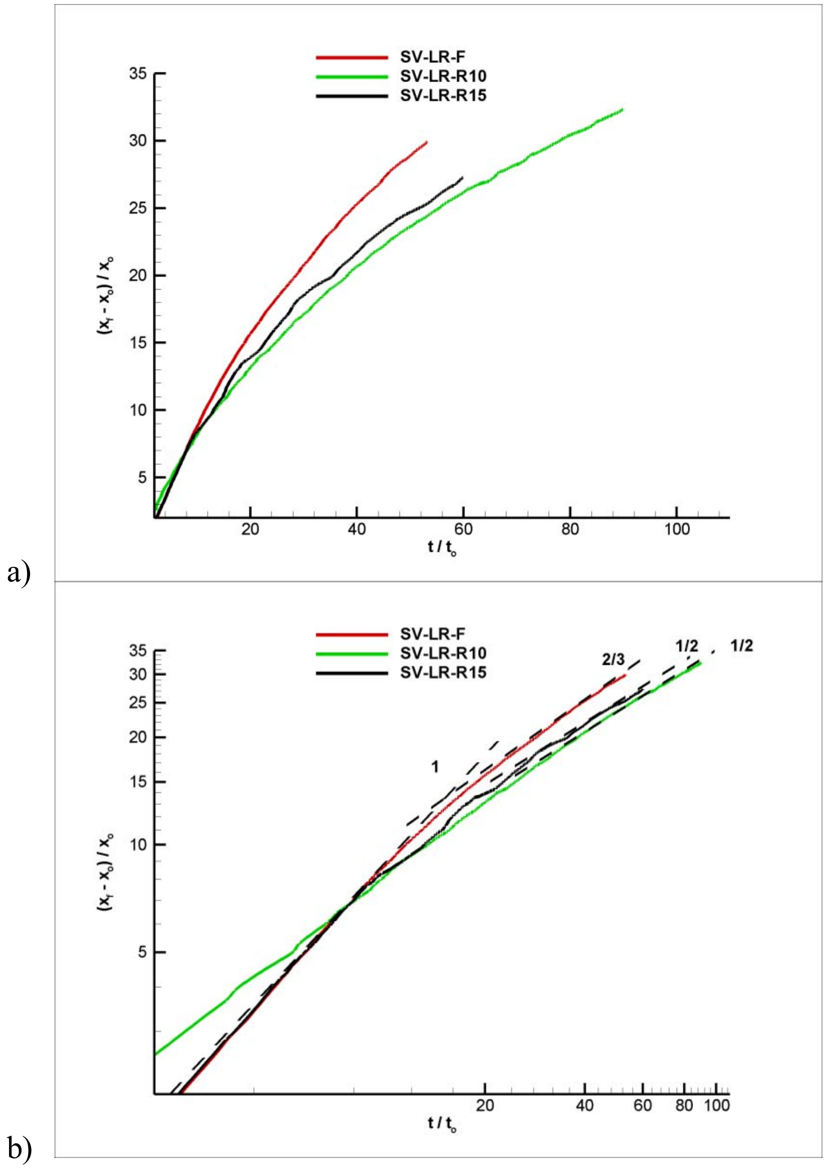

Figure 5.28 Time variation of the non-dimensional position of the front, $(x_f-x_0)/x_0$, function of the non-dimensional time, t/t_0, in the SV-LR-F, SV-LR-R10 and SV-LR-R15 simulations. a) linear scale; b) log-log scale.

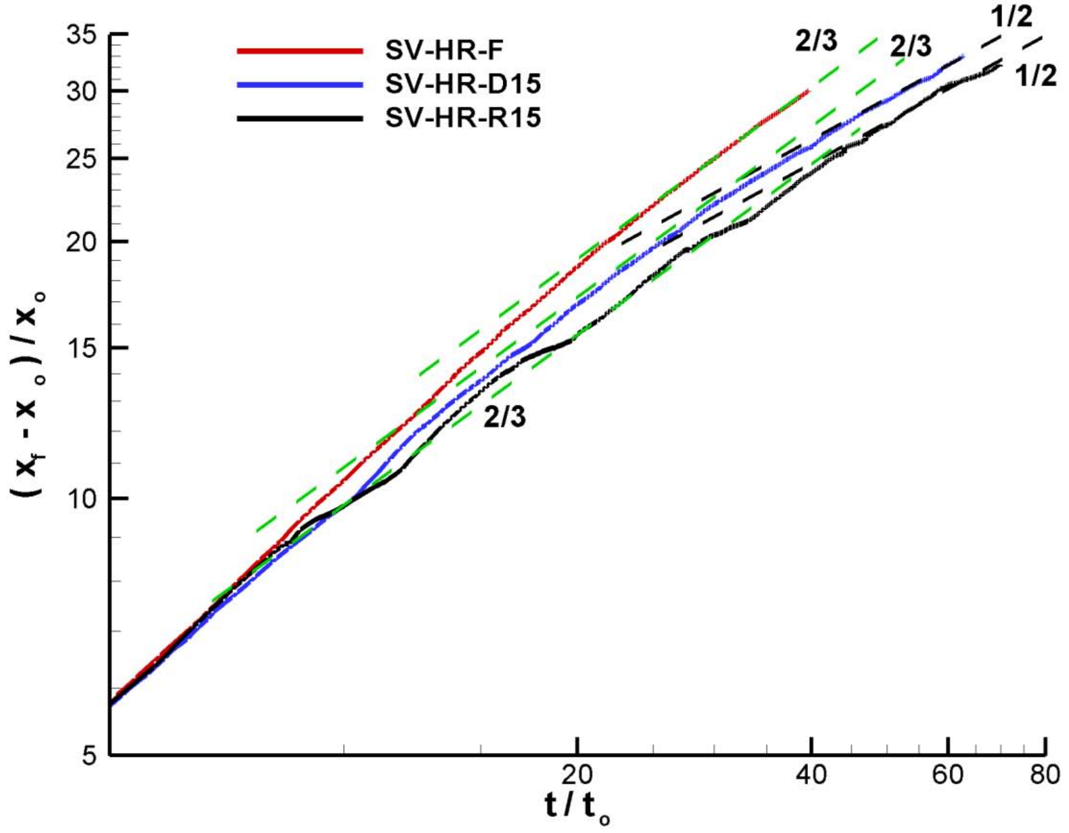

Figure 5.29 Time variation of the non-dimensional position of the front, $(x_f-x_0)/x_0$, function of the non-dimensional time, t/t_0 (log-log scale) in the high Reynolds number simulations SV-HR-F, SV-HR-D15 and SV-HR-R15.

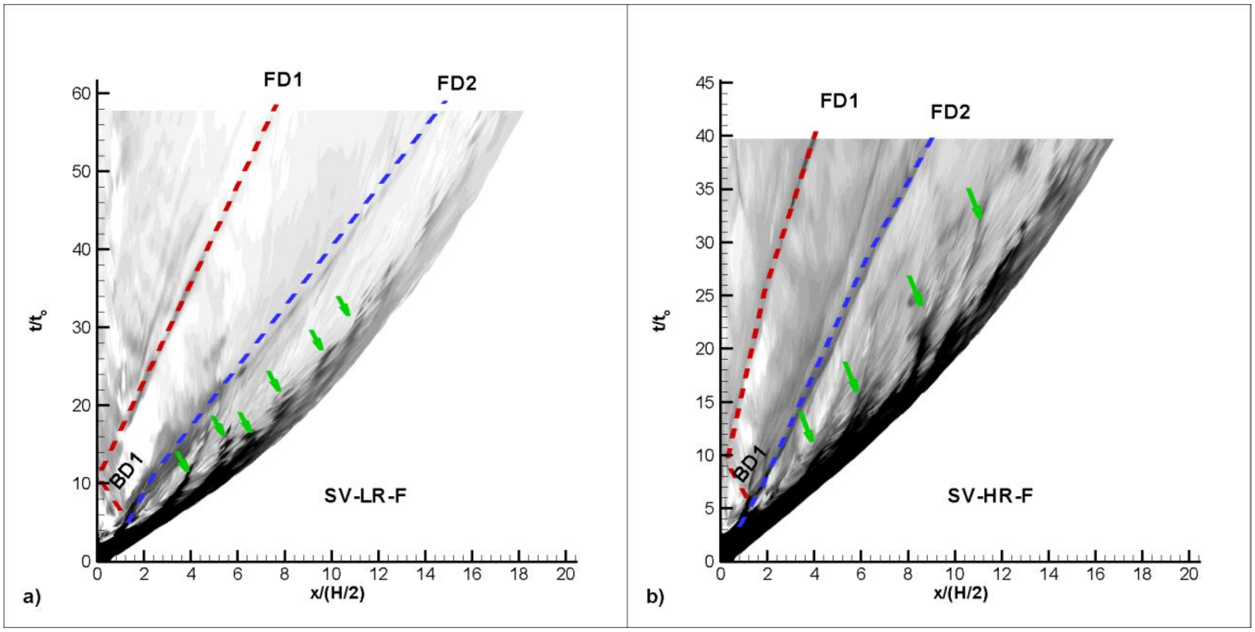

Figure 5.30 Evolution of the concentration with time along the x axis. The distance from the bottom wall is y/(H/2)=0.09. a) SV-LR-F simulation; b) SV-HR-F simulation. The dashed lines correspond to the forward propagating disturbances FD1 and FD2 and to the backward propagating disturbance BD1. After reflection BD1 is called FD1.

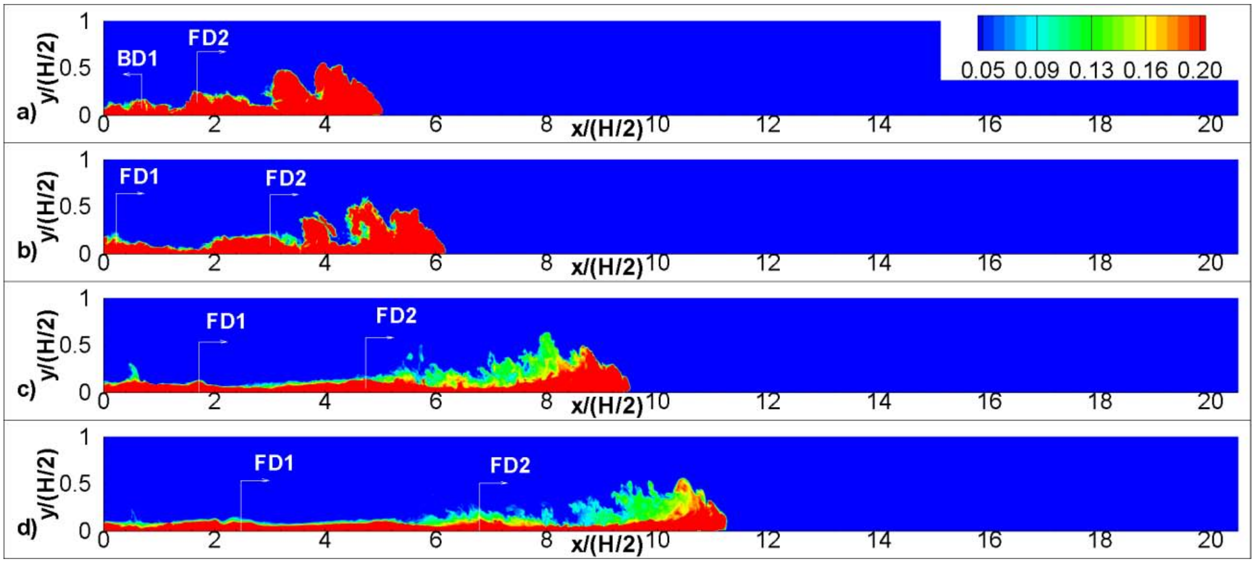

Figure 5.31 Visualization of the structure of the gravity current in the SV-LR-F simulation using concentration contours. The position and direction of propagation of the flow disturbances are shown using arrows. a) $t=9t_0$; b) $t=11.5t_0$; c) $t=20.5t_0$; d) $t=26.5_0$. The aspect ratio is 1:2 in the x-y contour plots.

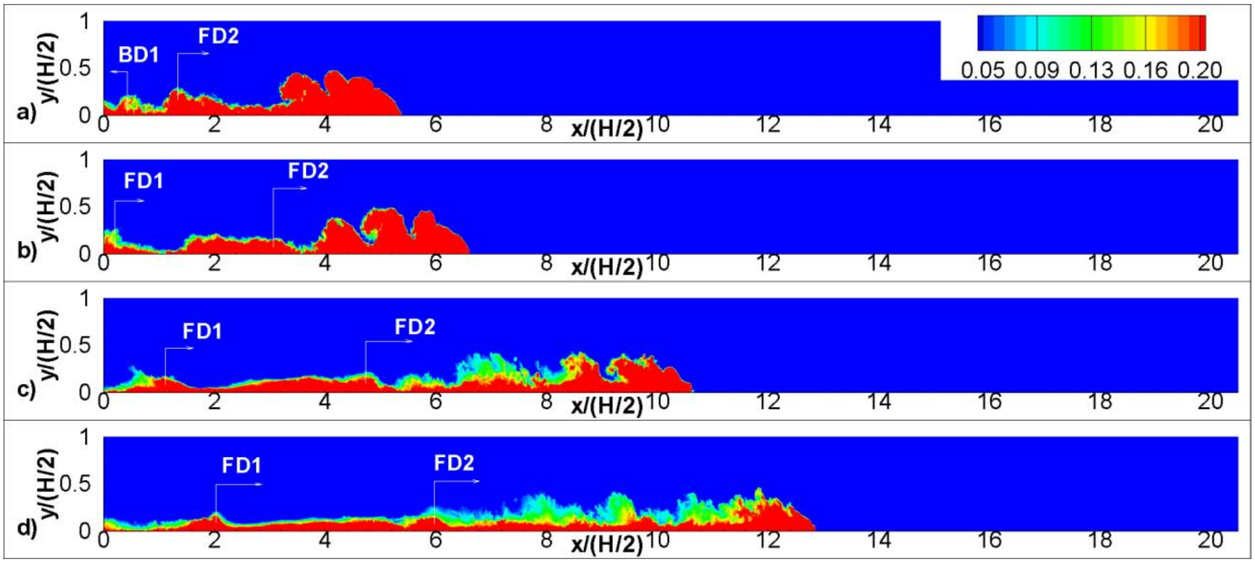

Figure 5.32 Visualization of the structure of the gravity current in the SV-HR-F simulation using concentration contours. The position and direction of propagation of the flow disturbances are shown using arrows. a) $t=9t_0$; b) $t=11.5t_0$; c) $t=20.5t_0$; d) $t=26.5_0$. The aspect ratio is 1:2 in the x-y contour plots.

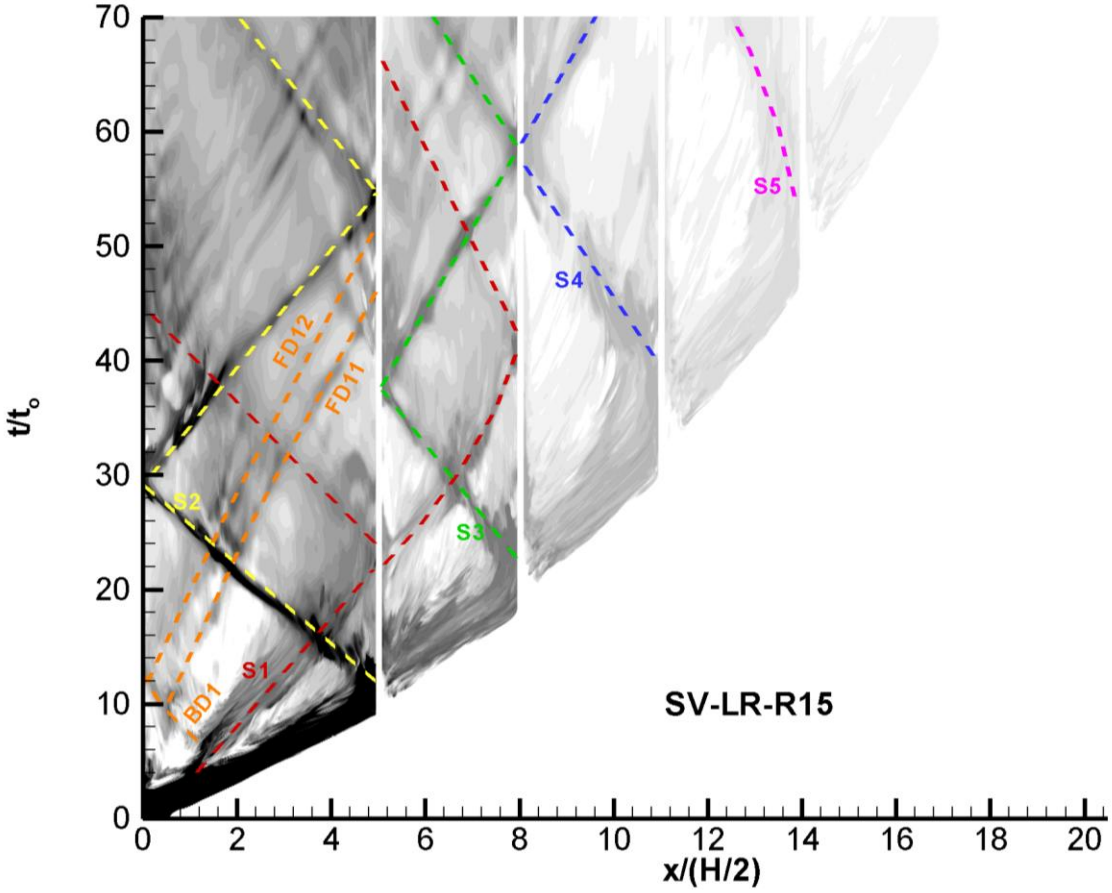

Figure 5.33 Evolution of the concentration with time along the x axis in the SV-LR-R15 simulation. The distance from the bottom wall is y/(H/2)=0.09. The dashed lines visualize the main forward and backward propagating flow disturbances. S1, BD1, FD11 and FD12 form due to the collapse of a large interfacial billow on the channel bottom. S2 to S5 form due to the partial reflection of the gravity current fluid as the front passes Rib1 to Rib4, respectively.

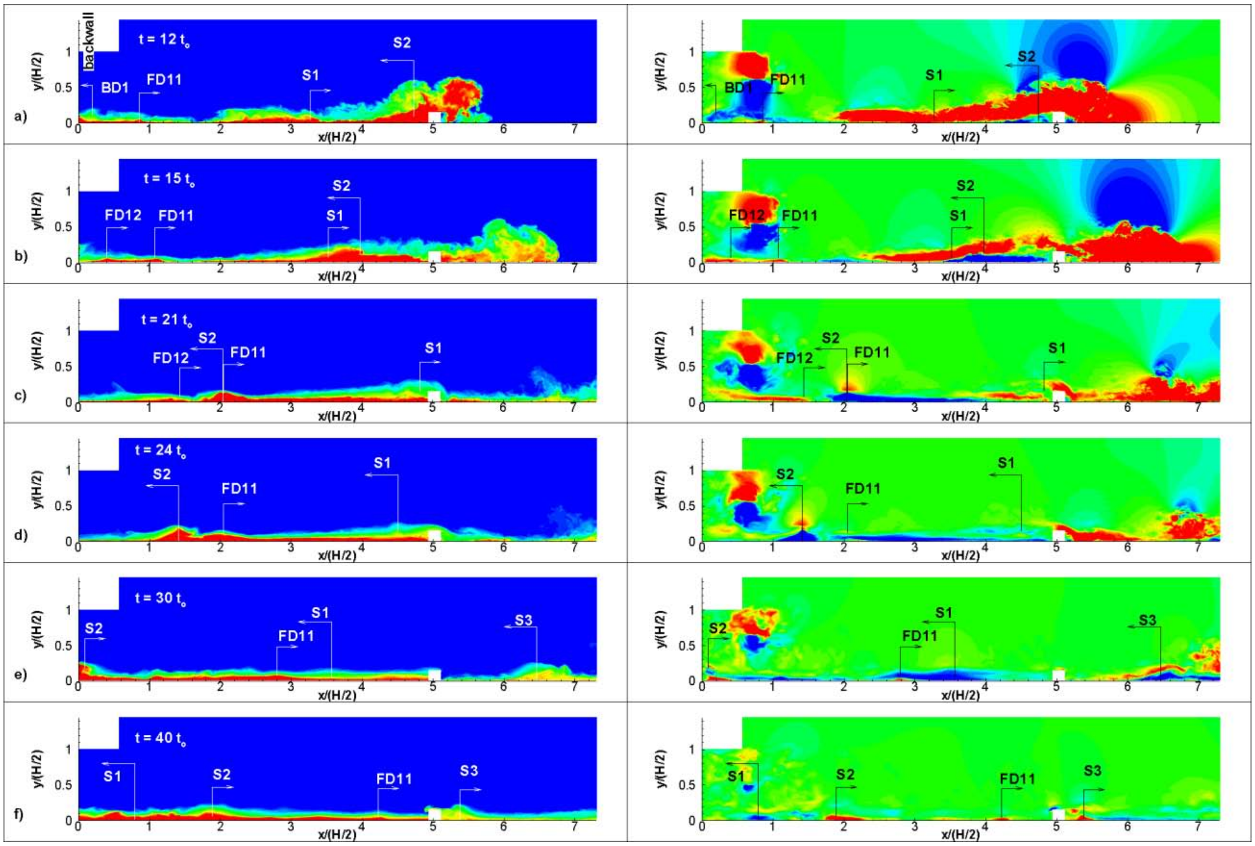

Figure 5.34 Visualization of the structure of the current between the end wall and Rib1 in the SV-LR-R15 simulation using non-dimensional concentration contours (left) and streamwise velocity contours (right). Also shown are the position and direction of propagation of the main flow disturbances. a) $t=12t_0$; b) $t=15t_0$; c) $t=21t_0$; d) $t=24_0$; e) $t=30t_0$; f) $t=40t_0$.

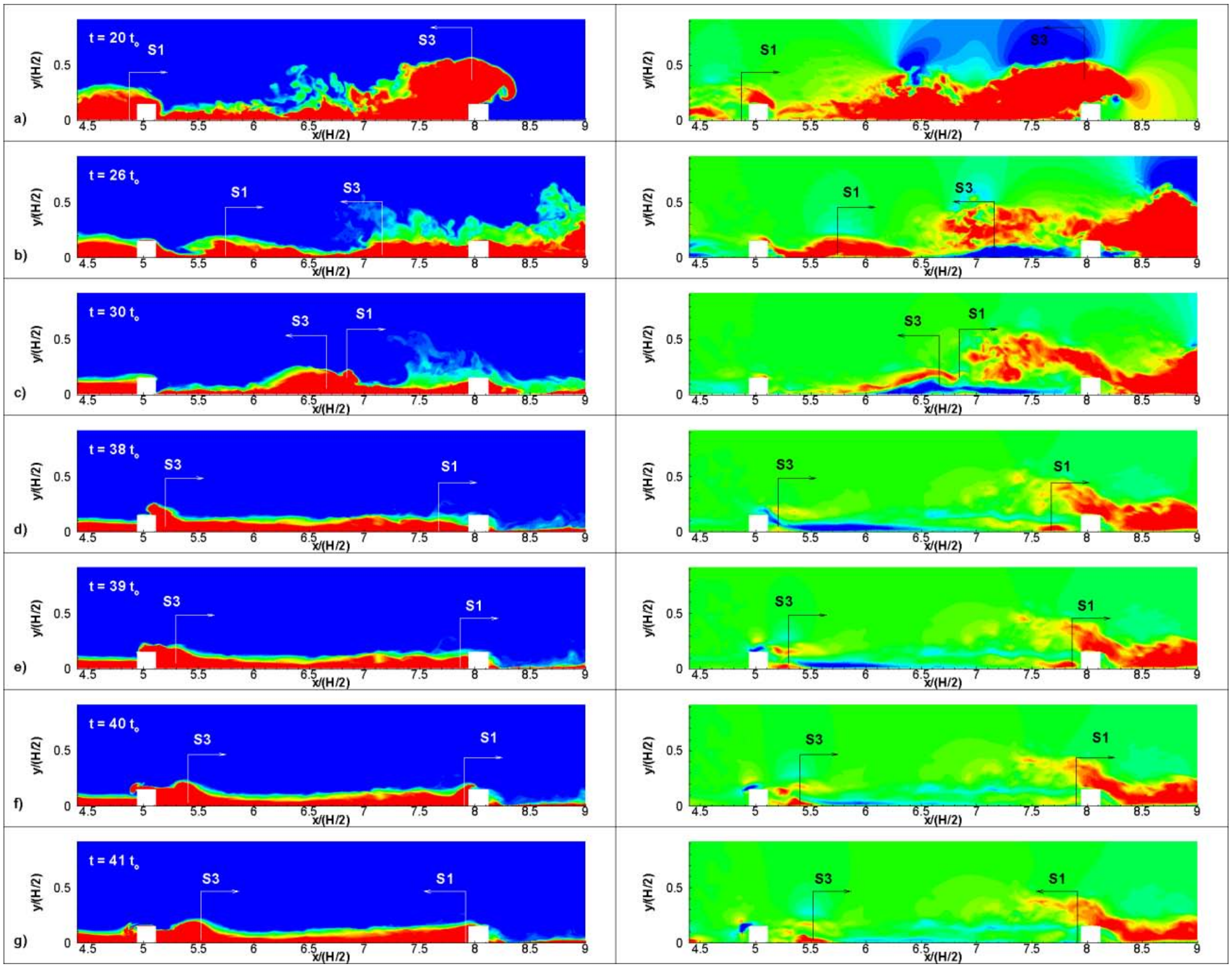

Figure 5.35 Visualization of the structure of the current between Rib1 and Rib2 in the SV-LR-R15 simulation using non-dimensional concentration contours (left) and streamwise velocity contours (right). Also shown are the position and direction of propagation of the main flow disturbances. a) t=20t$_0$; b) t=26t$_0$; c) t=30t$_0$; d) t=38$_0$; e) t=39t$_0$; f) t=40t$_0$; g) t=41t$_0$.

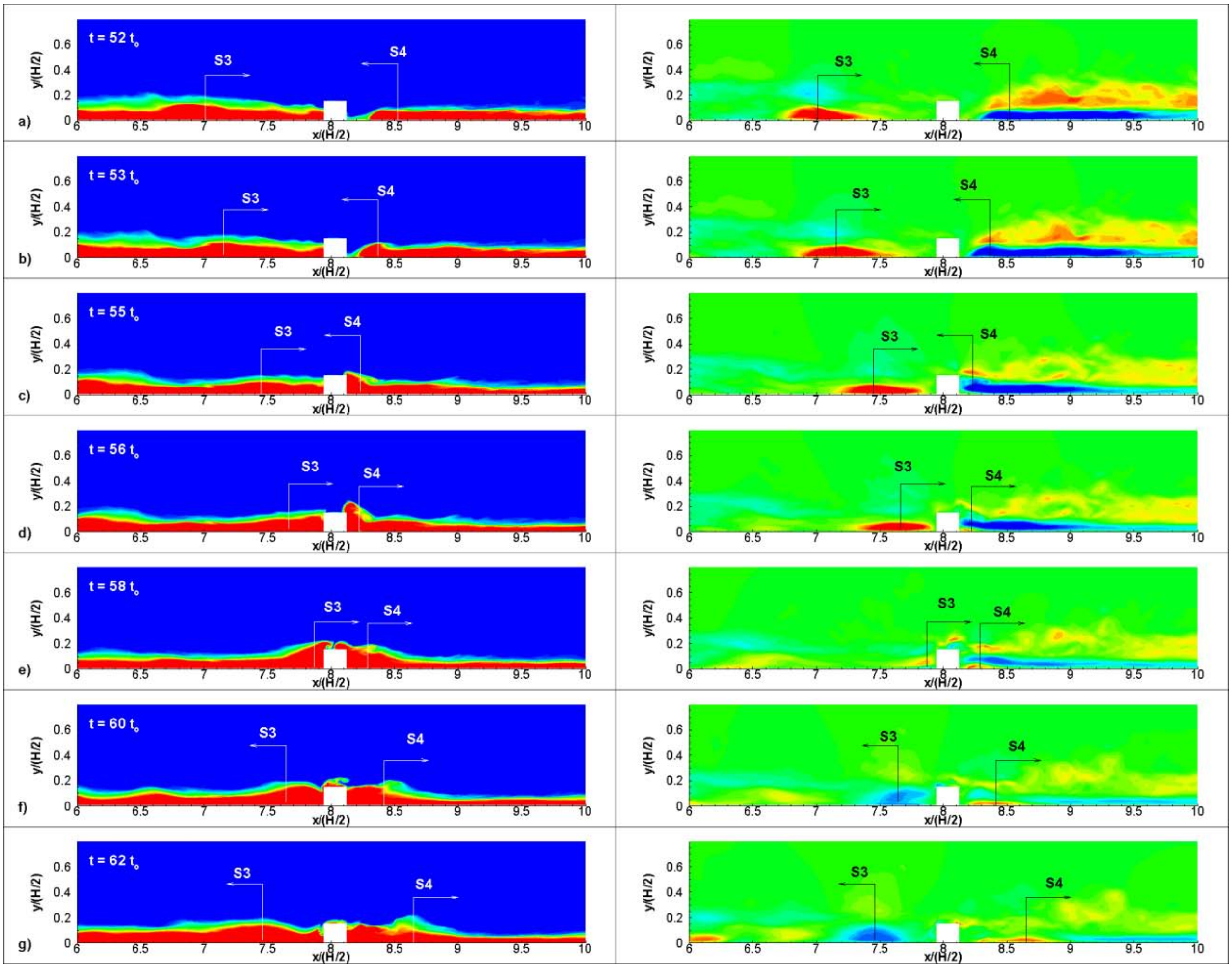

Figure 5.36 Visualization of the structure of the current around Rib2 in the later stages of the SV-LR-R15 simulation using non-dimensional concentration contours (left) and streamwise velocity contours (right). Also shown are the position and direction of propagation of the main flow disturbances. a) $t=52t_0$; b) $t=53t_0$; c) $t=55t_0$; d) $t=56_0$; e) $t=58t_0$; f) $t=60t_0$; g) $t=62t_0$.

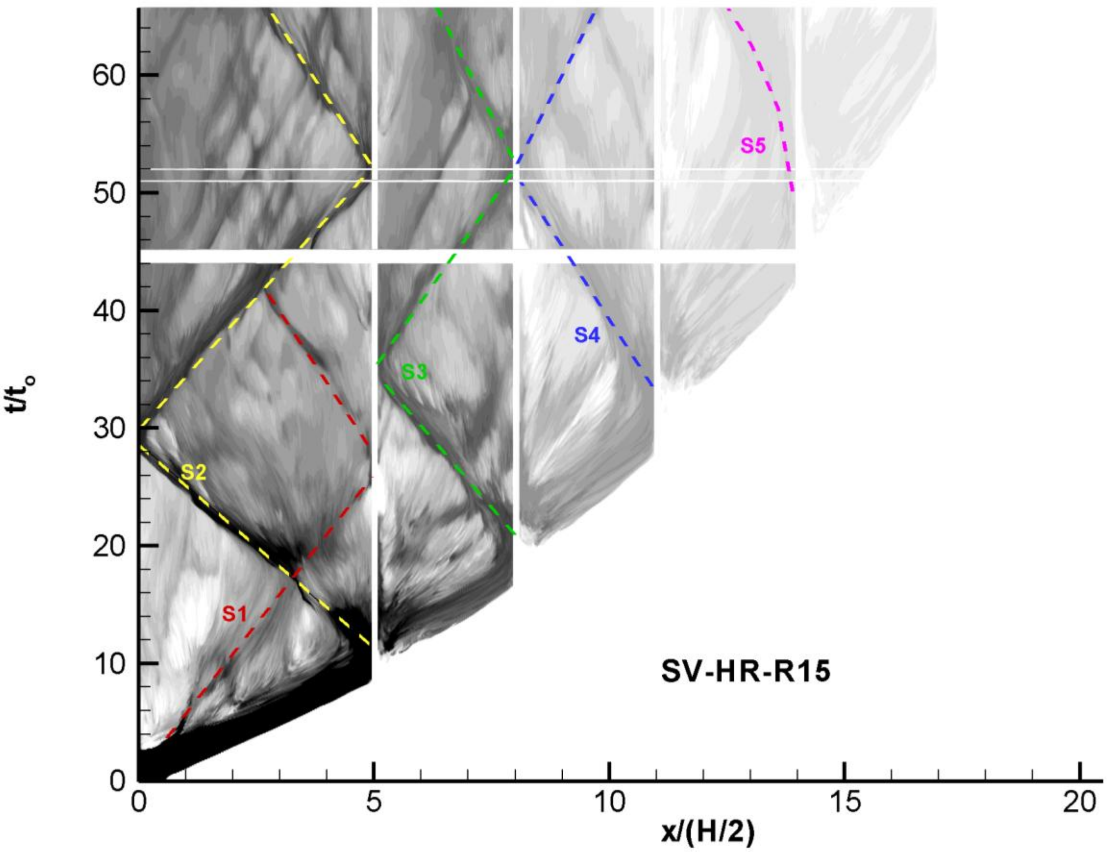

Figure 5.37 Evolution of the concentration with time along the x axis in the SV-HR-R15 simulation. The distance from the bottom wall is y/(H/2)=0.09. The dashed lines visualize the main forward and back propagating flow disturbances. S1 forms due to the collapse of a large interfacial billow on the channel bottom. S2 to S5 form due to the partial reflection of the gravity current fluid as the front passes Rib1 to Rib4, respectively.

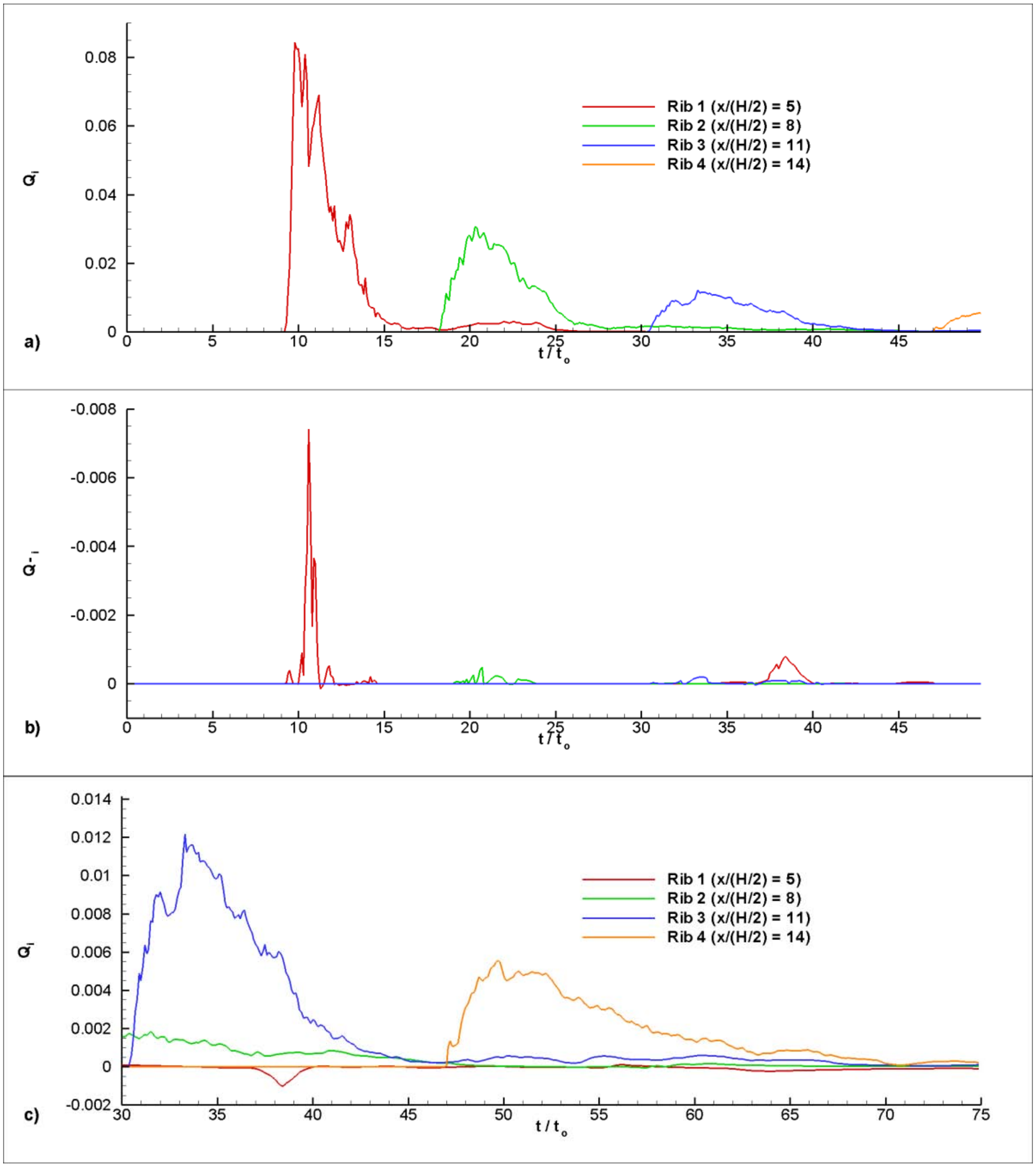

Figure 5.38 Time variation of the total volumetric flux of heavier fluid $Q_i = (4/u_b H^2)\int CudA$ and of the volumetric flux of heavier fluid moving upstream $Q_{-i} = (1/u_b H^2)\int Cu\_dA$ at the streamwise locations corresponding to the center of the ribs in the SV-LR-R15 simulation. a) Q_i, $t/t_0<45$; b) Q_{-i}, $t/t_0<45$; c) Q_i, $30<t/t_0<75$.

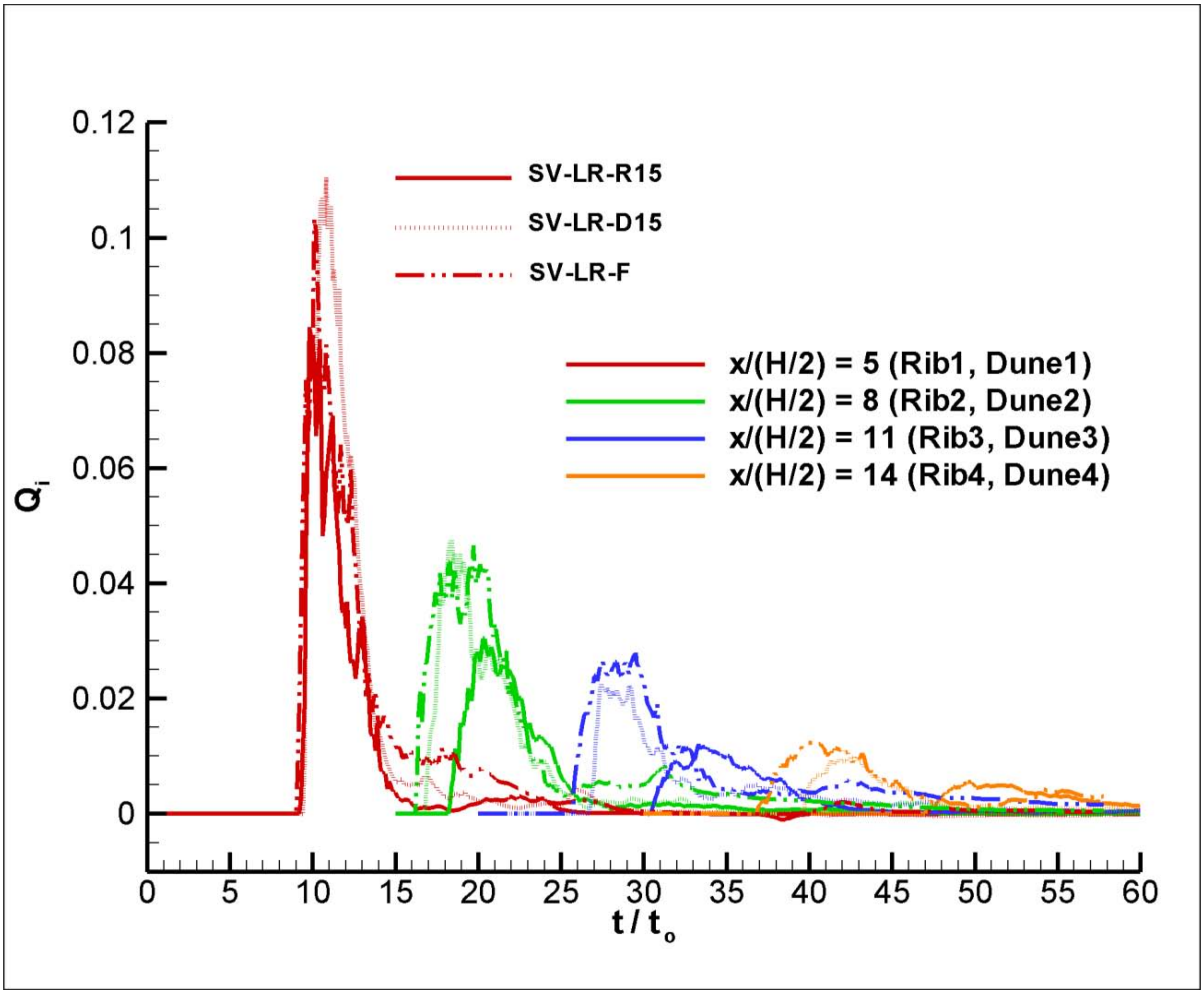

Figure 5.39 Time variation of the total volumetric flux of heavier fluid $Q_i = (4/u_b H^2)\int C u dA$ at the streamwise locations (x/(H/2)=5, 8, 11, and 14) corresponding to the center of the ribs and the crest of the dunes in the SV-LR-F, SV-LR-R15 and SV-LR-D15 simulations.

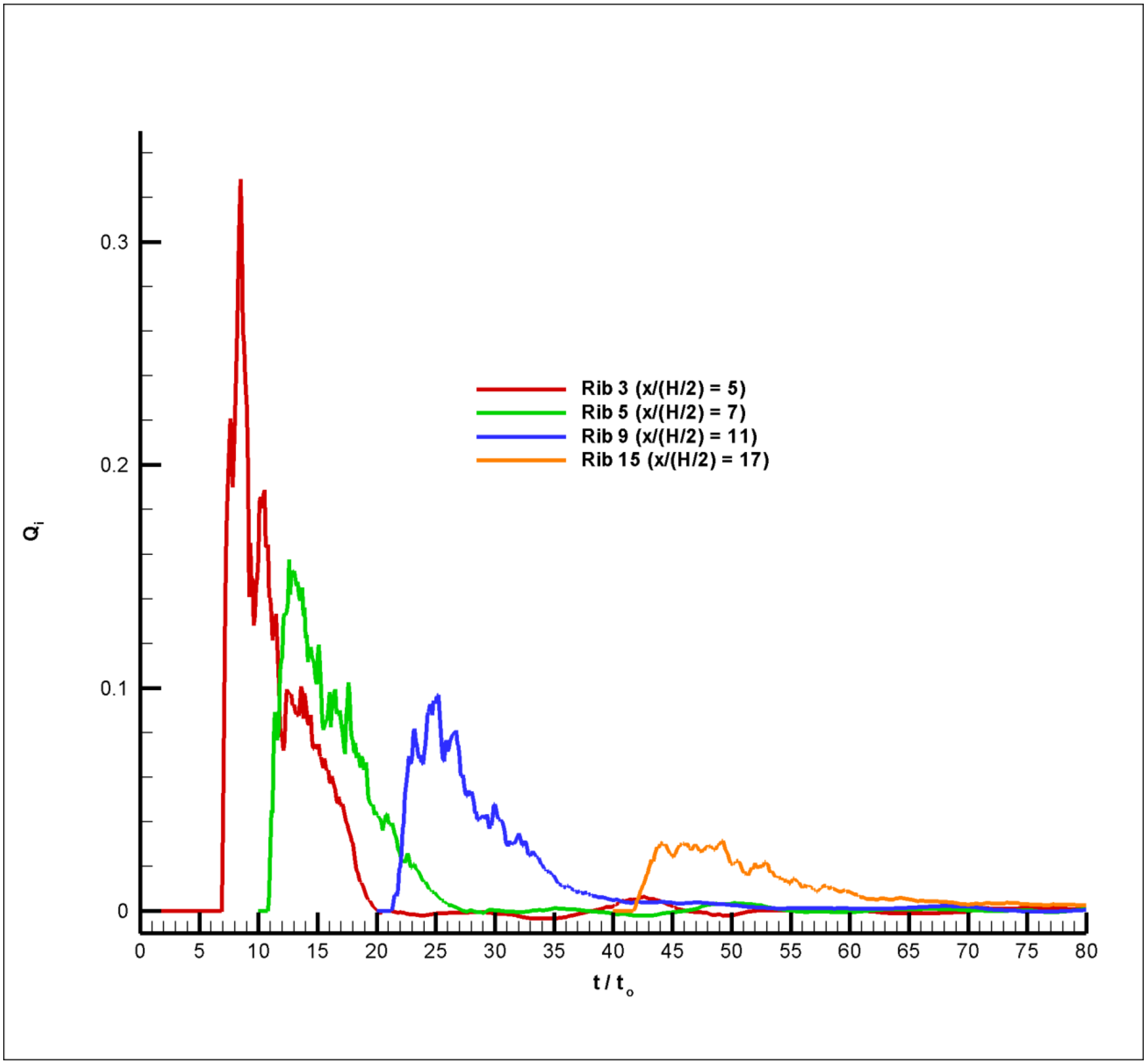

Figure 5.40 Time variation of the total volumetric flux of heavier fluid $Q_i = (4/u_b H^2)\int CudA$ at the streamwise locations (x/(H/2)=5, 7, 11, and 17) corresponding to the center of Rib3, Rib5, Rib9 and Rib15 in the SV-LR-R10 simulation.

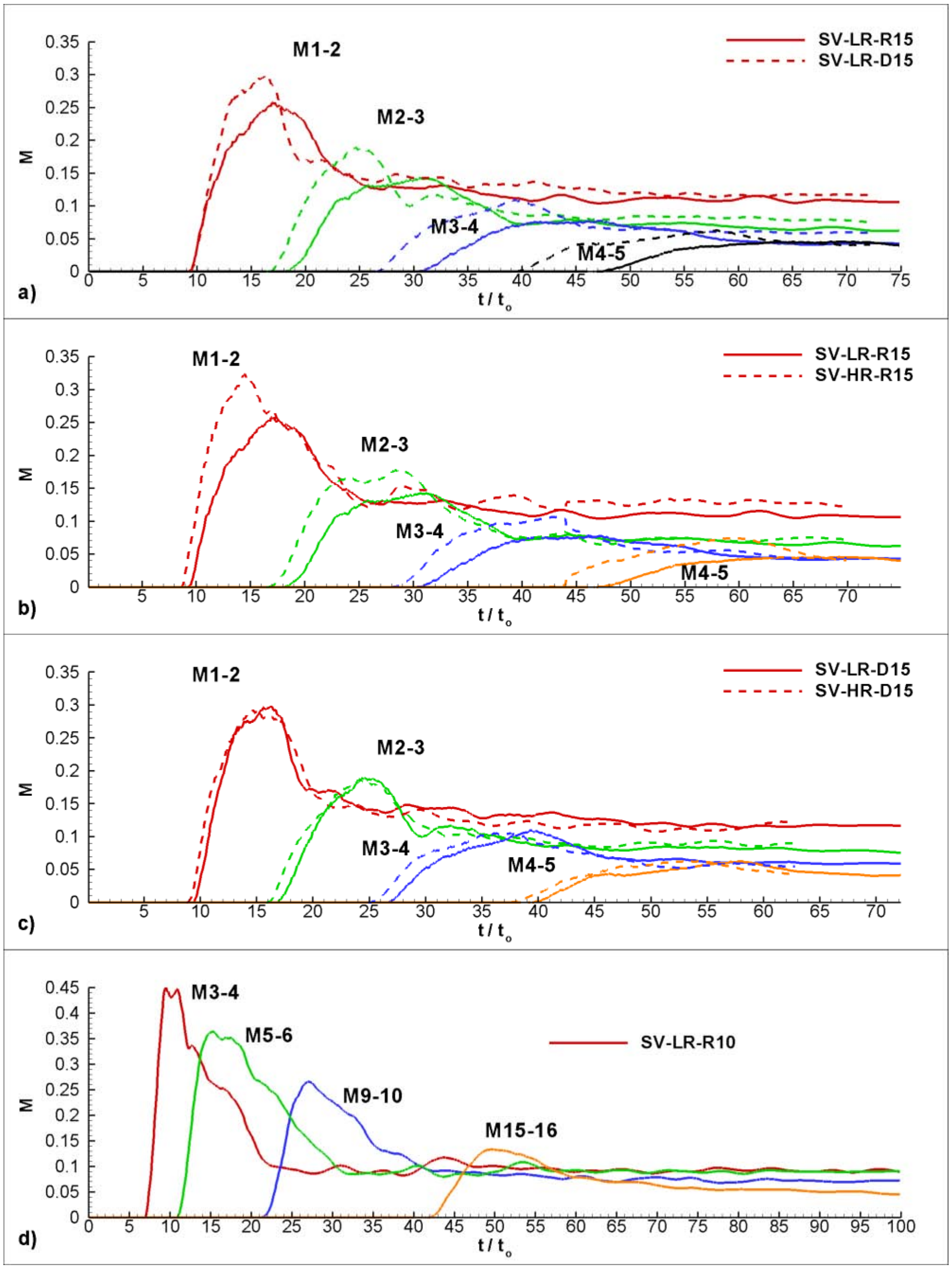

Figure 5.41 Time variation of the volume of heavier fluid $M_{i\text{-}i+1}$ in between the crests or centers of two successive obstacles (i and i+1). a) SV-LR-D15 and SV-LR-R15 simulations; b) SV-LR-R15 and SV-HR-R15 simulations; c) SV-LR-D15 and SV-HR-D15 simulations; d) SV-LR-R10 simulation.

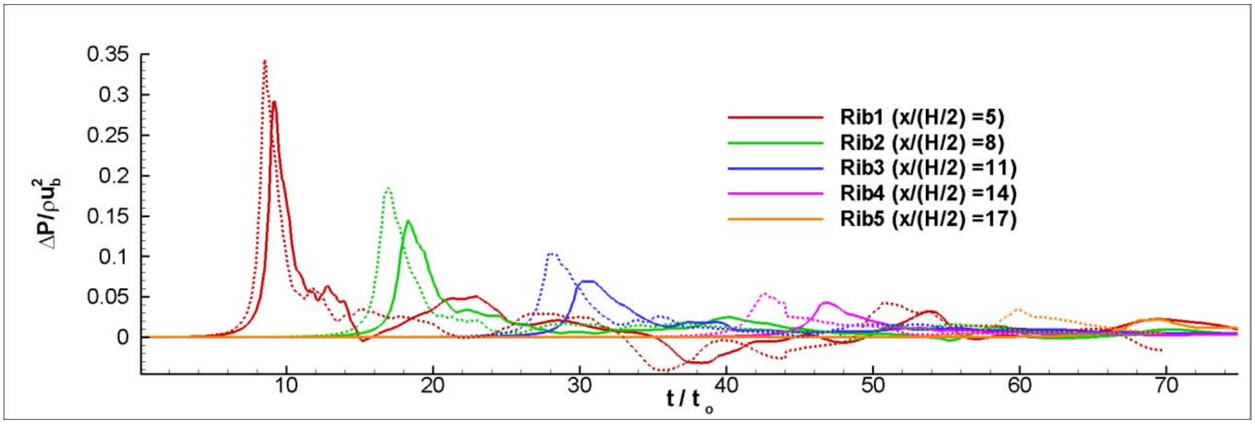

Figure 5.42 Time variation of the mean pressure difference between the upstream and downstream faces of Rib1, Rib2, Rib3, Rib4 and Rib5, $\Delta P/\rho u_b^2$, in the SV-LR-R15 and SV-HR-R15 simulations.

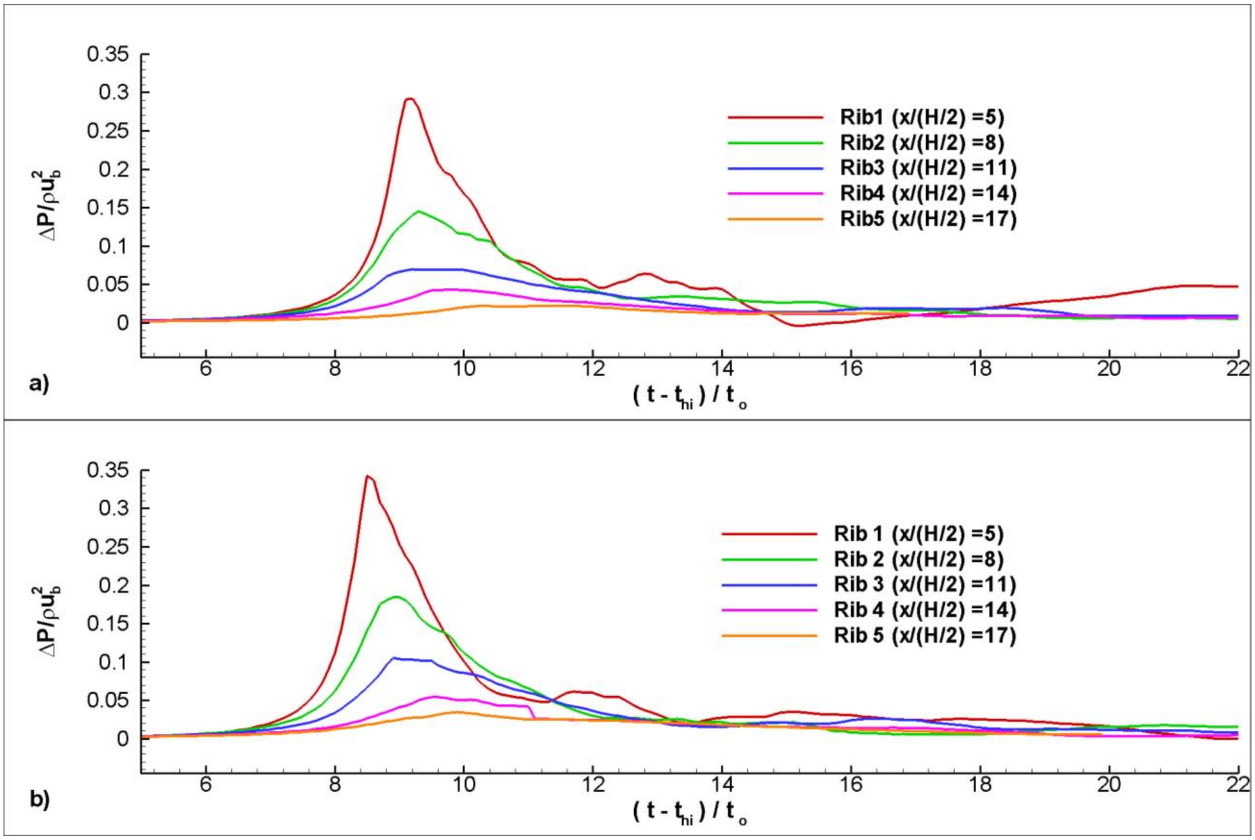

Figure 5.43 Time variation of the mean pressure difference between the upstream and downstream faces of Rib1, Rib2, Rib3, Rib4 and Rib5, $\Delta P/\rho u_b^2$. a) SV-LR-R15 simulation; b) SV-HR-R15 simulation. The profiles were translated in time such that the impact stage starts at $t/t_0=0$ for all the five ribs.

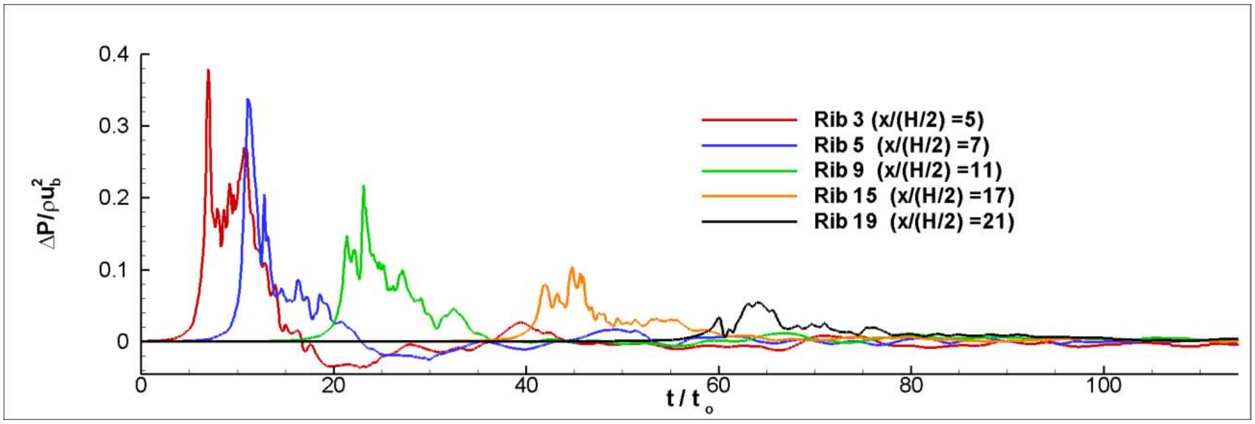

Figure 5.44 Time variation of the mean pressure difference between the upstream and downstream faces of Rib3, Rib5, Rib9, Rib15 and Rib19, $\Delta P/\rho u_b^2$, in the SV-LR-R10 simulation.

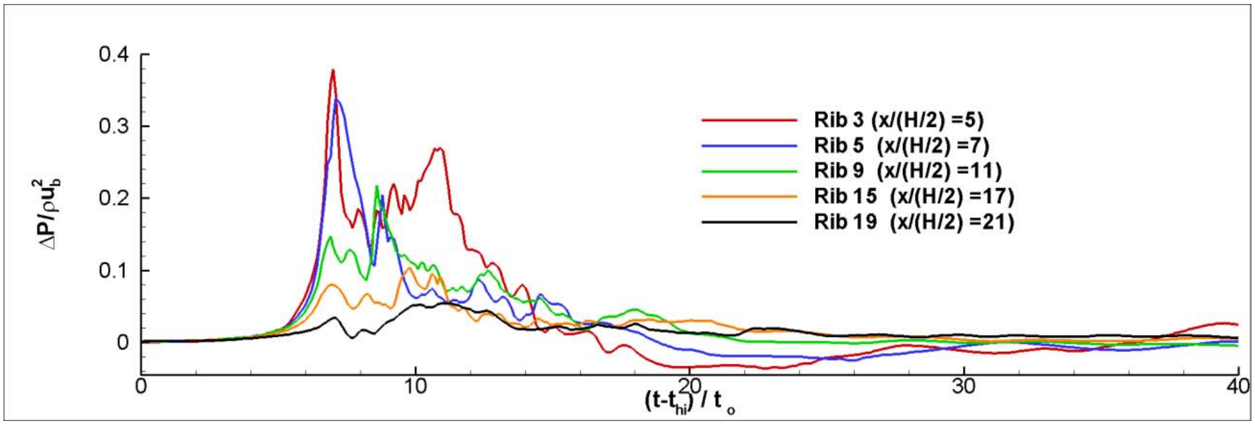

Figure 5.45 Time variation of the mean pressure difference between the upstream and downstream faces of Rib3, Rib5, Rib9, Rib15 and Rib19, $\Delta P/\rho u_b^2$, in the SV-LR-R10 simulation. The profiles were translated in time such that the impact stage starts at $t/t_0=0$ for all the five ribs.

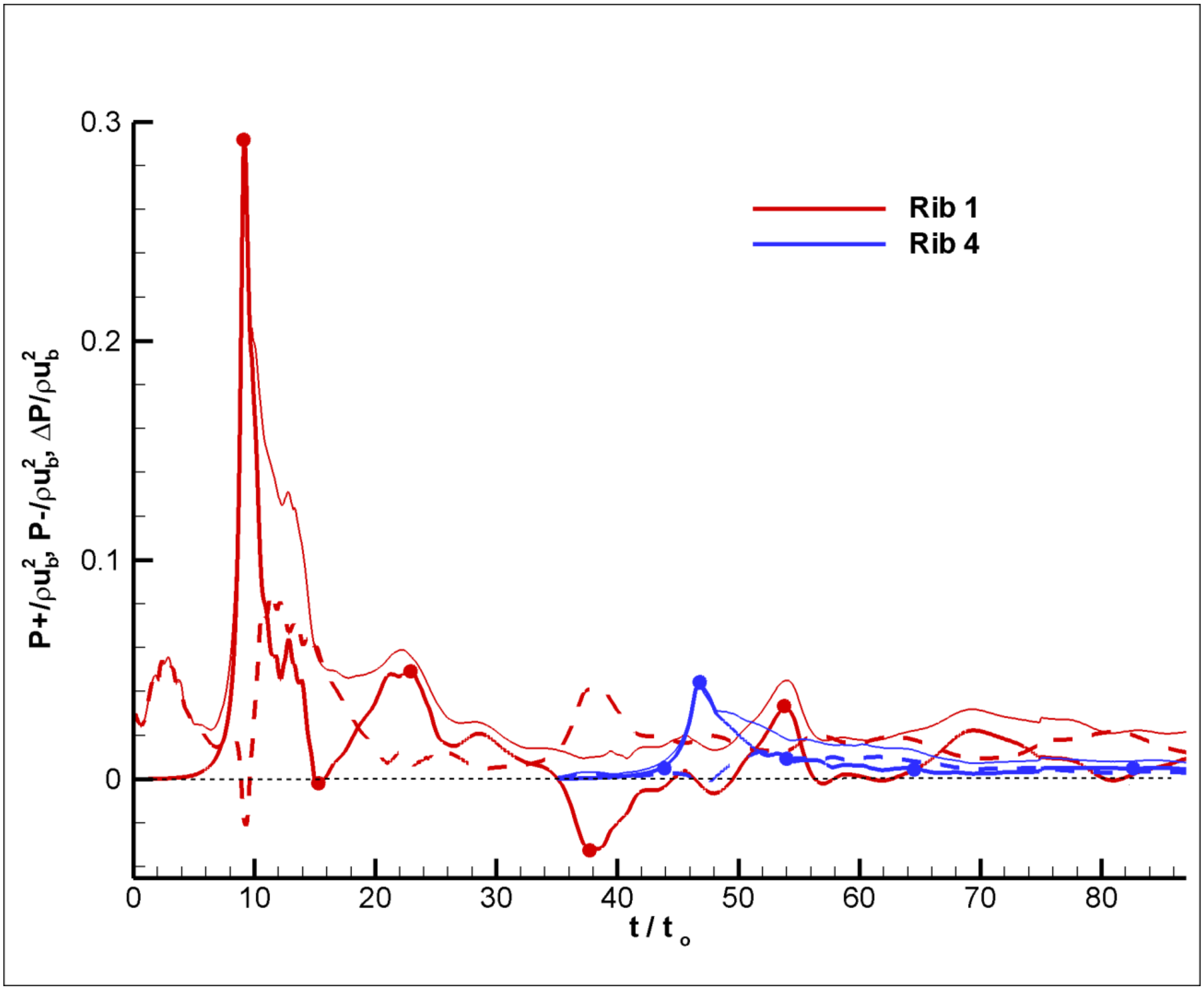

Figure 5.46 Time variations of the mean pressure on the upstream face of the ribs, $P^+/\rho u_b^2$, mean pressure on the downstream face of the ribs, $P^-/\rho u_b^2$, and mean pressure difference between the upstream and downstream faces of the ribs, $\Delta P/\rho u_b^2$, in the SV-LR-R15 simulation. Results are shown for Rib1 and Rib4.

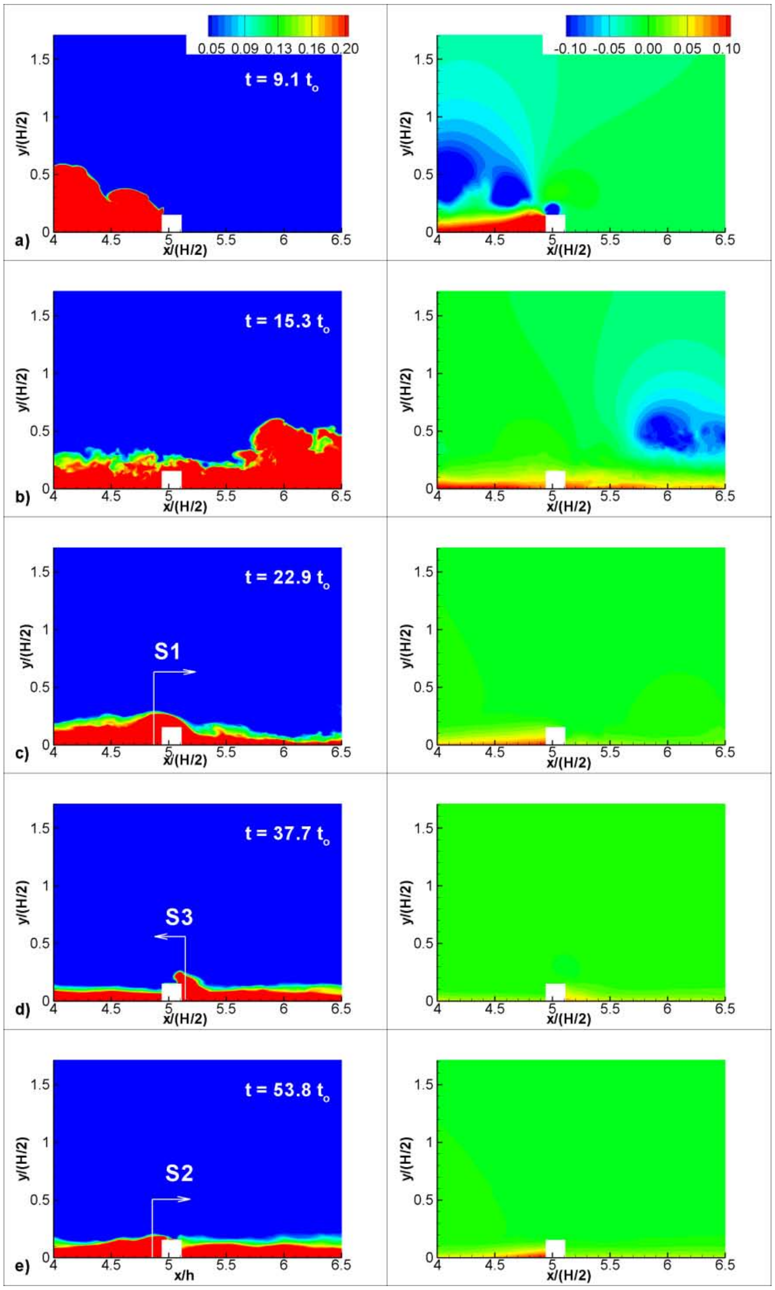

Figure 5.47 Contour plots showing the concentration, C, (left) and pressure, $p/\rho u_b^2$, (right) distributions in a vertical x-y plane around Rib1 in the SV-LR-R15 simulation at representative time instants. a) t=9.1t$_0$; b) t=15.3t$_0$; c) t=22.9t$_0$; d) t=37.7$_0$; e) t=53.8t$_0$.

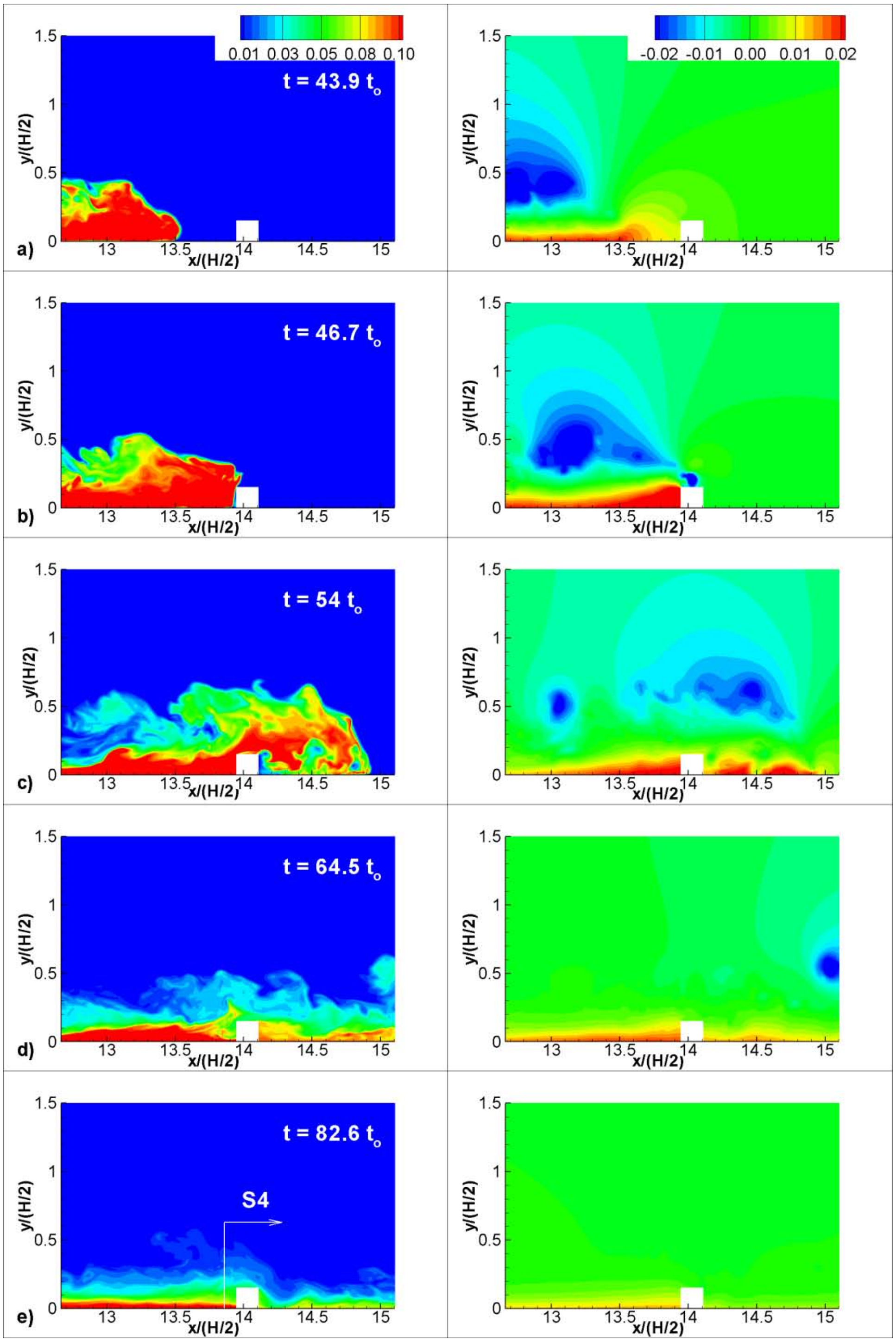

Figure 5.48 Contour plots showing the concentration, C, (left) and pressure, $p/\rho u_b^2$, (right) distributions in a vertical x-y plane around Rib4 in the SV-LR-R15 simulation at representative time instants. a) t=43.9t$_0$; b) t=46.7t$_0$; c) t=54.0t$_0$; d) t=64.5$_0$; e) t=82.6t$_0$.

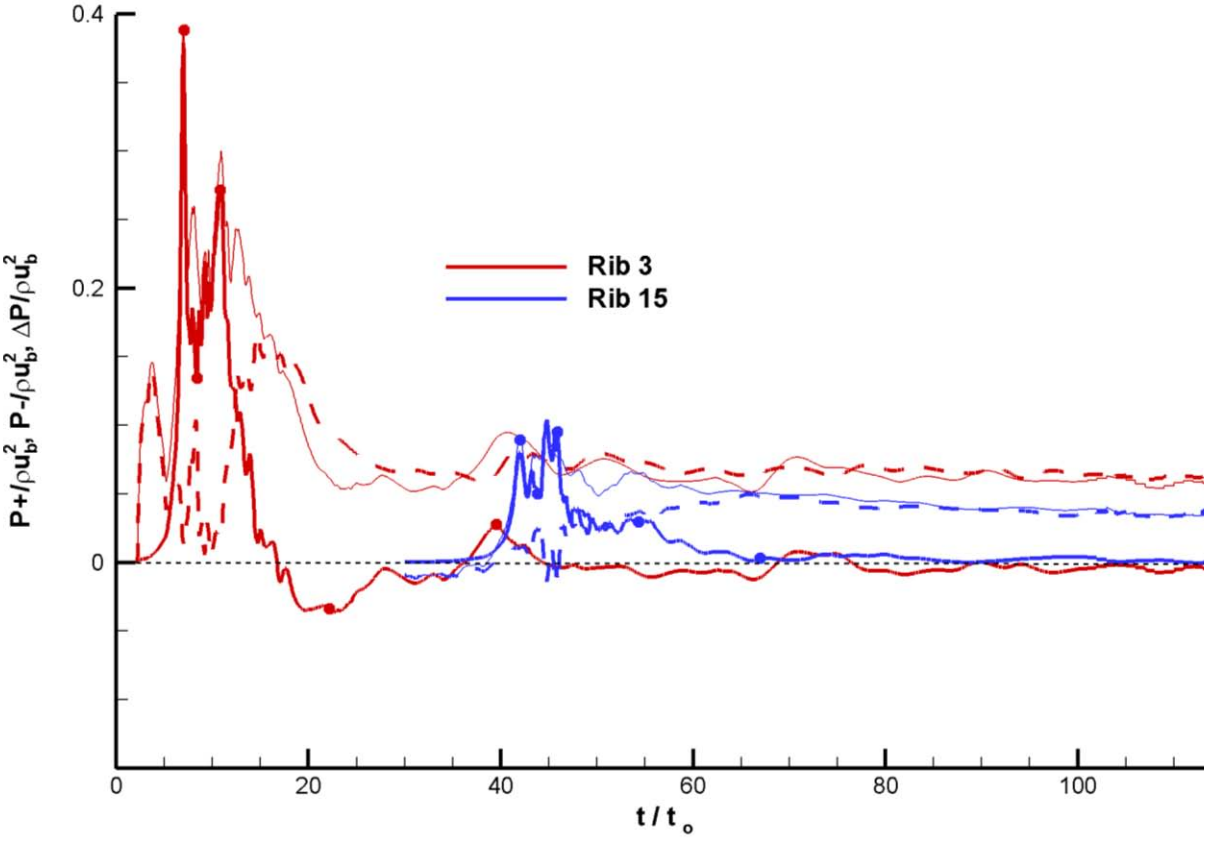

Figure 5.49 Time variations of the mean pressure on the upstream face of the ribs, $P^+/\rho u_b^2$, mean pressure on the downstream face of the ribs, $P^-/\rho u_b^2$, and mean pressure difference between the upstream and downstream faces of the ribs, $\Delta P/\rho u_b^2$, in the SV-LR-R10 simulation. Results are shown for Rib3 and Rib15.

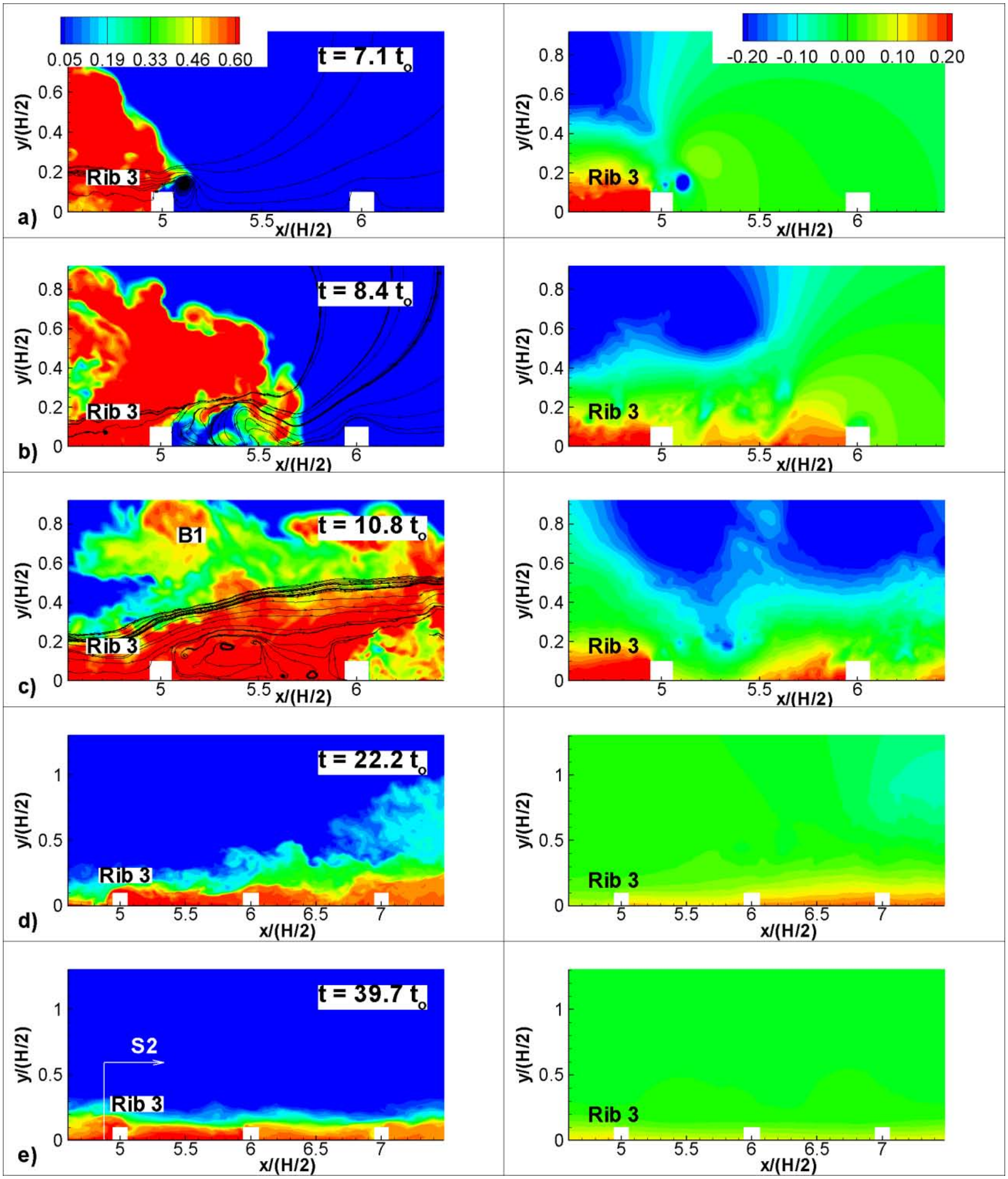

Figure 5.50 Contour plots showing the concentration, C, (left) and pressure, $p/\rho u_b^2$, (right) distributions in a vertical x-y plane around Rib3 in the SV-LR-R10 simulation at representative time instants. a) t=7.1t$_0$; b) t=8.4t$_0$; c) t=10.8t$_0$; d) t=22.2$_0$; e) t=39.7t$_0$.

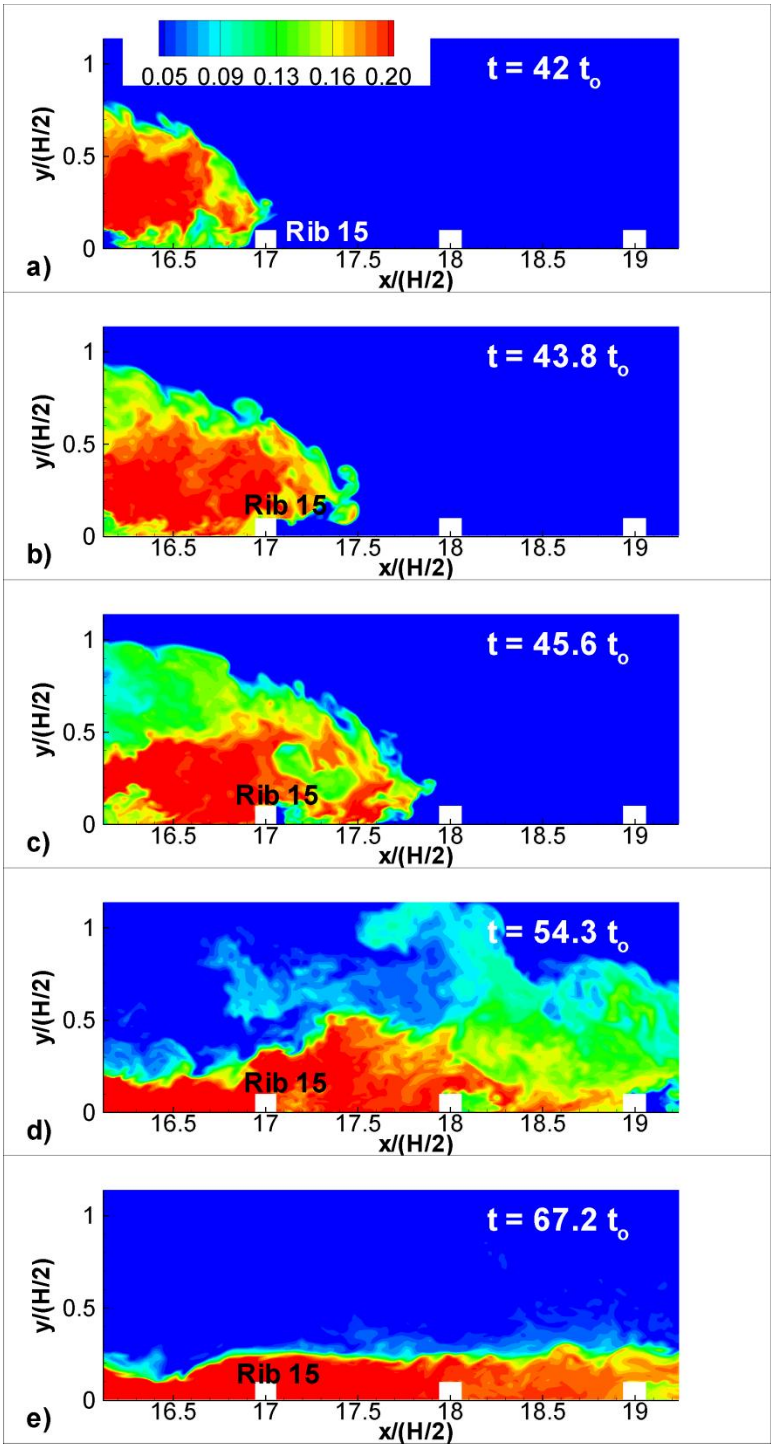

Figure 5.51 Contour plots showing the concentration, C, distribution in a vertical x-y plane around Rib15 in the SV-LR-R10 simulation at representative time instants. a) $t=42.0t_0$; b) $t=43.8t_0$; c) $t=45.6t_0$; d) $t=54.3_0$; e) $t=67.2t_0$.

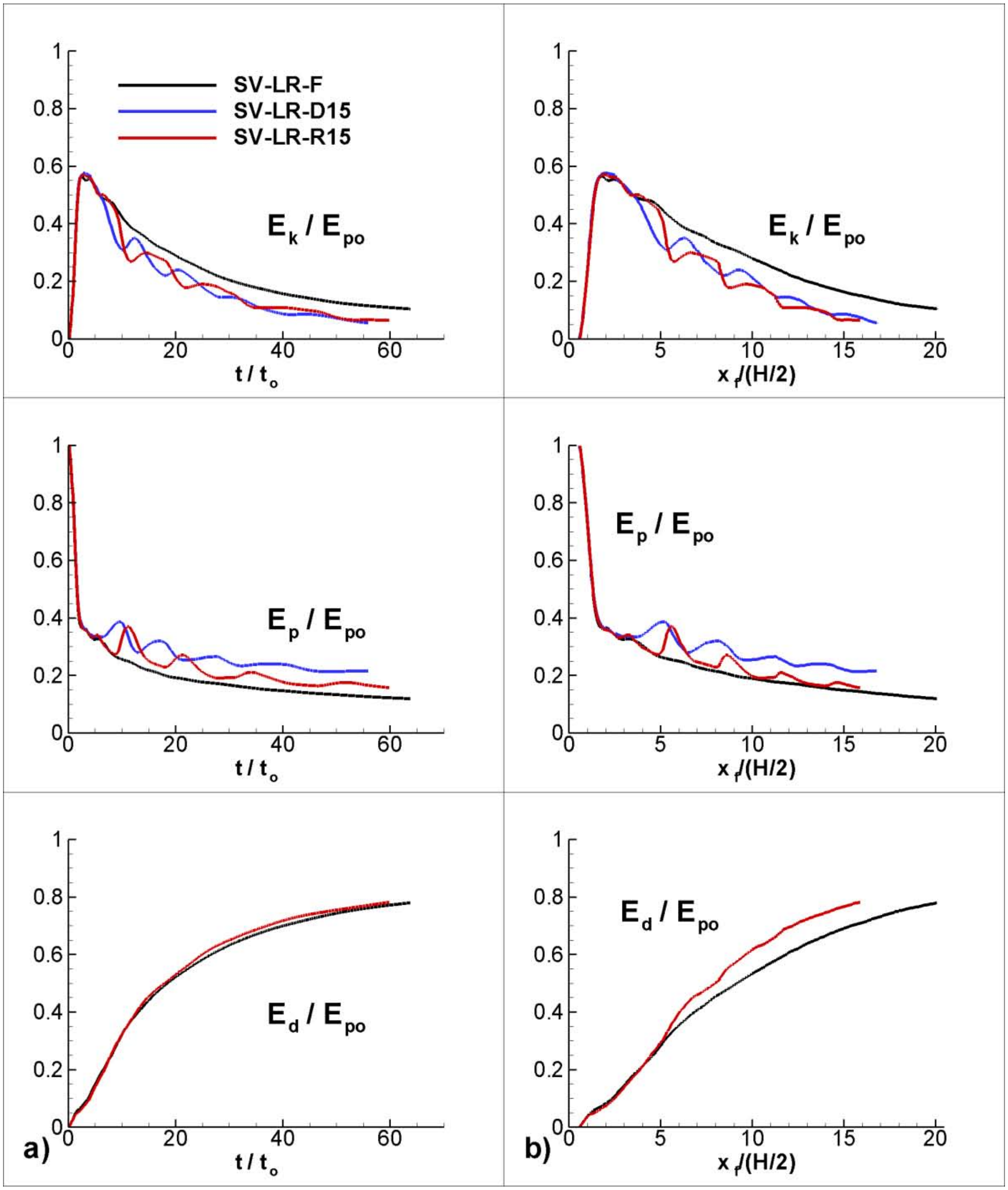

Figure 5.52 Variation of the potential energy, E_p, kinetic energy, E_k, and integral of the total dissipation, E_d, in the SV-LR-F, SV-LR-D15 and SV-LR-R15 simulations. a) plotted versus time in linear-linear scale; b) plotted versus the front position in linear-linear scale.

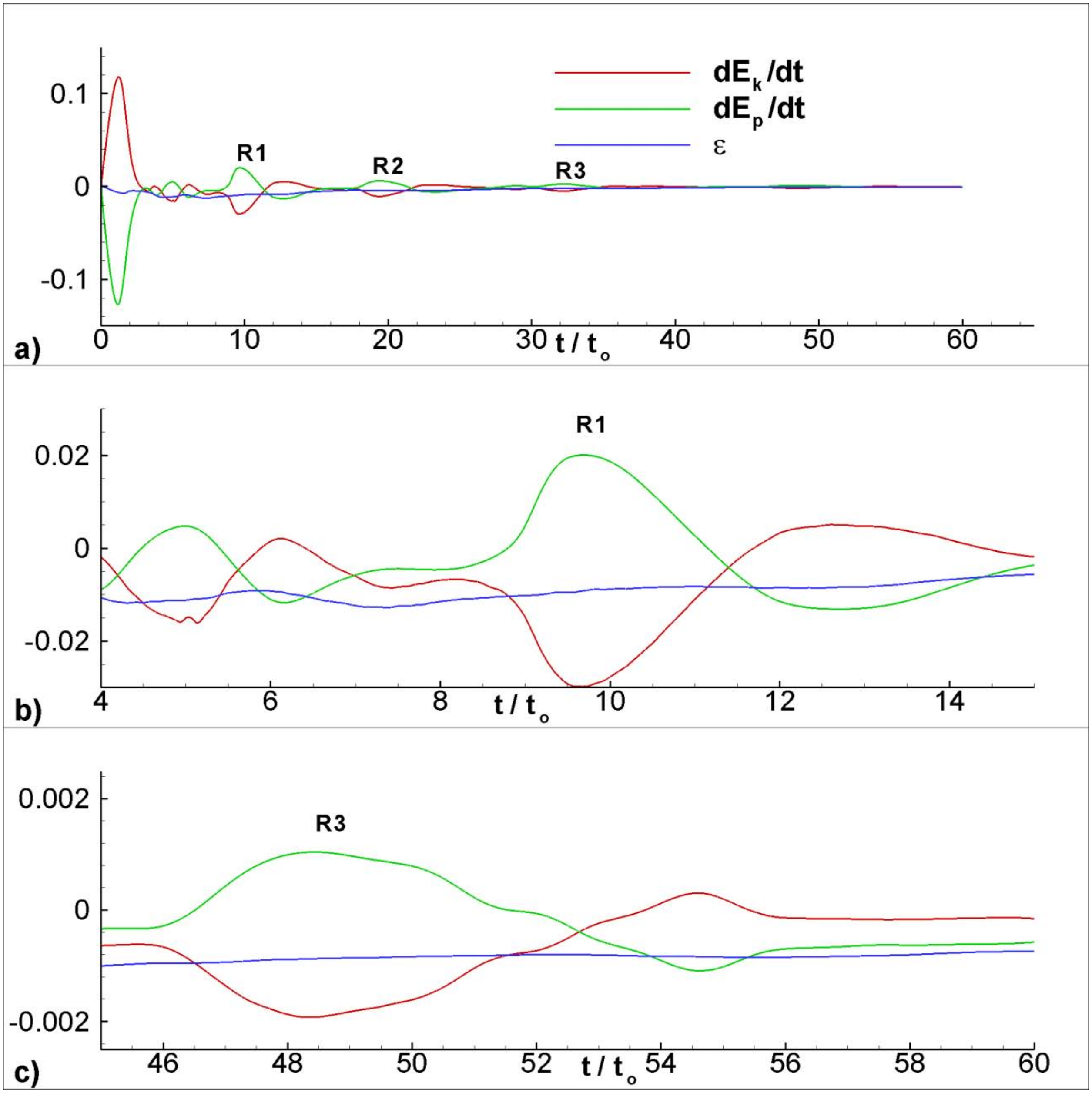

Figure 5.53 Time variation of the terms (-dE_k/dt, dE_p/dt and ε) in the differential equation of the mechanical energy in the SV-LR-R15 simulation. All the terms are nondimensionalized by $u_b^3(H/2)^2$.

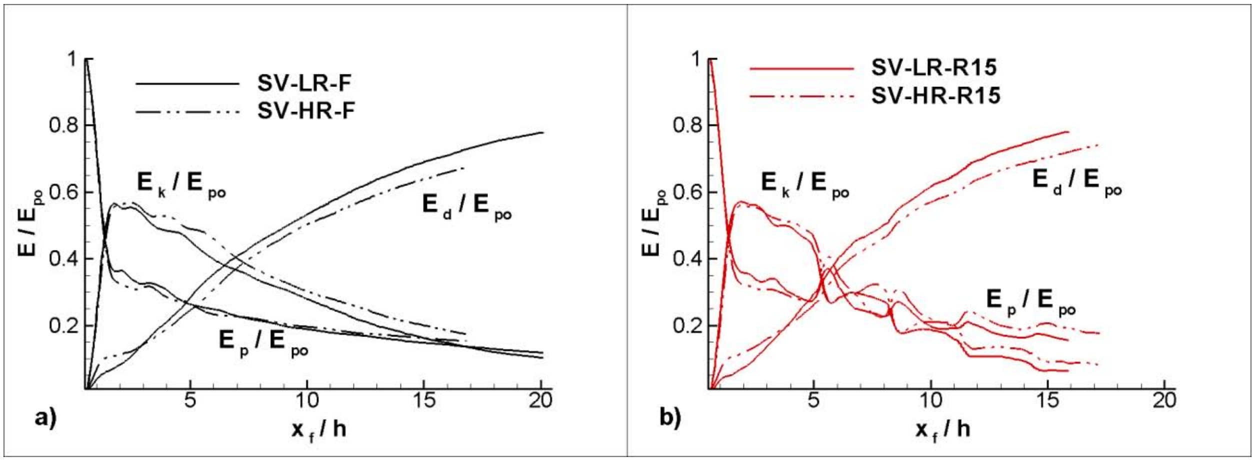

Figure 5.54 Variation of the potential energy, E_p, kinetic energy, E_k, and integral of the total dissipation, E_d, with the front position, $x_f/(H/2)$ in the: a) SV-LR-F and SV-HR-F simulations; b) SV-LR-R15 and SV-HR-R15 simulations.

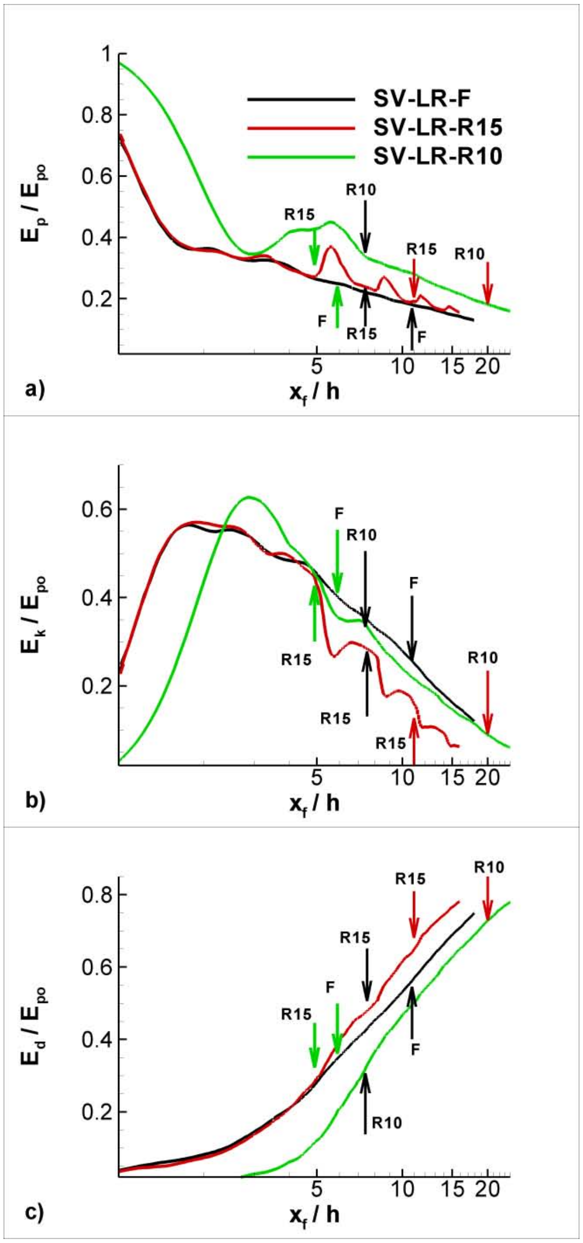

Figure 5.55 Variation of the potential energy, E_p (a), kinetic energy, E_k (b), and integral of the total dissipation, E_d (c), with the front position, $x_f/(H/2)$, plotted in linear-log scale for the SV-LR-F, SV-LR-R15 and SV-LR-R10 simulations. The green arrows show the end of the slumping phase. The black arrows show the start of the buoyancy-inertia phase. The red arrows show the start of the drag-dominated phase.

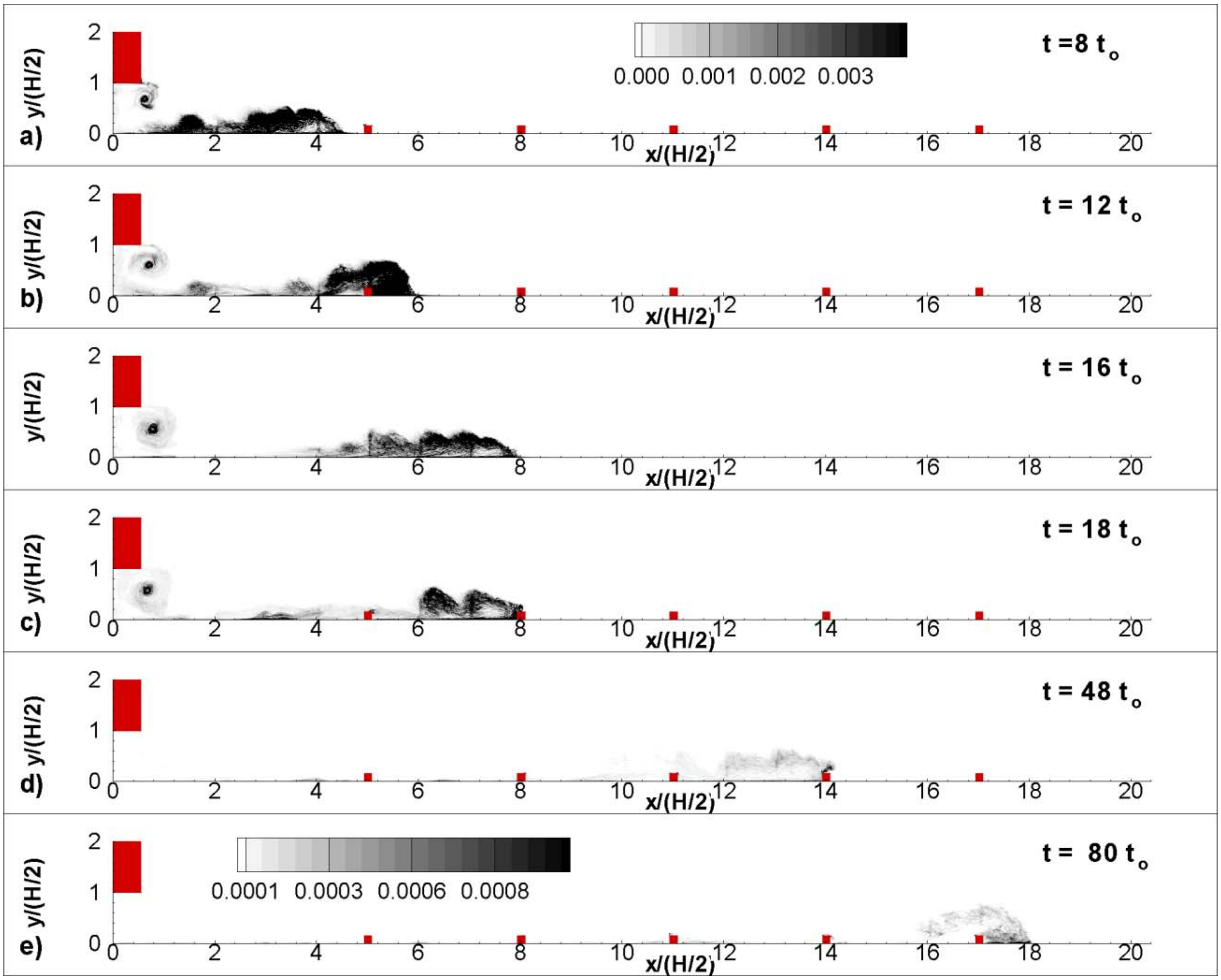

Figure 5.56 Spatial distributions of the non-dimensional spanwise-averaged local dissipation rate $\varepsilon_r/(u_b^3/(H/2))$ in the SV-LR-R15 simulation. a) t/t_0=8; b) t/t_0=12; c) t/t_0=18; d) t/t_0=48; e) t/t_0=80.

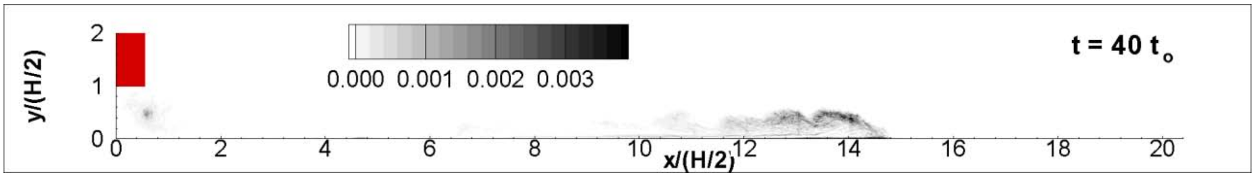

Figure 5.57 Spatial distribution of the non-dimensional spanwise-averaged local dissipation rate $\varepsilon_r/(u_b^3/(H/2))$ in the SV-LR-F simulation at t/t_0=40.

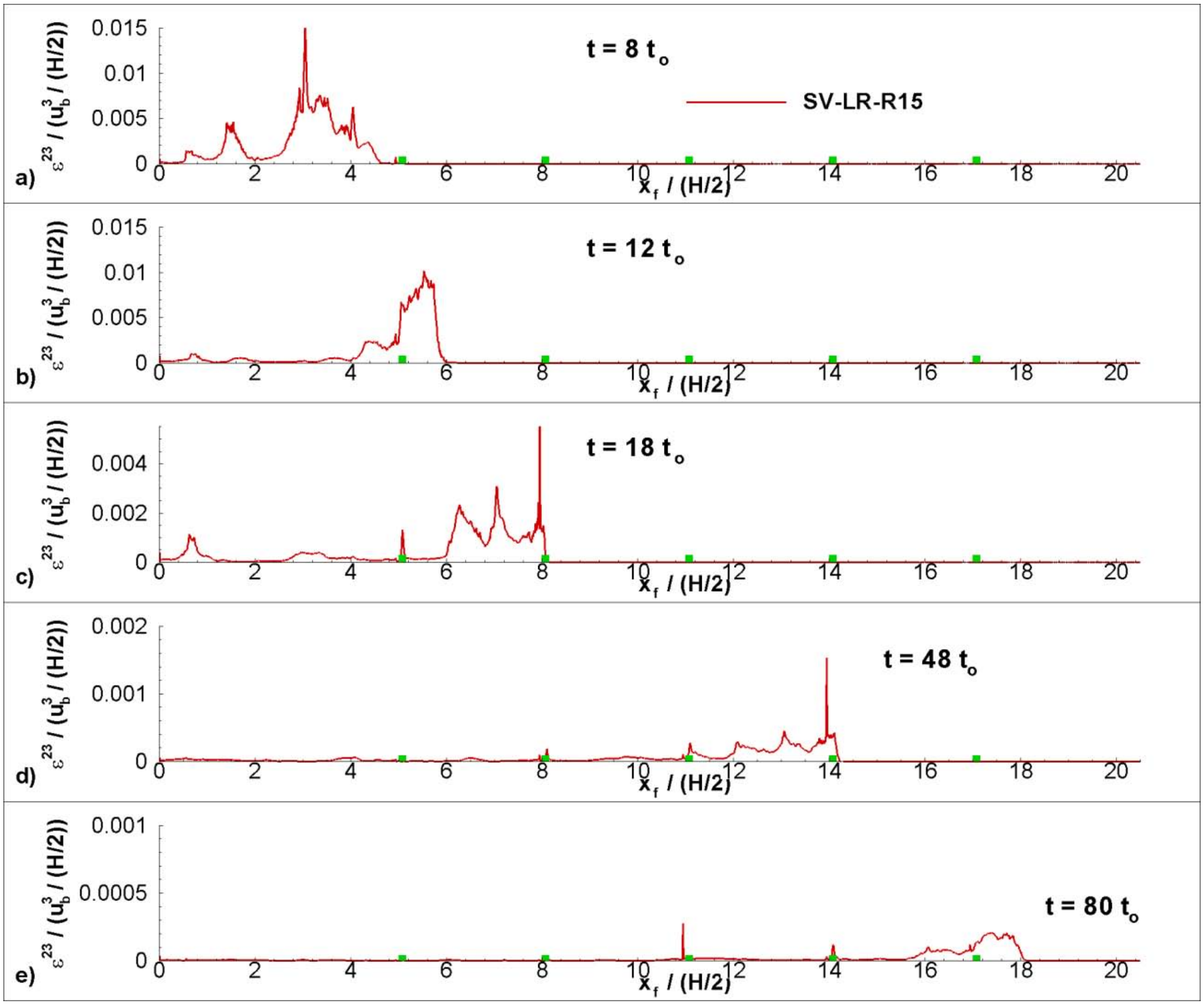

Figure 5.58 Streamwise distributions of $\varepsilon^{23}(x_1)/(u_b^3(H/2))$ in the SV-LR-R15 simulation. a) t/t$_0$=8; b) t/t$_0$=12; d) t/t$_0$=18; b) t/t$_0$=48; e) t/t$_0$=80.

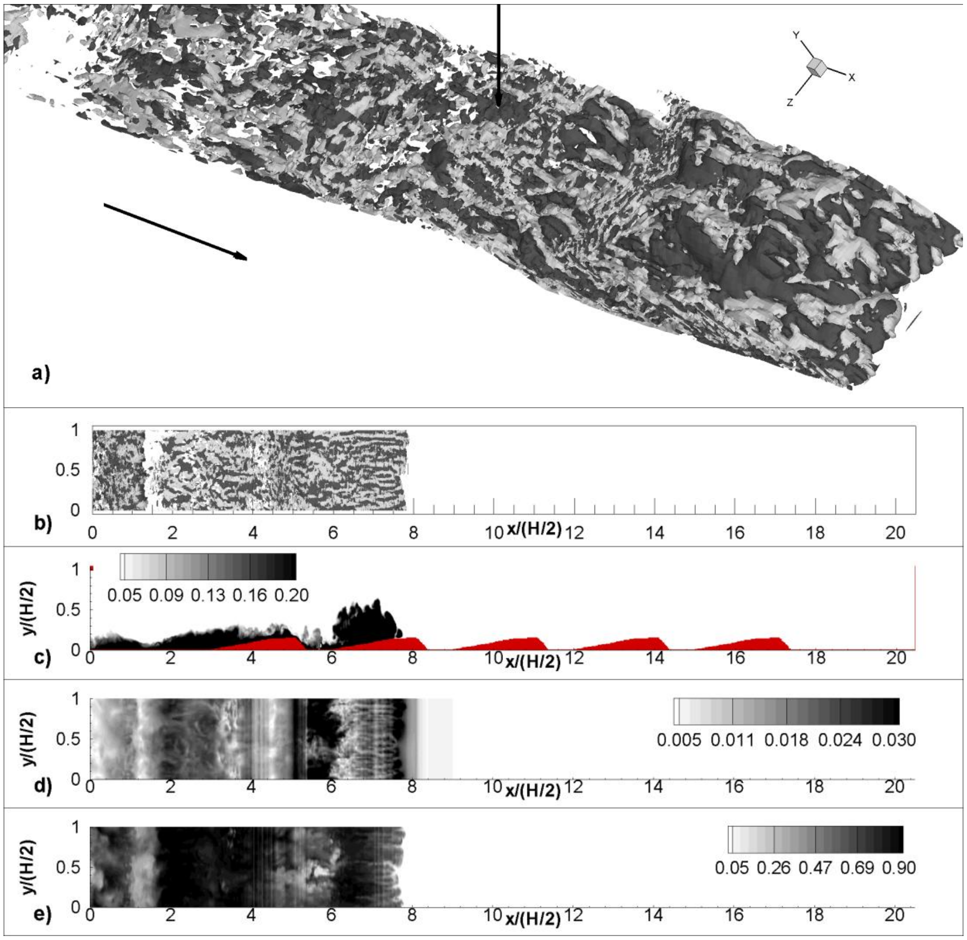

Figure 5.59 Visualization of the flow structure in the vicinity of the channel bottom in the SV-LR-D15 simulation during the buoyancy-inertia phase when the front is situated $x_f/(H/2)=7.7$. a) vertical vorticity contours, the view is lateral and from above the bottom propagating current; b) vertical vorticity contours, $\omega_y(H/2)/u_b$, on the bottom wall, the view is from below the bottom propagating current; c) spanwise-averaged concentration contours; d) bed friction velocity, u_τ/u_b, contours showing the positions of the regions containing streaks of high and low streamwise velocity; e) concentration contours in a horizontal plane situated close to the channel bottom. The light and dark vorticity contours in frames a) and b) correspond to $\omega_y = 2u_b/(H/2)$ and $\omega_y = -2u_b/(H/2)$, respectively. The arrows in frame a) indicate the position of the crest of each rib. The aspect ratio is 1:2 in the x-y plots in frame c) and in the x-z plots in frames b) and d).

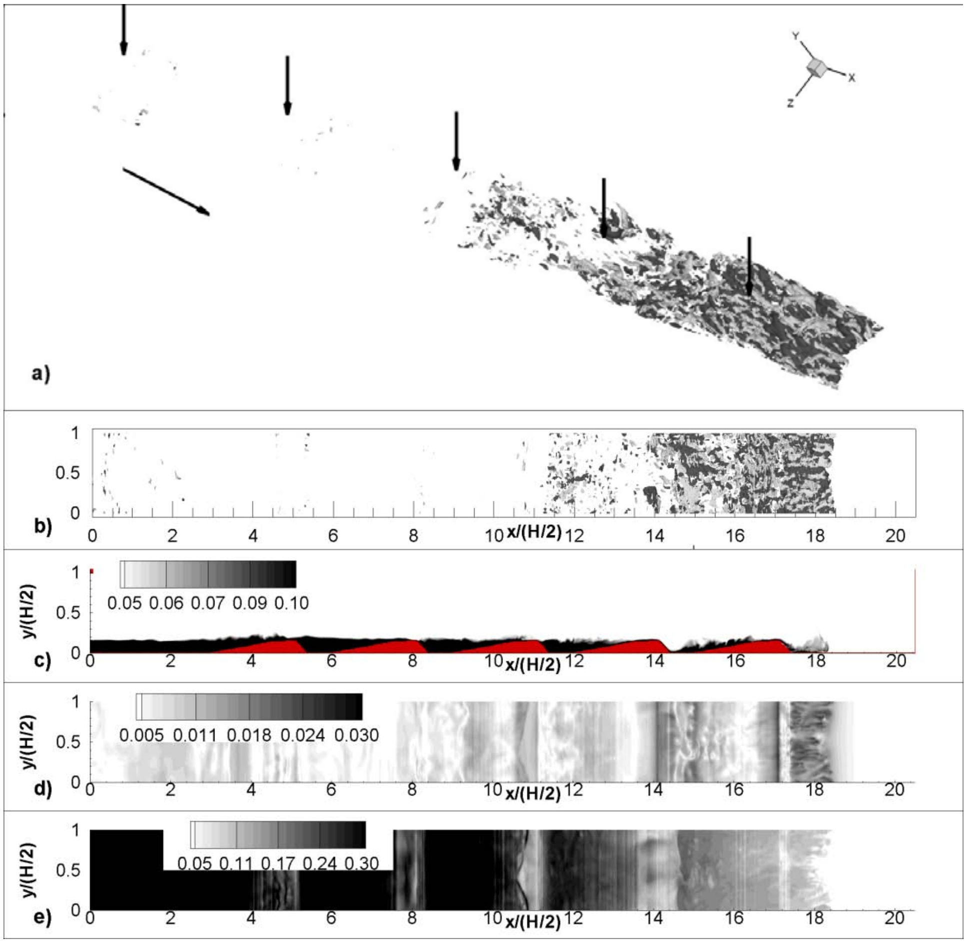

Figure 5.60 Visualization of the flow structure in the vicinity of the channel bottom in the SV-LR-D15 simulation during the drag-dominated phase when the front is situated $x_f/(H/2)=18.5$. a) vertical vorticity contours, the view is lateral and from above the bottom propagating current; b) vertical vorticity contours, $\omega_y(H/2)/u_b$, on the bottom wall, the view is from below the bottom propagating current; c) spanwise-averaged concentration contours; d) bed friction velocity, u_τ/u_b, contours showing the positions of the regions containing streaks of high and low streamwise velocity; e) concentration contours in a horizontal plane situated close to the channel bottom. The light and dark vorticity contours in frames a) and b) correspond to $\omega_y = 2u_b/(H/2)$ and $\omega_y = -2u_b/(H/2)$, respectively. The arrows in frame a) indicate the position of the crest of each rib. The aspect ratio is 1:2 in the x-y plots in frame c) and in the x-z plots in frames b) and d).

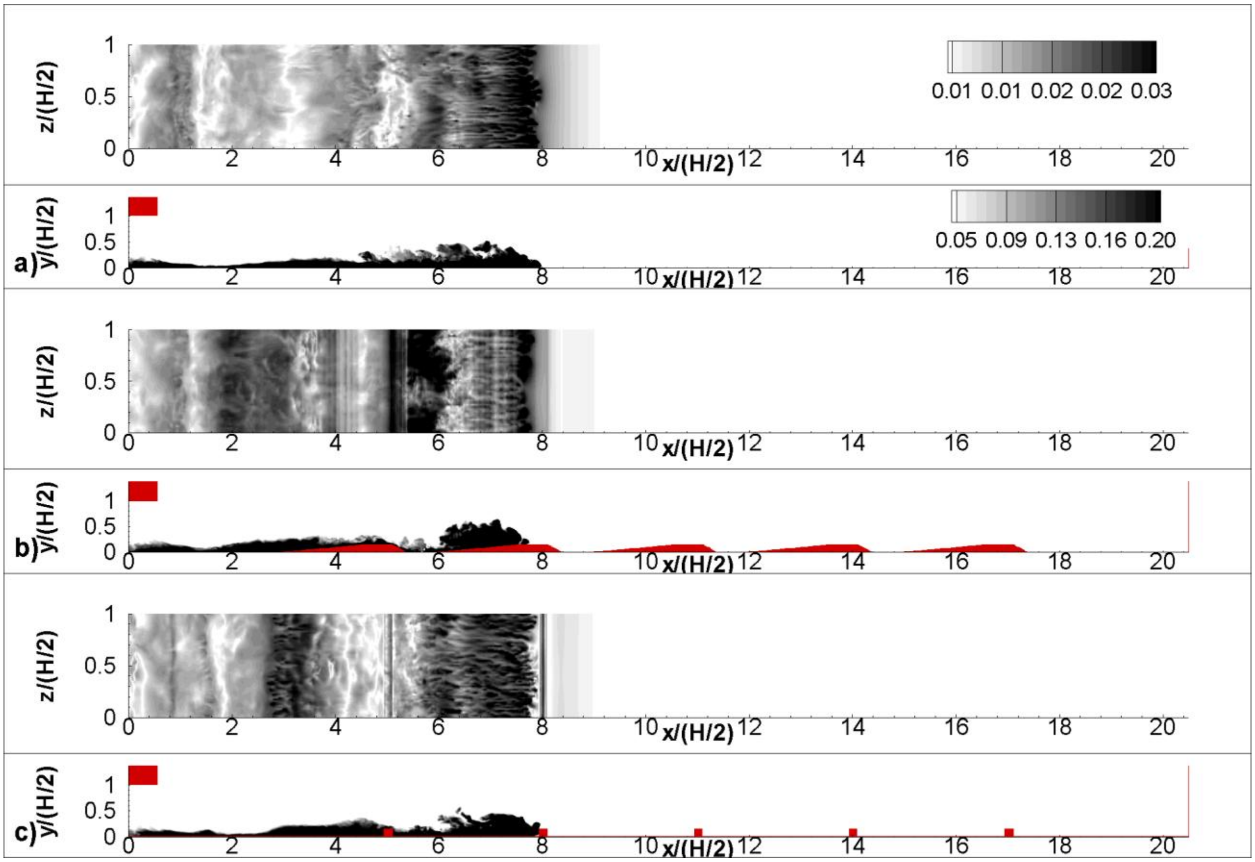

Figure 5.61 Spatial distribution of the bed friction velocity, u_τ/u_b, during the buoyancy-inertia phase when the front position is $x_f/(H/2)=8$. a) SV-LR-F simulation; b) SV-LR-D15 simulation; c) SV-LR-R15 simulation. Also shown are the concentration contours in an x-y section. The aspect ratio is 1:2 in the x-y plots.

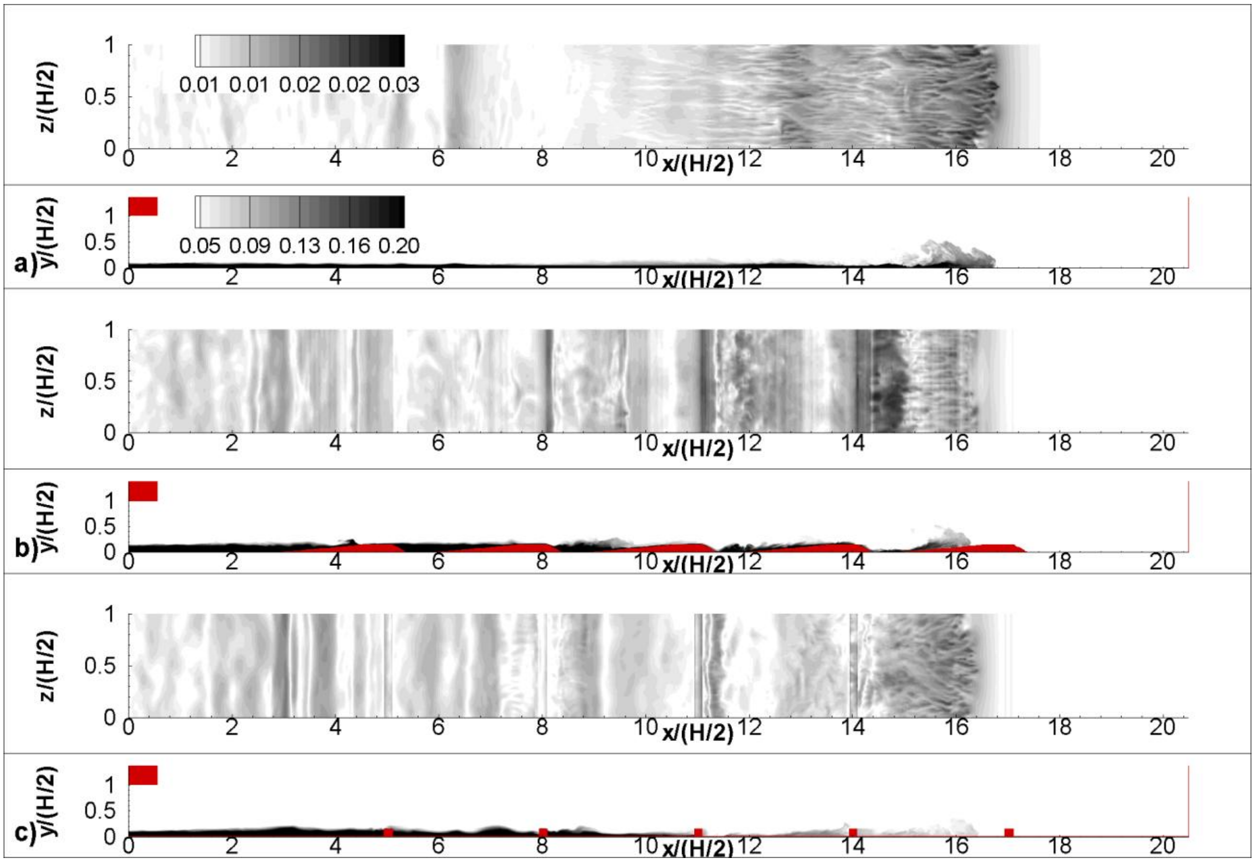

Figure 5.62 Spatial distribution of the bed friction velocity, u_τ/u_b, during the drag-dominated phase (simulations with roughness elements only) when the front position is $x_f/(H/2)=16.5$. a) SV-LR-F simulation; b) SV-LR-D15 simulation; c) SV-LR-R15 simulation. Also shown are the concentration contours in an x-y section. The aspect ratio is 1:2 in the x-y plots.

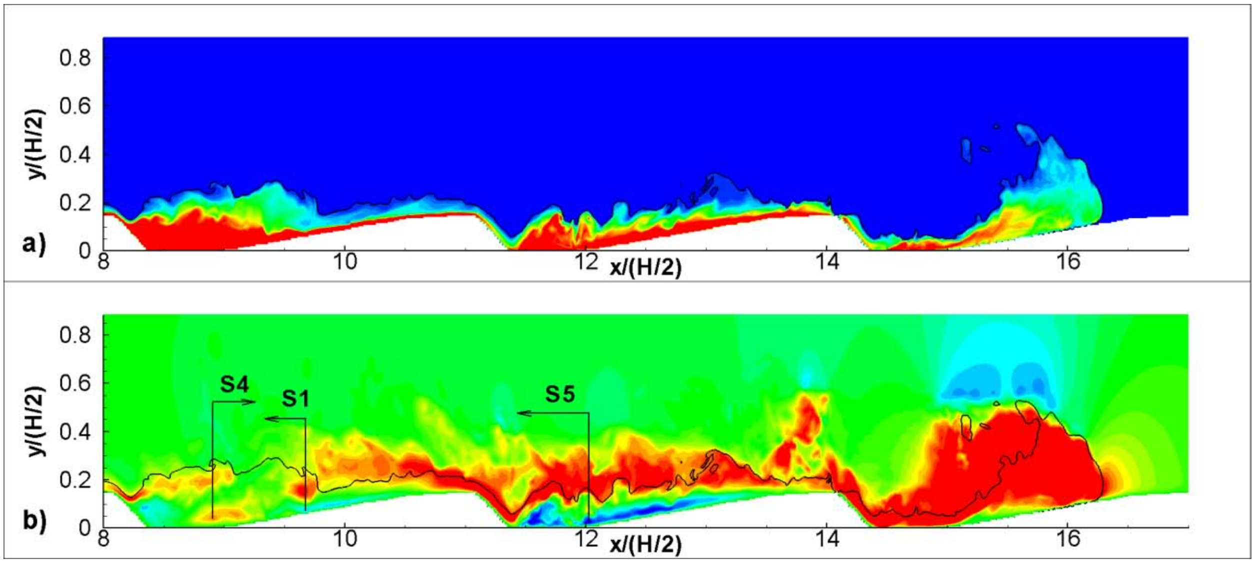

Figure 5.63 Visualization of the structure of the gravity current in an x-y plane between x/(H/2)=8 and the front, in the SV-LR-D15 simulation, when the front position is x_f/(H/2)=16.5. a) concentration; b) streamwise velocity. The solid lines correspond to the concentration isosurface C=0.05.

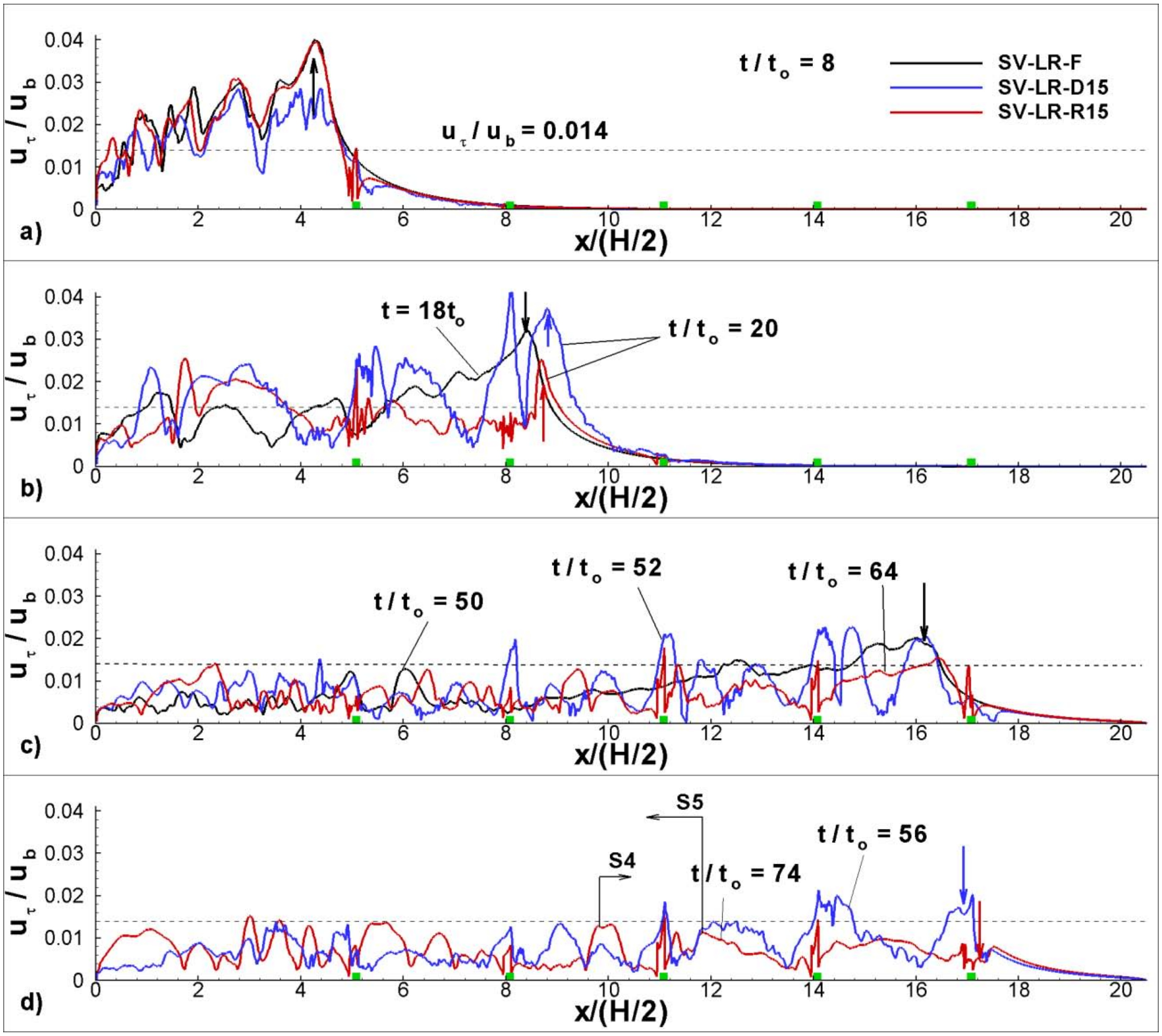

Figure 5.64 Streamwise distribution of the spanwise-averaged bed friction velocity in the SV-LR-F, SV-LR-R15 and SV-LR-D15 simulations. a) $x_f/(H/2)$~4.5; b) $x_f/(H/2)=8.5$; c) $x_f/(H/2)=16.2$; d) $x_f/(H/2)=17$. The dotted line corresponds to $u_{\tau c}=0.014u_b$.

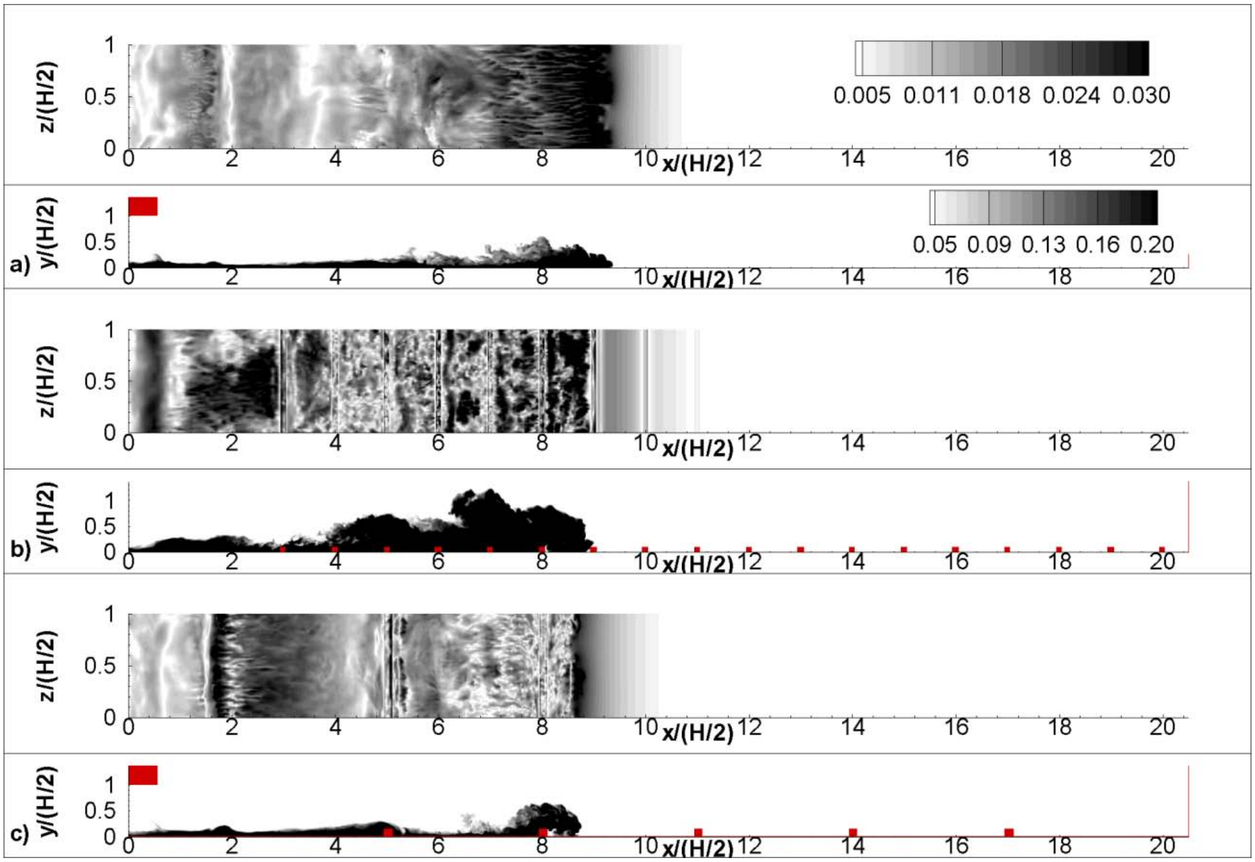

Figure 5.65 Spatial distribution of the bed friction velocity u_τ/u_b during the buoyancy-inertia phase when the front position is $x_f/(H/2)=9$. a) SV-LR-F simulation; b) SV-LR-R10 simulation; c) SV-LR-R15 simulation. Also shown are the concentration contours in an x-y section. The aspect ratio is 1:2 in the x-y plots.

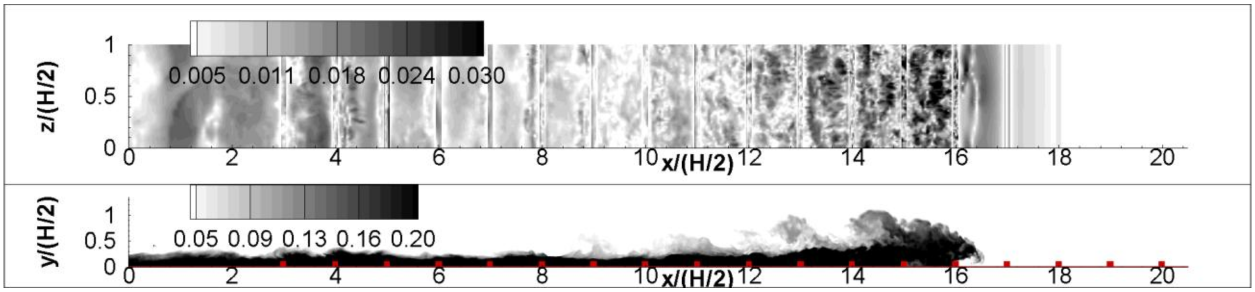

Figure 5.66 Spatial distribution of the bed friction velocity u_τ/u_b during the transition to the drag-dominated phase when the front position is $x_f/(H/2)=16.5$ in the SV-LR-R10 simulation. Also shown are the concentration contours in an x-y section. The aspect ratio is 1:2 in the x-y plot.

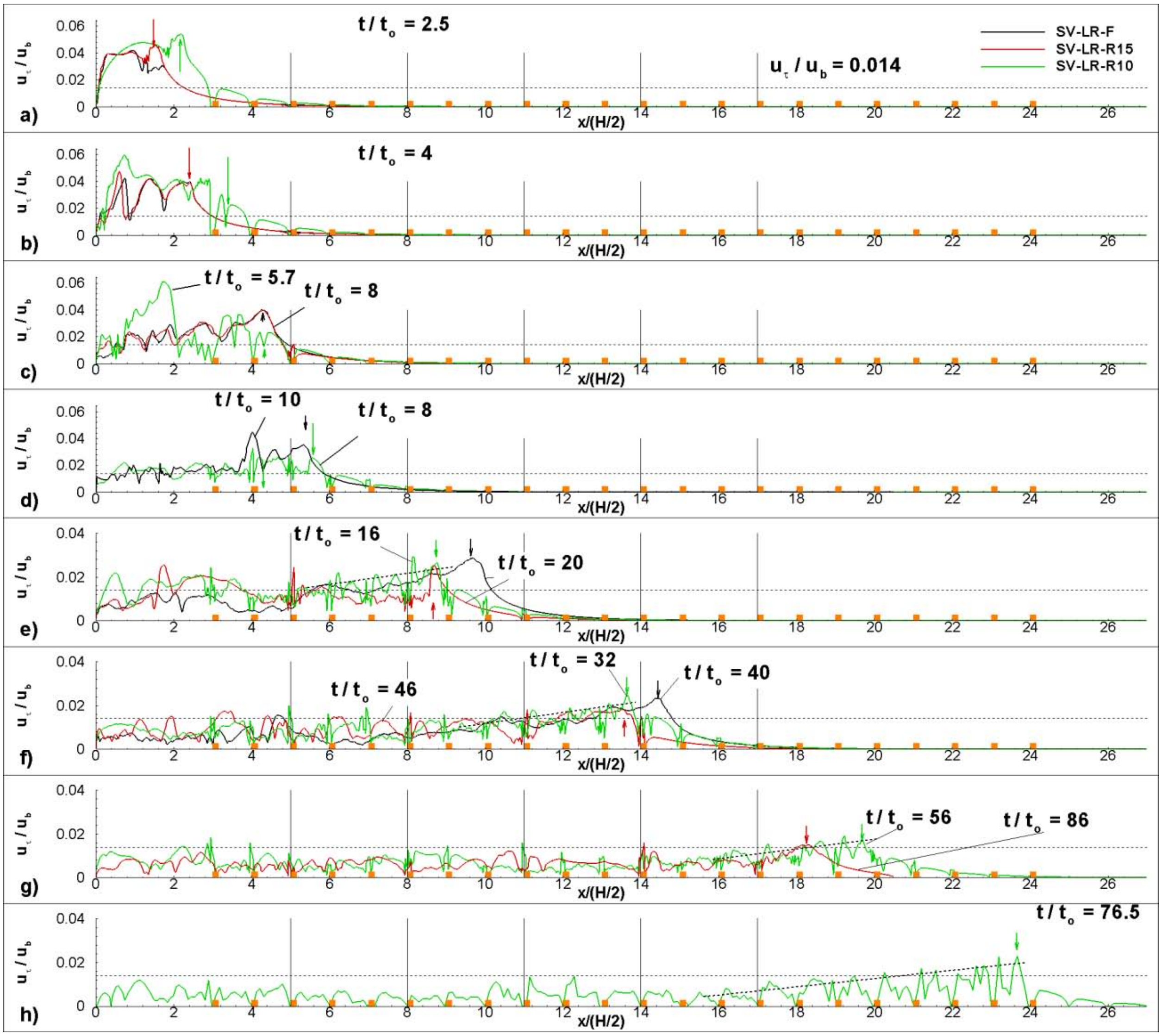

Figure 5.67 Streamwise distribution of the spanwise-averaged bed friction velocity in the SV-LR-F, SV-LR-R15 and SV-LR-R10 simulations. a) $t/t_0=2.5$; b) $t/t_0=4$; c) $x_f/(H/2)\sim4.5$; d) $x_f/(H/2)\sim5.5$; e) $x_f/(H/2)=8.5-9.5$; f) $x_f/(H/2)=13.5-14.5$; g) $x_f/(H/2)=18-19.5$; h) $x_f/(H/2)=23.5$. The dotted line corresponds to $u_{\tau c}=0.014u_b$. The dashed line shows the region where the overall decay of the bed friction velocity in the SV-LR-R10 simulation is linear. The solid vertical lines show the position of the ribs in the SV-LR-R15 simulation.

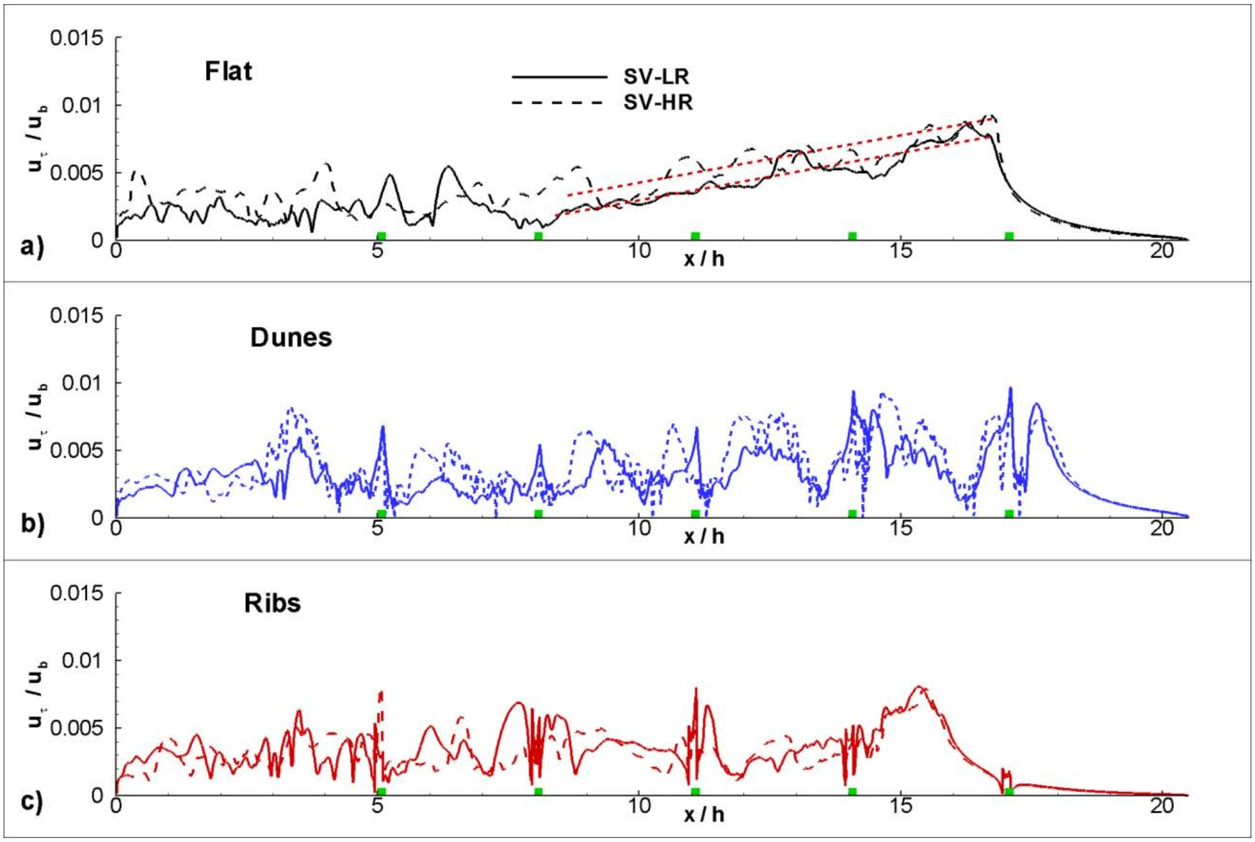

Figure 5.68 Streamwise distribution of the spanwise-averaged bed friction velocity in the high Reynolds number simulations with flat bed and obstacles of height D=0.15H when the front position is $x_f/(H/2)$=15.5-16.5. Also shown are the distributions of the spanwise-averaged bed friction velocity in the corresponding low Reynolds number simulations multiplied by a factor α=0.43. a) SV-LR-F vs. SV-HR-F; b) SV-LR-D15 vs. SV-HR-D15; c) SV-LR-R15 vs. SV-HR-R15.

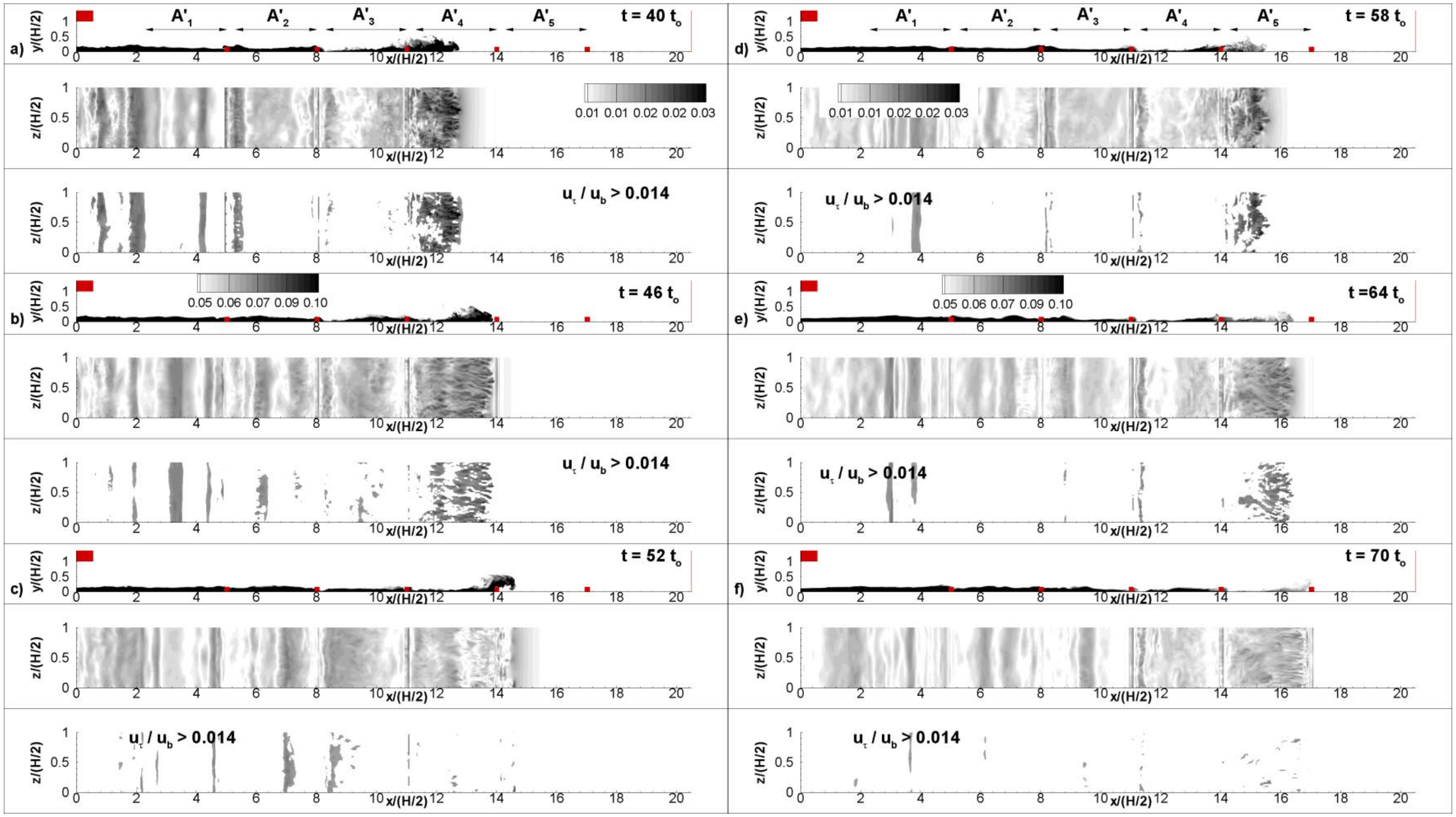

Figure 5.69 Spatial distributions of the bed friction velocity, u_τ/u_b, in the SV-LR-R15 simulation at representative time instances. Also shown at each time instant are the concentration distributions in an x-y section and the regions where sediment is entrained ($u_\tau > u_{\tau c}$) assuming $u_{\tau c}/u_b$=0.014. The concentration plots also show the integration domain A'' associated with each rib that is used to quantify the time variation of the amount of sediment entrained over a certain region of the bed. a) t/t_0=40; b) a) t/t_0=46; c) t/t_0=52; d) t/t_0=58; e) t/t_0=64; f) t/t_0=70. The aspect ratio is 1:2 in the x-y plots.

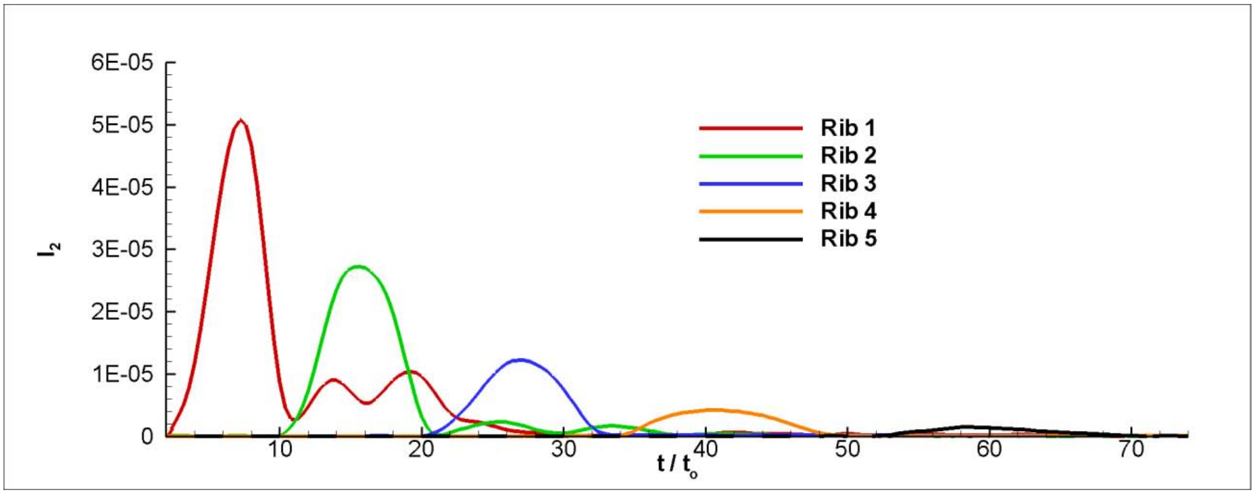

Figure 5.70 Time variation of I_2 calculated over the region associated with each of the ribs present in the SV-LR-R15 simulation. I_2 characterizes the flux of sediment of a certain particle size entrained from the bed, assuming no sediment is entrained if $u_\tau < u_{\tau c}$.

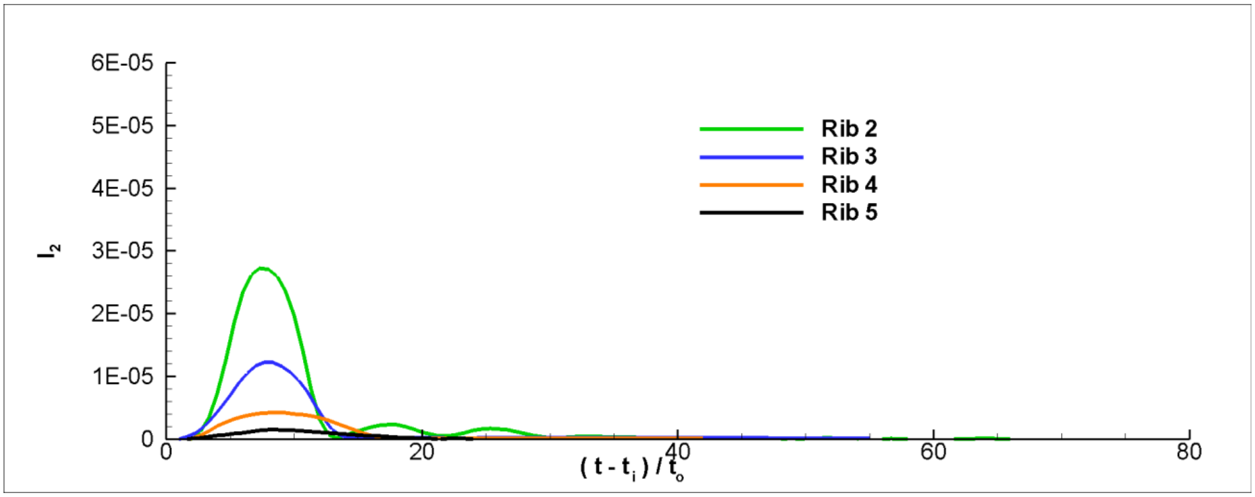

Figure 5.71 Time variation of I_2 calculated over the region associated with Rib2 to Rib5 in the SV-LR-R15 simulation. I_2 characterizes the flux of sediment of a certain particle size entrained from the bed, assuming sediment is entrained at all values of u_τ. The distributions for Rib2 to Rib5 were translated along the time axis such that I_2 becomes non zero at $t/t_0=0$.

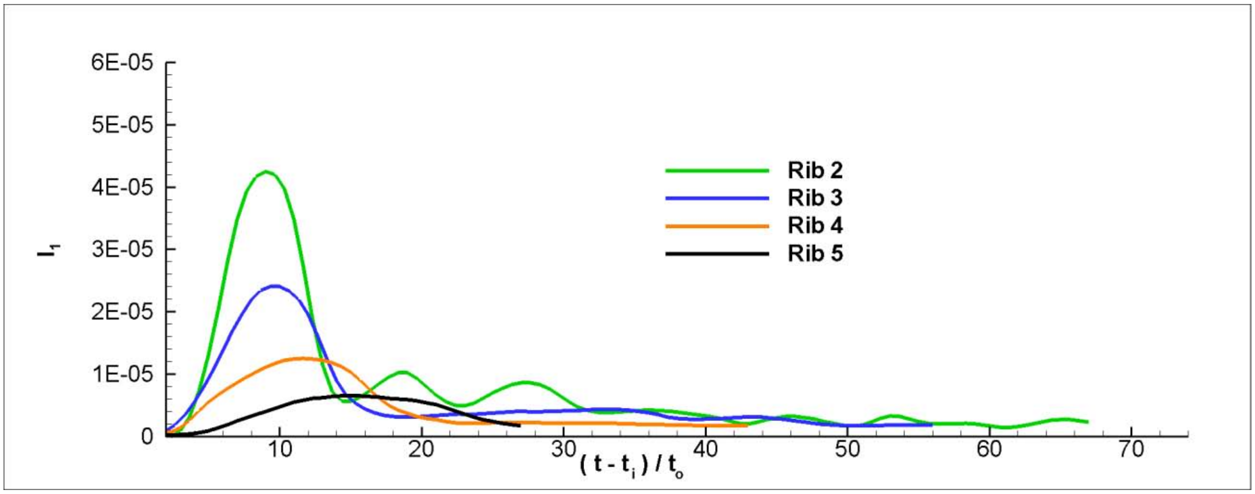

Figure 5.72 Time variation of I_1 calculated over the region associated with Rib2 to Rib5 in the SV-LR-R15 simulation. I_1 characterizes the flux of sediment of a certain particle size entrained from the bed, assuming sediment is entrained at all values of u_τ. The distributions for Rib2 to Rib5 were translated along the time axis such that I_1 becomes non zero at $t/t_0=0$.

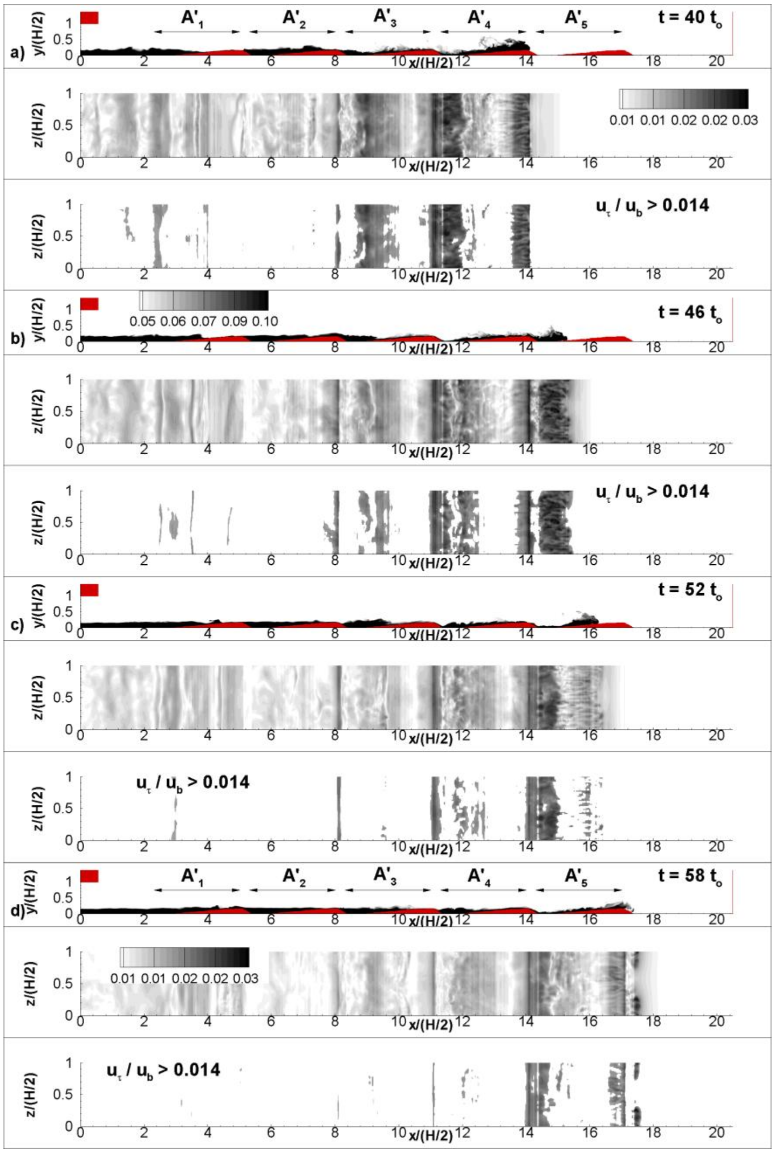

Figure 5.73 Spatial distributions of the bed friction velocity u_τ/u_b in the SV-LR-D15 simulation at representative time instances. Also shown at each time instant are the concentration distributions in an x-y section and the regions where sediment is entrained ($u_\tau > u_{\tau c}$) assuming $u_{\tau c}/u_b$=0.014. The concentration plots also show the integration domain A“ associated with each dune that is used to quantify the time variation of the amount of sediment entrained over a certain region of the bed. a) t/t_0=40; b) a) t/t_0=46; c) t/t_0=52; d) t/t_0=58. The aspect ratio is 1:2 in the x-y plots.

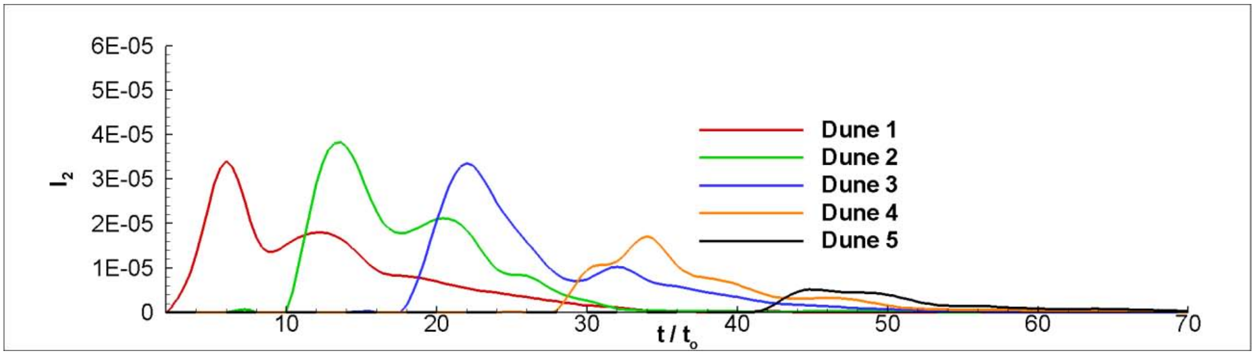

Figure 5.74 Time variation of I_2 calculated over the region associated with each of the dunes present in the SV-LR-D15 simulation. I_2 characterizes the flux of sediment of a certain particle size entrained from the bed, assuming no sediment is entrained if $u_\tau < u_{\tau c}$.

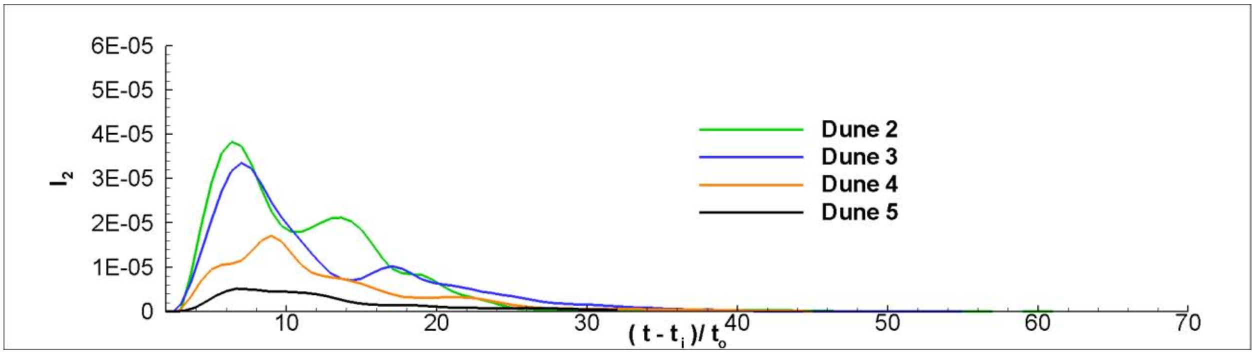

Figure 5.75 Time variation of I_2 calculated over the region associated with Dune2 to Dune5 in the SV-LR-D15 simulation. I_2 characterizes the flux of sediment of a certain particle size entrained from the bed, assuming sediment is entrained at all values of u_τ. The distributions for Dune2 to Dune5 were translated along the time axis such that I_2 becomes non zero at $t/t_0=0$.

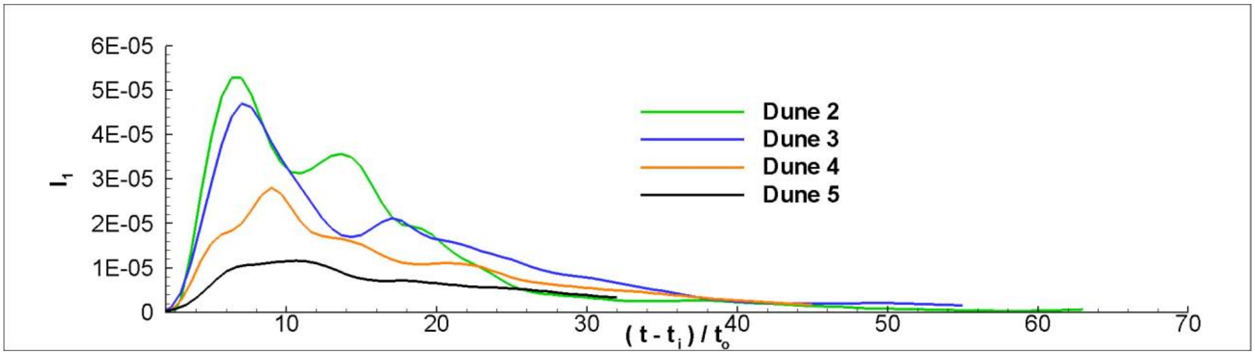

Figure 5.76 Time variation of I_1 calculated over the region associated with Dune2 to Dune5 in the SV-LR-D15 simulation. I_1 characterizes the flux of sediment of a certain particle size entrained from the bed, assuming sediment is entrained at all values of u_τ. The distributions for Dune2 to Dune5 were translated along the time axis such that I_1 becomes non zero at $t/t_0=0$.

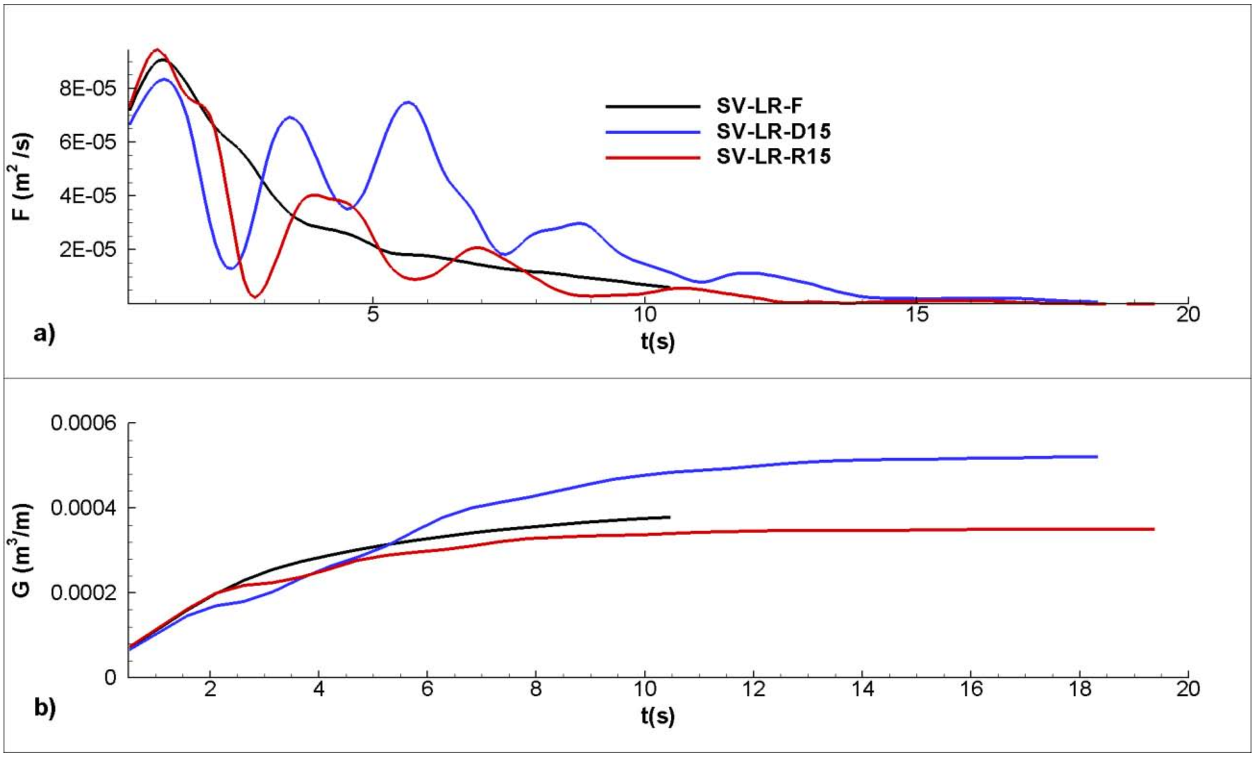

Figure 5.77 Comparison of the capacity of the bottom propagating current to entrain sediment particles of diameter *d=0.14 μm* over its whole length during its propagation in the SV-LR-F, SV-LR-R15 and SV-LR-R15 simulations. a) non-dimensional flux of sediment particles entrained from the bed per unit time and unit width, F(t); b) non-dimensional mass of sediment particles entrained from the bed per unit width between the time the lock gate is released and the current time, $G(t)=\int_0^t F(t)dt$. The flux F(t) is calculated based on van Rijn (1984) formula for the pick-up rate.

CHAPTER 6 GRAVITY CURRENT-SUBMERGED DAM INTERACTION

6.1 Introduction

This chapter investigates the interaction between a bottom-mounted triangular obstacle and a bottom-propagating gravity current with no net flow (see sketch in Figure 6.1). Barriers of triangular cross-sectional shape are, in many cases, a good approximation to submerged dams used to control the sediment depositing in reservoirs, to obstacles that are installed in rivers to reduce the speed of the incoming gravity current and its capacity to entrain sediment, and to obstacles designed to partially or fully arrest gravity currents containing pollutants or hazardous materials (e.g., accidental emissions of heavy hazardous gases propagating in the form of a bottom gravity current away from the source).

Once they form, density (compositional or particulate) currents follow the thalweg of the lake or reservoir, as they move toward deeper regions. For example, turbidity currents often form during flooding events, when a large quantity of fine sediments is entrained from the river bed. As the surface water containing entrained sediments flows into the reservoir containing less dense, relatively stagnant, water, the denser water plunges beneath the free surface and forms a bottom propagating gravity current. Often, the deepest region is situated close to a dam. Additionally, the passage of the density current, especially on a sloped bottom, can entrain substantial amounts of sediment from the bottom of the reservoir. In most cases, these sediments are carried for some distance and deposit in the vicinity of the hydropower dam. As they deposit in large quantities, these sediments can cover bottom outlet and power intake structures, and reduce the storage capacity of the reservoir (Oehy, 2003). These currents are responsible to a large degree for the redistribution of the sediments within the reservoir.

The presence of obstacles in the path of the currents is a popular measure to reduce the amount of sediment deposited in the vicinity of the dam. Submerged dams or groynes could be built to stop the current, or at least to weaken it, to divert the current toward regions situated away from the dam and the hydraulic structures that can be adversely affected by deposition of sediments, or to divert the current toward shallower regions where the deposited sediment can be dredged. For example, Oehy (2003) has shown experimentally that obstacles provide efficient blocking of sediments transported by turbidity currents if the approaching current is subcritical. He recommended using obstacles of height equal to at least twice that of the incoming current and placing the obstacle in a region of the reservoir where the slope is weak or horizontal. This also motivates the main focus of this chapter which is the study of subcritical currents propagating on a horizontal channel bottom.

However, the design of these obstacles is still empirical mainly because it is not possible to quantify their effect on the sediment transported by or with the current. Also, knowledge of the temporal variations of the forces and moments on the structure during and after the impact with the current is needed to insure the structural stability of the submerged dam. In many cases, these dams are built from erodible material. For example, submerged erodible embankment dams are often built from recycling of the excavation materials resulted during the building of the hydropower dams or other large structures. Thus, proper design requires knowledge of the bed shear stress distributions induced by the passage of the current. These distributions can then be used to estimate the amount of material removed from the erodible dam due to the passage of the current.

As a result of the impact between the obstacle and the current, if the height of the obstacle is not much larger than that of the current, some of the heavier (denser) fluid flows up and may continue over the obstacle, while the rest is reflected back as a moving hydraulic jump, as a rarefaction wave, or as a combination of a jump and a rarefaction wave (Lane-Serff et al., 1995). The hydraulic jump may assume the form of a sharp (turbulent breaking) bore or of an undular bore with a series of waves (smooth jump). The internal bore dissipates energy. Such bores were observed in freshwater outflows by Thorpe et al. (1983). Numerical simulations can provide a better description of these waves in terms of their velocity and wavelength and can quantitatively estimate the energy dissipated by the bore.

The influence of the hydraulic jump on the solution is important especially in cases in which the height of the incoming current is comparable to that of the obstacle. The heavier fluid in between the jump and the obstacle continues to move toward the obstacle, but with a smaller speed than that of the heavier fluid in the undisturbed current upstream of the jump. Experiments (Lane Serff et al., 1995) have shown that the presence of an upper boundary (e.g., rigid lid vs. free surface) can have significant effects on the flow if the height of the gravity current is only a few times smaller than that of the channel.

The present investigation considers only the simpler case of a “two-dimensional” flow in which the direction of propagation of the current (aligned with the streamwise direction, x) is perpendicular to the axis of the obstacle (aligned with spanwise direction z). Also, the widths of the current and of the channel, and the extent of the obstacle in the spanwise direction are identical. Under these conditions, the reflected jump is traveling in the opposite direction to that of the gravity current.

Depending on the ratio between the height of the obstacle and that of the incoming current, the flow within the lower layer containing heavier fluid can be **partially blocked** or **fully blocked** (total reflection).

In the partially-blocked regime, which is the main focus of the present chapter, when the gravity current propagating over a no-slip surface hits the obstacle, part of the flow is convected over the obstacle and continues to propagate as a bottom propagating (downstream) current after it passes the obstacle. Depending also on the degree of bluntness of the obstacle, a splash of heavier fluid can form during the initial impact stage. The convection of the splash over the obstacle and its interaction with the ambient fluid is characterized by a stronger mixing compared to the one associated with the convection of the heavier fluid from the tail of the incoming current. The heavier fluid at the head of the current decelerates as it approaches the crest of the obstacle. Meanwhile, the returning internal bore starts forming and accelerates toward the constant speed associated with the quasi-steady regime. The flow inside the lower layer of heavier fluid is strongly accelerated as it is convected over the downstream face of the obstacle. In most cases, the flow inside the lower layer becomes supercritical at, or some distance past, the crest of the obstacle. The flow within the lower layer then transitions back to the subcritical regime via a hydraulic jump. For the type of obstacles considered in the present investigation (triangular obstacles with an inclined downslope), the jump associated with the transition from supercritical flow to subcritical flow downstream of the obstacle is smooth, of small amplitude and stationary. Away from the obstacle, the heavier fluid propagates as a gravity current with an approximately constant front velocity. The speed of the bottom propagating (downstream) current that passed the obstacle, v_f, is smaller than the one of the (upstream) current before it reaches the obstacle, u_f.

The ratio between the gravity current flow convected over the obstacle and the incoming gravity current flow, q_d/q_0, depends on the ratio between the height of the obstacle, D, and the height of the undisturbed lower layer (gravity current), d_0, the ratio between the height of the undisturbed lower layer, and the channel depth, H, and the Froude number of the undisturbed lower layer, $Fr_0 = u_0 / \sqrt{g' d_0}$, where u_0 is the mean velocity inside the undisturbed lower layer (tail region of the upstream gravity current). As the height of the obstacle relative to that of the incoming current increases, the flux of heavier lock fluid over the obstacle decreases. At some point, depending also on the shape of the obstacle and the degree of bluntness of its upstream side, no heavier lock fluid can pass the obstacle continuously. This corresponds to the transition to the fully-blocked regime.

In the fully-blocked regime, the depth of the reflected flow behind the hydraulic jump is between two and three times that of the lower layer in the undisturbed region upstream of the jump. The heavier fluid is reflected as a result of its interaction with the upstream face of the obstacle. However, if the height of the obstacle is less than four to five times that of the incoming gravity current, a small splash, or a series of small splashes, of heavier fluid can pass the obstacle. Knowledge of the volume of heavier lock fluid convected by these splashes is particularly important in applications where gravity currents carry hazardous materials.

Though theoretical models based on the shallow-flow equations were used to predict the main flow parameters describing the interaction of the incoming current with the obstacle, the details of the flow structure was less investigated. Most of the information on the flow structure comes from video-recordings of the evolution of the dye-colored heavier current in laboratory experiments. These video-recordings do not allow exact measurement of some of the important flow parameters describing the flow over the obstacle. Also, not much is known about the temporal variation of the impact forces on the obstacle, and on the spatial and temporal distributions of the bed-friction velocity, which are needed to estimate the amount of sediment entrained by the current over the obstacle and in its vicinity. High-resolution numerical simulations can provide this information. They can also allow verifying the validity of some of the assumptions made in the theoretical models.

6.2 Description of Test Cases

Both the case of lock-exchange gravity current with a relatively large volume of release and the case of a continuously-fed constant-flux gravity current are considered. The positions of the lock gate in the first case (Figure 6.1a) and of the open slot through which a constant discharge of lock fluid is introduced in the channel in the second case (Figure 6.1b) are the same. In the cases of a gravity current in a lock-exchange configuration, the net flow is equal to zero. In other words, there is a return flow toward the lock gate in the upper layer of ambient fluid. This return flow is absent in the case of a constant-flux gravity current in which the heavier lock fluid is introduced over the whole depth of the gate opening.

A total of seven 3-D simulations were performed. The channel bottom was horizontal. Thus, the incoming gravity current was subcritical. The case of an incoming supercritical gravity current that typically occurs when the current propagates over a sloped bottom was not studied. Three of the simulations were conducted in lock-exchange configurations and four of the simulations were conducted with a constant inflow of lock fluid at the lock-gate position. In the simulations conducted in a lock-exchange configuration, the length scale, h_0, was equal to the lock-gate opening, h (Figure 6.1a). In the simulations with a constant-flux of lock fluid introduced at the lock-gate position ($x_0=8.125h_0$), the height of the opening was $h=0.566h_0$ (Figure 6.1b), such that the average non-dimensional depth of the tail of the current forming downstream of the lock gate, d_0/h_0, was similar (0.37-0.39) in all the simulations. The height of the head of the incoming current before it starts interacting with the obstacle, also referred to as the upstream current, was close to $0.5h_0$. This allows to directly compare simulations conducted in lock exchange configurations with simulations conducted with a constant incoming flux of lock fluid. The buoyancy velocity $u_b=\sqrt{g'h_0}$ is used to scale the velocities. The time scale is $t_0=h_0/u_b$.

In all but one of the simulations, the Reynolds number was around 7,200. In all but one of the simulations, the shape of the obstacle was triangular. The angle α between the faces of the obstacle and the channel bottom varied between 32^0 and 51^0 (see Figure 6.1 and Table 6.1). In all but one of the simulations, the non-dimensional channel depth, H/h_0, was equal to 5.354. This corresponds to a partial-depth-release current whose height is couple of times smaller that that of the ambient fluid. This is the case encountered in most practical applications when gravity currents occur in lake, sea and reservoir environments.

The distance between the crest of the obstacle and the gate position was $L_0=7.78h_0$. The length of the computational domain measured from the lock-gate position was $15.94h_0$. In the lock-exchange simulations, the distance between the back-wall and the lock gate was $x_0=8.125h_0$. To make the comparison of the results easier, the lock gate was situated at $x_G=8.125h_0$ and the center (crest) of the obstacle was situated at $x_c=15.9$ in all the simulations.

All the simulations conducted with an isolated obstacle have a „D" at the start of the notation. The simulations conducted in a lock exchange configuration are denoted „LE". The simulations conducted with a constant flux of lock fluid are denoted „CF". The non-dimensional height of the obstacle, D/h_0*100 is indicated by a number. The presence of a Gaussian-shape obstacle is marked by a „G" at the end of the name used to identify the simulation. The simulation conducted at Re=250,000 contains an „HR" at the end of the notation. The main parameters of the simulations discussed in this chapter are summarized in Table 6.1 (see also Figure 6.1).

As the Boussinesq approximation is used, the changes in the height of the free surface can be neglected, and symmetry boundary conditions (shear-free rigid-lid approximation) are employed at the top boundary. The back-wall, the channel bottom and the submerged part of the lock gate are treated as no-slip boundaries. A convective outflow boundary condition was used at the right extremity of the computational domain in the simulations with a constant-flux current. The value of the convective velocity U_c was equal to the estimated front velocity of the current when reaching the right end boundary. The Schmidt number was $Sc=600$. The flow field was initialized with fluid at rest. The flow was assumed to be periodic in the spanwise direction.

A zero normal gradient was imposed for the concentration at the top boundary and at all the wall boundaries. The non-dimensional concentration field was initialized with a constant value of one in the region containing the lock fluid (e.g., inlet section in the simulations conducted with a constant inflow of lock fluid) and a constant value of zero in the rest of the computational domain containing initially ambient fluid. The time step was $0.001t_0$.

In the simulations conducted with Re<10,000, the grid size was 2016×48×256 in the streamwise, spanwise (domain width $L_3=h_0$), and vertical (domain height $L_2=H$) directions, respectively. Away from the walls and the obstacle, the grid spacing in the three directions was about $0.02h_0$. To resolve the viscous sub-layer in the simulations conducted with Re<10,000, the grid spacing in the wall-normal direction was reduced to $0.006h_0$ near the wall surfaces of the computational domain. The mesh was finer in the D-CF-D068-HR simulation, due to the need to resolve the viscous sublayer.

The flow parameters in simulations D-LE-D034a and D-LE-D034b (Table 6.1) correspond to those in two of the lock-exchange experiments conducted by Lane-Serff et al. (1995) in which the non-dimensional height of the triangular obstacle, D/h_0, was equal to 0.34, the bottom length of the dam, B/h_0, was equal to 1.1, and h_0 was equal to 0.048 m. The main difference between the two test cases is the value of the non-dimensional channel depth, $H/h_0=1.042$ (very close to a full-depth-release case) vs. $H/h_0=5.354$ (partial-depth-release case). Comparison of these two test cases allows investigating the influence of the height of the layer of ambient fluid. The only difference between the computational domain and the experimental setup was the presence of a fixed barrier inside the region that was initially filled with lock fluid. The sliding barrier was situated at a small distance downstream of the fixed barrier. Only the sliding barrier (lock gate in the open position) was present in the simulations. It is not clear to what extent the presence of the fixed barrier affects the heavier flow propagating over the channel bottom downstream of the lock-gate position.

The effect of the size of the obstacle on the interaction between a gravity current and an obstacle is analyzed based on comparison of simulations D-LE-D034b and D-LE-D068 conducted with an obstacle of height $D=0.34h_0$ and $D=0.68h_0$, respectively. The length of the base in the two simulations is the same ($B=1.1h_0$). The partially-blocked regime is observed in both simulations.

Additionally, a simulation with an obstacle of height $D=1.37h_0$ is conducted. In this simulation, the obstacle is high enough such that the fully-blocked regime is observed.

The effect of the way the gravity current is set up is investigated by comparing the results of simulations D-LE-D068 and D-CF-D068 conducted in a lock exchange configuration and with a constant influx of lock fluid at the lock-gate position, respectively. The mean streamwise velocity within the tail of the undisturbed current, u_0, and its height, d_0, are used to characterize the bulk properties of the incoming current before it reaches the obstacle. In fact, at a given streamwise position, these two variables remain close to constant until the bore reaches that position. Because of the raised head, the front velocity is slightly lower than u_0. The measured values of d_0/h_0 (0.39 vs. 0.37) and u_0/u_b (0.54 vs. 0.50) were close, but not identical. The flux of incoming lock fluid $q_0=(u_0d_0)/(u_bh_0)$ was slightly higher (0.21 vs. 0.185) in the D-LE-D068 simulation.

Scale effects are investigated by comparing the results of simulations D-CF-068 and D-CF-068-HR conducted with a constant influx of lock fluid at Re=7,141 and Re=250,000 respectively. The simulation conducted at Re=250,000 allows to better understand the physics of the interaction between a gravity current and an isolated obstacle for flow conditions that are closer to those encountered in practical applications.

As in most practical applications the shape of the submerged dams is not exactly triangular, the effect of the shape of the obstacle is investigated by comparing the results of simulations D-CF-068 and D-CF-068-G conducted with an obstacle of triangular and, respectively, Gaussian shape. The exact shape is given by $y/h_o = 0.6875e^{-8(x/h_o - x_c/h_o)^2}$, where x_c is the streamwise position of the crest of the obstacle. The height of the obstacle in the two simulations is the same. The Gaussian shape is characterized by a smoother change in the elevation of the obstacle face and, for many cases, is a better approximation of the shape of submerged dams encountered in the field.

An integral approach is used to estimate the height of the current and the velocity of the flow at a certain streamwise location cutting through the body of the gravity current. The non-dimensional height is defined as,

$$d / h_0 = \int_0^{H/h_0} C d(y / h_0) \tag{6.1}$$

and the non-dimensional mean velocity at a certain section is defined as,

$$u / u_b = \frac{\int_0^{H/h_0} C(u_x / u_b) d(y / h_0)}{d / h_0} \tag{6.2}$$

where $u_x(x,y)$ is the time- and spanwise- averaged velocity component in the x direction.

For example, equations 6.1 and 6.2 were used to estimate u_0 and d_0 for the undisturbed current. The same equations are also used to estimate the non-dimensional flux of heavier fluid at a certain streamwise location, $q=(u_d)/u_b h_0$. The front speed of the current upstream (u_f) and downstream (v_f) of the obstacle is calculated by tracking the front of the current, $x_f(t)$ during the time intervals the front speed is close to constant (x_f increases linearly with time).

In the present numerical simulations, the upstream propagating hydraulic jump was observed to resemble an undular bore. This is consistent with experiments (Woods and Simpson, 1984, Lane-Serff et al., 1995) which found that undular bores occur when the change in depth across the hydraulic jump, d_{l1}/d_0, is smaller than 2.5 (see Table 6.4 and Figure 6.2). The undular bore is characterized by the formation of a train of internal waves which resembles a group of solitary waves (Edwards et al., 1994). The bore dissipates energy. In the particular case of an undular bore, each of the internal waves carries energy as it travels upstream. For very strong bores, additional energy is dissipated by the strong turbulence at the front.

The present simulations allowed characterizing the undular bore in terms of wavelengths and wave speeds. They also allowed measuring in an accurate way the flow depths in the regions where the flow is quasi-steady, the velocities of the backward disturbances, the flux of the heavier fluid convected over the obstacle, q_d, and the flux reflected away from the obstacle, q_0-q_d. All these quantities are difficult to accurately estimate from experiments. The velocities of the backward disturbances (e.g., waves associated with the backward propagating undular bore) are calculated by simply observing the changes in the positions of the disturbances with time.

6.3 Flow regimes

Assuming a constant-flux incoming current, or an incoming current with a large volume of release, and a partially blocked flow at the obstacle, the flow around the obstacle becomes quasi-steady and the backward propagating hydraulic jump moves with approximately constant velocity after a sufficiently large amount of time (see also sketch in Figure 6.2a). This first quasi-steady state regime (SS1) lasts until the reflected bore starts interacting with the submerged part of the lock gate and reflects back toward the obstacle. The disturbances are much stronger in the case of a constant-flux current for which all the heavier fluid convected with the bore is reflected. The reflection is accompanied by a strong disturbance of the heavier fluid propagating close to the channel bottom in the downstream direction. In the case of a lock exchange configuration, most of the heavier fluid traveling with the bore is convected upstream, past the lock gate position, into the region that was initially filled with lock fluid. In the present simulations conducted in lock-exchange configurations, the maximum height of the bore was smaller than the gate opening, h. This is why the amount of heavier fluid reflected at the lock gate was negligible.

In the case of a constant-flux current, a new type of quasi-steady regime (SS2) is reached when most of the region between the lock gate (rear end wall) and the obstacle becomes filled with heavier fluid, and the level of the interface between the mixed fluid and the ambient fluid becomes close to constant from the lock gate until close to the obstacle (see sketch in Figure 6.2b). This generally happens after several reflections of the flow disturbances at the lock gate and at the obstacle. Whether or not this quasi-steady regime will also be reached in the case of a lock-exchange current is not clear. This is because in the case of a lock-exchange current some of the reflected heavier fluid moves past the lock gate, back into the region that was initially filled with lock fluid. In the case of a constant-flux current, the heavier fluid moving with the bore does not penetrate the lock gate opening. Rather, it accumulates on top of the current containing heavier lock fluid that enters the domain through the whole height of the lock-gate opening.

The level of the interface upstream of the obstacle is higher than that observed during the first type of quasi-steady state regime. The flow inside the lower layer of heavier fluid moves over the crest and down the downstream face of the obstacle. The fast shallow layer flow past the crest of the obstacle resembles the constant density (single layer) flow of a fluid over a weir, with a constant free surface elevation upstream of the weir.

This second quasi-steady regime is also observed in the case of the fully blocked regime, assuming the volume of lock fluid is large enough to fill the region in between the lock gate and the obstacle, up to the crest of the obstacle (e.g., a constant-flux incoming current will always reach this regime after a sufficiently long time). At least for the case of a constant flux of incoming lock fluid, during this quasi-steady regime (SS2), the flux of heavier lock fluid past the obstacle, q_d, is close to constant and oscillates around the value of the flux of incoming lock fluid at the inlet section, q_g.

The time variations of the non-dimensional discharges at the lock gate position, q_g, and at the crest of the obstacle, $q_d=(u_d d_d)/(u_b h_0)$, allow estimating the duration of the first quasi-steady state regime at representative sections. One should mention that q_g is equal to the flux of lock fluid calculated in the tail of the incoming current $q_0=(u_0 d_0)/(u_b h_0)$.

The variations of q_d and q_g with time for case D-LE-D034b (Figure 6.3a) are representative for simulations conducted in lock-exchange configurations. After the release of the lock fluid, q_g increases slowly in a non-monotonic way and then starts oscillating along a constant value ($q_g \sim 0.21$ for case D-LE-D034b). As the reflected bore approaches the lock gate position ($t > 35t_0$), a small decrease in q_g is observed. At the crest of the obstacle, q_d first increases sharply, as the heavier fluid starts being convected over the obstacle, and the decreases toward a constant value. The regime in which the flow is close to steady (SS1) is reached at $t \sim 20t_0$, after the bore has formed ($x_{b1}/h_0 \sim 15$) and the interface between the two layers becomes close to horizontal in the vicinity of the obstacle. During SS1, $q_d < q_g$ (e.g., $q_d = 0.14$ in case D-LE-D034b). If the flow disturbances forming when the waves associated with the undular bore reach the lock gate are small, this quasi-steady-state regime can last until most of the lock fluid has left the region situated upstream of the lock gate. This is the case in the present simulations conducted in lock-exchange configurations.

The first quasi-steady regime is also observed in all the simulations (e.g., see Figures 6.3b and 6.3c) conducted with a constant-flux incoming current, in which the flow of heavier fluid is partially blocked. In these simulations, q_g is fixed (e.g., $q_g = 0.185$ for cases D-CF-D068 and D-CF-068-HD). Similar to case D-LE-D034b, after the initial transient, q_d becomes close to constant (e.g., $q_d = 0.019$-0.025 for cases D-CF-D068 and D-CF-068-HD) when the bore has formed and the interface with the ambient fluid in between the bore and the crest of the obstacle is close to horizontal (e.g., $t \sim 20t_0$ for case D-CF-D068). The first wave of the undular bore starts interacting with the lock gate at $t = 33t_0$. The reflection is complete at $t = 38t_0$. The reflection induces lots of flow disturbances not only inside the region situated close to the interface with the upper layer of ambient fluid, but also in the lower part of the lower layer. This is why, a short time after the reflection is complete (e.g., $t = 38t_0$ for case D-CF-D068), q_d starts increasing monotonically until the reflected heavier fluid reaches the crest ($t = 47t_0$). Part of this fluid is convected over the crest and part of it reflects back toward the lock gate. At later times, q_d is subject to large-scale oscillations of decaying amplitude, as the mean level of the interface in between the lock gate and the obstacle increases, and some of the heavier fluid is convected back and forth in between the lock gate and the obstacle.

In case D-CF-D068, q_d starts oscillating around the value of the flux of incoming heavier fluids, $q_g=0.185$, at $t \sim 65t_0$. This is when the second quasi-steady regime, SS2, is reached close to the obstacle. The time variation of q_d is similar in the other simulations with a constant-influx current (e.g., see Figure 6.3c for case D-CF-D068-HR).

In case D-CF-D137 the flow of heavier fluid is fully blocked. Thus, if one ignores the small splashes of heavier fluid convected over the crest of the obstacle, q_d remains equal to zero until the top of the lower layer in between the lock gate and the upstream face of the obstacle raises above the crest of the obstacle. This happens when $t \sim 52t_0$. After a transient stage ($52<t/t_0<88$), the height of the lower layer upstream of the obstacle becomes close to constant and q_d starts oscillating around the value of the flux of incoming lock fluid, $q_g=0.185$. The quasi-steady regime SS2 is reached and will continue indefinitely, assuming q_g remains constant.

6.4 Comparison of the main flow parameters describing the flow past the obstacle among the test cases

The values of the front velocity of the upstream current, u_f, are compared in Table 6.2. As in all the simulations the upstream gravity current reaches the slumping phase a short distance past the lock gate position, the size of the obstacle does not affect the value of u_f. For example, the results in Table 6.2 show that u_f/u_b is equal to 0.57 in two lock-exchange simulations (D-LE-D034b and D-LE-D068) in which the only difference is the obstacle height ($D=0.34h_0$ vs. $D=0.68h_0$).

However, if the height of the opening, h, is kept the same, u_f increases as H increases. This is because at a given elevation $y<h$ ($y=0$ at the channel bottom), the hydrostatic pressure difference between two points situated immediately upstream and downstream of the lock-gate position increases with H. Indeed, comparison of simulations D-LE-D034a and D-LE-

D034b shows that u_f/u_b increases from 0.45 to 0.57 as H/h_0 increases from 1.042 to 5.354. The increase in $q_g=q_0$ (Table 6.3) is similar, from 0.155 to 0.21.

The value of q_g in the D-CF-D068 simulation conducted with a constant-flux gravity current was chosen such the front velocity ($u_f=0.56$) is very close to the value ($u_f=0.57$) predicted in the corresponding lock-exchange simulation (D-LE-D068). Despite the close to identical values of u_f, the incoming flux of heavier fluid, q_g, was slightly lower in the D-CF-D068 simulation (0.185 vs. 0.21). The difference is due to the fact that the head of the current was larger in the D-LE-D068 simulation. Combined with the fact that the height of the tail was slightly smaller in the D-CF-D068 simulation ($d_0/h_0=0.37$ vs. 0.39), which is expected as the density gradient is sharper near the interface, the mean velocity in the tail, u_0/u_b, was smaller by about 8% (0.50 vs. 0.54) in the D-CF-D068 simulation.

To allow a direct comparison among the simulation results, q_g was left unchanged in all the other simulations conducted with a constant-flux gravity current. As expected, the presence of an obstacle of same height, but of different shape (D-CF-D068-G), or of an obstacle of larger height (D-CF-D137), did not affect the front velocity of the incoming current. In fact, the effect of the shape of the obstacle was negligible on all the main parameters characterizing the flow before and after the gravity current reaches the obstacle. Figure 6.5 compares the structure of the current in the D-CF-D068 and D-CF-D068-G simulations at two representative time instants during the initial impact stage ($t=15t_0$) and after the downstream current has formed ($t=29t_0$). The shape of the downstream current and the deformations of the interface upstream and downstream of the obstacle are identical. This is the reason why Table 6.3 does not report results for case D-CF-D068-G.

Meanwhile, the increase of the Reynolds number from Re=7,141 to Re=250,000 resulted in an increase of u_f/u_b by about 10% (0.56 vs. 0.61). The mean velocity in the tail (lower layer) and the tail height measured at large distances behind the head, where the interface is close to horizontal, were not affected by the increase in the Reynolds number.

Comparison of simulations D-LE-D034a ($H/h_0=1.042$) and D-LE-D034b ($H/h_0=5.354$), conducted in lock-exchange configurations ($h=h_0$), allows to quantify the effect of increasing $Fr_0 = u_0 / \sqrt{g' d_0} = (u_0 / u_b)/(\sqrt{d_0 / h}_{0})$ on the interaction between the current and the obstacle. The increase in Fr_0 from 0.69 to 0.86 is mainly due to the increase of u_0 with H (e.g., by about 25% from $H/h_0=1.042$ to $H/h_0=5.354$). By comparison, the relative increase of d_0 is about 5%.

As expected, the upstream current was subcritical in all the simulations ($Fr_0<1$). If the height of the obstacle is kept unchanged, the fraction of the incoming heavier fluid that propagates past the obstacle, $q_d = u_d d_d / u_0 d_0$, increases as the inflow Froude number, Fr_0, increases. This is because the heavier fluid within the incoming current has, relatively speaking, a larger streamwise momentum. Assuming h is constant (same gate opening), that means that $u_d d_d / u_0 d_0$ increases with increasing H or H-h (height of the layer of ambient fluid). Indeed, results in Table 6.3 show that $u_d d_d / u_0 d_0$ increases from 0.58 to 0.67 as H/h_0 increases from 1.042 to 5.354. The larger proportion of the heavier fluid flow convected over the obstacle translates into a smaller decrease of the front velocity of the downstream current, v_f, compared to the front velocity of the upstream current, u_f (e.g., from 0.45 to 0.39 in the D-LE-D034a case and from 0.57 to 0.54 in the D-LE-D034b case). Due to the larger depth of the layer of ambient fluid in case D-LE-D034b, the velocity of the return flow in the upper layer of ambient fluid is much smaller.

The most dramatic change is observed for the velocity of the bore, u_{b1}. In the case of an undular bore, u_{b1} denotes the speed of the first wave after it reaches the steady state value. As pointed out by Lane Serff et al. (1995), when the layer of ambient fluid is thicker, the return flow in it should be slower, as the net flow is equal to zero. The height of the lower layer behind the bore is smaller (d_{l1}/h_0 increases from 0.59 in the D-LE-D034a case to 0.66 in the D-LE-D034b case) and the speed of the bore is faster. Indeed, comparison of simulations D-LE-D034a ($H/h_0=1.042$) and D-LE-D034$_b$ ($H/h_0=5.354$) shows that u_{b1}/u_b is larger by about 10% (Table 6.2) in the simulation with a shallower layer of ambient fluid. Thus, the trend in the variation of the bore velocity is different than the one observed for the front velocity, u_f/u_b, which is much smaller (0.45 vs. 0.57) in the simulation with a shallower layer of ambient fluid.

As the bore velocity is mainly controlled by the relative thickness of the layer of ambient fluid, increasing the height of the obstacle from $0.34h_0$ to $1.37h_0$ should not result into a significant variation of u_{b1}. Comparisons of simulations conducted with the same height of the layer of ambient fluid, but with varying obstacle heights, do not show a clear trend in the variation of u_{b1}/u_b with increasing the height of the obstacle (see Table 6.2). The increase in the Reynolds number from 7,141 to 250,000 in the simulations with $D=0.68h_0$ has minimal effects on u_{b1}/u_b, which decreases from 0.39 to 0.38. Table 6.2 also shows the values of the bore velocity, (u_{b1}/u_b)“ obtained by assuming a sharp bore and applying the continuity equation across the moving front. This is a standard assumption made in all the theoretical models used to predict the interaction of a gravity current with an obstacle. The agreement is quite satisfactory for the simulations with $D>0.68h_0$. However, the velocity of the first wave of the undular bore is underpredicted by about 30% in the simulations with $D=0.34h_0$.

With the exception of case D-LE-D034a, the bore had a pronounced undular shape in all the other simulations (e.g., see Figure 6.4). However, especially in the simulations with a constant-flux gravity current, the interaction of the first wave with the lock gate resulted in a strong disturbance of the flow in between the gate and the obstacle, which made it difficult to infer the velocity and wavelength of the secondary waves. In the simulations D-LE-D034b and D-CF-D137, the bore was undular, but the first wave did not reach a close to constant velocity before it approached the lock gate. This is why Table 6.2 does not contain a value for u_{b2}.

The wavelength of the first wave was close to $3.7h_0$ in the D-LE-D034b simulation (Figure 6.4a). Increasing the height of the obstacle to $D=0.68h_0$ resulted in a slight decrease of the wavelength of the first wave to $3.5h_0$. The temporal evolution of the interface in the D-LE-D068 case (Figure 6.4b) allowed estimating the speed of propagation of the second wave ($u_{b2}=0.35u_b$).

The increase of the Reynolds number resulted in a large increase of the amplitude of the waves forming behind the bore front (e.g., see Figure 6.4c). This means the internal waves transport a much higher amount of energy in the case of high Reynolds number currents. The increase of their amplitude made the measurement of their velocities and wavelengths easier. As a result of the increase in the Reynolds number from Re=7,141 to Re=250,000, the velocity of the first wave decreased by about 5% and its wavelength decreased by about 15%, from $3.5h_0$ to $3h_0$. At both Reynolds numbers, the velocity of the second wave was lower than the velocity of the first wave. In the high Reynolds number simulation the wavelength of the second wave (Figure 6.4c) was $2.8h_0$, slightly smaller than that of the first wave ($3h_0$).

If no obstacle is present, then v_f is equal to u_f. If an obstacle is present, v_f is smaller than u_f because $q_d<q_0$ and of the mixing occurring at the head of the downstream current as a result of the impact of the current with the obstacle. The reduction with respect to u_f is mainly function of the height of the obstacle, D, relative to that of the incoming current, d_0. In both simulations with $D=0.34h_0$, for which $q_d / q_0 \cong 0.6$, v_f is about 10% less than u_f. The difference increases to about 30% in all the low Reynolds number simulations with $D=0.68h_0$, for which $q_d / q_0 \cong 0.025$. In the high Reynolds number simulation with $D=0.68h_0$, v_f is slightly larger compared to the lower Reynolds number simulation, but the relative decay of v_f with respect to u_f is close to identical (~30%).

As expected, the fraction of the incoming heavier fluid that propagates past the obstacle, q_d / q_0, decreases as the height of the obstacle increases (e.g., from 0.67 for $D=0.34h_0$ to 0.14 for $D=0.68h_0$ in the lock exchange simulations with $H=5.354h_0$). For the same flow conditions, q_d / q_0 is larger in the case of a lock-exchange current (e.g., $q_d / q_0 =0.14$ for $D=0.68h_0$) compared to the case of a constant-flux current (e.g., $q_d / q_0 =0.11$ for $D=0.68h_0$). Results in Table 6.3 confirm that once the gravity current past the obstacle is established, and the height of the region between the downstream face of the obstacle and the back of the tail becomes close to constant in time, $q_d = u_d d_d = v_3 d_3 = q_3$ in the simulations in which the flow of heavier fluid is partially blocked.

However, as the head of the downstream current is approached, larger variations in the instantaneous flux of lock fluid are observed. Close examination of the time variation of v_f shows that, at times, the front of the downstream current accelerates for some small periods of time with respect to the value observed at most times (this "steady state" value is quoted in Table 6.2). These oscillations are probably related to the unsteady dynamics associated with the shedding of billows behind the head of the downstream current. The height of the downstream current close to the front was calculated assuming continuity $d_f=q_d/v_f$.

The effect of the increase in the height of the obstacle is to also reduce the height of the lower layer at the location of the crest, d_d/h_0 (e.g., from 0.27 for $D=0.34h_0$ to 0.13 for $D=0.68h_0$ in the lock-exchange simulations) and the height and velocity of the downstream current (e.g., the height of the lower layer downstream of the obstacle d_3/h_0 decreases from 0.3 for $D=0.34h_0$ to 0.12 for $D=0.68h_0$ in the lock-exchange simulations). Consistent with the fact that, for the same flow conditions, the height of the tail is slightly smaller in the case of a constant-flux current compared to the case of a lock-exchange current (e.g., by about $0.02h_0$ for $D=0.68h_0$), the same trend is observed for d_d and d_3 (e.g., by 0.02-$0.03h_0$ for $D=0.68h_0$). Finally, the variation of the depth of the lower layer behind the jump, d_{11}, is similar to that of d_d, as in all the simulations d_{11} is close (within $0.02h_0$) to d_d+D. This means theoretical models that assume $d_{11}=d_d+D$ (e.q., Rottman et al., 1985) during the first quasi-steady state regime do not introduce large errors. During the first quasi-steady state regime, the elevation of the interface with the upper layer of ambient fluid is close to horizontal over the upstream face of the obstacle in all the simulations with $D=0.68h_0$ ($d_{11}\sim d_d+D$). LES results show that scale effects on d_d, d_3 and d_{11} related to the increase of the Reynolds number from 7,141 to 250,000 in the simulations with $D=0.68h_0$ are negligible.

Finally, at the crest of the obstacle the Froude number is, in most cases, much smaller than one ($0.64<Fr_d<1$). This means that assuming $Fr_d=1$ can be a potential source of errors for theoretical models that try to predict the flow characteristics during the first quasi-steady state.

Still, simulation results show that the flow becomes supercritical over the downstream face of the obstacle.

As discussed in the previous section, the constant-flux current cases reach a second type of quasi-steady state, SS2, after the heavier fluids fills the region in between the lock gate and the obstacle. Table 6.4 shows a comparison of the main flow parameters during SS2 for the D-CF-D068, D-CF-D068-HR and D-CF-D137 simulations. The variables measured during the second quasi-steady-state regime have a “b” subscript. In the simulation with D=0.137h$_0$, the incoming gravity current is fully blocked, so the first type of quasi-steady state regime is not present. As during SS2 the flux of heavier fluid over the obstacle is equal to the incoming flux at the lock gate position ($u_d d_d / u_0 d_0 = 1$), the difference between the height of the lower layer away from the obstacle, d_{l1}, and the height of the obstacle, D, has to be larger than the one observed during SS1 for which $u_d d_d / u_0 d_0 < 1$. For example in the case of the lower Reynolds number simulation with D=0.68, (d_{l1}-D) increases by a factor of five, from 0.08h$_0$ to 0.39h$_0$. The increase in the depth of the layer of heavier fluid at the location of the crest is slightly lower (four times), from 0.08h$_0$ to about 0.32h$_0$. This is because the interface elevation decays as the crest of the obstacle is approached (e.g., by about 0.05-0.09h$_0$). In contrast to the first steady-state regime where $d_{l1} \sim d_d + D$, assuming the interface is close to horizontal until the crest of the obstacle can be a source of errors when the main flow parameters characterizing the flow structure during the second quasi-steady-state regime are estimated. On the other hand, the Froude number at the crest of the obstacle is close to one ($0.92 < Fr_{db} < 1.11$). Thus, assuming $Fr_{db} = 1$ at the crest is justified.

The increase in $u_d d_d / u_0 d_0$ between the two regimes is close to nine times in the simulations with D=0.68h$_0$. The difference is, in part, due to the increase (by 2-3 times) of the mean velocity of the heavier fluid moving over the crest of the obstacle.

The mean velocity, v_{3b}, and height, d_{3b}, of the tail of the current forming past the obstacle are also larger during the second type of quasi-steady state. Both quantities are measured at relatively large distances downstream of the obstacle (x/h$_0$=21), where the height of the lower layer (tail) is close to constant. In the case of an obstacle of height $D=0.68h_0$, during SS2, v_{3b} is larger by about three times and d_{3b} is larger by more than three times compared to the values observed during SS1. For both types of steady-state regimes, the flow inside the lower layer remains supercritical for some distance downstream of the obstacle. However, especially for relatively high obstacles, the distance over which the flow remains supercritical is significantly larger during the second type of quasi-steady-state regime. This is confirmed by comparison of the values of the Froude number at section 3 in Tables 6.3 and 6.4. While during the second quasi-steady-state regime, $Fr_{3b}>1$ in all the simulations, the flow transitioned back to subcritical ($Fr_3<1$) at section 3 in most of the simulations during the first quasi-steady regime.

Assuming that upstream of the obstacle, the mean flow velocity close to the interface is very small, then, similar to the case of constant density flow over a weir, the discharge is mainly function of the difference between the elevation of the interface away from the crest and the elevation of the crest, d_{I1b}-D. As in all the constant-flux current simulations, $q_g=q_d$=constant (=0.185), one expects d_{I1b}-D to be also constant. Results in Table 6.4 confirm this (d_{I1b}-$D=0.39h_0$). As already mentioned, the elevation of the interface decreases as the crest is approached (e.g., by about $0.07h_0$ for $D=0.68h_0$ and by about $0.09h_0$ for $D=1.37h_0$). As d_{I1b}-D and d_{db} are close to independent of the size of the obstacle, and the discharge passing the obstacles is the same, the values of the mean velocity inside the layer of heavier fluid at the location of the crest, u_{db}, are also expected to be close. Results in Table 6.4 confirm that u_{db}~0.6 in both simulations. The effect of the height of the obstacle is larger on the speed and height of the tail of the downstream current. As the height of the obstacle increases, the flow at the bottom of the downstream face of the obstacle acquires a larger velocity. Thus, the velocity in the tail of the downstream current, after steady state conditions are reached at a certain streamwise location, is expected to increase with increasing height of the obstacle. As the discharge is constant, the height of the tail should decrease proportionally. For example, results in Table 6.3 show that an increase on the height of the obstacle from $D=0,68h_0$ to $D=0.137h_0$ results in a 30% increase of the tail velocity, from $0.63u_b$ to $0.90u_b$ at section 3 situated at $x=21h_0$.

The effect of increasing the Reynolds number from Re=7,141 to Re=250,000 is a slight increase of the height of the lower layer at the crest, from $0.32h_0$ to $0.34h_0$, and a reduction of the height of the tail of the downstream current (e.g., from $0.29h_0$ to $0.24h_0$ at section 3). Interestingly, d_{l1b}-D does not change as a result of the increase in the Reynolds number.

6.5 Validation and comparison with predictions given by theoretical models

Besides comparing the evolution of the current in numerical simulations with the one observed in the experiments conducted by Lane-Serff et al. (1995), the LES predictions of the main flow parameters are compared to those given by the theoretical models of Lane-Serff et al. (1995), Oehy and Schleiss (2007), and Gonzales-Juez and Meiburg (2009). These models are based on shallow flow theory, assume inviscid Boussinesq flow, neglect mixing between the lower and upper layers, and apply for the partially-blocked cases.

The evolution of the current in two of the lock-exchange simulations (D-LE-D034a and D-LE-D034b) is compared with the one observed in the experiments conducted by Lane Serff et al. (1995) for equivalent flow and geometrical conditions. Figures 6.5 and 6.6 compare the concentration fields predicted by LES with the ones obtained from video-recordings performed during the experiments. In these figures the comparison is shown at the times when frames were available from the experiment. The time interval between successive frames was not always the same. The fixed barrier was not present in the computational domain used to perform the LES simulations. The effect of not including the fixed barrier is not clear but it may explain some of the differences observed between simulation and experiment.

In both experiments, the height of the lock-gate opening was $h=h_o=0.048$ m and that of the obstacle was $D=0.34h_0$. The main difference was the height of the channel H ($1.042h_0$ vs. $5.354h_0$). The conditions in case D-LE-D034b were close to the ones corresponding to a current advancing in a deep environment. The non-dimensional density difference between the lock fluid and the ambient fluid $\Delta\rho/\rho_o$ was 6.1% in the D-LE-D034a case and 4.7% in the D-LE-D034b case. These values are within the range in which the Boussinesq approximation is valid. The values of the buoyancy velocity, $u_b = \sqrt{g' h_o}$, and of the time scale, $t_o = h_o / u_b$ were 0.169 m/s and 0.284 s in the D-LE-D034a case, and 0.149 m/s and 0.322 s in the D-LE-D034b case.

In both experiments the gravity current fluxes were estimated by multiplying the speed of advance of the gravity current, u_f, by the height of the tail of the current behind the raised head, d_0. In the simulations, the front speed was replaced by the mean velocity in the tail of the current behind the raised head, u_0, measured at the location where the height of the tail is d_0. This velocity (Table 6.2) is generally 6-10% higher than u_f. In both test case, the gravity current is partially reflected and an internal bore traveling upstream is observed. In the experiments, the reflected flux was estimated by multiplying the speed of the reflected jump, u_{b1}, by the difference in the depths of the gravity current downstream and upstream of the jump, (d_{l1}-d_0).

Similar to the experimental results, the height of the head of the incoming current before reaching the obstacle is very close to that of the tail region in case D-LE-D034a. Meanwhile, in case D-LE-D034b, the head is raised and its height is noticeable higher than that of the tail. Compared to the experiment, in both cases the interfacial billows shed at the back of the head maintain their coherence for a longer distance behind the head and induce larger disturbances of the interface. In both simulations, the head decelerates as it reaches the obstacle and starts moving upwards. Due to the relatively low angle of the upstream face of the obstacle with the channel bottom ($\alpha=32^0$), and the initial splash that forms when a gravity current interacts with an obstacle of high bluntness is relatively small. The flow becomes critical some distance downstream of the crest of the obstacle. The front accelerates as it is convected over the downstream face of the obstacle. After it reaches the flat bottom of the channel, downstream of the obstacle, the front speed starts decreasing until it reaches a constant value, v_f. The effect of the obstacle is to induce more mixing in the downstream current at the interface with the layer of ambient fluid (the sizes of the light gray areas behind the head are much larger in both experiment and simulation after the current passes the obstacle compared to before the current reaches the obstacle). Also, the presence of the obstacle induces a decrease of the concentration in the head region of the downstream current due to the mixing with the ambient fluid, in particular with some of the ambient fluid trapped beneath the nose of the current after it passes the crest of the obstacle. The amount of mixing is function of the height of the obstacle relative to that of the incoming current, the streamwise momentum of the incoming current when it reaches the obstacle and the degree of bluntness of the obstacle.

The agreement between the front position in the simulation and experiment is excellent in case D-LE-D034a both before and after the current passes the obstacle. The only difference is that the height of the tail region containing high-density fluid behind the downstream current is smaller in the simulation. This is also why in the simulation the head height of the downstream current is larger than the tail height. By comparison, the heights of head and tail are very close in the experiment.

As shown by the comparison of Figures 6.7f to 6.7h, in case D-LE-D034b, the simulation predicts a faster front velocity for the downstream gravity current. However, good qualitative agreement is observed for the shape of the raised head and of the tail region after the current overtakes the obstacle. In particular, the thickness of the layer of high concentration fluid within the tail increases between the obstacle and the back of the head. In case D-LE-D034b, the incoming current has enough streamwise momentum such that the core of higher concentration fluid is convected past the crest of the obstacle at a certain distance above the downstream face of the obstacle. As a result, lower ambient fluid being is trapped in between the core of higher density fluid moving over the obstacle and the downstream face of the obstacle (see Figure 6.7e). By contrast, in case D-LE-D034a, the core of high-density fluid does not have enough momentum to detach from the surface of the obstacle (see Figure 6.6e).

Some qualitative differences are observed between the internal hydraulic jumps in the two cases. In both simulation and experiment, no waves can be observed behind the reflected hydraulic jump in case D-LE-D034a. The change in the height of the lower layer around the location of the jump is very smooth. This suggests the hydraulic jump is not sharp. The conditions in the D-LE-D034a simulation were the closest to the ones for which the theoretical model of Lane-Serff et al. (1995) would predict a combination of bore and rarefaction (see Figure 5.5). The positions of the jump in experiment and simulation are in very good agreement even at large times after the jump has formed. The position of the jump is taken to be the point where the lower layer depth is halfway between its extreme values on the two sides of the jump.

In the D-LE-D034b simulation, the shape of the jump was closer to that of a classical undular bore. For example, two waves are observed at $t=29t_0$ in Figure 6.7h. The presence of the second wave is clearer in the concentration field obtained from LES. An undular bore was also observed to form in all the other simulations discussed in this chapter. The ratio of the depth of the lower layer downstream of the jump to the depth of the lower layer upstream of the jump, d_{11}/d_0, was between 1.6 and 2.2 in all these simulations. Wood and Simpson (1984) found that undular bores occur when $d_{11}/d_0<2.5$. Despite the differences in the front position observed between simulation and experiment, a much better agreement is observed for the bore position.

Next, the values of the main flow parameters describing the interaction of the gravity current with the obstacle inferred from LES are compared with the ones predicted by theoretical models.

The model of Lane Serff et al. (1995) considers the case in which there is a small return flow in the upper layer of ambient fluid. This is generally the case of lock-exchange gravity currents. The model assumes that the flow is controlled at the section cutting through the crest of the obstacle, where the composite Froude number, calculated using the Froude numbers in the upper and lower layers, is equal to one. Additionally, LES results are compared with another model based on the shallow-water equations. The model is summarized in Oehy (2003) and Oehy and Schleiss (2007). The model assumes the flow in the upper layer of ambient fluid is stagnant and the flow over the crest of the obstacle is critical. This model is expected to give more accurate predictions for cases with a constant-flux gravity current. All these models assume the density currents are conservative and neglect the entrainment between the two layers.

The model proposed by Lane Serff et al. (1995) predicts the proportion of the incoming flux of heavier lock fluid that passes the obstacle, $u_d d_d / u_0 d_0$, the ratio between the velocity of the reflected hydraulic jump and the mean velocity inside the tail the gravity current before it starts interacting with the obstacle, u_{b1}/u_0, and the ratio of the height of the gravity current behind the jump to the height of to the tail in the undisturbed region, d_{l1}/d_0 (see Figures 6.1 and 6.2). The model assumes the reflected flow is a simple sharp jump despite the fact that in the experiments a combination of jump and rarefaction is sometimes observed.

Lane-Serff et al. (1995) proposed an empirical equation to estimate the ratio $z = H/d_o$ between the total channel depth and the undisturbed height of the tail:

$$z = (1.77 \pm 0.05)(H/h)^{(1.26\pm0.06)} \tag{6.3}$$

Based on the value of z obtained from equation 6.3, Lane-Serff et al. (1995) estimated the Froude number of the incoming gravity current as:

$$Fr_{0f} = u_f/\sqrt{g'd_0} = (0.56 \pm 0.02)z^{(0.22\pm0.04)} \tag{6.4}$$

where u_f rather than u_0 was used to estimate Fr_{0f} from experiments. This is because in the experiments u_0 cannot be measured accurately in a simple way.

The LES predictions of z and Fr_{0f} are compared with the empirical predictions given by equations 6.3 and 6.4 in Table 6.5 and Figure 6.9. The flow variables are estimated during the time period the first quasi-steady regime is observed. This is why case D-CF-D137 is excluded from the comparison. Additionally, Figure 6.9 shows that the agreement for the Froude number of the incoming current improves noticeably if u_f rather than u_0 is used to define Fr_0 in the tail region. With the exception of case D-LE-D034a, for which the values of Fr_{0f} and z predicted by the simulation are larger and respectively lower than the values predicted by the theoretical model of Lane-Serff et al. (1995), the values of Fr_{0f} and z predicted by LES are within the range predicted by theory. The disagreement observed for case D-LE-D034a is due to the fact that theory predicts a much larger value of d_0 compared to LES.

Figure 6.8 is used to infer the predicted values of $u_d d_d / u_f d_0$, u_{b1} / u_f and d_{l1} / d_0 using the model of Lane-Serff et al. (1995) for the test cases considered in the numerical study. One should also point out that the predictions of the model of Lane Serff et al. (1995) are reliable only for z<14. This is because Equation (6.3) predicts infinite values of z and Fr_0 for h going to zero. Four of the test cases have values of z very close to the threshold value (Table 6.5).

Based on the better agreement between LES and theory observed for the Froude number when u_f rather than u_0 is used to define it, u_f was also used to obtain the non-dimensional bore velocity in Table 6.5. Despite the relatively poor agreement obtained for Fr_{0f} and z, the LES and model predictions of u_{b1}/u_f and d_{l1}/d_0 in case D-LE-D034a are in excellent agreement (2-3% difference). In fact, the maximum difference between the values predicted by LES and theory for these two quantities is less than 10%, which can be considered good agreement. Though the predictions of u_{b1} are in overall good agreement with LES, one should point out that the theoretical model predictions are based on the assumption of a sharp jump, which is not the case in both experiments and simulations. Larger differences (up to 18%) are observed for the predictions of the incoming flux that continues over the obstacle. However, the percentage errors tend to be high for cases with small values of $u_d d_d / u_f d_0$. Compared to LES simulations, the model of Lane-Serff et al. (1995) systematically underpredicts $u_d d_d / u_f d_0$ and overpredicts d_{l1}/d_0.

The model described in Oehy (2003) uses the conservation of mass and momentum at the jump, written in a reference frame moving with the jump velocity, u_{b1}, that is assumed constant.

$$(u_0 - u_{b1}) d_0 = (u_{l1} - u_{b1}) d_{l1} \tag{6.5}$$

$$(u_0 - u_{b1})^2 = \frac{1}{2}(g' d_0) \frac{d_{l1}}{d_0}\left(1 + \frac{d_{l1}}{d_0}\right) \tag{6.6}$$

The flow over the crest of the obstacle is assumed to be critical and steady, such that

$$u_d = \sqrt{g' d_d} \tag{6.7}$$

Additionally, the model assumes the free surface between the jump and the crest of the obstacle is flat, such that $d_d = d_{l1} - D$. The results in Table 6.2 allow estimating the error of making these assumptions for the different cases. As already discussed, during SS1 the assumption that $d_d = d_{l1} - D$ is consistent with LES results, while that of critical flow over the crest of the obstacle is more questionable.

Continuity between a section situated in between the jump and the obstacle and the section cutting through the crest of the obstacle provides an additional equation:

$$u_{l1} d_{l1} = u_d d_d \tag{6.8}$$

Assuming, the flow of heavier fluid is partially-blocked by the obstacle ($d_{l1} > D$), the previous four equations can be combined to get d_{l1} / d_0 and u_{b1} function of Fr_0 and D/h_0. Once u_{b1} is known, one can calculate the proportion of the incoming current that continues over the obstacle as

$$q_d = \frac{u_d d_d}{u_0 d_0} = \frac{\sqrt{g' d_d}\, d_d}{u_0 d_0} = \frac{\sqrt{g'(d_{l1} - D)^3}}{u_0 d_0} \tag{6.9}$$

The variation of d_{l1} / d_0 and $q_d = \eta = (u_d d_d)/(u_0 d_0)$ function of Fr_0 and D/h_0 are shown in graphical form in Figures 6.10a and 6.10b, respectively. These figures are taken from Oehy (2003). The values of q_d and d_{l1} / d_0 predicted by LES are compared in Tables 6.6 and 6.7 with the predictions given by the model of Oehy (2003) and Lane-Serff et al. (1995). For consistency, u_f rather than u_0 was used to calculate q_d.

The predictions of d_{l1} / d_0 and q_d by the model of Oehy (2003) show somewhat better agreement with LES, especially for the constant-flux gravity current cases. The level of agreement with LES shown by the two theoretical models is similar for the lock-exchange cases. One interesting observation is that, compared to LES, the model of Oehy (2003) consistently underpredicts d_{l1} / d_0, while the model of Lane-Serff et al. (1995) consistently overpredits the same variable.

The model of Gonzales-Juez and Meiburg (2009) predicts the non-dimensional velocity, $v_f / \sqrt{g' d_0}$, and height, d_f/d_0, of the downstream gravity current for partially-blocked cases. Similar to the model of Oehy (2003), the model of Gonzales-Juez and Meiburg (2009) neglects the horizontal velocities in the upper layer, assumes the ambient fluid is very deep (H/h>>1), and assumes critical flow at the obstacle position. The original model assumes the volume flux per unit width, *ud*, is constant and the velocity of the current can be calculated as $u = C(g'ud)^{1/3}$, where C=$2^{1/3}$ based on inviscid theory. For the purpose of comparing with experiments or simulations, u_0 is set equal to the front speed u_f. Gonzales-Juez and Meiburg (2009) found that the original model overpredicted $v_f / \sqrt{g'd_0}$ by about 40% and underpredicted d_f/d_0 by about 30%. The value of the constant C in the model of Gonzales-Juez and Meiburg (2009) was later calibrated (C=0.92) based on results obtained for square cylinders mounted on a no-slip bottom surface. The calibrated value mainly accounts for the effect of bottom friction on the propagation speed of the current.

The results of the present LES simulations are compared in Figure 6.11 with the original model of Gonzales-Juez and Meiburg (2009). The present test cases extend the range of flow conditions for which the model of Gonzales-Juez and Meiburg (2009) was originally tested. This is because the present study considers obstacles of different shape (triangular vs. rectangular) and especially obstacles with a lower degree of bluntness. The Reynolds numbers are also significantly higher compared to the ones in the 2D simulations performed by Gonzales-Juez and Meiburg (2009). Triangular obstacles with a low angle α (Figure 6.1) have a much lower degree of bluntness compared to rectangular obstacles or with triangular obstacles with large values of α. The theoretical model consistently overpredicts the flux of heavier flow within the downstream current $v_f d_f / \sqrt{g'd_0^3}$. The errors are of the order of 20% for the two simulations with D=0.34h_0, for which α has the smaller value ($\alpha=32^0$). For a given obstacle height, the proportion of the incoming flux that continues over the obstacle is expected to be larger for obstacles with a lower degree of bluntness. For these cases, one does not expect necessarily Fr~1 at the crest of the obstacle, which is assumed in the model of Gonzales-Juez and Meiburg (2009). The model predictions of $v_f d_f / \sqrt{g'd_0^3}$ are closer to LES for cases with a larger degree of bluntness of the obstacle.

Comparison with present LES results show that for obstacles of small height and reduced degree of bluntness, the velocity of the downstream current is overpredicted by the theoretical model by 10-20% and the current depth is underpredicted, when no effort is made to calibrate the model constant C. However, the opposite is true for the case of higher obstacles with a larger degree of bluntness, including for the simulation with Re=250,000 where the front velocity is relatively close to the inviscid limit. In particular, the LES predictions of $v_f / \sqrt{g' d_0}$ are in excellent agreement with the theoretical model for case D-LE-D068. Thus, trying to calibrate C may not result in better overall predictions by the model for a wide range of flow and geometrical parameters. One problem may be that when the front velocity is estimated using $u = C(g' ud)^{1/3}$, one does not take into account the reduction of the front velocity as a result of the mixing occurring at the head of the current as it overtakes the obstacle. The amount of mixing is function of the relative height of the obstacle and the degree of bluntness of the obstacle.

A simple approach can be proposed to estimate the main flow parameters during the second quasi-steady state. In this case there is no bore (the flow disturbances have dissipated after successive reflections) and the proportion of the incoming flux that continues over the obstacle is always equal to one. Assuming the flow is critical at the location of the crest, which is fully justified based on the LES results (Table 6.4), one obtains

$$u_{db} d_{db} = u_0 d_0 \tag{6.10}$$

$$u_{db}^2 = g' d_{db} \tag{6.11}$$

Solving eqns. 6.10 and 6.11, one obtains

$$d_{db} / h_0 = ((u_0 d_0)/(u_b h_0))^{2/3} = q_0^{2/3} = q_{db}^{2/3} \tag{6.12}$$

As in all the three simulations for which the second quasi-steady state regime was reached q_{db}=0.185, the predicted value of d_{db} / h_0 is 0.32, which is in very good agreement with the values predicted by LES in the three cases (0.3-0.34). The other important parameter to estimate is the height of the lower layer away from the obstacle, d_{l1}. A first approximation is to assume that d_{l1b}=D+d_{db}. This was shown to be a reasonable assumption during the first quasi-steady regime. However, results in Table 6.4 show that during the second quasi-steady regime the elevation of the interface decays as the crest is approached. One can assume that Bernoulli applies between the section where d=d$_{l1b}$ and the crest, in which case:

$$d_{l1b}u_{l1b} = d_{db}u_{db} = q_{db}(u_b h_0) \tag{6.13}$$

$$d_{l1b} + u_{l1b}^2 / 2g' = D + d_{db} + u_{db}^2 / 2g' \tag{6.14}$$

This system of two equations has two positive solutions and one negative solution. The positive solution for which the flow is subcritical is the correct one. If $d_{l1b} >> d_{db}$, then $d_{l1b} / h_0 \sim D / h0 + d_{db} / h_0 + (u_{db} / u_b)^2 / 2$. Both the approximate and exact values of d_{l1b} / h_0 are slightly larger than the ones predicted by LES. For example, the approximate solution gives $(d_{l1b} - D) / h_0 \sim d_{db} / h_0 + (u_{db} / u_b)^2 / 2 = 0.487$, while all the three simulations predict $(d_{l1b} - D) / h_0 = 0.39$. The improvement shown by the exact solution ($(d_{l1b} - D) / h_0 = 0.39 - 0.41$) is relatively minor for all the three cases. The main reason for the disagreement (~20%) is the fact that the velocity at the interface, away from the obstacle, is larger than the mean velocity in the section.

6.6 Analysis of the temporal changes in the structure of the gravity current as a result of its interaction with the obstacle

Figures 6.12 and 6.13 show the distributions of the concentration, C, out-of-plane vorticity, $\omega_z(h_0/u_b)$ and local dissipation rate $\varepsilon / (u_b^3 \cdot h_0^2)$ at representative times before and after the gravity current reaches the obstacle in the D-CF-D068 and D-CF-D068-HR simulations. Figure 6.14 shows similar information for case D-CF-D137 until the second quasi-steady state regime is reached. The focus is on the changes in the flow structure during the impact stage and at later times, after the formation of the downstream current and of the undular bore. Of particular interest are the effects of the waves associated with the undular bore on the distributions of vorticity and dissipation within the flow, and the structure of the flow in between the crest of the obstacle and the back of the head of the downstream current. Finally, Figures 6.15 and 6.16 show the streamwise distributions of the spanwise and vertically integrated local dissipation rate ε[23] at some of the time instances at which ε is shown in Figures 6.12 to 6.14.

Figure 6.12a shows the upstream gravity current before it starts interacting with the obstacle. With the exception of the head and dissipative wake region, most of the vorticity and dissipation is concentrated in the thin interfacial shear layer and the bottom boundary layer. As expected, the vorticity and dissipation are strongly amplified in the region where interfacial billows are present.

Figure 6.12b shows the gravity current during the impact stage. The height and degree of bluntness of the obstacle are large enough to induce the formation of a significant splash of heavier fluid. The splash was convected past the crest of the obstacle but did not yet reattach on the downstream face of the obstacle. Due to the impact with the obstacle, the fluid within the splash has very little streamwise momentum. Moreover, the strongly turbulent eddies generated by the impact increase significantly the mixing between the splashed fluid and the surrounding ambient fluid. As the heavier fluid within the splash plunges downwards, it traps a significant amount of the ambient fluid situated beneath it (Figure 6.12b). These phenomena induce a significant decay of the concentration inside the head of the downstream current compared to that inside the head of the upstream current (e.g., see Figure 6.12c). In Figure 6.12b, the first wave, B1, of the undular bore has formed and is still accelerating as it moves away from the obstacle. Observe the strong amplification of the vorticity and dissipation both within the splash of heavier fluid and in between B1, that in the initial stages resembles more a sharp bore, and the downstream face of the obstacle. This amplification of the turbulence within the splashed fluid is observed not only near the interface with the ambient fluid and the solid boundaries but over the whole height of the lower layer.

In Figure 6.12c the undular bore contains two waves, B1 and B2, and the downstream current has formed. The lower layer is very thin over the downstream face of the obstacle. A very small recirculation region forms near the crest, but the flow remains attached over most of the downstream face of the obstacle. The height of the head of the downstream current is much larger than that of the tail region behind it. It is also larger than the height of the upstream current. Meanwhile, the average density within the head of the downstream current is much smaller that than the one in the head of the upstream current. Here the height of the head is defined as the height of the region containing mixed fluid rather than the equivalent height of unmixed lock fluid at that location. It roughly corresponds to the position of the shear layer forming in between the region containing mixed fluid and the surrounding ambient fluid.

The formation of the undular jump has important consequences for the structure of the flow upstream of the obstacle. In contrast to Figure 6.12b, the vorticity and dissipation levels are relatively small close to the upstream face of the obstacle. This is because most of the amplification of the turbulence at that location is due to the formation of the jump. In Figure 6.12c, the region of high vorticity and high dissipation has separated from the obstacle. This region occupies only the deeper part of the lower layer. The correspondence between the two waves and the region of high turbulence amplification is evident. It also confirms the dissipative nature of the flow created by the undular bore. The formation of strongly turbulent eddies beneath the undular jump induces ejections of eddies from the bottom boundary layer and flow separation. These strong eddies can also locally induce sediment entrainment when they pass very close to the channel bottom.

Despite the presence of strong eddies close to the interface with the ambient fluid, unmixed lock fluid is still present very close to the downstream face of the obstacle once the interface between the two layers, upstream of the obstacle, becomes stable. This happens once the first quasi-steady state regime is approached in the region around the obstacle (e.g., see Figure 6.12d). The impact of the high-speed heavier fluid propagating over the downstream face with the channel bottom results in an additional amplification of the turbulence around the impact region. Due to the very small height of the lower layer past the crest of the obstacle, the instabilities propagating over the interface with the ambient fluid can, at times, penetrate until very close to the bottom surface. As a result of the mixing, the height of the lower layer increases monotonically with the distance from the obstacle, while the mean concentration decays. Meanwhile, a strong vorticity sheet, within which the dissipation is also very high, forms at the interface between the two layers, in between the end of the obstacle ($x/h_0=16.45$) and the start of the dissipative wake of the downstream current. The strength of the vorticity sheet decreases as the dissipative wake region in approached. No unmixed lock fluid is observed past $x/h_0=20$, after the first quasi-steady regime is reached around the obstacle (Figures 6.12d) and before the transition to the second type of steady state regime does not start.

The distributions of the dissipation and vorticity in Figure 6.12d show that regions of high turbulence amplification can form as a result of the interaction between an incoming wave of the undular bore and the lock-gate or when a reflected wave interacts with an incoming wave. However, in most practical applications, the gravity current forms very far from the obstacle. Thus, one does not expect reflections of the upstream propagating waves to occur for a relatively long time. The disturbances propagating at the interface are strongly damped in time, as they reflect back and forth between the lock-gate and the obstacle. Once the flow transitions toward the second type of quasi-steady regime, the interface becomes close to horizontal. With the exception of the shear layers forming on the two sides of the incoming gravity current, close to the lock-gate position, the turbulence remains low in between the lock gate and the obstacle.

Finally, Figure 6.12e shows the flow structure during the second quasi-steady state ($t=80t_0$). The dissipation levels upstream of the obstacle are very small. Similar to the case when a gravity current passes an obstacle of lower height, a strong shear layer forms at the interface between the layer of heavier fluid and the ambient fluid. This shear layer extends for some distance upstream of the crest of the obstacle (see Figures 6.12e and 6.13f).

The flux of the heavier fluid over the obstacle is much larger than the one recorded during the first quasi steady state. Also, the elevation of the interface has increased in the region situated in between the lock gate and the obstacle. As a result, the velocity and depth of the lower layer over the downstream face of the obstacle and over some distance downstream of the region where the plunging flow of heavier fluid reaches the channel bed (e.g., compare Figures 6.12d and 6.12e). Comparison of the distributions of the local dissipation rate in Figures 6.12d and 6.12e and of ε^{23} in Figures 6.15d and 6.15e show that the turbulence intensity and dissipation in these regions are much during larger SS2 (e.g., by as much as 3-4 times larger for the dissipation based on the values of ε^{23}). In contrast to Figure 6.12d, the lower layer propagating over the downstream face of the obstacle contains mostly unmixed lock fluid. The mixing and dissipation increase strongly in the region where the plunging current of heavier fluid reaches the bed. Then, the mixing inside the lower layer increases gradually in the streamwise direction and the dissipation starts decaying. At a certain distance from the obstacle, the height of the lower layer becomes close to constant.

Comparison of Figures 6.13 and 6.12 allow quantifying Reynolds-number-induced scale effects. The Reynolds number in the D-CF-D068-HR simulation is sufficiently high (Re=250,000) such that no important qualitative changes are expected to occur for test cases conducted at even higher Reynolds number. The interaction between the incoming current and the obstacle, the dynamics of the splashed fluid, and the formation and evolution of the downstream current in the two simulations are qualitatively and, in many respects, quantitatively similar. For example, the maximum height of the splash is about two times the obstacle height in both simulations. The front velocities of the downstream current are also relatively close.

One difference is the eddy content in the regions where the turbulence is high. As expected, as the Reynolds number increases, the average size of the energetic eddies decreases. For example, in the low Reynolds number case, most of the large-scale eddies behind the head correspond to the large-scale interfacial billows. The region in between the interface and the channel bottom is depleted of large-scale eddies. In the high-Reynolds number case, the average size of these eddies is much smaller but eddies occupy the whole region in between the channel bottom and the interface with the upper layer of ambient fluid. This means the vertical mixing is much stronger in the high Reynolds number case. This is confirmed by comparison of the concentration distributions in the lower layer, in between the crest of the obstacle and the front of the downstream current. Comparison of Figures 6.12d and 6.13d-e shows that, past the middle of the downstream face, no unmixed lock fluid is present near the dam surface. By contrast, unmixed lock fluid is still present in the low Reynolds number simulation for about $2h_0$ past the end of the downstream face of the dam. In fact, Figures 6.13d-e show that the concentration distribution within the lower layer, in between the crest of the obstacle and the start of the dissipative wake of the downstream current, is characterized by a much higher degree of uniformity in the vertical direction. This is because the turbulent eddies are relatively uniformly distributed over the whole height of the lower layer in this region. Finally, the distributions of the local dissipation rate in Figures 6.13d and 6.13e show that a significant amount of dissipation occurs with the layer of ambient fluid behind the dissipative wake region of the downstream current. This is important, as theoretical models generally assume all the dissipation takes place in the lower layer.

Finally, comparison of Figures 6.13f and 6.12d shows that the decay of the dissipation in the streamwise direction in the region situated downstream of the obstacle is milder in the high Reynolds number simulation. The smaller size and more uniform distribution of the turbulent eddies within the lower layer in the high Reynolds number simulation results in a stronger vertical mixing. However, in both simulations the height of the lower layer becomes close to constant for $x/h_0>21$ and most of the dissipation takes place in the lower layer. The height of the lower layer is about 20% less in the high Reynolds number simulation in the region where the height is close to constant.

Before the transition to the second steady-state regime starts, most of the important scale effects are observed in the region situated upstream of the obstacle. In the low Reynolds number case, the thickness of the attached boundary layer is comparable, though smaller, to that of the sheet of vorticity forming at the interface with the layer of ambient fluid. By contrast, in the high Reynolds number case the thickness of the attached boundary layer is so small that the layer of negative vorticity at the channel bottom is hardly observable in Figure 6.13, while the thickness of the layer of high positive vorticity associated with the interface has grown significantly.

Similar to the low Reynolds number case, an undular bore is observed. The passage of the waves induces a large amplification of the vorticity and dissipation over most of the thickness of the lower layer around the position of the crest of the wave. The amplification is the largest in the region close to the channel bed. This high amplification of the turbulence in the near-bed region is expected to significantly contribute to the local entrainment of sediment. The most important scale effect is related to the large increase of the amplitude of the waves associated with the undular bore. As the Reynolds number is increased, these waves transport more energy and are more stable. This is also the reason why their effect on the turbulence in the near-bed region is, relatively speaking, larger. Results in Figure 6.13 show that the amplitude of the waves increases with the distance from the obstacle. However, the turbulence intensity in the near-bed region situated beneath each wave decays as the distance from the obstacle increases. Thus, low Reynolds number simulations are expected to substantially underestimate the effect of the undular bore on the flow and turbulence upstream of the obstacle.

Comparison of the distributions of ε^{23} between the low and high Reynolds number simulations with obstacles of height $D=0.68h_0$ allows a more quantitative assessment of the effect of the Reynolds number on the spatial and temporal variation of the dissipation within the flow. Simulations of turbulent gravity currents ($Re>10,000$) propagating over a flat bed have shown that as the Reynolds number is increased, the dissipation remains comparable in the head and dissipative wake, but decays significantly in the tail of the current. The distributions of ε^{23} are consistent with this observation. The larger values of ε^{23} around $x/h_0=12.5$ in the lower Reynolds number simulation are due to the presence of a strongly coherent billow.

Following the formation of the splash and the formation of the first wave of the bore, B1, the dissipation is high in between the front of the bore and the front of the current (e.g., see Figure 6.13b). Figure 6.15b show that the values of ε^{23} over this region are comparable and scale effects are not significant. As the bore B1 gets away from the upstream face of the obstacle, the values of ε^{23} decay by about 100%. On the other hand, as shown in Figure 6.15c, ε^{23} increases sharply in the region where the splashed fluid convected over the crest reaches the channel bottom and the head of the downstream current starts forming. Once the wave B1 has separated from the obstacle, the values of ε^{23} decay very little as the wave moves upstream (compare levels of ε^{23} around the position of B1 at $t=20t_0$ and $t=28t_0$ in the high Reynolds number simulation). For both Reynolds numbers, the second wave B2 is less dissipative than the first wave B1 (e.g., see Figure 6.15d), but the decay is larger in the higher Reynolds number simulation. Finally, Figure 6.15d shows that the distributions of ε^{23} are similar over the region occupied by the downstream current in the high and the low Reynolds number simulations.

The changes in the flow structure during and after the impact of the incoming current with the upstream face of the obstacle are qualitatively similar in the case the flow is fully blocked or partially blocked, as observed from comparison of cases D-CF-D068 and D-CF-D137 in Figures 6.12 and 6.14. The only difference is that in case D-CF-D137, in which the height of the obstacle is three times larger than that of the incoming current, only a negligible amount of heavier fluid is convected past the obstacle until the volume of lock fluid in between the lock gate and the obstacle is not large enough for the interface to raise above the crest of the obstacle. The maximum height reached by the initial splash (about 3.3 times that of the incoming current) is only slightly higher than that of the obstacle. This is different from the case of an obstacle with a higher degree of bluntness (e.g., obstacle with a vertical upstream face), where the maximum height of the initial splash of heavier fluid can be 4-5 times that of the incoming current. Once the initial splash passes the crest of the obstacle, if forms a small gravity current that accelerates as it propagates over the inclined downstream face of the obstacle. Figures 6.14c and 6.14e visualize the gravity current generated by the first and the second splash at about the time the current reaches the channel bottom. Most of the vorticity and dissipation is concentrated in the head and dissipative wake regions.

Once the interface starts raising above the crest of the obstacle, the transition to the (second) quasi-steady regime starts ($t>45t_0$) and a continuous flow of heavier fluid is observed over the downstream face of the obstacle (e.g, see Figure 6.14f). Except close to the crest, the flow remains attached over most of the downstream face of the obstacle. Interestingly, though most of the larger-scale vortical eddies are situated inside the head and dissipative wake of the current forming due to the convection of a finite splash of heavier fluid, the region of high dissipation extends for some distance behind the dissipative wake region, into the layer of ambient fluid. Thus, a significant part of the dissipation induced by the propagation of these small gravity currents occurs in the top layer. This is similar to what is observed in the D-CD-D068-HR simulation (Figures 6.13d and 6.13e).

If one makes abstraction of the splashed fluid convected over the crest in case D-CF-D068, the structure of the flow in between the lock gate and the upstream face of the obstacle are very similar in Figures 6.12b and 6.14b. In both cases a region of high dissipation (see also Figure 6.16b) and vorticity is observed in the vicinity of the channel bottom, around the position of B1. The near-bed regions of high vorticity and dissipation move away from the obstacle together with the traveling waves (Figures 6.12c with Figure 6.14d). As B1 moves away from the obstacle, the total dissipation induced by its passage decays (e.g., compare levels of ε^{23} in region with $13<x/h_0<14.9$ in Figure 6.16b and region with $9<x/h_0<11$ in Figure 6.16c). Also similar, the passage of the reflected wave and its interaction with one of the waves traveling upstream can result in a large amplification of the turbulence (e.g., compare ε^{23} in Figures 6.16d and 6.16c). However, after several reflections ($t>40t_0$, Figures 6.14e-g) the turbulence intensity and the dissipation are very small in the region situated upstream of the obstacle (e.g., see Figs 6.16e-h). This is also true for cases with a partially-blocked flow, once the second quasi-steady regime is reached (e.g., for case D-CF-D067).

In case D-CF-D137, the discharge and the height of the lower layer past the crest of the obstacle increase in a non-monotonic way until they become close to constant. The same is true for the dissipation rate past the crest of the obstacle (e.g., compare streamwise distribution of ε^{23} in Figures 6.16e-g for $x/h_0>15.9$). Once the quasi-steady regime is reached (e.g., see Figure 6.14g), the discharge in the lower layer past the obstacle oscillates around the inflow discharge. As the proportion of the incoming flux that continues over the obstacle is equal to one, the thickness of the lower layer during the second quasi-steady regime is larger than the one observed during the first quasi-steady regime (if it exists).

Similar to cases D-CF-D068 and D-CF-D068, the height of the lower layer increases slowly in the streamwise direction, past the end of the obstacle. Large-scale energetic eddies are present within the whole height of the lower layer. The turbulence intensity and the dissipation peak close to the junction line between the obstacle and the channel bed, where the high-speed fluid within the lower layer changes direction (see also Figures 6.16f and 6.16g). After the quasi-steady state regime is reached ($t>80t_0$), the distribution of ε^{23} is characterized by a rapid increase from the crest ($x/h_0=15.9$) until the end of the obstacle ($x/h_0=17.6$). Then, as the height of the lower layer increases, ε^{23} starts decreasing. The decrease of ε^{23} with x is close to logarithmic until $x/h_0\sim22$. Thus, during the second quasi-steady regime most of the dissipation takes place past the crest of the obstacle and includes the upstream part of the tail of the downstream gravity current. The length of the region characterized by a large turbulence intensity and large dissipation is expected to increase with the height of the obstacle and the discharge convected over the obstacle.

Figure 6.17 compares the 2-D distributions of the friction velocity u_τ/u_b at $t=28t_0$ in the low and high Reynolds number simulations conducted with an obstacle of height $D=0.68h_0$. At this time instant the flow around the obstacle is close to finish its transition to the first type of quasi-steady regime. Also shown are the distributions of the spanwise-averaged values of the bed friction velocity at the same time instant.

The spanwise resolution in the low Reynolds number simulation is large enough to accurately capture the near-bed streaks. Indeed, streaks form behind the head of the downstream current and extend over the whole tail of the current, until the recirculation bubble present close to the crest of the obstacle is approached. The streaky structure is also observed in the high Reynolds number simulation in which the decrease in the width of the streaks is limited by the grid resolution. As expected, the values of u_τ/u_b are smaller in the high Reynolds number simulation. However, the variation of u_τ/u_b past the crest of the obstacle in the two simulations is qualitatively similar. The bed friction velocity peaks at the crest of the obstacle. It then decays sharply beneath the small recirculation eddy. Downstream of this eddy u_τ/u_b increases sharply and reaches a close to constant value until close to the bottom of the downstream face of the obstacle, where the high-speed flow inside the thin lower layer of heavier fluid changes direction. The change in the direction occurs in a more gradual way in the high Reynolds number simulations, such that the values u_τ/u_b past the junction line between the obstacle and the channel bottom are smaller than those observed over the downstream face. In the low Reynolds number simulation u_τ/u_b decreases sharply downstream of the impact region. Then, in both simulations, u_τ/u_b decreases mildly until close to the front of the downstream current. This decrease is consistent with the thickening of the tail, which triggers a small decrease with x of the mean streamwise velocity. In the low Reynolds number simulation, u_τ/u_b increases slightly as the front is approached, which is generally observed for currents propagating over flat surfaces. This increase close to the front is not present in the high Reynolds number simulation.

Some important qualitative similarities are also observed in the distributions of u_τ/u_b upstream of the obstacle. The relationship between the values of u_τ/u_b and the flow structure is easier to infer in the high Reynolds number simulation. The spanwise distribution of u_τ/u_b in between the front of the undular bore (x/h_0~10.2 at $t=28t_0$) and the obstacle is characterized by small scale variations. This confirms the highly turbulent nature of the near bed flow behind the front of the undular bore. By contrast, the variation of u_τ/u_b in the spanwise direction is negligible in between the lock gate and the front of the bore. The passage of the bore induces flow separation in the near bed region. The near-bed flow is moving upstream beneath the first wave B1. This is why u_τ/u_b decays sharply at the location of the front of the bore. In the high Reynolds number simulation, u_τ/u_b decays mildly behind the crest of the first wave, B1. Behind the region associated with B1, the values of u_τ/u_b are close to constant despite the presence of a second wave B2. Though a region of strong turbulence amplification is also observed at the position of B2, this region does not penetrate until close to the channel bottom (see also Figure 6.13d).

In the low Reynolds number simulation, the values of u_τ/u_b are also the highest behind the extremity of the near-bed region containing highly turbulent heavier fluid that moves upstream together with the first wave, B1 (see Figure 6.12c). The near-bed flow advancing with B1 separates at x/h_0~11, slightly behind the front of the bore in the interface region, which is situated at x/h_0~10.5. The bed friction velocity decays over the region associated with the first wave, B1. The decay is much milder over the region associated with the second wave, B2. Behind the region associated with B2, the levels of u_τ/u_b are very small. The fact that the levels of u_τ/u_b around the position of B2 are significantly larger than the ones behind it is explained by the position of the region of high turbulence in Figure 6.12c. Though the turbulence intensity within the region associated with B2 is slightly lower than the one within the region associated with B1, both regions are penetrating up to the bed (this was not the case in the high Reynolds number simulation). Thus, both beneath B1 and B2 a patch of highly turbulent fluid is moving upstream. This patch induces relatively high bed friction velocity values.

Figure 6.18 compares the 2-D distributions of the friction velocity u_τ/u_b at $t=80t_0$ in the low Reynolds number simulations conducted with obstacles of height $D=0.68h_0$ and $D=1.37h_0$, respectively. The inlet discharges in the two simulations are identical. At this time instant, the second type of quasi-steady regime is observed. Also shown are the distributions of the spanwise-averaged values of the bed friction velocity at the same time instant.

As expected, the flow velocities are very small in the region situated in between the lock gate and the obstacle everywhere except very close to the opening through which the higher density fluid is entering the domain. Consistent with this, the bed friction velocity decays sharply away from the inlet section and then remains very low until the obstacle. Then, the bed friction velocity increases sharply as the flow accelerates over the upstream face of the obstacle. The bed friction velocity decays sharply beneath the small recirculation bubble that forms past the crest of the obstacle. After the flow within the lower layer reattaches, u_τ/u_b increases fast again. The distributions of u_τ/u_b in between the lock gate and the end of the obstacle are qualitatively similar in the two simulations. The main quantitative differences are the larger values of u_τ/u_b in the D-CF-D137 simulation on the upstream and downstream faces of the obstacles. They are due to the fact that the interface between the two layers is situated closer to the crest of the obstacle in the D-CF-D137 simulation. As the discharge in the two simulations is the same, the thickness of the lower layer of heavier fluid will be smaller and the mean velocity within the lower layer will be larger in the simulation with a higher obstacle.

After the high-speed higher density fluid within the lower layer changes direction at the end of the obstacle, the bed friction velocity starts decaying fairly rapidly in the simulation with a larger obstacle. This decay is mainly due to the gradual thickening of the lower layer, which reduces the mean velocity within the lower layer. A similar, but milder, decay is also observed in the D-CF-D068 simulation. The decay starts around $x/h_0=18$, some distance downstream of the end of the obstacle. The main reason for the milder decay of u_τ/u_b is the higher angle of the downstream face of the obstacle with the horizontal that induces large velocity gradients in the region where the high speed flow over the downstream face of the obstacle reaches the channel bottom. Finally, the lower height of the tail explains the slightly larger values of u_τ/u_b predicted beneath the upstream part of the tail of the downstream current in the D-CF-D137 simulation. The difference reduces with the distance from the obstacle because of the higher growth rate of the tail height in the D-CF-D137 simulation.

6.7 Drag force on the obstacle

Figure 6.19 compares the time evolutions of the non-dimensional drag force in the streamwise direction divided by the obstacle height, $\Delta P/(\rho u_b^2)=(F/D)/(\rho u_b^2)=(P^+-P^-)/(\rho u_b^2)$, where the normalized force component on the upstream face is denoted P^+ and the one on the downstream face is denoted P^-. One should mention that $\Delta P/(\rho u_b^2)$, $P^+/(\rho u_b^2)$ and $P^-/(\rho u_b^2)$ are calculated based on the values of the piezometric pressure $p=p''+\rho_0 gz-C$, that includes the hydrostatic component associated with the ambient fluid of density ρ_0. The LES code provides at each time step the piezometric pressure distribution, p, rather than the pressure, p''. At each time step, the constant C is determined such that $p''+\rho_0 gz-C=0$ inside the stagnant region containing ambient fluid. Thus, before the lock fluid is released, the flow is at rest and $P^+/(\rho u_b^2)=P^-/(\rho u_b^2)=0$. The LES results are used to estimate $P^+/(\rho u_b^2)$ and $P^-/(\rho u_b^2)$ by calculating the pressure force component in the streamwise direction induced by the predicted piezometric pressure distribution over the upstream and downstream faces of the obstacle. As shown by previous studies (e.g., Gonzales-Juez et al., 2009), at sufficiently high Reynolds numbers (Re>>1,000), the friction drag component is not significant.

Comparison of the time variations of $\Delta P/(\rho u_b^2)$ in Figures 6.19a-c between the time the incoming current approaches the obstacle and the time the first quasi-steady regime is reached, shows that the drag force peaks at the end of the impact stage. Then it reaches a relative minimum as the splashed fluid starts being convected past the crest of the obstacle, loses its momentum and plunges downwards toward the downstream face of the obstacle. It then increases again as the head of the downstream current forms and is convected away from the obstacle. In all the test cases considered in this chapter the height of the incoming current is comparable or lower than that of the obstacle ($d_0/D<1.2$). Qualitatively, this variation of $\Delta P/(\rho u_b^2)$ is similar to the one observed for gravity currents interacting with an obstacle of significantly lower height (e.g., see Figure 4.28 for Rib1, $d_0/D>2$). Then, depending on the flow conditions and the geometry of the obstacle (e.g., angle α), large-scale oscillations of smaller or higher amplitude are observed during the transition to the first quasi-steady regime when $\Delta P/(\rho u_b^2)$ becomes close to constant. This is essentially the scenario observed in the lock exchange simulations (e.g., see Figure 6.19a).

In the simulations conducted with a constant-flux current, due to the relatively short distance between the lock gate and the obstacle, the time interval over which the first quasi-state regime is observed is relatively small (e.g., $28<t/t_0<33$). As the first wave of the undular bore reflects at the lock gate, the elevation of the interface with the ambient current is disturbed and the transition to the second quasi-state regime starts. Strong non-linear interactions take place with the other waves that move upstream. When one of the reflected waves reaches the crest of the obstacle, the discharge over the obstacle and the elevation of the interface around the obstacle increase temporarily. This explains why first $\Delta P/(\rho u_b^2)$ increases due to an increase of the piezometric pressure on the upstream face of the obstacle and then decreases due both to an increase of the piezometric pressure on the downstream face of the obstacle and a decrease of the piezometric pressure on the upstream face of the obstacle. This is the mechanism responsible for the large-scale oscillations of $\Delta P/(\rho u_b^2)$ during the transition to the second quasi-steady regime. Comparison of Figures 6.19b and 6.19c shows that the amplitude of the large-scale oscillations is significantly higher during the transition to the second quasi-steady regime compared to the one observed during the transition to the first quasi-steady regime. In the simulation in which the fully-blocked regime is observed (D-LE-D137, see Figure 6.19d), most of the large-scale oscillations of $\Delta P/(\rho u_b^2)$ take place before the interface rises above the crest of the obstacle. At the time that happens, the disturbances traveling close to the interface are relatively weak. The amplitude of the large-scale oscillations during the transition to the second type of quasi-steady regime (Figure 6.19d) and the period of time corresponding to this transition are much smaller than the ones in the simulations in which the partially-blocked regime is observed (e.g., see Figure 6.19c).

The values of $\Delta P/(\rho u_b^2)$ during the two quasi-steady states increase with the height of the obstacle, the difference $(d_{l1}-D)/h_0$ between the height of the layer of heavier fluid upstream of the obstacle and the obstacle height, and the flux q_0 of the incoming current. The increase of $\Delta P/(\rho u_b^2)$ with the height of the obstacle and $(d_{l1}-D)/h_0$ is mainly due to the increase of the hydrostatic pressure at the center of mass of the upstream face of the obstacle (e.g., neglecting inertial effects and P^-, $\Delta P/(\rho u_b^2) \sim P^+/(\rho u_b^2) \sim (d_{l1}-D+D/2)D/(Dh_0) \sim (d_{l1}-D)/h_0+(D/2)/h_0$).

For example, in the simulations with $D=0.34h_0$, an increase of $(d_{l1}-D)/h_0$ from 0.25 (D-LE-D034a) to 0.32 (D-LE-D034b) resulted in an increase of $\Delta P/(\rho u_b^2)$ from 0.22 to 0.28. The increase of $\Delta P/(\rho u_b^2)$ from 0.35 in the constant-flux simulation with $D=0.68h_0$ to 0.41 in the lock-exchange simulation with $D=0.68h_0$ is mainly due to the slightly larger flux of the incoming current in the lock-exchange simulation ($q_0=0.21$ vs. 0.185).

The change in the value of $\Delta P/(\rho u_b^2)$ during SS2 is mainly related to the differences in the height of the obstacle, as both q_0 (=0.185) and $(d_{l1}-D)/h_0$ (=0.39) are close to identical in the constant-flux simulations with $D=0.68h_0$ and $D=0.134h_0$. The increase of $\Delta P/(\rho u_b^2)$ from 0.49 to 0.84 is consistent with the effect of the increase in the obstacle height ($(D/2)/h_0$ increases from 0.34 to 0.68). The difference of 0.07 between the values of $\Delta P/(\rho u_b^2)$ predicted during SS1 in the simulations with D=0.34h_0 (D-LE-D034b) and D=0.68h_0 (D-CF-D068) can be approximately explained based on the increase in (D/2)/h_0 by 0.14 and the decrease in (d_{l1}-D)/h_0 by 0.1.

Figure 6.20 shows the time histories of $\Delta P/(\rho u_b^2)$, $P^+/(\rho u_b^2)$ and $P^-/(\rho u_b^2)$ in the D-CF-D068 simulation. The concentration and pressure distributions in Figure 6.20 allow understanding the relationship between the flow structure and the variation of the drag force on the obstacle.

During the impact stage (12<t/t_0<16), P^+ increases sharply as the kinetic energy of the heavier fluid at the front of the incoming current is transformed into potential energy, and the heavier fluid close to the upstream face of the obstacle starts raising. As the splash of heavier fluid passes the crest of the obstacle, a strong vortex forms over the downstream face, close to the crest. Before this vortex detaches, its effect is to decrease the pressure over the downstream face of the obstacle (e.g., a region of low pressure is present in the pressure distribution shown in Figure 6.21a). This is why P^- decreases between t=12t_0 and the end of the impact stage in Figure 6.20.

Between the end of the impact phase and the time the first quasi-steady regime is reached (t~28t_0), P^+ continues to grow at an increasingly smaller rate as the level of the interface raises, and the average density of the heavier fluid convected over the crest increases gradually. The variation of P^- is more complex. Immediately after the end of the impact stage, P^- increases sharply, as the heavier fluid from the splash convected over the crest starts moving downwards. P^- peaks at t~18.6t_0 (Figure 6.21b), when the fluid from the splash reaches the face of the obstacle. Then, P_- increases again during the time the fluid from the splash reaches the channel bottom and the front of the downstream current forms. Once the head of the downstream current forms and detaches from the downstream face of the obstacle, P^- becomes close to constant until the end of the first quasi-steady regime (e.g., see Figure 6.21c).

During SS1, the distribution of the piezometric pressure upstream of the obstacle is close to hydrostatic (e.g., the constant iso-pressure contours are close to horizontal in between the lock gate and the crest of the obstacle). After the downstream gravity current forms, the piezometric pressure continues to be close to zero away from the downstream face of the obstacle. This is the main reason why the values of $P^{-}/(\rho u_b^2)$ are much smaller than those of $P^{+}/(\rho u_b^2)$. Two factors contribute to the decrease and, respectively, the increase of $P^{-}/(\rho u_b^2)$ after heavier fluid starts flowing over the downstream face. Because of the high speed flow of higher-density fluid past the downstream face of the obstacle, the piezometric pressure becomes slightly negative. This decrease, which can be easily explained using Bernoulli"s principle, is larger than the increase due to the added hydrostatic pressure component induced by the presence of a layer of fluid over the face of the obstacle, whose density is higher than that of the ambient fluid. As the high-speed higher-density fluid approaches the base of the downstream face, it encounters the channel bottom and changes direction. The piezometric pressure becomes positive in the vicinity of the impact region and induces a positive component to $P^{-}/(\rho u_b^2)$. The resultant piezometric force in the streamwise direction is positive (it is oriented toward the obstacle), but its magnitude is relatively small compared to $P^{+}/(\rho u_b^2)$.

Once the waves of the undular bore start reflecting, the interface starts rising and the flow starts transitioning toward the second quasi-steady regime. As the interface rises, the proportion of the incoming flux that continues over the obstacle increases in a non-monotonic fashion until the flux of heavier fluid over the crest becomes equal to the flux of the incoming current at the inflow section (lock-gate). As this happens, the thickness and mean velocity of the layer of heavier fluid convected over the downstream face of the obstacle increase. The main effect is a strong increase of the piezometric pressure in the region where the high-speed flow changes direction from being parallel to the obstacle face to being parallel to the channel bottom (e.g., compare pressure distributions in Figures 6.21c and 6.21d). This is the main reason for the gradual increase of P^- between $38t_0$ and $50t_0$.

As one of the reflected disturbances approaches the crest, the interface rises locally and increases the piezometric pressure on the upstream face of the obstacle (e.g., see Figure 6.21d). As a result, P^+ increases sharply (Figure 6.20). Once the disturbance passes the crest of the obstacle, P^+ decreases, while P^- starts increasing rapidly because of the larger amount of heavier fluid that is convected over the crest with the disturbance (e.g., compare the pressure distributions in Figures 6.21d and 6.21e close to the downstream face of the obstacle).

The amplitudes of the oscillations of ΔP induced by the propagation of a flow disturbance over the obstacle are smaller than those observed in the variation of P^+. The reason is that, at most times after the transition to the second steady state regime started ($t>50t_0$), the highs in P^+ are correlated with the lows in P^- (e.g., $t\sim66.8t_0$ Figure 6.20, see also Figure 6.21f) and vice versa (e.g., $t\sim60t_0$ in Figure 6.20, see also Figure 6.21e). The reason for this out-of-phase variation of P^+ and P^- is the finite propagation speed of the disturbance over the two faces of the obstacle. The flux of heavier fluid and the height of the lower layer are significantly larger during SS2. Consequently, the increase of the piezometric pressure close to the end of the obstacle (e.g., compare pressure distribution in Figure 6.21c and Figure 6.21f) is much larger. This is the main reason why the average level of $P^-/(\rho u_b^2)$ during SS2 (see Figure 6.20) is higher (0.18) than the one observed during SS1 (0.06). However, due to the increase of the elevation of the interface upstream of the obstacle crest, the average level of $P^+/(\rho u_b^2)$ during SS2 (0.67) is larger than the one observed during SS1 (0.41). The global effect is an increase of $\Delta P/(\rho u_b^2)$ from 0.28 during the first quasi-steady state regime to 0.35 during the second quasi-steady state regime.

Figure 6.22 shows the time histories of $\Delta P/(\rho u_b^2)$, $P^+/(\rho u_b^2)$ and $P^-/(\rho u_b^2)$ in the D-CF-D137 simulation in which the flow within the lower layer is fully-blocked and the first type of quasi-steady regime is not present. The concentration and pressure distributions at representative time instants are shown in Figure 6.23. Similar to the case in which the flow within the lower layer is partially blocked (e.g., see Figure 6.20 for case D-CF-D137), P^+ increases sharply as the front of the incoming current reaches the obstacle and heavier fluid is pushed upwards, over the upstream face of the obstacle (Figure 6.23a). There is also a small decrease in P^- due to the dislocation of ambient fluid around the crest of the obstacle by the raising level of the interface and to the convection over the crest of the obstacle of a small splash of heavier fluid (Figure 6.23a). Between $16t_0$ and $19t_0$ the interface level close to the obstacle decreases sharply, as the front of the bore starts getting away from the obstacle. The interface remains close to horizontal (e.g., Figure 6.23b) until the bore reaches the lock gate and reflects. During this time interval, both P^+ and P^- are close to constant. The first large reflected disturbance reaches the obstacle around $t=35t_0$. The disturbance is strong enough to strongly tilt the interface and to convect a small volume of heavier fluid over the crest (Figure 6.23c). The increase in ΔP between $t=35t_0$ and $t=40t_0$ is driven by the increase of P^+ which is induced by the rising level of the interface in the vicinity of the upstream face of the obstacle. After the upstream propagating disturbance reflects, the interface level decays below its mean level in the vicinity of the obstacle. This induces a strong reduction in P^+ and ΔP until $t=47t_0$ (Figure 6.23d). The interface is subject to several seiching motions of increasingly smaller amplitude during the time the average level of the interface upstream of the obstacle raises. For $t>62t_0$ a continuous current of heavier fluid is established over the crest of the obstacle. P^- starts increasing mainly due to the increase of the piezometric pressure in the region where the heavier current propagating over the downstream face of the obstacle reaches the channel bottom (e.g., see Figures 6.23e-g). Once the mean level of the interface rises above the crest of the obstacle, the transition to SS2 is not characterized by strong large scale oscillations in P^+ and P^-, as was the case during the transition to SS2 in the D-LE-D068 simulation. For $t>78t_0$ (Figures 6.23f-g), the disturbances propagating at the interface are strongly damped, the interface level stabilizes. Consequently, both P^+ and P^- are close to constant (Figure 6.22). Similar to case D-CF-D068, the interface elevation decays sharply close to the crest. Over the downstream face of the obstacle, the flow within the lower layer is characterized by large scale streamwise momentum oscillations and generation of large scale billows at the interface with the ambient fluid. This explains the presence of patches of high and low pressure over the downstream face of the obstacle. Despite the fact that the discharge within the lower layer is the same as in case D-CF-D068, $P^- /(\rho u_b^2)$ is slightly smaller (0.15 vs. 0.18, see also Table 6.9). This is mainly because the angle between the face of the obstacle and the channel bottom is smaller (39.5^0 vs. 51^0) in case D-CF-D137. This reduces the increase of the piezometric pressure over the impact region (e.g., compare pressure distributions in Figures 6.21f and 6.23g).

Next, theoretical models will be used to predict the resultant drag force in the streamwise direction and its two components on the upstream and downstream faces of the obstacle, respectively, during the two types of quasi-steady regimes. The idea is to determine P^+ using the momentum equation between a vertical section situated upstream of the obstacle (section l1) and the section cutting through the crest of the obstacle, where one will assume the flow is critical (section d). Similarly, P^- can be determined using the momentum equation between the section cutting through the crest and a section cutting some distance downstream of the obstacle where the streamlines are parallel to the channel bottom and the pressure distribution is close to hydrostatic (section 3). The resultant force is $\Delta P=P^+-P^-$. Alternatively, ΔP can be estimated directly by applying the momentum equation between the sections situated upstream and downstream of the obstacle. The two predictions should be very close.

The values of P^+ and P^- determined based on theoretical model prediction of the mean velocity and height of the lower layer at these three sections and use of the momentum equation are denoted P_{uT} and P_{dT}, respectively (see Table 6.9). This is needed to make the distinction with the values calculated by integrating the pressure distribution predicted by LES around the obstacle (P^+ and P^-) without use of the momentum equation (see Table 6.9). The values of the flow variables in the same three sections predicted by the theoretical model of Oehy and Schleiss (2007), that assumes the flow over the crest is critical, are given in Table 6.8. These predictions are for the first type of quasi-steady regime. For the second type of quasi-steady regime, the values of the flow parameters at the three sections are estimated using the simplified model proposed in section 6.4 (see equations 6.10-6.14), that also assumes the flow at the crest is critical. Using continuity between section d and section 3, and applying the Bernoulli‟s equation between the same two sections, one can determine the velocity u_3/u_b and height d_3/h_0 of the lower layer at this section.

$$d_d u_d = q_d/(u_b h_0) = d_3 u_3 \tag{6.15}$$

$$d_3 + u_3^2/2g' = D + d_{db} + u_{db}^2/2g' \tag{6.16}$$

The two equations are solved for the variables at section 3. Out of the three solutions, only two are physical. They correspond to the flow being subcritical and, respectively, supercritical at section 3. For both types of steady-state regime, the flow at section 3 is assumed to be supercritical, consistent with present LES results.

Table 6.8 also contains the values of the same flow variables predicted by LES. The LES predictions are considered to give "true" values of these flow quantities obtained from a numerical experiment that does not assume any of the simplifying assumptions made in theoretical models (e.g., critical flow at the crest, sharp hydraulic jump, no mixing between the lower and upper layer), nor the ones associated with the momentum equation (hydrostatic distribution of the pressure at the two sections, uniform flow in the two sections, neglect losses at the interface with the ambient fluid and friction losses upstream and downstream of the obstacle, etc.).

Finally, Table 6.9 contains the values of the drag force on the upstream (P_{uLES}) and downstream faces (P_{uLES}) of the obstacle determined using the momentum equation and based on the "true" values of the flow parameters at the three sections predicted by LES, rather than the values predicted by the theoretical model. In principle, ΔP_{uLES} should be closer to ΔP than ΔP_T because only errors associated with application of the momentum equation are present in the estimation of ΔP_{uLES}. The difference between ΔP and ΔP_{uLES} will allow quantifying the errors induced by the use of the momentum equation to estimate the pressure force in the streamwise direction. If the values are comparable, it means the use of momentum equation to estimate the drag force on the faces of the obstacle is justified.

For example, the quasi-steady value of the mean pressure, P_u, and mean pressure force component in the streamwise direction on the upstream face of the obstacle, $F_u=P_uD$, can be estimated as:

$$\frac{F_u}{\rho g' D h_0} = \frac{P_u}{\rho g' h_0} = \frac{P_u}{\rho u_b^2} = \frac{1}{D/h_0}\left(\frac{1}{2}\frac{d_{l1}^2}{h_0^2} + \frac{u_{l1}^2}{u_b^2}\frac{d_{l1}}{h_0} - \frac{1}{2}\frac{d_d^2}{h_0^2} - \frac{u_{db}^2}{u_b^2}\frac{d_d}{h_0}\right) \qquad (6.17)$$

Similarly, P_d and mean pressure force component in the streamwise direction on the downstream face of the obstacle, $F_d=P_dD$, can be estimated as:

$$\frac{F_d}{\rho g' D h_0} = \frac{P_d}{\rho g' h_0} = \frac{P_d}{\rho u_b^2} = \frac{1}{D/h_0}\left(\frac{1}{2}\frac{d_3^2}{h_0^2} + \frac{u_3^2}{u_b^2}\frac{d_3}{h_0} - \frac{1}{2}\frac{d_d^2}{h_0^2} - \frac{u_{db}^2}{u_b^2}\frac{d_d}{h_0}\right) \qquad (6.18)$$

As already mentioned, for first quasi-steady regime (SS1), the model of Oehy and Schleiss (2007) is used to estimate the pressure forces on the faces of the obstacle. Assuming q_0 and d_0/h_0 are known (Table 6.3), the model predictions of q_d/q_0 and d_{l1}/d_0 are used to calculate q_d and $d_{l1}/h_0=(d_{l1}/d_0)(d_0/h_0)$. Then, using the fact that the model assumes the flow at the crest is critical, one can calculate $d_d/h_0 = q_d^{2/3}$ and $u_d/u_b = q_d/(d_d/h_0)$. Finally, using continuity one obtains the velocity at section l1, $u_{l1}/u_b = q_d/(d_{l1}/h_0)$. Using continuity and Bernoulli‟s equation between section d and section 3, and choosing the supercritical flow solution, one can calculate the velocity and height at section 3 and then estimate $P_d/(\rho u_b^2)$ using equation 6.18.

Table 6.9 shows that during SS1, ΔP is underpredicted in all the cases by 0-25%. The largest contribution to the error in the prediction of ΔP is due to an underestimation of P^+ by the analytical model. Thus, for SS1 one recommends using $1.3\Delta P_T$ for design purposes, assuming the maximum value of ΔP during the transient toward SS1 is smaller or equal than the quasi steady state value, which is the case for the simulations considered in the present study (see Figure 6.19).

For the second quasi-steady regime one can neglect u_{l1b}/u_b. Using Bernoulli equation between section l1 and section d, one can show that $d_{l1b}/h_0 \sim D/h0 + d_{db}/h_0 + (u_{db}/u_b)^2/2$. As in all the three simulations that reached the second quasi-steady regime q_{db}=0.185, one obtains $d_{db}/h_0 = q_{db}^{2/3}$ =0.32, $u_{db}/u_b = 0.578$ and $d_{l1b}/h_0 \sim 0.487 + D/h_0$. Finally, substituting $d_d=d_{db}$ and

$u_d=u_{db}$ in eqn. 6.17, one can calculate $P_u/(\rho u_b^2)$. Then, using continuity and Bernoulli‟s equation between section d and section 3, and assuming the flow is supercritical at section 3, one can calculate the velocity and height of the lower layer at section 3. Finally, $P_d/(\rho u_b^2)$ is estimated using equation 6.18.

Table 6.9 shows that that during SS2, ΔP is overpredicted in all the cases by 15-20%. The largest contribution to the error in the prediction of ΔP is due to an overestimation of P^+ by the analytical model. Thus, for SS2 one recommends using ΔP_T for design purposes. The 15-20% overprediction by the model of ΔP during SS2, should also account for the fact that during the transitions to SS2, ΔP can overshoot the quasi-steady state value by as much as 10-15% (e.g., see Figure 6.19c).

6.8 Mean flow and turbulence statistics around the obstacle during the quasi-steady state regimes

The distributions of the time- and spanwise-averaged concentration, C, streamwise velocity u_x/u_b, velocity magnitude, u_{mag}/u_b, piezometric pressure, $p/\rho u_b^2$, and turbulent kinetic energy, k/u_b^2, during the first type of steady-state regime are compared in Figures 6.24 to 6.26 for the D-LE-D034b, D-CF-D068 and D-CF-D068-HR simulations, respectively. Also shown in the same figures are line plots of the non-dimensional height d/h_0 (see eqn. 6.1), streamwise (with respect to the local mean flow direction in the lower layer) velocity, u_s/u_b, Froude number, $Fr=(u_s/u_b)/\sqrt{(d/h_0)}$, and mean bed-friction velocity, $\bar{u}_\tau/u_b$. The statistics were calculated over a time interval in which the flow can be considered quasi-steady (e.g., $30<t/t_0<40$ in the D-LE-D034b simulation, see Figure 6.3) in the region $13<x/h_0<20$ which surrounds the obstacle. Analysis of the mean flow statistics allow a more clear understanding of the extent of the regions of high velocity and strong turbulence that develop in the vicinity of the obstacle. This is important, as most of the scour is expected to occur beneath these regions.

Figures 6.27-6.29 show the distributions of the same variables during the second type of steady state regime (SS2) that is reached in the D-CF-D068, D-CF-D068-HR and D-CF-D137 simulations. Figure 6.3 shows the time intervals over which the mean flow variables were calculated in each of the three simulations.

Qualitatively, the largest differences among the simulations are not necessarily between the SS1 and SS2 cases, but rather between cases in which the proportion of the incoming flow that continues over the obstacle, q_d/q_0 is large and cases in which q_d/q_0 is relatively small. Of course, all the SS2 cases fall into the first category as $q_d/q_0=1$. Depending mainly on the ratio between the height of the incoming current and the height of the obstacle, SS1 cases (e.g., D-LE-D034a and D-LE-D034b in which $q_d/q_0>0.5$) may fall into the first or the second (e.g., D-LE-D068, D-CF-D068 in which $q_d/q_0<0.2$) category. Other factors are the front velocity of the incoming current and the degree of bluntness of the upstream face of the obstacle.

The other quantity that controls the flow structure over and around the obstacle is the relative difference in elevation between the interface upstream of the obstacle and the crest of the obstacle, $(d_{11}-D)/D$. Cases with low q_d/q_0 are also generally characterized by low values of $(d_{11}-D)/D$. However, cases with high q_d/q_0, including SS2 cases in which $q_d/q_0=1$, are not necessarily characterized by high values of $(d_{11}-D)/D$, if the obstacle height is relatively large (e.g., case D-CF-D137 offers a good example) or the flux over the crest of the obstacle is relatively small.

A general characteristic of the cases with large values of q_d/q_0 and $(d_{11}-D)/D$ is that a large recirculation bubble forms past the crest of the obstacle, in between the downstream face and the core of high speed fluid within the bottom layer. This recirculation region can extend over the whole face of the obstacle (e.g., see Figure 6.24b during SS1 and Figures 6.27b and 6.28b during SS2). The main effect is to reduce the bed friction velocity and the sediment entrainment on the downstream face of the obstacle with respect to the case the flow remains attached. In contrast, in all the cases with low values of q_d/q_0 and $(d_{11}-D)/D$, only a small recirculation bubble forms in the vicinity of the crest, and the flow within the bottom layer remains attached over most of the downstream face of the obstacle. Case D-CF-D137 during SS2 is a good example of a case with relatively low $(d_{l1}\text{-}D)/D$ and high q_d/q_0. The recirculation bubble occupies only about one third of the total length of the downstream face of the obstacle.

q_d/q_0 and $(d_{l1}\text{-}D)/D$ are also the main two parameters that control the mean velocity and mean height of the lower layer over the downstream face of the obstacle. As the values of these two parameters and that of the angle α increase, the pressure forces in the region situated close to the junction line between the downstream face of the obstacle and the channel bottom increase too (e.g., compare the piezometric pressure distributions in frame d of Figures 6.24 to 6.29). The increase of the piezometric pressure at the toe of the obstacle is the most important component that contributes to the pressure drag force on the downstream face of the obstacle, $F^{-}=P^{-}{}_{*}D$.

All simulations show the distribution of the piezometric pressure is close to hydrostatic in the region situated upstream of the obstacle. The pressure drag force on the upstream face of the obstacle is mainly dependent on the elevation of the interface in this region. For small values of $(d_{l1}\text{-}D)/D$, the interface remains close to horizontal until the crest of the obstacle. For high values of $(d_{l1}\text{-}D)/D$, the lines of constant piezometric pressure curve toward the obstacle, as the crest of the obstacle is approached.

The degree of mixing at the interface between the two layers, past the crest of the obstacle, is mainly function of the turbulence intensity. In particular, the height of the region containing fluid of density that is higher than that of the ambient fluid increases strongly in the regions of high turbulent kinetic energy, especially inside the shear layer forming at the outer side of the jet like flow, where turbulence production by shear is strong. The strong turbulence observed within the downstream part of the separation bubble, and close to the junction line between the obstacle and the channel bottom, where the jet-like flow changes direction, has less effect on mixing because those regions contain, for the most part, unmixed lock fluid.

For example, the lowest degree of mixing is observed during SS1 in the D-CF-D068 simulation (Figure 6.25a). The vertical density gradient over the downstream face of the obstacle remains very sharp until close to the junction line with the channel bottom. The mixing increases noticeably only past the junction line $(x/h_0>16.5)$, where the turbulence kinetic energy is amplified inside the shear layer forming on the outer side of the jet–like flow. A second region characterized by a smaller amplification of the turbulence corresponds to the shear layer forming on the inner side of the jet-like flow. The amplification of the turbulence within this second region is due to the fact that the jet-like flow is oriented slightly away from the channel bottom past the junction line (see Figures 6.25b and 6.25e), similar to the case when a gravity current passes the lee side of a dune.

In the higher Reynolds number simulation D-CF-D068-HR (Figure 6.26a), the extent of the region of high turbulence amplification has increased significantly. In particular, high turbulent kinetic energy values are observed at the interface between the two layers over the whole length of the downstream face. This is the main reason why no unmixed lock fluid is observed past the middle of the downstream face in the D-CF-D068-HR simulation and the density gradient at the interface between the two layers is much smaller. Also, the region of high values of k/u_b^2 extends farther downstream. This further intensifies the mixing within the lower layer, past the obstacle, in the higher Reynolds number simulation (e.g., compare the distributions of C for $x/h_0>17$ in Figures 6.26a and 6.27a).

The mixing between the two layers over the beginning of the downstream face of the obstacle remains relatively low during SS1 in the D-LE-D034b simulation (Figure 6.24a). This is consistent with the low values of k/u_b^2 observed over the upstream part of the interfacial shear layer. However, the strong amplification of the turbulence within the shear layer over the downstream part of the downstream face of the obstacle and past the obstacle ($16.5<x/h_0<19$) induces a rapid growth of the thickness of interfacial mixed fluid. Downstream of the region of high turbulence ($x/h_0>19$), the vertical profile of the concentration within the bottom layer are much less dependent on the streamwise location.

The distributions of the concentration downstream of the crest of the obstacle are qualitatively similar during SS1 in the D-LE-D034b simulation (Figure 6.24a) and during SS2 in the D-CF-068 simulation (Figure 6.27a). However, in the D-CF-D068 simulation the values of k/u_b^2 within the shear layers on the two sides of the jet-like flow are larger and the turbulence is strongly amplified in the shear layer forming on the outer side, starting close to the crest of the obstacle. This is the main reason why the thickness of the layer of mixed fluid is larger during SS2 in the D-CF-068 simulation at all sections situated downstream of the crest of the obstacle.

Similar, to the case when simulations D-CF-D068 and D-CF-D068-HR were compared during SS1, the increase of the Reynolds number during SS2 increases the longitudinal extent of the region of high k/u_b^2 (see Figures 6.27e and 6.28e) and intensifies the vertical mixing within the lower layer, especially at sections situated downstream of the obstacle (e.g., compare Figures 6.27a and 6.28a for $x/h_0>16.5$).

Finally, the strong interfacial mixing occurring over the whole extent of the downstream face of the obstacle during SS2 in the D-CF-D137 simulation is due to the strong amplification of k/u_b^2 within the interfacial shear layer starting at the crest of the obstacle.

Scale effects are also affecting the position and strength of the core of high velocities within the jet-like flow during both SS1 and SS2. The increase of the Reynolds number increases the penetration distance of the region of high velocity within the jet like flow and moves its centerline closer to the channel bottom in the region situated downstream of the obstacle.

The streamwise variation of the Froude number is discussed, next. A first important observation is that the Froude number remains subcritical at the crest of the obstacle during SS1 in the simulations with small q_d/q_0 and $(d_{l1}-D)/D$ (e.g., Fr~0.6-0.7 in the D-LE-D034a, D-CF-D068 and D-CF-D068-HR cases). In these simulations (e.g., see Figures 6.25h and 6.26h), the Froude number increases rapidly between the crest of the obstacle and the section where the change in direction of flow within the lower layer is complete and the flow streamlines become parallel the horizontal channel bottom (x/h_0~16.7). Then, the Froude number starts decaying slowly. The decay has an exponential shape which continues even after the flow transitions back to subcritical. The increase in the Reynolds number from Re=7,141 to Re=250,000 results in an increase of the maximum Froude number at x/h_0~16.7, from 3 to 4, and an increase of the distance from the obstacle where the flow transitions back to subcritical, from $x/h_0=18$ to $x/h_0=20.5$.

By contrast, the flow within the lower layer is very close to critical at the crest of the obstacle during SS1 in the simulations with large q_d/q_0 and $(d_{l1}-D)/D$ (e.g., case D-LE-D034b). In these simulations, rather than continuing to increase, the Froude number remains close to critical over the first half of the downstream face. It then starts to increase over the second half of the downstream face. The increase continues past the junction line, until $x/h_0 \sim 16.9$, where it reaches a maximum value of about 1.5. Similar to the other simulations, past this location the Froude number starts decaying slowly. The flow becomes subcritical at $x/h_0=19.5$.

The streamwise variations of the Froude number during SS2 in the D-CF-D068, D-CF-D068-HR and D-CF-D137 simulations are qualitatively similar to the one observed during SS1 in the simulations with large q_d/q_0 and $(d_{l1}-D)/D$. The Froude number at the crest of the obstacle is close to critical and it remains so over most of the downstream face of the obstacle. As the bottom of the obstacle is approached, the flow becomes supercritical and the Froude number peaks at a small distance ($\sim 0.5h_0$) from the junction line between the obstacle and the channel bottom. This is followed by a region of a slow decay of the Froude number.

The differences in the distributions of the Froude number during SS2 are mostly of quantitative nature. The increase the Reynolds number from Re=7,141 to Re=250,000 in the simulations with $D=0.68h_0$ results in an increase of the maximum Froude number during SS2, from 1.7 to 2.2. As the rate of decay of the Froude number is similar, the flow remains supercritical over a significantly longer distance in the high Reynolds number simulation. In the D-CF-D137 simulation, in which the relative height of the lower layer over the obstacle during SS2 is smaller than in the D-CF-D068 simulation, the peak value of the Froude number is close to 2.5. The rate of decay of the Froude number is again comparable to the one observed in the other simulations during SS2. Thus, the flow remains supercritical over a much longer region downstream of the obstacle during SS2 compared to during SS1.

In all the simulations, during both SS1 and SS2, the bed friction velocity remains low upstream of the obstacle, starts increasing over the upstream face of the obstacle, and peaks at the crest. The values of $\bar{u}_\tau / u_b$ over the downstream face of the obstacle are comparable to those at the crest only if the separation bubble extends over a small fraction of the total length of the downstream face. This is the case in the D-CF-D068 (Figure 6.25i) and D-CF-D068-HR (Figure 6.26i) simulations during SS1 and in the D-CF-D137 simulation (Figure 6.29i) over SS2. In all the other simulations the values of $\bar{u}_\tau / u_b$ remain relatively low, thus the entrainment of sediment is expected to be low over the downstream face of the obstacle.

As in all the simulations the flow reattaches around the junction line between the obstacle and the channel bottom, the bed friction velocity is strongly amplified in the region where the jet-like flow encounters the channel bottom and changes direction. In the case the separation bubble extended over most of the length of the downstream face, the values of $\bar{u}_\tau / u_b$ downstream of the junction line are expected to be significantly higher than those over the downstream face (e.g., during SS2 in the D-CF-D068 case, during SS1 in the D-LE-D034b case). This can result in the rapid development of a large scour hole immediately downstream of the obstacle. If the separation bubble covers only the upstream part of the downstream face of the obstacle, than the values of $\bar{u}_\tau / u_b$ downstream of the junction line are expected to be comparable to those recorded over the downstream face (e.g., during SS1 in the D-CF-D068 case).

In all the simulations, $\bar{u}_\tau / u_b$ starts decaying slowly after it peaks near the junction line. The rate of decay of $\bar{u}_\tau / u_b$ is similar to the one of the streamwise velocity within the core of the jet-like flow. The streamwise variation of $\bar{u}_\tau / u_b$ in the lower Reynolds number simulations shows the presence of regions with different rates of decay. By contrast, the rate of decay is much more uniform in the high Reynolds number simulations (e.g., compare Figures 6.25i and 6.26i during SS1 and Figure 6.27i and 6.28i during SS2 for the simulations with D=0.68h_0). The main reason for the smaller rate of decay is that the core of high-speed fluid remains parallel to the channel bottom in the high Reynolds number simulation rather than getting away from the channel bottom (e.g., compare Figures 6..25c and 6.26c). During SS2, the main effect of increasing the obstacle height is to reduce the height of the lower layer. If the discharge is the same (e.g., compare D-CF-D068 and D-CF-D137 simulations during SS2) the fluid within the lower layer will have a higher velocity. Moreover, past the crest, the core of high velocities is situated closer to the bed. This explains the larger values (by about 20%) of $\bar{u}_\tau / u_b$ past the obstacle in the D-CF-D137 simulation compared to the D-CF-D068 simulation.

6.9 Sediment entrainment capacity

The distributions of u_τ/u_b during the two quasi-steady regimes SS1 and SS2 were analyzed in the previous section. Figures 6.24i to 6.29i contain a horizontal dashed line corresponding to u_τ/u_b=0.06. Assuming the fluid is water, and the ratio of the density difference between the heavier lock fluid and the ambient fluid, to the density of the ambient fluid, $\Delta\rho/\rho_o$, is 4.7% in the simulations conducted at Re=7,141, one obtains h_0=0.048 m and $u_b = \sqrt{g' h_0}$ =0.15 m/s, similar to the values used in the experiments (cases D-LE-D034a and D-LE-D034b) conducted by Lane Serff et al. (1995). Using Shields‟ diagram, one can show that $u_{\tau c}/u_b$=0.06 is the non-dimensional critical value of the bed friction velocity ($u_{\tau c}$=0.009 m/s) for sediment particles with a diameter of 50μm. The non-dimensional time scale is t_0=0.32 s.

The flux of sediment of diameter d=50μm entrained per unit time and unit width over a certain zone by the gravity current is denoted F(t) and is calculated using the expression proposed by van Rijn (1984), as described by equations 4.12 and 4.13. Sediment of a certain size is entrained only if $u_\tau > u_{\tau c}$.

Four zones are chosen to compare the distributions of $F_i(t)$, where i is the zone number. These zones are shown in the sketch in Figure 6.30. They allow quantifying the sediment entrained by the current upstream of the obstacle (Zone 1, $10<x/h_0<14.5$, the lock gate is situated at $x/h_0=8.2$), over the upstream face of the obstacle (Zone 2), over the downstream face of the obstacle (Zone 3), and downstream of the obstacle (Zone 4, $16.5<x/h_0<20$ for cases except case D-CF-D137 for which $17.6<x/h_0<20$). As already discussed in the introduction, most of the submerged dams installed in rivers are built of erodible material. Thus, it is important to be able to quantify the amount of sediment entrained from the dam in these cases.

The time histories of the fluxes $F_i(t)$ in the D-LE-D034b and D-CF-D068 simulations are compared in Figure 6.31. Figure 6.32 compares the time histories of the fluxes $F_i(t)$ in the D-CF-D068 and D-CF-D137 simulations.

Over Zone 1 (Figures 6.31a and 6.32a), in all the three simulations sediment is entrained only beneath the head and dissipative wake of the upstream current ($2<t/t_0<15$). The time variations of $F_1(t)$ are very similar in all the three simulations. This is expected, as the temporal evolution of the gravity current before it reaches the obstacle is not expected to be influenced by the size of the obstacle. The maximum values of $F_1(t)$ are around $2*10^{-6}$ m^2/s. After the current reaches the obstacle, $F_1(t)$ is equal or very close to zero. The small non-zero values of the flux around $t=30t_0$ in the D-CF-D068 simulation are due to the amplification of the bed friction velocity beneath the first wave of the undular jump, when the crest of the first wave is situated at $x\sim11h_0$. Thus, the potential for erosion of sediment with $d=50$ μm over Zone 1 is small in all the three simulations.

Comparison of Figures 6.31b and 6.32b shows that the distributions of $F_2(t)$ over the upstream face of the dam are qualitatively similar. The largest values of $F_2(t)$ are recorded during the impact stage between the front of the incoming current and the upstream face of the obstacle. The maximum values are comparable in the D-LE-D034b and D-CF-D068 simulations in which part of the heavier current is convected over the top of the dam. The values of $F_2(t)$ are about one order of magnitude larger during the impact stage in the D-CF-D137 simulation in which the flow is fully blocked. Part of this difference is due to the fact that the length of the upstream face is about two times larger in the D-CF-D137 case compared to the other two cases. Then, after the first wave of the undular bore detaches from the obstacle, $F_2(t)$ decreases to very low values. The distributions of the bed friction velocity over the upstream face are qualitatively similar after the first type of quasi-steady state regime is reached in the D-LE-D034b and D-CF-D068 simulations (e.g., see Figures 6.24i and 6.25i). However, as $u_\tau/u_b<0.06$ in the D-CF-D068 simulation, $F_2(t)$ is equal to zero. The average level of $u_\tau/u_b<0.06$ is about two times larger in the D-LE-D034b simulation, in which $u_\tau/u_b>0.06$ over the second half of the upstream face of the obstacle. The mean value of $F_2(t)$ during SS1 is close to $2.5*10^{-6}$ m^2/s in the D-LE-D034b simulation. The first type of quasi steady state regime is not present in the D-CF-D137 simulation. However, the seiching motions induced by the passage over the upstream face of the obstacle of the disturbances that reflected at the lock gate can induce small values of $F_2(t)$ during the transition to SS2 (e.g., around $t=37t_0$ in the D-CF-D137 simulation). Finally, after the transition to SS2 is complete in the D-CF-D068 and D-CF-D137 simulations, $F_2(t)$ oscillates around $1.8*10^{-6}$ m^2/s in case D-CF-D068 and around $1.8*10^{-5}$ m^2/s in case D-CF-D137. As shown by the comparison of u_τ/u_b during SS2 in Figures 6.28i and 6.29i, the main reasons for the larger values of $F_2(t)$ in case D-CF-D137 are the larger amplification of the bed friction velocity close to the crest and the larger size of the region where $u_\tau/u_b>0.06$.

Comparison of Figures 6.31c and 6.32c shows that the distributions of $F_3(t)$ over the downstream face of the dam depend strongly on the streamwise extent of the separation bubble that starts at the crest of the obstacle. This is true during both SS1 and SS2. In the D-LE-D034b simulation, $F_3(t)$ becomes non-zero over the downstream face immediately after the front passes the crest of the obstacle. After a short transient, $F_3(t)$ becomes close to constant and oscillates around $1.0*10^{-6}$ m^2/s, which is less than half the value predicted over the upstream face during SS1. This can look surprising, as one expects the sediment flux to be larger over the face with positive slope over which the mean velocity of the fluid within the lower layer is large. The main reason is that during SS1 the separation bubble extends over the whole length of the downstream face of the obstacle in case D-LE-D034b (Figure 6.24). The values of $F_3(t)$ during SS1 are also low (less than $1.0*10^{-6}$ m^2/s) in the D-CF-D068 simulation, in which the flow remains attached over the most part of the downstream face. However, the values of the bed friction velocity are low and comparable to those observed during SS1 in the D-LE-D034b simulation mostly because the discharge of heavier fluid convected over the dam is much smaller in the D-CF-D068 simulation compared to the D-LE-D034b simulation ($q_d/q_0=0.11$ vs 0.67, q_0 is comparable in both cases). $F_3(t)$ increases monotonically during the transition to SS2 in cases D-CF-D068 and D-CF-D137. Once SS2 is reached, the mean values of $F_3(t)$ are $3.5*10^{-4}$ m^2/s in case D-CF-

D137 and only $1.8*10^{-6}$ m^2/s in case D-CF-D068. As shown by the distribution of u_τ/u_b during SS2 in case D-CF-D137 (Figure 6.29i), most of the sediment is entrained over the second half of the downstream face. The fluxes of sediment entrained over the upstream and downstream faces of the dam during SS2 are similar in the D-CF-D068 simulation ($F(t)\sim 2.0*10^{-6}$ m^2/s). In contrast to this, in case D-CF-D137 the flux of sediment entrained over the downstream face of the dam during SS2 ($F_3(t)\sim 3.5*10^{-4}$ m^2/s) is more than one order of magnitude higher than the one predicted over the upstream face ($F_2(t)\sim 1.8*10^{-5}$ m^2/s). Thus, in cases in which the flow remains attached over most of the downstream face during SS2 (e.g., see Figure 6.29), the flux of sediment entrained over the downstream face is much larger than the one entrained over the upstream face. If SS2 is expected to last over long periods of time, one has to protect against erosion not only the crest region but the entire downstream face of the dam or, at least, the region close to the end of the obstacle.

The flux of sediment entrained over Zone 4 during SS1 is $9.0*10^{-6}$ m^2/s, which is about two times larger than the value of the flux over the downstream face ($1.8*10^{-6}$ m^2/s). Most of the sediment in entrained in between the junction line and $x/h_0\sim 17.5$. As shown in Figure 6.24i, u_τ/u_b decays below the critical value for $x/h_0>18$. Thus, a scour hole of limited extent is expected to develop downstream of the obstacle. The flux is very small during SS1 in the D-CF-D068 simulation in which q_d/q_0 is very low (0.11). During SS2, the flux in the D-CF-D068 is about $3.0*10^{-5}$ m^2/s. This value is about three times larger than the one predicted during SS1 in the D-LE-D034b simulation in which the structure of the lower layer past the crest of the obstacle was similar (e.g., compare Figures 6.24 and 6.27). The differences are mostly due to the fact that u_τ/u_b decays slower with the distance from the obstacle during SS2 in the D-CF-D068 simulation. For example, the region of entrainment extends up to $x/h_0\sim 19$ rather than 17.5, as was the case during SS1 in the D-LE-D034 case. Thus, the extent of the scour hole is expected to be larger during SS2 in the D-CF-D068 simulation. Also, during SS2 the amount of sediment entrained downstream of the obstacle should be much larger than the one entrained over the downstream face, as F_3 ($=2.0*10^{-6}$ m^2/s) is about one order of magnitude lower than F_4 ($=3.0*10^{-}$

^{5} m^2/s). Finally, $F_4(t)$ increases close to linearly with time once heavier fluid starts being convected over the crest of the obstacle. It peaks once the transition to SS2 is complete when $F_4 \sim 3.0*10^{-5}$ m^2/s. In fact, the total flux of sediment entrained downstream of the obstacle during SS2 in the D-CF-D137 simulation should be larger, as u_τ/u_b is still larger than 0.06 at the end of Zone 4 (see Figure 6.29i). Compared to case D-CF-D068 during SS2, u_τ/u_b is larger by at least 20% at locations situated at the same distance form the end of the obstacle. This is the main reason why $F_4(t)$ is larger during SS2 in the D-CF-D137 simulation. Thus, similar to case D-CF-D068, one expects a large scour hole to develop downstream of the obstacle. However, as opposed to case D-CF-D068, the scoured region will also extend over the downstream face of the obstacle, where $F_3(t)$ is very large during SS2.

6.10 Summary and Conclusions

The reflection of a gravity current from an obstacle was studied based on results of highly-resolved LES simulations. The study considered only the case of a horizontal channel bottom in which the incoming gravity current was subcritical. The study focused on the case of a deep submerged incoming current that encounters an obstacle of varying height. Both cases in which the flow within the lower layer containing heavier fluid was partially blocked and, respectively, fully blocked (total reflection) were considered. Scale effects were investigated between simulations conducted at $Re \sim 10^4$ and Re=250,000, at which the structure of the current is closer to the one encountered at field conditions.

The study considered both lock-exchange gravity currents and constant-flux gravity currents. In the later case, two types of quasi-steady states are observed in the partially-blocked cases. The first one (SS1) is identical to the one observed in lock-exchange simulations, where the bore reflections are insignificant at the lock gate position, or the distance between the lock gate and the obstacle is very large. During SS1 the discharge at the crest of the obstacle is smaller than the one at the lock-gate position. The second one (SS2) is observed after the region between the lock gate and the obstacle becomes filled with lock fluid, and the flow over the obstacle resembles to the flow of a constant density fluid past a weir. During SS2, the discharge at the crest of the obstacle is equal to the inlet discharge at the lock gate position. The difference between the height of the lower layer upstream of the obstacle and the obstacle height, $(d_{l1}\text{-D})/h_0$ is larger during the SS2 regime compared to during the SS1 regime. The same value of $(d_{l1}\text{-D})/h_0$ was predicted during SS2 in the simulations with varying obstacle heights. SS2 is the only quasi-steady state observed in the fully-blocked cases.

A simple one-layer approach was proposed to estimate the main flow parameters during SS2. Simulation results showed that the Froude number at the crest was close to unity during SS2. However, that was not always the case during SS1, where, in some of the simulations, the flow became critical over the downstream face of the obstacle. All single-layer theoretical models assume Fr=1 at the crest.

The numerical predictions of the main flow parameters during SS1 were compared to predictions of analytical models based on shallow-water theory (e.g., Lane Serff et al., 1995, Oehy and Schleiss, 2007, Gonzales-Juez and Meiburg, 20009). The changes in the overall shape of the current as it interacted with the obstacle were found to be similar to those observed in experiments conducted with similar flow conditions. Compared to the LES simulations, the model of Lane-Serff et al. (1995) systematically underpredicted the proportion of the incoming flux that continues over the obstacle $u_d d_d / u_f d_0$ and overpredicted d_{l1}/d_0. The predictions of d_{l1} / d_0 and $u_d d_d / u_f d_0$ by the model of Oehy (2003) show somewhat better agreement with LES, especially for the constant-flux gravity current cases. The level of agreement with LES shown by the two theoretical models was similar for the lock-exchange cases.

Comparison between the LES simulations and the theoretical model of Gonzales0-Juez and Meiburg (2009) showed that for obstacles of small height and reduced degree of bluntness, the velocity of the downstream current is overpredicted by the theoretical model by 10-20% and the current depth is underpredicted, when no effort was made to calibrate the model constant C. However, the opposite was true for the case of higher obstacles with a larger degree of bluntness, including for the simulation conducted with Re=250,000, in which the front velocity is relatively close to the inviscid limit.

In most cases, the simulations predicted the formation of an undular bore with a series of waves. The amplitude of the waves was found to increase strongly with the increase in the Reynolds number. Simulation results showed the waves of the undular bore induced regions of high turbulence and strong dissipation beneath them. In the case these regions are situated close to the channel bottom, additional sediment can be entrained from the bed.

The temporal evolution of the drag force showed that during the transient stage the drag force was, at most, 10-15% larger than the values recorded during the quasi-steady regimes, SS1 and SS2. The momentum equation was then used to predict the drag force, including its two components on the upstream and downstream faces of the dam, during SS1 and SS2 based on the predictions of the main flow parameters by the analytical models. During SS1, ΔP was underpredicted in all the cases by 0-25% by the analytical model. The largest contribution to the error in the prediction of ΔP was due to an underestimation of pressure force on the upstream face of the dam by the analytical model. Thus, for SS1 one recommends using 1.3ΔP for design purposes, assuming the maximum value of ΔP during the transient toward SS1 is smaller or equal than the quasi-steady-state value. During SS2, ΔP was overpredicted (15-20%) by the analytical model in all the cases. The largest contribution to the error in the prediction of ΔP was again due to an overestimation of the pressure force on the upstream face of the dam by the analytical model. Thus, for SS2 one recommends using ΔP predicted by the analytical model for design purposes.

LES also allowed a detailed analysis of the mean flow, turbulence structure and bed friction velocity distributions around and over the obstacle during the two quasi-steady regimes. The mixing between the two layers and the vertical mixing over the lower layer were strongly enhanced in the regions of high turbulence amplification. In the high Reynolds number simulations the mixing was larger and the core of large velocities within the jet-like flow remained closer to the channel bottom compared to the lower Reynolds number simulations.

Simulation results showed that in cases in which a recirculation bubble covers most of the downstream face of the obstacle, the amount of sediment entrained over the downstream face is much smaller compared to cases in which the flow remains attached. Thus, separation is an effective way to protect from erosion the downstream face of the obstacle. This is important as the downstream face has, in general, a much higher potential for erosion compared to the upstream face of the obstacle (e.g., by about 20 times during SS2 in the D-CF-D137 simulation). As the bed friction velocity is high close to the crest in all the simulations, one recommends the use of local protection against scour near the crest of the obstacle (e.g., rip rap, etc.). If the flow conditions are such that in most cases the flow of heavier fluid past the crest of the obstacle will remain attached over a large part of its downstream face, one recommends scour protection methods to be implemented over the whole downstream face of the obstacle and, of course, over some distance downstream of the junction line between the obstacle and the channel bottom. LES allowed estimation of the length of the region downstream of the obstacle over which the bed friction velocity remains high during SS1 and SS2. The length of this region and the flux of sediment entrained over it are much larger during SS2 and increase with the height of the obstacle. The strong decay of the velocity in between the bore and the upstream face of the obstacle suggests that the deposition rates will be increased upstream of the obstacle in the case in which the gravity current transports particulates.

Thus, results from LES simulations can be used to insure the force acting on the obstacle (submerged dam) does not dislocate the structure, to estimate the amount of sediment entrained over the faces of the obstacle and around it due to the passage of the current, and to identify regions of high bed friction velocity where local scour can develop. Based on this information one can decide the extent of the regions over which scour protection should be applied (e.g., rip rap, etc.).

Table 6.1 Main geometrical parameters of the simulations with a lock-exchange gravity current and with a constant-flux gravity current.

	Lock Exchange	**h/h_o**	**B/h_o**	**D/h_o**	**H/h_o**	**α**	**L_o/h_o**	**L/h_o**	**x_o/h_o**	**Re**
1	D-LE-D034a	1	1.1	0.34	1.042	32^o	7.78	15.94	8.125	8135
2	D-LE-D034b	1	1.1	0.34	5.354	32^o	7.78	15.94	8.125	7141
3	D-LE-D068	1	1.1	0.68	5.354	51^o	7.78	15.94	8.125	7141
	Constant Flux									
4	D-CF-D068	0.566	1.1	0.68	5.354	51^o	7.78	15.94	-	7141
5	D-CF-D068-HR	0.566	1.1	0.68	5.354	51^o	7.78	15.94	-	250,000
6	*D-CF-D068-G	0.566	2	0.68	5.354	-	7.78	15.97	-	7141
7	D-CF-D137	0.566	3.33	1.37	5.354	39.5^o	7.78	15.94	-	7141

Table 6.2 Comparison of the front velocities of the gravity current before and after it passed the obstacle and of the velocities of the first two waves of the undular bore. (u_{b1}/u_b)“ denotes the non-dimensional bore velocity assuming a sharp bore is present and applying the continuity equation across the moving front. This is a standard assumption made in all the theoretical models used to predict the interaction of a gravity current with an obstacle.

	u_f/u_b	u_{b1}/u_b	(u_{b1}/u_b)’	u_{b2}/u_b	v_f/u_b
D-LE-D034a	0.45	0.40	0.29	-	0.39
D-LE-D034b	0.57	0.36	0.26	-	0.54
D-LE-D068	0.57	0.39	0.44	0.35	0.34
D-CF-D068	0.56	0.39	0.42	0.35	0.34
D-CF-D068-G	0.57	0.39	0.42	0.35	0.34
D-CF-D068-HR	0.61	0.38	0.4	0.35	0.38
D-CF-D137	0.57	0.34	0.37	-	-

Table 6.3 Comparison of the main flow parameters during the first type of quasi-steady regime, SS1.

	D-LE-D034a	**D-LE-D034b**	**D-LE-D068**	**D-CF-D068**	**D-CF-D068-HR**
$\mathbf{H/h}$	1.042	5.354	5.354	5.354	5.354
$\mathbf{D/h_o}$	0.34	0.34	0.68	0.68	0.68
$\mathbf{d_o/h_o}$	0.37	0.39	0.39	0.37	0.37
$\mathbf{D/d_o}$	0.92	0.87	1.74	1.89	1.89
$\mathbf{1/z = d_o/H}$	0.36	0.07	0.07	0.07	0.07
$\mathbf{z = H/d_o}$	2.8	13.7	13.7	14.9	14.9
$\mathbf{u_o/u_b}$	0.42	0.54	0.54	0.50	0.50
$\mathbf{d_{l1}/h_o}$	0.59	0.66	0.80	0.76	0.77
$\mathbf{u_d/u_b}$	0.33	0.51	0.23	0.21	0.24
$\mathbf{d_d/h_o}$	0.27	0.27	0.13	0.09	0.10
$\mathbf{v_4/u_b}$	0.38	0.46	0.24*	0.21	0.31
$\mathbf{d_4/h_o}$	0.24	0.30	0.12*	0.09	0.08
$q_g = q_o = u_o d_o / u_b h_o$	0.155	0.21	0.21	0.185	0.185
$q_d = u_d d_d / u_b h_o$	0.09	0.14	0.03	0.019	0.025
$q_3 = v_3 d_3 / u_b h_o$	0.09	0.14	0.03*	0.019	0.025
$q_d / q_o = u_d d_d / u_o d_o$	0.58	0.67	0.14	0.11	0.13
$Fr_o = u_o / \sqrt{g' d_o}$	0.69	0.86	0.86	0.82	0.82
$Fr_d = u_d / \sqrt{g' d_d}$	0.63	0.98	0.64	0.68	0.76
$Fr_3 = v_3 / \sqrt{g' d_3}$	0.77	0.84	0.7	0.7	1.1

Table 6.4 Comparison of the main flow parameters during the second type of quasi-steady regime, SS2.

	D-CF-D068	**D-CF-D068-HR**	**D-CF-D137**
u_{db} / u_b	0.54	0.51	0.61
d_{db} / h_o	0.34	0.36	0.30
v_{3b} / u_b	0.63	0.75	0.90
d_{3b} / h_o	0.29	0.24	0.20
d_{l1b} / h_o	1.07	1.07	1.76
$q_{3b} = (v_{3b} d_{3b}) / (u_b h_o)$	0.185	0.185	0.185
$q_{db} = (u_{db} d_{db}) / (u_b h_o)$	0.185	0.185	0.185
$(d_{l1b} - D) / h_o$	0.39	0.39	0.39
$Fr_{db} = u_{db} / \sqrt{g' d_{db}}$	1.03	0.92	1.11
$Fr_{3b} = u_{3b} / \sqrt{g' d_{3b}}$	1.28	1.53	1.98

Table 6.5 Comparison of the LES and theoretical model predictions of the main parameters describing the evolution of the flow before and after the gravity current passes the obstacle (during the first type of quasi-steady regime).

	D-LE-D034a			**D-LE-D034b**			**D-LE-D068**		
	Theory	**LES**	**%Error**	**Theory**	**LES**	**%Error**	**Theory**	**LES**	**%Error**
$z = H/d_o$	1.81-1.92	2.8	-	12.9-16.7	13.7	-	12.9-16.7	13.7	-
$Fr_{of} = u_f / \sqrt{g'd_o}$	0.6-0.69	0.74	-	0.86-1.21	0.91	-	0.86-1.21	0.91	-
$u_d d_d / u_f d_o$	0.45	0.52	13	0.55	0.63	13	0.13	0.14	7
u_{b1} / u_f	0.92	0.89	3	0.56	0.63	11	0.74	0.68	9
d_{l1} / d_o	1.63	1.59	2	1.86	1.69	10	2.17	2.05	6

	D-CF-D068			**D-CF-D068-HR**		
	Theory	**LES**	**%Error**	**Theory**	**LES**	**%Error**
$z = H/d_o$	12.9-16.7	14.9	-	12.9-16.7	14.9	-
$Fr_{of} = u_f / \sqrt{g'd_o}$	0.86-1.21	0.92	-	0.86-1.21	1.0	-
$u_d d_d / u_f d_o$	0.09	0.09	0	0.09	0.11	18
u_{b1} / u_f	0.76	0.70	8	0.76	0.72	5
d_{l1} / d_o	2.22	2.05	8	2.22	2.05	8

Table 6.6 Comparison of the predictions of the models of Lane–Serff et al. (1995) and Oehy and Schleiss (2007) with those given by LES for the proportion of the incoming flux that continues over the obstacle during the first type of quasi-steady regime.

Simulations	**LES**	**Oehy and Schleiss (2007)**	**%error**	**Lane-Serff et al.(1995)**	**%error**
D-LE-D034a	0.52	0.6	15	0.45	13
D-LE-D034b	0.63	0.58	8	0.55	13
D-LE-D068	0.14	0.13	7	0.13	7
D-CF-D068	0.09	0.1	11	0.09	0
D-CF-D068-HR	0.11	0.1	9	0.09	18

Table 6.7 Comparison of the predictions of the models of Lane–Serff et al. (1995) and Oehy and Schleiss (2007) with those given by LES for the ratio between the depth of the lower layer behind the bore and the depth of the undisturbed lower layer upstream of the bore during the first type of quasi-steady regime.

Simulations	**LES**	**Oehy and Schleiss (2007)**	**%error**	**Lane-Serff et al. (1995)**	**%error**
D-LE-D034a	1.59	1.50	6	1.63	3
D-LE-D034b	1.69	1.62	4	1.86	10
D-LE-D068	2.05	1.95	5	2.17	6
D-CF-D068	2.05	1.97	4	2.22	8
D-CF-D068-HR	2.05	1.97	4	2.22	8

Table 6.8 Main flow parameters predicted by LES and theoretical models that are used to estimate the pressure forces on the upstream and downstream faces of the obstacle during the two quasi steady regimes.

	LES							**Theory**						
Simulation	d_{l1}/h_o	u_d/u_b	d_d/h_o	$q_d/(u_b h_o)$	u_{l1}/u_b	u_3/u_b	d_3/h_o	d_{l1}/h_o	u_d/u_b	d_d/h_o	$q_d/(u_b h_o)$	u_{l1}/u_b	u_3/u_b	d_3/h_o
D-LE-D034a (SS1)	0.61	0.33	0.27	0.09	0.15	1.21	0.074	0.56	0.48	0.21	0.10	0.18	1.22	0.082
D-LE-D034b (SS1)	0.67	0.5	0.28	0.14	0.21	0.11	0.126	0.63	0.51	0.26	0.13	0.20	1.1	0.12
D-CF-D068 (SS1)	0.78	0.17	0.11	0.019	0.02	1.25	0.015	0.73	0.27	0.08	0.02	0.03	1.25	0.017
D-CF-D068 (SS2)	1.07	0.54	0.34	0.185	0.17	1.44	0.128	1.167	0.578	0.32	0.185	0.16	1.6	0.12
D-CF-D068-HR (SS1)	0.76	0.2	0.12	0.025	0.03	1.26	0.020	0.73	0.28	0.08	0.02	0.03	1.25	0.018
D-CF-D068-HR (SS2)	1.07	0.51	0.36	0.185	0.17	1.44	0.128	1.167	0.578	0.32	0.185	0.16	1.6	0.12
D-CF-D137 (SS2)	1.76	0.61	0.3	0.185	0.11	1.875	0.099	1.857	0.578	0.32	0.185	0.1	1.97	0.09

Table 6.9 Comparison between the predictions of LES obtained by integrating the pressure over the two faces of the obstacle and those obtained using the flow parameters predicted by the theoretical models and applying the momentum equation (subscript "T") of the mean pressure on the upstream face of the obstacle, $P^+/\rho u_b^2$, mean pressure on the downstream face of the obstacle, $P^-/\rho u_b^2$, and mean pressure difference between the upstream and downstream faces of the obstacle, $\Delta P/\rho u_b^2$ during the two quasi steady regimes. Also shown are the predictions of these three quantities obtained using the momentum equation and the flow parameters predicted by LES (subscript "LES").

	LES						**Theory**		
Simulation	**$P^+/\rho u_b^2$**	**$P^-/\rho u_b^2$**	**$\Delta P/\rho u_b^2$**	**$P_{uLES}/\rho u_b^2$**	**$P_{dLES}/\rho u_b^2$**	**$\Delta P_{LES}/\rho u_b^2$**	**$P_{uT}/\rho u_b^2$**	**$P_{dT}/\rho u_b^2$**	**$\Delta P_T/\rho u_b^2$**
D-LE-D034a (SS1)	0.34	0.11	0.22	0.39	0.14	0.26	0.31	0.16	0.15
D-LE-D034b (SS1)	0.45	0.17	0.28	0.42	0.16	0.26	0.36	0.15	0.23
D-CF-D068 (SS1)	0.41	0.06	0.35	0.43	0.02	0.41	0.38	0.03	0.35
D-CF-D068 (SS2)	0.67	0.18	0.49	0.66	0.17	0.48	0.81	0.21	0.61
D-CF-D068-HR (SS1)	0.45	0.07	0.38	0.41	0.03	0.38	0.38	0.03	0.35
D-CF-D068-HR (SS2)	0.68	0.15	0.53	0.66	0.17	0.48	0.81	0.21	0.61
D-CF-D137 (SS2)	0.99	0.15	0.84	1.02	0.14	0.89	1.16	0.15	1.0

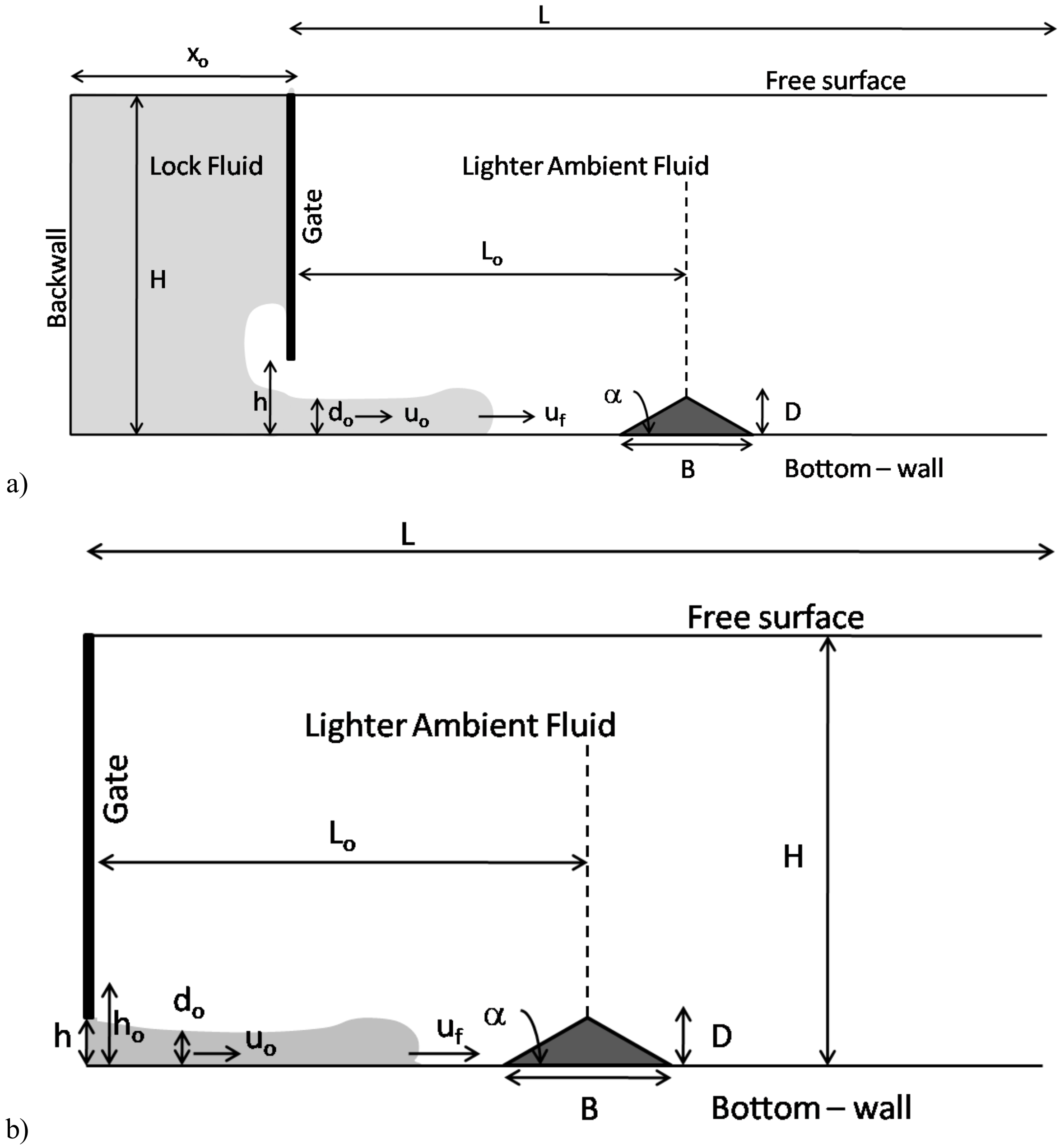
L
x_o
Free surface
Backwall
Lock Fluid
H
Gate
Lighter Ambient Fluid
L_o
h
d_o
u_o
u_f
α
D
B
Bottom – wall
a)
L
Free surface
Gate
Lighter Ambient Fluid
L_o
H
h
h_o
d_o
u_o
u_f
α
D
B
Bottom – wall
b)

Figure 6.1 Sketch of the computational domain used to study the interaction between a bottom propagating gravity current an obstacle (submerged dam). a) lock-exchange gravity current; b) constant-flux gravity current.

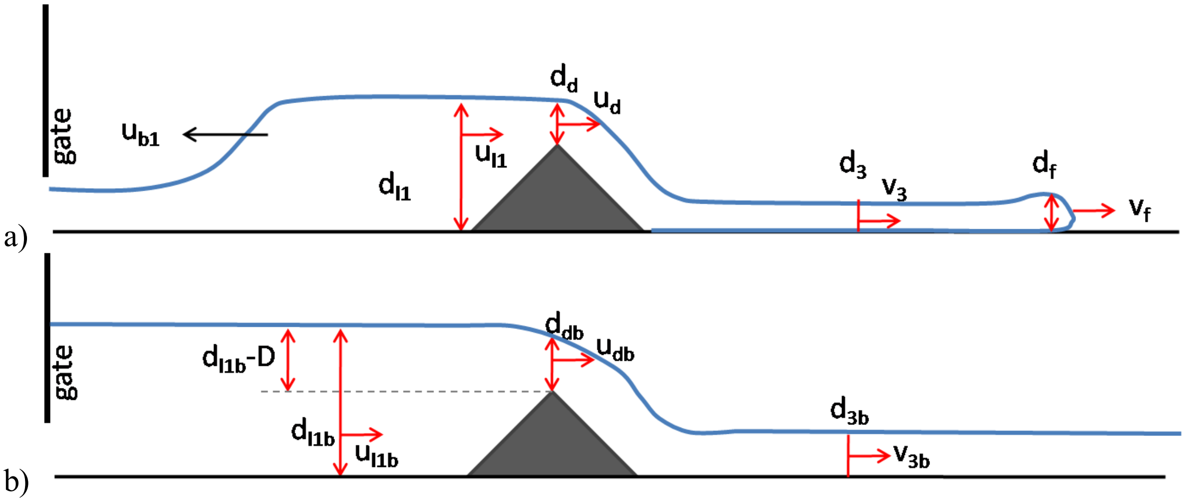
gate
u_b1
d_d
u_d
u_l1
d_l1
d_3
V_3
d_f
V_f
a)
gate
d_l1b-D
d_db
u_db
d_l1b
u_l1b
d_3b
V_3b
b)

Figure 6.2 Sketch of the flow structure during a) the first type of quasi-steady regime (SS1) showing the main flow parameters upstream and downstream of the obstacle and the moving submerged hydraulic jump; b) the second type of quasi-steady regime (SS2) showing the main flow parameters upstream and downstream of the obstacle. The index “b” refers to the values of the variables during SS2.

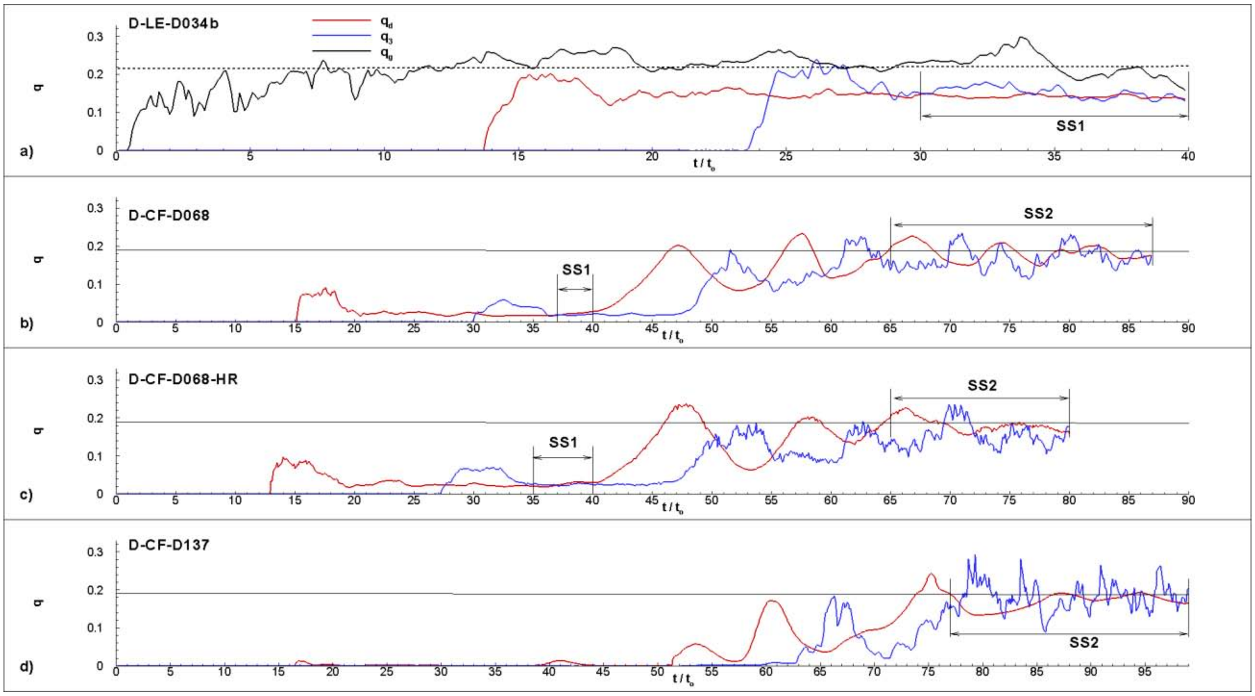

Figure 6.3 Time variation of the non-dimensional discharges at the inlet section (q_g), at the section cutting through the crest of the obstacle (q_d) and at a section situated at about $5h_0$ downstream of the crest of the obstacle (q_3). a) D-LE-D034b; b) D-CF-D068; c) D-CF-D068-HR; d) D-CF-D137. The horizontal lines denote the mean values of q_g during the quasi-steady regimes. In the constant-flux current simulations, q_g is constant in time.

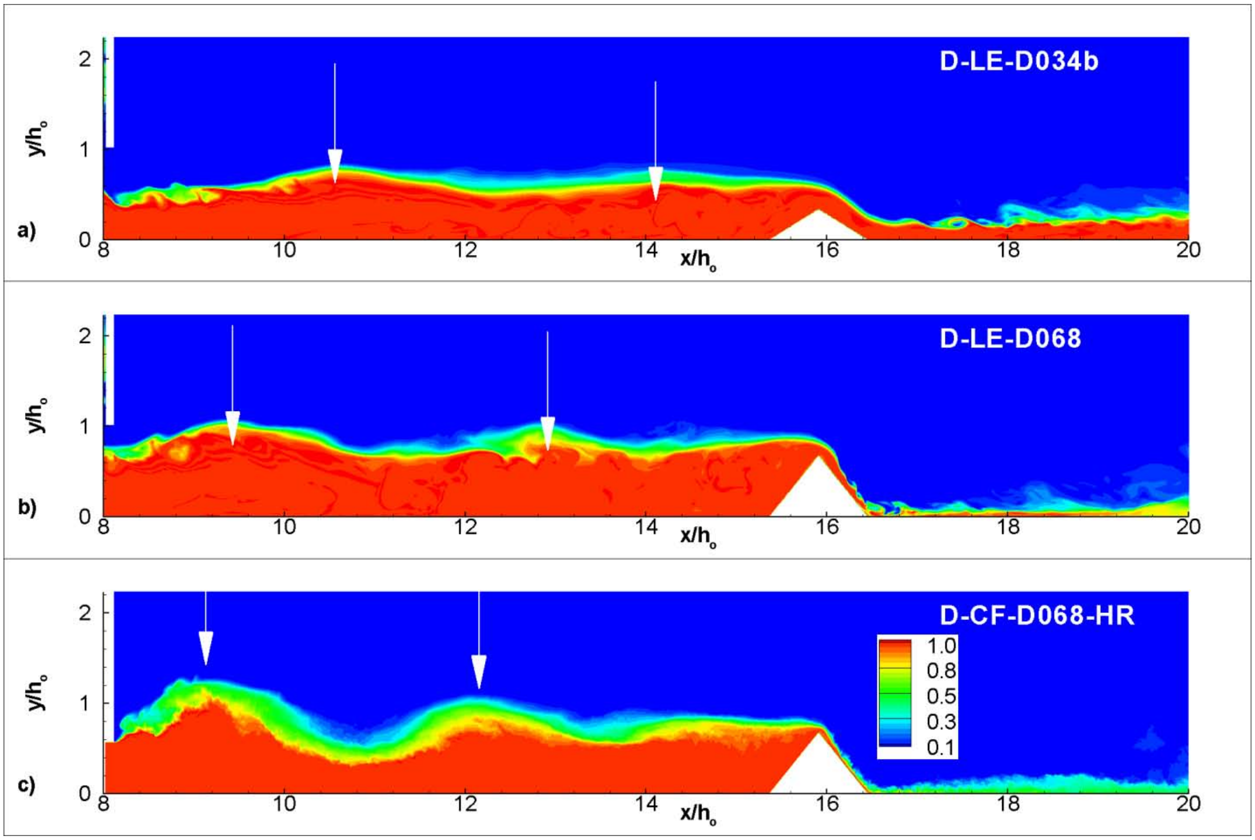

Figure 6.4 Comparison of the shape of the undular bores based on the distribution of the concentration contours near the interface. a) D-LE-D034b; b) D-LE-D068; c) D-CF-D068-HR. The vertical arrows indicate the crest of the first and second waves of the undular bore.

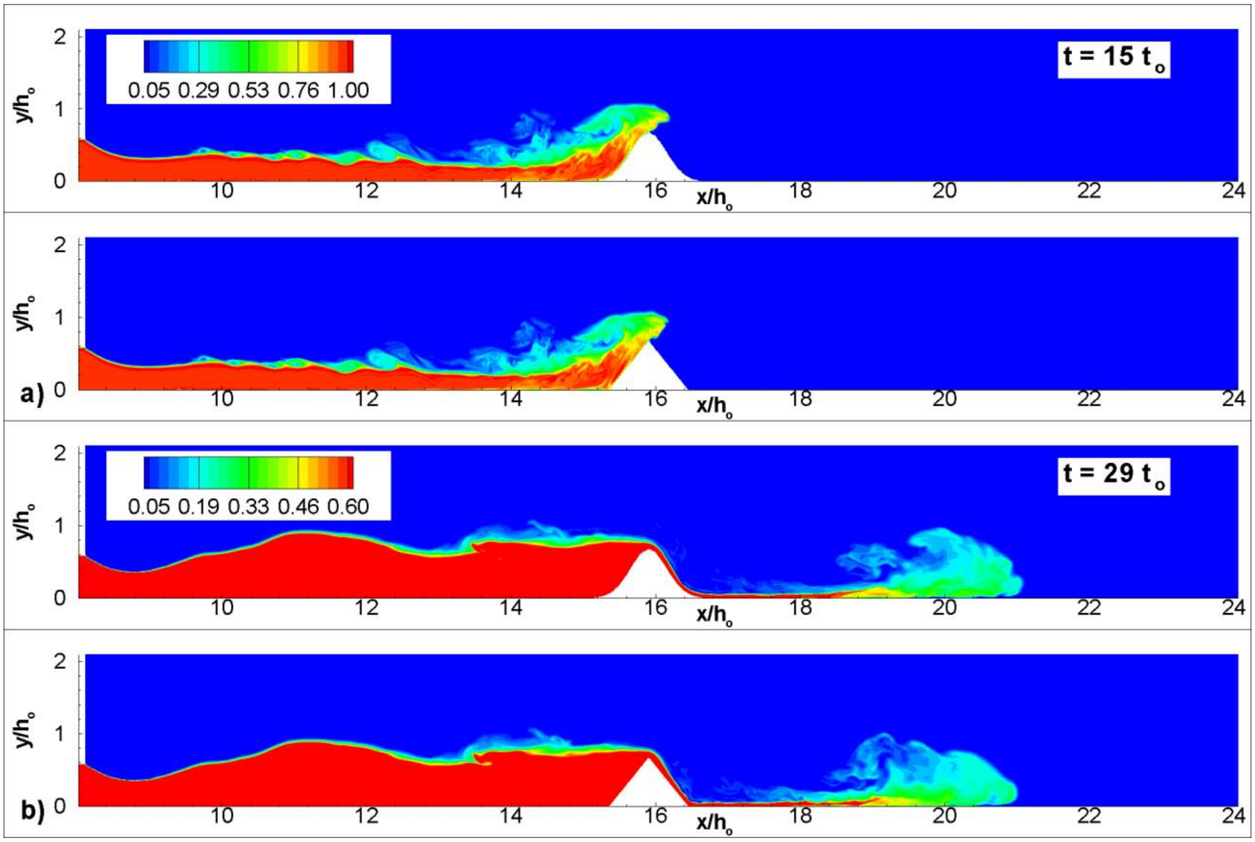

Figure 6.5 Comparison of the structure of the gravity current in the simulations with a triangular obstacle (D-CF-D068) and a Gaussian-shape obstacle of same height (D-CF-D068-G). a) $t=15t_0$; b) $t=29t_0$.

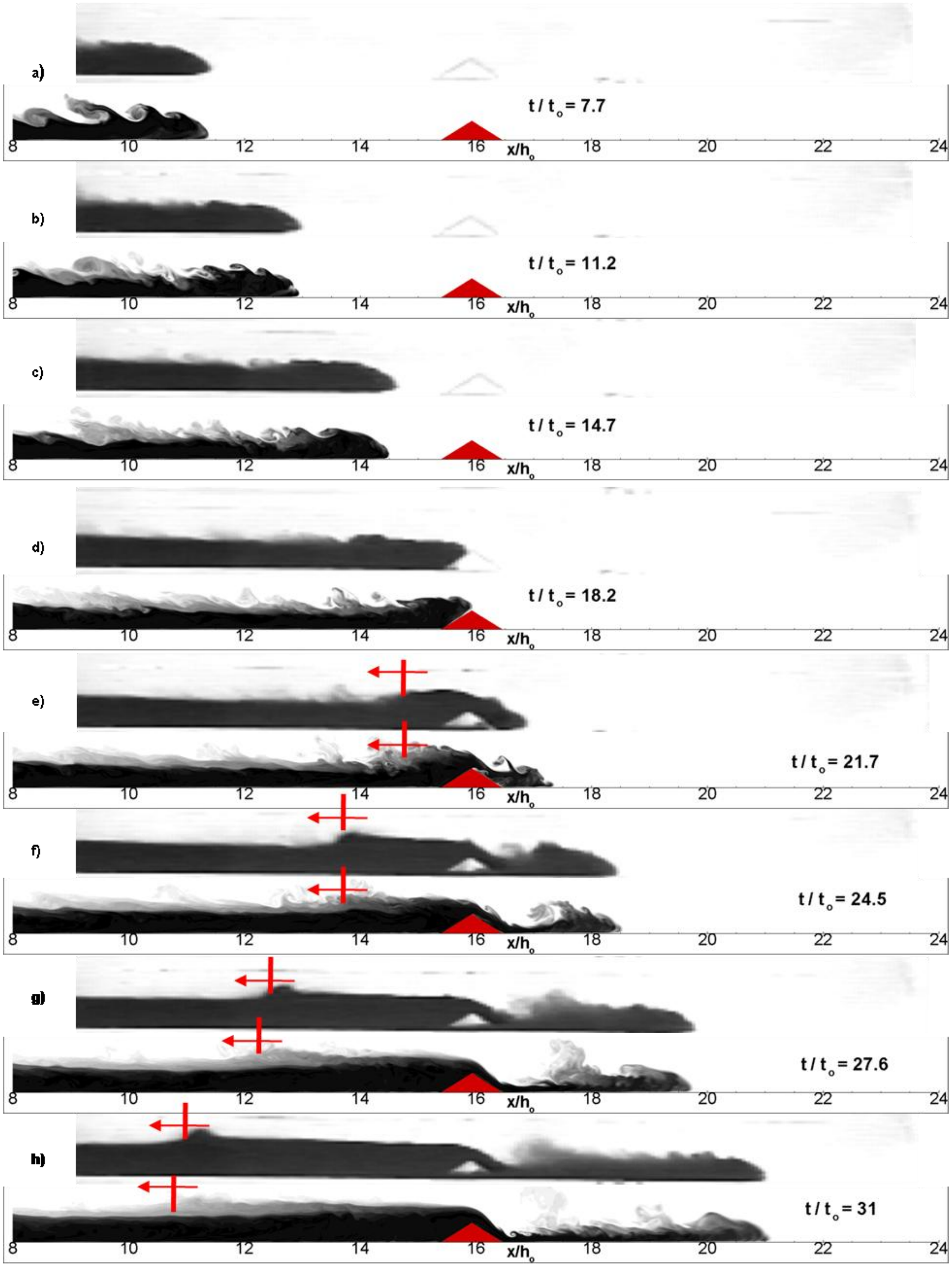

Figure 6.6 Comparison between the evolutions of the gravity current in the experiment (Lane Serff et al., 1995) and LES simulation for case D-LE-D034a. The arrow indicates the position of the front of the bore. The time scale is t_0=0.28 s.

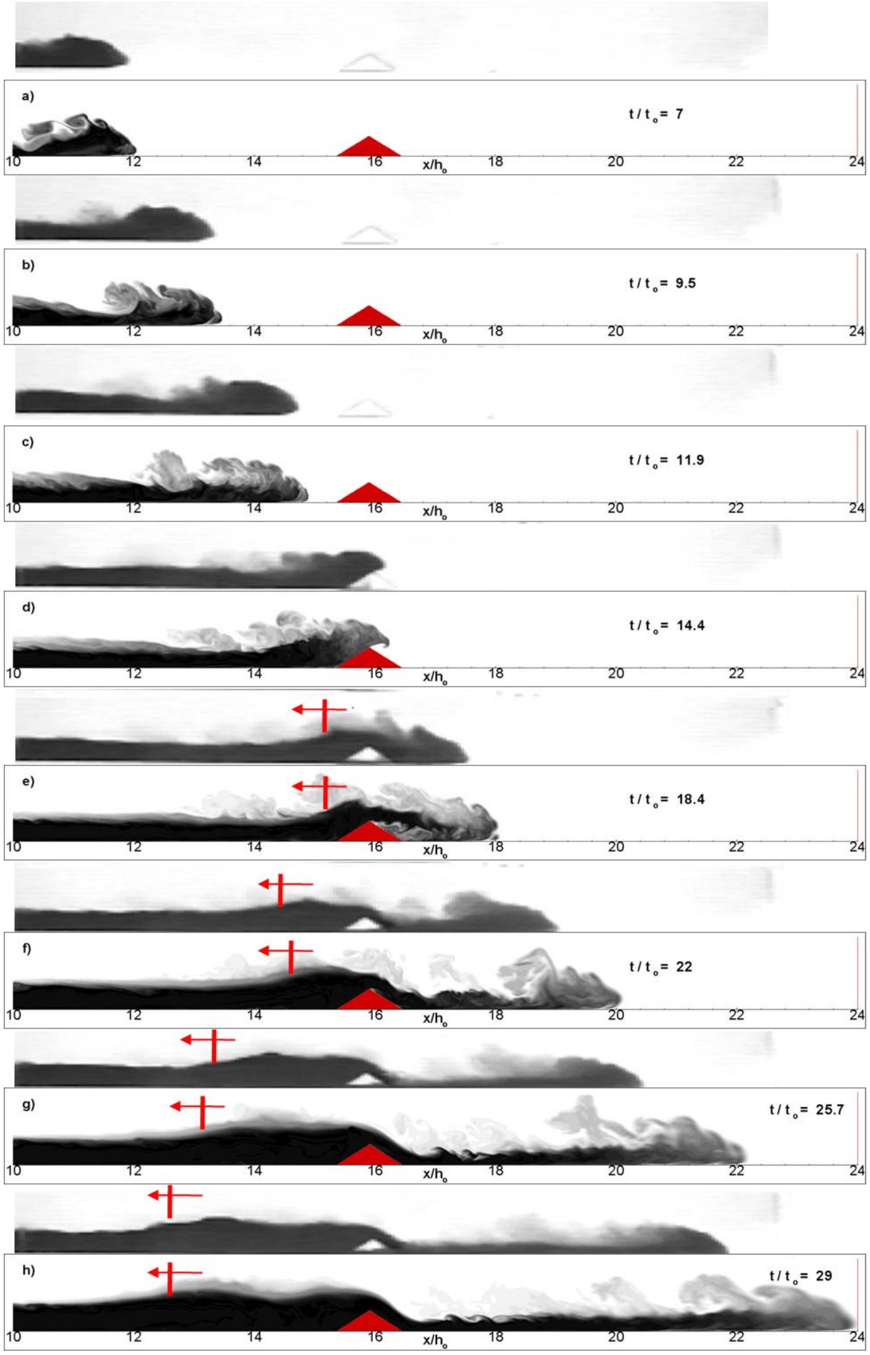

Figure 6.7 Comparison between the evolutions of the gravity current in the experiment (Lane Serff et al., 1995) and LES simulation for case D-LE-D034b. The arrow indicates the position of the front of the bore. The time scale is t_0=0.38 s.

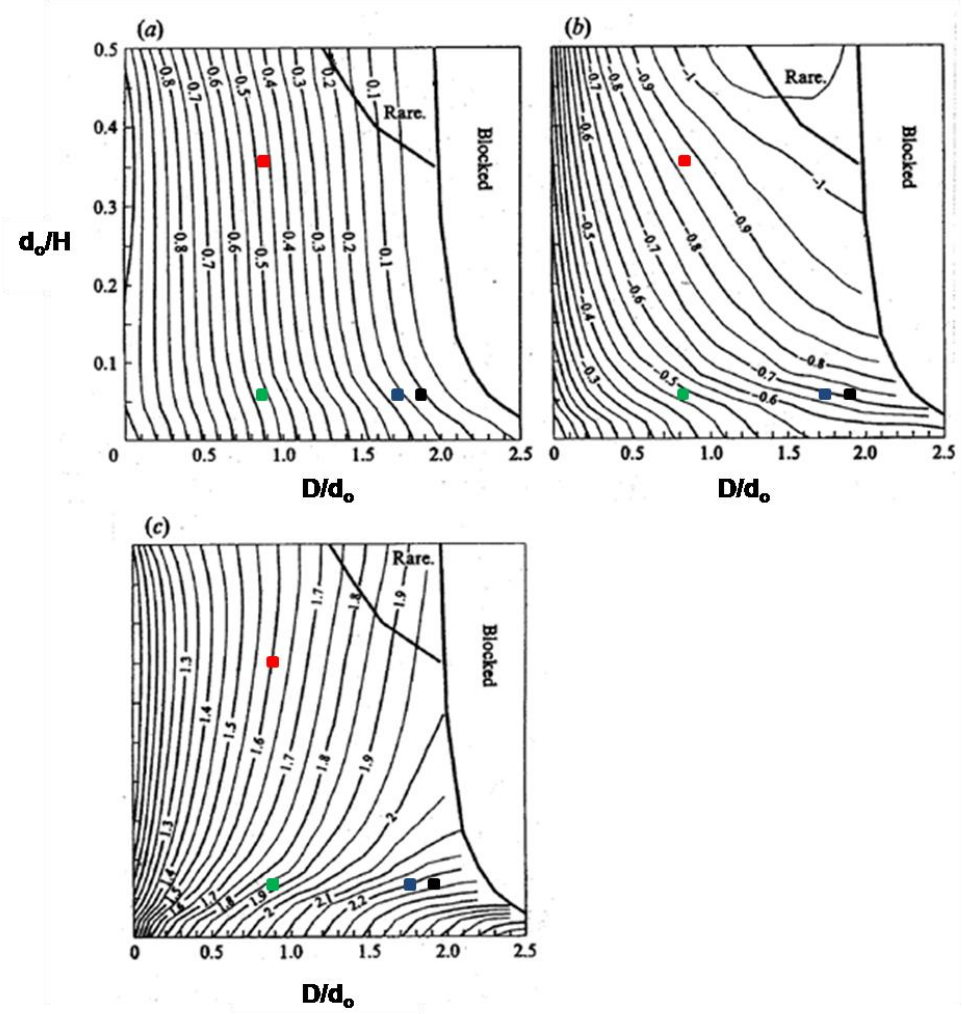

Figure 6.8 Contour plots given by Lane Serff et al. (1995) to predict the main parameters describing the evolution of the flow after the gravity current passes the obstacle. The theoretical model predictions apply during the first type of quasi-steady regime. a) the proportion of the incoming flux over the obstacle, q_d/q_0; b) the ratio of the hydraulic jump velocity to the velocity of the lower layer behind the head of the current, u_{b1}/u_0; c) the ratio of the height of the lower layer behind the hydraulic jump to the height of the undisturbed tail, d_{l1}/d_0. The rectangles correspond to the theoretical model predictions for cases D-LE-D034a (red), D-LE-D034b (green), D-LE-D068 (blue), D-CF-D068 and D-CF-D068-HR (black).

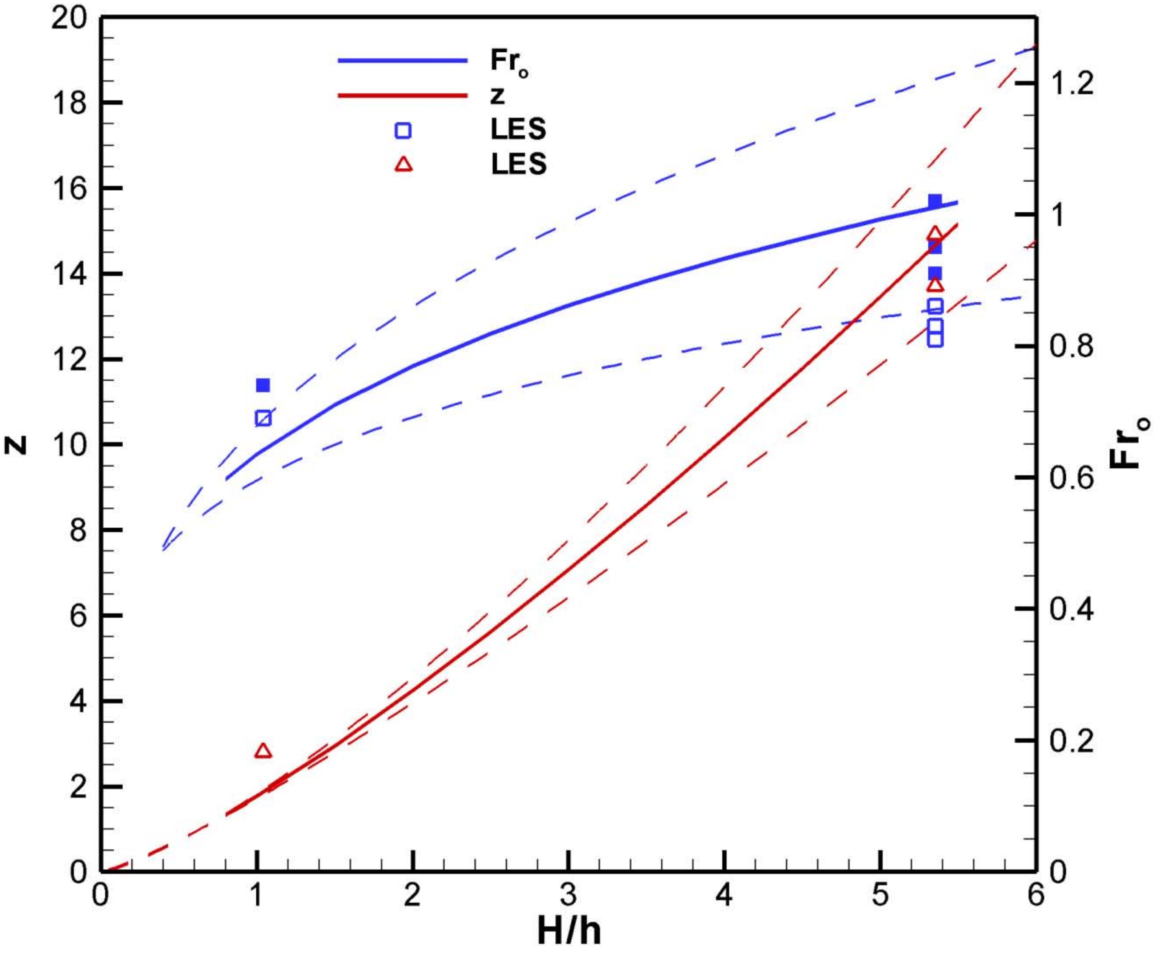

Figure 6.9 Variation of the relative depth of the gravity current, z=H/d$_0$ (red line) and the Froude number of the incoming current, $Fr_0 = u_0 / \sqrt{g' d_0}$ (blue line) based on the experimental data of Lane-Serff et al. (1995). The dashed lines correspond to the upper and lower bound of the variable based on the scatter of the experimental data. The LES predictions of z are shown using red triangles. The LES predictions of $Fr_0 = u_0 / \sqrt{g' d_0}$ are shown using hollow blue rectangles. The LES predictions of $Fr_{0f} = u_f / \sqrt{g' d_0}$ are shown using filled blue rectangles.

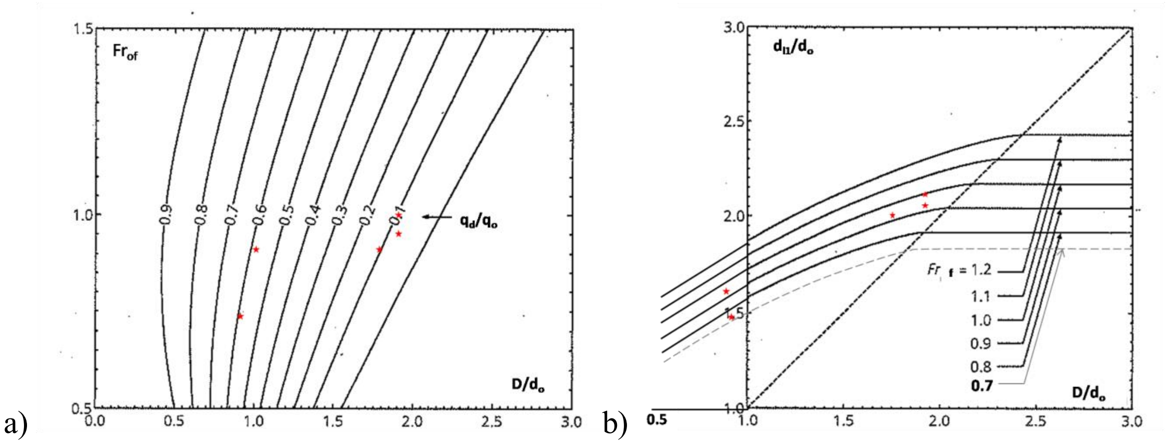

Figure 6.10 Contour plots given by Oehy (2003) to predict the main parameters describing the evolution of the flow after the gravity current passes the obstacle. The theoretical model predictions apply during the first type of quasi-steady regime. a) the proportion of the incoming flux over the obstacle, q_d/q_0; b) the ratio of the height of the lower layer behind the hydraulic jump to the height of the undisturbed tail, d_{l1}/d_0.

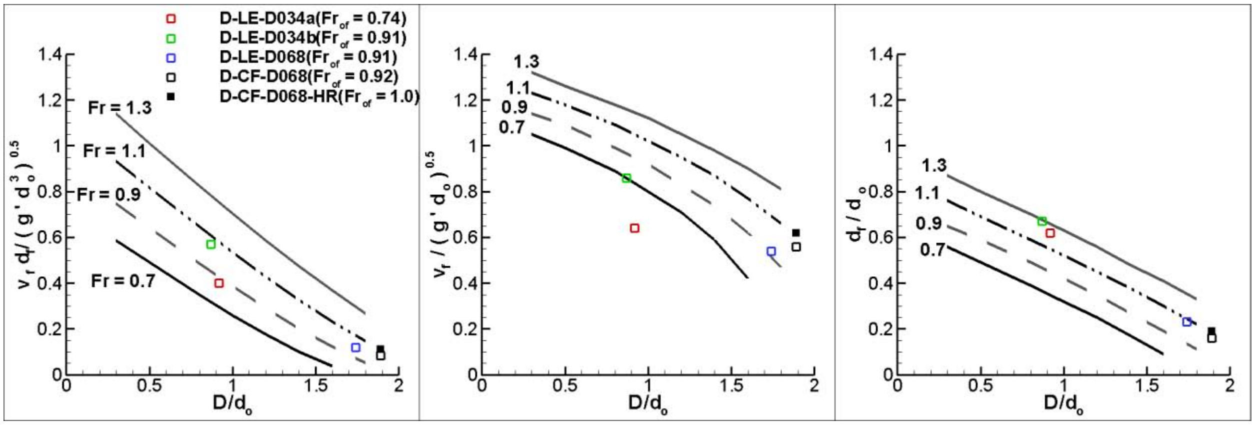

Figure 6.11 Comparison between the predictions given by the theoretical model of Gonzales-Juez and Meiburg (2009) and those of LES. a) nondimensional discharge of the downstream current $v_f d_f / \sqrt{g' d_0^3}$; b) non-dimensional front velocity of the downstream current, $v_f / \sqrt{g' d_0}$; c) non-dimensional height of the lower layer behind the front of the downstream current, d_f/d_0.

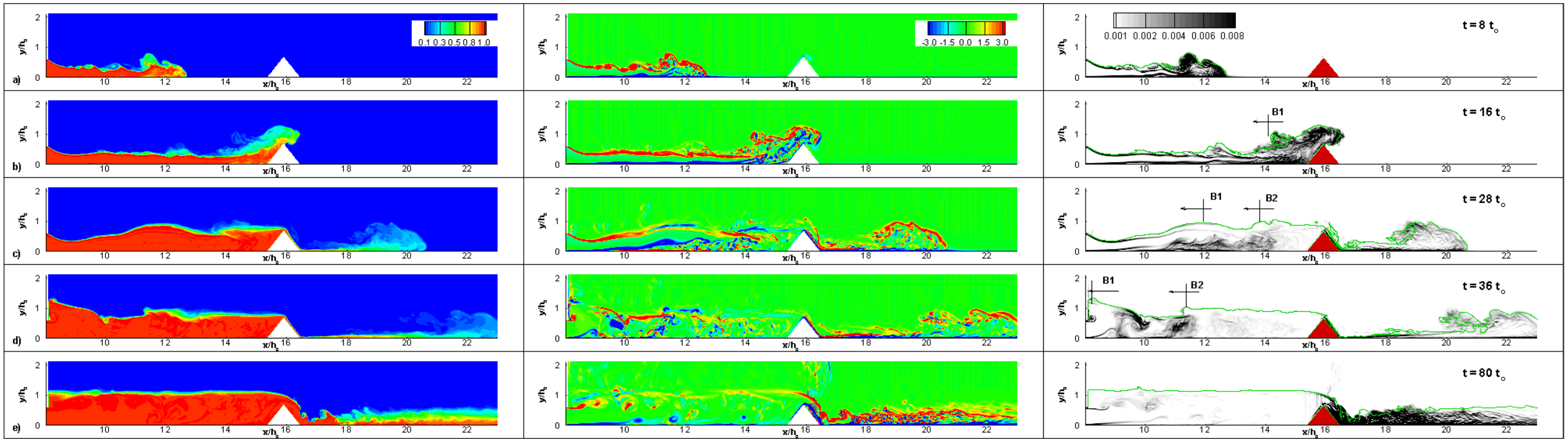

Figure 6.12 Distribution of the concentration, C, out-of-plane vorticity, $\omega_z h_0 / u_b$ and spanwise-averaged local dissipation rate, $\varepsilon_r/(u_b^3 / h_0)$ in the D-CF-D068 simulation. a) $t/t_0=8$; b) $t/t_0=16$; c) $t/t_0=28$; d) $t/t_0=36$; e) $t/t_0=80$. The vertical arrows indicate the position of the crest of the waves of the undular bore.

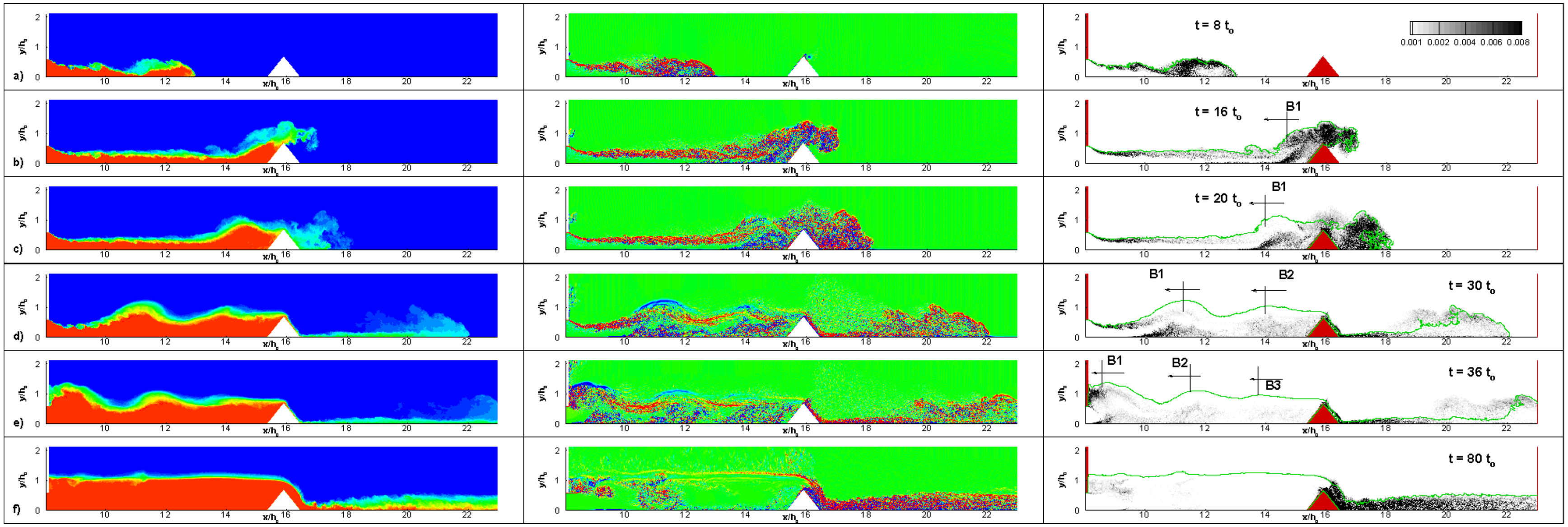

Figure 6.13 Distribution of the concentration, C, out-of-plane vorticity, $\omega_z h_0 / u_b$ and spanwise-averaged local dissipation rate, $\varepsilon_r/(u_b^3/h_0)$ in the D-CF-D068-HR simulation. a) $t/t_0=8$; b) $t/t_0=16$; c) $t/t_0=20$; d) $t/t_0=30$; e) $t/t_0=36$; f) $t/t_0=80$. The vertical arrows indicate the position of the crest of the waves of the undular bore.

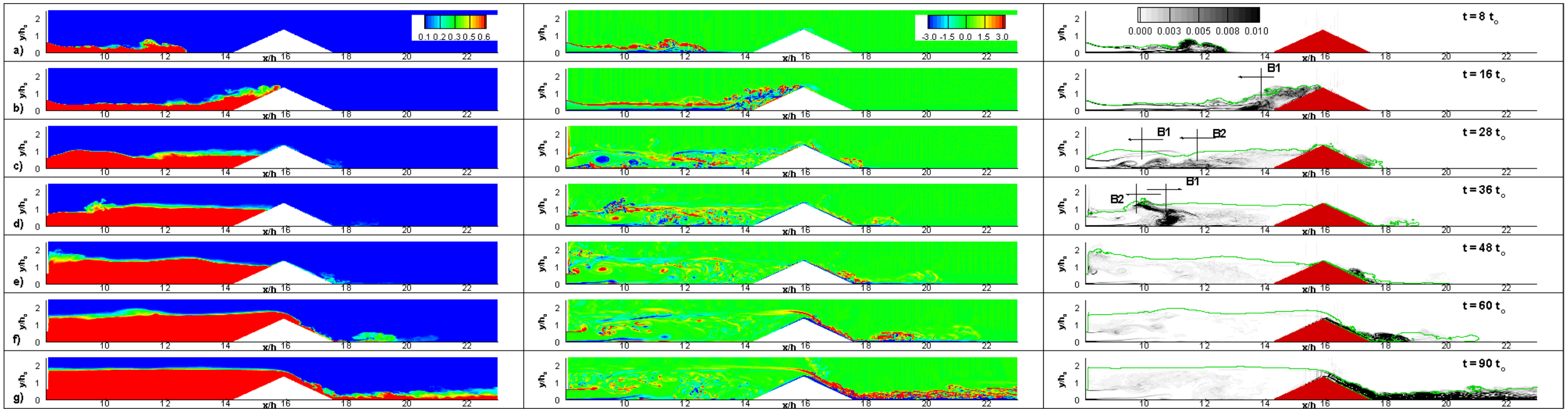

Figure 6.14 Distribution of the concentration, C, out-of-plane vorticity, $\omega_z h_0 / u_b$ and spanwise-averaged local dissipation rate, $\varepsilon_r/(u_b^3 / h_0)$ in the D-CF-D137 simulation. a) $t/t_0=8$; b) $t/t_0=16$; c) $t/t_0=28$; d) $t/t_0=36$; e) $t/t_0=48$; f) $t/t_0=60$; g) $t/t_0=90$. The vertical arrows indicate the position of the crest of the waves of the undular bore.

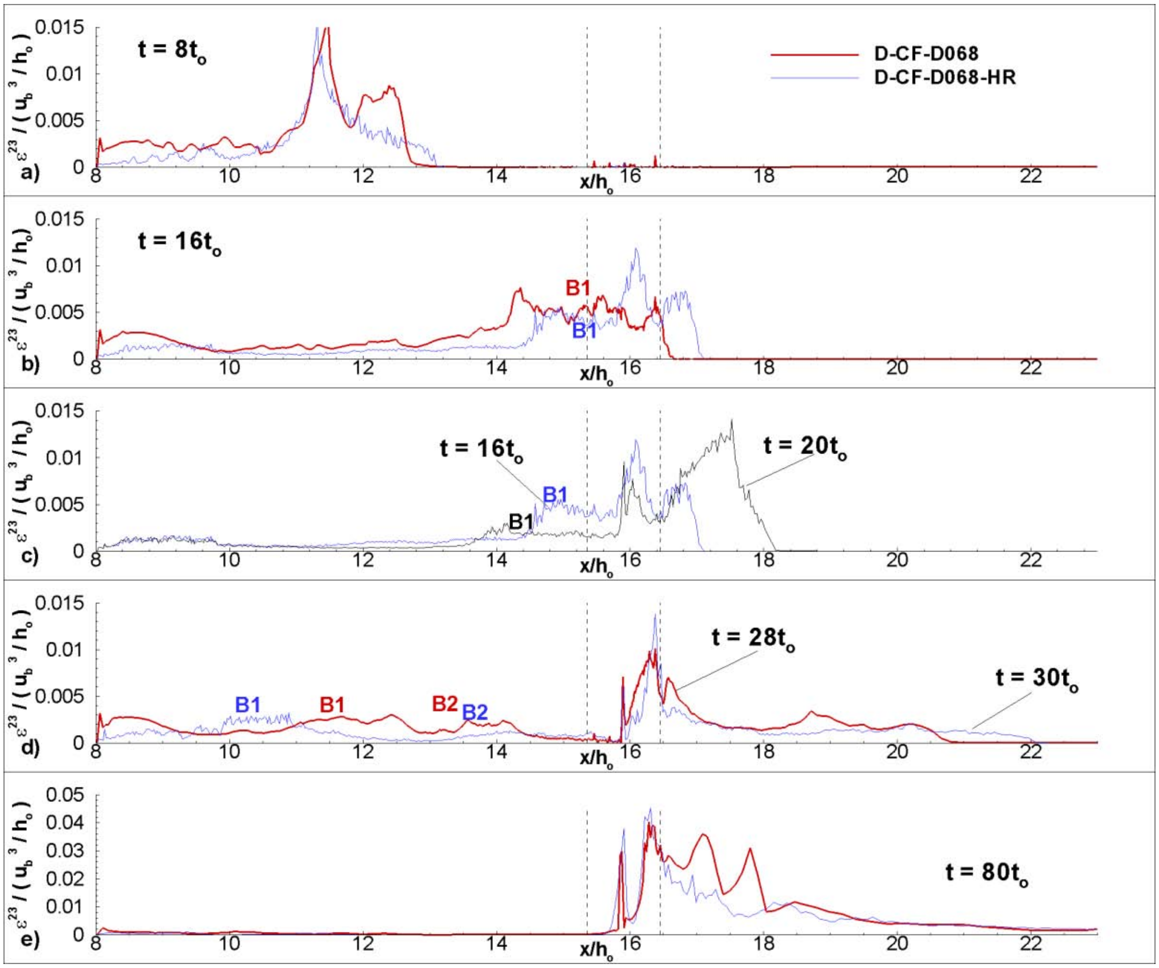

Figure 6.15 Streamwise distributions of $\varepsilon^{23}(x_1)/(u_b^3 h_0)$ in the D-CF-D068 (red line) and D-CF-D068-HR (blue line) simulations. B1 and B2 mark the regions of large dissipation induced by the passage of the waves of the undular bore.

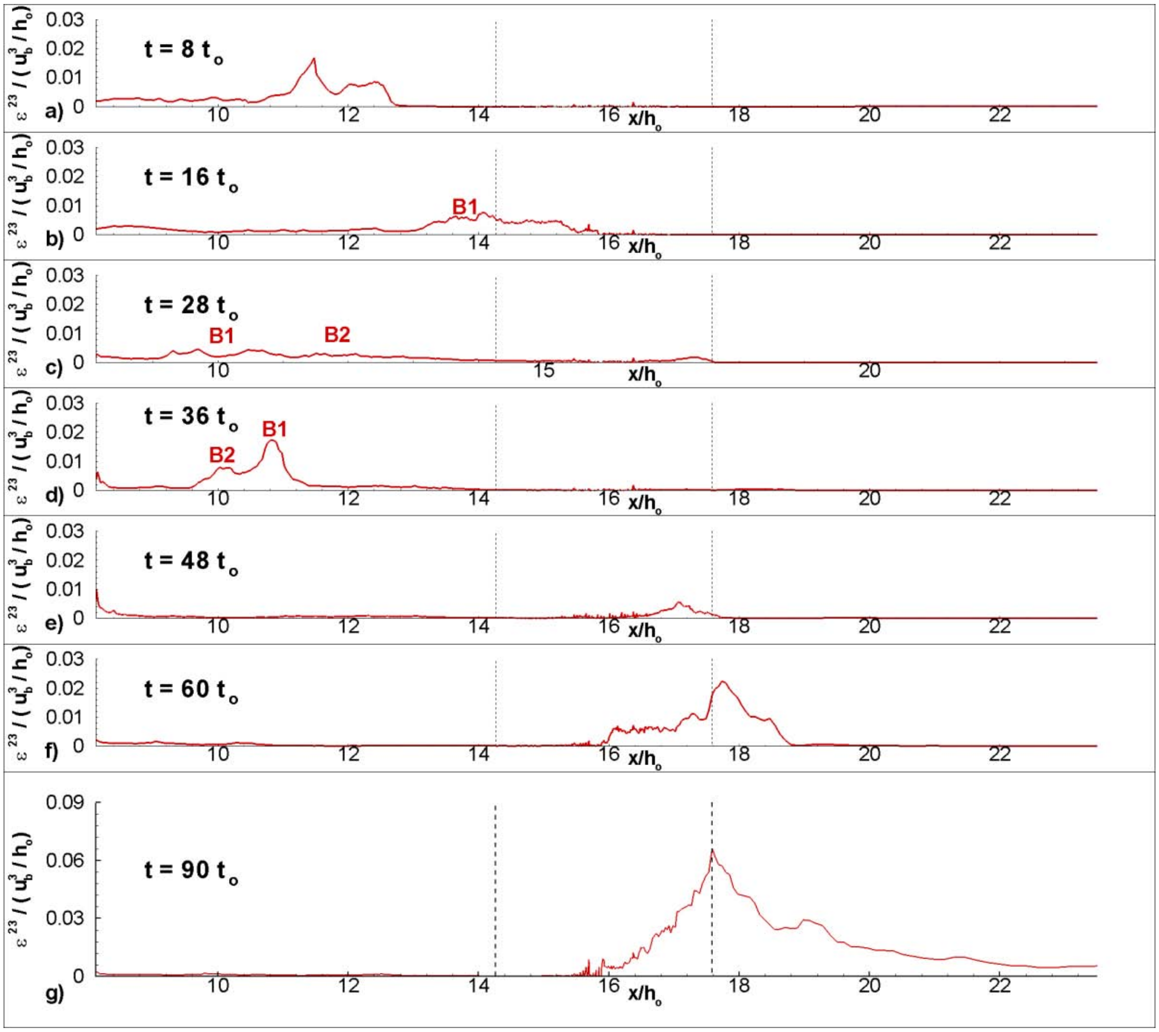

Figure 6.16 Streamwise distributions of $\varepsilon^{23}(x_1)/(u_b^3 h_0)$ in the D-CF-D137 simulation. B1 and B2 mark the regions of large dissipation induced by the passage of the waves of the undular bore. a) t/t_0=8; b) t/t_0=16; c) t/t_0=28; d) t/t_0=36; e) t/t_0=48; f) t/t_0=60; g) t/t_0=90.

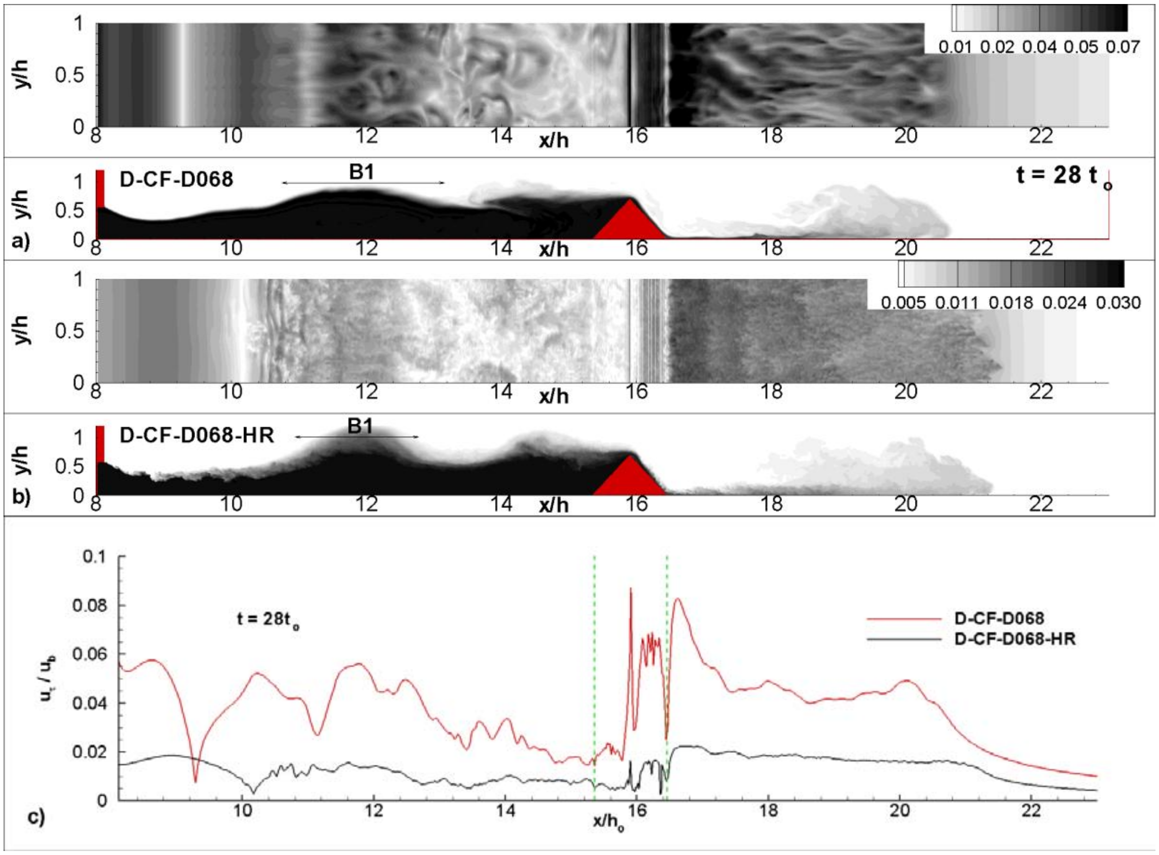

Figure 6.17 Comparison of the spatial distributions of the bed friction velocity u_τ/u_b after the current has passed the obstacle ($t=28t_0$) in the D-CF-D068 (a) and the D-CF-D068-HR (b) simulations during SS1. Also shown are the concentration contours in an x-y section. The aspect ratio is 1:2 in the x-y plot. Frame c shows the comparison of the streamwise distributions of the spanwise-averaged bed friction velocity in the two simulations at $t=28t_0$.

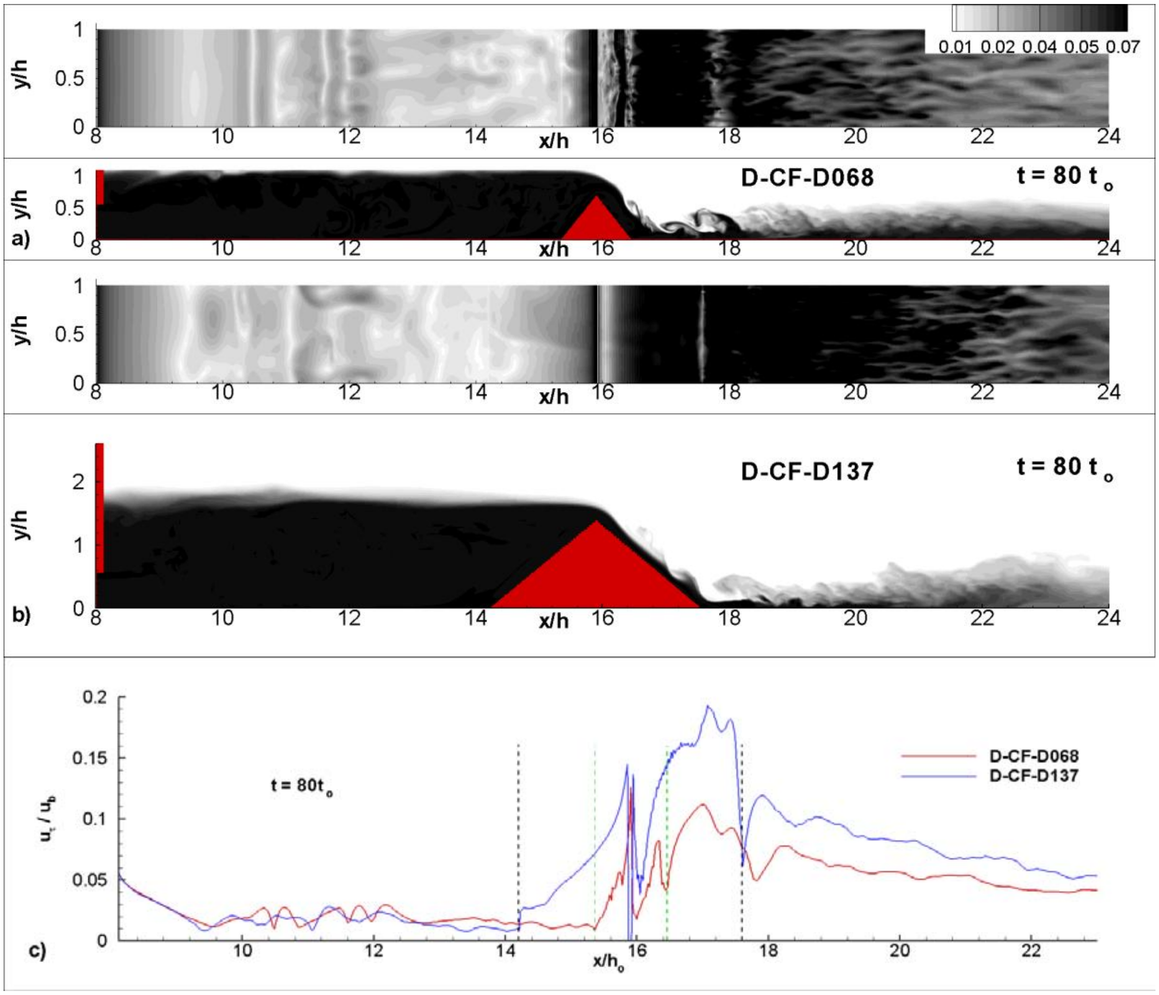

Figure 6.18 Comparison of the spatial distributions of the bed friction velocity u_τ/u_b after the current has passed the obstacle ($t=80t_0$) in the D-CF-D068 (a) and D-CF-D137 (b) simulations, during SS2. Also shown are the concentration contours in an x-y section. The aspect ratio is 1:2 in the x-y plot. Frame c shows the comparison of the streamwise distributions of the spanwise-averaged bed friction velocity in the two simulations at $t=80t_0$.

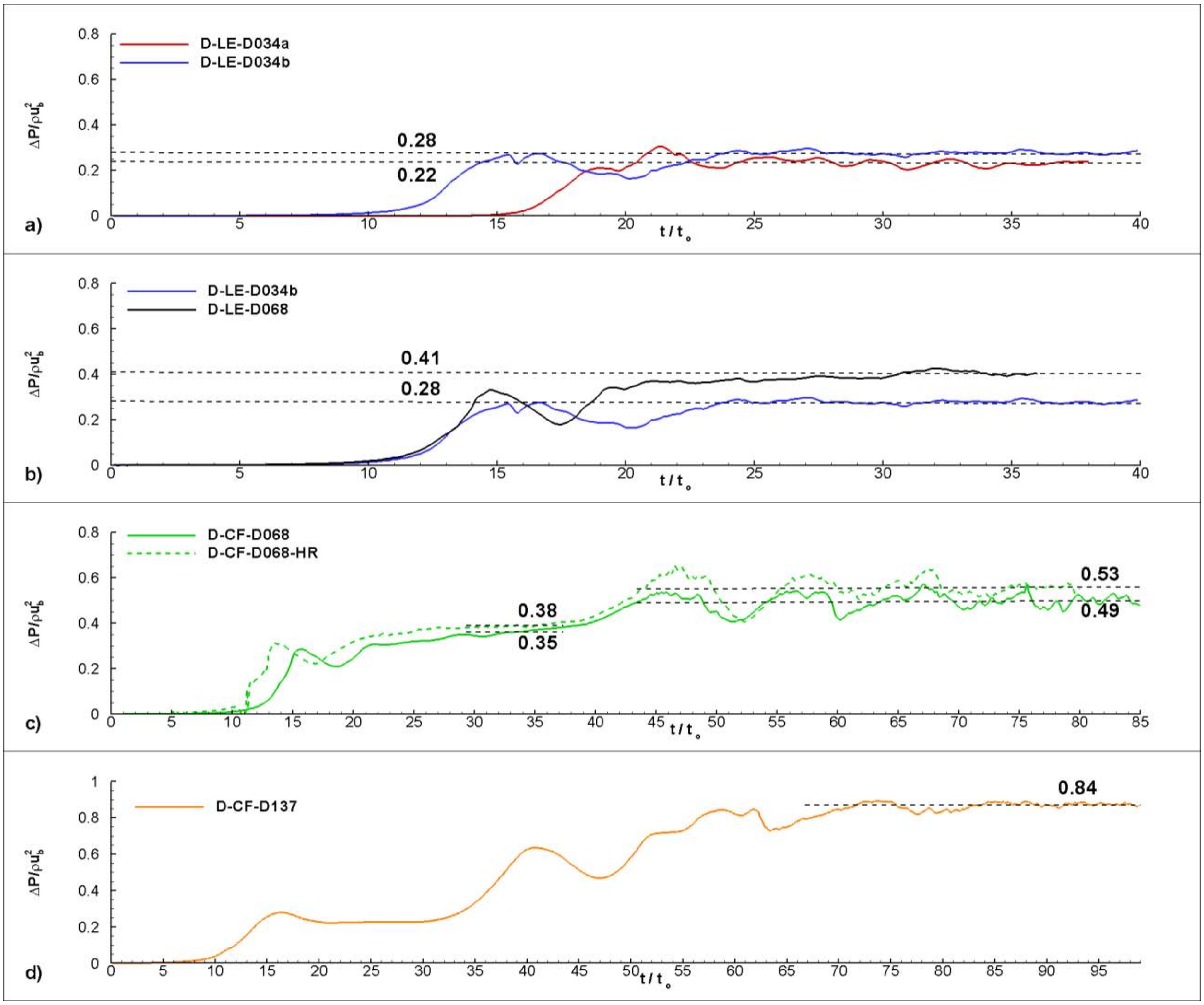

Figure 6.19 Time variation of the mean pressure difference (streamwise drag force divided by the obstacle height) between the upstream and downstream faces of the obstacle, $\Delta P/\rho u_b^2$. a) D-LE-D034a vs. D-LE-D034b; b) D-LE-D034b vs. D-LE-D068; c) D-CF-D068 vs. D-CF-D068-HR; d) D-CF-D137.

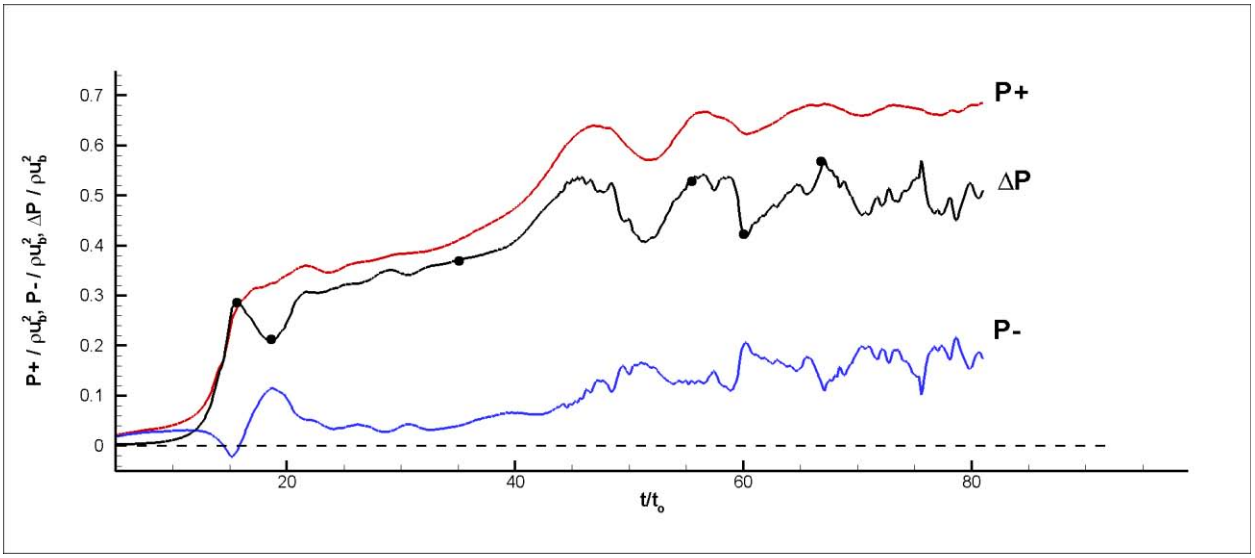

Figure 6.20 Time variations of the mean pressure on the upstream face of the obstacle, P$^+$/ ρu_b^2, mean pressure on the downstream face of the obstacle, P$^-$/ ρu_b^2, and mean pressure difference between the upstream and downstream faces of the obstacle, ΔP/ ρu_b^2, in the D-CF-D068 simulation.

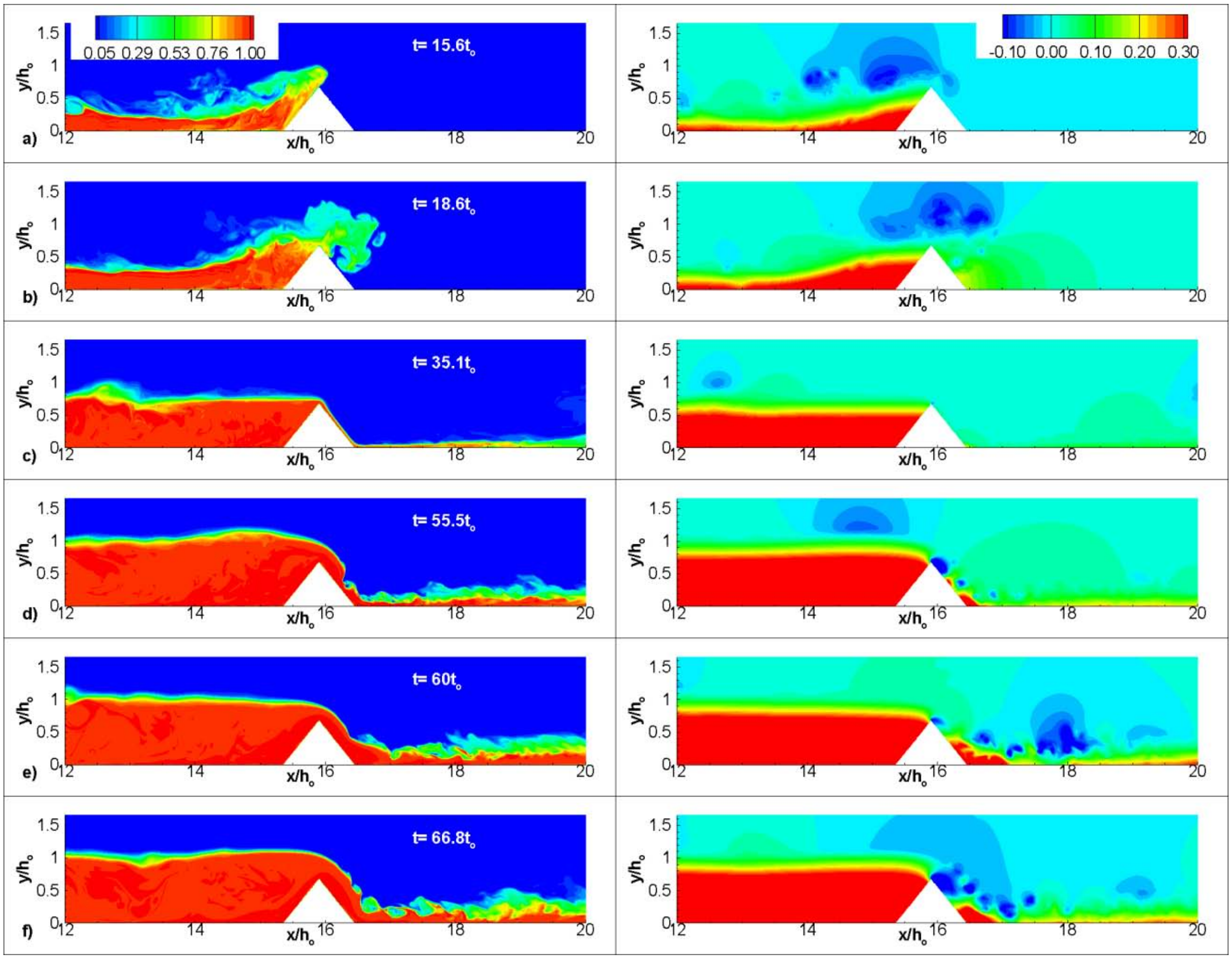

Figure 6.21 Contour plots showing the concentration, C, (left) and piezometric pressure, $p/\rho u_b^2$, (right) distributions in a vertical x-y plane around the obstacle in the D-CF-D068 simulation at representative time instants. a) t=15.6t$_0$; b) t=18.6t$_0$; c) t=35.1t$_0$; d) t=55.5t$_0$; e) t=60t$_0$; f) t=68.8t$_0$.

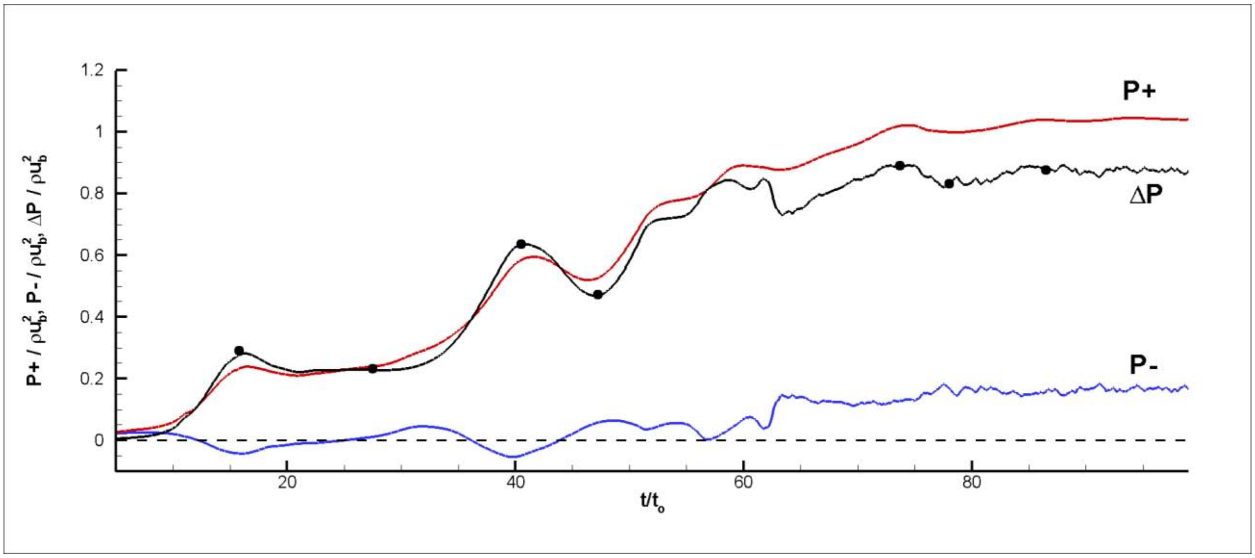

Figure 6.22 Time variations of the mean pressure on the upstream face of the obstacle, P$^+$/ ρu_b^2, mean pressure on the downstream face of the obstacle, P$^-$/ ρu_b^2, and mean pressure difference between the upstream and downstream faces of the obstacle, ΔP/ ρu_b^2, in the D-CF-D137 simulation.

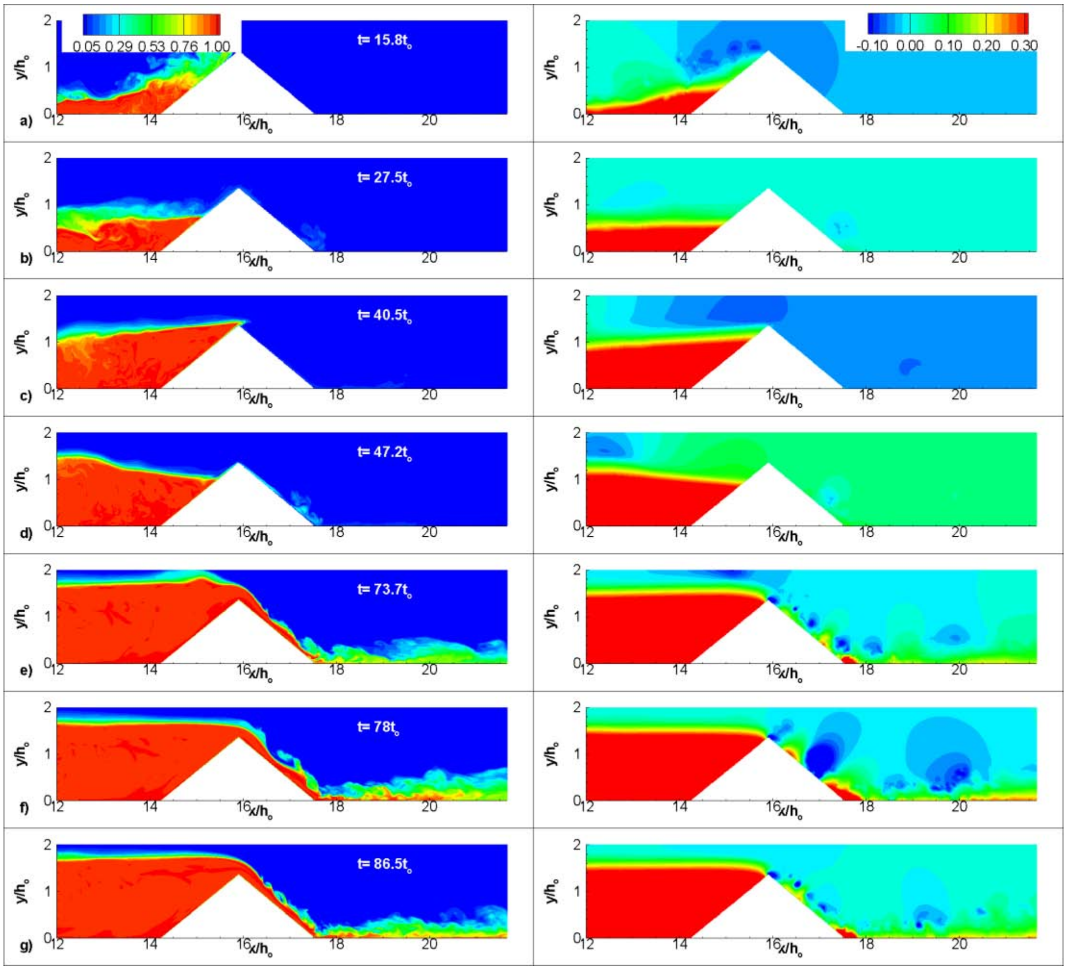

Figure 6.23 Contour plots showing the distribution of the concentration, C, (left) and piezometric pressure, $p/\rho u_b^2$, (right) in a vertical x-y plane around the obstacle in the D-CF-D137 simulation at representative time instants. a) $t=15.8t_0$; b) $t=27.5t_0$; c) $t=40.5t_0$; d) $t=47.2t_0$; e) $t=73.7t_0$; f) $t=78t_0$; g) $t=86.5t_0$.

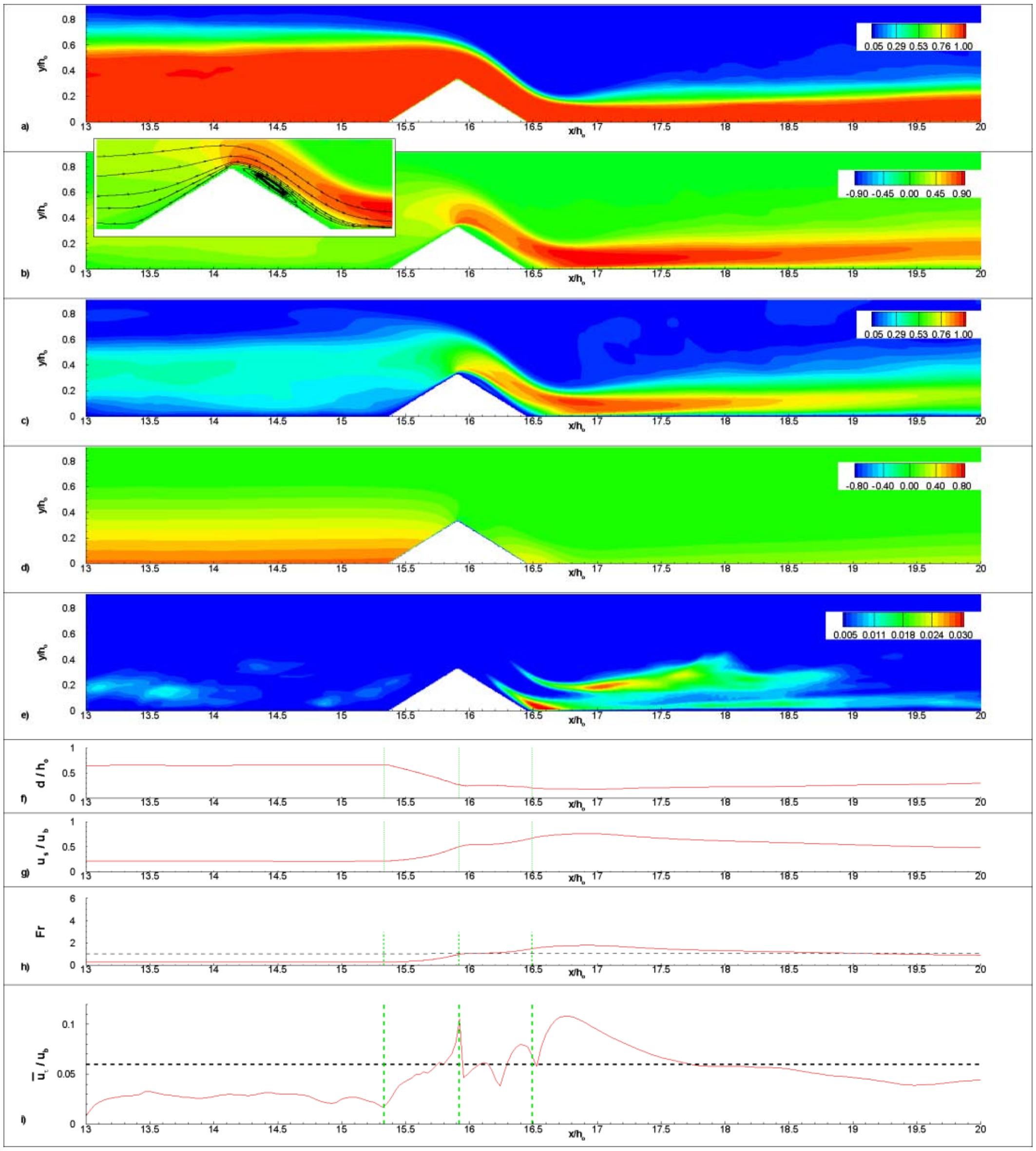

Figure 6.24 Contour and line plots showing the structure of the mean flow around the obstacle during SS1 in the D-LE-D034b simulation. a) concentration, C; b) streamwise velocity, u_x / u_b; c) velocity magnitude, u_{mag}/u_b; d) piezometric pressure $p/\rho u_b^2$; e) turbulent kinetic energy k/u_b^2; f) depth of the lower layer, d/h_0; g) mean streamwise (with respect to the bottom surface) velocity in the lower layer, u_s/u_b; h) Froude number of the flow in the lower layer, Fr; i) bed friction velocity, $\bar{u}_\tau / u_b$. The dashed line in frame i corresponds to $\bar{u}_\tau / u_b$=0.06.

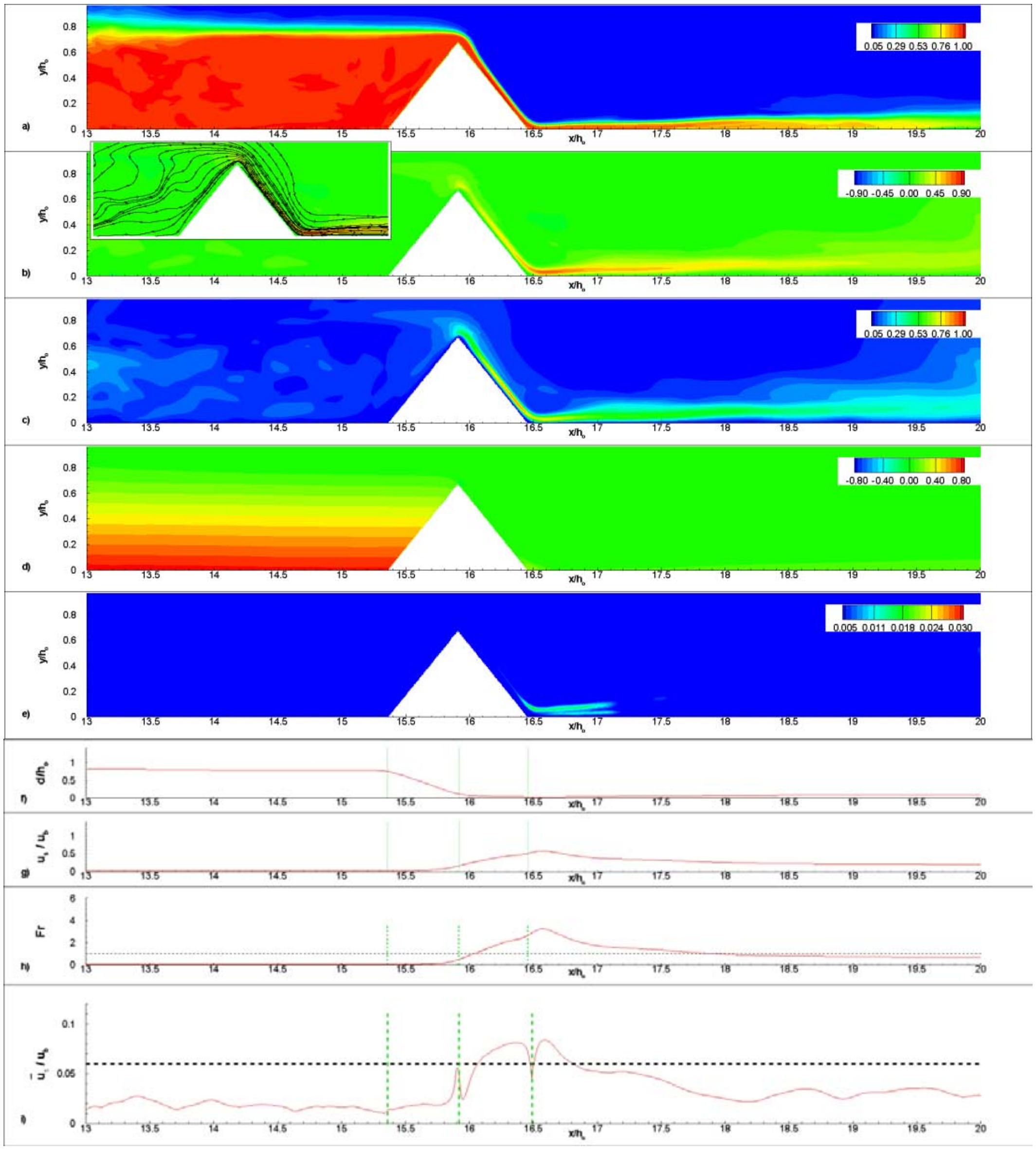

Figure 6.25 Contour and line plots showing the structure of the mean flow around the obstacle during SS1 in the D-CF-D068 simulation. a) concentration, C; b) streamwise velocity, u_x/u_b; c) velocity magnitude, u_{mag}/u_b; d) piezometric pressure $p/\rho u_b^2$; e) turbulent kinetic energy k/u_b^2; f) depth of the lower layer, d/h_0; g) mean streamwise (with respect to the bottom surface) velocity in the lower layer, u_s/u_b; h) Froude number of the flow in the lower layer, Fr; i) bed friction velocity, $\bar{u}_\tau/u_b$. The dashed line in frame i corresponds to $\bar{u}_\tau/u_b$=0.06.

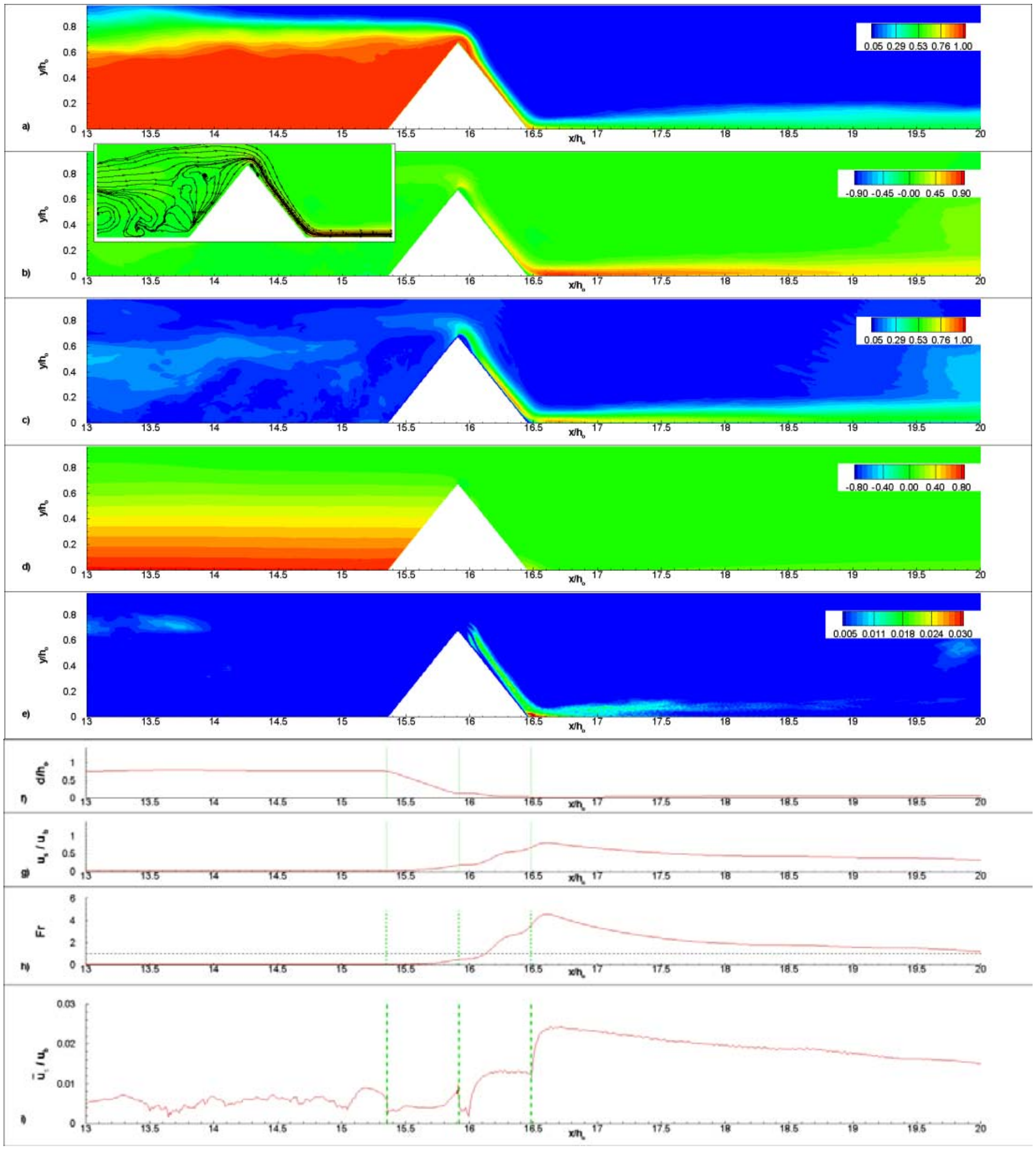

Figure 6.26 Contour and line plots showing the structure of the mean flow around the obstacle during SS1 in the D-CF-D068-HR simulation. a) concentration, C; b) streamwise velocity, u_x/u_b; c) velocity magnitude, u_{mag}/u_b; d) piezometric pressure $p/\rho u_b^2$; e) turbulent kinetic energy k/u_b^2; f) depth of the lower layer, d/h_0; g) mean streamwise (with respect to the bottom surface) velocity in the lower layer, u_s/u_b; h) Froude number of the flow in the lower layer, Fr; i) bed friction velocity, $\bar{u}_\tau/u_b$. The dashed line in frame i corresponds to $\bar{u}_\tau/u_b$=0.06.

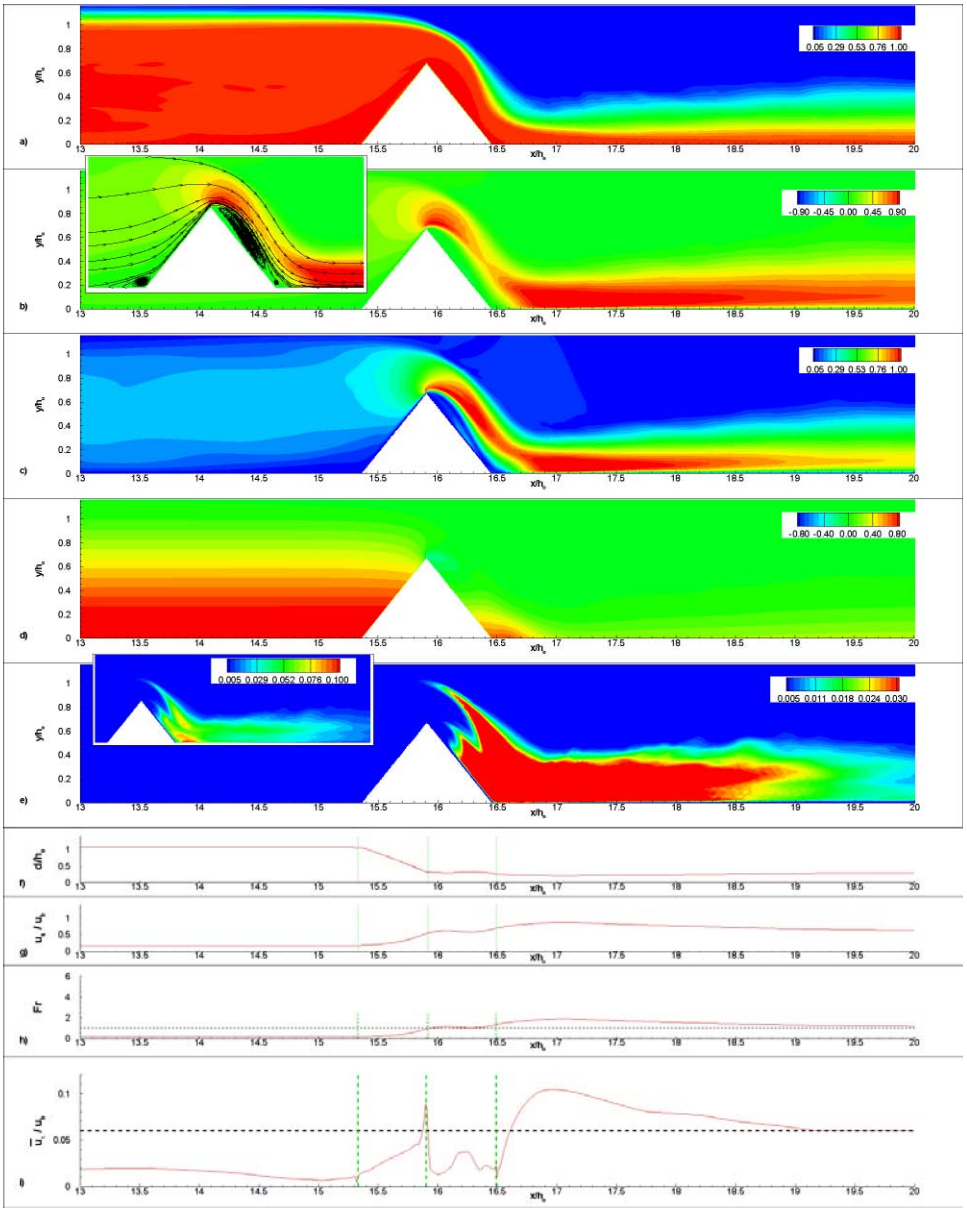

Figure 6.27 Contour and line plots showing the structure of the mean flow around the obstacle during SS2 in the D-CF-D068 simulation. a) concentration, C; b) streamwise velocity, u_x / u_b; c) velocity magnitude, u_{mag}/u_b; d) piezometric pressure $p/\rho u_b^2$; e) turbulent kinetic energy k/u_b^2; f) depth of the lower layer, d/h_0; g) mean streamwise (with respect to the bottom surface) velocity in the lower layer, u_s/u_b; h) Froude number of the flow in the lower layer, Fr; i) bed friction velocity, $\bar{u}_\tau / u_b$. The dashed line in frame i corresponds to $\bar{u}_\tau / u_b$ =0.06.

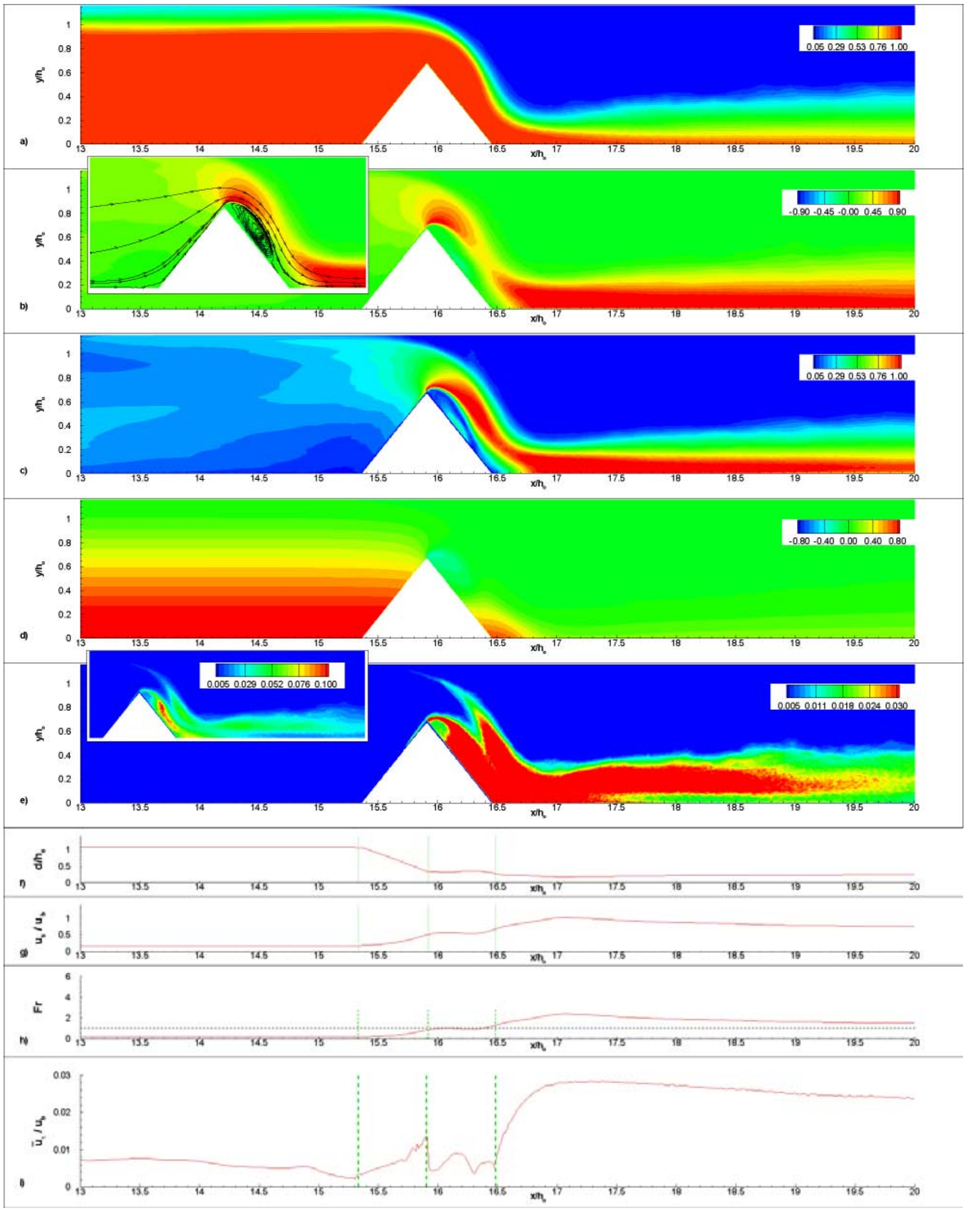

Figure 6.28 Contour and line plots showing the structure of the mean flow around the obstacle during SS2 in the D-CF-D068-HR simulation. a) concentration, C; b) streamwise velocity, u_x / u_b; c) velocity magnitude, u_{mag}/u_b; d) piezometric pressure $p/ \rho u_b^2$; e) turbulent kinetic energy k/ u_b^2; f) depth of the lower layer, d/h_0; g) mean streamwise (with respect to the bottom surface) velocity in the lower layer, u_s/u_b; h) Froude number of the flow in the lower layer, Fr; i) bed friction velocity, $\bar{u}_\tau / u_b$. The dashed line in frame i corresponds to $\bar{u}_\tau / u_b$ =0.06.

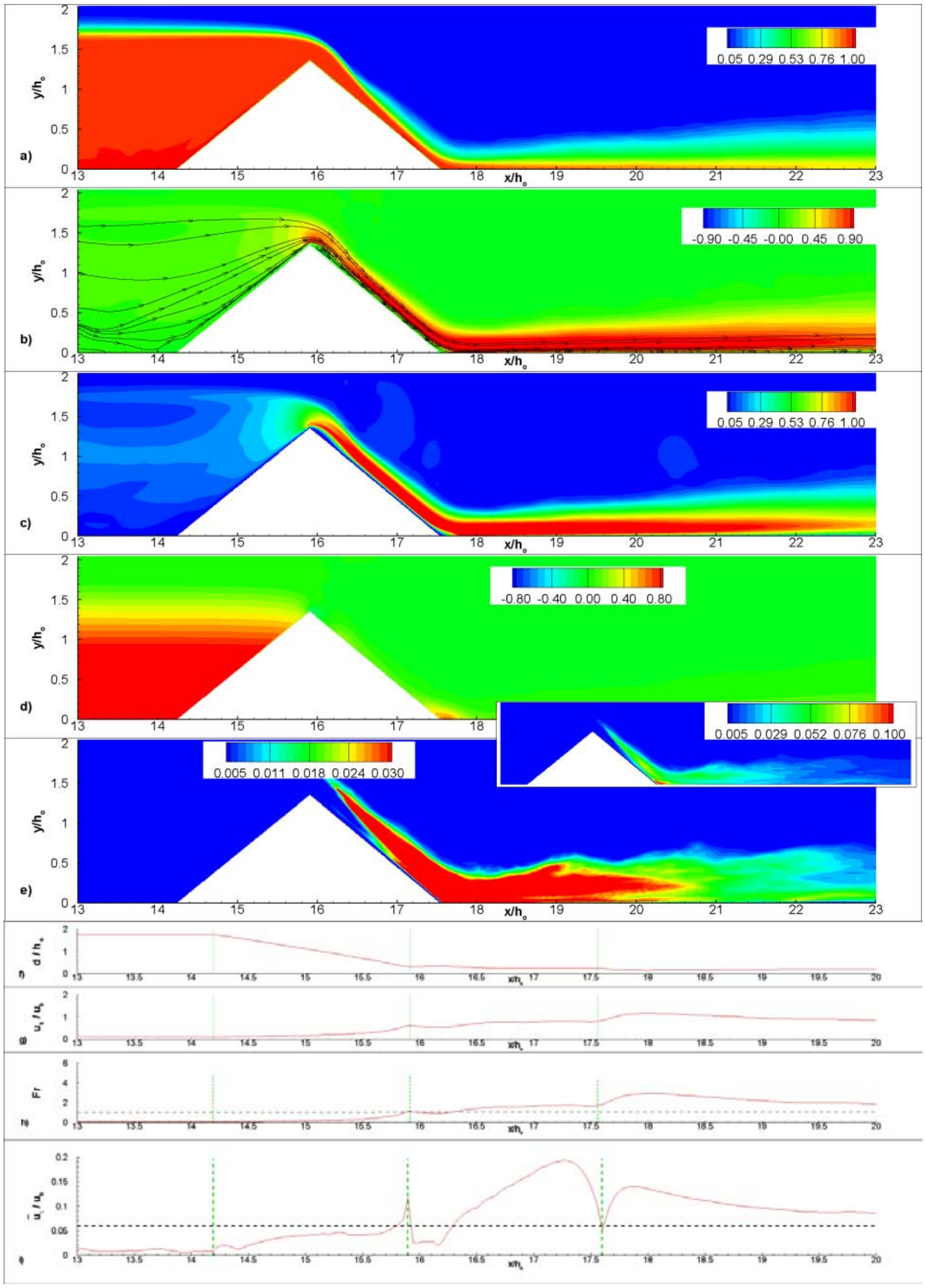

Figure 6.29 Contour and line plots showing the structure of the mean flow around the obstacle during SS2 in the D-CF-D137 simulation. a) concentration, C; b) streamwise velocity, u_x/u_b; c) velocity magnitude, u_{mag}/u_b; d) piezometric pressure $p/\rho u_b^2$; e) turbulent kinetic energy k/u_b^2; f) depth of the lower layer, d/h_0; g) mean streamwise (with respect to the bottom surface) velocity in the lower layer, u_s/u_b; h) Froude number of the flow in the lower layer, Fr; i) bed friction velocity, $\bar{u}_\tau/u_b$. The dashed line in frame i corresponds to $\bar{u}_\tau/u_b$=0.06.

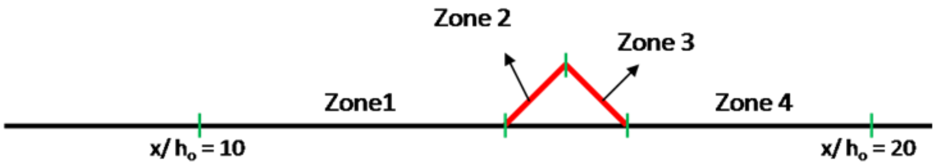

Figure 6.30 Sketch showing the extent of the four zones over which the flux of sediment entrained from the bed surface over surface i, $F_i(t)$, is estimated using van Rijn‟s formula.

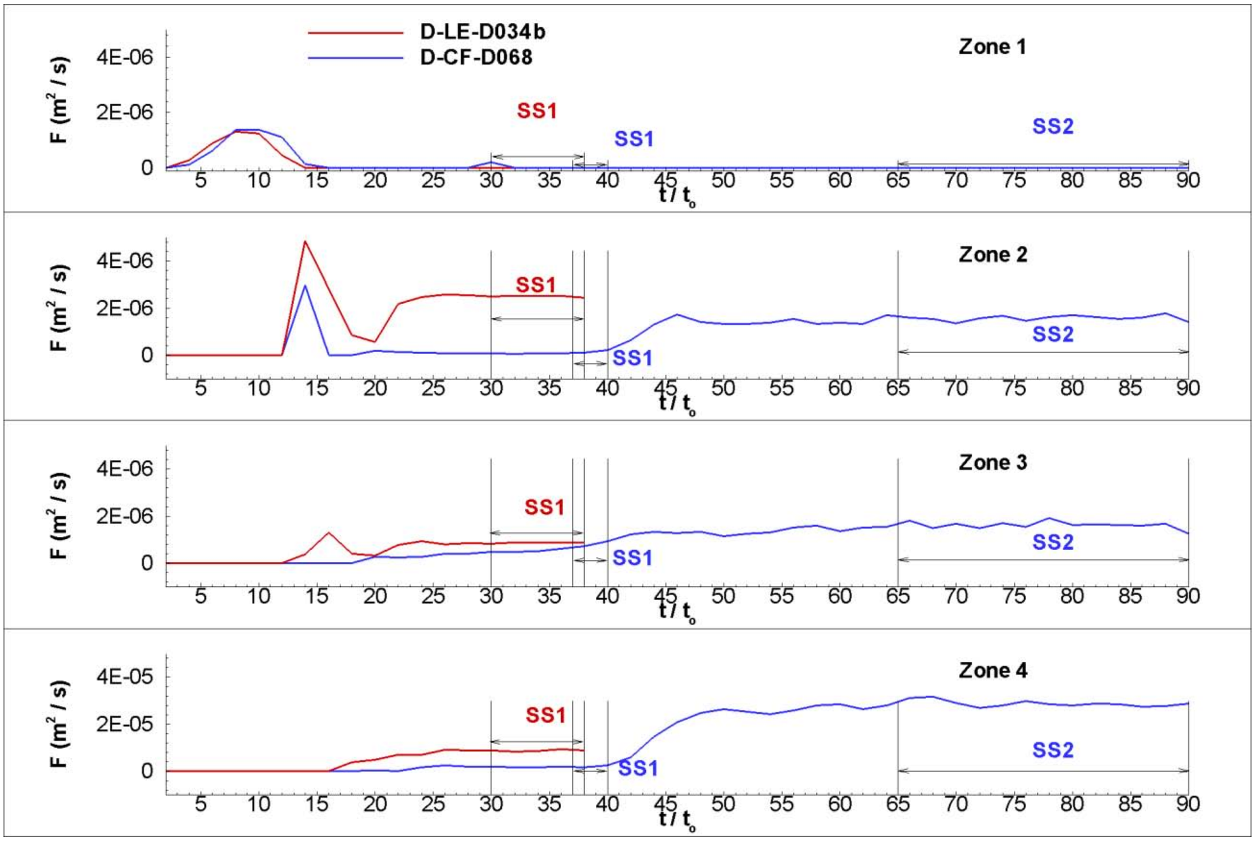

Figure 6.31 Comparison between the time variations of the flux of sediment particles of diameter *d=50μm* ($u_{\tau c}/u_b = 0.06$) entrained from a certain zone in the D-LE-D034b and D-CF-D068 simulations. The time scale is t_0=0.32 s. a) Zone 1; b) Zone 2; c) Zone 3; d) Zone 4.

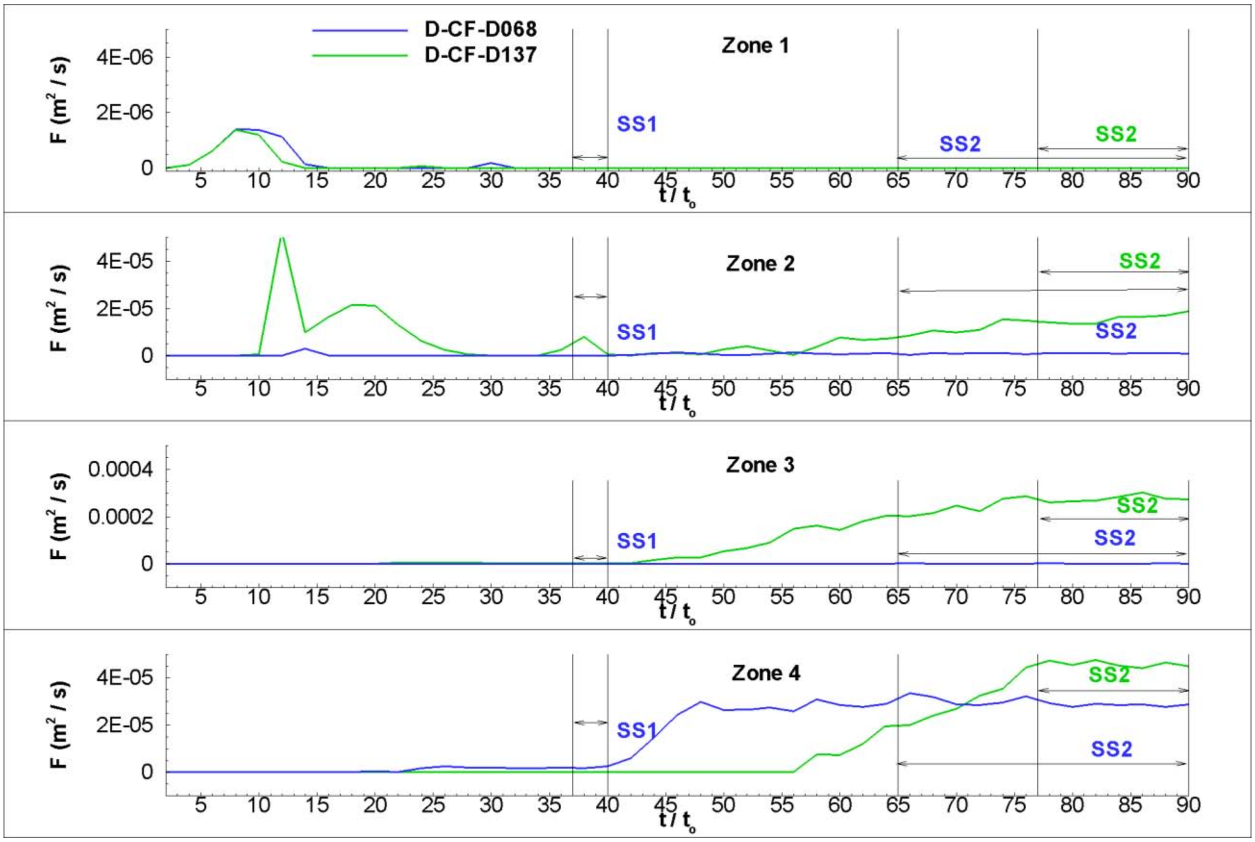

Figure 6.32 Comparison between the time variations of the flux of sediment particles of diameter *d=50μm* ($u_{\tau c} / u_b = 0.06$) entrained from a certain zone in the D-CF-D068 and D-CF-D137 simulations. The time scale is t_0=0.32 s. a) Zone 1; b) Zone 2; c) Zone 3; d) Zone 4.

CHAPTER 7 CONCLUSIONS AND FUTURE WORK

7.1 Conclusion

The present study provided a detailed investigation of the physics of high Reynolds number compositional Boussinesq gravity currents with large and small volume of release in lock-exchange configurations, and their dynamic effects on various obstacles (e.g., bedforms, flow retarding obstacles in the form of rectangular ribs, submerged dams of triangular shape that are used to control sediment deposition in reservoirs). The study focused on compositional gravity currents propagating over arrays of 2-D obstacles (roughness elements) and over isolated obstacles of triangular shape. The study mainly considered gravity currents in lock-exchange configurations in which the current is generated by the instantaneous removal of a vertical lock gate separating two fluids at rest and of different densities in a straight horizontal channel of rectangular section. The method of investigation was based on highly-resolved LES simulations performed using a non-dissipative Navier-Stokes solver in which the subgrid-scale terms are calculated dynamically. This allowed the study of gravity currents at Reynolds numbers that are high enough for the flow to be highly turbulent in the head and dissipative wake regions ($Re_f>10^4$ during the slumping phase). This is the case of interest in most environmental applications.

The study allowed understanding how the large-scale instabilities in the flow, interfacial billows and flow disturbances (e.g., forward and backward propagating hydraulic jumps, etc.) affect the evolution of the bottom propagating turbulent current and its capacity to entrain sediment when it propagates over a surface containing large-scale obstacles. The study of the propagation of high Reynolds number gravity currents over rough surfaces containing large-scale obstacles is of practical relevance for many applications in river, coastal and ocean engineering, where, in most cases, gravity currents propagate over loose surfaces containing bedforms (e.g., dunes).

The interaction of a gravity current with an array of retarding obstacles, whose main role is to decelerate the current, is another class of important civil engineering applications. This is because the propagation of a gravity current may be accompanied by disastrous damage. For example, arrays of obstacles are often used as protective measures on hilly terrains to stop or slow down gravity currents in the form of powder-snow avalanches before they reach populated areas. Similarly, defense structures such as baffle blocks are designed to slow down gravity currents in river environments or to stop the spreading of gravity currents containing pollutants or hazardous substances. The LES study allowed determining the characteristic times and magnitudes of the hydrodynamic impact forces over the different phases characterizing the impact of the current with the submerged obstacle and how the time histories of these forces vary with the rank of the obstacle in the series.

The result of the impact between a gravity current and a submarine structure (e.g., dam, barrier) can result in an environmentally hazardous situation. Evaluation of such scenarios is extremely important in environmental engineering applications. LES simulations of flow past triangular obstacles was used to obtain information on the flow structure upstream and downstream of the obstacle, the proportion of the flow convected over the structure, the variation of the flow regime as the gravity current is convected over the obstacle, the speed of the reflected hydraulic jump and its characteristics (e.g., sharp vs. undular), the depth of the reflected flow, the generation of intensified mixing vortices around the obstacle, and the temporal evolution of the forces and moments on the obstacle. In particular, LES allowed understanding how the time variation of the forces is related to the different flow structures that develop within the flow and the physical mechanisms behind the formation of such structures.

The simulations provided detailed information on the temporal evolutions of the front velocity, energy balance, sediment entrainment capacity and the flow instabilities, and of the distributions of the density, velocity, local dissipation rate and bed shear stresses at different stages of the propagation of the gravity current. Most of these quantities are very difficult to measure experimentally. The study allowed quantifying the effect of the shape and relative size of the obstacles, with respect to the current height, on the structure of the current, the energy balance, the bed shear distributions and sediment entrainment capacity of the current, and understanding, qualitatively and quantitatively, the differences with the simpler, but much more widely studied, case of a gravity current propagating over a flat smooth surface.

The LES simulations of gravity currents propagating past arrays of ribs and isolated triangular obstacles provided a straightforward way to estimate the characteristic times and magnitudes of the hydrodynamic impact forces on the obstacles. This information is crucial for the proper design of these structures and to develop strategies for controlling the interaction of the gravity current with the obstacles.

The main results and conclusions of the present study are summarized below:

1) In the case of gravity currents with a large volume of release (R<<1), the present study showed that currents propagating over an array of 2-D large-scale roughness elements reach, under certain conditions, a slumping phase in which the front velocity is approximately constant. The front velocity is smaller than the one reached by the same gravity current propagating over a flat surface (no obstacles) and is function of the size and relative degree of bluntness of the obstacles in the series (e.g., compared to flat bed case, the front velocity is smaller by 12% for dunes and by 24% for ribs of height D=0.15H and spacing λ=3H, where H is the channel depth and the current height is close to H/2). During this regime, the kinetic energy was found to increase in time proportional to $t^{1/3}$. This is different from the case of a gravity current with a high volume of release propagating over a flat bed during the slumping phase, in which a regime is reached where the variation of the kinetic and potential energies are linear. The condition that a slumping phase is present and lasts for a relatively long time, during which the front propagates over a large number of obstacles in the series, depends on the magnitude of the drag force per unit length induced by the presence of the obstacles. If the conditions are such that the slumping phase is present and lasts for a relatively long time, than the flow past the obstacles situated far

behind the front becomes quasi-steady, similar to the case of constant density flow over a series of identical obstacles.

2) The simulations of gravity currents with a high volume of release also showed that if the drag force per unit length increases due to an increase in the size of the obstacles or to a decrease in their spacing, then the slumping phase can be very short or not present. The simulations with obstacles showed that in contrast to the case of a current with a high volume of release propagating over a flat surface, for which the front velocity remains constant until the reflected disturbance reaches the front, the front velocity starts decaying with time due to the added drag force induced by the obstacles. A simulation conducted with densely-spaced ribs in a long channel showed that the current transitioned directly to a turbulent drag-dominated regime in which the front velocity decays proportional with t^{α}, with α~-0.28. Such a regime was previously shown to exist for gravity currents with a large volume of release propagating into a porous medium of uniform porosity, but not for the case in which the drag force acts only over the lower part of the bottom propagating current. The present study showed that, as a result of the spatial differences in the distribution of the drag force acting on the gravity current, the shape of the current propagating over bottom mounted obstacles (relatively horizontal interface until close to the head) is very different from the shape (interface with ambient fluid is straight and inclined with respect to the horizontal) observed for currents propagating into a porous medium, in which the drag force is relatively uniformly distributed over the whole height of the current. Due to these differences, one does not expect α to be the same for the two types of gravity currents. However, the LES simulation showed that after a certain time after the release of the lock gate, the flux of heavier fluid convected at the position of the gate becomes close to constant. This mean that the theoretical model proposed by Hatcher et al. (2000) to estimate the decay of the front velocity for high Reynolds number gravity currents propagating in a porous medium for the case in which the total volume of lock fluid increases linearly with time does apply. Indeed, the value of α predicted by LES (α=-0.28) was close to the one predicted by the theoretical model (α=-0.25). Simulation results also showed that, after the flux becomes constant

and the front velocity starts decaying with $t^{-0.28}$, the kinetic energy starts decaying linearly with time and with the front position. This is consistent with the current reaching a drag-dominated regime in which the front velocity decays continuously in time.

3) For gravity currents with a large volume of release for which the slumping phase lasts a long time, the structure of the flow in the head and dissipative wake was found to change dramatically as a result of the presence of large-scale roughness elements compared to the case the current propagates over a horizontal flat surface. A strong jet-like flow formed downstream the top or crest of each roughness element, a short time after the front started getting away from the obstacle. The flow became supercritical in the region of strong flow acceleration, in which the high-concentration fluid inside the jet-like flow plunges toward the lower regions of the bed, at least for the roughness elements situated close to the front. Significant changes were also observed over the tail region. The stably stratified tilted interface, depleted of large-scale eddies, which develops behind the dissipative wake in the flat bed simulations, was absent in the simulations with obstacles. Rather, a layer of varying height containing mixed fluid developed between the regions containing heavier fluid and lighter ambient fluid. The top of the layer of mixed fluid is close to horizontal at large distances behind the front. The bottom of this layer undergoes quasi-regular deformations with the same wavelength as that of the roughness elements.

4) For gravity currents with a large volume of release for which the slumping phase lasts for a long time, the flow past the obstacles situated at large distances behind the front becomes quasi-steady, similar to the widely studied case of constant density flow propagating over an array of identical 2D obstacles (e.g., dunes, ribs). The characteristics of the quasi-steady flow developing over these obstacles are important, as most of the sediment may be entrained from the bed beneath the tail region where the quasi-steady regime was reached. The non-dimensional distributions of the concentration, velocity magnitude and Reynolds stresses were found to be dependent on the shape of the roughness elements, but relatively independent of the Reynolds number. The largest amplification of the turbulence was observed in the shear layer region

forming on the outer part of the jet-like flow. The spatial distributions of the local dissipation rate in the simulations with obstacles showed that, in the later stages of the slumping phase, most of the dissipation takes places over the tail of the current. By contrast, in the flat bed simulations most of the dissipation occurred in the dissipative wake region.

5) The establishment of a quasi-steady flow past obstacles situated far behind the front allowed using the double-averaging technique to investigate the global changes in the flow and turbulence structure between the case of a bottom surface containing 2D obstacles of different shapes and the case when the bed surface is flat. For the flat bed cases, LES confirmed previous experimental results that showed that the turbulent kinetic energy (tke) peaks at the interface between the mixing layer and the heavier bottom propagating current, and that the position of the minimum value of the tke is also that of the maximum in the streamwise velocity. The high correlation between the regions of high tke and those of high streamwise velocity gradient showed that in the simulations with obstacles most of the turbulence production was due to shear. The presence of the obstacles induced significant differences in the 1-D profiles of the concentration, streamwise velocity and tke over the height of the heavier current. For example, compared to the flat bed case the overall amplification of the tke was close to five times as a result of the presence of roughness elements with a height of 0.15H. Most of this amplification was due to the formation of shear layers induced on both sides of the jet-like flow, which has no equivalent in the case the current propagates over a flat bed. Comparison of the 1-D profiles of the concentration, streamwise velocity and tke showed that Reynolds induced scale effects were much less significant in the simulations in which roughness elements were present at the bed.

6) The analysis of the temporal evolution of the drag force acting on the ribs showed that the important role played by the backward propagating hydraulic jumps. For example, in the simulations with a high volume of release the passage of the hydraulic jump originating at the first rib downstream of the one where the drag force is analyzed induced a reduction of up to 20% of the drag force acting on the rib. The peak values of ΔP at the end of the impact stage

decreased much faster with the rank of the rib in the simulations with a small volume of release compared to the simulations of gravity currents with a large volume of release.

7) After the formation of the tilted stably stratified interface, the distribution of the bed-friction velocity in the flat bed simulations with a high volume of release reached a maximum at the front of the current and then decayed smoothly over most of the tail region. By contrast, in the simulations in which obstacles were present at the bed, the largest values of u_τ were observed in the regions where the jet-like flow reattached to the bed surface and over the crest of the dunes. For obstacles situated at large distances behind the front, the distribution of u_τ between two consecutive roughness elements was found to be relatively independent of the rank of the obstacle.

8) In the case of gravity currents with a small volume of release (R=O(1)), the present study showed that currents propagating over large-scale roughness elements reach a turbulent drag-dominated regime in which the front velocity decays with time proportional to t^α, where $\alpha=-1/2$. This value is the same with the one predicted by theory (Hatcher et al., 2000) and measured experimentally in the case of gravity currents with a small volume of release propagating within a porous medium. One important observation is that the shape of the gravity current with a small volume of release propagating over obstacles is qualitatively similar to that observed in experiments conducted in porous media, thus the good agreement for α is expected. The fact that even in an LES simulation in which the ratio between the height of the ribs and the current height was quite low, the current reached the drag dominated regime in which $\alpha=-1/2$, shows that gravity currents propagating in an environment containing obstacles that induce a significant drag force on the current have a similar evolution to that of gravity currents propagating into a porous medium of uniform porosity.

9) Analysis of the energy balance in the simulations of gravity currents with a small volume of release propagating over a flat bed and over a series of obstacles showed that the variations of the total kinetic energy, total potential energy, and the integral of the total dissipation rate with the front position are logarithmic after the end of the transition to the buoyancy-inertia phase.

10) The LES simulations conducted at Re=10^6 helped to better understand the physics of finite-volume lock-release currents and their interactions with obstacles for flow conditions that are closer to the inviscid state that is often assumed in theoretical models, and to conditions encountered in practical applications in rivers, lakes and oceans. In particular, the increase of the Reynolds number from Re=48,000 to Re=10^6 in the flat bed simulations with a large and with a small volume of release resulted in a large decay of the overall levels of u_τ. However, the two distributions remained qualitatively similar. For example, the ratio between the bed friction velocity in the flat bed simulations with a large volume of release was close to 0.58 over the whole length of the current. More important, simulation results showed the same ratio can be used to successfully scale the low and high Reynolds number simulations in which ribs or dunes were present at the channel bottom. This means that the shape of the bed shear stress distributions is basically independent of the Reynolds number at Reynolds numbers that are high enough for the flow at the head of the current to be strongly turbulent. This means laboratory experiments and simulations performed at lower Reynolds numbers (around 10,000) can provide valuable information that is needed used to understand the capacity of a gravity current to entrain sediment at field conditions. This is in contrast to the case when the evolution of high Reynolds number currents is compared to that observed for currents at Re around 1,000 (e.g., see discussion in Ooi et al., 2009). In this case, the Reynolds number is too low for the flow to be strongly turbulent even in the head region and the growth of the 3D instabilities is much slower. As a result the break up of the KH billows is also very slow and the structure of the current is very different than the one observed for Re>10,000.

11) The simulation results showed that, independently of the volume of release, gravity currents propagating over dunes have a much larger capacity to entrain particles with a relatively high critical friction velocity (of about 50% of the average bed friction velocity induced by the current during the slumping phase) than gravity currents propagating over ribs of same height and same spacing or gravity currents propagating over a flat bed.

12) In the case of gravity current – submerged dam interaction, the temporal evolution of the drag force showed that during the transient stage the drag force was, at most, 10-15% larger than the values recorded during the type I and type II quasi-steady state regimes. The momentum equation was then used to predict the drag force, including its two components on the upstream and downstream faces of the dam, during first quasi-steady state and second quasi-steady state based on the predictions of the main flow parameters by the analytical models. During first quasi-steady state, ΔP was underpredicted in all the cases by 0-25% by the analytical model. The largest contribution to the error in the prediction of ΔP was due to an underestimation of pressure force on the upstream face of the dam by the analytical model. Thus, for first quasi-steady state one recommends using 1.3ΔP for design purposes, assuming the maximum value of ΔP during the transient toward first quasi-steady state regime is smaller or equal than the quasi-steady-state value.

13) Results from LES simulations can be used to insure the force acting on the obstacle (submerged dam) does not dislocate the structure, to estimate the amount of sediment entrained over the faces of the obstacle and around it due to the passage of the current, and to identify regions of high bed friction velocity where local scour can develop. Based on this information one can decide the extent of the regions over which scour protection should be applied (e.g., rip rap, etc.).

7.2 Future Work

The present investigation of gravity currents propagating over isolated or arrays of obstacles have proved that high-resolution LES can be successfully used to investigate the fundamental flow physics and to predict quantities that are very difficult or impossible to determine experimentally. The model can be further enhanced to allow the study of other applications of fundamental or applied nature related to gravity current flows.

- Perform a more detailed parametric study of the effects of the size, shape and wavelength of the roughness elements, the Schmidt number and the Reynolds number on the physics and main integral parameters characterizing the propagation of gravity currents over rough surfaces.
- Study gravity currents propagating on surfaces of constant or variable slope, with or without arrays of roughness elements. This is important especially for the case of gravity currents with a small volume of release. The evolution of the gravity current may change significantly as a result of the acceleration/deceleration of the flow propagating over a sloped surface.
- Study the case of gravity currents propagating at the bottom of a turbulent channel flow. Consider the case of a flat bed and the case in which bed forms or obstacles are present. This problem is more complex and adds several new parameters that can influence the evolution of the gravity current propagating over flat or rough surfaces (e.g., the ratio between the mean channel velocity and the buoyancy velocity, the shape of the mean velocity profile in the channel, the turbulence intensity of the channel flow).
- Study gravity currents propagating in a porous medium (e.g., array of rigid cylinders). Investigate the changes in the structure of the current as a result of changes in the porosity, arrangement of the cylinders and the Reynolds number. The Reynolds number plays a more important role in the case of gravity currents propagating in a porous medium because the drag coefficient on an individual cylinder can vary significantly with the cylinder Reynolds number. The spacing between the cylinders is another important parameter, as the drag coefficient can vary significantly in the case when the wake created by a cylinder modifies significantly the flow past the downstream cylinders. The numerical simulations have the advantage of providing the time history of the forces on the individual cylinders at all stages of the propagation of the gravity current. This information can be used to obtain a better parametrization of the drag terms in the turbulence models used to model vegetated flows.
- Study gravity currents propagating in a channel containing a layer of higher porosity close to the bed. This case is particularly relevant for gravity currents propagating over a

submerged layer of vegetation (e.g., canopy of aquatic plants). Investigate the changes in the structure of the gravity current function of the ratio between the thickness of the vegetation layer and the thickness of the channel.

- Study evolution of particulate (turbidity) currents containing a uniform or a non-uniform sediment size distribution. Study dynamics of turbidity currents induced by the passage of a compositional gravity current over a loose bed (quantification of the amount of sediment entrained and carried each time a lock facility is operated is one of the main applications of practical concern in river engineering).
- Study non-Boussinesq gravity currents in which the density differences between the lock and the ambient fluid may be important. Especially at flood conditions, the differences between the concentration of a turbidity current and that of the water in the river or estuary can be substantially higher than the threshold value above which the use of the Boussinesq approximation is not acceptable.

REFERENCES

1. Alexander, J. and Morris, S., (1994), “Observations on experimental, nonchannelized, high-concentration turbidity currents and variations in deposits around obstacles”, Journal of Sedimentary Research, Vol. A64A, Issue 4, 899-909.

2. Baas, J.H., McCaffrey, W.D., Haughton P.D.W., and Choux, C., (2005), “Coupling between suspended sediment distribution and turbulence structure in a laboratory turbidity current”, Journal of Geophysical Research, Vol. 110.

3. Baines, P., (2004), “Topograpic effects in stratified flows”, Cambridge Monographs on Mechanics, Cambridge University Press.

4. Benjamin, T.B., (1968), “Gravity currents and related phenomena”, Journal of Fluid Mechanics, Vol. 31, 209-248.

5. Birman, V.K., Martin, J.E., and Meiburg, E., (2005), “The non-Boussinesq lock-exchange problem. Part 2. High-resolution simulations”, Journal of Fluid Mechanics, Vol. 537, 125-144.

6. Blanchette, F., Strauss, M., Meiburg, E., Kneller, B., and Glinsky, M.E., (2005), “High-resolution numerical simulation of resuspending gravity currents: Conditions for self-sustainment”, Journal of Geophysical Research, Vol. 110.

7. Blanchette, F., Piche, V., Meiburg, E., and Strauss, M., (2006), “Evaluation of a simplified approach for simulating gravity currents over slopes of varying angles”, Computers and Fluids, Vol. 35, 492-500.

8. Bonnecaze, R.T., Huppert, E.H., and Lister, J.R., (1993), “Particle-driven gravity currents”, Journal of Fluid Mechanics, Vol. 250, 339-369.

9. Bournet, P.E., Dartus, D., Tassin, B., and Vincon-Leite, B., (1999), “Numerical investigation of plunging density current”, Journal of Hydraulic Engineering, Issue 6, 584-594.

10. Britter, R.E and Simpson, J.E., (1978), “Experiments on dynamics of a gravity current head”, Journal of Fluid Mechanics, Vol. 88, 223-240.

11. Bursik, M.I. and Woods, A.W., (2000), “The effects of topography on sedimentation from particle-laden turbulent density currents”, Journal of Sedimentary Research, Vol. 70, Issue 1, 53-63.

12. Cantero, M.I., Balachandar, S., and Garcia, M.H., (2006), “Direct numerical simulations of planar and cylindrical density currents”, Journal of Applied Mechanics, Vol. 73, Issue 6, 923-930.

13. Cantero, M.I., Lee, J.R., Balachandar, S., and Garcia, M.H., (2007), “On the front velocity of gravity currents”, Journal of Fluid Mechanics, Vol. 586, 1-39.

14. Chang, K.S., Constantinescu, G., and Park, S.O., (2006), “Analysis of the flow and mass transfer processes for the incompressible flow past an open cavity with a laminar and a fully turbulent incoming boundary layer”, Journal of Fluid Mechanics, Vol. 561, 113-145.

15. Chang, K.S., Constantinescu, G., and Park, S.O., (2007), “The purging of a neutrally buoyant or a dense miscible contaminant from a rectangular cavity. Part II: The case of an incoming fully turbulent overflow”, Journal of Hydraulics Engineering, Vol. 133, Issue 4, 373-385.

16. Chen, G. and Lee, J.H.W., (2001), “Turbulent lock release gravity current”, Science in China (Series E), Vol. 44, Issue 5, 449-462.

17. Choi, S.U. and Garcia, M., (1995), “Modeling of one-dimensional turbidity currents with a dissipative-Galerkin Finite element method”, Journal of Hydraulic Research, Vol. 33, Issue 5, 623-648.

18. Choi, S.U. and Garcia, M.H., (2002), “k-ε Turbulence modelling of density currents developing two dimensionally on a slope”, Journal of Hydraulics Engineering, Vol. 128, Issue 1, 55-63.

19. Cui, J., Patel, V.C., and Lin, C.L., (2000), “Large eddy simulation of turbulent flow over rough surfaces”, IIHR-Technical Report, No. 413, Iowa City, IA.

20. Cui, J., Patel, V.C., and Lin, C.L., (2003), “Large eddy simulation of turbulent flow in a channel with rib roughness”, International Journal of Heat and Fluid Flow, Vol. 24, 372-388.

21. Djenidi, L., Elavarasan, R., and Antonia, R. A., (1999), “The turbulent boundary layer over transverse square cavities”, Journal of Fluid Mechanics, Vol. 395, 271–294.

22. Edwards, D.A., (1993), “Turbidity Currents: Dynamics, Deposits and Reversals”, Springer-Verlag, Berlin, pp. 173.

23. Ellison, T.H. and Turner, J.S., (1959), “Turbulent entrainment in stratified flows”, Journal of Fluid Mechanics, Vol. 6, Issue 3, 423-448.

24. Ermanyuk, E.V. and Gavrilov, N.V., (2005), “Interaction of an internal gravity current with a submerged circular cylinder”, Journal of Applied Mechanics and Technical Physics, Vol. 46, Issue 2, 216–223.

25. Ermanyuk, E.V. and Gavrilov, N.V., (2005), “Interaction of an internal gravity current with an obstacle on the channel bottom”, Journal of Applied Mechanics and Technical Physics, Vol. 46, Issue 4, 489–495.

26. Farmer, D.M., and Armi, L., (1986), “Maximal two-layer exchange over a sill and through the combination of a sill and contraction with barotropic flow”, Journal of Fluid Mechanics, Vol. 164, 53–76.

27. Fannelop, T.K., (1994), “Fluid Mechanics for Industrial Safety and Environmental Protection”, Elsevier.

28. Fannelop, T.K. and Waldman, G.D., (1972), "Dynamics of oil slicks", AIAA Journal, Vol. 10, 506-510.

29. Faust, K.M. and Plate, E.J., (1984), "Experimental investigation of intrusive gravity currents entering stably stratified fluids", Journal of Hydraulic Research, Vol. 22, 315-323.

30. Garcia, M. and Parker, G., (1993), "Experiments on the entrainment of sediment into suspension by a dense bottom current", Journal of Geophysical Research, Vol. 98 (C3)

31. Germano, M., Piomelli, U., Moin, P., and Cabot, W. H., (1991), "A dynamic subgrid-scale eddy viscosity model", Physics of Fluids, Vol. 31(7), 1760–1765.

32. Gonzalez-Juez, E. and Meiburg, E., (2009), "Shallow water analysis of gravity current flows past isolated obstacles", Journal of Fluid Mechanics, in press.

33. Gonzalez-Juez, E., Meiburg, E., and Constantinescu, G.S., (2009a), "Gravity currents impinging on bottom mounted square cylinders: Flow fields and associated forces", Journal of Fluid Mechanics, Vol. 631, 65-102.

34. Gonzalez-Juez, E., Meiburg, E., and Constantinescu, G.S., (2009b), "The interaction of gravity current with a circular cylinder mounted above a wall: Effect of the gap size", Journal of Fluids and Structures, Vol. 25, 629-640.

35. Gonzalez-Juez, E., Meiburg, E., T. Tokyay and Constantinescu, G.S. (2009c), "Gravity current flow past a circular cylinder: Forces and wall shear stresses", submitted to Journal of Fluid Mechanics.

36. Gray, T.E., Alexander, J., and Leeder, M.R., (2006), "Quantifying velocity and turbulence structure in depositing sustained turbidity currents across breaks in slope", Sedimentology, Vol. 52, 467-488.

37. Greenspan, H.P. and Young, R.E., (1978), "Flow over a containment dyke", Journal of Fluid Mechanics, Vol. 87, Page Numbers.

38. Grobelbauer, H.P., Fannelop, T.K., and Britter, R.E., (1993), "The propagation of intrusion fronts of high density ratios", Journal of Fluid Mechanics, Vol. 250, Page Number.

39. Hacker, J., Linden, P.F., and Dalziel, S.B., (1996), "Mixing in lock-release gravity currents", Dynamics of Atmospheres and Oceans, Vol. 24, 183-195.

40. Hallez, Y., and Magnaudet, J., (2008), "Effects of channel geometry on buoyancy-driven mixing", Physics of Fluids, Vol. 20.

41. Hallworth, M.A., Hogg, A.J., and Huppert, H.E., (1998), "Effects of external flow on compositional and particle gravity currents", Journal of Fluid Mechanics, Vol. 359, 109-142.

42. Hartel, C., Carlsson, F., and Thunblom, M., (2000a), "Analysis and direct numerical simulation of the flow at a gravity-current head. Part 2. The lobe-and-cleft instability", Journal of Fluid Mechanics, Vol. 418, 213–229.

43. Hartel, C., Meiburg, E, and Necker, F., (2000b), “Analysis and direct numerical simulation of the flow at a gravity-current head. Part 1. Flow topology and front speed for slip and no-slip boundaries”, Journal of Fluid Mechanics, Vol. 418, 189–212.

44. Hatcher, L., Hogg, A.J., Woods, A.W., (2000), “The effects of drag on turbulent gravity currents”, Journal of Fluid Mechanics, Vol. 416, 297-314.

45. Hopfinger, E. J., (1983), “Snow avalanche motion and related phenomena”, Annual Review of Fluid Mechanics, Vol.15, 47–76.

46. Hoult, D.P., (1972), “Oil spreading on the sea”, Annual Review of Fluid Mechanics, Vol. 4, 341-368.

47. Huang, H., Imran, J., and Pirmez, C., (2005), “Numerical model of turbidity currents with a deforming bottom boundary”, Journal of Hydraulic Engineering, Issue 4, 283-293.

48. Huang, H., Imran, J., and Pirmez, C., (2007), “Numerical modeling of poorly sorted depositional turbidity currents”, Journal of Geophysical Research, Vol. 112, 1–15.

49. Huppert, H.E., (1982), “The propagation of two-dimensional and axisymmetric viscous gravity currents over a rigid horizontal surface”, Journal of Fluid Mechanics, Vol. 121, 43-58.

50. Huppert, H., and Simpson, J.E., (1980), “The slumping of gravity currents”, Journal of Fluid Mechanics, Vol. 99, 785–799.

51. Jacobsen, O., and Magnussen, B.F., (1987), “3-D numerical simulation of heavy gas dispersion”, Journal of Hazardous Materials, Vol. 16, 215-230.

52. Jamali, M., Zhang, X., Nepf, H.M., (2008), “Exchange flow between canopy and open water”, Journal of Fluid Mechanics, Vol.611, 237-254.

53. Johannesson, T., Lied, K., Margreth, S., and Sanderson, F., (1996), “An overview of the need for avalanche protection measures in Iceland”, Report prepared for the Icelandic Ministry for the Environment and local authorities in towns threatened by avalanches. Reykjavik.

54. Kassem, A., and Imran, J., (2004), “Three-dimensional modeling of density current. II. Flow in sinuous confined and unconfined channels”, Journal of Hydraulics Research, Vol. 42, Issue 6, 591-602.

55. Keller, J.J., and Chyou, Y.P., (1991), “On the hydraulic lock-exchange problem” Journal of Applied Mathematics and Physics, Vol. 42, 874-910.

56. Klemp, J.B., Rotunno, R., and Skamarock, W.C., (1994), “On the dynamics of gravity currents in a channel”, Journal of Fluid Mechanics, Vol. 269, 169-198.

57. Kneller, B.C., Edwards, D.A., McCaffrey, W.D., and Moore, R.M., (1991), “Oblique reflection of turbidity currents”, Geology, Vol. 19, 250-252.

58. Kneller, B., Bennett, S.J., and McCaffrey, W.D. (1999), “Velocity structure, turbulence and fluid stresses in experimental gravity currents”, Journal of Geophysical Research-Ocean, Vol. 104 (C3), 5381–5391.

59. Keulegan, G.H., (1957). “An experimental study of the motion of saline water from locks into fresh water channels” U.S. Natl. Bur. Stand. Rep. 5168.

60. Lane-Serff, G.F., Beal, L.M., and Hadfield, T.D., (1995), “Gravity current flow over obstacles”, Journal of Fluid Mechanics, Vol. 292, 39–53.

61. Linden, P.F. and Simpson, J.E., (1986), “Gravity driven flows in a turbulent fluid”, Journal of Fluid Mechanics, Vol. 172, 481-497.

62. Lowe, R.J., Rottman, J.W., and Linden, P.F., (2005), “The non-Boussinesq lock-exchange problem. Part 1. Theory and experiments”, Journal of Fluid Mechanics, Vol. 537, 101–124.

63. Maxworthy, T., Leilich, J., Simpson, J.E., and Meiburg, H.E., (2002), “The propagation of a gravity current into a linearly stratified fluid”, Journal of Fluid Mechanics, Vol. 453, 371-394.

64. McElwaine, J. and Patterson, M., (2004), “Lobe and cleft formation at the head of a gravity current”, Proceedings of XXI International Congress of Theoretical and Applied Mechanics.

65. Mierlo, M.C. and de Ruiter, J.C., (1988). “Turbulence measurements over artificial dunes”, Report Q789. Delft Hydraulics Laboratory, Delft, Netherlands.

66. Necker, F., Hartel, C., Kleiser, L., and Meiburg, E., (2002), “High-resolution simulations of particle-driven gravity currents”, International Journal of Multiphase Flow, Vol. 28, 279-300.

67. Necker, F., Hartel, C., Kleiser, L., and Meiburg, E., (2005), “Mixing and dissipation in particle-driven gravity currents”, Journal of Fluid Mechanics, Vol. 545, 339-372.

68. Nikora, V., Koll, K., McEwan, I., McLean, S., and Dittrich, A., (2004), “Velocity distribution in roughness layer of rough-bed flows”, Journal of Hydraulic Engineering, Vol.130, 1036-1042.

69. Nikora, V., Goring, D., McEwan, I., and Griffiths, G., (2001), “Spatially averaged open-channel flow over rough bed”, Journal of Hydraulic Engineering, Vol. 127, 123-133.

70. Oehy, C.D., (2003), “Effects of obstacles and jets on reservoir sedimentation due to turbidity currents”, Ph.D. Thesis, Ecole Polytechnique Federale de Lausanne.

71. Oehy, C.D. and Schleiss, A.J., (2007), “Control of turbidity currents in reservoirs by solid and permeable obstacles”, Journal of Hydraulic. Engineering, Vol. 133, 637–648.

72. Ooi, S.K., Constantinescu, S.G., and Weber, L. (2009), “Numerical simulations of lock exchange compositional gravity currents”, Journal of Fluid Mechanics, Vol. 635, 361-388.

73. Ooi, S.K., Constantinescu, S.G., and Weber, L. (2007a), “A numerical study of intrusive compositional gravity currents”, Physics of Fluids Vol.19.

74. Ooi, S.K., Constantinescu, S.G., and Weber, L. (2007b), “Two-dimensional large-eddy simulation of lock-exchange gravity current flows at high Grashof numbers”, Journal of Hydraulic Engineering, Vol. 9, 1037–1047.

75. Ozgokmen, T.M., Fischer, P.F., Duan, J., and Iliescu, T., (2004), “Entrainment in bottom gravity currents over compex topography from three-dimensional non-hydrostatic simulations”, Geophysical Research Letters, Vol. 31.

76. Parker, G., Garcia, M.H., Fukushima, Y., and Yu W., (1987), “Experiments on turbidity currents over an erodible bed”, Journal of Hydrological Research, Vol. 25, 191–244.

77. Parsons, J., and Garcia, M., (1998), “Similarity of gravity current fronts”, Physics of Fluids, Vol. 10, Issue 12, 3209–3213.

78. Patin, H.M and Leeder, M.R., (1987), “Reverse flow in turbidity currents: role of internal solitons”, Sedimentology, Vol. 34, 1143-1156.

79. Patterson, M.D., Simpson, J.E., and Dalziel, S.B., (2006), “Vortical motion in the head of an axisymmetric gravity current”, Physics of Fluids, Vol. 18.

80. Pierce, C.D., (2001), “Progress-variable approach for large eddy simulation of turbulent combustion”, PhD thesis, Stanford University.

81. Pierce, C.D. and Moin, P., (2004), “Progress-variable approach for large-eddy simulation of nonpremixed turbulent combustion”, Journal of Fluid Mechanics, Vol. 504, 73–97.

82. Rottman, J.W. and Simpson, J.E., (1983), “Gravity currents produced by instantaneous releases of a heavy fluid in a rectangular channel”, Journal Fluid Mechanics, Vol. 135, 95–110.

83. Rottman, J.W., Simpson, J.E., Hunt, J.C.R., and Britter, R.E., (1985), “Unsteady gravity current flows over obstacles: Some observations and analysis related to the phase II trials”, Journal of Hazardous Materials, Vol. 11, 325–340.

84. Sequeiros, E. O., Naruse, H., Endo, N., Garcia, H.M., and Parker, G., (2009), “Experimental study on self-accelerating turbidity current”, Journal of Geophysical Research-Oceans, Vol. 114.

85. Shin, J., Dalziel, S., and Linden, P.F., (2004), “Gravity currents produced by lock exchange”, Journal of Fluid Mechanics, Vol. 521, 1-34.

86. Simpson J.E., (1997), “Gravity currents in the environment and the laboratory”, 2nd Edition, Cambridge University Press.

87. Simpson, J.E., (1972), “Effects of the lower boundary on the head of a gravity current”, Journal of Fluid Mechanics, Vol. 53, Issue 4, 759–768.

88. Simpson, J.E. and Britter, R.E., (1979), “The dynamics of the head of a gravity current advancing over a horizontal surface”, Journal of Fluid Mechanics, Vol. 94, Issue 3, 477-495.

89. Stacey, M.W. and Bowen, A.J., (1988), “The vertical structure of turbidity currents and a necessary condition for self-maintenance”, Journal of Geophysical Research, 94(C4), 3543-3553.

90. Stoesser, T., Braun, C., Garcia-Villalba, M., and Rodi, W., (2008), “Turbulence structure in flow over two-dimensional dunes”, Journal of Hydraulic Engineering, Issue 1, 42-55.

91. Sutherland, B., Kyba, P.J., and Flynn, M.R., (2004), “Intrusive gravity currents in two-layer fluids”, Journal of Fluid Mechanics, Vol. 514, 327-353.

92. Tanino, Y., Nepf, H.M., and Kulis, P.S., (2005), “Gravity currents in aquatic canopies”, Water Resources Research, Vol. 41.

93. Turner, J., (1986), “Turbulent entrainment: the development of the entrainment assumption, and its application to geophysical flows”, Journal of Fluid Mechanics, Vol. 173, 431–471.

94. Van Rijn, L.C., (1984). “Sediment pick-up functions”, Journal of Hydraulics Engineering, Vol. 110, Issue 10, 1494-1503.

95. Von Karman, T., (1940), “The engineer grapples with nonlinear problems”, Bulletin of American Mathematical Society, Vol. 46, 615–683.

96. Yoon, J.Y. and Patel, V.C., (1996), “Numerical model of turbulent flow over sand dune”, Journal of Hydraulic Engineering, Issue 1, 10-18.